The mechanical and physical properties of volcanic rocks: application to volcanic hazards and building conservation

Michael HEAP
Habilitation à diriger des recherches

Institut de Physique de Globe de Strasbourg
UMR 7516 CNRS, Université de Strasbourg/EOST
5 rue René Descartes
67084 Strasbourg cedex
FRANCE

21st June 2018

Committee

Yves GUÉGUEN
Benjamin VAN WYK DE VRIES
Beatriz MENÉNDEZ
Mai-Linh DOAN
Jean-Luc GOT
and Patrick BAUD

Table of contents

Acknowledgements

1. Introduction

2. The mechanical behaviour of volcanic rocks

3. The permeability of volcanic rocks

4. The use of volcanic rocks in construction

5. Some perspectives for future work

Acknowledgements

CHAPTER ONE – Introduction

1.1 The mechanical behaviour of porous rocks

Our understanding as to how porous rocks deform has increased significantly over the last thirty years. This understanding began with porous sandstones (e.g., see early studies by Menéndez et al., 1996; Wong et al., 1997) and has more recently moved towards porous limestones (e.g., Vajdova et al., 2004, Baud et al., 2009; Vajdova et al., 2010; Zhu et al., 2010; Vajdova et al., 2012; Baud et al., 2017a). These studies, and many others, have shown that porosity is one of the main factors that controls the mechanical behaviour and failure mode of rocks. High-porosity rocks are typically characterised by lower brittle strengths and transition to ductile behaviour at lower pressures than low-porosity rocks (Wong and Baud, 2012). Studies that investigate the mechanical behaviour and failure mode of porous rocks typically perform suites of triaxial deformation experiments that are conducted over a range of effective pressures (often simply defined as the confining pressure minus the pore fluid pressure). Examples of such experiments on a porous sandstone (Bentheim sandstone; data from Baud et al., 2006) and a porous limestone (Tavel limestone; data from Vajdova et al., 2004) are shown in Figure 1.
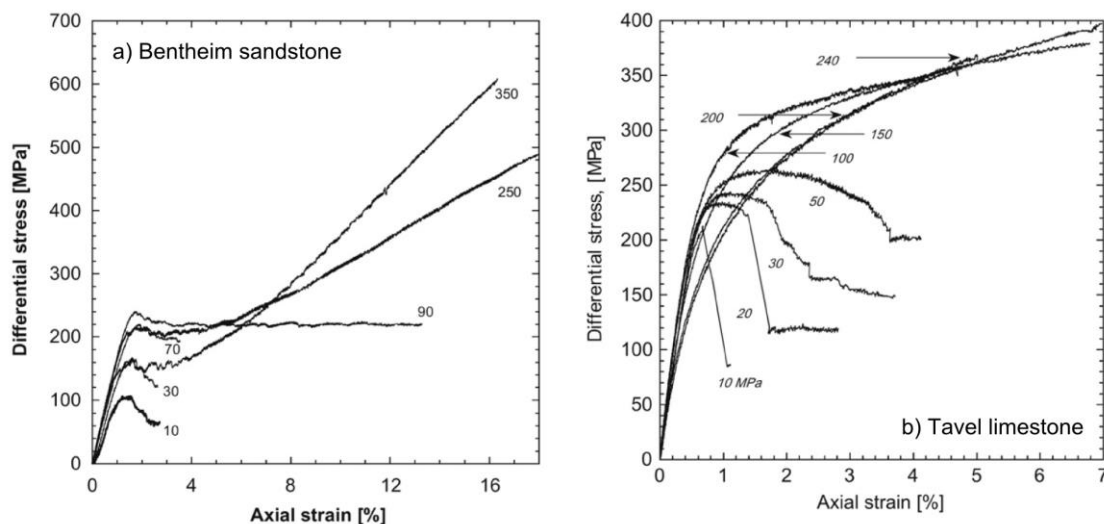

Figure 1. Stress-strain curves for triaxial experiments performed on (a) Bentheim sandstone (Baud et al., 2006) and (b) Tavel limestone (Vajdova et al., 2004). The numbers next to the curves corresponds to the effective pressure.

It can be seen from the experiments in Figure 1 that the mechanical behaviour changes as the effective pressure is increased (the number next to each of the curves). Brittle experiments are characterised by a peak stress followed by a phase of strain softening (a stress drop). In the example of Figure 1a, Bentheim sandstone was brittle at effective pressures up to 70 MPa. In the brittle regime, an increase in effective pressure results in an increase in peak stress – the strength of Bentheim sandstone was increased from about 100 MPa at an effective pressure of 10 MPa up to about 200 MPa at an effective pressure of 70 MPa (Figure 1a). Failure under brittle conditions either leads to axial splitting (in the case of very low pressures) or the formation of a shear fracture (e.g., Paterson and Wong, 2005). Brittle failure is typically associated with increases in porosity (e.g., Read et al., 1995), a result of the formation, growth, and coalescence of microcracks (e.g., Lockner et al., 1991).

Ductile experiments, on the other hand, are characterised by the absence of strain softening (i.e. there is no stress drop) and sometimes, in the case of the experiments shown in Figure 1, strain hardening. Bentheim sandstone, for example, was ductile at effective pressures above 90 MPa (strain hardening was only observed at effective pressures of 250 and 350 MPa; Figure 1a). Deformation in the ductile regime is associated with decreases in porosity (e.g., Wong and Baud, 2012). Failure under ductile conditions can manifest in one of two ways. First, deformation can be distributed and the sample "flows". The micromechanism responsible for this behaviour is cataclastic flow (i.e. microcracking) and grain crushing in sandstones (e.g., Menéndez et al., 1996; Wong et al., 1997;) and cataclastic pore collapse in limestones (e.g., Vajdova et al., 2004; Zhu et al., 2010; Vajdova et al., 2010). Second, the deformation can be localised into compaction bands. Compaction bands are planes of lower porosity than the surrounding host rock and, in porous sandstone, are typically a few grains in thickness (0.5-1.5 mm) (Figure 2) (e.g., Baud et al., 2006; Fortin et al., 2006; Stanchits et al., 2009). Compaction bands have also been documented in porous limestones (e.g., Baud et al., 2009; Cilona et al., 2014; Baud et al., 2017b). The occurrence of compaction localisation in sandstones is thought to be related to the initial grain size distribution: sandstones with a wide grain size distribution will deform via cataclastic flow and compaction in sandstones with a narrow grain size distribution will manifest as compaction bands (Cheung et al., 2012). Compaction localisation in limestones is also thought to depend on rock heterogeneity (e.g., Cilona et al., 2014)
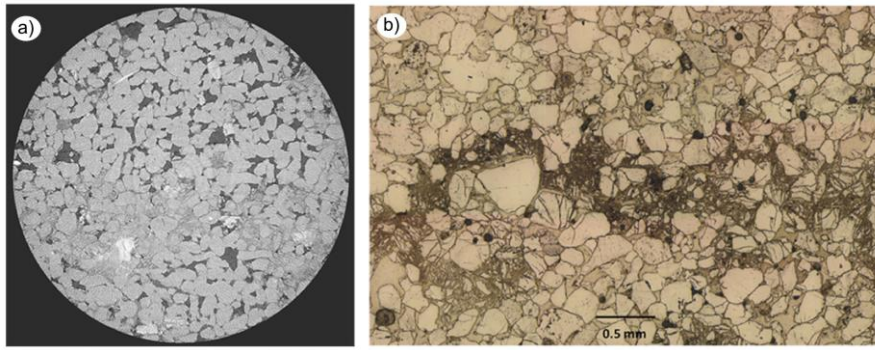
Figure 2. Images of compaction bands in Bentheim sandstone. (a) X-ray computed tomographic image of a compaction band in a sample of Bentheim sandstone (sample is 20 mm in diameter). (b) Thin section photomicrograph of a compaction band in a sample of Bentheim sandstone.

Triaxial deformation data at different effective pressures permit the construction of failure envelopes that can be summarised graphically as differential stress (Q) versus effective mean stress (P). Graphs of this type provide insight on the mechanical behaviour and failure modes of materials, and provide a useful way to compare rocks with different properties and/or different rock types (e.g., Wong and Baud, 2012).
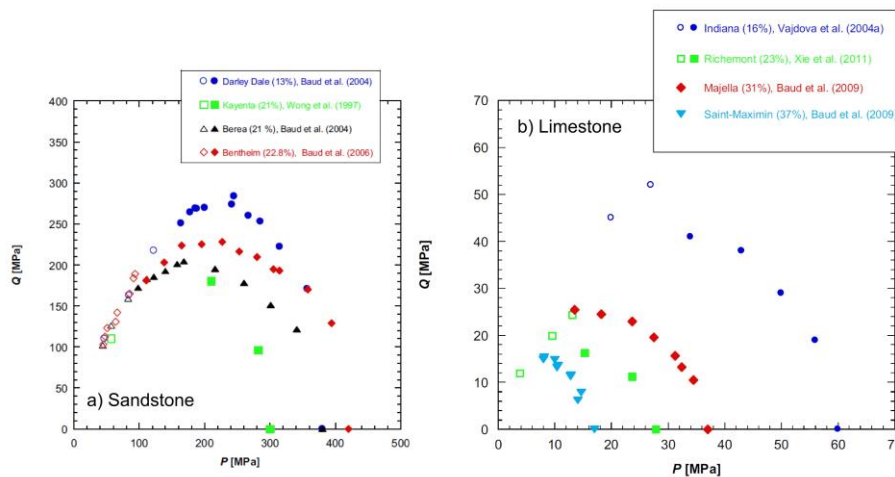
Figure 3. Failure envelopes for porous sandstones (a) and porous limestones (b). Figures taken from Wong and Baud (2012).

The peak differential stress delineates the brittle failure envelope, while the differential stress at the onset of shear-enhanced compaction (C^*) constrains the ductile yield cap (Wong et al., 1997; Wong and Baud, 2012 and references therein). Therefore, a sample would be pre-failure if the stress state plots inside the failure envelope. If the state of stress plots the rock outside the failure envelope on the left hand side, the rock will fail in a brittle manner (shear fracture). By

contrast, the rock will suffer a ductile mode of failure (cataclastic pore collapse or compaction bands) if it plots outside the failure envelope on the right hand side. Examples of failure envelopes for sandstones and limestones with different porosities are shown in Figure 3 (from Wong and Baud, 2012 and references therein). The onset of inelastic deformation at $Q = 0$ marks the effective mean stress capable of crushing grains and/or pores and is termed P* (e.g., Zhang et al., 1990).

The sheer number of experiments on sedimentary rocks has resulted in a deep understanding. For example, experimental studies have shown that the mechanical behaviour and failure mode of sedimentary rock depends on the grain size (e.g., Zhang et al., 1990; Baud et al., 2006; Wong and Baud, 2012), the grain size distribution (e.g., Cheung et al., 2012), clay content, cementation, and bedding (e.g., David et al., 1998; Baud et al., 2006; Tembe et al., 2008; Wong and Baud, 2012; Baud et al., 2017a), pore size (e.g., Ashby and Sammis, 1990; Wong and Baud, 2012), the dual nature of the porosity (e.g., Zhu et al., 2010), and the presence of water (e.g., Baud et al., 2000), amongst others. However, while sedimentary rocks are well characterised, much less is known about the mechanical behaviour and failure mode of volcanic materials.

A thorough understanding of the mechanical behaviour and failure mode of volcanic materials is important to assess the stability of a volcanic edifice (e.g., Voight, 2000; Watters et al., 2000; Okubo, 2004; Apuani et al., 2005). For example, measurements of strength are required in models of slope stability (e.g., Apuani et al., 2005), important to assess potentially devastating volcanic hazards (McGuire, 1996; Keating and McGuire, 2000). The mechanical behaviour of volcanic materials is also important for the modelling of surface displacement routinely monitored at many active volcanoes worldwide (e.g., Got et al., 2013; Carrier et al., 2015; Got et al., 2017). Further, the failure modes of volcanic rock (brittle or ductile) could help inform on instability induced by faulting (e.g., Lagmay et al., 2000) and volcano spreading (van Wyk de Vries and Borgia, 1996; van Wyk de Vries and Francis, 1997; Delcamp et al., 2008). However, and despite this importance, studies focussed on the mechanical behaviour and failure mode of porous volcanic materials are comparatively few (when compared to sedimentary rocks). Early work by Shimada (1986) showed that porous basalt deforms in a ductile manner at room temperature and at high confining pressures. Shimada (1986) found that compaction in the ductile field was driven by cataclastic flow (the crushing of crystals and pores). Since Shimada (1986), notable studies on the mechanical behaviour of porous volcanic rocks include Zhu et al., (2011), Loaiza et al. (2012), and Adelinet et al. (2013). These studies also showed that porous

volcanic rock can deform in the ductile regime at room temperature. The experiments in these three studies showed that the stress-strain curves of porous volcanic rock, in both the brittle and ductile regimes, are not dissimilar to those for porous sedimentary rocks (Figure 4a). Further, deformation in the brittle regime was facilitated by microcracking and resulted in a shear fracture (Zhu et al., 2011; Loaiza et al. 2012; Adelinet et al., 2013). The micromechanism behind deformation in the ductile regime was cataclastic pore collapse, which can either be distributed (e.g., the porous tuffs of Zhu et al., (2011); Figure 4b-c) or localised into bands (e.g., the basalts of Loaiza et al. (2012) and Adelinet et al. (2013); Figure 4d-f).
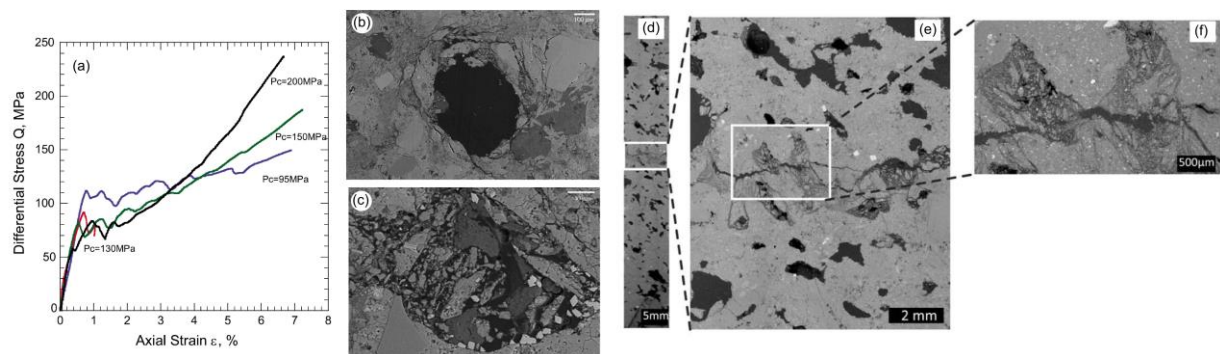

Figure 4. (a) Stress-strain curves for basalt deformed at different confining pressures. Pc – confining pressure (from Loaiza et al., 2012). (b and c) Scanning electron micrographs of pores within tuff deformed at high pressure (from Zhu et al., 2011). (d, e, and f) Scanning electron micrographs of bands of collapsed pores in basalt (from Loaiza et al., 2012).

The aforementioned studies on volcanic rocks, no doubt, improved our understanding of how porous volcanic rocks deform, but these studies all performed experiments on a single rock type. Based on the paucity of data, it is therefore challenging to comment on the influence of porosity, pore size, pore shape, crystal size, and crystal content on the mechanical behaviour and failure mode of volcanic rocks. In other words, more data are now required. Further, these studies did not consider how these data could be of use for understanding large-scale volcanic processes. The important unanswered questions include:

- ➢ **What are the key microstructural controls in the deformation of porous volcanic rocks?**
- ➢ **What controls compaction localisation in porous volcanic rocks?**
- ➢ **How can laboratory experimental studies on mechanical behaviour and failure mode inform large-scale volcanic processes?**

1.2 The permeability of porous rocks

The permeability (a measure of the ability of a material to transmit fluids) of rock has received considerable attention in the literature, due to its importance in governing, for example, fault behaviour (e.g., Caine et al., 1996; Doan et al., 2006; Faulkner et al., 2010; Aben et al., 2016, 2017), the viability of geothermal resources (e.g., Barbier, 2002), and locating suitable sites for the sequestration of carbon dioxide (e.g., Holloway, 2005). For these reasons, and others, many studies that have measured the permeability of granites (e.g., Brace et al., 1968; Zoback and Byerlee, 1975; Mitchell and Faulkner, 2008) and sedimentary rocks (e.g., Bourbié and Zinszner, 1985; Doyen, 1988; Nelson et al., 1994; Zhu and Wong, 1997; Baud et al., 2017a).

Work on porous rocks has shown that porosity exerts a first-order control on permeability: rocks containing a higher porosity are generally more permeable (e.g., Bourbié and Zinszner, 1985; Nelson, 1994; Figure 5). The data of Figure 5 shows that the relationship between porosity and permeability is nonlinear. The data of Nelson (1994) could be well-described by a single power law and the data of Bourbié and Zinszner (1985) are perhaps better described by two power laws that intersect at a porosity of about 10% (Figure 5).
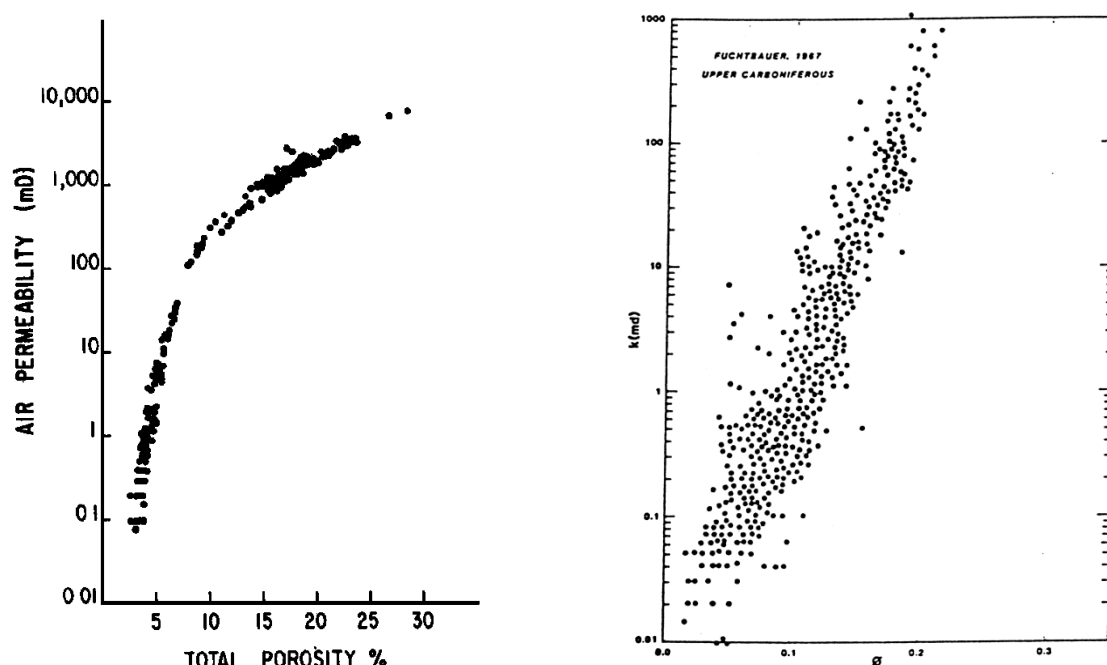

Figure 5. Porosity and permeability relationships. Left graph: air permeability as a function of total porosity for Fontainebleau sandstone (from Bourbié and Zinszner, 1985). Right graph: permeability (in md) as a function of porosity for Upper Carboniferous sandstones (from Nelson, 1994).

Although porosity is a useful indicator of permeability, large datasets often find that the permeability of samples containing the same porosity can vary by orders of magnitude (as demonstrated by the data of Nelson (1994) shown in Figure 5). This variability for a constant porosity is the consequence of differences in pore architecture, namely the size, shape, and connectivity of the microstructural elements responsible for flow (e.g., Guéguen and Dienes, 1989; Guéguen et al., 1997; Bernabé et al., 2010). To emphasise, a rock containing a high-porosity can have a low permeability if the porosity is poorly connected. Conversely, a low-porosity rock can be surprisingly permeable if the porosity is well connected, as is sometimes the case for microcracked rocks (e.g., Le Ravalec and Guéguen, 1994; David et al., 1999; Menéndez et al., 1999; Darot and Reuschlé, 2000; Guéguen and Schubnel, 2003; Fortin et al., 2011; Meredith et al., 2012).
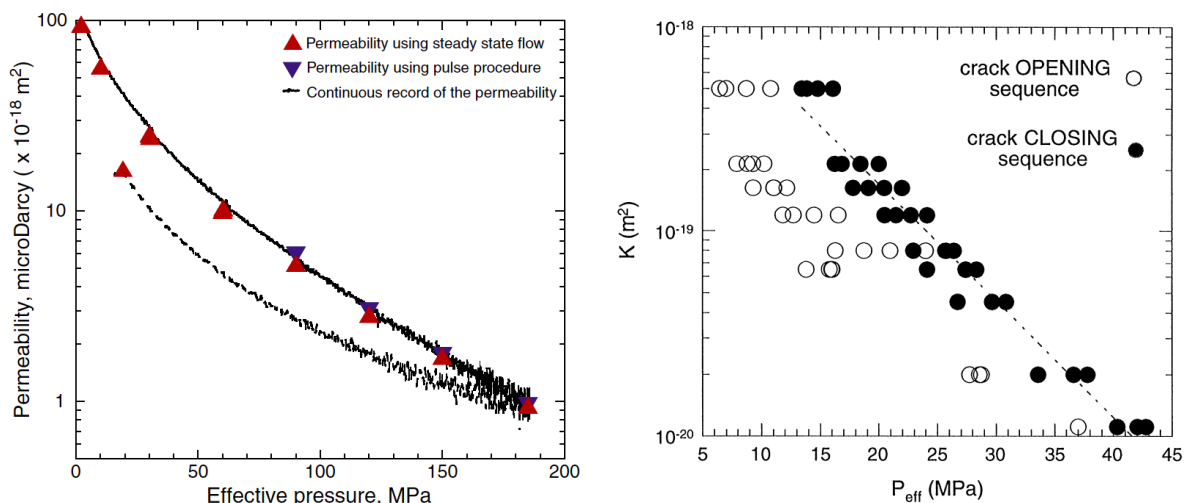
Figure 6. Permeability as a function of effective pressure. Left graph: permeability of a naturally microcracked basalt as a function of effective pressure (from Fortin et al., 2011). Right graph: permeability (K) as a function of effective pressure (P_{eff}) for a thermally microcracked granite (from Darot and Reuschlé, 2000).

The permeability of rock can be influenced by external factors such as confining pressure and deformation (induced by stresses, either mechanical or thermal). The influence of confining pressure on the permeability of rock depends on the nature of the porosity (e.g., Benson et al., 2006). If the permeability is supported by compliant microcracks, for example, permeability can be reduced by many orders of magnitude at high confining pressures due to the pressure-dependent closure of microcracks (e.g., Gavrilenko and Guéguen, 1989; Benson et al., 2006; Nara et al., 2011; Fortin et al., 2011; Figure 6). It can also be seen in the data of Figure 6, from

studies by Fortin et al. (2011) and Darot and Reuschlé (2000), that a high confining pressure can permanently close microcracks: permeability is higher for a given effective pressure during the pressurisation than during the depressurisation of the sample. When permeability is supported by backbone of pores, which often do not close at high confining pressures due to their aspect ratio, the influence of confining pressure on permeability is diminished (e.g., Farrell et al., 2014).
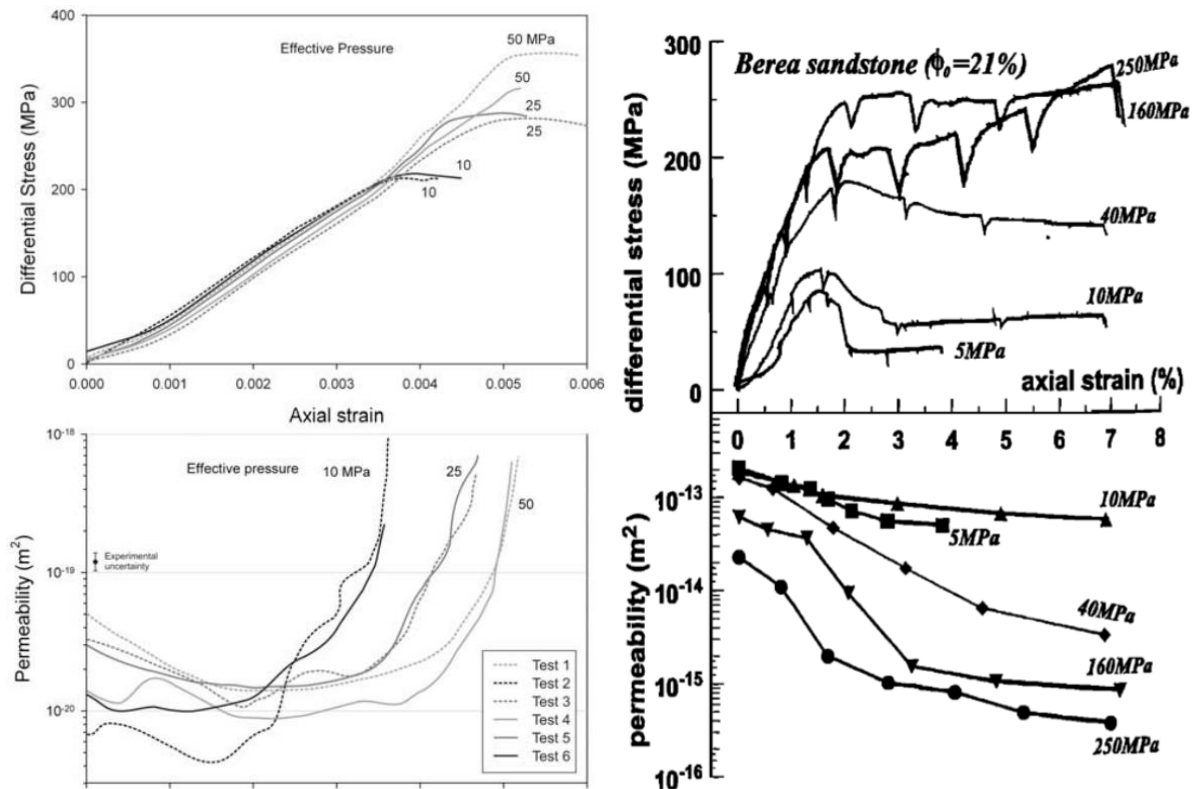
Figure 7. Permeability as a function of axial strain (numbers next to each curve indicate the effective pressure). Left graphs: differential stress as a function of axial strain (stress-strain curves) for samples of granite deformed in the brittle regime (top graph) and their permeability evolution as a function of axial strain (bottom graph) (from Mitchell and Faulkner, 2008). Right graphs: differential stress as a function of axial strain (stress-strain curves) for samples of porous sandstone deformed in the brittle and ductile regimes (top graph) and their permeability evolution as a function of axial strain (bottom graph) (from Zhu and Wong, 1997).

Since the mechanical deformation of rock can greatly influence porosity (see section 1.1), it follows that deformation will also yield changes to rock permeability. Whether the permeability increases or decreases in response to deformation depends on the failure mode (brittle or ductile) and the porosity architecture. In the brittle field, deformation is associated with

increases in permeability for low-porosity rock such as granite (e.g., Zoback and Byerlee, 1975; Mitchell and Faulkner, 2008; Figure 7). However, studies on porous sandstones show that permeability can decrease with deformation in the brittle field (Zhu and Wong, 1997; Figure 7). In the ductile field, the inelastic compaction of porous rocks is associated with decreases to permeability (David et al., 1994; Zhu et al., 1997; Zhu and Wong, 1997; David et al., 2001; Fortin et al., 2005; Baud et al., 2012; Figure 7).

For a volcanic system, permeability is considered an extremely important metric. In short, volcanic eruptions can be driven by gas overpressures and, as a result, the ease at which exsolving magmatic volatiles can escape the system can dictate the eruptive behaviour: effusive or explosive (e.g., Eichelberger et al., 1986; Sparks, 1997; Melnik et al., 2005; Mueller et al., 2005; Lavallée et al., 2013). Although many laboratory studies have been dedicated to the porosity and permeability of volcanic materials, often high-porosity pumice (e.g., Klug and Cashman, 1996; Saar and Manga, 1999; Rust and Cashman, 2004; Wright et al., 2009), the vast variability in the porosity (from 0 to almost 1 in the case of reticulite) and porosity architecture (pore size and shape, connectivity, and porosity type (microcracks and pores), amongst others) of volcanic rocks demands further study. The important unanswered questions include:

- ➤ **What are the key microstructural attributes that control the permeability of porous volcanic rocks?**
- ➤ **How does deformation (brittle and ductile) influence the permeability of volcanic rocks?**
- ➤ **How can values of permeability measured in the laboratory be upscaled (e.g., see Guéguen et al., 1996) to the volcano-scale?**

1.3 The use of volcanic rocks in construction

Volcanic rocks have been used in construction for millennia. Buildings are often constructed using local rocks and, in the case of settlements close to sites of ancient or present-day volcanic activity, volcanic rocks were and are widely used. For example, the gothic cathedral in Clermont-Ferrand (France) is built entirely from local basalt – Volvic basalt (Figure 8).

Figure 8. The Cathédrale Notre-Dame-de-l'Assomption in Clermont-Ferrand, built entirely from Volvic basalt.

In particular, volcanic tuffs were and are widely used due to their easy workability (tuffs can be easily cut by a saw), their low density (tuffs are easy to transport), and their wide availability (tuffs usually form extremely voluminous deposits). Indeed, tuffs have been used worldwide as a building stone for millennia and cities built on and constructed using tuff span six of the seven continents (all except Antarctica) (Heiken, 2006). The use of tuffs in Europe was documented by Roman architect Vitruvius who, in his De Architectura works, stated that:

"*There are also many other kinds, such as red and black tuff in Campania, [and] in Umbria, Piceno and in Venetia white, which, indeed, can be cut like wood by means of a serrated or toothed saw. So long as these soft stones are sheltered under plaster they will hold up and do their work but if they are laid bare or exposed in the open air, ice and frost accumulate within them and they crumble*

apart and dissolve. Also along the sea coast salt eats at them and they dissolve apart; neither do they endure sea tides and spray." (De Architectura 2.7.1-2; Jackson et al., 2006).

Further information as to the use of tuff in early construction was provided by Tactius, a Roman senator and historian, who wrote that the Romans considered peperino tuff (lapis Albanus) as fire resistant (Tacitus, Annales 15.43). Indeed, Tactius stated that Nero specified its use in the reconstruction of Rome after the fire of AD 64 (Tacitus, Annales 15.43). Interestingly, the implication of these writings is that other types of tuff must have been less resistant to fire, or not resistant at all.

Due to the widespread use of tuff as a building stone worldwide, many studies are devoted to understanding, for example, their resistance to fire (e.g., Duvarcı et al., 2005; Gomez-Heras et al., 2006), resistance to salt weathering (e.g., Török et al., 2004; Zedef et al., 2007; Vacchiano et al., 2008; Oguchi and Yuasa, 2010; Yavuz, 2012; La Russa et al., 2017), resistance to freeze-thaw weathering (e.g., Chen et al., 2004; Török et al., 2004; Oguchi and Yuasa, 2010; Nijland et al., 2010; Ruedrich et al., 2011; Yavuz, 2012), and their strength in the presence of water and following wetting-drying cycles (e.g., Jackson et al., 2005; Siedel, 2010; Oguchi and Yuasa, 2010; Zhu et al., 2011; Di Benedetto et al., 2015).

The widespread use of tuffs in construction is certainly of interest due to their extreme variability in mineral content (tuffs can contain minerals that are sensitive to fire and water, as discussed by Vitruvius and Tactius), porosity, strength, and microstructure, amongst others. It is because of this variability that more studies are required to understand their physical and mechanical properties, and their resistance to the elements (such as fire and water). This research is important to promote the use of natural volcanic rocks in construction, rather than continue our overreliance on concretes that are associated with an additional CO_2 fingerprint (e.g., Worrell et al., 2001), a low resistance to fire (for example), and a short service life. The important unanswered questions include:

- ➢ **How tough are tuffs in the event of fire and what factors influence their fire resistance?**
- ➢ **Are all tuffs weaker when wet and what factors influence water-weakening?**

CHAPTER TWO – The mechanical behaviour of volcanic rocks

This chapter outlines recent work from laboratory at IPG Strasbourg on the mechanical behaviour and failure mode of volcanic rocks. One of the first studies from our laboratory to focus on the physical properties of volcanic rocks was "Microstructural controls on the physical and mechanical properties of edifice-forming andesites at Volcán de Colima, Mexico" (Heap et al., 2014a, *Journal of Geophysical Research*). This paper exposed that the highly variable physical properties (uniaxial compressive strength, elastic wave velocities, and permeability) of a suite of andesites from Volcán de Colima (Mexico) is the result of their highly variable microstructural attributes (microcrack density, pore number density, pore size distribution, and pore shape).
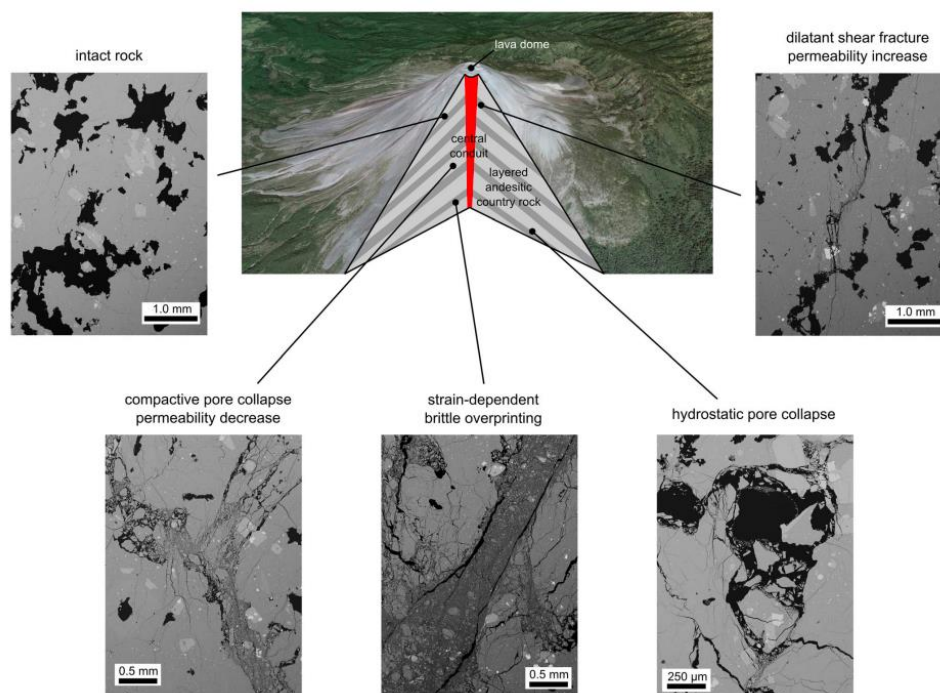
Figure 9. Schematic cross section of Volcán de Colima (layered andesitic edifice host rocks with a central conduit of dykes. The cross section is annotated with back-scattered scanning electron microscope pictures of the intact material and the various deformation microstructures (from Heap et al., 2015a).

This paper led to a number of studies that focussed on performing suites of triaxial deformation experiments on volcanic rocks to better understand their mechanical behaviour and failure modes. Namely, "Fracture and compaction of andesite in a volcanic edifice" (Heap et al., 2015a,

Bulletin of Volcanology), "Mechanical behaviour and failure modes in the Whakaari (White Island volcano) hydrothermal system, New Zealand" (Heap et al., 2015b, *Journal of Volcanology and Geothermal Research*), "Mechanical behaviour of dacite from Mount St. Helens (USA): A link between porosity and lava dome extrusion mechanism (dome or spine)?" (Heap et al., 2016, *Journal of Volcanology and Geothermal Research*), and "Closing an open system: Pore pressure changes in permeable edifice rock at high strain rates" (Heap and Wadsworth, 2016, *Journal of Volcanology and Geothermal Research*).

Heap et al. (2015a), probably the most significant of the aforementioned studies, performed suites of triaxial experiments on andesites from Volcán de Colima to better understand the influence of porosity on the mechanical behaviour and failure mode of volcanic rocks. The experiments in this study showed that (1) porosity and pore size are important in governing their mechanical behaviour and (2) edifice-forming rocks can deform in a ductile manner at pressures relevant for a volcano. Importantly, this study tried to link the experimental deformation microstructures, and their impact on permeability, to regions of the edifice (Figure 9). Similar experiments were performed on hydrothermally altered volcanic materials from Whakaari volcano (New Zealand), with an emphasis using the results of these experiments to inform on the interpretation of seismic signals, outgassing, ground deformation, and the volcanic structural stability of Whakaari volcano (Heap et al., 2015b). Triaxial experiments on dacite from Mt. St. Helens (USA) highlighted a potential link between the porosity of extruded lava and the extrusion mechanism (dome or spine) (Heap et al., 2016). Further experiments on andesites from Volcán de Colima showed how pore fluid pressure can change during "undrained" deformation in the brittle and ductile regimes (Heap and Wadsworth, 2016).

The experimental studies discussed thus far were all performed at room temperature. The publication "From rock to magma and back again: The evolution of temperature and deformation mechanism in conduit margin zones" (Heap et al., 2017a, *Earth and Planetary Science Letters*) represents one of the first studies to investigate deformation mechanisms and the failure mode of porous volcanic rocks at high-pressure and high-temperature. These experiments showed that increasing the temperature above the threshold glass transition temperature not only changed the deformation mechanism from cataclastic pore collapse to viscous flow, but also the manifestation of failure changed from localised (into compaction bands) to distributed (Figure 10). Deformation driven by viscous flow resulted in much larger

reductions to porosity (Figure 10), and presumably permeability (not measured in this study), with implications for pore pressure augmentation and explosive volcanic behaviour.
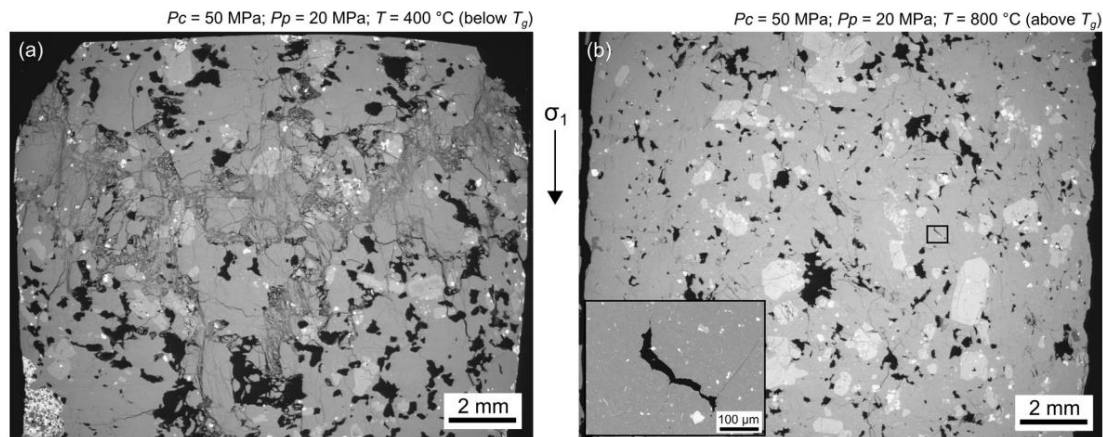

Figure 10. *Ductile deformation microstructures below and above Tg. (a) Scanning electron microscope (SEM) image of the sample deformed at 400 °C showing the band of crushed pores. (b) SEM image of the sample deformed at 800 °C showing distributed viscous compaction. Inset shows a viscously flattened pore (from Heap et al., 2017a).*

Jamie Farquharson's Ph.D at IPG Strasbourg (2013-2016) was focussed on the impact of failure mode on permeability evolution in volcanic rocks. During this time, he also contributed to our understanding of the mechanical behaviour of volcanic materials. His paper "Pore pressure embrittlement in a volcanic edifice" (Farquharson et al., 2016a, *Bulletin of Volcanology*) shows that increasing the pore pressure, whilst holding the rock at a constant differential stress, results in brittle failure. These data suggest that only small increases in pore pressure could trigger failure in previously damaged rocks and therefore promote flank/slope instability.

Attached to this chapter are three of the most relevant papers on this topic (all the of papers published on this topic can be found in Appendix B).

➢ "**Microstructural controls on the physical and mechanical properties of edifice-forming andesites at Volcán de Colima, Mexico**" (Heap et al., 2014a).
➢ "**Fracture and compaction of andesite in a volcanic edifice**" (Heap et al., 2015a).
➢ "**From rock to magma and back again: The evolution of temperature and deformation mechanism in conduit margin zones**" (Heap et al., 2017a).

Correspondence to:
M. J. Heap,
heap@unistra.fr

Microstructural controls on the physical and mechanical properties of edifice-forming andesites at Volcán de Colima, Mexico

M. J. Heap[1], Y. Lavallée[2], L. Petrakova[3], P. Baud[1], T. Reuschlé[1], N. R. Varley[4], and D. B. Dingwell[3]

[1]Laboratoire de Déformation des Roches, Équipe de Géophysique Expérimentale, Institut de Physique de Globe de Strasbourg (UMR 7516 CNRS, Université de Strasbourg/EOST), Strasbourg, France, [2]School of Environmental Sciences, University of Liverpool, Liverpool, UK, [3]Earth and Environment, University of Munich, München, Germany, [4]Facultad de Ciencias, Universidad de Colima, Colima, Mexico

Abstract The reliable assessment of volcanic unrest must rest on an understanding of the rocks that form the edifice. It is their microstructure that dictates their physical properties and mechanical behavior and thus the response of the edifice to stress perturbations during unrest. We evaluate the interplay between microstructure and rock properties for a suite of edifice-forming rocks from Volcán de Colima (Mexico). Microstructural analyses expose (1) a pervasive, isotropic microcrack network, (2) a high, subspherical vesicle density, and (3) a wide vesicle size distribution. This complex microstructure severely impacts their physical and mechanical properties. In detail, porosities are high and range from 8 to 29%. As a consequence, elastic wave velocities, Youngs moduli, and uniaxial compressive strengths are low, and permeabilities are high. All of the rock properties demonstrate a wide range. For example, strength decreases by a factor of 8 and permeability increases by 4 orders of magnitude over the porosity range. Below a porosity of 11–14%, the permeability-porosity trend follows a power law with a much higher exponent. Microstructurally, this represents a critical vesicle content that efficiently connects the microcrack population and permits a much more direct path through the sample, rather than restricting flow to long and tortuous microcracks. Values of tortuosity inferred from the Kozeny-Carman permeability model support this hypothesis. However, we find that the complex microstructure precludes a complete description of their mechanical behavior through micromechanical modeling. We urge that the findings of this study be considered in volcanic hazard assessments at andesitic stratovolcanoes.

1. Introduction

A comprehensive description of the microstructural, physical, and mechanical properties of edifice-forming rocks represents essential input for the development of effective and robust volcanic unrest models [e.g., *Sparks*, 2003]. In the assessment of the response of a volcanic edifice to the stress perturbations likely to accompany any unrest activity, details of the response of the rocks become central to the question of ascribing the permissible mechanistic sources behind geophysical, geodetic, and geochemical signals of unrest [e.g., *Gottsmann et al.*, 2011]. An improved understanding of the relationships between rock microstructure (e.g., microcracks and vesicles), rock physical properties (e.g., porosity, bulk density, elastic wave velocities, and permeability), and rock mechanical properties (e.g., strength) of representative materials should therefore allow us to (1) improve the imaging of subsurface activity [e.g., *Manconi et al.*, 2007], (2) construct a better scheme to assess the structural stability of the volcano [e.g., *Voight*, 2000; *Gudmundsson*, 2011], and (3) better understand the role of the host rocks in dictating eruption characteristics and progression [e.g., *Jaupart*, 1998; *Costa et al.*, 2009].

Volcanic structures are haphazardly assembled from the products of successive effusive and explosive eruptions. The rapid and heterogeneous construction, in both time and space, of volcanic edifices renders them inherently unstable [e.g., *McGuire*, 1996]. During this rapid construction, volcanic rocks are subjected to variable but rapid solidification due to the temperature changes associated with their eruptive and emplacement history. In this process, disequilibrium crystallization, gas exsolution, degassing, sintering/welding, and partial vitrification/devitrification contribute to generate a wide range of volcanic materials. Complex variations in temperature, stress, strain, and strain rate during magma ascent may further promote the development of additional microstructural and macrostructural features (e.g., microcracks and flow bands), both in the eruptive products and in the host rock. As a result, volcanic structures are generally made

up of many layers that harbor very different microstructural, physical, and mechanical properties [e.g., *Gudmundsson*, 2011]. To emphasize, the porosity of volcanic rocks can vary from essentially zero up to 97% in the case of reticulite. Experimental rock deformation has been dominated by studies of homogeneous sedimentary and intrusive igneous rocks [see *Paterson and Wong*, 2005]. Only recently have studies begun to investigate the microstructural, physical, and mechanical properties of volcanic rocks [e.g., *Rocchi et al.*, 2004; *Balme et al.*, 2004; *Vinciguerra et al.*, 2005; *Stanchits et al.*, 2006; *Jeong et al.*, 2007; *Benson et al.*, 2008; *Smith et al.*, 2009; *Fortin et al.*, 2011; *Heap et al.*, 2011; *Zhu et al.*, 2011; *Loaiza et al.*, 2012; *Adelinet et al.*, 2013]. Though few in number, these studies have already exposed a wide range of physical properties and mechanical behavior owing to a wide variety of microstructure.

In this study, we evaluate the microstructure (i.e., microcrack density and anisotropy, and vesicle density, shape, and size distribution) and the physical (i.e., porosity, dynamic and static elastic moduli, elastic wave velocities and anisotropy, and permeability) and mechanical properties (i.e., strength) of a representative suite of andesitic rocks from the active Volcán de Colima, Mexico. The focus of this study is to characterize edifice host rocks; the host rock will very rarely exceed its glass transition temperature (740°C) [*Lavallée et al.*, 2012], and therefore the room temperature experiments reported in this study should correspond closely to the state of the rocks comprising the edifice. We then explore the adequacy of micromechanical models (pore-emanated crack and sliding wing-crack modeling) in an attempt to decipher their mechanical behavior and geometrical permeability modeling (Kozeny-Carman) to understand the physics underpinning fluid transport. With the aim of a better understanding of volcanically active provinces, we complement our data with an assessment of the impact of temperatures representative of conduit margins (450°C) on the microstructural, physical, and mechanical properties of the andesites. Thermal microcracks form as a result of the buildup of internal stresses due to the following: (1) the thermal expansion mismatch between the different phases present in the material, (2) thermal expansion anisotropy within individual minerals, and (3) thermal gradients [e.g., *Richter and Simmons*, 1974; *Yong and Wang*, 1980]. Thermal microcracking has been previously shown to induce changes to the physical properties of rocks [e.g., *David et al.*, 1999]. However, few studies have investigated the propensity of volcanic rocks to develop thermal microcracks and their consequences on rock physical properties. In a volcanic setting, thermal microcracking of the conduit wall rock and the surrounding country rock could have consequences on the progression of the eruption [e.g., *Costa et al.*, 2009], and, importantly, on the stability of the volcanic edifice as a whole [e.g., *Donnadieu et al.*, 2001; *Gudmundsson*, 2011]. Finally, we discuss some implications of our findings for andesitic stratovolcanoes.

2. Case Study: Volcán de Colima (Mexico)

Volcán de Colima (Mexico, 19°30′N, 103°37′W, Figure 1) is a persistently active and frequently collapsing volcano located at the western end of the Trans-Mexican Volcanic Belt. Locally, the stratovolcano marks the intersection between the N-S trending Colima Rift Zone and the NE-SW trending Tamazula Fault [*Norini et al.*, 2010]. The volcanic complex comprises the older, extinct edifice of Nevado de Colima and the active (<50 ka) Fuego de Colima, constructed in the amphitheater of an earlier collapse structure (Figure 1). At least five collapse events during the last 18,500 years have occurred with widely distributed debris avalanche deposits found to the south [*Cortés et al.*, 2010], the most recent being 2550 B.P.

Recent eruptive activity at Volcán de Colima has been described as occurring in cycles with an interval of approximately 100 years [*Luhr*, 2002]. The last two cycles of which ended in 1818 and 1913 with volcanic explosivity index four explosive eruptions (between larger Plinian or sub-Plinian eruptions). Typical activity is characterized by episodes of both effusive and Vulcanian explosive events. Multifaceted transitions between styles of activity point to a complex plumbing system with multiple pathways [*Lavallée et al.*, 2012] and various magma reservoirs located at different depths. Studies of melt inclusions have defined a range of crystallization depths based upon the entrapment pressure of both dissolved H_2O and CO_2 for the 1998–2005 period [*Reubi et al.*, 2013]. The majority indicate depths less than 4 km, matching depths for volcano-tectonic seismicity recorded as precursors to the 1998–1999 eruption [*Zobin et al.*, 2002a].

The most recent eruption commenced in January 2013 with Vulcanian explosions and the emplacement of a new lava dome and flow and is ongoing as of February 2014. The previous prolonged episode lasted from November 1998 until June 2011. During this period, there were five episodes of dome growth, of varying duration and effusion rate, from 2.5 months and $8\,m^3\,s^{-1}$ in 2004 [*Varley et al.*, 2010] to the excessively low rate of $0.02\,m^3\,s^{-1}$ for
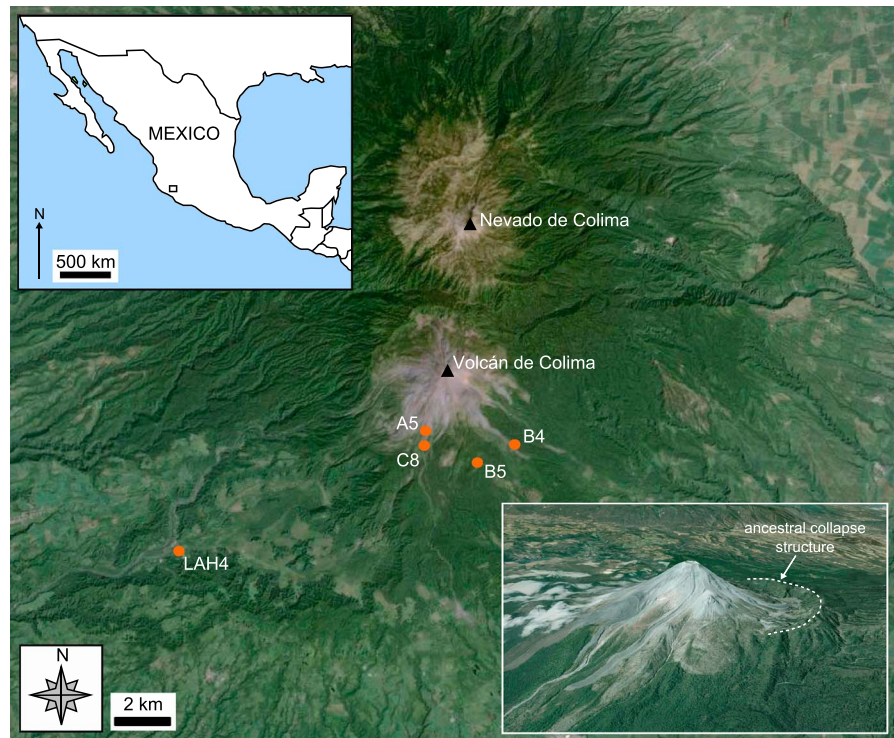
Figure 1. A Google Earth^TM map showing the locations of the sampling sites with respect to Volcán de Colima. Insets show a map of Mexico (the rectangular box corresponds to the position of the locality map) and a Google Earth^TM image of Volcán de Colima showing the ancestral collapse structure (dashed white line).

the final episode, which lasted 4.5 years. Slow protracted dome growth occurred in 2001–2003 and 2007–2011, while fast episodes, more typical for this type of volcano, were witnessed in 1998–1999, 2004, and 2005, the former two extending to form substantial lava flows. Two types of explosive activity have also characterized the recent eruption: larger Vulcanian events that have often destroyed a previously emplaced dome and small events of variable ash contents, which have been generated with a repose period of the order of a few hours. The most intense period of activity occurred in 2005 during which at least 30 larger explosions produced pyroclastic flows, reaching 5.4 km to the SE of the volcano [*Varley et al.*, 2010].

Recent eruptive activity has been extensively monitored by seismicity [*Arámbula-Mendoza et al.*, 2011], with also gas geochemistry [*Taran et al.*, 2002; *Varley and Taran*, 2003], infrared imaging [*Hutchinson et al.*, 2013; *Stevenson and Varley*, 2008], and deformation [*Zobin et al.*, 2002b]. The local population has increased since the 1913 Plinian eruption whose impact was relatively minimal [*Saucedo et al.*, 2010]. The increased vulnerability has been highlighted by the impact of lahars during recent years, which have shown a clear relationship with the volume of pyroclastic period deposited in the ravines [*Dávila et al.*, 2007]. Modeling collapse events has emphasized the need to understand and ideally predict the failing of lava domes [*Sulpizio et al.*, 2010] while stochastic flank collapse probability modeling has yielded two scenarios: (1) that Colima is 110 years overdue for a debris avalanche event (DAE) and (2) that this next DAE will occur 345 years from the present [*Borselli et al.*, 2011].

The magma erupts at temperatures of 960–1031°C [*Reubi and Blundy*, 2008], and the temperature of fumaroles at the surface has been measured to be 820°C in 2001 [*Varley and Taran*, 2003]. The temperature of the outer carapace of a lava dome is dependent upon its size and the effusion rate; temperatures can reach >500°C when the dome is small with exogenic growth and, when large, the temperature is dependent on the effusion rate (for fast growing domes this can be >300°C). The core of the dome remains hot, as evidenced by routine thermal imaging of internal dome structures, occasionally exposed by the partial shedding of the talus [*Mueller et al.*, 2013]. The erupted products of Volcán de Colima have varied only slightly in bulk composition during recent years, being andesitic and containing ~58–61 wt % SiO_2 [*Luhr*, 2002; *Savov et al.*, 2008]. Recent field-based studies [*Lavallée et al.*, 2012, and references therein] have revealed the porosity of eruptive products to be, in general, lower than 40%.

Table 1. Averaged X-ray Fluorescence Analysis of the Bulk Geochemical Composition of Each of the Studied Andesites

Sample	B5	B4	A5	C8	LAH4
SiO_2	59.72	60.23	58.87	61.41	59.10
Al_2O_3	16.85	17.56	17.87	17.84	17.45
Fe_2O_3	6.25	5.95	5.89	5.43	6.13
MnO	0.12	0.11	0.10	0.10	0.11
MgO	3.90	3.08	3.63	2.29	4.04
CaO	6.05	5.86	6.44	5.49	6.62
Na_2O	4.51	4.73	4.61	4.88	4.52
K_2O	1.27	1.32	1.18	1.44	1.19
TiO_2	0.60	0.60	0.60	0.55	0.62
P_2O_5	0.18	0.20	0.18	0.20	0.19
LOI	0.05	0.03	0.10	0.00	0.00
Total	99.47	99.59	99.27	99.61	99.97

3. Experimental Materials and Methods

3.1. Experimental Materials

For the purpose of our study we selected five andesitic blocks (A5, B4, B5, C8, and LAH4) to represent the variability of the material forming the volcanic edifice [*Lavallée et al.*, 2012]. A5 is from the 1998–1999 lava flow in the Cordoban ravine, B4 was taken from the 1975–1976 lava flow from the southeast slope of the volcano, B5 is from an older lava flow of unknown age, C8 was taken from the 1998–1999 blow-and-ash flow in the San Antonio ravine, and LAH4 is a block of unknown age collected from a lahar deposit on the west flank of the volcano (in the El Zarco riverbed near La Becerrera). The locations of the collection sites are indicated in Figure 1.

X-ray fluorescence analysis of the bulk geochemical composition of each andesite block is presented in Table 1 and shows that the andesites contain between 58 and 61 wt % silica (similar to the bulk chemical compositions provided by *Luhr* [2002]). Optical microscopic analysis (Figure 2a) under crossed polarized transmitted light has shown the andesites to have a porphyritic texture containing (commonly microcracked) phenocrysts (<1.5 mm) of plagioclase (13–25%), orthopyroxene (2–4%), and clinopyroxene (3–4%) within a microlitic groundmass (59–68%). The plagioclase crystals are commonly zoned and twinned (Figure 2a). The groundmass contains interstitial glass with a glass transition temperature of about 740°C at a rate of 10°C/min [*Lavallée et al.*, 2012]. Under reflected light (Figure 2b) and using a scanning electron microscope (SEM, Figure 2c), methods that permit a better examination of rock microstructure, we observe that the andesites are pervasively microcracked and contain many vesicles.

Numerous cylindrical core samples were prepared from each of the five blocks of andesite. Samples were cored to a diameter of 20 mm and precision ground to a nominal length of 40 mm. The collected andesite blocks were loose blocks selected from lava, block-and-ash flow, and lahar deposits (Figure 1) and are therefore unorientated with respect to any volcanological feature and with respect to each other. In this study we refer to an *X*, *Y*, and *Z* directions for each of the blocks. Our *Z* direction was chosen to maximize the number of cylindrical core samples we could take from each block; *X* and *Y* are orthogonal to this coring direction.

3.2. Experimental Methods

The methods used in this study are presented below. In each case, further details can be found in Appendix A.

3.2.1. Microstructural Characterization

Two-dimensional quantitative microcrack and vesicle analyses were performed on thin sections (in the *XY* plane) prepared from fluorescent-epoxy-impregnated samples of each andesite. Volcanic rocks are persistently exposed to a combination of thermal and mechanical stresses and, as a result, are often highly fractured. Microcrack surface area per unit volume was determined using classical stereological techniques [*Underwood*, 1970], and microcrack anisotropy was measured using the modified Cantor-dust method [*Volland and Kruhl*, 2004] included in the automated pattern quantification toolbox AMOCADO [*Gerik and Kruhl*, 2009]. Vesicles in volcanic rocks represent the solidified relics of degassing processes in magmas. For this reason, their statistical analysis can provide information relating to the physical processes that drive magma ascent and eruption [see *Shea et al.*, 2010, and references therein]. In this study we are interested in vesicle size and shape distributions in order to evaluate the micromechanics responsible for their deformation. Vesicle area, density, circularity, aspect ratio, and roundness were determined using image processing software ImageJ.

3.2.2. Connected and Total Porosities

The connected water porosities of the samples were measured using the triple-weight water saturation (distilled water) method, using Archimedes' principal [see *Guéguen and Palciauskas*, 1994]. The powder skeletal densities required for the calculation of total porosity were measured using a helium pycnometer (AccuPyc II 1340).
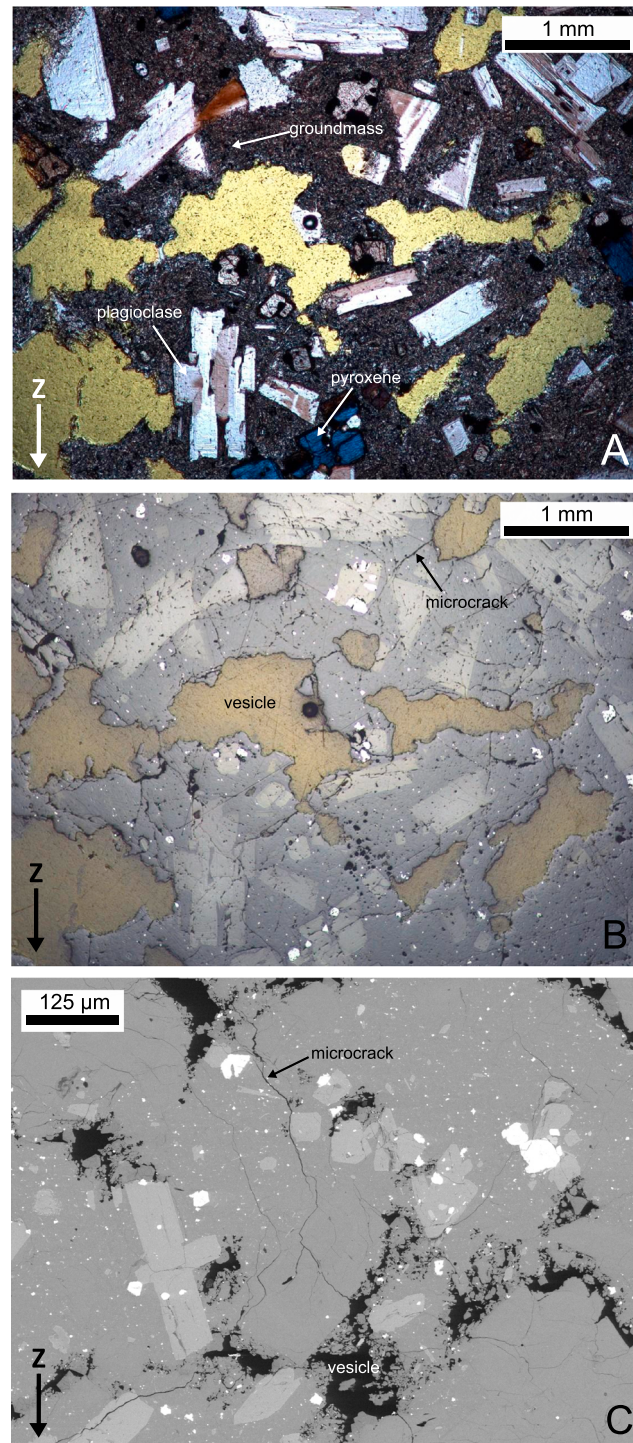
Figure 2. (a) A photomicrograph (taken under transmitted cross-polarized light) of one of the andesites investigated in this study (in this case C8). The common minerals are identified on the figure (note: the green areas are vesicles, see Figure 2b). (b) A photomicrograph (taken under reflected light) of the same area. The microstructural elements are identified on the figure. (c) Scanning electron microscope image of a sample of B5. The microstructural elements are identified on the figure.

3.2.3. Elastic Wave Velocities

P and S wave velocities were measured along the long axis of the cylindrical samples (i.e., the Z direction) under both dry conditions (i.e., the samples were dried for at least 24 h in a vacuum oven at 40°C, and then the measurements were made under ambient humidity conditions) and water-saturated (i.e., vacuum saturated with distilled water) conditions. All measurements were collected under ambient laboratory conditions and an axial stress of 1.9 MPa. To investigate the anisotropic nature of the andesites we machined cubes (approximately $50 \times 50 \times 50$ mm) from each of the andesite blocks. P and S wave velocities could then be measured in each of the X, Y, and Z directions with a reduced risk of sample variability influencing the results (as may be the case if three orthogonal cores were prepared).

3.2.4. Elastic Moduli

The measured elastic wave velocities (see section 3.2.3) were subsequently used to calculate the dynamic Young's modulus E_d and the dynamic Poisson's ratio v_d [see *Guéguen and Palciauskas*, 1994]. For the static Young's moduli E_s, we used the tangent moduli defined as the local slope of the stress-strain curves collected during the uniaxial compressive strength (UCS) experiments described in section 3.2.6. The moduli were calculated at the axial stress level corresponding to the maximum slope (typically at axial stresses between 15 and 100 MPa, depending on the sample).

3.2.5. Permeability Measurements

Water (distilled) permeability measurements were made in a hydrostatic pressure vessel along the long axis of the cylindrical samples (i.e., the Z direction). Permeabilities were measured for a suite of samples that best cover the observed range of connected water porosities (from 7.4 to 23.8%). Fluid volume flux was measured during steady state flow (under a confining pressure of 2 MPa), and permeability was calculated using
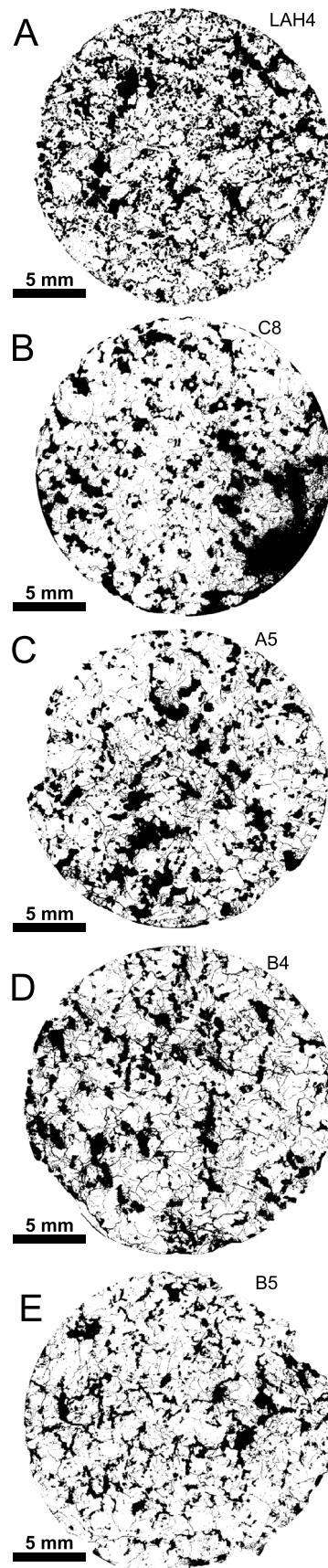
Darcy's law. All measurements were collected under ambient laboratory temperatures.

3.2.6. Uniaxial Compressive Strength Experiments

UCS tests were performed on two cylindrical samples (dried in a vacuum oven at 40°C for at least 24 h prior to experimentation) of similar porosity from each of the five blocks of andesite. The experiments were conducted in a uniaxial press under ambient laboratory conditions at a constant strain rate of $10^{-5}\,s^{-1}$ until failure. During deformation, axial strain, axial stress, and acoustic emissions (AEs) were continuously monitored. Further, the received AE signals were statistically analyzed using the analogous seismic b value [Aki, 1965] to characterize the nature of the microcracking in our samples.

3.2.7. Thermal Stressing Experiments

Thermal stressing experiments (to 450°C) were performed on cylindrical samples from each of the five blocks of andesite. During thermal stressing, we continuously recorded the furnace temperature, the temperature adjacent to the sample, axial stress, and the output of AE (to be used as a proxy for the initiation and propagation of thermal microcracks). Samples were taken to 450°C at a rate of 1°C/min, held at 450°C for 60 min, and then cooled back to the ambient laboratory temperature at a rate of 1°C/min. Each sample underwent a systematic physical property characterization (see above) before and after thermal stressing (except UCS, which was only determined following thermal stressing). Thin sections of the thermally stressed andesites were also prepared for microcrack density and anisotropy analysis (described in section 3.2.1).

4. Results

4.1. Rock Microstructural Analysis

The photomicrograph maps of each of the andesites (following binary conversion using ImageJ) are presented as Figure 3. As a first-order observation, the andesites are intensely and pervasively microcracked and contain many vesicles.

4.1.1. Microcrack Analyses

Quantitative stereological analysis of the andesites yielded average microcrack densities ranging between 35 and 45 mm^{-1} (Table 2). For an isotropic material (this is confirmed in section 4.2), the microcrack surface area per unit volume S_v can be inferred from the average of the linear intercept measurements in the two directions P [Underwood, 1970; Wong, 1985]:

$$S_v = 2P \qquad (1)$$

To visualize the spatial distribution of microcrack surface area density, contour plots of the stereological measurements in the 121 subregions are presented as Figure 4. In most cases, the microcracks appear to be largely homogeneously distributed. Values of S_v reach a maximum of about 90 mm^{-1} in all our samples. Figure 4 shows that, with the

Figure 3. Photomicrograph maps of each of the andesite samples using a transmitted fluorescent light source, converted to binary images using ImageJ. The photomicrographs are all taken in the XY plane. The black areas represent the porosity (microcracks and vesicles), and the white areas represent the groundmass/crystals.

Table 2. The Results of the Quantitative Microcrack Density and Anisotropy Analysis on Both As-Collected and Thermally Stressed Samples (450°C) of the Studied Andesites[a]

Sample	B5 As-Collected	B5 450°C	B4 As-Collected	B4 450°C	A5 As-Collected	A5 450°C	C8 As-Collected	C8 450°C	LAH4 As-Collected	LAH4 450°C
P (mm^{-1})	21.1	20.7	21.4	19.2	23.0	22.4	20.4	15.4	12.4	15.5
S_v (mm^{-1})	42.2	41.5	42.7	39.4	46.0	44.7	40.8	30.9	24.8	31.1
Average accuracy of log-log fit (%)	94.86	93.92	94.79	95.25	93.29	94.43	92.83	95.24	94.91	96.61
Anisotropy (with error in %)	1.102 (3.35)	1.055 (2.71)	1.168 (3.99)	1.134 (7.66)	1.002 (2.58)	1.034 (3.13)	1.069 (5.26)	1.046 (4.26)	1.059 (2.93)	1.029 (3.33)
Change in anisotropy (%)		−4.70		−3.40		3.20		−2.30		−3.00

[a]The first two rows correspond to the optical microscopic method, and the final three rows correspond to the AMOCADO toolbox method. P is the number of linear intercepts per millimeter, and S_v is the microcrack area (in square millimeter) per cubic millimeter. See Appendix A for further details.

exception of LAH4, all of the samples appear to contain approximately the same S_v (see also Table 2).

A detailed examination of the microcrack anisotropy (on the same images) was obtained with the AMOCADO toolbox. The quality of the log-log fits of all 180 fractal regressions for each degree of orientation is between 93% and 97% for each sample (Figure 5 and Table 2). These fits suggest a microcrack network with anisotropy values between 1.002 and 1.168.

4.1.2. Vesicle Analyses

Two-dimensional quantitative vesicle analysis of the andesites yielded average vesicle densities n_A ranging between 3.3 and 8.1 mm^{-2} (Table 3). While vesicle densities are similar for samples A5, B4, and C8 (all between 3.3 and 3.7 mm^{-2}), vesicle densities are much higher in samples B5 (6.1 mm^{-2}) and LAH4 (8.1 mm^{-2}). However, the vesicles of A5, C8, and LAH4 are much larger (average areas ranged between 0.033 and 0.049 mm^2) than those of B4 and B5 (between 0.015 and 0.023 mm^2). The shape of the vesicles in all of the andesites is very similar. Average circularity, aspect ratio, and roundness are about 0.75, 1:1.85, and 0.63, respectively (Table 3). The cumulative relative frequency distributions of the vesicle area and the equivalent vesicle radii for each of the andesites are given as Figure 6, while Figure 7 shows the density n_A of the distribution of vesicle radii for each andesite. We can observe that (1) most vesicle radii lie between 0.01 and 0.1 mm (although the range in size is large) and that (2) B5 contains a larger proportion of smaller vesicles than the other andesites.

4.2. Rock Physical and Mechanical Properties

The rock physical properties (density, porosity, elastic wave velocities, the ratio between P and S wave velocities (the V_p/V_s ratio), elastic moduli, and permeability) of the five andesites are summarized in Table 4.

The connected porosities of the andesites range from about 7 to about 27% (Table 4 and Figure 8). We note that, for these andesites, (1) there is a significant trapped porosity (average of about 2.2% and a maximum of about 4.5%, see Figure 8) and (2) the amount of trapped porosity, in general, increases as total porosity increases (Figure 8b).

Benchtop P and S wave velocities of dry samples range from 2.34 to 3.11 km s^{-1} and 1.09 to 1.45 km s^{-1}, respectively. Using these values, dynamic Young's moduli and Poisson's ratio were calculated to be between 6.4–13.3 GPa and 0.31–0.39, respectively, and V_p/V_s ratios between 1.9 and 2.4. The static Young's moduli (determined from the stress-strain curves), also given in Table 4, range between 8.6 and 31.8 GPa. In general, elastic wave velocities and Young's moduli decrease as porosity increases. The P wave velocity of all the samples greatly increases when the rocks are saturated with distilled water (Table 4). Our elastic wave velocity anisotropy measurements, measured on machined cubes of each material (see section 3.2.3 for details), are presented in Table 5. Our data show that, for each andesite, P and S wave velocities are very similar in the three orthogonal directions, i.e., that the andesites are, within error, seismically isotropic.

Water permeability is plotted as a function of connected water porosity (i. e., the porosity potentially useful for the flow of water) on a log-log scale in Figure 9. The data show that the water permeability of the measured
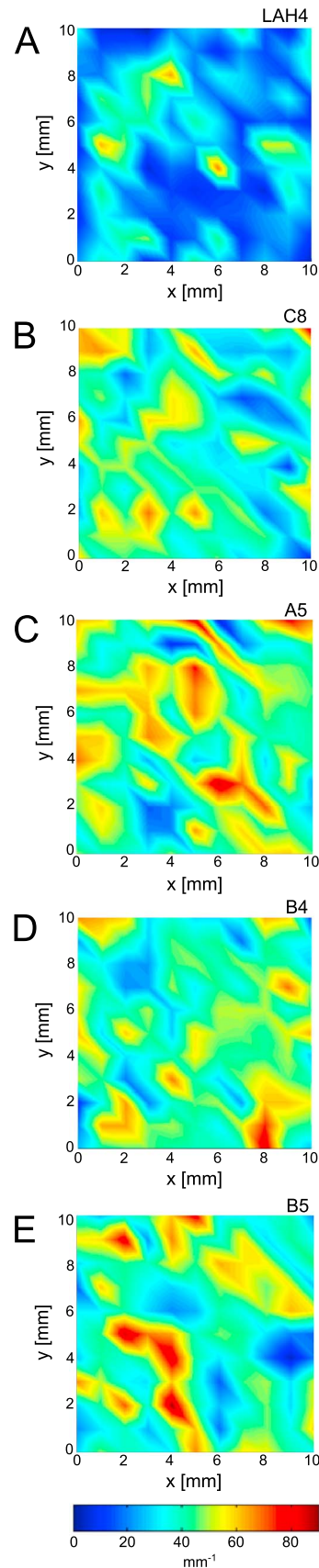
andesites varies between 3.6×10^{-17} and $7.0 \times 10^{-13}\,m^2$. Water permeability increases by about 4 orders of magnitude as porosity is increased by a factor of 3 (from 7 to 24%).

Representative stress-strain curves for each of the studied andesites are presented in Figure 10, together with the AE output during deformation and the evolution of the seismic b value. A synoptic plot, showing the stress-strain curves only, is given as Figure 11. The stress-strain curves of Figure 11 show that the andesites exhibit all of the stages of brittle failure in compression. The failure process of brittle rock in compression can be broken down into a number of stages [see *Brace et al.*, 1966; *Hoek and Bieniawski*, 1965; *Scholz*, 1968], characterized by the shape of the stress-strain curve. First, the stress-strain curve is convex; this behavior can be attributed to the closure of microcracks aligned subperpendicular to the direction of loading. Second, the stress-strain curve is very nearly linear as the rock deforms elastically (i.e., recoverable). Third, the stress-strain curve is concave (strain hardening) as the rock is taken to a stress where dilatant microcracks can initiate. Here the rock is deforming inelastically (i.e., nonrecoverably). Fourth, after the peak stress (i.e., the UCS of the material) is reached, there is an axial strain hardening stage before the rock succumbs to failure, usually marked by a substantial stress drop. Post peak behavior ensues, but its observation depends on the stiffness of the testing machine [see *Cook*, 1981]. We note that, although we do not offer complementary tensile strength measurements, the ratio of uniaxial compressive to tensile strength is close to 12 [*Jaeger et al.*, 2007]. In particular, we note that all of the samples show a substantial convex, initial portion. Sample failure is marked by a stress drop (indicating macroscopically brittle behavior) [see *Rutter*, 1986] and is usually accompanied by macroscopic axial splitting (this is especially true for the high-strength, low-porosity samples, see Figure 10). Figure 11 and Table 4 show that the andesites span a large range of UCS (from about 20 MPa for C8 to about 135 MPa for B4).

During deformation, the progression of stress-induced microcracking was monitored via the output of AEs. In our experiments, the rate of AE output increases as the rock approaches failure, and failure is accompanied by a large spike in AE output (Figure 10). The stress at the onset of dilatant microcracking (or C') [see *Brace et al.*, 1966] was inferred using the AE data (in detail, we selected the point where the AE starts its acceleration to failure). The stress at the onset of C' ranges between 3.5 and 38 MPa for the andesites of this study (Table 4). However, we suggest that radial strain measurements would help to better constrain C'. As failure approaches, we also observe a decrease in the seismic b value, from 1.4–2.0 to 0.4–0.6 at failure. In general, the lower porosity samples exhibit a larger b value range. In the experiments where failure was less abrupt, an increase in the b value occurs following the peak stress. Photomicrographs of the samples deformed to failure are shown in

Figure 4. The spatial distribution of the specific surface area of the microcracks in the andesite samples. Warm colors (yellow, orange, and red) are indicative of high microcrack surface areas, while cold colors (dark blue and blue) are indicative of low microcrack surface areas.
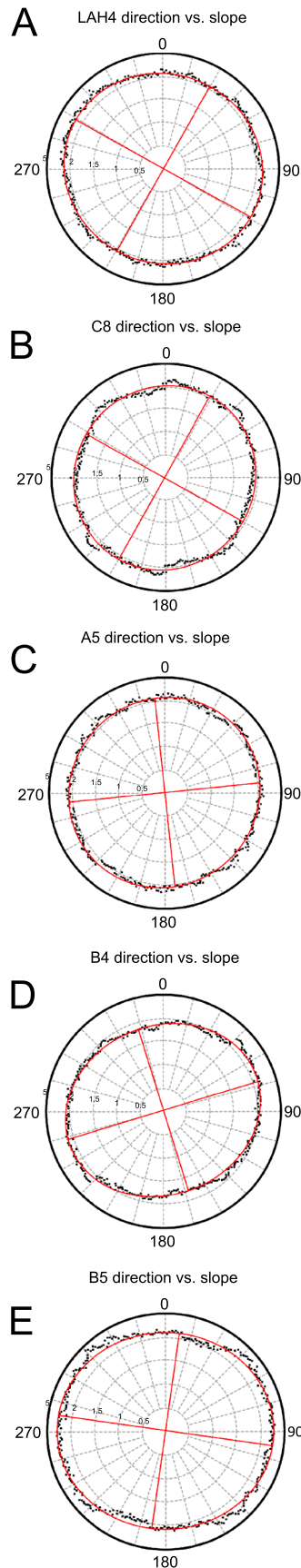
Figure 12. In general, we find that microcracking is significantly increased in all samples (when compared to the as-collected samples of Figure 2). We note (1) that the microcracks are aligned with the direction of the maximum principal stress (i.e., the Z direction) and (2) that they often emanate from vesicles (see inset in Figure 12a).

The relationship between rock physical properties (total porosity and P wave velocity) and rock mechanical properties (strength) is presented as Figure 13. We note that there is a strong correlation between UCS and total porosity (Figure 13a): UCS increases as total porosity decreases. Although the relationship with P wave velocity is less striking, there is still a general trend that UCS decreases as P wave velocity decreases (Figure 13b).

4.3. The Influence of Thermal Stressing

The results of the thermal stressing procedure (plots of AE output against time, together with the sample and furnace heating/cooling curves) for each rock type are presented as Figure 14. The results suggest that the AE response of the andesites to thermal stressing varies from sample to sample. Whereas B4 and B5 do not experience much thermal microcracking, LAH4 suffers thermal microcracking during the heating segment only, while C8 and A5 experience thermal microcracking during both the heating and cooling segments. We note that the initiation temperature for thermal microcracking also varies from sample to sample.

Quantitative microstructural analysis has revealed that there is no systematic change in two-dimensional microcrack surface area per unit volume and microcrack network anisotropy upon exposure to 450°C (Table 2). In fact, for the majority of the andesites, the S_v and the microcrack network anisotropy are marginally lower for the thermally stressed samples. We find that thermal stressing only slightly modifies the physical properties of the samples (Table 4). The connected porosities show a modest increase ($< 1\%$), while the V_p/V_s ratios, dry elastic wave velocities, dynamic Young's moduli, and dynamic Poisson's ratios all show a modest decrease (Table 4). We detect no variations (outside the natural variability of the materials) between the strength of the as-collected samples and those thermally stressed (Figure 15 and Table 4). Further, and due to the natural variability between samples, we cannot draw any firm conclusions as to whether thermal stressing has any impact on the onset of dilatancy or static Young's modulus (Table 4).

5. Discussion

5.1. Microstructure of Andesites From Volcán de Colima

Our study has shown that the andesites, representative of those that comprise the volcanic edifice at Volcán de Colima, are pervasively microcracked, as evidenced through microstructural observations and quantitative stereological techniques. Microcrack surface area per unit volume reach values as high as 90 mm^{-1}. To emphasize, the

Figure 5. Crack anisotropy analysis for the andesite samples using the modified Cantor-dust method included in the automated pattern quantification toolbox AMOCADO. Plots are the log-log fits. See Appendix A for details.

Table 3. The Results of the Quantitative Connected Vesicle Size, Shape, and Density Analysis on Each of the Studied Andesites Using ImageJ[a]

	B5	B4	A5	C8	LAH4
Total vesicle area (mm^2)	28.83	26.59	41.46	50.34	84.86
Vesicle porosity (%)	9.2	8.5	13.2	16.0	27.0
Vesicle density (mm^{-2})	6.13	3.69	3.26	3.27	8.13
Average area of a vesicle (mm^2)	0.0150	0.0229	0.0405	0.0490	0.0332
Maximum area of a vesicle (mm^2)	1.108	0.775	2.880	2.535	4.858
Minimum area of a vesicle (mm^2)	0.00019	0.00019	0.00020	0.00021	0.00019
Average equivalent radius (mm)	0.0690	0.0855	0.1136	0.1248	0.1028
Maximum equivalent radius (mm)	0.5938	0.4966	0.9574	0.8982	1.2434
Minimum equivalent radius (mm)	0.00777	0.00770	0.00798	0.00807	0.00780
Average circularity	0.79	0.75	0.76	0.74	0.76
Average aspect ratio	1:1.81	1:1.94	1:1.84	1:1.89	1:1.80
Average roundness	0.65	0.60	0.62	0.62	0.64

[a]See Appendix A for further details.

maximum S_v (using the same method) obtained for a sample of Darley Dale sandstone (porosity = 13%) containing a shear fault was only 40 mm^{-1} [*Wu et al.*, 2000]. Further evidence for high microcrack densities is provided by the pronounced convex shape of the initial portion of the stress-strain curves, generally explained as the closure of subperpendicular microcracks [e.g., *David et al.*, 2011]. Microcrack densities are slightly lower in sample LAH4 (Figure 4), although this could be a product of its high vesicle size and density (Table 3). Microcrack network anisotropy values (that ranged between 1.002 and 1.168), and our *P* wave anisotropy analysis, suggest that the microcrack network is isotropic (for example, anisotropies of 1.353 have been reported for deformed andesitic lavas) [*Lavallée et al.*, 2008]. The isotropic nature of the microcrack network suggests that the microcracking may be of thermal origin. Thermal microcrack networks are often isotropic (for initially isotropic materials), while mechanical microcracking normally produces an anisotropic crack network [see *David et al.*, 1999]. We therefore propose that the pervasive microcrack network is the result of the relatively rapid cooling history associated with their eruptive origin. A similar conclusion was drawn in reference to a highly microcracked basaltic lava from Mount Etna [*Vinciguerra et al.*, 2005]. Despite the large natural variability in connected water porosity (7 to 27%), the microcrack surface area densities of the andesites are remarkably similar (with the exception of LAH4). This implies (1) that the cooling histories of these andesites were similar and (2) that the differences in porosities must largely be due to a variable vesicle density and/or vesicle size. Indeed, we note that the two-dimensional vesicle porosity or vesicularity (Table 3) is very close to the average connected water porosities listed in Table 4. This is largely to be expected, since the extremely low aspect ratio of microcracks makes them inefficient at generating porosity (although their effect on physical and mechanical properties can be significant, see section 5.2).
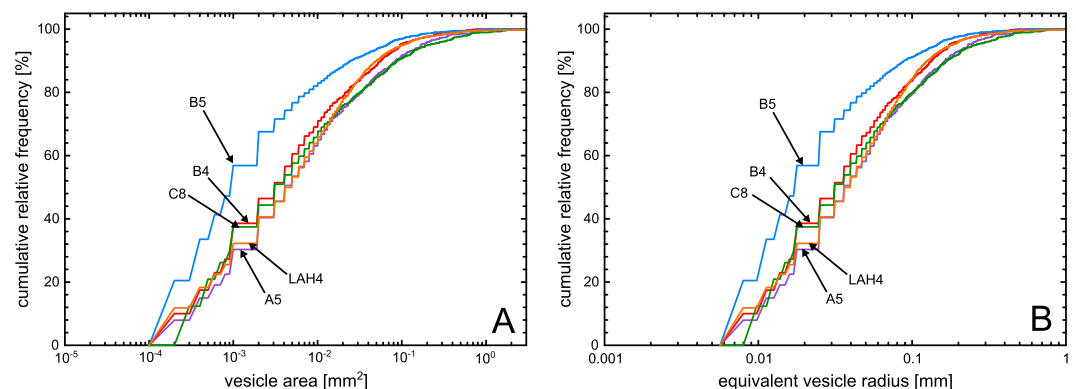
Figure 6. Cumulative relative frequencies of (a) vesicle area and (b) equivalent vesicle radius for each of the andesites. Blue–B5; red–B4; green–C8; orange–LAH4; purple–A5.
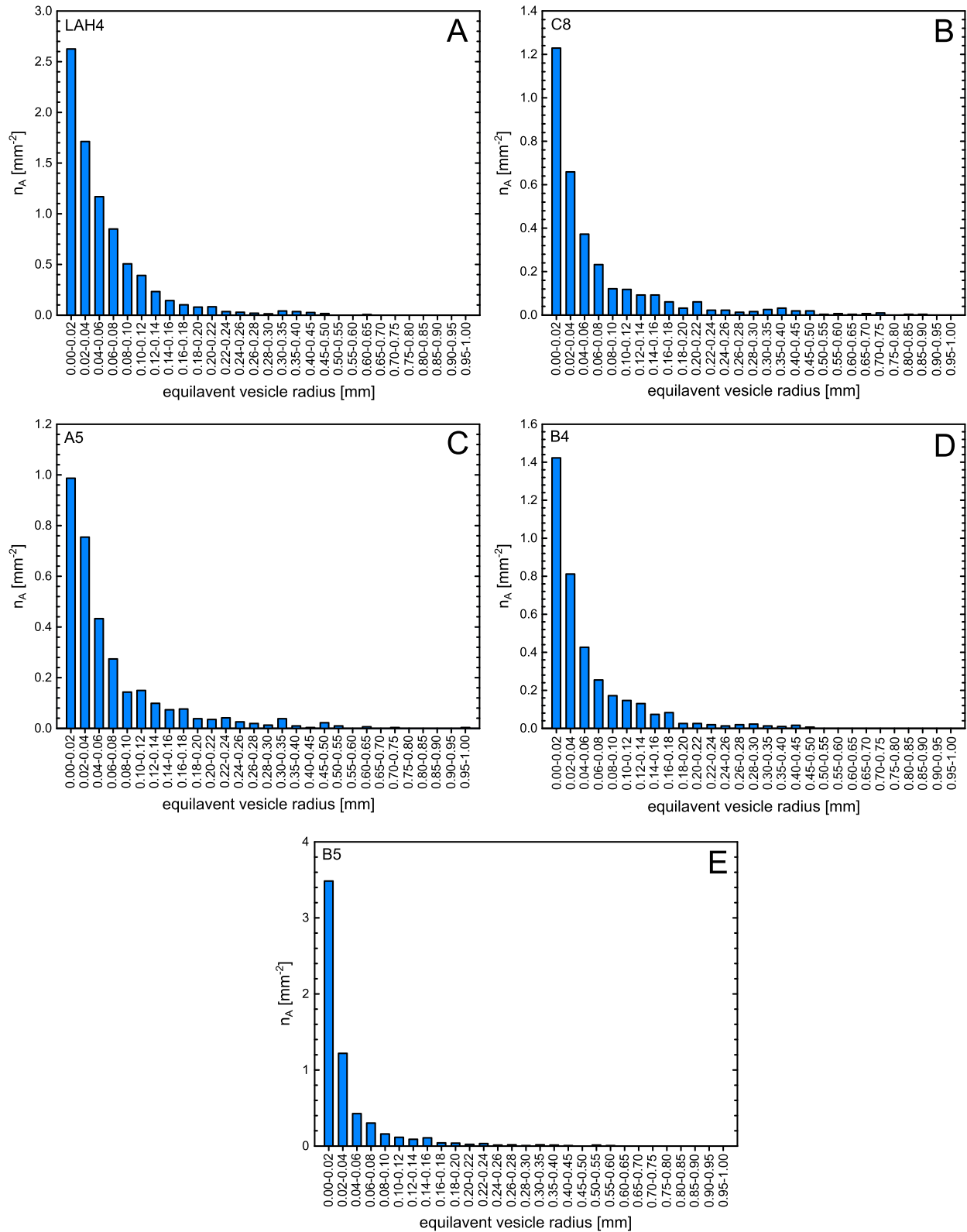
Figure 7. Equivalent vesicle radius densities for each of the andesites. The histogram bars represent 0.02 mm intervals up to 0.30 mm; after 0.30 mm the interval increases to 0.05 mm. Note that, to show the full vesicle radius distribution for each andesite, the y axes are not always identical.

Table 4. Average Physical and Mechanical Properties of the Andesites Investigated in This Study: Bulk Sample Density, Connected Water Porosity, Elastic Wave Velocities, Water Permeability, Dynamic Young's Modulus and Poisson's Ratio, Static Young's Modulus, Uniaxial Compressive Strength (UCS), and the Stress at Which C' Was Observed in Our Acoustic Emission Data (C' Is Not an Average, It Is Just the Data From Figure 10)[a]

| Sample		B5 As-Collected	B5 450°C	B4 As-Collected	B4 450°C	A5 As-Collected	A5 450°C	C8 As-Collected	C8 450°C	LAH4 As-Collected	LAH4 450°C
Bulk sample density (g/cm³)	Dry	2.48		2.48		2.40		2.13		1.96	
	Water-saturated	2.53		2.50		2.48		2.30		2.21	
Connected water porosity (%)		7.9	8.1	8.6	8.9	11.2	11.6	17.6	17.7	25.0	25.2
Total porosity (%)		12.1	-	14.0	-	14.3	-	23.8	-	29.8	-
P wave velocity (km s⁻¹)	Dry	3.11	2.71	2.69	2.52	3.11	2.85	2.56	2.31	2.34	1.89
	Water-saturated	4.84	4.67	4.98	4.96	4.97	4.78	4.30	4.31	3.91	4.01
S wave velocity (km s⁻¹)	Dry	1.30	1.23	1.42	1.33	1.45	1.34	1.24	1.21	1.09	1.00
V_p/V_s ratio	Dry	2.39	2.19	1.90	1.77	2.21	2.15	2.07	1.90	2.15	1.89
Dynamic Young's modulus (GPa)	Dry	11.8	10.4	13.0	11.3	13.3	11.5	8.8	8.2	6.4	5.1
Dynamic Poisson's ratio	Dry	0.39	0.36	0.31	0.26	0.33	0.34	0.35	0.30	0.36	0.30
Static Young's modulus (GPa)	Dry	21.6[b]	23.1[b]	31.8[b]	35.6[b]	23.6[b]	23.8[b]	8.6[b]	9.9[b]	9.2[b]	11.6[b]
Water permeability (m²) at Pc = 2 MPa	Water-saturated	1.62 × 10⁻¹⁶	-	8.64 × 10⁻¹⁷	-	2.55 × 10⁻¹⁶	-	1.08 × 10⁻¹²	-	1.45 × 10⁻¹²	-
Uniaxial compressive strength (MPa)	Dry	87.5	86.3	124.0	128.8	74.0	88.1	23.9	30.5	29.9	35.4
C' (MPa)	Dry	38.0	28.5	19.2	19.6	9.8	14.0	3.5	5.8	7.5	12.4

[a]Data for both as-collected and thermally stressed (450°C) samples are shown. "Dry" and "water-saturated" refer to measurements on samples dried in a vacuum oven at 40°C and samples saturated with distilled water in a vacuum, respectively. Elastic wave velocities (and therefore the resultant dynamic elastic moduli), UCS, permeability, and static Young's modulus have been determined in the Z direction. The physical property characterization was performed under the lowest possible stress conditions (to avoid damaging the samples). The bulk densities and porosities were measured at ambient pressure, the elastic wave velocities and dynamic moduli were determined using an axial stress of 1.9 MPa, and permeability was measured at a confining pressure of 2 MPa. The static Young's moduli were measured at axial stresses between 15 and 100 MPa, depending on the strength of the sample. Therefore, direct comparison with the dynamic Young's moduli is ill-advised (see text for details).
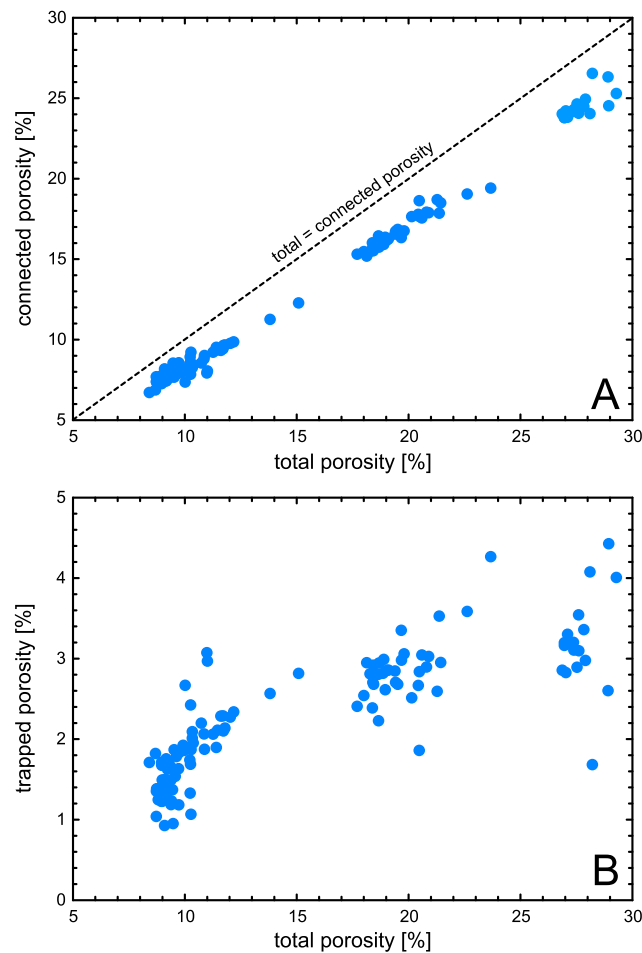
[b]The static Young's moduli were measured at axial stresses between 15 and 100 MPa, depending on the strength of the sample.

Figure 8. (a) The connected porosity as a function of the total porosity for the studied andesites (dashed line is the 1:1 line). (b) The trapped porosity as a function of the total porosity for the studied andesites.

Although our study has highlighted that andesites from Volcán de Colima contain high vesicle densities, a distinguishing feature of these materials, when compared with nonvolcanic rocks, is the extremely large range of vesicle or pore sizes (radii between 0.008 and 1.24 mm). For nonvolcanic rocks, this range of pore size is largely unprecedented. Similar analyses on limestones (that analyze pores with radii larger than 0.003 mm) showed that the pores have radii between 0.003 and 0.015 mm [*Vajdova et al.*, 2010] and 0.003 and 0.25 mm [*Vajdova et al.*, 2012]. However, while limestones typically contain a significant micropore contribution (i.e., below the resolution of the analyses), we note that our two-dimensional porosities (Table 3) were very similar to those calculated using the triple-weight water saturation technique (Table 4), suggesting that, in the measurements presented in this study, we captured most, if not all, of the vesicularity. For volcanic rocks, the range of vesicle size can range from the submicron scale to the meter scale [e.g., *Walker*, 1989; *Shea et al.*, 2010, and references therein]. While a detailed textural description of the vesicles is beyond the scope of this study (our blocks were collected from a block-and-ash flow, lahar flow, and lava deposits), one interesting aspect of the vesicles is that they are not circular (average vesicle circularity for the andesites was between 0.74 and 0.79, Table 3). Departure from noncircularity could be the result of deformation within the conduit, although we note that there is no preferred vesicle shape orientation (Figure 2).

5.2. Physical and Mechanical Properties of Andesites From Volcán de Colima

The complex microstructure (pervasive microcrack network, large vesicle size, and high vesicle density) of these andesites severely impacts their rock physical and mechanical properties.

5.2.1. Density and Porosity

Bulk sample densities are low and porosities are high as a result of the combined presence of microcracks and vesicles. The complexity of these andesites is emphasized by their substantial trapped porosities, although this is not unexpected for volcanic rocks [e.g., *Bernard et al.*, 2007]. We note that while such trapped porosity could play an important role for some physical and mechanical properties (elastic velocities, strength, and elastic moduli) others, such as water permeability, rely only on the connected water porosity.

5.2.2. Elastic Wave Velocities

The andesites have very low elastic wave velocities (*P* and *S* wave velocities range from 2.34 to 3.11 km s^{-1} and 1.09 to 1.45 km s^{-1}, respectively). For comparison, the *P* and *S* wave velocities of an aphyric basalt from Seljadur (Iceland; porosity = 4.5%) are 5.43 and 3.03 km s^{-1}, respectively [*Vinciguerra et al.*, 2005]. The elastic wave velocities are low for these andesites because they are very sensitive to microcrack porosity [e.g., see *O'Connell and Budiansky*, 1974], much more so than vesicle porosity. For instance, the *P* wave velocity of the aforementioned basalt from Iceland can be reduced by almost 60% by thermal microcracks alone

Table 5. Elastic Wave Velocities in the X, Y, and Z Directions for All of the Studied Andesites

	B5		B4		A5		C8		LAH4	
	P Wave Velocity (km s^{-1})	S Wave Velocity (km s^{-1})	P Wave Velocity (km s^{-1})	S Wave Velocity (km s^{-1})	P Wave Velocity (km s^{-1})	S Wave Velocity (km s^{-1})	P Wave Velocity (km s^{-1})	S Wave Velocity (km s^{-1})	P Wave Velocity (km s^{-1})	S Wave Velocity (km s^{-1})
X	2.69	1.23	2.62	1.40	2.43	1.31	2.39	1.23	2.41	1.15
Y	2.81	1.25	2.70	1.42	2.34	1.40	2.45	1.22	2.43	1.20
Z	2.73	1.26	2.59	1.35	2.38	1.47	2.46	1.19	2.46	1.19
V_{max}/V_{min}	1.04	1.02	1.04	1.05	1.04	1.12	1.03	1.03	1.02	1.04

[*Vinciguerra et al.*, 2005]. We also find that the *P* wave velocity of the andesites increased significantly upon water saturation (*P* waves travel faster through water than air). This corroborates with the fact that the microcracks are a significant contributor to the low elastic wave velocities, as, upon their saturation, *P* wave velocity would be expected to increase significantly (for the andesites of this study, *P* wave velocities were increased from the above-quoted values to between 3.91 and 4.97 km s^{-1}, see Table 4).

5.2.3. Young's Modulus

The stiffness (Young's modulus) of these andesites is very low (dynamic and static Young's moduli ranged between 6.38 and 13.34 GPa and 9.05 and 34.17 GPa, respectively). For comparison, the static Young's modulus of an aphyric basalt from Iceland was measured to be 66.5 GPa [*Heap et al.*, 2010]. It has long been established that static and dynamic elastic moduli differ, due to the large difference in frequency [e.g., *Simmons and Brace*, 1965; *Cheng and Johnston*, 1981; *Eissa and Kazi*, 1989; *Ciccotti et al.*, 2000; *Ciccotti and Mulargia*, 2004]. However, dynamic moduli are commonly much higher than static moduli, particularly when the rock is highly fractured [e.g., *Gudmundsson*, 2011]. The opposite appears to be true for the andesites of this study (under the implemented experimental conditions, see Table 4). We note, however, that the moduli were calculated at different axial stresses. The dynamic moduli were calculated from elastic wave velocities measured at 1.9 MPa whereas the static moduli were calculated using stress-strain data between 15 and 100 MPa, depending on the stress level at which the slope of the stress-strain curve is at a maximum. This may preclude direct comparison. In an attempt to resolve this issue, we performed a pilot experiment in which we measured the static (tangent) and dynamic Young's modulus at the same axial stress (Figure 16). We note that both moduli increase with increasing axial stress (although the static values below about 25 MPa are, as per our definition, not strictly static elastic moduli). Figure 16 aptly shows that (1) when the moduli are compared at the same level of stress, the dynamic modulus is always significantly higher than the static modulus (as reported by previous studies on a variety of rock types) [see *Gudmundsson*, 2011] and (2) the dynamic modulus measured at 1.9 MPa (the stress used for the physical property characterization, see Table 4) is lower than the static modulus measured using the method outlined in Appendix A (in this case, 30 MPa). These observations can be explained by the progressive closure of microcracks during stressing. These results clearly demonstrate that for pervasively microcracked materials such as the andesites of this study, static and dynamic Young's moduli should only be compared when measured at the same stress.

5.2.4. Permeability

The water permeability of these andesites is high (up to ~10^{-13} m^2) and increases as connected water porosity increases (Figure 9). Water permeability measurements on andesites from Volcán de Colima have been previously measured to be within the range of ~10^{-13} to ~10^{-16} m^2 [*Kolzenburg et al.*, 2012; *Kendrick et al.*, 2013]. As a comparison, low-porosity (4.5%) aphyric basalts can have a water permeability as low as ~10^{-21} to ~10^{-19} m^2 [*Vinciguerra et al.*, 2005; *Nara et al.*, 2011]. The permeability of volcanic rocks has been shown to display an extremely wide range, owing to the vast assortment of microstructures. For example, the gas permeability of porous (35–94%) pumices have been measured to be in the range of ~10^{-13} to ~10^{-10} m^2 [*Klug and Cashman*,
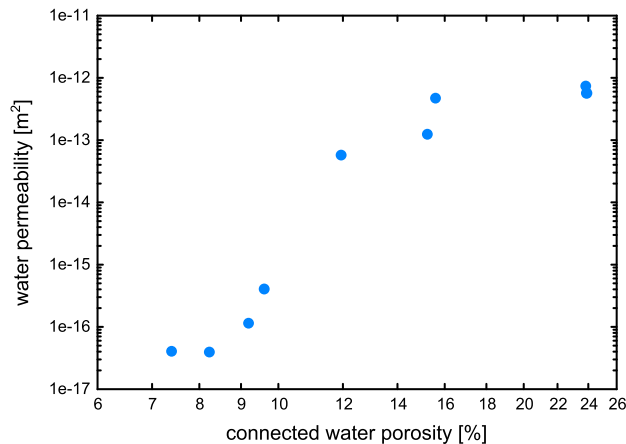
Figure 9. The water (distilled water) permeability of andesites from Volcán de Colima as a function of connected water porosity, plotted on log-log axes.

1996; *Rust and Cashman*, 2004; *Mueller et al.*, 2005; *Wright et al.*, 2006; *Bernard et al.*, 2007; *Wright and Cashman*, 2013]. However, the gas permeability of effusive volcanic rocks demonstrate a much wider range: ~10^{-17} to ~10^{-11} m^2 [*Saar and Manga*, 1999; *Rust and Cashman*, 2004; *Mueller et al.*, 2005; *Bernard et al.*, 2007]. A compilation of data on both explosive and effusive rocks is presented in *Wright et al.* [2009]. Several of these studies have described their data using a single power law; however, a close examination of our data reveals that there are two families with different permeability-porosity power law exponents (Figure 19a). The low-porosity (7–12%) family has an exponent of about 15.9 and the high-porosity (15–24%) family has an exponent of about 3.2. The crossover porosity, where the two trends meet, is in the range of 11–14%. The permeability-porosity relationship of the andesites is similar to that of Fontainebleau sandstone [*Bourbié and Zinszner*, 1985]. The power law exponent of Fontainebleau sandstone was increased from 3.05 to 7.33 below a crossover porosity of about 9%. The existence of a crossover porosity for rocks from Volcán de Colima is emphasized when one compiles the available published data (Figure 19c). For volcanic rocks, it is clear that a simple relationship between porosity and permeability simply does not exist. To emphasize, two volcanic rocks (porosities as different as 3 and 85%) can both have permeabilities on the order of ~10^{-12} m^2 (see compilation in *Mueller et al.* [2008]). The permeability of andesites from Volcán de Colima is discussed further in sections 5.3.2 and 5.5.

5.2.5. Uniaxial Compressive Strength

The UCS of the studied andesites, in comparison to other rocks, is low. It must be noted that while typical values of UCS for low-porosity (< 1%) granitic rocks are about 205–240 MPa [e.g., *Heap and Faulkner*, 2008; *Blake et al.*, 2013], the UCS of volcanic rocks can be extremely variable (see the examples in Table 6), a result of their varied composition and microstructure. We note that the strengths of the andesites of this study, in comparison to those volcanic rocks in Table 6, are still low (with the exception of the highly porous tuffs). This is a result of their highly microcracked and porous nature. We also note that we observe a decrease in b value as sample failure is approached (Figure 10). A decrease in b value indicates that the proportion of large cracking events increased as failure was approached (as observed previously for other volcanic rocks) [see *Smith et al.*, 2009]. The reincrease following sample failure is likely to represent smaller-scale microcracking occurring on the newly formed macroscopic fractures.

The relationship between physical and mechanical properties of the andesites is illustrated in Figure 13. It is well known in experimental rock deformation that the strength of rock decreases as porosity increases [*Zoback*, 2010; *Baud et al.*, 2014]. A conclusion also resolved in experimental volcanology [*Spieler et al.*, 2004], although the relative contributions from microcrack porosity and vesicularity remains unconstrained. This premise entails that rock strength should decrease with increasing preexisting "damage" (a combination of microcracks and pores/vesicles). The relationship between P wave velocity and UCS is more clouded (Figure 13b); although there is a general trend where UCS decreases as P wave velocity decreases. Similar cloudy P wave velocity-UCS relationships have also been observed for sedimentary rocks [*Chang et al.*, 2006]. Microcrack density and P wave velocity are intrinsically connected (for instance, it is possible to invert ultrasonic velocities to calculate microcrack densities) [see *Schubnel et al.*, 2006]. Therefore, if one were to increase microcrack porosity in a material without vesicles, the relationship between UCS and P wave velocity should be more clear-cut. In the case of andesites from Volcán de Colima (Figure 13b), it is therefore clear that microcracks alone are not controlling the reduction in strength. This is corroborated by the fact that (1) microcrack densities do not differ greatly between the andesites (Table 2) and (2) failure in compression may be heavily influenced by vesicle-emanating microcracking (Figure 12a, see also the next section).
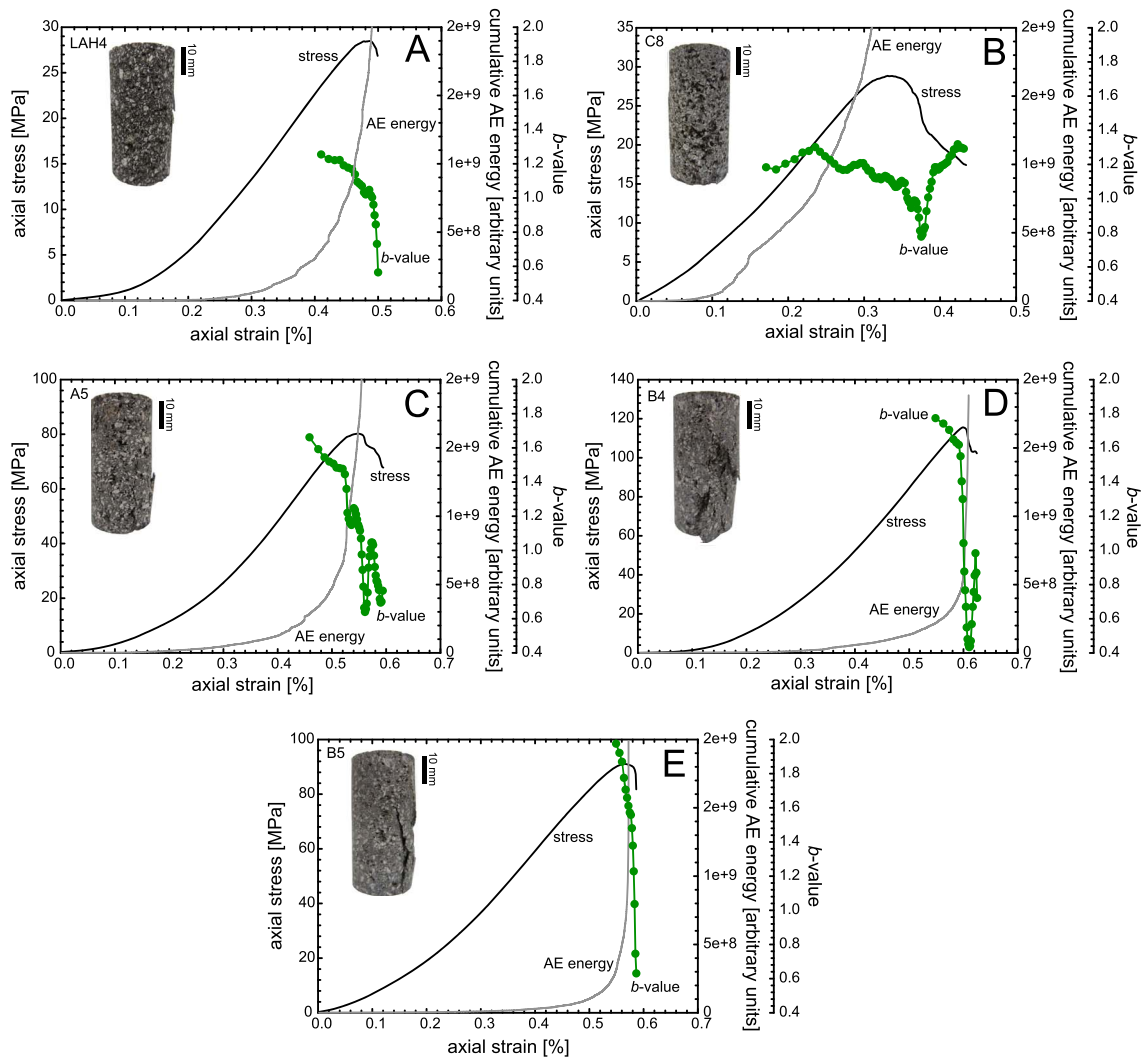
HEAP ET AL.   2939

Figure 10. Stress-strain curves for the andesite samples from constant strain rate ($1.0 \times 10^{-5}\,\mathrm{s}^{-1}$) uniaxial deformation experiments. Data are plotted with the cumulative acoustic emission "energy" and the evolution of the seismic b value. Photographs of the post failure samples are also included on the graphs. Note that the axial stress and axial strain axes are not always identical.

5.3. Application of Micromechanical and Geometrical Permeability Models

While extracting empirical relationships between rock properties may appear inviting (e.g., the relationships presented in Figures 9 and 13), we advise extreme caution based on their lack of physical basis (the parameters are not easily related to independently measurable quantities). For volcanic rocks this is especially true, since their genesis and therefore microstructure can vary significantly. Micromechanical and geometrical permeability models hold the potential to be better constrained as their parameters often have a clear physical meaning. In this section, we perform a pilot study to test the applicability of micromechanical modeling (pore- and wing-crack modeling) [see *Sammis and Ashby*, 1986; *Ashby and Sammis*, 1990] and geometrical permeability modeling (using the Kozeny-Carman equation) [see *Kozeny*, 1927; *Carman*, 1937; *Guéguen and Palciauskas*, 1994]. In fact, the andesites of this study represent the ideal case to test such models since (1) their chemical composition is identical (Table 1) and (2) they are all products of the same volcano.

5.3.1. Micromechanical Modeling: Pore- and Wing-Crack Modeling

Micromechanical modeling can provide useful insights in the mechanics of compressive failure in brittle rock [*Wong and Baud*, 2012]. However, they have rarely been applied to volcanic rocks [e.g., *Zhu et al.*, 2011; *Vasseur et al.*, 2013]. In most cases, the microstructure can be idealized in terms of an inclusion model with
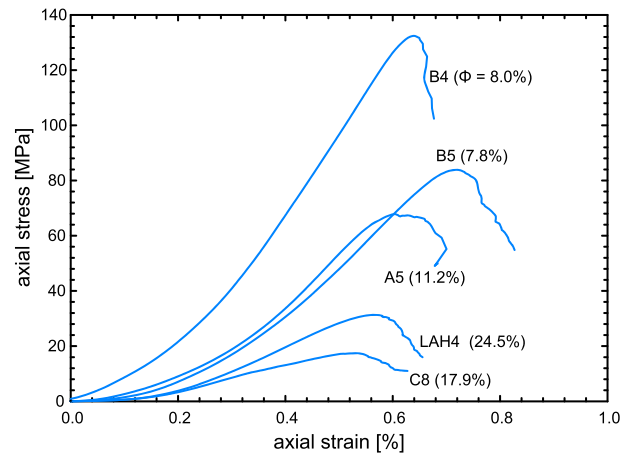
Figure 11. Synopsis plot showing representative stress-strain curves for all the andesite blocks. The porosity of each sample is provided next to the relevant curve.

microcracks or equant vesicles embedded in an elastic continuum. The preexisting microcracks or vesicles act as stress concentrators for the initiation of extensile cracks which then propagate through the porous medium. The mechanical behavior is controlled by the evolution of such damage. The initiation and propagation of these stress-induced microcracks can be analyzed using linear elastic fracture mechanics [*Wong and Baud*, 2012]. Since the andesite samples contain both microcracks and vesicles (see Figures 2b and 2c), we performed a pilot study to test the applicability of two micromechanical models: one that considers only vesicles (the pore-emanated crack model of *Sammis and Ashby* [1986]) and one that considers only microcracks (the sliding wing-crack model of *Ashby and Sammis* [1990]). If the experimental data can be adequately described by one of these models, and not the other, then we can glean information regarding
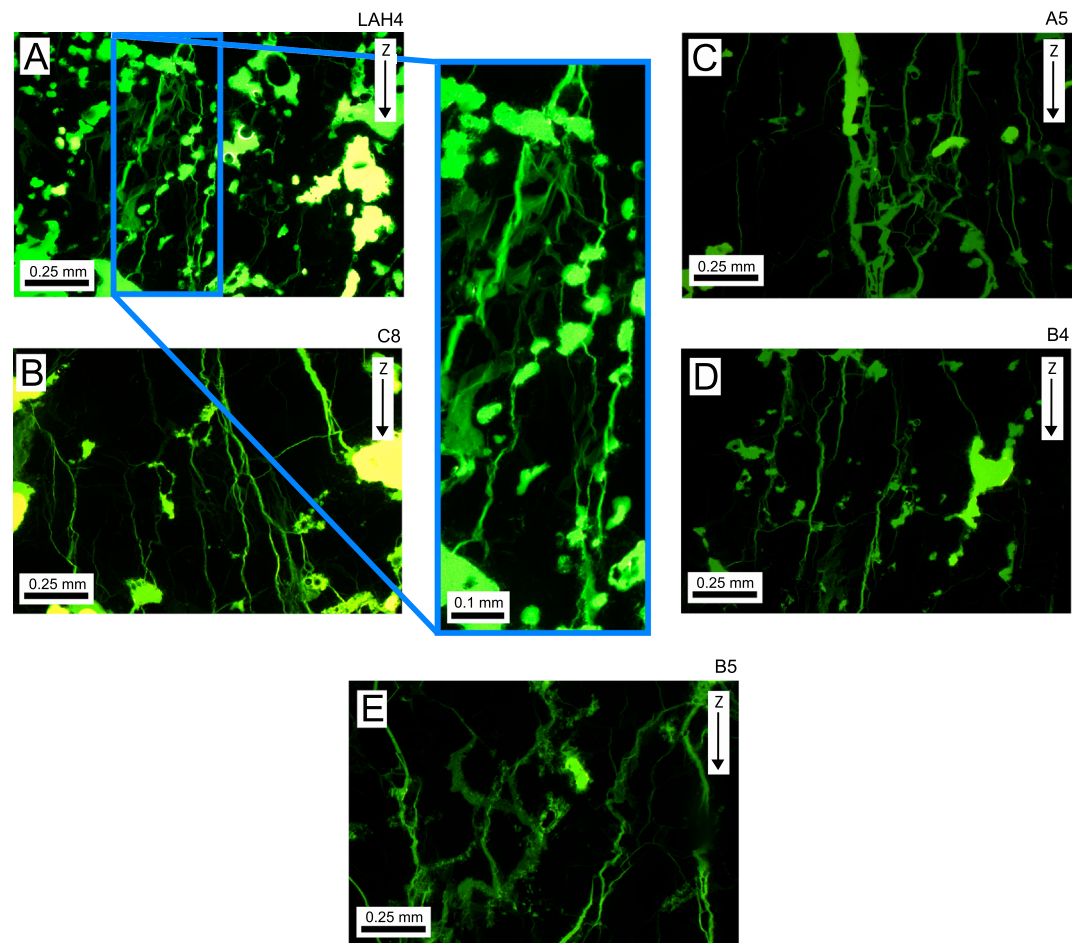

Figure 12. (a–e) Photomicrographs of the andesite samples deformed to failure during uniaxial compression tests, using a transmitted fluorescent light source. The inset in Figure 12a zooms in on vesicle-emanated microcracking. The light green areas represent the porosity (microcracks and vesicles), and the dark green/black areas represent the solid rock (groundmass/crystals).
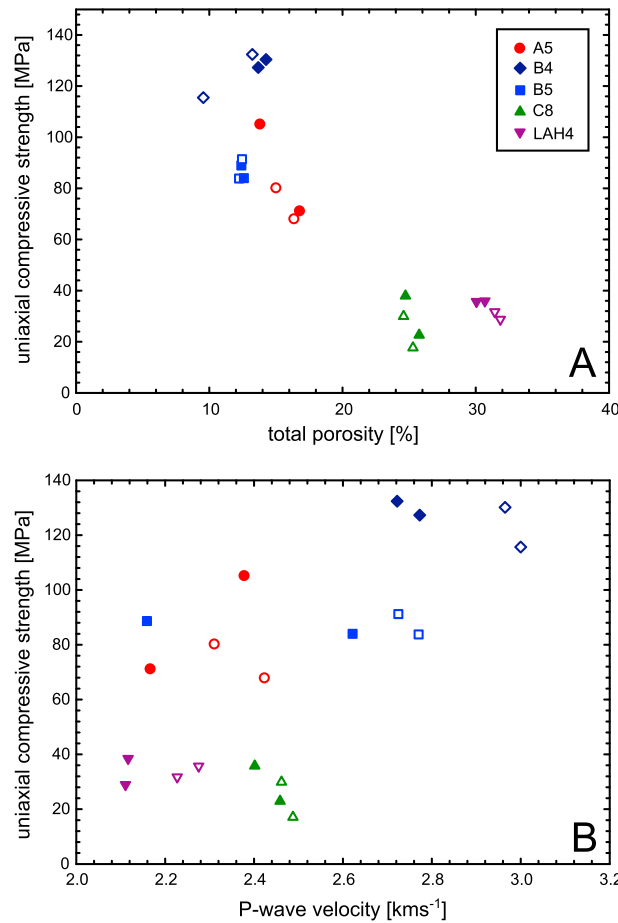
Figure 13. The relationship between uniaxial compressive strength and (a) total porosity and (b) P wave velocity.

the control of the microcracks and the vesicles on the strength of these materials in compression. Unfortunately, a model that combines both elements is yet to be formulated.

The pore-emanated crack model of *Sammis and Ashby* [1986] describes a two-dimensional elastic medium populated by circular holes of uniform radius *r*. As the applied stress (*σ*) increases, cracks emanate from the circular holes (parallel to the direction of the applied stress) when the stress at the tip of a small crack on the circular surface reaches a critical value (K_{IC}, the critical stress intensity factor or "fracture toughness"). The newly formed cracks propagate to a distance *l* in the direction of the maximum principal stress. Once the cracks are long enough, they can interact, thus increasing the local tensile stress intensity. Eventually, they coalesce and conspire to induce the macroscopic failure of the elastic medium (Figures 17a–17c). In the case of uniaxial compression, *Zhu et al.* [2010] derived an analytical approximation of *Sammis and Ashby*'s [1986] pore-emanated crack model to estimate UCS ($σ_p$, the peak stress) as a function of the bulk sample porosity (*φ*):

$$\sigma_p = \frac{1.325}{\varphi^{0.414}} \frac{K_{IC}}{\sqrt{\pi r}} \qquad (2)$$

Alternatively, the sliding wing-crack model (Figures 17d–17f) considers the tensile stress concentrators to be the tips of inclined (45°) preexisting cracks (of length 2*c*) undergoing frictional slip [*Horii and Nemat-Nasser*, 1986; *Ashby and Sammis*, 1990; *Kemeny and Cook*, 1991]. Similar to the pore-emanating crack model, the inclined cracks populate a two-dimensional elastic medium. However, the frictional resistance of the closed crack must first be overcome, by shear traction induced by an applied stress, before the wing cracks can propagate (parallel to the direction of the applied stress). As before, the wing cracks cannot propagate until K_{IC} is exceeded. In the case of uniaxial compression, another analytical estimate was also inferred for $σ_p$ [*Baud et al.*, 2014]:

$$\sigma_p = \frac{1.346}{\sqrt{1+\mu^2}-\mu} \frac{K_{IC}}{\sqrt{\pi c}} D_0^{-0.256} \qquad (3)$$

where *μ* is the friction coefficient of the sliding crack and D_0 is an initial damage (a function of the angle of the initial microcrack with respect to the maximum principal stress and the initial number of sliding cracks per unit area) [*Ashby and Sammis*, 1990]. It should also be noted that in both models, a comparable term (the ratio of the fracture toughness over the square root of the default size) appears.

The predictions of the pore-emanated crack model are presented on a plot of total porosity against UCS in Figure 18. Our experimental data could not be fitted using a single value of $\frac{K_{IC}}{\sqrt{\pi r}}$ but can be bracketed between two theoretical curves where $\frac{K_{IC}}{\sqrt{\pi r}}$ equals 7 and 44 MPa. In detail, the data can be divided into two groups (excluding the much stronger B4 samples): (1) high-porosity end-members (LAH4 and C8) that can be bracketed between theoretical curves where $\frac{K_{IC}}{\sqrt{\pi r}}$ equals about 7 and 17 MPa and (2) low-porosity end-
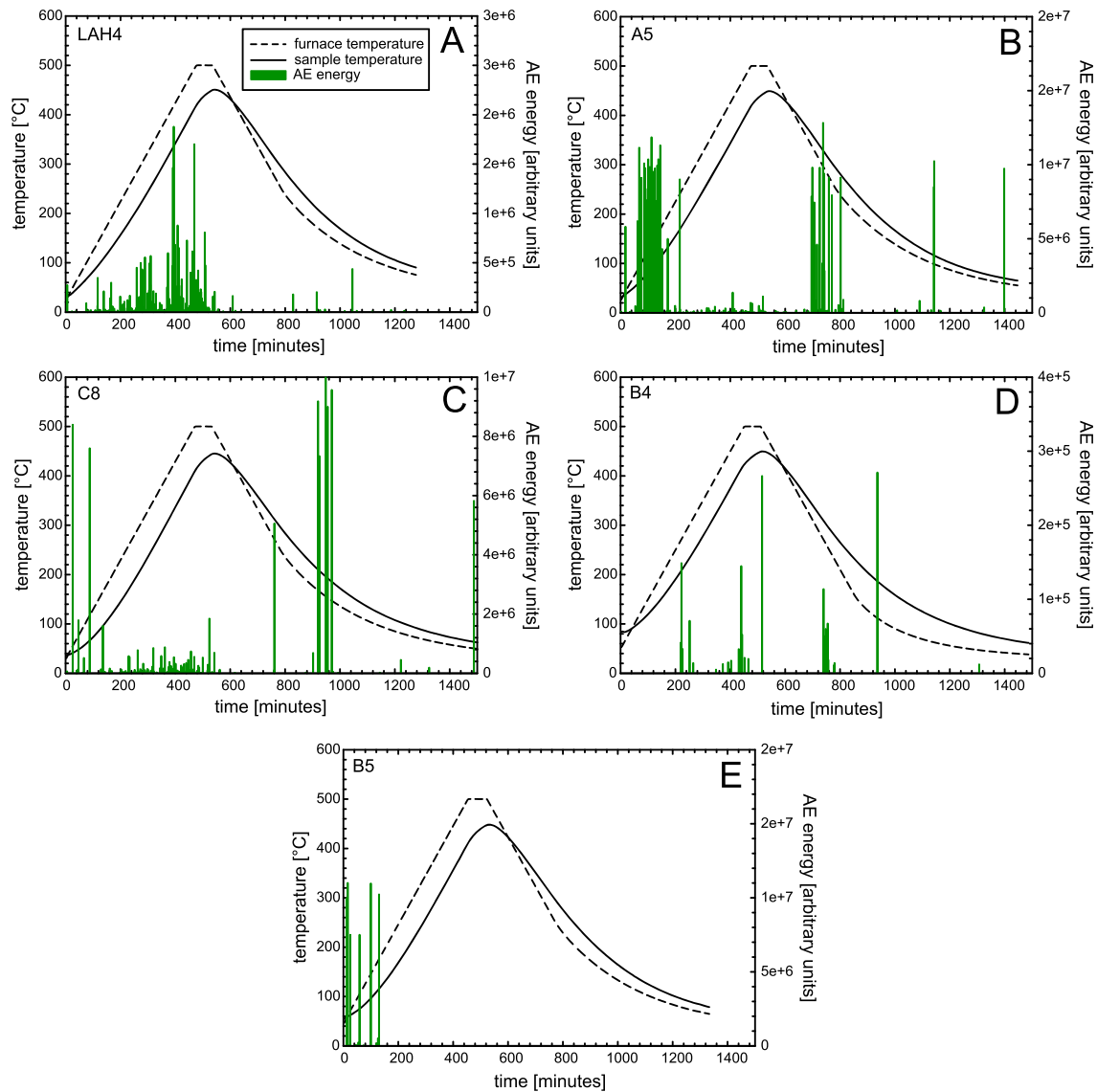
Figure 14. Acoustic emission energy (the area under the received AE waveform envelope) in 1 min bins, sample temperature, and furnace temperature against time for each of the studied andesites during our thermal stressing experiments. Note that the acoustic emission energy axes are not the same between samples.

members (A5 and B5, excluding the A5 sample with a UCS of 105.1 MPa) that can be bracketed between curves where $\frac{K_{IC}}{\sqrt{\pi r}}$ equals about 24 and 29 MPa. If we assume a fixed value r (using the average equivalent vesicle radius for each andesite, Table 3) we can estimate the range of K_{IC} for these rocks, and likewise, if we assume a fixed value for K_{IC} we can investigate the range of r. The inferred values of K_{IC} range from 0.40 to 2.28 MPa m$^{-1/2}$; we obtained low values for the high-porosity andesites ($K_{IC} = 0.40$–1.06 MPa m$^{-1/2}$) and high values for the low-porosity andesites ($K_{IC} = 1.12$–2.28 MPa m$^{-1/2}$). Previous studies on andesite reported a value of K_{IC} of about 1.5–2.0 MPa m$^{-1/2}$ [*Ouchterlony*, 1990; *Obara et al.*, 1992; *Keles and Tutluoglu*, 2011; *Nara et al.*, 2012]. The values inferred for the low-porosity andesites are therefore in qualitative agreement with these data. However, the inferred values of K_{IC} for the high-porosity andesites are significantly lower than those previously reported in the literature. This suggests that, beyond a certain porosity, the larger vesicles may play a more dominant role in the failure process than the average vesicle size. To conclude, although the pore-crack model seems to capture part of the phenomenology of brittle failure in the andesites (excluding the B4 samples), new laboratory experiments should now be performed to constrain K_{IC} and check the quantitative prediction of this model.
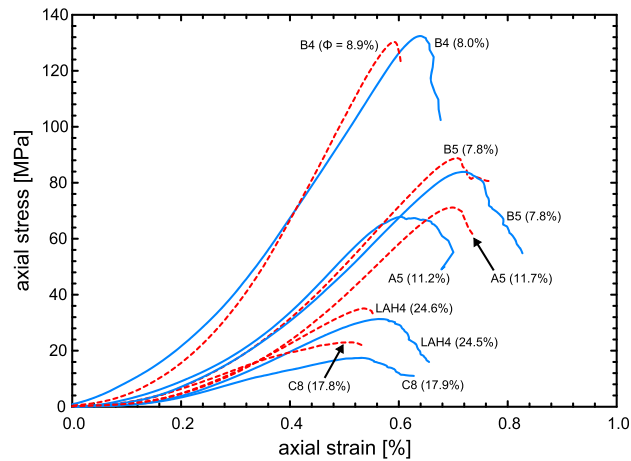
Figure 15. Synopsis plot showing representative stress-strain curves for all the as-collected andesites (the same as those in Figure 11, solid blue lines), together with representative stress-strain curves for the thermally stressed andesite samples (red dashed lines). The porosity of each sample is provided next to the relevant curve.
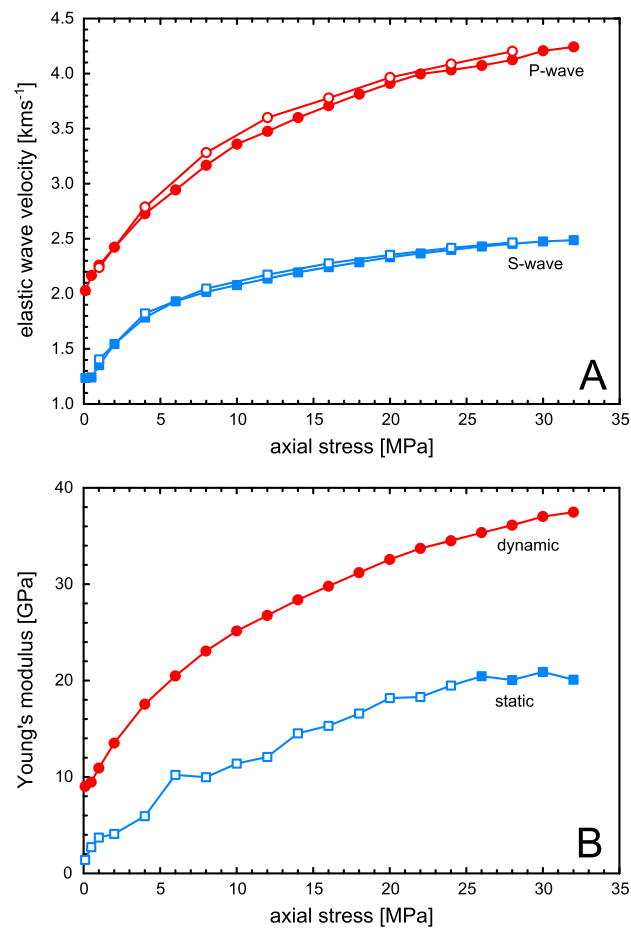
Figure 16. The evolution of (a) P and S wave velocities and (b) dynamic and static Young's moduli with increasing axial stress. The experiment was performed on a sample of A5 (porosity = 9.2%) using the uniaxial compression apparatus (Figure A2). Modified endcaps containing piezoelectric crystals were used to measure P and S wave velocities. The unfilled shapes in Figure 16a are measurements taken during the unloading of the sample, showing that the process is reversible. The unfilled shapes in Figure 16b highlight the static moduli that, according to our definition, are not strictly elastic moduli; we include them here for completeness.

Table 6. Values of Porosity and Uniaxial Compressive Strength for Various Volcanic Rocks

Rock Type	Connected Porosity (%)	Uniaxial Compressive Strength (MPa)	Reference
Etna basalt	4.4	140	*Heap et al.* [2009]
Icelandic basalt	4.5[a]	360	*Heap et al.* [2010]
Vesuvian basalt	8–10	86–93	*Rocchi et al.* [2004]
Etnean basalt	8–10	102–138	*Rocchi et al.* [2004]
Stromboli basalt	13[a]	100	*Heap et al.* [2010]
Mount Shasta andesite	7.2	82–125	*Smith et al.* [2009]
Colima andesite	8–11	115–138[b]	*Kolzenburg et al.* [2012]
Mount Saint Helen's andesite	9.5	140	*Smith et al.* [2011]
Mount Hood andesite	10–12	120	*Bauer et al.* [1981]
Kumamoto andesite	13[a]	130	*Jeong et al.* [2007]
Neapolitan Yellow Tuff	44	3.5	*Heap et al.* [2012]
Piperno Tuff	48	1.6	*Heap et al.* [2012]
Welded Grey Ignimbrite	49	9	*Heap et al.* [2012]

[a]The porosity was remeasured (and therefore is different from the porosity quoted in the original study; the porosity of Kumamoto andesite was not quoted in *Jeong et al.* [2007]).
[b]The measurements were performed at in situ temperatures of 940°C. We include these data here for two reasons: (1) they were measured on the most pertinent rock type and (2) the materials were not glassy and, even at 940°C, behavior was entirely brittle [see *Kolzenburg et al.*, 2012].

Considering that the andesite samples all have a high microcrack density (Table 2), another possibility would be to assume that the microcracks play the dominant role in their brittle failure in compression. To test this theory, we can use the sliding wing-crack model (Figures 17d–17f) [*Horii and Nemat-Nasser*, 1986; *Ashby and Sammis*, 1990]. The predicted UCS (σ_p) given by equation (3) contains four parameters: K_{IC}, m, c, and D_0. We can partially constrain these parameters using the stress at which we inferred the onset of dilatancy, C' (i.e., the onset of the acceleration in AE activity, see Figure 10). Assuming that C' corresponds to the propagation of the most favorably orientated microcracks, the stress at the onset of dilatancy ($\sigma_{C'}$) predicted by the wing-crack model [*Ashby and Sammis*, 1990; *Baud et al.*, 2000] is given by

$$\sigma_{C'} = \frac{\sqrt{3}}{\sqrt{1+\mu^2}-\mu} \frac{K_{IC}}{\sqrt{\pi c}} \qquad (4)$$

The initial damage D_0 can be inferred directly from

$$D_0^{0.256} = 0.777 \frac{\sigma_{C'}}{\sigma_p} \qquad (5)$$

Using the data of Table 4, we find that $D_0 < 0.012$ for all the andesites. However, these values are significantly lower than the results compiled for rocks by *Paterson and Wong* [2005], including some low-porosity (< 1%) end-members such as Westerly granite. Our inferred values for D_0 are therefore suspiciously low for such pervasively microcracked and porous rocks. Several factors could explain this discrepancy. First, our estimation hinges on the precise determination of C', which is difficult when relying only on AE data (C' can be more accurately determined using radial strain data). Second, equation (5) assumes that the microcracks involved in the dilatancy process are those involved in the failure process. *Baud et al.* [2014] recently suggested that this assumption may well be invalid for materials with complex mineralogy and microstructure and that consequently the crack lengths and/or the K_{IC} considered in equations (3) and (4) could be different. It is clear that more laboratory data are now needed to better constrain the model parameters and to verify its applicability to these materials.

In summary, the micromechanical analysis of uniaxial data from a suite of andesites from Volcán de Colima suggests that the pore-emanated crack model is more appropriate than the sliding wing-crack model. This is consistent with the fact that our microstructural observations on post failure samples have shown a high degree of pore-emanated microcracking (Figure 12a). More definitive conclusions could be drawn using laboratory-determined K_{IC} measurements. However, our analysis may highlight the limit of such micromechanical models, where a complex and heterogeneous microstructure cannot be boiled down to a single parameter such as a mean crack length or mean pore size. Ideally, a new micromechanical model incorporating both microcracks
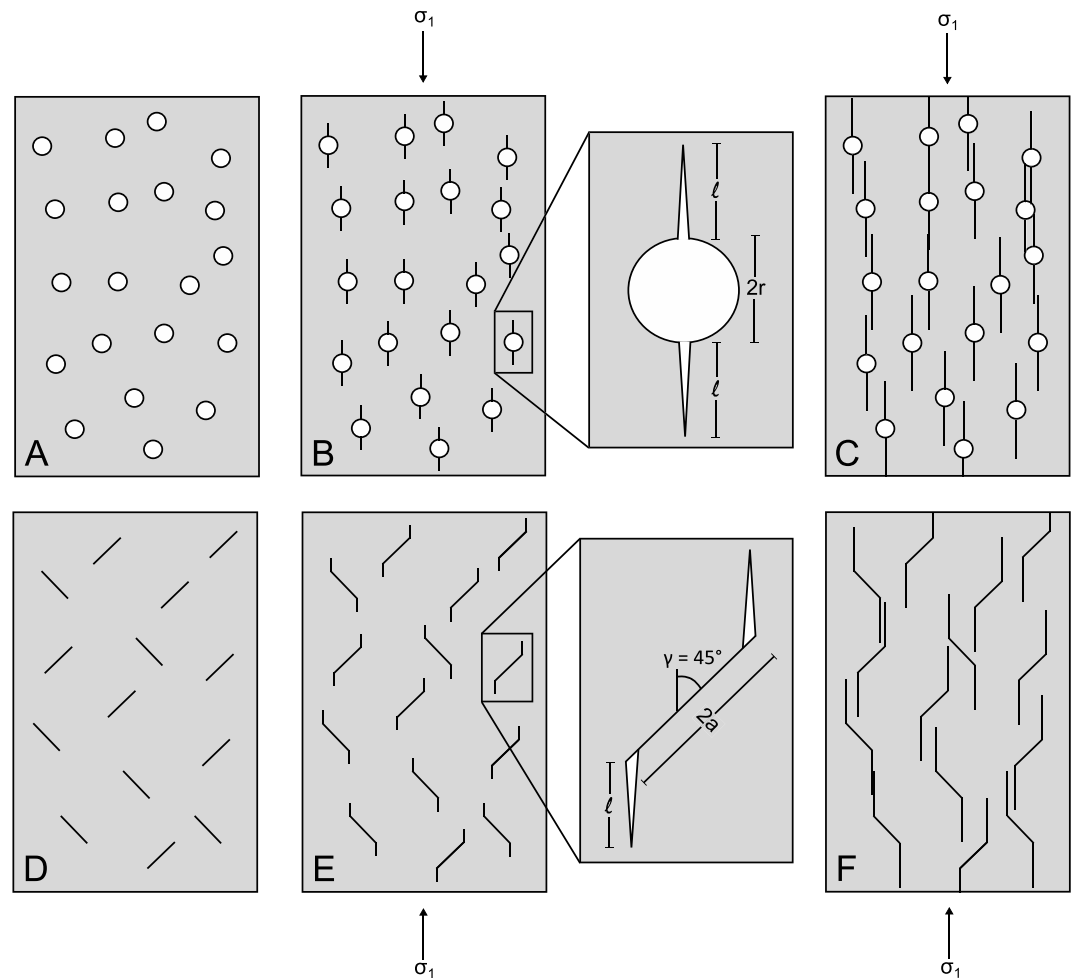
Figure 17. (a) *Sammis and Ashby's* [1986] two-dimensional elastic medium populated by circular holes of uniform radius *r*. (b) Pore-emanated cracks propagate from the pores (to a length *l*) upon the application of an axial stress (one large enough to overcome K_{IC}). (c) Eventually, as axial stress increases, the cracks grow further, interact, and promote macroscopic failure. (d) The sliding wing-crack model [*Horii and Nemat-Nasser*, 1986; *Ashby and Sammis*, 1990; *Kemeny and Cook*, 1991], consisting of a two-dimensional elastic medium populated by cracks of uniform length *2a*. (e) Upon the application of an axial stress (one large enough to overcome the frictional resistance of the crack and the K_{IC}), wing cracks propagate to a length *l*. (f) Eventually, as axial stress increases, the wing cracks grow further, interact, and promote macroscopic failure.

and pores should be developed. While building such a model is beyond the scope of this study, we highlight that this suite of andesites presents an ideal material to formulate such a model.

5.3.2. Geometrical Permeability Modeling: Kozeny-Carman

Permeability models can be grouped into two families, (1) "tube or crack" or statistical permeability models and (2) hydraulic radius or geometrical permeability models where a single equivalent channel is considered [*Guéguen and Palciauskas*, 1994], that are commonly referred to as Kozeny-Carman models. Kozeny-Carman models have been widely used in the earth sciences [e.g. *Paterson*, 1983; *Walsh and Brace*, 1984], due largely to a combination of their simplicity and the fact that the variables can be easily constrained in the laboratory.

The Kozeny-Carman relation has been previously used to model the permeability of volcanic rocks [e.g., *Saar and Manga*, 1999; *Costa*, 2006; *Bernard et al.*, 2007; *Yokoyama and Takeuchi*, 2009]. Several studies have simplified this relation by neglecting variations in element shape (e.g., tube or crack), specific surface area, and tortuosity, instead using an empirically derived constant [*Klug and Cashman*, 1996; *Rust and Cashman*, 2004; *Mueller et al.*, 2005; *Lavallée et al.*, 2013]. While these further assumptions may be somewhat appropriate for rocks with a simple microstructure, such simplification does not adequately pay tribute to the complexity of volcanic rock microstructure. Indeed, even Fontainebleau sandstone suffers void space
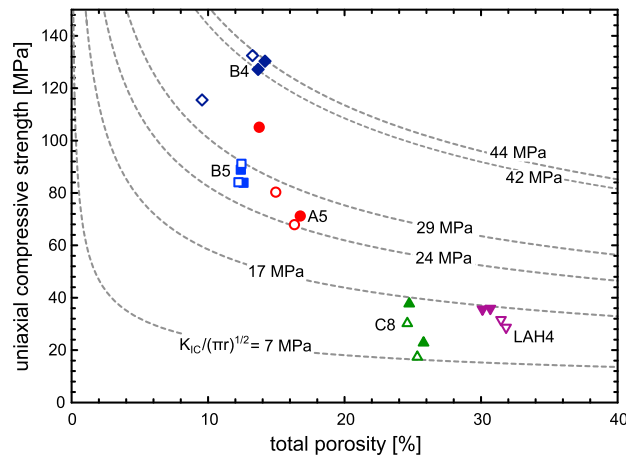
Figure 18. Plot of uniaxial compressive strength against total porosity showing all of the experimental data, together with the theoretical curves from the pore-emanated crack micromechanical modeling (see text for details). Unfilled shapes–as-collected samples; filled shapes–thermally stressed samples.

connectivity issues below 9% porosity [*Bourbié and Zinszner*, 1985]. Further, the use of empirical relations does not permit us to glean information regarding the key factors controlling their fluid transport behavior. Here we take a different approach where we determine the hydraulic radius using Brunauer, Emmett, and Teller (BET) krypton (Kr) adsorption measurements. Krypton adsorption was used as our values for specific surface were approximately at the resolution of nitrogen adsorption. A summary of these data, and the measured water permeability, connected water porosity, and bulk density data, is presented in Table 7. We note that the specific surface of sample B5 is much higher than the other andesites and likely reflects the fact that B5 contains a much greater proportion of small vesicles (Figures 6 and 7).

The Kozeny-Carman relation is of the form

$$k_{KC} = \frac{\varphi (r_H)^2}{b\tau^2} \tag{6}$$

where k_{KC} is the permeability, φ is the connected porosity, b is a geometrical factor, τ is the tortuosity of the flow channel (i.e., the ratio of its actual to nominal length), and r_H is the hydraulic radius. The hydraulic radius can be defined as follows:

$$r_H = \frac{V_{pores}}{S_{pores}} \tag{7}$$

where V_{pores} is the volume of pores and S_{pores} is the surface of the pores. The specific surface area of the connected pore space inside a rock can be determined using BET krypton adsorption. This technique can be used to determine the hydraulic radius:

$$r_H = \frac{\varphi}{\rho_b S_{BET}} \tag{8}$$

where ρ_b is the bulk density and S_{BET} is the specific surface area as determined by BET. The Kozeny-Carman relation can therefore be recast as

$$k_{KC} = \frac{\varphi^3}{b\tau^2 \rho_b^2 S_{BET}^2} \tag{9}$$

Table 7. Data Summary for the Andesite Samples Used for the Permeability Measurements and Modeling

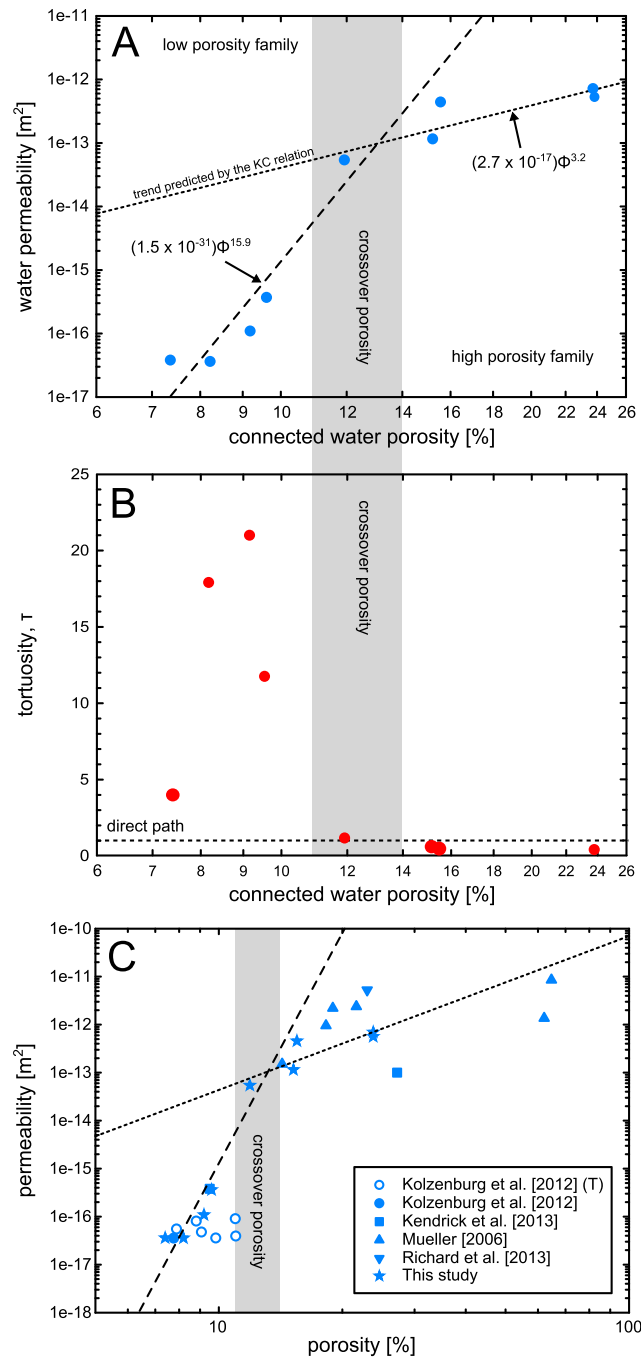| Connected Water Porosity (%)	Sample	Water Permeability (m^2)	Bulk Density (kg/m^3)	Specific Surface Area S_{BET} (m^2/kg)	Tortuosity Assuming Cracks ($b = 12$)
7.4	B5-5	3.61×10^{-17}	2474.64	100	3.9
8.2	B4-2	3.59×10^{-17}	2443.04	26	17.8
9.2	A5-11	1.09×10^{-16}	2446.08	15	21.0
9.6	A5-1	3.62×10^{-16}	2403.23	16	11.7
11.9	A5-7	5.45×10^{-14}	2317.94	20	1.1
15.2	C8-9	1.15×10^{-13}	2188.72	35	2.3
15.5	C8-8	4.57×10^{-13}	2127.07	28	0.4
23.8	LAH4-9	5.65×10^{-13}	1971.65	57	0.4
23.8	LAH4-7	6.96×10^{-13}	1998.97	51	0.4

Figure 19. (a) Log-log plot of water permeability against connected water porosity. The dashed and dotted lines are the best fit trends for the low-porosity family (steep curve) and the high-porosity family (shallow curve), respectively. Both lines are accompanied by their power law exponent. The "crossover porosity" (11–14%), where the two trends meet, is shaded in grey. (b) Log-linear plot of tortuosity against connected water porosity. The crossover porosity range (11–14%) is shaded in grey. (c) Permeability against porosity for rocks from Volcán de Colima, plotted on log-log axes. The *Kolzenburg et al.* [2012] and the *Kendrick et al.* [2013] data are water permeabilities measured on andesitic rocks under a confining pressure of 5 MPa and a pore fluid pressure gradient of 1 MPa. (T)–samples that contain healed tuffisites. The *Mueller* [2006] data are gas (argon) permeabilities measured under a confining pressure of 0 MPa using the pulse decay method (2.5 MPa on one side and 0 MPa on the other). The low-porosity samples of *Mueller* [2006] were performed on lava samples from the 1999 block-and-ash flow deposit, and the high-porosity samples were pumiceous samples from the 1913 eruption. The *Richard et al.* [2013] datum is for a sample collected from the 1999 block-and-ash flow deposits; gas (argon) permeability was measured under a confining pressure of 0 MPa using the pulse decay method (4 MPa on one side and 0 MPa on the other). The dashed and dotted lines are the power law trends shown in Figure 19a. The crossover porosity range (11–14%) is shaded in grey.
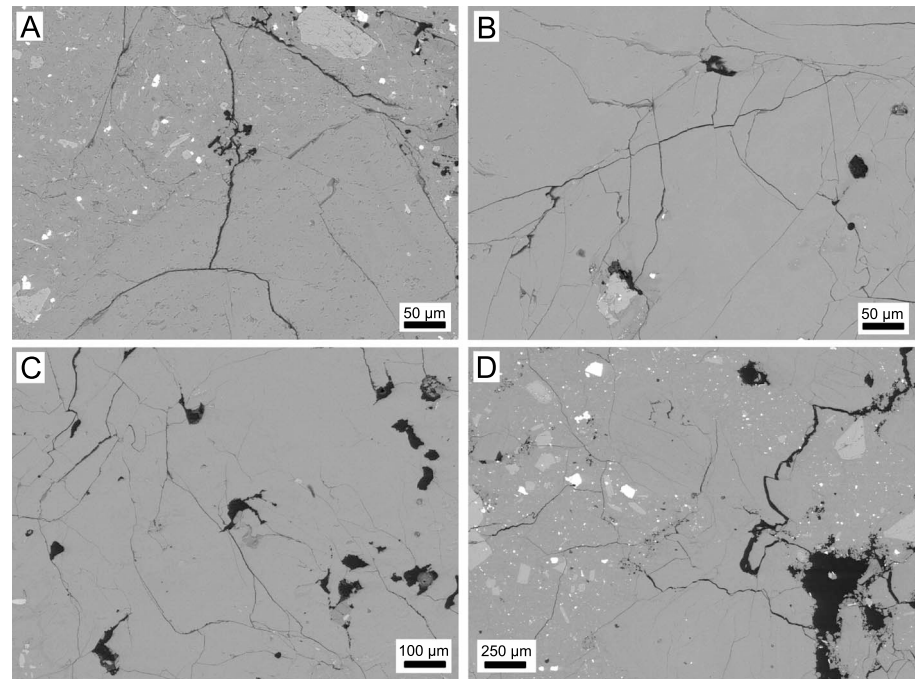
HEAP ET AL.   2948

Figure 20. Scanning electron microscope photographs of an as-collected sample of B5 highlighting the tortuous nature of the microcracking.

We find the power law exponent for our high-porosity (15–24%) andesites to be close to 3 (Figure 19a), a value in agreement with the Kozeny-Carman model [see *Bourbié and Zinszner*, 1985; *Doyen*, 1988]. In detail, one would expect a power law exponent of 3 if the elements controlling the permeability are cracks [*Guéguen and Palciauskas*, 1994]. For this range of porosities, we can assume that the tortuosity and the specific surface area are largely independent of the porosity (a power law exponent of 3 is indicative of this independency). In theory, if these microstructural parameters remained unchanged when the porosity is reduced, samples of lower porosity should follow the same trend (the dotted line on Figure 19a). This is however not the case (i.e., one or more of the parameters is changing as porosity is reduced). The power law exponent for the low-porosity (8–12%) samples is much larger (about 16) and can be explained in terms of a dramatic reduction in void space connectivity which, in turn, results in a significant increase in tortuosity below the crossover porosity (11–14%). We note that crossover porosity for the andesites is only slightly higher than that for Fontainebleau sandstone (about 9%) [*Bourbié and Zinszner*, 1985].

Microstructurally, the crossover porosity (Figure 19) in the andesites is likely to represent a critical vesicle content (a combination of vesicle size and density) that efficiently connects the microcrack population and allows the water to travel a much more direct path through the sample, rather than restricting flow to long and tortuous microcracks. Indeed, SEM analysis of one of the low-porosity andesites aptly demonstrates the convoluted path the water must take to pass through the sample; the SEM photographs show "cross roads," "dead ends," and multiple pathways for fluid flow (Figure 20).

Although it is clear that no single Kozeny-Carman relationship will be able to describe the full suite of data, we can use the model to support our hypothesis by estimating values for the tortuosity, τ. Using our experimentally determined values for water permeability, BET specific surface area, density, and porosity (Table 7), we can solve equation (9) to find values for the unknown term $b\tau^2$. Values for geometrical factor b can vary [*Bernabé et al.*, 2003], but it can be assumed that $b = 8$ if the transport elements are "tubelike" and $b = 12$ if they are "crack-like" [*Bernabé et al.*, 2010]. Since cracks are controlling the permeability of the andesites of this study (the power law exponent is 3) [see *Guéguen and Palciauskas*, 1994], we will assume that $b = 12$ and solve for τ. Values for τ are commonly between 1 (direct path) and 3 [*Dullien*, 1979]. We find that, when $b = 12$, τ ranges from 0.4 to 21.0 (Table 7). Values of τ for each sample, for a constant value of b (12 in this case), are plotted against porosity in Figure 19b. Figure 19b shows that there is a large increase in tortuosity

below the crossover porosity. We find τ values below 1 above the crossover porosity and values almost 20 below the crossover porosity (such high values of tortuosity are not uncommon for volcanic rocks) [see *Wright et al.*, 2009]. While we note that values of τ below 1 are impossible (true values likely to be close to, albeit higher, than 1), we emphasize the striking difference in tortuosity above and below the crossover porosity. This analysis supports our initial conjecture that the deviation from Kozeny-Carman behavior is related to inefficient element connectivity and high tortuosity in the samples below a porosity of about 12%. A similar interpretation may explain the low permeabilities of the rhyolite and obsidian samples of *Eichelberger et al.* [1986] below 60% porosity. Our data are plotted alongside previously published permeability data for rocks from Volcán de Colima (Figure 19c). This compilation plot shows that our power law trends and the position of the crossover porosity are in agreement with the available published data.

To conclude we would like to highlight that, even using samples from the same volcano with an identical chemical composition, understanding their permeability still remains a challenge. We suggest that a deviation from Kozeny-Carman behavior may exist in other extrusive volcanic rocks that contain a combination of vesicles and microcracks. We implore that the complex controls on permeability in volcanic rocks require a deeper understanding. Further discussion on the implications of these permeability data can be found in section 5.5.

5.4. The Influence of Thermal Stressing on Andesites From Volcán de Colima

Our AE analysis suggests that the onset temperature and the extent of thermal microcracking differed greatly between the samples, perhaps reflecting the broad crystal size distribution, crystal/glass fraction, and porosity of volcanic rocks. Volcanic rocks often have a heterogeneous (often bimodal) crystal size distribution and may therefore react to thermal stressing in a different way to granites or sandstones. *Tang et al.* [2011] stress the importance of crack propagation at the mortar/coarse aggregate interface in heterogeneous concrete, somewhat analogous to the groundmass/phenocryst interface in volcanic rocks. We also observed that, for some of the andesites of this study, thermal microcracking was more prevalent during the cooling stage of the thermal stressing experiment (Figure 14). While previous studies largely attribute thermal microcracks as the result of thermal expansion mismatches between minerals, our study highlights that the thermal contraction of minerals can also be important. While data on this phenomenon in rocks are rare, it has been previously observed in studies on porcelain [*Kirchhoff et al.*, 1982] and concrete [*Heap et al.*, 2013].

Stereological microcrack analysis provided lower microcrack densities and a higher anisotropy for the samples thermally stressed to 450℃. We do not suggest that thermal stressing has reduced the microcrack density or changed the anisotropy of the andesite samples. This difference is likely due to the fact that the counting did not take place on the same sample, i.e., both before and after thermal stressing (as was the case for the physical properties described above and listed in Table 4). We must conclude that the thermal microcracking that took place in our samples was much less than the natural variability between samples taken from the same block of material. Unfortunately, no firm conclusions can be drawn from such stereological techniques for the studied materials. We observed modest changes in rock physical properties as a result of thermal stressing. We saw a modest increase in connected porosity, and modest decreases in ultrasonic wave velocities and dynamic elastic moduli. This can be interpreted as a result of a small increase in the already extensive thermal microcrack network, as evidenced by the output of AE during our thermal stressing experiments.

Thermal microcracking has been previously shown to induce changes to the physical properties of rocks [e.g., *David et al.*, 1999]. However, few studies have investigated the propensity of volcanic rocks to develop thermal microcracks and their consequences on rock physical properties [*Jones et al.*, 1997; *Lebedev and Kern*, 1999; *Vinciguerra et al.*, 2005; *Heap et al.*, 2009; *Smith et al.*, 2009; *Nara et al.*, 2011]. In general, the influence of thermal stressing on the physical properties of volcanic rocks is not so clear. In the case of a basaltic lava deposit from Mount Etna, the permeability, elastic wave velocities [*Vinciguerra et al.*, 2005], and elastic moduli [*Heap et al.*, 2009] remained unchanged after exposure to 900℃. Similarly, *Smith et al.* [2009], in triaxial experiments on an andesite from Mount Shasta (California, USA), found that, at in situ temperatures from 25 to 600℃, the static Young's modulus of their andesites remained constant. However, some studies report large thermally induced physical property modifications for volcanic rocks. For an aphyric basalt from Iceland, *Jones et al.* [1997] showed that thermal stressing increases the permeability above temperatures of 300℃ (later reinforced by *Nara et al.* [2011]), and *Vinciguerra et al.* [2005] showed that its *P* wave velocity was

reduced from 5.2 to 4.0 km s^{-1} upon exposure to 900°C. What we can conclude from this incomplete data set is that, in the absence of mineralogical changes, aphyric (or low porosity) volcanic rocks appear more susceptible to thermal microcracking than porphyritic volcanic rocks, a conclusion also surmised by *Jones et al.* [1997]. It is also possible that the immunity of some materials to further thermal microcracking is linked to the presence of a preexisting thermal microcrack network (i.e., materials that have already undergone one or more heating/cooling episodes), a concept linked to the Kaiser "temperature-memory" effect [*Yong and Wang*, 1980]. This interpretation has been previously proposed for the highly microcracked basalt from Mount Etna [*Vinciguerra et al.*, 2005; *Heap et al.*, 2009].

The data from our study suggest that thermal stressing to 450°C does not influence the UCS of our suite of andesite samples. While we can cite that natural variability could again obscure any observable difference in UCS (as-collected and thermally stressed UCS cannot be measured on the same sample), the influence of thermal stressing on the strength of materials, as portrayed throughout the literature, is unclear. Some materials weaken as a result of thermal microcracking (e.g., granites) [*Homand-Etienne and Houpert*, 1989], and others weaken as a result of chemical changes (e.g., tuffs) [*Heap et al.*, 2012]. However, in some materials (largely of volcanic origin), no weakening was observed over a wide range of temperature [*Bauer et al.*, 1981; *Meredith et al.*, 2005; *Balme et al.*, 2004; *Heap et al.*, 2009; *Smith et al.*, 2009], even though the rocks host an abundance of feldspars (feldspars have an extremely anisotropic thermal expansion coefficient) [see *Tribaudino et al.*, 2010]. For example, the UCS of a basaltic lava deposit from Mount Etna did not decrease after exposure to 900°C [*Heap et al.*, 2009] and can be explained by the fact that this material appears to resist further thermal microcracking, as evidenced by its unchanged *P* wave velocity after exposure to 900°C [*Vinciguerra et al.*, 2005]. However, in the case of the aphyric basalt from Iceland (porosity = 4.5%), the *P* wave velocity was reduced from 5.2 to 4.0 km s^{-1} [*Vinciguerra et al.*, 2005] upon exposure to 900°C but its UCS and indirect tensile strength were unaffected [*Meredith et al.*, 2005]. Another study found that high in situ temperatures had little impact on fracture toughness of basaltic lava deposits from Mount Etna and Vesuvius [*Balme et al.*, 2004] and the compressive strength of andesite [*Bauer et al.*, 1981; *Smith et al.*, 2009]. From these observations we can conclude that, if a volcanic rock is exposed to thermal stressing, it does not necessarily change the most deleterious microcrack (i.e., new thermal microcracks are relatively small), which plays a large role in failure in compression. However, and owing to the paucity of data, we conclude that a complete picture of the effect of thermal stressing on volcanic rocks does not exist to date. We suggest that thermal stressing (on short timescales) does not significantly modify the andesites due to a combination of (1) the stability of its mineral phases, (2) the presence of a preexisting pervasive thermal microcrack network, (3) their porphyritic texture, and (4) their high porosities (i.e., the thermal expansion of the minerals could simply be accommodated by the porosity).

5.5. Volcanological Implications

The main goal of this study was to characterize the microstructural, physical, and mechanical properties for a representative range of andesitic rocks that form the volcanic edifice at Volcán de Colima. Our findings demonstrate that the physical and mechanical properties of these volcanic rocks are strongly controlled by their microstructure. The andesitic rocks from Volcán de Colima are intensely fractured, a result of their relatively fast cooling history, and contain high vesicle densities and a wide vesicle size distribution. As a result they have high porosities and permeabilities and low bulk densities, elastic wave velocities, Young's moduli, and compressive strengths. The nature of volcanic rock formation, combined with the relatively unstable conditions in which they exist, suggests that this is may be the case for many volcanic rocks. The wide range of microstructural, physical, and mechanical properties exhibited by this representative suite of andesites highlights the heterogeneous nature of the rocks comprising the edifice at Volcán de Colima. Although it may appear counterintuitive, stratovolcanoes constructed from rock strata with vastly different physical and mechanical properties may be "stronger" as a result. Layers of rock with different Young's moduli and strengths impact the distribution of stress and strain and can promote the deflection or arrest of propagating dykes and fractures at the contacts between layers [*Gudmundsson*, 2011], thus increasing the amount of strain energy required for large-scale edifice failure [*Gudmundsson*, 2012].

Due to the sensitivity of elastic waves to microcracks, an increase in microcracking (due to thermal or mechanical stresses) and/or the movement of fluids within a region of the volcanic edifice hosting highly microcracked rocks could alter seismic velocities at Volcán de Colima. We suggest that such findings should

be considered in tomographic, seismic data inversion of subvolcanic structures, and V_p/V_s anomaly analysis. Knowledge of the elastic moduli for representative volcanic rock is important for (1) the reliable modeling of the ground deformation at volcano edifices [e.g., *Manconi et al.*, 2007, 2010], (2) the calibration of damage mechanics criteria and the development of appropriate time-to-failure laws [e.g., *Voight*, 1989; *Kilburn*, 2003; *Kilburn and Sammonds*, 2005], and (3) the distribution of stress and strain and the understanding of the propagation and arrest and fractures and dykes [e.g., *Gudmundsson*, 2011], amongst many more. All require a robust knowledge of the elastic moduli of the representative rocks and their modification under mechanical and thermal stresses. The heterogeneous nature of the rocks comprising the edifice at Volcán de Colima highlights that the currently common assumption of rock homogeneity in volcano modeling is an oversimplification that can lead to misinterpretations of derived source (e.g., a magma chamber, a zone of overpressurized fluids, or a combination of the two) parameters [*Manconi et al.*, 2007, 2010]. Previously, ground deformation [*Murray and Ramírez Ruiz*, 2002; *Murray and Wooller*, 2002; *Pinel et al.*, 2011] and viscoelastic [*De la Cruz-Reyna and Reyes-Davila*, 2001] modeling have been employed as forecasting tools at Volcán de Colima. For instance, *Pinel et al.* [2011] used a Young's modulus of 3 MPa and, although they remark that this value is very low compared to previously published values for rock, perhaps (when one accounts for the fact that laboratory Young's modulus measurements exclude macroscopic fractures; laboratory measurements are commonly 1.5–5 times greater than the in situ modulus of the same rock) [*Gudmundsson*, 2011] their estimate is not so unrealistic, as evidenced by the low values of Young's moduli obtained in this study. We suggest (1) that low values of Young's modulus should be considered when choosing the parameters for the modeling of unrest phenomena and (2) that the assumption of rock homogeneity is an oversimplification at andesitic stratovolcanoes. Further, we highlight that recent finite element modeling [*Manconi et al.*, 2010] and experimental studies [*Heap et al.*, 2009, 2014] suggest that the static values may be more appropriate in volcanic hazard modeling.

The ease at which exsolved gases can escape from rising magma during periods of unrest can have drastic consequences on the eruption style: effusive or explosive [*Woods and Koyaguchi*, 1994]. The permeability of magma, and the surrounding host rock, is therefore of crucial importance. For magma, the percolation threshold is likely to represent an abrupt transition between essentially zero permeability to reasonably high permeability. Above the percolation threshold for magma, exsolved gas can escape vertically but can also escape horizontally, assuming a lateral connection of bubbles and a permeable host rock. We also speculate that the gas in bubbles on the outermost edges of the conduit (i.e., in contact with the host rock) could escape below the percolation threshold for magma. While a variety of studies discuss magma permeability using data from explosive or effusive volcanic products, we stress that we consider our permeability measurements as representative of the host (country and wall) rock, not the magma in the conduit. However, and as discussed above, we consider that host rock permeability is likely to play an important role in shaping eruption characteristics [see also *Jaupart*, 1998]. We have shown that the host rock can be very permeable ($\sim 10^{-13}$ m^2, i.e., similar to magma permeability estimates above the percolation threshold) and could therefore allow significant horizontal gas loss, reducing the potential for large explosive eruptions. Evidence for host rock gas transport include the following: (1) lava close to the conduit wall can be devoid of vesicles, suggesting efficient gas escape [*Jaupart*, 1998] and (2) the presence of tuffisites [*Stasiuk et al.*, 1996; *Tuffen et al.*, 2003, and references therein] that are extremely common at Volcán de Colima [*Kolzenburg et al.*, 2012]. Further, it is likely that lateral permeability may be preferentially enhanced by microcracking within the magma at the conduit boundary [*Laumonier et al.*, 2011; *Lavallée et al.*, 2013; *Plail et al.*, 2014]. "Hydrofracturing," due to rising pore pressures inside the host rock, could further increase the microcrack density and permeability of the adjacent host rock [*Caricchi et al.*, 2011]. We suggest that horizontal gas escape should be considered in volcanic permeability models at Volcán de Colima and at other stratovolcanoes worldwide.

Another goal of this study was to make some of the first steps in understanding the micromechanical processes responsible for the deformation of volcanic rocks and to revisit the potential of geometrical permeability models. A deeper understanding of the micromechanics of edifice-forming volcanic rocks, and the physics underpinning their permeability, allows for a better assessment of volcano hazards [e.g., *Jaupart*, 1998; *Costa et al.*, 2009]. Previous studies have shown that the pore-emanated crack model can adequately describe the mechanical behavior of porous tuffs [*Zhu et al.*, 2011] and bubbly magma [*Vasseur et al.*, 2013].

Perhaps this is not surprising since the microcrack density for such materials is usually very low (in other words, the porosity consists of vesicles only). However, for lava deposits, where microcracks and vesicles are both abundant, both microstructural elements contribute to their deformation (since pore-emanated or wing-crack modeling could not capture the mechanics). Unfortunately, no model that combines both elements exists. We envisage that future work on the micromechanics of volcanic rocks, including the formation of a multielement model, will help unravel their complex micromechanics and provide vital information for volcanic hazard assessment. While permeability models (such as Kozeny-Carman) have been adopted for volcanic rocks [*Costa*, 2006], the validity of empirically derived relationships between porosity and permeability is questionable due to their heterogeneity (even those from the same eruption). We found that Kozeny-Carman permeability modeling does not accurately capture the fluid flow properties of the andesites of this study. While other statistical permeability models are available, and should be the focus of future studies, we anticipate that understanding fluid flow will certainly represent a challenge for volcanic materials.

This study has shown that, on short timescales, thermal stressing will not significantly weaken the edifice-forming andesites at Volcán de Colima and therefore the edifice as a whole. However, we should emphasize that the heating/cooling rates used in this study were perhaps high when compared with heating/cooling rates in nature. Prolonged deformation at higher temperatures could provide the time needed for the chemical alteration of unstable mineralogical assemblages or for healing, providing that the deformation timescale exceeds the time required for the structural relaxation of the interstitial melt phase [e.g., *Tuffen et al.*, 2003]. We suggest that, for a deeper understanding of the influence of thermal stressing, further experimentation using longer timescales is required.

6. Conclusions

1. Our study has shown that a representative suite of andesites from Volcán de Colima is pervasively microcracked and has high vesicle densities and a wide vesicle size distribution. Due to the isotropic nature of this microcracking (and the origin of the samples), we suggest that the microcracks are predominantly of thermal origin and formed as a result of rapid cooling. Since microcrack densities are similar (their cooling histories are therefore likely to be similar), the large differences in porosity are the result of varying vesicle size and density.
2. The complex microstructure (i.e., microcracks and vesicles) of these andesites has left them with high porosities and permeabilities and low densities, elastic wave velocities, Young's moduli, and compressive strengths.
3. The wide range of microstructural, physical, and mechanical properties exhibited by this representative suite of andesites highlights the heterogeneous nature of the rocks comprising the edifice at Volcán de Colima.
4. Micromechanical modeling (pore-emanated crack versus sliding wing-crack modeling), implemented to decipher the micromechanical controls on deformation, was unable to accurately capture the micromechanics of the tested andesites, due to their microstructural complexity. These analyses highlight the need for a micromechanical model that combines both microcracks and vesicles. We suggest that these andesites are an ideal material to formulate such a model.
5. A unique Kozeny-Carman permeability model does not exist for the studied suite of andesites. Two families exist that can be distinguished by their void space connectivity and tortuosity. Below the crossover porosity, flow occurs mainly through highly tortuous microcracks. Above the crossover porosity, the fluid pathways are simplified by an increasing vesicle content (a combination of size and density). These analyses highlight that understanding the permeability of volcanic rocks still remains a challenge and requires a deeper understanding.
6. We found that thermally stressing these andesites to 450°C slightly increases their porosities and slightly decreases their elastic wave velocities and dynamic elastic moduli. This is interpreted as the result of a small increase in the already extensive microcrack network, as evidenced by the output of AE during thermal stressing. We suggest that thermal stressing (on short timescales) does not significantly modify the andesites due to a combination of (1) the stability of its mineral phases, (2) the presence of a preexisting pervasive thermal microcrack network, (3) their porphyritic texture, and (4) their high porosities (i.e., the thermal expansion of the minerals is simply accommodated by the porosity).

7. Thermal stressing to 450°C does not influence the UCS of the andesite samples (within the expected natural variability of the tested samples). We interpret that thermal stressing does not change the most deleterious microcrack, which plays a large role in failure in compression.

8. We suggest that our findings should be considered in (1) edifice stability assessment, (2) the interpretation of volcano seismic tomography and V_p/V_s anomaly analysis, (3) the modeling of unrest phenomena at andesitic stratovolcanoes, and (4) assessing the potential contribution of the host rock in magma degassing.

Appendix A: Additional Methods

A1. Microstructural Characterization

For both analyses, photomicrograph maps of each sample were collated using an optical microscope under transmitted fluorescent light. The maps were then converted to binary images. In this study we refer to microcracks and vesicles. Both are void space within the rock. While there is a clear difference in genesis between the two microstructural features, they were differentiated in thin section by their aspect ratio. The aspect ratio of a microcrack is typically above 1:100. Vesicles typically range from 1:1 (a perfect circle) down to 1:10. We note that these analyses represent only the connected microstructural elements (i.e., those impregnated with the fluorescent epoxy).

A1.1. Microcrack Analysis

The two-dimensional "connected" microcrack surface area S_v for each sample was measured by counting perpendicular $(P_L)_I$ and parallel $(P_L)_{II}$ microcrack intercepts within an 11 × 11 mm^2 grid, containing both horizontal and vertical lines spaced by 0.1 mm (Figure A1) [*Underwood*, 1970; *Wu et al.*, 2000]. The method provides the microcrack density in two orthogonal directions within the studied plane.

A complementary assessment of the microcrack anisotropy was performed using the modified Cantor-dust method [*Volland and Kruhl*, 2004] included in the automated pattern quantification toolbox AMOCADO [*Gerik and Kruhl*, 2009]. In detail, a set of 260 to 420 parallel lines (spaced by three pixels; equivalent to percentage rate of the radius) was superimposed onto a circular 1–1.5 cm^2 area of the binary images, and the number of segments $N(s)$ of length s that covers the microcrack-line intercept was plotted cumulatively versus the corresponding segment length on a log-log diagram. The threshold for the detection of a microcrack intercepted by a scan line was set to a length of three pixels. The data points in the cumulative segment-length plot formed a straight line (i.e., exponential distribution), and the slope calculated by the linear regression (excluding the 5% end tails of the data sets) provided a size distribution coefficient. From its initial horizontal position, the set of scan lines were subsequently rotated counterclockwise stepwise by an angle of 1° around the center point and the procedure was repeated up to an angle of rotation $\Sigma\omega < 180°$ (due to the rotational symmetry of the scan lines). All computed slope values were plotted in a direction versus slope diagram and approximated with a best fit ellipse. Analyses of anisotropic complex patterns (long axis to short axis ratio) yield oriented ellipses as best fits to the data point distributions.

A1.2. Vesicle Analysis

Two-dimensional connected vesicle area, density, circularity, aspect ratio, and roundness were determined using ImageJ. For these analyses, the binary images were further thresholded to select only the vesicles (Figure A1). The above vesicle parameters were automatically calculated using ImageJ using the following formulae:

$$\text{circularity} = 4\pi \left(\frac{\text{area}}{[\text{perimeter}]^2} \right) \tag{A1}$$

$$\text{aspect ratio} = \frac{\text{major axis}}{\text{minor axis}} \tag{A2}$$

$$\text{roundness} = 4 \left(\frac{\text{area}}{\pi(\text{major axis})^2} \right) \tag{A3}$$
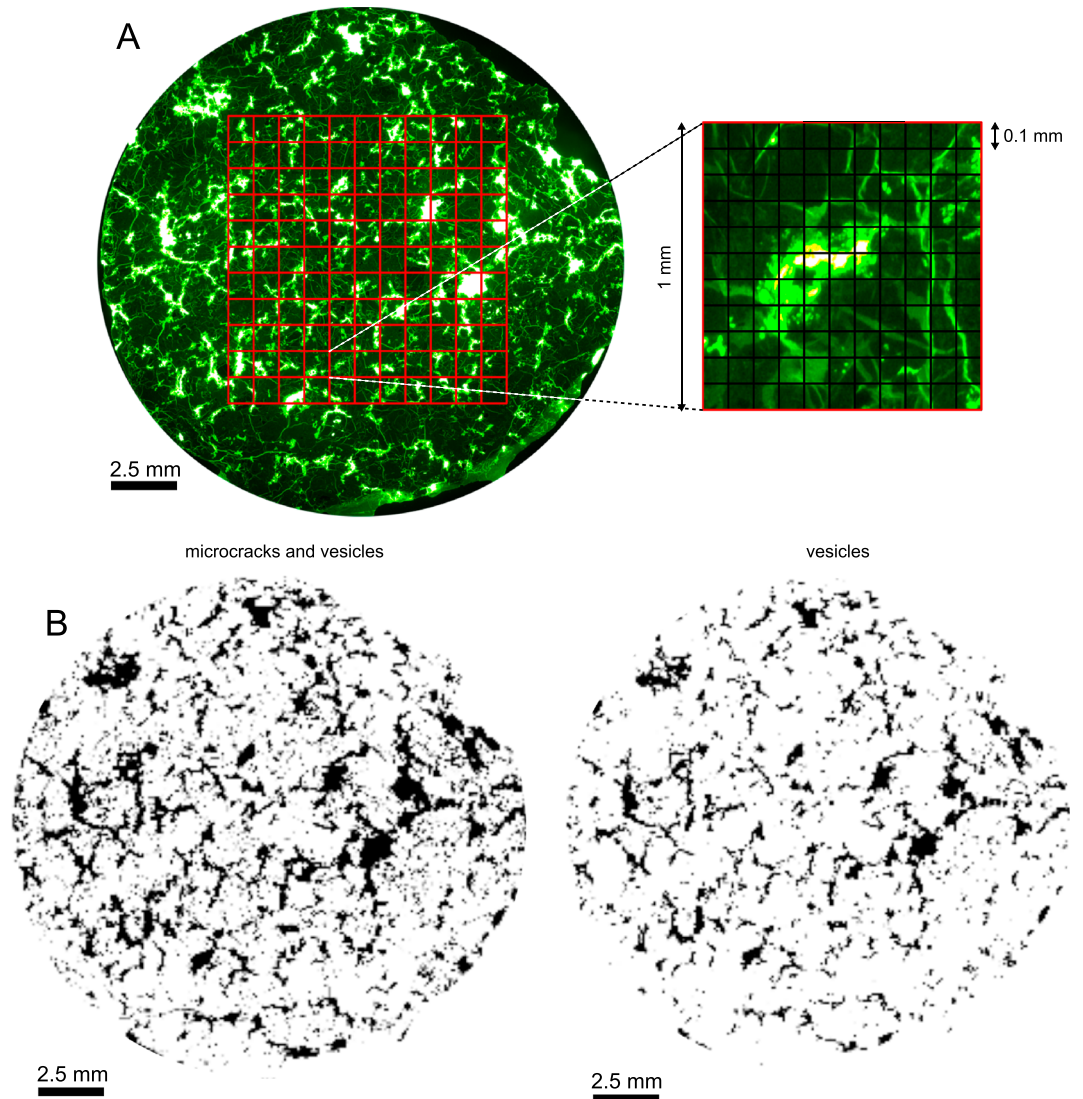
Figure A1. Diagrams outlining the two-dimensional stereological method for counting perpendicular $(P_L)_I$ and parallel $(P_L)_{II}$ microcrack intercepts within an $11 \times 11\,\text{mm}^2$ grid containing both horizontal and vertical lines spaced by 0.1 mm [see *Underwood*, 1970].

The equivalent vesicle radii were then determined, assuming circular vesicles and using the following formula:

$$\text{equivalent vesicle radius} = \sqrt{\frac{\text{area}}{\pi}} \tag{A4}$$

A.2. Connected and Total Porosities

The connected water porosities of the samples were measured using the triple-weight water saturation (distilled water) method, using Archimedes' principal [see *Guéguen and Palciauskas*, 1994]:

$$\varphi_w = \frac{m_2 - m_1}{m_2 - m_3} \tag{A5}$$

where m_1, m_2, and m_3 are the dry mass (vacuum dried at 40°C for at least 24 h), saturated mass (saturated with distilled water under a vacuum), and saturated submerged mass, respectively. Powdered skeletal densities

Table A1. Powdered Skeletal Densities for Each of the Five Blocks of Andesite

Block	Powdered Skeletal Density, ρ_{s_p} (kg m^3)
B5	2738.1
B4	2712.8
A5	2729.3
C8	2679.1
LAH4	2737.5

ρ_{s_p} were measured using a helium pycnometer (AccuPyc II 1340) using Boyle's law (Table A1). Total φ_t porosities were then calculated using the following formulae:

$$\varphi_t = 1 - \frac{\rho_b}{\rho_{s_p}} \tag{A6}$$

where ρ_b is the bulk sample density.

Water and total porosities were measured on many core samples from each of the five blocks of andesite. First, this provides insight into the variability of the materials. Second, in order to be able to compare the mechanical data of samples from the same block, we used these data to select core samples of similar porosities. Third, we were interested in sampling a range of porosities for our permeability measurements.

A3. Elastic Wave Velocities

The measurements were all performed (at the Laboratoire de Déformation des Roches, Strasbourg, Figure A2) using a device coupling: (1) a digital oscilloscope (Agilent Technologies DSO5012A digital storage oscilloscope), (2) a waveform pulse generator (Agilent Technologies 33210A, 10 MHz function/waveform generator), (3) two piezoelectric transducers, located within steel endcaps at the top and bottom of the sample, with a resonant frequency up to 1 MHz, (4) a load cell, and (5) a signal amplifier. Samples were held in the device at a constant contact force of 600 N (equating to a stress of about 1.9 MPa) to ensure the adequate transmission of the signal between the endcaps and the sample and to ensure reproducibility between one measurement and the next. In the case of sample material LAH4 (the sample with the highest porosity), a force of 200 N (about 0.6 MPa) was chosen to avoid inducing any damage. The frequency of generated signal was set at 700 kHz for P waves and 300 kHz for S waves.

Elastic wave velocities were subsequently used to calculate the dynamic Young's modulus E_d and the dynamic Poisson's ratio v_d using the following formulae:

$$E_d = \rho_b \frac{V_s^2 \left(3V_p^2 - 4V_s^2\right)}{V_p^2 - V_s^2} \tag{A7}$$

$$v_d = \frac{V_p^2 - 2V_s^2}{2\left(V_p^2 - V_s^2\right)} \tag{A8}$$

where ρ_b is the bulk sample density and V_p and V_s are the P wave and S wave velocities, respectively.

The tangent moduli or static Young's moduli E_s were calculated using the stress-strain data collected during the unconfined compressive strength (UCS) experiments. First, each stress-strain curve was fitted with a third-order polynomial. The resultant equations were then differentiated and the tangent modulus (i.e., the Young's modulus) was determined over their entire lengths. We take the Young's modulus from the region where the moduli did not change (corresponding to the maximum slope) [e.g., see *Heap and Faulkner*, 2008]. The axial stress at the region of maximum slope varied from sample to sample (typically between 15 and 100 MPa). We note that this only represents one Young's modulus in a deforming rock sample, since the elastic moduli will be developing in an anisotropic manner.

A4. Permeability Measurements

Water (distilled water) permeability measurements were made in a hydrostatic pressure vessel (at the Laboratoire de Déformation des Roches, Strasbourg, Figure A2) along the long axis of the cylindrical samples (i.e., the Z direction). Permeabilities were measured for a suite of samples that best covers the observed range of connected water porosities (from 7.4 to 23.8%). All measurements were collected under ambient laboratory temperatures. Prior to experimentation the samples were vacuum saturated with distilled water. The measured sample was then inserted into a viton jacket, placed between two steel endcaps, and lowered into the pressure vessel. A confining pressure (provided by distilled water) of 2 MPa was then applied to the sample. Water permeability was measured using the steady state flow method where the differential pore pressure ($P_{up} - P_{down}$) was kept constant (0.5 MPa). The flow rate Q was measured at the downstream side of
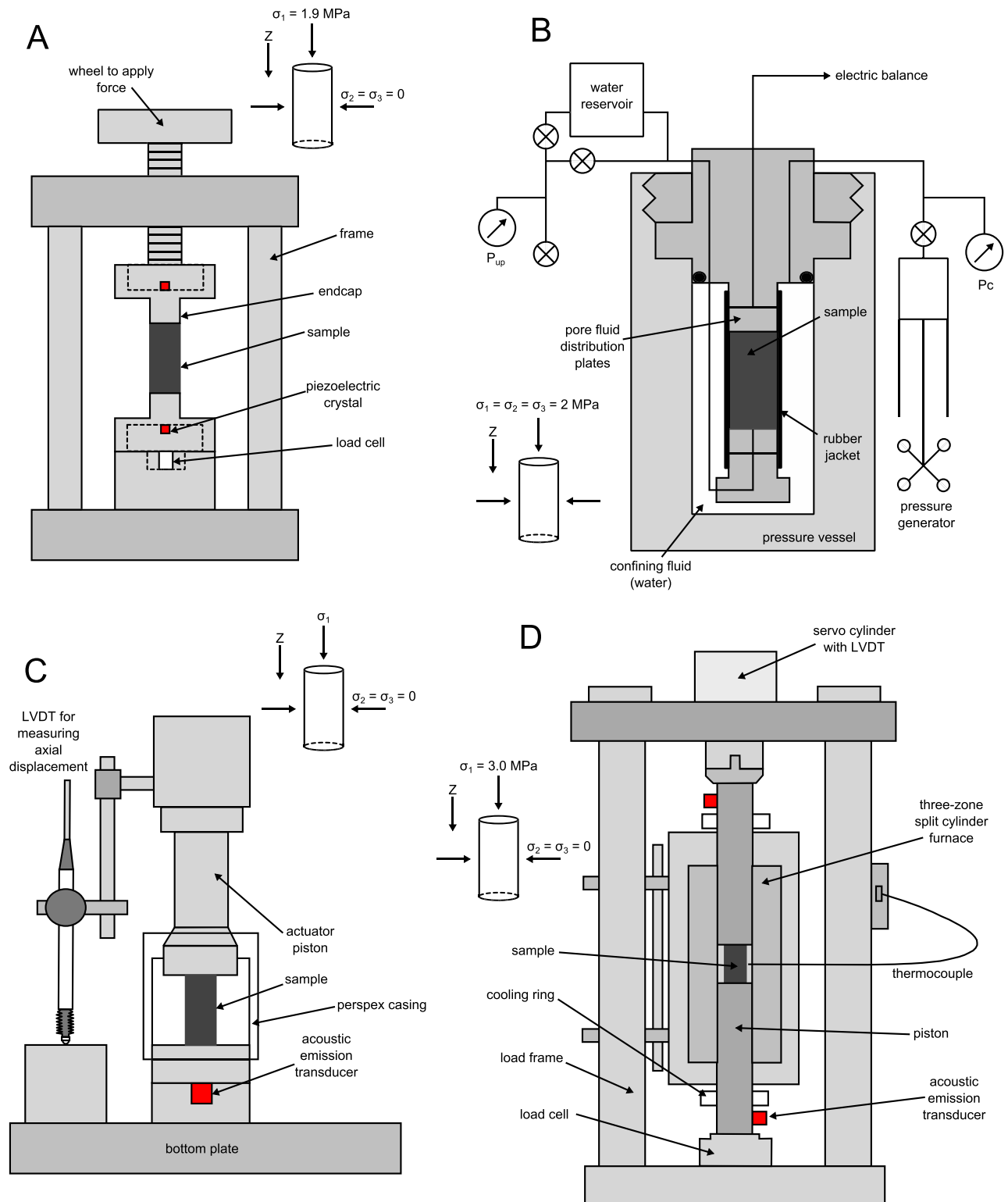
Figure A2. (a) Schematic diagram of the experimental arrangement used to determine benchtop elastic wave velocities. (b) Schematic diagram of the experimental arrangement used for our thermal stressing experiments. (c) Schematic diagram of the experimental arrangement used for our uniaxial compression experiments.

the sample using an electronic balance. After equilibration, water permeability (κ_{water}) could be calculated using Darcy's law:

$$\frac{Q}{A} = \frac{\kappa_{water}}{\eta L}\left(P_{up} - P_{down}\right) \tag{A9}$$

where Q is the volume of fluid measured per unit time (fluid volume flux), A is the cross-sectional area of the sample, η is the viscosity of the pore fluid, and L is the length of the sample.

A5. Uniaxial Compressive Strength Measurements

Uniaxial compressive strength (UCS) tests were performed on two cylindrical samples (dried in a vacuum oven at 40°C for at least 24 h prior to experimentation) of similar porosity from each of the five blocks of andesite. The experiments were conducted in a uniaxial press (Laboratoire de Déformation des Roches, Strasbourg, see Figure A2) under ambient laboratory conditions (i.e., ambient humidity, room pressure, and temperature) at a constant strain rate of $10^{-5}\,s^{-1}$ until failure. Although such a strain rate exceeds characteristic tectonic strain rates (that are typically on the order of $10^{-14}\,s^{-1}$) [see *Whitten*, 1956; *Wood*, 1973], volcano-tectonic environments, affected by magmatic and eruptive activities, will undoubtedly experience much higher strain rates [*Borgia*, 1994; *Takada*, 1994]. Indeed, this experimental strain rate is equivalent to strain rates observed in lava domes and inferred along the margins of magma conduits [*Rust et al.*, 2003]. Whereas we understand that unconfined compression experiments performed under ambient laboratory conditions may not accurately represent the natural case, this method is nevertheless considered as the "standard" way to assess rock strength [*International Society of Rock Mechanics*, 2007] allowing our data (1) to be compared with the wealth of preexisting data and (2) to be used in micromechanical modeling.

During deformation, axial strain and stress were continuously monitored by an LVDT (linear variable differential transducer) displacement transducer and a load cell, respectively. The output of acoustic emissions (AEs) during deformation was continuously monitored using a piezoelectric AE transducer (WD wideband sensors from Physical Acoustics Corporation) located within the bottom endcap (Figure A2) connected to a PCI-2 MISTRAS AE system (sampling at a rate of 5 MHz). AEs are high-frequency elastic wave packets generated by the rapid release of strain energy such as during brittle microfracturing (see *Lockner* [1993] for a review). During experimentation, an AE hit was recorded if a signal exceeded the set threshold of 30 dB. The amplitude and "energy" (the area under the received AE waveform envelope) of each received AE signal were provided by the AEwin software. Further, the received AE signals were also statistically analyzed using the analogous seismic *b* value [*Aki*, 1965] to characterize the nature of the microcracking in our samples. The *b* value describes the slope of the amplitude to frequency distribution of AEs, commonly used to describe the size-frequency distribution of microcracking events in rock deformation experiments [*Meredith and Atkinson*, 1983; *Main et al.*, 1989; *Smith et al.*, 2009; *Sammonds et al.*, 1992].

A6. Thermal Stressing Experiments

The rocks that comprise a volcanic edifice are, as a result of sustained magmatic and hydrothermal activity, subjected to high temperatures (e.g., 300–700°C). Numerical simulations of dyke emplacement highlight the potential for thermal stressing of the host rocks on a scale of several meters [*Carrigan et al.*, 1992], whereas larger bodies (such as magma reservoirs) can generate kilometer-scale thermal aureoles [*Bonaccorso et al.*, 2010]. With the aim of a better understanding of volcanically active provinces, we have assessed the impact of thermal stressing (to 450°C, representative of the temperatures at conduit margins) on the microstructural, physical, and mechanical properties of the andesites. We note that this temperature is within the stability field of the mineralogical assemblage, as well as the brittle limit set by the glass transition [*Lavallée et al.*, 2012]. First, each sample underwent a systematic physical property characterization. Second, each sample was thermally stressed in a high-temperature uniaxial press (at Earth and Environment, LMU, Munich, Figure A2). Samples were placed between the two pistons, and an axial stress of about 3 MPa was applied to the sample (provided simply by the mass of the upper piston). The furnace temperature was then set to climb to 500°C at 1°C/min, hold at 500°C for 60 min, and then cool back to the ambient laboratory temperature at a rate of 1°C/min (Figure 5). This procedure ensured that the sample temperature reached the target of 450°C (measured by an additional thermocouple adjacent to the sample, see Figure A2). We note that the heating
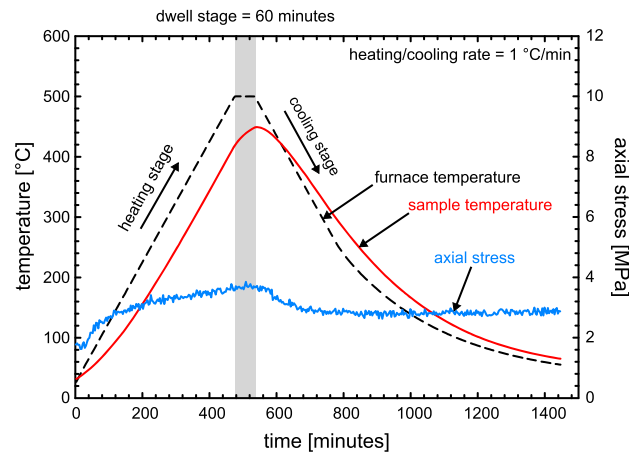
Figure A3. A time-temperature plot outlining the methodology for our thermal stressing experiments.

rate of the sample accurately matched the furnace heating rate (above temperatures of 100°C). However, the sample cooling rate was lower than that of the furnace, and the furnace could not cool at 1°C/min below furnace temperatures of about 250°C (Figure A3). During thermal stressing we continuously recorded the furnace temperature, the temperature adjacent to the sample, axial stress, and the output of AE (to be used as a proxy for the initiation and propagation of thermal microcracks). The generation of thermal microcracks during thermal stressing experiments has been previously monitored using the output AE [e.g., *Meredith et al.*, 1990; *Glover et al.*, 1995; *Jones et al.*, 1997; *Heap et al.*, 2013]. The pistons of the press were used as waveguides for the monitoring of AE using the same AE system described above (although the amplitude threshold was increased to 50 dB to eliminate electrical and background noise). Third, each sample underwent a systematic physical property recharacterization. Fourth, we determined their UCS (again using two samples per rock type). To best compare the mechanical behavior of the "as-collected" (i.e., samples that have undergone no additional heating or deformation) and thermally stressed andesites, we selected core samples that contained similar initial porosities. Finally, thin sections, again in the *XY* plane, of the thermally stressed andesites were prepared for microcrack density and anisotropy analysis.

References

Adelinet, M., J. Fortin, A. Schubnel, and Y. Guéguen (2013), Deformation modes in an Icelandic basalt: From brittle failure to localized deformation bands, *J. Volcanol. Geotherm. Res.*, *255*, 12–25.

Aki, K. (1965), Maximum likelihood estimate of b in the formula log N = a-bM and its confidence limits, *Bull. Earthquake Res. Inst.*, *43*, 237–239.

Arámbula-Mendoza, R., P. Lesage, C. Valdés-González, N. R. Varley, G. Reyes-Dávila, and C. Navarro (2011), Seismic activity that accompanied the effusive and explosive eruptions during the 2004–2005 period at Volcán de Colima, Mexico, *J. Volcanol. Geotherm. Res.*, *205*, 30–46.

Ashby, M. F., and C. G. Sammis (1990), The damage mechanics of brittle solids in compression, *Pure Appl. Geophys.*, *133*, 489–521.

Balme, M. R., V. Rocchi, C. Jones, P. R. Sammonds, P. G. Meredith, and S. A. Boon (2004), Fracture toughness measurements on igneous rocks using a high-pressure, high-temperature rock fracture mechanics cell, *J. Volcanol. Geotherm. Res.*, *132*, 159–172.

Baud, P., W. Zhu, and T.-F. Wong (2000), Failure mode and weakening effect of water on sandstone, *J. Geophys. Res.*, *105*, 16,371–16,389.

Baud, P., T.-f. Wong, and W. Zhu (2014), Effects of porosity and crack density on the compressive strength of rocks, *Int. J. Rock Mech. Mining Sci.*, *67*, 202–211, doi:10.1016/j.ijrmms.2013.08.031.

Bauer, S. J., M. Friedman, and J. Handin (1981), Effects of water-saturation on strength and ductility of three igneous rocks at effective pressures to 50 MPa and temperatures to partial melting, *The 22nd U.S. Symposium on Rock Mechanics (USRMS)*, June 29–July 2, 1981, Cambridge, Mass.

Benson, P. M., S. Vinciguerra, P. G. Meredith, and R. P. Young (2008), Laboratory simulation of volcano seismicity, *Science*, *322*, 249–252.

Bernabé, Y., U. Mok, and B. Evans (2003), Permeability-porosity relationships in rocks subjected to various evolution processes, *Pure Appl. Geophys.*, *160*, 937–960.

Bernabé, Y., M. Li, and A. Maineult (2010), Permeability and pore connectivity: A new model based on network simulations, *J. Geophys. Res.*, *155*, B10203, doi:10.1023/2010JB007444.

Bernard, M.-L., M. Zomara, Y. Géraud, and G. Boudon (2007), Transport properties of pyroclastic rocks from Montagne Pelée volcano (Martinique, Lesser Antilles), *J. Geophys. Res.*, *112*, B05205, doi:10.1029/2006JB004385.

Blake, O. O., D. R. Faulkner, and A. Reitbrock (2013), The effect of varying damage history in crystalline rocks on the P- and S-wave velocity under hydrostatic confining pressure, *Pure Appl. Geophys.*, *170*, 493–505.

Bonaccorso, A., G. Currenti, C. Del Negro, and E. Boschi (2010), Dike deflection modelling for inferring magma pressure and withdrawal, with application to Etna 2001 case, *Earth Planet. Sci. Lett.*, *293*, 121–129.

Borgia, A. (1994), Dynamic basis of volcanic spreading, *J. Geophys. Res.*, *99*, 17,791–17,804.

Borselli, L., L. Capra, D. Sarocchi, and S. De la Cruz-Reyna (2011), Flank collapse scenarios at Volcán de Colima, Mexico: A relative instability analysis, *J. Volcanol. Geotherm. Res.*, *208*, 51–65.

Bourbié, T., and B. Zinszner (1985), Hydraulic and acoustic properties as a function of porosity in Fontainebleau Sandstone, *J. Geophys. Res.*, *90*, 11,524–11,532.

Brace, W. F., B. W. Paulding, and C. H. Scholz (1966), Dilatancy in the fracture of crystalline rocks, *J. Geophys. Res.*, *71*, 3939–3953.

Caricchi, L., A. Pommier, M. Pistone, J. Castro, A. Burgisser, and D. Perugini (2011), Strain-induced magma degassing: Insights from simple-shear experiments on bubble bearing melts, *Bull. Volcanol.*, *73*, 1245–1257.

Carman, P. (1937), Fluid flow through a granular bed, *Trans. Inst. Chem. Eng.*, *15*, 150–167.

Carrigan, C. R., G. Schubert, and J. C. Eichelberger (1992), Thermal and dynamical regimes of single- and two-phase magmatic flow in dikes, *J. Geophys. Res.*, *97*, 17,377–17,392.

Chang, C., M. D. Zoback, and A. Khaksar (2006), Empirical relations between rock strength and physical properties in sedimentary rocks, *J. Pet. Sci. Eng.*, *51*, 223–237.

Cheng, C. H., and D. H. Johnston (1981), Dynamic and static moduli, *Geophys. Res. Lett.*, *8*, 39–42.

Ciccotti, M., and F. Mulargia (2004), Differences between static and dynamic elastic moduli of a typical seismogenic rock, *Geophys. J. Int.*, *157*, 474–477.

Ciccotti, M., N. Negri, L. Sassi, G. Gonzato, and F. Mulargia (2000), Elastic and fracture parameters of Etna, Stromboli, and Vulcano lava rocks, *J. Volcanol. Geotherm. Res.*, *98*, 209–217.

Cook, N. W. G., (1981), Stiff testing machines, stick slip sliding, and the stability of rock deformation, in *Mechanical Behavior of Crustal Rocks: The Handin Volume*, edited by N. L. Carter et al., pp. 93–102, AGU, Washington, D. C., doi:10.1029/GM024p0093.

Cortés, A., V. H. Garduño, J. L. Macías, C. Navarro-Ochoa, J. C. Komorowski, R. Saucedo, and J. C. Gavilanes (2010), Geologic mapping of the Colima volcanic complex (Mexico) and implications for hazard assessment, *Geol. Soc. Am. Special Pap.*, *464*, 249–264.

Costa, A. (2006), Permeability-porosity relationship: A reexamination of the Kozeny-Carman equation based on a fractal pore-space geometry assumption, *Geophys. Res. Lett.*, *33*, L02318, doi:10.1029/2005GL025134.

Costa, A., R. S. J. Sparks, G. Macedonio, and O. Melnik (2009), Effects of wall-rock elasticity on magma flow in dykes during explosive eruptions, *Earth Planet. Sci. Lett.*, *288*, 455–462.

David, C., B. Mendez, and M. Darot (1999), Influence of stress-induced and thermal cracking on physical properties and microstructure of La Pyrette Granite, *Int. J. Rock Mech. Mining Sci.*, *36*, 433–448.

David, E. C., N. Brantut, A. Schubnel, and R. W. Zimmerman (2011), Sliding crack model for nonlinearity and hysteresis in the uniaxial stress-strain curve of rock, *Int. J. Rock Mech. Mining Sci.*, *52*, 9–17.

Dávila, N., L. Capra, J. C. Gavilanes-Ruiz, N. Varley, G. Norini, and Á. Gómez-Vázquez (2007), Recent lahars at Volcán de Colima (Mexico): Drainage variation and spectral classification, *J. Volcanol. Geotherm. Res.*, *165*, 127–141.

De la Cruz-Reyna, S., and G. A. Reyes-Davila (2001), A model to describe precursory material-failure phenomena: Applications to short-term forecasting at Colima volcano, Mexico, *Bull. Volcanol.*, *63*, 297–308.

Donnadieu, F., O. Merle, and J. C. Besson (2001), Volcanic edifice stability during cryptodome intrusion, *Bull. Volcanol.*, *63*, 61–72.

Doyen, P. M. (1988), Permeability, conductivity, and pore geometry of sandstone, *J. Geophys. Res.*, *93*, 7729–7740.

Dullien, F. A. L. (1979), *Porous Media: Fluid Transport and Pore Structure*, Academic, New York.

Eichelberger, J. C., C. R. Carrigan, H. R. Westrich, and R. H. Price (1986), Non-explosive silicic volcanism, *Nature*, *323*, 598–602.

Eissa, E. A., and A. Kazi (1989), Relation between static and dynamic Young's moduli of rocks, *Int. J. Rock Mech. Mining Sci. Geomechanics Abstr.*, *25*, 479–482.

Fortin, J., S. Stantchits, S. Vinciguerra, and Y. Guéguen (2011), Influence of thermal and mechanical cracks on permeability and elastic wave velocities in a basalt from Mt. Etna volcano subjected to elevated pressure, *Tectonophysics*, *503*, 60–74, doi:10.1016/j.tecto.2010.09.028.

Gerik, A., and J. H. Kruhl (2009), Towards automated pattern quantification: Time-efficient assessment of anisotropy of 2D patterns with AMOCADO, *Comput. Geosci.*, *35*, 1087–1097.

Glover, P. W. J., P. Baud, M. Darot, P. G. Meredith, S. A. Boon, M. LeRevelec, S. Zoussi, and T. Reuschlé (1995), α/β phase transition in quartz monitored using acoustic emissions, *Geophys. J. Int.*, *120*, 775–782.

Gottsmann, J., S. De Angelis, N. Fournier, M. Van Camp, S. Sacks, A. Linde, and M. Ripepe (2011), On the geophysical fingerprint of Vulcanian explosions, *Earth Planet. Sci. Lett.*, *306*, 98–104.

Gudmundsson, A. (2011), *Rock Fractures in Geological Processes*, Cambridge Univ. Press, Cambridge, U. K.

Gudmundsson, A. (2012), Strengths and strain energies of volcanic edifices: Implications for eruptions, collapse calderas, and landslides, *Nat. Hazards Earth Syst. Sci.*, *12*, 2241–2258.

Guéguen, Y., and V. Palciauskas (1994), *Introduction to the Physics of Rocks*, Princeton Univ. Press, Princeton, N. J.

Heap, M. J., and D. R. Faulkner (2008), Quantifying the evolution of static elastic properties as crystalline rock approaches failure, *Int. J. Rock Mech. Mining Sci.*, *45*, 564–573.

Heap, M. J., S. Vinciguerra, and P. G. Meredith (2009), The evolution of elastic moduli with increasing crack damage during cyclic stressing of a basalt from Mt. Etna volcano, *Tectonophysics*, *471*, 153–160.

Heap, M. J., D. R. Faulkner, P. G. Meredith, and S. Vinciguerra (2010), Elastic moduli evolution and accompanying stress changes with increasing crack damage: Implications for stress changes around fault zones and volcanoes during deformation, *Geophys. J. Int.*, *183*, 225–236.

Heap, M. J., P. Baud, P. G. Meredith, S. Vinciguerra, A. F. Bell, and I. G. Main (2011), Brittle creep in basalt and its application to time-dependent volcano deformation, *Earth Planet. Sci. Lett.*, *307*, 71–82.

Heap, M. J., Y. Lavallée, A. Laumann, K.-U. Hess, P. G. Meredith, and D. B. Dingwell (2012), How tough is tuff in the event of fire?, *Geology*, *40*, 311–314.

Heap, M. J., Y. Lavallée, P. G. Meredith, D. B. Dingwell, S. Huismann, and F. Weise (2013), The influence of thermal-stressing (up to 1000 °C) on the physical, mechanical, and chemical properties of siliceous-aggregate, high-strength concrete, *Construction Building Mater.*, *42*, 248–265.

Heap, M. J., P. Baud, P. G. Meredith, S. Vinciguerra, and T. Reuschlé (2014), The permeability and elastic moduli of tuff from Campi Flegrei, Italy: Implications for ground deformation modelling, *Solid Earth*, *5*, 25–44.

Hoek, E., and Z. T. Bieniawski (1965), Brittle fracture propagation in rock under compression, *Int. J. Fract.*, *1*, 137–155.

Homand-Etienne, F., and R. Houpert (1989), Thermally induced microcracking in granite: Characterisation and analysis, *Int. J. Rock Mech. Mining Sci. Geomech. Abstr.*, *26*(2), 125–134.

Horii, H., and S. Nemat-Nasser (1986), Brittle failure in compression: Splitting, faulting and brittle-ductile transition, *Phil. Trans. Royal Soc. London*, *319*, 337–374.

Hutchinson, W., N. Varley, D. M. Pyle, and T. A. Mather (2013), Airborne thermal remote sensing of the Volcán de Colima (Mexico) lava dome from 2007 to 2010, in *Remote Sensing of Volcanoes & Volcanic Processes: Integrating Observation & Modelling*, edited by D. L. Pyle and T. A. Mather, pp. 203–228, Geological Society of London, London, U. K.

International Society of Rock Mechanics (2007), Part 1 - SM for determination of the uniaxial compressive strength of rock materials, in *The Complete ISRM Suggested Methods for Rock Characterization, Testing and Monitoring: 1974–2006*, edited by R. Ulusay and J. A. Hudson, pp. 151–156, IRSM Turkish National Group, Ankara, Turkey.

Jaeger, J., N. G. W. Cook, and R. Zimmerman (2007), *Fundamentals in Rock Mechanics*, 4th ed., Blackwell Publishing, London.

Jaupart, C. (1998), Gas loss from magmas through conduit walls during eruption, *Geol. Soc. London, Special Publ.*, *145*, 73–90.

Jeong, H.-s., S.-s. Kang, and Y. Obara (2007), Influence of surrounding environments and strain rates on the strength of rocks subjected to uniaxial compression, *Int. J. Rock Mech. Mining Sci.*, *44*, 321–331.

Jones, C., G. Keaney, P. G. Meredith, and S. A. F. Murrell (1997), Acoustic emission and fluid permeability measurements on thermally cracked rocks, *Phys. Chem. Earth*, *22*(1-2), 13–17.

Keles, C., and L. Tutluoglu (2011), Investigation of proper specimen geometry for mode I fracture toughness testing with flattened Brazilian disc method, *Int. J. Fract.*, *169*, 61–75.

Kemeny, J. M., and N. W. G. Cook (1991), Micromechanics of deformation in rocks, in *Toughening Mechanisms in Quasi-Brittle Materials*, edited by S. P. Shah, pp. 155–188, Kluwer Academic Publishers, Dordrecht, Netherlands.

Kendrick, J. E., Y. Lavallée, K.-U. Hess, M. J. Heap, H. E. Gaunt, P. G. Meredith, and D. B. Dingwell (2013), Tracking the permeable porous network during strain-dependent magmatic flow, *J. Volcanol. Geotherm. Res.*, *260*, 117–126.

Kilburn, C. R. J. (2003), Multiscale fracturing as a key to forecasting volcanic eruptions, *J. Volcanol. Geotherm. Res.*, *125*, 271–289.

Kilburn, C. R. J., and P. R. Sammonds (2005), Maximum warning times for imminent volcanic eruptions, *Geophys. Res. Lett.*, *32*, L24313, doi:10.1029/2005GL024184.

Kirchhoff, G., W. Pompe, and H.-A. Bahr (1982), Structure dependence of thermally induced microcracking in porcelain studied by acoustic emission, *J. Mater. Sci.*, *17*, 2809–2816.

Klug, C., and K. V. Cashman (1996), Permeability development in vesiculating magmas: Implications for fragmentation, *Bull. Volcanol.*, *58*, 87–100.

Kolzenburg, S., M. J. Heap, Y. Lavallée, J. K. R. Russell, P. G. Meredith, and D. B. Dingwell (2012), Strength and permeability recovery of tuffisite-bearing andesite, *Solid Earth*, *3*, 191–198.

Kozeny, J. (1927), Ueber kapillare Leitung der Wasser in Boden, *Sitzungsber. Akad. Wiss. Wien*, *136*, 271–306.

Laumonier, M., L. Arbaret, A. Burgisser, and R. Champallier (2011), Porosity redistribution enhanced by strain localisation in crystal-rich magmas, *Geology*, *39*, 715–718.

Lavallée, Y., P. G. Meredith, D. B. Dingwell, K. U. Hess, J. Wassermann, B. Cordonnier, A. Gerik, and J. H. Kruhl (2008), Seismogenic lavas and explosive eruption forecasting, *Nature*, *453*, 507–510.

Lavallée, Y., N. Varley, M. A. Alatorre-Ibargüengoitia, K.-U. Hess, U. Kueppers, S. Mueller, D. Richard, B. Scheu, O. Spieler, and D. B. Dingwell (2012), Magmatic architecture of dome-building eruptions at Volcán de Colima, Mexico, *Bull. Volcanol.*, *74*, 249–260.

Lavallée, Y., P. M. Benson, M. J. Heap, K.-U. Hess, A. Flaws, B. Schillinger, P. G. Meredith, and D. B. Dingwell (2013), Reconstructing magma failure and the degassing network of dome-building eruptions, *Geology*, *41*, 515–518.

Lebedev, E. B., and H. Kern (1999), The effect of hydration and dehydration reactions on wave velocities in basalts, *Tectonophysics*, *308*, 331–340.

Loaiza, S., J. Fortin, A. Schubnel, Y. Guéguen, S. Vinciguerra, and M. Moreira (2012), Mechanical behavior and localized failure modes in a porous basalt from the Azores, *Geophys. Res. Lett.*, *39*, L19304, doi:10.1029/2012GL053218.

Lockner, D. (1993), The role of acoustic emission in the study of rock fracture, *Int. J. Rock Mech. Mining Sci. Geomech. Abstr.*, *30*, 883–889.

Luhr, J. F. (2002), Petrology and geochemistry of the 1991 and 1998–1999 lava flows from Volcán de Colima, México: Implications for the end of the current eruptive cycle, *J. Volcanol. Geotherm. Res.*, *117*, 169–194.

Main, I. G., P. G. Meredith, and C. Jones (1989), A reinterpretation of the precursory seismic b-value anomaly from fracture-mechanics, *Geophys. J. Oxford*, *96*, 131–138.

Manconi, A., T. R. Walter, and F. Amelung (2007), Effects of mechanical layering on volcano deformation, *Geophys. J. Int.*, *170*, 952–958.

Manconi, A., T. R. Walter, M. Manzo, G. Zeni, P. Tizzani, E. Sansosti, and R. Lanari (2010), On the effects of 3D mechanical heterogeneities at Campi Flegrei caldera, southern Italy, *J. Geophys. Res.*, *115*, B08405, doi:10.1029/2009JB007099.

McGuire, W. J. (1996), Volcano instability: A review of contemporary themes, *Geol. Soc. London*, *110*, 1–23.

Meredith, P. G., and B. K. Atkinson (1983), Stress corrosion and acoustic emission during tensile crack propagation in Whin Sill dolerite and other basic rocks, *Geophys. J. R. Astron. Soc.*, *75*, 1–21.

Meredith, P. G., I. G. Main, and C. Jones (1990), Temporal variations in seismicity during quasi-static and dynamic rock failure, *Tectonophysics*, *175*, 249–268.

Meredith, P. G., O. Lewis, S. Vinciguerra, C. Trovato, and P. M. Benson (2005), The influence of microcracks on the physical and mechanical properties of Etna and Iceland basalt, Abstract #V24B-08 presented at 2005 Fall Meeting, AGU, San Francisco, Calif.

Mueller, S. B., N. R. Varley, U. Kueppers, P. Lesage, G. Á. Reyes Davila, and D. B. Dingwell (2013), Quantification of magma ascent rate through rockfall monitoring at the growing/collapsing lava dome of Volcán de Colima, Mexico, *Solid Earth*, *4*, 201–213.

Mueller, S. P. (2006), Permeability and porosity as constraints on the explosive eruption of magma: Laboratory experiments and field investigations, PhD thesis, University of Munich, Munich, Germany.

Mueller, S., O. Melnik, O. Spieler, B. Scheu, and D. B. Dingwell (2005), Permeability and degassing of dome lavas undergoing rapid decompression: An experimental study, *Bull. Volcanol.*, *67*, 526–538.

Mueller, S., B. Scheu, O. Spieler, and D. B. Dingwell (2008), Permeability control on magma fragmentation, *Geology*, *36*, 399–402.

Murray, J. B., and J. J. Ramírez Ruiz (2002), Long-term predictions of the time of eruptions using remote distance measurement at Volcán de Colima, México, *J. Volcanol. Geotherm. Res.*, *117*, 79–89.

Murray, J. B., and L. K. Wooller (2002), Persistent summit subsidence at Volcan de Colima, Mexico,1982–1999: Strong evidence against Mogi deflation, *J. Volcanol. Geotherm. Res.*, *117*, 69–78.

Nara, Y., P. G. Meredith, T. Yoneda, and K. Kaneko (2011), Influence of macro-fractures and micro-fractures on permeability and elastic wave velocities in basalt at elevated pressure, *Tectonophysics*, *503*, 52–59.

Nara, Y., K. Morimoto, N. Hiroyoshi, T. Yoneda, K. Kaneko, and P. M. Benson (2012), Influence of relative humidity on fracture toughness of rock: Implications for subcritical crack growth, *Int. J. Solids Struct.*, *49*, 2471–2481.

Norini, G., L. Capra, G. Groppelli, F. Agliardi, A. Pola, and A. Cortés (2010), Structural architecture of the Colima Volcanic Complex, *J. Geophys. Res.*, *115*, B12209, doi:10.1029/2010JB007649.

Obara, Y., K. Sakaguchi, T. Nakayama, and K. Sugawara (1992), Anisotropy effect on fracture toughness of rock, in *ISRM Symposium Eurock 1992 "Rock Characterisation"*, edited by J. A. Hudson, pp. 7–12, British Geotechnical Society, London, U. K.

O'Connell, R. J., and B. Budiansky (1974), Seismic velocities in dry and saturated cracked solids, *J. Geophys. Res.*, *79*, 5412–5426.

Ouchterlony, F. (1990), Fracture toughness testing or rock with core based specimens, *Eng. Fracture Mech.*, *35*, 351–366.

Paterson, M. S. (1983), The equivalent channel model for permeability and resistivity in fluid-saturated rock - A re-appraisal, *Mech. Mater.*, *2*, 345–352.

Paterson, M. S., and T.-F. Wong (2005), *Experimental Rock Deformation: The Brittle Field*, Springer, New York.

Pinel, V., A. Hooper, S. De la Cruz-Reyna, G. A. Reyes-Davila, M. P. Doin, and P. Bascou (2011), The challenging retrieval of the displacement field from InSAR data for andesitic stratovolcanoes: Case study of Popocatepetl and Colima Volcano, Mexico, *J. Volcanol. Geotherm. Res.*, *200*, 49–61.

Plail, M., M. Edmonds, C. S. Humphreys, J. Barclay, and R. A. Herd (2014), Geochemical evidence for relict degassing pathways preserved in andesite, *Earth Planet. Sci. Lett.*, *386*, 21–33.

Reubi, O., and J. Blundy (2008), Assimilation of plutonic roots, formation of high-K exotic melt inclusions and genesis of andesitic magmas at Volcan De Colima, Mexico, *J. Petrol.*, *49*, 2221–2243.

Reubi, O., J. Blundy, and N. R. Varley (2013), Volatiles contents, degassing and crystallisation of intermediate magmas at Volcan de Colima, Mexico, inferred from melt inclusions, *Contrib. Mineral. Petrol.*, *165*, 1087–1106.

Richard, D., B. Scheu, S. P. Mueller, O. Spieler, and D. B. Dingwell (2013), Outgassing: Influence on speed of magma fragmentation, *J. Geophys. Res. Solid Earth*, *118*, 862–877, doi:10.1002/jgrb.50080.

Richter, D., and G. Simmons (1974), Thermal expansion behaviour of igneous rocks, *Int. J. Rock Mech. Mining Sci.*, *11*, 403–411.

Rocchi, V., P. R. Sammonds, and C. R. J. Kilburn (2004), Fracturing of Etnean and Vesuvian rocks at high temperatures and low pressures, *J. Volcanol. Geotherm. Res.*, *132*, 137–157.

Rust, A. C., M. Manga, and K. V. Cashman (2003), Determining flow type, shear rate and shear stress in magmas from bubble shapes and orientations, *J. Volcanol. Geotherm. Res.*, *122*, 111–132.

Rust, A., and K. V. Cashman (2004), Permeability of vesicular silicic magma: Inertial and hysteresis effects, *Earth Planet. Sci. Lett.*, *228*, 93–107.

Rutter, E. (1986), On the nomenclature of mode of failure transitions in rocks, *Tectonophysics*, *122*, 381–387.

Saar, M. O., and M. Manga (1999), Permeability-porosity relationship in vesicular basalts, *Geophys. Res. Lett.*, *26*, 111–114.

Sammis, C. G., and M. F. Ashby (1986), The failure of brittle porous solids under compressive stress states, *Acta. Metall.*, *34*, 511–526, doi:10.1016/0001-6160(86)90087-8.

Sammonds, P. R., P. G. Meredith, and I. G. Main (1992), Role of pore fluids in the generation of seismic precursors to shear fracture, *Nature*, *359*, 228–230.

Saucedo, R., J. L. Macías, J. C. Gavilanes, J. L. Arce, J. C. Komorowski, J. E. Gardner, and G. Valdez-Moreno (2010), Eyewitness, stratigraphy, chemistry, and eruptive dynamics of the 1913 Plinian eruption of Volcán de Colima, México, *J. Volcanol. Geotherm. Res.*, *191*, 149–166.

Savov, I. P., J. F. Luhr, and C. Navarro-Ochoa (2008), Petrology and geochemistry of lava and ash erupted from Volcán Colima, Mexico, during 1998–2005, *J. Volcanol. Geotherm. Res.*, *174*, 241–256.

Scholz, C. H. (1968), Microfracturing and the inelastic deformation of rock in compression, *J. Geophys. Res.*, *73*, 1417–1432.

Schubnel, A., P. M. Benson, B. D. Thompson, J. Hazzard, and R. P. Young (2006), Quantifying damage, saturation and anisotropy in cracked rocks by inverting elastic wave velocities, *Pure Appl. Geophys.*, *163*, 947–973.

Shea, T., B. F. Houghton, L. Gurioli, K. V. Cashman, J. E. Hammer, and B. J. Hobden (2010), Textural studies of vesicles in volcanic rocks: An integrated methodology, *J. Volcanol. Geotherm. Res.*, *190*, 271–289.

Simmons, G., and W. F. Brace (1965), Comparison of static and dynamic measurements of compressibility of rocks, *J. Geophys. Res.*, *70*, 5649–5656.

Smith, R., P. R. Sammonds, and C. R. J. Kilburn (2009), Fracturing of volcanic systems: Experimental insights into pre-eruptive conditions, *Earth Planet. Sci. Lett.*, *280*, 211–219.

Smith, R., P. Sammonds, H. Tuffen, and P. G. Meredith (2011), Evolution of the mechanics of the 2004–2008 Mt. St. Helens lava dome with time and temperature, *Earth Planet. Sci. Lett.*, *307*, 191–200.

Sparks, R. S. J. (2003), Forecasting volcanic eruptions, *Earth Planet. Sci. Lett.*, *210*, 1–15.

Spieler, O., B. Kennedy, U. Kueppers, D. B. Dingwell, B. Scheu, and J. Taddeucci (2004), The fragmentation threshold of pyroclastic rocks, *Earth Planet. Sci. Lett.*, *226*, 139–148.

Stanchits, S., S. Vinciguerra, and G. Dresen (2006), Ultrasonic velocities, acoustic emission characteristics and crack damage of basalt and granite, *Pure Appl. Geophys.*, *163*, 975–994.

Stasiuk, M. V., J. Barclay, M. R. Carroll, C. Jaupart, J. C. Ratté, R. S. J. Sparks, and S. R. Tait (1996), Degassing during magma ascent in the Mule Creek vent (USA), *Bull. Volcanol.*, *58*, 117–130.

Stevenson, J. A., and N. Varley (2008), Fumarole monitoring with a handheld infrared camera: Volcán de Colima, Mexico, 2006–2007, *J. Volcanol. Geotherm. Res.*, *177*, 911–924.

Sulpizio, R., L. Capra, D. Sarocchi, R. Saucedo, J. C. Gavilanes-Ruiz, and N. R. Varley (2010), Predicting the block-and-ash flow inundation areas at Volcán de Colima (Colima, Mexico) based on the present day (February 2010) status, *J. Volcanol. Geotherm. Res.*, *193*, 49–66.

Takada, A. (1994), The influence of regional stress and magmatic input on styles of monogenetic and polygenetic volcanism, *J. Volcanol. Geotherm. Res.*, *99*, 13,563–13,573.

Tang, S. B., C. A. Tang, Z. Z. Liang, and Y. F. Zhang (2011), Influence of heterogeneity on strength and failure characterization of cement-based composite subjected to uniform thermal loading, *Constr. Build. Mater.*, *25*, 3382–3392.

Taran, Y., J. C. Gavilanes, and A. Cortés (2002), Chemical and isotopic composition of fumarolic gases and the SO2 flux from Volcán de Colima, Mexico, between the 1994 and 1998 eruptions, *J. Volcanol. Geotherm. Res.*, *117*, 105–119.

Tribaudino, M., R. J. Angel, F. Cámara, F. Nestola, D. Pasqual, and I. Margiolaki (2010), Thermal expansion of plagioclase feldspars, *Contrib. Mineral. Petrol.*, *160*, 899–908.

Tuffen, H., D. B. Dingwell, and H. Pinkerton (2003), Repeated fracture and healing of silicic magma generate flow banding and earthquakes?, *Geology*, *31*, 1089–1092.

Underwood, E. E. (1970), *Quantitative Stereology*, Addison Wesley, Reading, Mass.

Vajdova, V., W. Zhu, T.-M. N. Chen, and T.-F. Wong (2010), Micromechanics of brittle faulting and cataclastic flow in Tavel limestone, *J. Struct. Geol.*, *32*, 1158–1169.

Vajdova, V., P. Baud, L. Wu, and T.-f. Wong (2012), Micromechanics of inelastic compaction in two allochemical limestones, *J. Struct. Geol.*, *43*, 100–117.

Varley, N. R., and Y. A. Taran (2003), Degassing processes of Popocatépetl and Volcán de Colima, Mexico, in *Volcanic Degassing*, edited by C. Oppenheimer, D. M. Pyle, and J. Barclay, pp. 263–280, Geological Society of London, London, U. K.

Varley, N., R. Arámbula-Mendoza, G. Reyes-Dávila, J. Stevenson, and R. Harwood (2010), Long-period seismicity during magma movement at Volcán de Colima, *Bull. Volcanol.*, *72*, 1093–1107.

Vasseur, J., F. B. Wadsworth, Y. Lavallée, K.-U. Hess, and D. B. Dingwell (2013), Volcanic sintering: Timescales of viscous densification and strength recovery, *Geophys. Res. Lett.*, *40*, 5658–5664, doi:10.1002/2013GL058105.

Vinciguerra, S., C. Trovato, P. G. Meredith, and P. M. Benson (2005), Relating seismic velocities, thermal cracking and permeability in Mt. Etna and Iceland basalts, *Int. J. Rock Mech. Mining Sci.*, *42*, 900–910.

Voight, B. (1989), A relation to describe rate-dependent material failure, *Science*, *243*, 200–203.

Voight, B. (2000), Structural stability of andesite volcanoes and lava domes, *Philos. Trans. Math. Phys. Eng. Sci.*, *358*(1770), Causes and Consequences of Eruptions of Andesite Volcanoes (May 15, 2000), 1663–1703.

Volland, S., and J. H. Kruhl (2004), Anisotropy quantification: The application of fractal geometry methods on tectonic fracture patterns of a Hercynian fault zone in NW Sardinia, *J. Struct. Geol.*, *26*, 1499–1510.

Walker, G. P. L. (1989), Spongy pahoehoe in Hawaii: A study of vesicle-distribution patterns in basalt and their significance, *Bull. Volcanol.*, *51*, 199–209.

Walsh, J. B., and W. F. Brace (1984), The effect of pressure on porosity and the transport properties of rock, *J. Geophys. Res.*, *89*, 9425–9431.

Whitten, C. A. (1956), Crustal movements in California and Nevada, *Trans. AGU*, *37*, 393–398.

Wong, T.-f. (1985), Geometric probability approach to the characterization and analysis of microcracking in rocks, *Mech. Mater.*, *4*, 261–276.

Wong, T.-f., and P. Baud (2012), The brittle transition in rocks: A review, *J. Struct. Geol.*, *44*, 25–53.

Wood, D. S. (1973), Patterns and magnitudes of natural strain in rocks, *Phil. Trans. R. Soc. London*, *274*, 373–382.

Woods, A. W., and T. Koyaguchi (1994), Transitions between explosive and effusive eruptions of silicic magmas, *Nature*, *370*, 641–644.

Wright, H. M. N., and K. V. Cashman (2013), Compaction and gas loss in welded pyroclastic deposits: Evolution of porosity and permeability in the Shevlin Park Tuff, *Geol. Soc. Am. Bull.*, *126*, 234–247, doi:10.1130/B30668.1.

Wright, H. M. N., J. J. Roberts, and K. V. Cashman (2006), Permeability of anisotropic tube pumice: Model calculations and measurements, *Geophys. Res. Lett.*, *33*, L17316, doi:10.1029/2006GL027224.

Wright, H. M. N., K. V. Cashman, E. H. Gottesfeld, and J. J. Roberts (2009), Pore structure of volcanic clasts: Measurements of permeability and electrical conductivity, *Earth Planet. Sci. Lett.*, *280*, 93–104.

Wu, X. Y., P. Baud, and T.-F. Wong (2000), Micromechanics of compressive failure and spatial evolution of anisotropic damage in Darley Dale sandstone, *Int. J. Rock Mech. Mining Sci.*, *37*, 143–160.

Yokoyama, T., and S. Takeuchi (2009), Porosimetry of vesicular volcanic products by a water-expulsion method and the relationship of pore characteristics to permeability, *J. Geophys. Res.*, *114*, B02201, doi:10.1029/2008JB005758.

Yong, C., and C.-Y. Wang (1980), Thermally induced acoustic emission in Westerly granite, *Geophys. Res. Lett.*, *7*(12), 1089–1092.

Zhu, W., P. Baud, and T.-f. Wong (2010), Micromechanics of cataclastic pore collapse in limestone, *J. Geophys. Res.*, *115*, B04405, doi:10.1029/2009JB006610.

Zhu, W., P. Baud, S. Vinciguerra, and T.-F. Wong (2011), Micromechanics of brittle faulting and cataclastic flow in Alban Hills tuff, *J. Geophys. Res.*, *116*, B06209, doi:10.1029/2010JB008046.

Zoback, M. D. (2010), *Reservoir Geomechanics*, Cambridge Univ. Press, Cambridge, U. K.

Zobin, V. M., M. González-Amezcua, and G. A. Reyes-Dávila (2002a), Seismotectonic deformation of the volcanic edifice prior to the 1998 lava eruption of Volcán de Colima, México, *Bull. Volcanol.*, *64*, 349–355.

Zobin, V. M., M. Gonzalez Amezcua, G. A. Reyes Davila, T. Dominguez, J. C. Cerda Chacon, and J. M. Chavez Alvarez (2002b), Comparative characteristics of the 1997-1998 seismic swarms preceding the November 1998 eruption of Volcan de Colima, Mexico, *J. Volcanol. Geotherm. Res.*, *117*, 47–60.

RESEARCH ARTICLE

Fracture and compaction of andesite in a volcanic edifice

M. J. Heap[1] · J. I. Farquharson[1] · P. Baud[1] ·
Y. Lavallée[2] · T. Reuschlé[1]

Abstract The failure mode of lava—dilatant or compactant—depends on the physical attributes of the lava, primarily the porosity and pore size, and the conditions under which it deforms. The failure mode for edifice host rock has attendant implications for the structural stability of the edifice and the efficiency of the sidewall outgassing of the volcanic conduit. In this contribution, we present a systematic experimental study on the failure mode of edifice-forming andesitic rocks (porosity from 7 to 25 %) from Volcán de Colima, Mexico. The experiments show that, at shallow depths (<1 km), both low- and high-porosity lavas dilate and fail by shear fracturing. However, deeper in the edifice (>1 km), while low-porosity (<10 %) lava remains dilatant, the failure of high-porosity lava is compactant and driven by cataclastic pore collapse. Although inelastic compaction is typically characterised by the absence of strain localisation, we observe compactive localisation features in our porous andesite lavas manifest as subplanar surfaces of collapsed pores. In terms of volcano stability, faulting in the upper edifice could destabilise the volcano, leading to an increased risk of flank or large-scale dome collapse, while compactant deformation deeper in the edifice may emerge as a viable mechanism driving volcano subsidence, spreading and destabilisation. The failure mode influences the evolution of rock physical properties: permeability measurements demonstrate that a throughgoing tensile fracture increases sample permeability (i.e. equivalent permeability) by about a factor of two, and that inelastic compaction to an axial strain of 4.5 % reduces sample permeability by an order of magnitude. The implication of these data is that sidewall outgassing may therefore be efficient in the shallow edifice, where rock can fracture, but may be impeded deeper in the edifice due to compaction. The explosive potential of a volcano may therefore be subject to increase over time if the progressive compaction and permeability reduction in the lower edifice cannot be offset by the formation of permeable fracture pathways in the upper edifice. The mode of failure of the edifice host rock is therefore likely to be an important factor controlling lateral outgassing and thus eruption style (effusive versus explosive) at stratovolcanoes.

✉ M. J. Heap
heap@unistra.fr

[1] Équipe de Géophysique Expérimentale, Institut de Physique de Globe de Strasbourg (UMR 7516 CNRS, Université de Strasbourg/EOST), 5 rue René Descartes, 67084 Strasbourg cedex, France

[2] Earth, Ocean and Ecological Sciences, University of Liverpool, Liverpool L69 3GP, UK

Introduction

Volcanic edifices, products of the accumulation of successive lava and volcaniclastic deposits and endogenous growth (Borgia and Linneman 1990; Kaneko 2002; Biggs et al. 2010), play a central role in governing volcanic hazards (Voight 2000). First, the structural stability of the edifice, and therefore its susceptibility to catastrophic collapse, depends on the integrity of this rapidly emplaced mélange of coherent lava flows and poorly consolidated volcaniclastic deposits (e.g. Gudmundsson 2011). Second, the ease with which exsolving magma can outgas into the country rock (e.g. Jaupart 1998; Collinson and Neuberg 2012), a factor

dictating the explosivity of the volcano, relies on the physical state (porosity, permeability) of the edifice host rocks (e.g. Eichelberger et al. 1986; Woods and Koyaguchi 1994; Mueller et al. 2008; Nguyen et al. 2014; Castro et al. 2014; Okumura and Sasaki 2014; Gaunt et al. 2014; Farquharson et al. 2015). Throughout edifice construction, edifice rocks are subject to a multitude of local and regional stresses that persistently alter their physical state, challenging edifice stability and influencing lateral outgassing; for example, local stress fields can rapidly change due to dyke propagation, regional stresses exist in the form of tectonic stresses, and lithostatic stresses build as effusive and explosive products that accumulate over time (e.g. Roman et al. 2004; Gerst and Savage 2004; Gudmundsson 2006). As a result, during the life cycle of a volcano, the initially steep conical structure evolves into a more dispersed and degraded landform (van Wyk de Vries and Borgia 1996; Borgia et al. 2000). Ultimately, this increasingly unstable structure can collapse, evidence of which is exposed in the geological record as sector collapse scars, amphitheatres, craters and calderas (e.g. Guest et al. 1984; Stoopes and Sheridan 1992; Hall et al. 1999; Tibaldi 2001). It follows that the mechanical response of the rocks that comprise the edifice to regional and local stresses must represent a fundamental factor in the progressive destabilisation of a volcano and the evolution of outgassing efficiency and thus explosivity.

When exposed to a differential stress, porous rock reacts in one of two ways. The porosity within the rock (a combination of microcracks and pores) will either increase (dilation) or decrease (compaction). The operative micromechanical process, dilatational microcracking or compactive pore collapse/ grain crushing, dictates the response of the rock to an applied stress and is dependent on both the initial physical properties of the rock (e.g. porosity, pore size) and the conditions (e.g. pressure, temperature, pore fluid) under which the rock deforms (see the review by Wong and Baud 2012 and references therein). At low confining pressures (shallow depths), both low- and high-porosity rocks will dilate resulting in a dilatant mode of failure, such as axial splitting (at very low confining pressures or depths) or shear failure (e.g. Paterson and Wong 2005). However, as confining pressure (depth) increases, while low-porosity rock will continue to form shear fractures, high-porosity rock will undergo shear-enhanced compaction driven by cataclastic pore collapse and grain crushing (Wong and Baud 2012).

Importantly, the mode of failure will severely impact the evolution of rock physical properties. Laboratory experiments have shown that shear fracturing (and associated dilatancy) is synonymous with an increase in porosity (Read et al. 1995) and a decrease in elastic wave velocity (Ayling et al. 1995). Some experimental data, however, suggest the impact of fracturing on permeability may depend on the initial porosity of the rock. While dilation and the formation of a macroscopic

shear fracture (e.g. Zoback and Byerlee 1975; Mitchell and Faulkner 2008) and tensile (extension) fractures (Nara et al. 2011) have been shown to increase the permeability of low-porosity rock by many orders of magnitude, experiments on high-porosity (>15 %) sandstones have shown that shear fractures can decrease permeability (Zhu et al. 1997a; Ngwenya et al. 2003). Indeed, some field studies on large faults in porous rocks have shown that permeability decreases as the fault is approached (Shipton et al. 2002; Farrell et al. 2014). Similar studies on large faults in low-porosity rock attest to a significant increase in permeability within the adjacent damage zone (Mitchell and Faulkner 2012), although the low permeability of the fault core can impart a permeability anisotropy (Faulkner and Rutter 2001; Wibberley and Shimamoto 2003).

By contrast, inelastic compaction will serve to increase elastic wave velocity (Fortin et al. 2005), decrease porosity (Wong and Baud 2012) and, in all cases, decrease permeability (David et al. 1994; Zhu et al. 1997b; Fortin et al. 2005; Baud et al. 2012). The failure mode also influences the output of acoustic emissions (AE, typically used as a proxy for microcracking) during deformation (Wong et al. 1997). An understanding of the mechanical behaviour and failure modes, and their impact on rock physical properties, of edifice-forming volcanic rocks is therefore of upmost importance. For example, the efficiency of lateral outgassing through the country rock (e.g. Jaupart 1998) is likely aided by a dilatant failure mode and hindered by a compactant failure mode.

Laboratory studies on the mechanical behaviour and failure modes of rock have been biased towards sedimentary rocks (Wong and Baud 2012). Studies on volcanic rocks—rocks with a greater microstructural complexity—are few (e.g. Kennedy et al. 2009; Zhu et al. 2011; Loaiza et al. 2012; Adelinet et al. 2013; Heap et al. 2014a, 2015), but have highlighted that volcanic rock can switch from dilatant to compactive modes of failure as effective pressure (i.e. depth) is increased. High-porosity tuffs (30–50 %) have been shown to switch to inelastic compaction at very low effective pressures (P_{eff}=5–10 MPa; P_{eff}=Pc−αPp, where Pc and Pp are the confining pressure and pore pressure, respectively, and poroelastic constant α is assumed to be 1), corresponding to depths of a couple of hundred metres (Zhu et al. 2011; Heap et al. 2014a, 2015). Studies on porous extrusive rocks have shown that inelastic compaction is encountered at much higher effective pressures. An aphanitic basalt from Reykjanes (Iceland) containing a porosity of 8 % switched to compactive behaviour at an effective pressure of 75 MPa (Adelinet et al. 2013), while an aphanitic trachyandesite from the Açores (Portugal) with a porosity of 18 % was compactant at 90 MPa (Loaiza et al. 2012), pressures corresponding to depths greater than 3 km. Kennedy et al. (2009) showed that low-porosity (8 %) dacite from Mount St. Helens (USA) exhibited shear faulting up to effective pressures of 75 MPa, while the deformation of high-porosity (20–24 %) dacite from

Augustine volcano (USA) was driven by distributed cataclastic flow at pressures of 25 MPa and higher. Despite these studies, the paucity of experimental data on the mechanical behaviour and failure modes of volcanic rock inhibits our understanding, a key element to interpret the evolution of edifice stability and sidewall outgassing. For instance, the rocks comprising a volcanic edifice are known to be variably porous (e.g. Melnik and Sparks 2002; Kueppers et al. 2005; Lavallée et al. 2012; Farquharson et al. 2015). However, little is known about the influence of porosity on the failure mode of representative edifice-forming rocks. To better understand the deformation of edifice-forming rock, we conducted a systematic experimental study on the mechanical behaviour and failure mode of a suite of edifice-forming andesites containing different porosities (7 to 25 %), deformed under volcanogically relevant pressures (corresponding to depths from a couple of hundred metres to about 3 km).

Case study, materials and methods

Case study: Volcán de Colima

For the purpose of this study, we selected edifice-forming andesitic rocks from Volcán de Colima (Trans-Mexican Volcanic Belt, Mexico, 19° 30′ N, 103° 37′ W, Fig. 1). Volcán de Colima was specifically chosen for this study as it is an active and frequently collapsing andesitic stratovolcano, with a construction and eruption history comparable to other active andesitic stratovolcanoes observed worldwide, such as Merapi (Indonesia), Santa María (Guatemala), Tungurahua (Ecuador) and Ruapehu (New Zealand). The volcanic complex comprises the active Fuego de Colima, constructed in the amphitheatre of an earlier collapse structure, and the older and extinct edifice of Nevado de Colima (Fig. 1). The most recent collapse event (2550 BP) was the last of at least five major collapses during the last 18,500 years (Stoopes and Sheridan 1992; Cortés et al. 2010). More recent activity has been characterised by lava effusion and Vulcanian explosions sandwiched between Plinian and sub-Plinian eruptions; these major explosive eruptions are thought to occur about every 100 years (Luhr 2002). Present day eruptive activity is extensively monitored through seismicity (Arámbula-Mendoza et al. 2011; Lamb et al. 2014; Lesage et al. 2014), gas geochemistry (Taran et al. 2002; Varley and Taran 2003), thermal infrared imaging (Hutchinson et al. 2013; Stevenson and Varley 2008; Webb et al. 2014), rockfall (Mueller et al. 2013) and deformation (Zobin et al. 2002). Between November 1998 and June 2011, there were five episodes of dome growth. Slow effusion and dome growth occurred in 2001–2003 and 2007–2011, interrupted by much faster episodes in 1998–1999, 2004 and 2005 (Varley et al. 2010). Explosive activity during this time was characterised by small
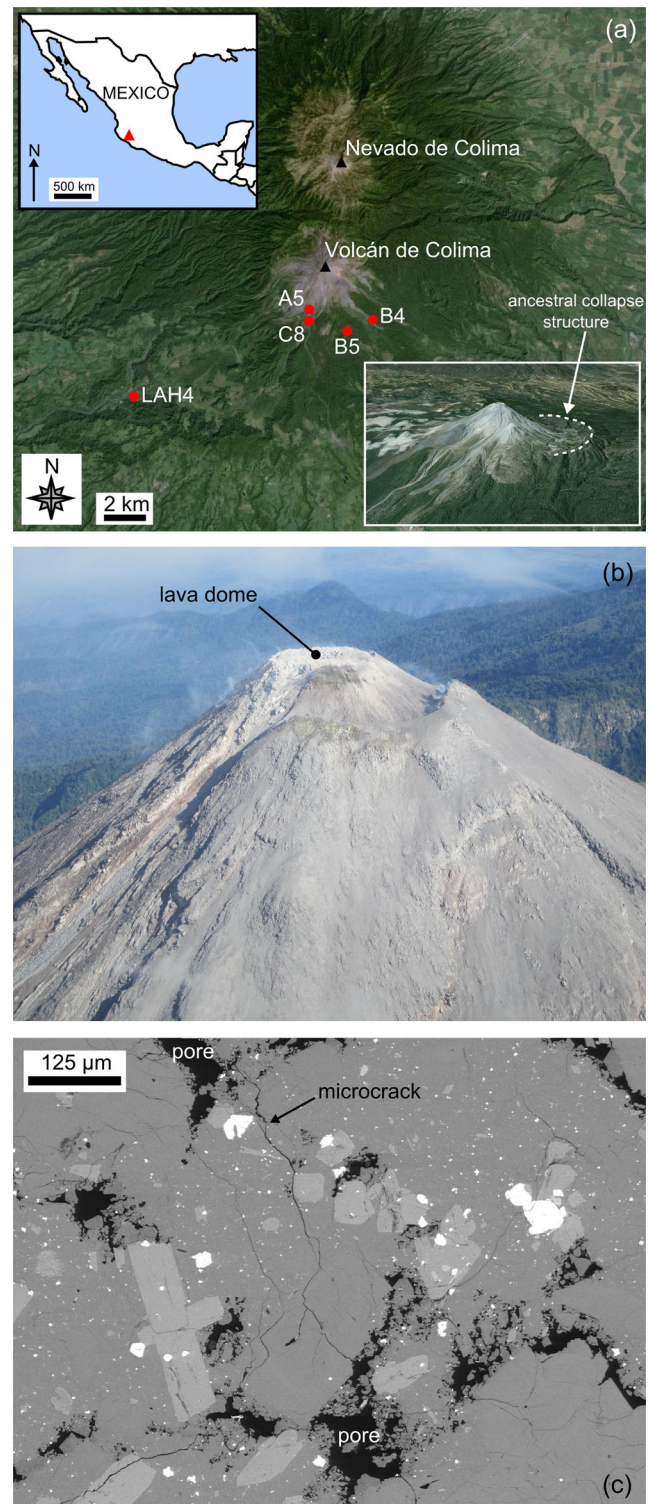
Fig. 1 **a** Google Earth™ map showing the locations of the sampling sites with respect to Volcán de Colima and Nevada de Colima. *Insets* show a map of Mexico (the *red triangle* corresponds to the position of Volcán de Colima) and a Google Earth™ image of Volcán de Colima showing the ancestral collapse structure (*dashed white line*). **b** Aerial photograph of the dome at Volcán de Colima (May 2014; photo credit: M. Heap). **c** Scanning electron microscope image showing the porosity network with a sample of andesite (B5) from Volcán de Colima. The microstructural elements are identified on the figure

gas-and-ash events and larger dome-disrupting Vulcanian events. The most intense period of activity provided at least 30 explosions, generating pyroclastic flows that reached distances as far as 5.4 km from the active vent (Varley et al. 2010). The most recent eruptive sequence, which started in January 2013, has involved dome growth and lava extrusion punctuated by pyroclastic density currents and Vulcanian explosions. Frequent explosive events were ongoing at the time of writing (i.e. May 2015).

Experimental materials

We selected four andesitic lava blocks (typically $30 \times 30 \times 30$ cm) to represent the variation in porosity typically seen within the materials forming the edifice at Volcán de Colima. A recent field-based study at Volcán de Colima (Farquharson et al. 2015) revealed the porosity of the eruptive products to be between 2 and 75 % (based on 542 hand samples). Using the method of Bernard et al. (2015), a weighted abundance analysis of these data shows that the predominant porosity class at Volcán de Colima is between 10 and 25 %. Using a similar field density technique, Mueller et al. (2011) found an average porosity of 16.4 % (based on 299 hand samples; see also Lavallée et al. 2012) and Lavallée et al. (2015) found that the average porosity of 2635 hand samples to be about 20 % (porosity ranged from 8 to 40 %). The range of porosities studied herein (from 7 to 25 %) is therefore representative of the rocks most frequently observed in the field.

The first block, A5, is from the 1998–1999 lava flow in the Cordoban ravine and contains a connected porosity of about 11 %. B5 is from an older lava flow of unknown age and contains a connected porosity of around 8 %. We note that B5 displays a certain degree of high-temperature alteration, as evidenced by the presence of vapour-deposited cristobalite within the pores (Fig. 1c; see Horwell et al. 2013 and Schipper et al. 2015). Block C8 was taken from the 1998–1999 blow-and-ash flow in the San Antonio ravine and contains a connected porosity of about 17 %. Finally, LAH4 is a block of unknown age collected from a lahar deposit on the west flank of the volcano (in the El Zarco river bed near La Becerrera); LAH4 contains a connected porosity of approximately 25 %. The locations of the collection sites are indicated in Fig. 1a. Using the classification scheme of Farquharson et al. (2015), B5 can be classified as "altered lava" and A5, C8 and LAH4 as "lava". All of the andesite blocks contain a dual porosity: a combination of microcracks and pores (Fig. 1c, Heap et al. 2014b). In detail, the andesites are pervasively microcracked (containing average microcrack densities between 35 and 45 mm^{-1}) and contain high pore number densities (between 3.3 and 8.1 mm^{-2}) and wide pore size distributions (the pore diameters range between about 0.02 and 2.0 mm; Heap et al. 2014b). The andesites have a porphyritic texture containing a microlitic groundmass (59–68 %)

containing commonly microcracked phenocrysts (<1.5 mm in diameter) of plagioclase (13–25 %), clinopyroxene (3–4 %) and orthopyroxene (2–4 %). All of the andesites contain between 58 and 61 wt% silica (Heap et al. 2014b), compositionally representative of recently erupted materials from Volcán de Colima (Luhr 2002; Savov et al. 2008). Cylindrical core samples, cored in the same orientation to a diameter of 20 mm and precision-ground to a nominal length of 40 mm, were prepared from each of the blocks. The connected water porosities of the samples were measured using the triple weight water-saturation (distilled water) method.

Experimental methods

All experiments were performed at the Géophysique Expérimentale laboratory at the Institut de Physique du Globe de Strasbourg. Uniaxial compressive strength (UCS; $\sigma_1 > \sigma_2 = \sigma_3 = 0$) experiments were performed on water-saturated samples of each andesite at a constant strain rate of 10^{-5} s^{-1} until failure. During uniaxial compression, axial stress was measured using a load cell and axial strain via a displacement transducer. The water-saturated samples were deformed inside a bath of distilled water. Triaxial deformation experiments were performed using a conventional triaxial apparatus ($\sigma_1 > \sigma_2 = \sigma_3$) on water-saturated samples at a constant strain rate of 10^{-5} s^{-1}. Our chosen strain rate is the standard for rock deformation experiments in compression, allowing our data to be compared with the wealth of pre-existing data (see review by Wong and Baud 2012). All triaxial experiments were performed under drained conditions. The pore fluid pressure was kept at a constant 10 MPa, and we ran experiments at confining pressures between 15 and 80 MPa (i.e. Peffs between 5 and 70 MPa), equivalent to depths between a couple of a hundred metres to about 3 km. For the purpose of this study, we assume a simple effective pressure (Peff) law such that Peff=Pc−αPp, where poroelastic constant α is assumed to be 1. Prior to deformation, the samples were left at the target effective pressure for at least 12 h to ensure microstructural equilibrium. During experimentation, we measured axial stress via a load cell and axial strain using a displacement transducer located on the top piston. Porosity change was measured using a pore pressure intensifier/volumometer and the output of acoustic emissions (AEs) and AE energy (the area under the received AE waveform) using a piezoelectric crystal attached to the top piston. Hydrostatic experiments—during which the confining pressure acting on a sample is increased while maintaining a constant pore fluid pressure—were also performed on a sample of each andesite. No differential stress is imposed on the sample during these experiments (i.e. $\sigma_1 = \sigma_2 = \sigma_3$). To ensure microstructural equilibration, the samples were first left for at least 12 h under a confining pressure of 12 MPa and a pore pressure of 10 MPa. The confining pressure was increased at a servo-controlled rate of

0.003 MPa s^{-1}, and the porosity change was monitored during the experiments using a pore pressure intensifier/ volumometer. Details of the triaxial experimental apparatus can be found in a previous contribution (Heap et al. 2014a). All of the experiments reported in this study were performed at room temperature. The focus of this study is to characterise the mechanical behaviour of edifice-forming andesites, which have long since cooled below the glass transition temperature (Tg) of their melt phase (~740 °C, Lavallée et al. 2012). While we are confident that viscous deformation will only occur within edifice rock in contact with a heat source (e.g. a dyke), we are aware that elevated temperatures may encourage subcritical crack growth (Brantut et al. 2013), although we note that increasing the temperature from room temperature to 75 °C did not significantly influence the deformation rate during a long-term triaxial experiment on a basalt from Mt Etna (Brantut et al. 2013). At the strain rates studied herein, we do not expect a temperature-induced change in failure mode at temperatures below Tg, exemplified by the brittle and dilatant behaviour of basalt and crystallised dacite samples deformed triaxially at high temperature (up to 900 °C; Smith et al. 2011; Violay et al. 2015). In this study, we adopt the convention that compressive stresses and strains are positive. An experimental summary, containing all of the data collected for this study, is given as Table 1.

Failure mode: dilatant or compactant?

The mechanical behaviour of rock is often classified as brittle or ductile (Rutter 1986; Evans et al. 1990; Paterson and Wong 2005; Wong and Baud 2012). Shear fracturing, a product of the coalescence of (predominately tensile) microcracks, is described as a brittle mode of failure. Ductile behaviour, however, defined simply as the capacity of a material to deform to a substantial strain without the tendency to localise the flow into faults (Rutter 1986), can be the result of a variety of microstructural deformation mechanisms, including microcracking (in the case of cataclastic flow); the description of ductility holds no mechanistic connotation (Rutter 1986). However, due to instances of compaction localisation (e.g. Baud et al. 2004), and because ductile behaviour can be driven by microcracking (i.e. "brittle" on the microscale), we have simplified our classification of the failure mode of rock in this manuscript to "dilatant" and "compactant".

Stress-strain curves and porosity reduction-strain curves for each of the andesite lavas, for different effective pressures (from 0 to 70 MPa or depths from 0 m to 3.2 km), are shown in Fig. 2. Dilatant behaviour (blue curves) is characterised by strain softening and large stress drops, typically associated with shear fracture formation (Fig. 2). The convex shape of the initial portion of the stress-strain curves (e.g. Fig. 2a) is typically attributed to the closure of microcracks aligned sub-

perpendicular to the loading direction. Indeed, the initial portion of the porosity reduction curves shows that the lava is compacting (e.g. Fig. 2a). The lavas then enter an elastic deformation stage where the stress-strain curve is quasi-linear, followed by a stage where the curves are concave. At the beginning of this latter stage, microcracks nucleate and grow (inelastic deformation). The onset of dilatancy, termed C' (Wong et al. 1997), is best observed using porosity change measurements (see discussion below) but can usually be observed as the start of an acceleration in AE activity (Fig. 3a), used as a proxy for the nucleation and growth of microcracks (e.g. Lockner 1993). The onset of dilatant microcracking can be observed as a reduction in the rate of porosity decrease in the porosity reduction curves (e.g. Fig. 2a; Wong et al. 1997), and eventually, as the rate of microcracking accelerates, the lava switches from compaction-dominated behaviour to dilation-dominated behaviour. The rate of microcracking, monitored by the output of AE (Fig. 3a), continues to accelerate up to the peak stress (σ_p). Following the peak stress, there is a strain softening phase before the lava succumbs to macroscopic failure, marked by a large stress drop and a rapid acceleration in AE activity (Fig. 3a). The stress-strain curves for the lavas are typical of those for rock in compression (e.g. Hoek and Bieniawski 1965; Brace et al. 1966; Scholz 1968). We note that, for the dilatant lavas, the peak stress and the strain-at-failure increases, and the magnitude of the stress drop decreases, with increasing effective pressure (see also Paterson and Wong 2005). We also highlight that the porosity reduction curves show that samples deformed at higher effective pressures show less net dilation (e.g. Fig. 2a). Visual inspection of the deformed samples confirmed that the samples contained localised shear fractures typically orientated at about 30° to the maximum principal stress.

Compactant behaviour (red curves) of the andesitic lavas is characterised by the lack of significant strain softening, strain hardening (in some cases) and many small stress drops (of a couple of MPa) (Fig. 2). Similar to the dilatant curves, the compactant curves contain an initial convex portion, associated with the closure of microcracks (the porosity reduction curves show that the lava is compacting; e.g. Fig. 2c, d) and an elastic deformation stage where the stress-strain curve is approximately linear. However, unlike the dilatant curves, there is no switch to dilation dominance. At a critical stress state, termed the onset of shear-enhanced compaction or C^* (Wong et al. 1997), the rate of compaction increases (e.g. Fig. 2c, d). As for C', C^* is best observed using porosity change measurements (see discussion below) but also usually marks the position of the onset of significant AE activity (Fig. 3b) whereat the lava begins to deform inelastically. We also note the presence of many small stress drops that are contemporaneous with sudden and temporary increases in the rate of AE output (Fig. 3b); such stress drops and AE bursts have previously been attributed to compaction

Table 1 Experimental summary of the 39 experiments performed for this study. All experiments were performed at the Géophysique Expérimentale laboratory at the Institut de Physique du Globe de Strasbourg. C* - onset of shear-enhanced compaction; P - effective mean stress; P* - onset of lithostatic inelastic compaction; N/A - not available (sample was too strong to break in our experimental setup under these pressure conditions)

| Block	Sample	Connected porosity (%)	Confining pressure (MPa)	Pore pressure (MPa)	Effective pressure (MPa)	Peak differential stress (MPa)	C* (MPa)	P (MPa)	P* (MPa)	Notes
B5	4_s1	7.9	0	0 (wet)	0	81.1	–	27.0	–	
B5	8	7.3	15	10	5	136.0	–	50.3	–	
B5	7	7.4	20	10	10	184.9	–	71.6	–	
B5	10	7.9	40	10	30	270.7	–	120.2	–	
B5	11	7.5	60	10	50	281.4	–	143.8	–	
B5	4	7.7	80	10	70	N/A	–	–	–	
B5	2	7.6	Hydro	10	Hydro	–	–	–	N/A	
B5	3	7.6	Hydro	10	Hydro	–	–	–	N/A	
A5	7	12.3	0	0 (wet)	0	64.8	–	21.6	–	
A5	17	9.3	15	10	5	128.7	–	47.9	–	
A5	10_s1	11.2	20	10	10	164.2	–	64.7	–	
A5	4_s1	11.7	40	10	30	209.1	–	99.7	–	
A5	14_s1	10.6	60	10	50	261.7	–	137.2	–	
A5	4	11.2	80	10	70	–	290.1	166.7	–	
A5	20	9.8	Hydro	10	Hydro	–	–	–	N/A	
C8	5_s1	17.6	0	0 (wet)	0	17.5	–	5.8	–	
C8	16	16.2	15	10	5	74.1	–	27.7	–	Microstructure
C8	4_s1	17.9	20	10	10	62.3	–	30.8	–	
C8	19	19.4	40	10	30	–	43.4	44.5	–	
C8	23	18.5	40	10	30	–	48.7	46.2		
C8	20	17.6	60	10	50	–	45.3	65.1	–	
C8	8	15.5	60	10	50	–	103.5	84.5	–	C*′ (20 % strain)
C8	21	16.5	60	10	50	–	60	70	–	Microstructure; 1.5 % strain
C8	5	16.3	60	10	50	–	78.3	76.1	–	Microstructure; 3 % strain
C8	4	16.4	60	10	50	–	60.3	70.1	–	Microstructure; 6 % strain
C8	26	16.7	60	10	50	–	59.5	69.8	–	Permeability, 1.5 % strain
C8	25	17.2	60	10	50	–	49.4	66.5	–	Permeability, 4.5 % strain
C8	22	19.0	80	10	70	–	26.5	78.8	–	
C8	6	16.7	Hydro	10	Hydro	–	–	–	126.0	
C8	7	16.7	Hydro	10	Hydro	–	–	–	151.7	Microstructure
C8	i	17.2	0	0	0	fractured in tension	–	–	–	Permeability
C8	ii	18.1	0	0	0	fractured in tension	–	–	–	Permeability
LAH4	7	23.8	0	0 (wet)	0	31.3	–	10.4	–	
LAH4	1	24.1	20	10	10	69.5	–	33.2	–	
LAH4	2	24.0	40	10	30	–	92.5	60.8	–	
LAH4	4	24.2	60	10	50	–	72.9	74.3	–	
LAH4	6	24.5	80	10	70	–	56.4	88.8	–	
LAH4	8	23.8	Hydro	10	Hydro	–	–	–	160.6	
LAH4	9	23.8	Hydro	10	Hydro	–	–	–	150.0	
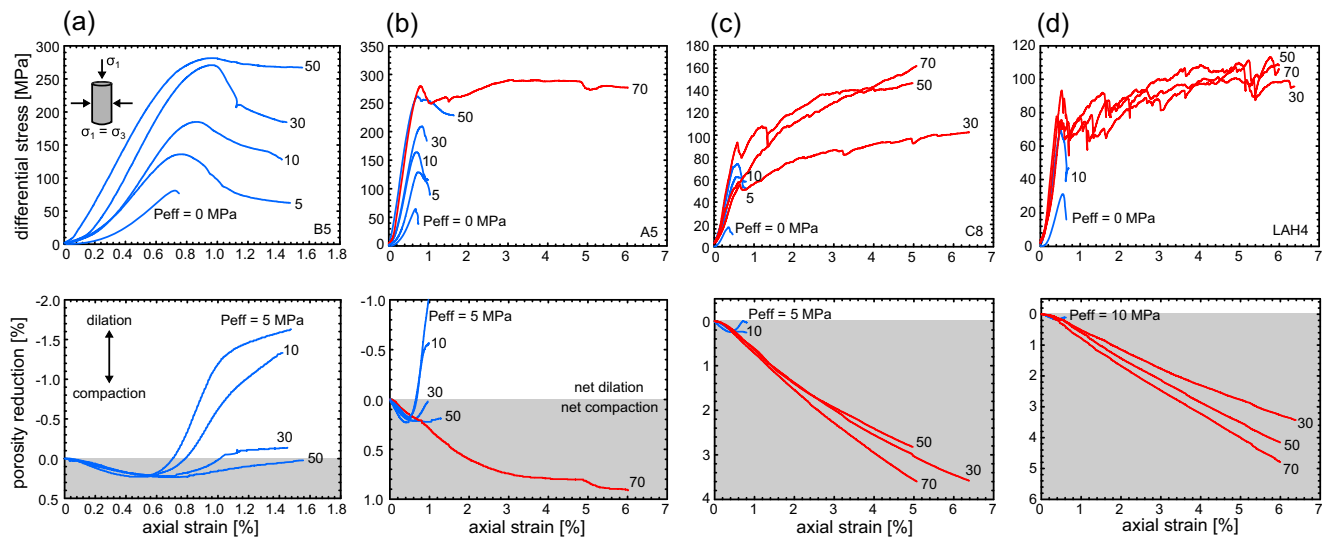
Fig. 2 Mechanical data. Stress-strain curves and porosity reduction curves for andesitic lava from Volcán de Colima: **a** B5, **b** A5, **c** C8 and **d** LAH4. The effective pressure (*Peff*) of the experiment is shown next to each curve. Dilatant curves are shown in *blue* and compactant curves are shown in *red*. Net compaction in the graphs of porosity reduction is highlighted in *grey*, net dilation in *white*

localisation in porous rock (Baud et al. 2004; this is discussed further in the "Operative micromechanical processes" section). Unlike failure in the dilatant regime, the differential stress required for the onset of shear-enhanced compaction decreases with increasing effective pressure. Our experiments highlight that the rate of compaction increases as the effective pressure increases (e.g. Fig. 2d); for example, at 6 % axial strain, LAH4 had lost about 3 and 5 % porosity at effective pressures of 30 and 70 MPa, respectively.

The transition between dilatant and compactant behaviour was observed at effective pressures of 30 MPa and above (equivalent to depths greater than about 1.6 km) for the higher

porosity lavas (C8 and LAH4), while the failure mode of the samples from the blocks containing the lowest porosities (B5 and A5) remained dilatant up to 50 MPa. Above 50 MPa (depth ~2.4 km), A5 switched from a dilatant to a compactive failure mode (B5 was too strong to break in our triaxial press at a Peff of 70 MPa).

Additional insights into the mechanical behaviour of the andesites can be gleaned by plotting the porosity reduction versus the effective mean stress (*P*), where $P=((\sigma 1+2\sigma 3)/3)$ $-Pp$. Such curves highlight the difference between hydrostatic ($\sigma_1=\sigma_2=\sigma_3$) and shear stresses ($\sigma_1>\sigma_2=\sigma_3$) on the evolution of porosity (Fig. 4). In the hydrostatic case, the onset of
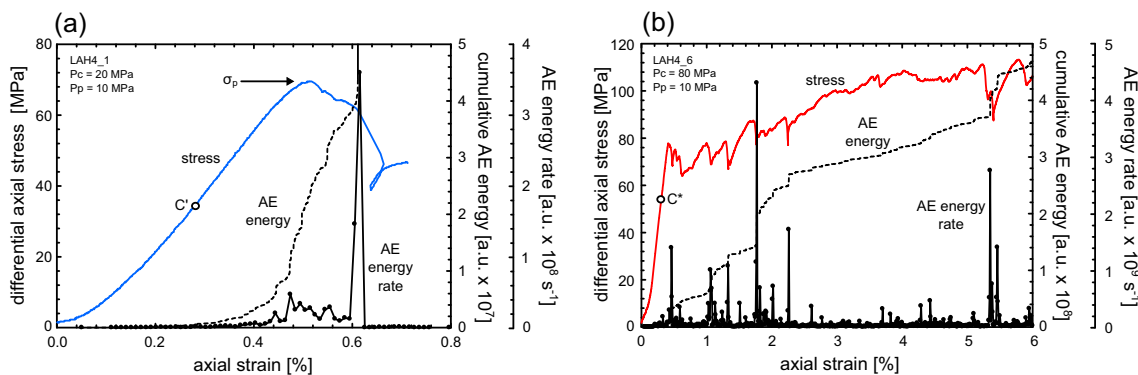

Fig. 3 Acoustic emission characteristics. Cumulative acoustic emission energy (*AE*) and AE energy rate (AE energy is given in arbitrary units, a.u.) during **a** a dilatant constant strain rate experiment (Peff=10 MPa) and **b** a compactant constant strain rate experiment (Peff=70 MPa) on porous andesite. The experiments shown here were performed on samples of LAH4 (the same experiments presented in Fig. 2d). The positions of the onset of dilatational microcracking (*C'*) and the peak stress (σ_p) are indicated in panel **a**, and the position of the onset of shear-enhanced compaction (*C**) is indicated in panel **b**
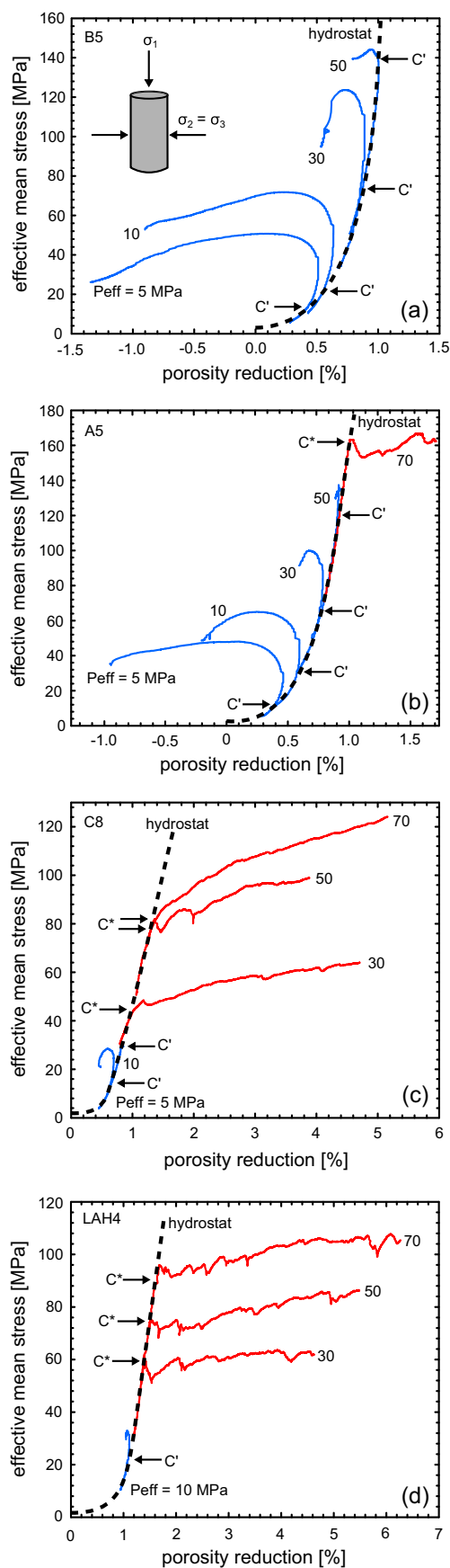
inelastic compaction is termed $P*$ (Wong et al. 1997; Fig. 4). $P*$ was attained for the two most porous samples (C8 and LAH4; see Table 1), but A5 and B5 contain porosities too low to observe $P*$ in our experimental setup. We note that, in all cases, an increase in hydrostatic stress resulted in a decrease in porosity. Prior to $P*$, this is attributed to the elastic closure of porosity as pressure is increased; the acceleration in porosity loss following $P*$ is attributed to inelastic compaction (Wong et al. 1997). Any deviation from the hydrostatic curve (or "hydrostat") during a constant strain rate triaxial experiment must therefore be the consequence of differential stress on the porosity evolution. A dilatant mode of failure is characterised by a deviation to the left (porosity increase), marked by C′, and a compactant mode of failure by a deviation to the right (porosity decrease), marked by C* (see Wong et al. 1997).

Constructing failure envelopes for porous andesite

The data of this study can be used to map failure envelopes for andesite lava containing different porosities (Fig. 5). In the dilatant regime, the peak stress maps the dilatant failure envelope on a plot of differential stress (Q) versus effective mean stress. In the compactant regime, it is the stress at the onset of shear-enhanced compaction C* that delineates the compactive yield envelope. The positions of $P*$, lithostatic inelastic compaction, plot along the x-axis ($Q=0$ MPa). The lava has failed (or yielded) if the stress state plots outside the failure envelope (shear fracture on the left and inelastic compaction on the right; see inset in Fig. 5a). It follows that stronger rocks will therefore be intact over a much larger P-Q space (i.e. the failure envelope will have a larger amplitude).

The complete failure envelopes are only available for the most porous lavas (C8 and LAH4); the low-porosity lavas (A5 and B5) were dilatant for the majority of the P-Q space attainable in our apparatus. The dilatant failure envelopes for the andesites highlight that differential stress at failure increases linearly with effective mean stress, in accordance with the Mohr-Coulomb criterion. While it is common for porous sedimentary rocks to have parabolic compactive yield envelopes (Wong and Baud 2012), the andesitic lavas of this study have linear compactive envelopes. This is likely the result of the duality of the porosity (microcracks and pores), as previously suggested by Zhu et al. (2010). As mentioned above, an
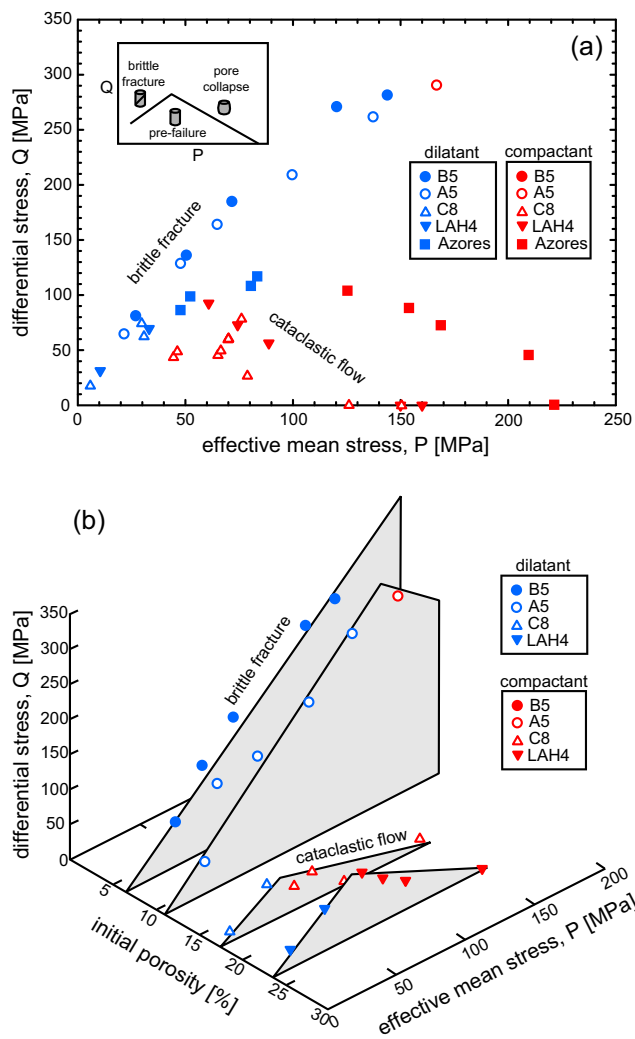
Fig. 5 Failure envelopes for andesitic lava from Volcán de Colima. **a** The experimental data plotted on differential stress Q at failure versus effective mean stress P. **b** A 3D plot of differential stress at failure and effective mean stress plotted alongside the initial connected porosity. Dilatant experiments are shown as *blue symbols* and compactant experiments as *red symbols*. Data for Açores trachyandesite (*squares*) from Loaiza et al. (2012) is also presented in panel **a**

increase in confining pressure on the compactive side of the failure envelope reduces the differential stress required for the onset of shear-enhanced compaction. However, in a rock containing microcracks and pores, an increase in confining pressure must also close a larger proportion of the pre-existing microcracks. Therefore, for the same increase in confining pressure, the decrease in the differential stress required for C^* may be less for a rock containing microcracks than for an initially microcrack-free rock. The result, in P-Q space, is a linear compactive envelope. We note that parabolic envelopes were observed for a porous trachyandesite from the Azores (Loaiza et al. 2012; Fig. 5a) and porous tuff (Zhu et al. 2011), both of which contain low initial microcrack densities.

We find, in general, that the amplitude of the failure envelope is lower when the porosity is higher. In other words, lava containing lower porosity is intact (or pre-failure) over a much larger stress space. This is best observed on our 3D plot where the differential stress at failure and the effective mean stress are plotted alongside the initial connected porosity (Fig. 5b). 3D yield caps are typically deployed in soil mechanics, but have also been successfully applied to rocks (see Cuss et al. 2003 and references therein). In these studies, the third axis is the porosity multiplied by the grain size; in our diagram, we have chosen to use initial connected porosity as our third axis, since volcanic rocks cannot be described by a grain size and, while an average pore size could be utilised here, we highlight that the pore size distribution of our rocks varies tremendously (Heap et al. 2014b), raising doubt over the applicability of an average pore size.

Contrary to our expectation, the 3D failure envelopes show that the amplitude of the failure envelope for LAH4 (porosity=25 %) is larger than that of C8 (porosity=18 %) (Fig. 5b). The cause of this discrepancy is likely the result of the difference in pore size distribution and the size of the largest pore between the two andesites. While LAH4 contains a large number of small pores, and few large pores (the largest is about just over 1 mm), C8 contains a much wider pore size distribution, including pores almost 2 mm in diameter (Heap et al. 2014b). The stress intensity is higher at the tips of cracks emanating from larger pores (Sammis and Ashby 1986). A crack will propagate when a critical stress is reached; therefore, the larger the pore, the lower the applied differential stress required for crack propagation (see also Heap et al. 2014c). Therefore, pore size should also be considered important in controlling the mechanical behaviour and failure mode of volcanic rocks, just as grain size is important for sandstones (Wong and Baud 2012). Another noteworthy observation is that the failure envelope for the trachyandesite from the Açores (porosity=18 %, Loaiza et al. 2012) has a much larger amplitude than that of the andesite from Volcán de Colima with a comparable porosity (C8, porosity=17 %; Fig. 5a). While this difference could be explained by the differences in microcrack density and/or the pore size, we highlight a potential role for the presence of phenocrysts. The trachyandesite from the Açores is aphanitic (the crystals are microlites), while the andesites from Volcán de Colima are porphyritic (crystals are as large as a couple of mm). Phenocrysts in volcanic rocks often contain microcracks and other defects (plagioclase can be twinned for example) and could therefore affect their mechanical behaviour, although no firm conclusions can be drawn from the available data.

Operative micromechanical processes

It is well known that the formation of a shear fracture is the result of the nucleation, growth and coalescence of

microcracks (e.g. Lockner et al. 1991). For porous materials, including rocks, microcracks usually emanate from pre-existing pores (e.g. Sammis and Ashby 1986; Wong and Baud 2012). Figure 6a shows a scanning electron microscope (SEM) image of a sample of andesite (C8) deformed within the dilatant regime (Peff=5 MPa). We clearly see pore-emanated microcracks that are orientated sub-parallel to the maximum principal stress. We note that the microcracks shown in Fig. 6a form part of the macroscopic localised (i.e. the microstructure appears undisturbed outside the fracture) shear fracture.
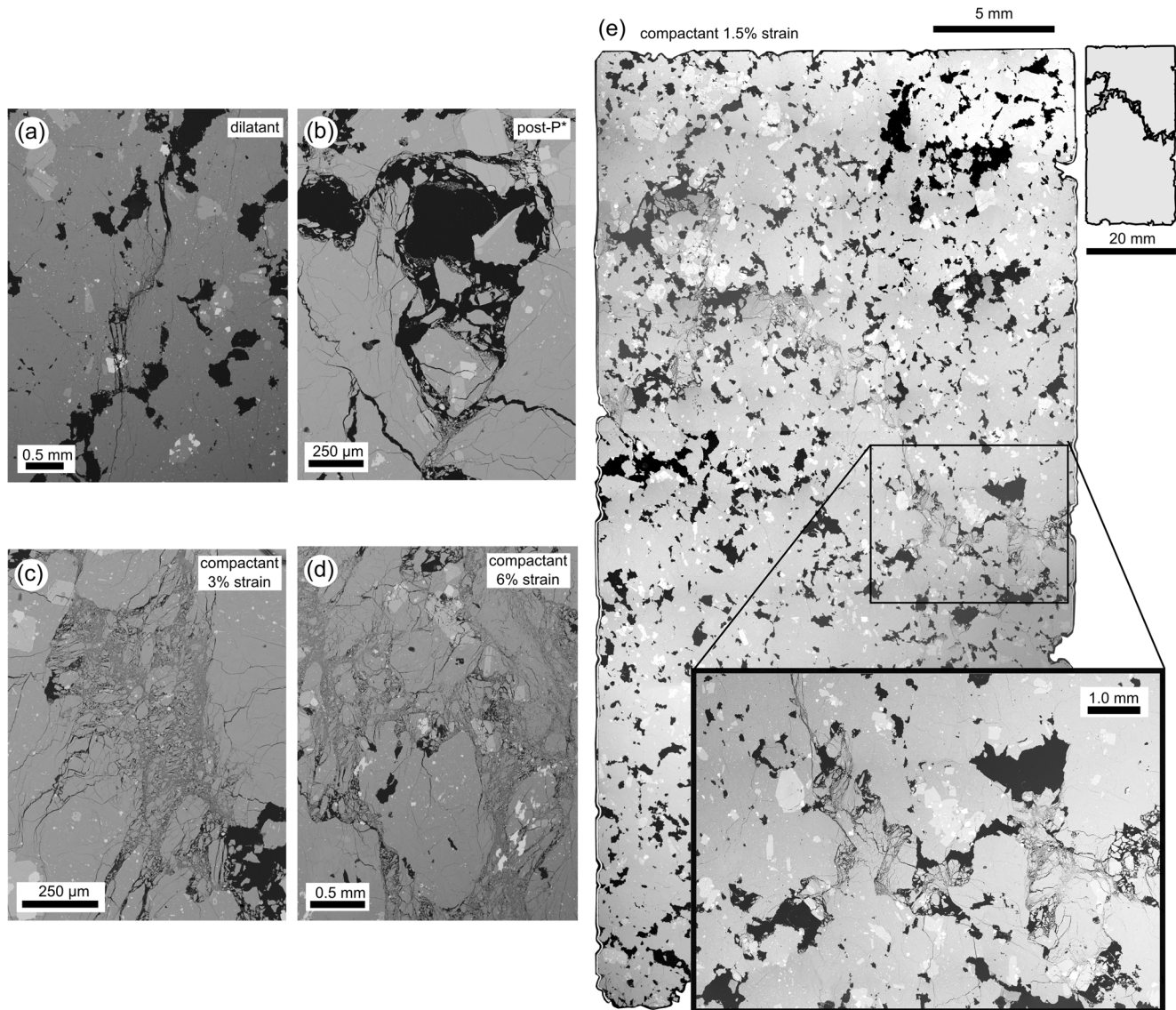
Microstructurally, the inelastic compaction of porous rocks is typically attributed to cataclastic pore collapse and grain crushing (e.g. Wong and Baud 2012). Although microstructural observations have shown that pore collapse and grain crushing can be distributed throughout the sample (e.g. Menéndez et al. 1996), there are cases of compactive localisation. These features are well documented (in the field and laboratory) in porous sandstones (e.g. Mollema and Antonellini 1996; Baud et al. 2004) and limestones (e.g. Cilona et al. 2014), and are called compaction bands. Compaction bands in sandstones, for example, are subplanar

Fig. 6 Microstructure. a Back-scattered scanning electron microscope (SEM) picture of pore-emanating microcracking from a dilatant constant strain rate experiment (Peff=5 MPa) on a sample of C8. b SEM picture of cataclastic pore collapse during hydrostatic loading of a sample of C8 beyond the onset of hydrostatic pore collapse (P*). c SEM picture of cataclastic pore collapse from a compactant constant strain rate experiment (Peff=50 MPa) on a sample of C8 taken to 3 % axial strain. d SEM picture of cataclastic pore collapse from a compactant constant strain rate experiment (Peff=50 MPa) on a sample of C8 taken to 6 % axial strain. e SEM map showing a compaction localisation feature (band of collapsed pores) from a constant strain rate experiment (Peff=50 MPa) on a sample of C8 taken to 1.5 % axial strain

surfaces of localised compaction—typically a few grains thick—orientated perpendicular to the maximum principal stress that show little or no evidence of shear. The porosity within the band is typically much lower than that of the surrounding host rock (e.g. Baud et al. 2006). During laboratory experiments, the appearance of compaction bands in sedimentary rock is typically associated with small stress drops (of a few MPa) and a sudden, temporary increase in the rate of AE activity (Baud et al. 2004, 2006).

Recently, two studies have shown evidence for compaction localisation in porous volcanic rocks (Loaiza et al. 2012; Adelinet et al. 2013). For example, Loaiza et al. (2012) showed that compaction localisation in porous trachyandesite deformed at a confining pressure of 130 MPa is manifest as bands of collapsed pores sub-perpendicular to the maximum principal stress. The structure was approximately 2 mm thick, roughly the average pore diameter. Small stress drops were seen in the stress-strain curves of these experiments, although AEs were not recorded during the experiments. The confining pressures required for the formation of compactive localisation in the trachyandesite were in excess of 95 MPa (i.e. at depths greater than about 4 km; Loaiza et al. 2012), perhaps too deep to be volcanologically relevant. The significance of these features within a volcano is that an experimental study on compactive localisation in sandstones has shown that permeability can be reduced by up to three orders of magnitude (Baud et al. 2012). As discussed above, the permeability of the country rock can impact sidewall outgassing, an important factor governing eruption explosivity (this is discussed further in the "Impact of failure mode on permeability" section).

To investigate the microstructural progression of our andesite lavas during compactive deformation, and to look for evidence of compaction localisation (as suggested by our mechanical data: we also observe the small stress drops associated with an increase in the rate of AE activity documented by Baud et al. 2004 and Baud et al. 2006), we performed three additional constant strain rate experiments on samples of C8 at an effective pressure of 50 MPa (corresponding to a depth of about 2 km) to axial strains of 1.5, 3 and 6 % (Table 1). As before (Fig. 3b), the stress-strain curves were punctuated by small stress drops associated with bursts of AE activity. We also performed an additional hydrostatic experiment to study the microstructure of a sample deformed beyond P^* (Table 1). Similarly to previous studies on porous sedimentary rocks (Wong and Baud 2012) and volcanic rocks (Zhu et al. 2011; Loaiza et al. 2012), the acceleration in porosity reduction at P^* seen here is the result of distributed pore collapse (Fig. 6b). Collapsed pores are partially filled with broken fragments of groundmass and are often bounded by microcracks (Fig. 6b).

An SEM map of the sample deformed to an axial strain of 1.5 %, i.e. immediately following the first stress drop, shows clear evidence of a compactive strain localisation feature (Fig. 6e). The feature, a band of collapsed pores (that have been infilled or partially filled with broken fragments of groundmass; see inset in Fig. 6e), traverses the diameter of the sample (20 mm) and is the thickness of the collapsed pore through which it passes (typically 0.25–0.5 mm). The band is not perpendicular to the maximum principal stress but is guided through the sample by the distribution of pores. Neighbouring collapsed pores are often connected by microcracks. We note that the pores appear undisturbed outside the band (i.e. the deformation is localised at the millimetre scale). Substantial pore collapse is seen in the samples deformed to 3 and 6 % strain (Fig. 6c, d). Due to the extent of the pore collapse, it is difficult to distinguish discrete bands of compacted pores. The observed deformation is likely the result of the amalgamation of several bands. We highlight that these cataclastic microstructures share similarities with the volcanic breccia found within the conduit zone of Unzen volcano, Japan (Goto et al. 2008).

Since a band is assumed to grow during a discrete stress drop and AE pulse (e.g. Baud et al. 2004), we can estimate (assuming uniaxial strain and that the bands are perpendicular to the maximum principal stress) that the inelastic axial strain associated with band growth is typically between 0.04 and 0.06 % for both C8 and LAH4 (corresponding to an axial shortening of about 20 μm). Microstructural observations indicate that the localised band has a thickness equal to the collapsed pore through which it passes (typically 0.25–0.5 mm), suggesting that the porosity reduction within the band is on the order of 4 to 8 %. In other words, the porosity is 17 % outside the band and about 10 % within the band. By contrast, the porosity of compaction bands in Bentheim sandstone was estimated to be about 8 %, considerably lower than the initial porosity of 23 % (Baud et al. 2004). These results are discussed further in the section "Impact of failure mode on permeability". The ubiquity of cataclastic pore collapse during the deformation of porous volcanic rocks at high confining pressures (Zhu et al. 2011; Loaiza et al. 2012; Adelinet et al. 2013; Heap et al. 2014a, 2015) highlights the universality of pore collapse as the operative micromechanical mechanism driving low-temperature (below Tg) compactant deformation in porous volcanic rocks.

Field, experimental and modelling evidence suggest that the development of compaction bands is enhanced in well-sorted sandstones (Wang et al. 2008; Cheung et al. 2012). When the grain size distribution is large, compaction bands do not form because the deformation is accommodated by the smaller grains (Cheung et al. 2012). However, extrusive volcanic rocks cannot be characterised by a grain size. Nevertheless, in a similar manner, could compactive localisation features only occur in volcanic rocks with a homogeneous pore size distribution? It follows that, if the pore size distribution is wide, the deformation may focus on the larger pores (e.g. Heap et al. 2014c), resulting in distributed cataclastic pore collapse (assuming that the large pores are

distributed throughout the sample). Compactive localisation features may therefore develop more easily when the pore size is relatively uniform. The collapse of one pore encourages the collapse of a neighbouring pore, due to the redistribution of stresses, promoting cascading pore collapse across the sample (in a similar way to cascading grain failure in the development of compaction bands in sandstones; Wang et al. 2008). However, we have observed compaction localisation in andesites with an extremely wide pore size distribution (C8; see Heap et al. 2014b; Fig. 6b). Firm conclusions on the favourable rock attributes for compaction localisation in volcanic rocks cannot be provided with currently available data, although we highlight a potentially important role for pore shape, a factor that displays much more variability in volcanic rocks than in sedimentary rocks. In a simplistic scenario where the pore shape is spherical, stresses are likely to focus on the larger pores, allowing the damage to be distributed throughout the sample. However, non-spherical pores may focus the deformation away from the larger pores and permit the formation of compactive localisation features through networks of misshapen pores. This interpretation is supported by the presence of large intact pores in C8 deformed to 1.5 % strain (Fig. 6).

Impact of failure mode on permeability

Our experimental data demonstrate that edifice-building lavas can either dilate or compact in response to stress, depending on their depth and porosity. To explore permeability evolution as a consequence of dilatant and compactant failure modes, we measured the change in permeability of samples of porous (17 %) andesite (block C8) deformed in both regimes. Two samples (20 mm in diameter and about 20 mm in length) were loaded diametrically in uniaxial compression (at a constant strain rate of 10^{-5} s^{-1}) until tensile failure, and two samples (20 mm in diameter and about 40 mm in length) deformed triaxially at a pore pressure of 10 MPa, a confining pressure of 60 MPa and a constant strain rate of 10^{-5} s^{-1} to axial strains of 1.5 and 4.5 %, respectively (Table 1). Gas (nitrogen) permeability was measured before and after deformation at a constant confining pressure of 1 MPa. We found that a tensile fracture—parallel to the imposed flow direction—serves to increase permeability by about a factor of two (permeability increased from 6.2×10^{-13} and 1.6×10^{-12} m^2 to 1.0×10^{-12} and 2.8×10^{-12} m^2 for the two samples, respectively). We note that (1) this increase may be reduced at confining pressures higher than 1 MPa (see Nara et al. 2011) and (2) a larger increase may be seen in andesites containing a lower initial porosity. The permeability of the fractured samples can be considered as an equivalent permeability (i.e. equal to the contribution of both the fracture and the host rock). Fracture permeabilities were calculated, using a fracture aperture of ~0.25 mm (determined through microstructural observations),

to be 3.0×10^{-11} and 9.8×10^{-11} m^2 for the two samples, respectively.

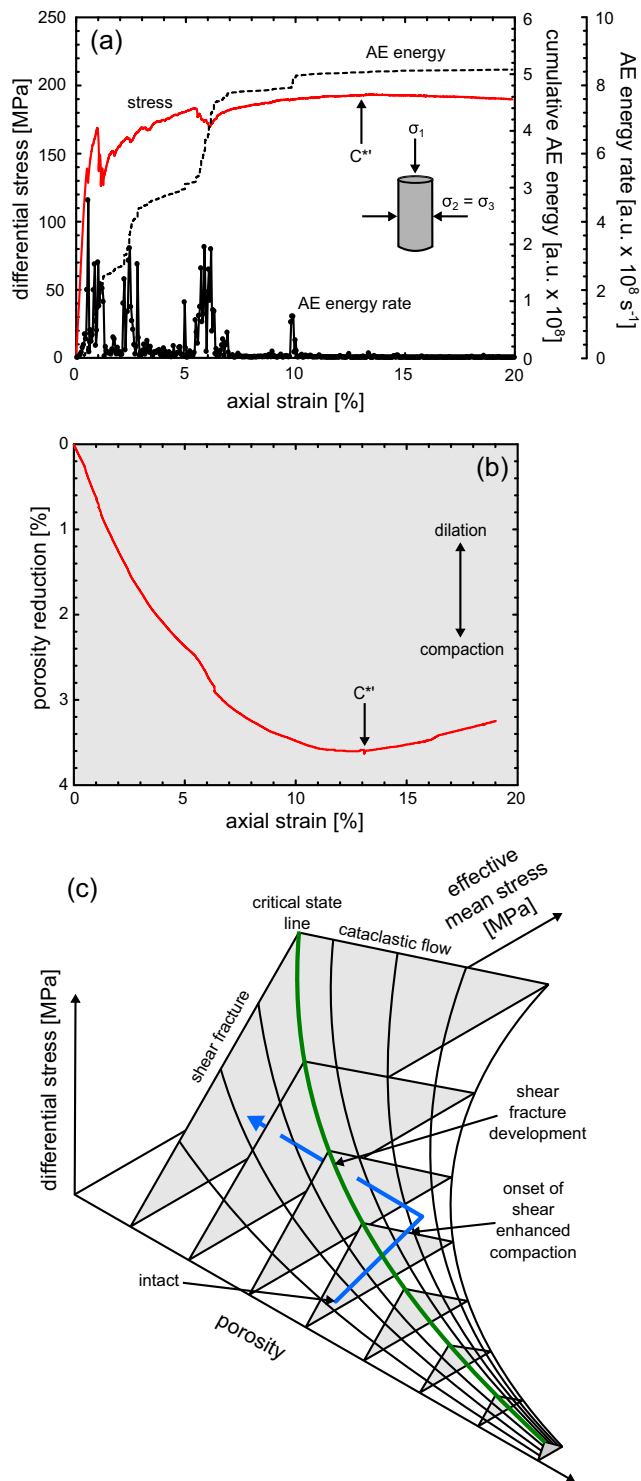Compaction to 1.5 % strain reduced permeability from 6.2×10^{-12} to 2.6×10^{-12} m^2 (a decrease by a factor of about two), and compaction to 4.5 % strain reduced permeability from 3.3×10^{-12} to 3.1×10^{-13} m^2 (a decrease by about an order of magnitude). We highlight that compaction bands in sandstones resulted in a dramatic reduction in sample permeability (by up to three orders of magnitude, Baud et al. 2012). Our data suggest that a single band of collapsed pores—orientated perpendicular to the imposed flow direction—does not significantly reduce permeability and that this may be a result of a combination of their tortuous nature (gaps may exist over the area of the band) and the fact that the estimated porosity reduction within the band (4–8 %) is less than that typically estimated for compaction bands in sandstones (~15 %; Baud et al. 2012).

Taken together, these data suggest that the failure mode of the host rock will play an important role in conduit outgassing and therefore in dictating eruption characteristics: a dilatant failure mode in the upper conduit (<1 km) will assist outgassing, and compaction in the deep edifice (>1 km) will hinder outgassing (this is discussed further in the "Volcanological significance" section).

Switching failure modes at high strains and the limit of compaction

As previously stated, porosity exerts a crucial role on the failure mode of rock (e.g. Wong and Baud 2012). However, we have also shown that porosity can be severely reduced during compactant deformation (Fig. 2). It follows that, after a certain degree of compaction, the rock may contain a porosity low enough to react to an applied stress in a dilatant manner. In rock mechanics, this strain-dependent switch in mechanical behaviour is referred to as $C^{*\prime}$ and has been observed in porous limestones (e.g. Baud et al. 2000) and sandstones (e.g. Schock et al. 1973; Baud et al. 2006). $C^{*\prime}$ will also provide us with a measure of the limit of inelastic porosity loss in porous andesitic edifice rocks. Prior to this study, this phenomenon had never been observed in porous extrusive volcanic rocks.

To explore this concept in porous andesite, we performed a constant strain rate experiment on a sample of C8 at an effective pressure of 50 MPa to an axial strain of 20 % (Fig. 7). We find that the switch from compactant to dilatant behaviour, $C^{*\prime}$, occurs at an axial strain of about 13 % and a porosity loss of about 3.6 % (for a sample containing an initial porosity of 15.5 %). In other words, for this sample, the maximum porosity loss as a result of inelastic compaction is 3.6 %, leaving the sample with a porosity of 11.9 %. Considerable porosity destruction may not therefore be obtainable in porous andesitic edifice rocks, although the porosity reduction at $C^{*\prime}$ should

places, of collapsed pores, intense fracturing and numerous anastomosing shear bands (Fig. 8b) containing fine-grained (from a few microns up to a few tens of microns) pulverised groundmass and crystals (Fig. 8c). Crystals on the boundary of the highly sheared bands have been fractured and the broken fragments have been transported parallel to the direction of shear (Fig. 8d). Outside the shear band, we notice that most of the pores are collapsed; the anastomosing shear bands often overprint evidence of cataclastic pore collapse (Fig. 8e). We again highlight the similarity between these microstructures and those of the volcanic breccia found within the conduit zone of Unzen volcano, Japan (Goto et al. 2008).

The switch in failure mode as porosity is reduced is best depicted on a 3D failure envelope (Fig. 7c). A theoretical "critical state line" can be mapped out schematically in *P-Q*-porosity space to delineate the transition between dilatant and compactant behaviour (see Fig. 7c); with progressive compaction (i.e. a reduction on the porosity axis), compactant volcanic materials will migrate towards this line. The switch in failure mode would be observed as the reduction in porosity allows the rock to cross the critical state line, as shown in Fig. 7c. We infer that highly strained rocks (in our experiment, $C*'$ required an axial strain of 13 %) near the conduit, or deep in the edifice, will be prone to this switch in failure mode (see "Volcanological significance" section). A strain-dependent switch to brittle failure has also been observed in high-temperature (940–945 °C) uniaxial deformation experiments on andesite from Volcán de Colima (Kendrick et al. 2013). However, in magma, the reduction in porosity required for a dilatant response is the consequence of viscous pore rearrangement and closure, rather than cataclastic pore collapse.

Volcanological significance

Our experimental data help constrain the depth of the transition between a dilatant and compactant failure mode in edifice-forming andesitic lavas. Based on these data, we have constructed a schematic cross section of Volcán de Colima that highlights regions of the volcano that are likely to (1) be intact (any deformation is elastic), (2) fail in a

increase for rocks containing higher initial porosities and at higher pressures (depths) (Baud et al. 2006).

In a sample that has surpassed $C*'$, compactive pore collapse should be overprinted by a shear fracture. An SEM map of the deformed sample beyond $C*'$ is presented as Fig. 8a and shows a well-developed shear zone, up to 10 mm thick in
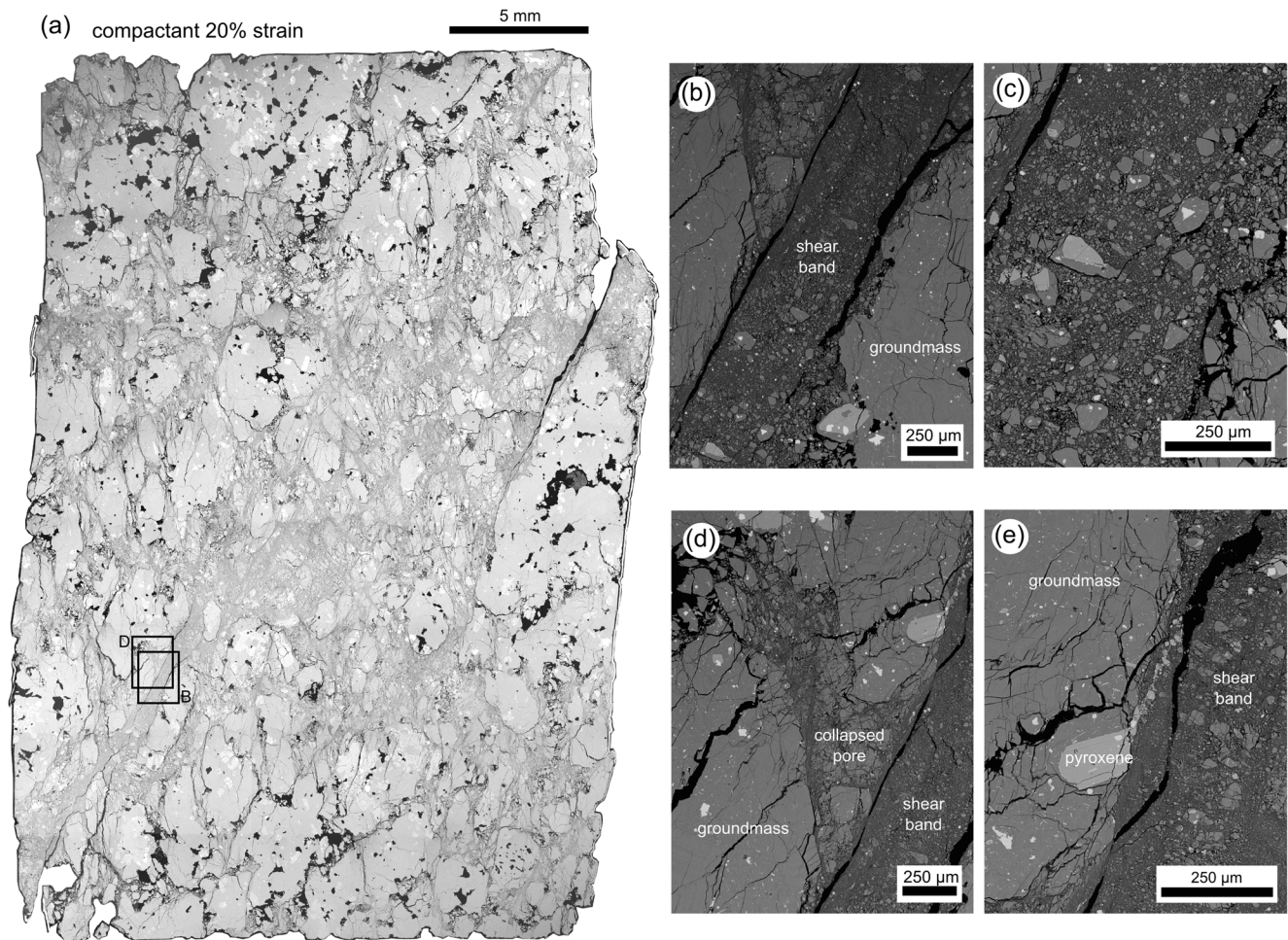
Fig. 8 Microstructure. **a** Back-scattered scanning electron microscope (SEM) map of a sample of C8 deformed at a constant strain rate (Peff= 50 MPa) to an axial strain of 20 %. **b** SEM picture of one of the anastomosing shear bands. **c** SEM picture showing the crushed groundmass and crystals within the anastomosing shear band shown in panel **b**. **d** Crosscutting relationships. An anastomosing shear band overprinting a collapsed pore. **e** Crystal fragments entrained by the shear band and transported along the direction of shear

dilatant manner, (3) fail in a compactant manner or, (4) fail via inelastic lithostatic compaction (Fig. 9). We anticipate that differential stress will be higher closer to the central conduit of dykes and that effective pressure will increase with depth. Porous andesites will react to regional and local stresses in a dilatant manner in the shallow edifice (<1 km) and in a compactant manner at depths greater than about 1 km. It is worthwhile noting that the depth of the transition between a dilatant and compactant failure mode is likely reduced for rocks containing higher porosities and increased for rocks containing lower porosities. The strain-dependent switch to dilatant behaviour ($C^{*'}$) is likely to be encountered deeper in the edifice, where older rocks have suffered significant inelastic strain. Inelastic lithostatic compaction (P^*) can occur far from the sources of deformation but requires depths of at least 4–5 km (although we note that very porous rocks—such as pumiceous or scoracious rocks (see Farquharson et al. 2015)—may encounter inelastic lithostatic compaction at volcanologically relevant depths).

Implications for lateral outgassing

The ease with which exsolved gases can escape the conduit can impact the style and intensity of an eruption; generally speaking, efficient outgassing promotes effusive behaviour whereas the retention of gas pressure promotes explosive behaviour (e.g. Eichelberger et al. 1986; Woods and Koyaguchi 1994; Rust et al. 2004; Mueller et al. 2008; Nguyen et al. 2014; Castro et al. 2014; Okumura and Sasaki 2014; Gaunt et al. 2014). The permeability of the edifice host lavas is likely to play an important role in the outgassing of the conduit magma (Jaupart 1998; Collombet 2009; Collinson and Neuberg 2012; Heap et al. 2014b; Farquharson et al. 2015); therefore, high-permeability host rocks may encourage effusive behaviour, and vice versa.

Our experimental data show that a throughgoing tensile fracture can increase sample permeability by a factor of two. Therefore, the dilatant deformation of edifice host rocks in the upper edifice (Fig. 9) may serve to increase permeability and
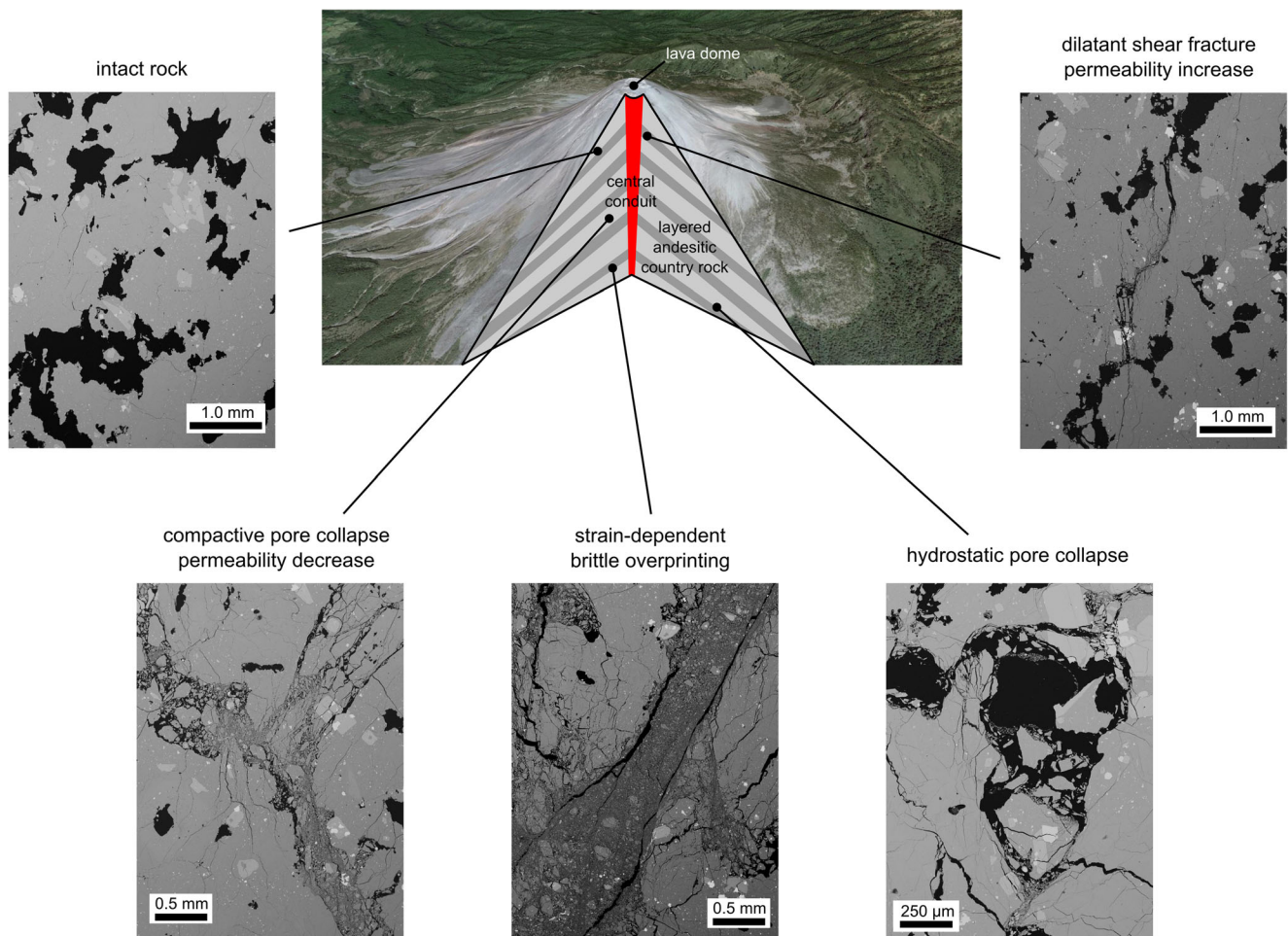
Fig. 9 Schematic cross section of Volcán de Colima (layered andesitic edifice host rocks with a central conduit of dykes; image taken from Google Earth^TM) . The cross section is annotated with back-scattered scanning electron microscope pictures of the intact material and the various deformation microstructures. See text for details

assist the lateral outgassing of the conduit. However, we note that this increase in permeability may be suppressed at pressures high enough to close fluid pathways (e.g. Nara et al. 2011). Recent field evidence has exposed the ubiquitous presence of fractures within the dome, near the dome and on the upper flanks of Volcán de Colima (Kolzenburg et al. 2012; James and Varley 2012; Lavallée et al. 2015). Their presence, anticipated throughout the upper edifice (e.g. Heiken et al. 1988), serves as a testament to the ongoing brittle deformation and outgassing of the shallow edifice. Dilatant failure near the central conduit (the volume inferred to experience higher stresses) may create a permeable halo around the conduit down to a depth of about 1.5 km (i.e. the depth of the dilatant to compactant transition) that provides an efficient outgassing channel (e.g. Rust et al. 2004; Lavallée et al. 2013; Young and Gottsmann 2015). Further, outgassing through large-scale fractures and faults in the edifice is also supported by detailed field studies (e.g. Varley and Taran 2003).

Although edifice rocks are rarely above the temperature of their melt phase, preventing the efficient viscous sintering of

fractures, we highlight that hot pressing (e.g. Kolzenburg et al. 2012) and mineral precipitation (e.g. Taran et al. 2001; Horwell et al. 2013; Schipper et al. 2015) may promote fracture sealing and permeability reduction between periods of unrest activity.

By contrast, rock will deform in a compactant manner deeper in the edifice (Fig. 9). Data from this study show that compaction can decrease permeability significantly (by an order of magnitude at a strain of 4.5 %). Therefore, the compactant deformation of deep edifice host rocks will serve to decrease permeability and impede the lateral outgassing of exsolving magma through the deep conduit wallrock. Evidence for persistent volcano subsidence at Volcán de Colima is provided by both in situ (Murray and Wooller 2002) and passive (Pinel et al. 2011) ground deformation methods. Subsidence rates as high as 93 mm per year (between 1982 and 1999) have been recorded at the edge of the dome, and based on the lack of consistency in horizontal movements, this subsidence has been interpreted as due to the compaction and settling of the edifice (Murray and

Wooller 2002). If the ongoing compaction of Volcán de Colima is the result of compactive deformation, as presented herein, it implies ongoing reduction in the permeability of deep-edifice rocks (>1 km). If faulting within the upper edifice cannot compensate for the continued compaction and permeability reduction of the rocks deeper in the edifice, the potential for explosivity at Volcán de Colima may be subject to increase over time.

Based on our data, we suggest that models of conduit outgassing (e.g. Collombet 2009; Collinson and Neuberg 2012) may be improved by considering permeability of the lower edifice (>1 km) to be lower than that of the upper edifice (<1 km).

Implications for volcano stability

Fracturing in the upper edifice, as evidenced by the ubiquitous presence of fractures, is likely to reduce the integrity and structural stability of the edifice, leading to an increased risk of flank or large-scale dome collapse. Fault movement can result in bulging, intense fracturing and landsliding within the flanks, greatly destabilising the volcano (Lagmay et al. 2000). Subsequent intrusions of magma preferentially infiltrate heavily faulted domains of the volcano resulting in additional instability (Voight et al. 1983; Lagmay et al. 2000; Donnadieu and Merle 1998). However, we highlight that fracture-induced instability may be offset by the healing of fractures (e.g. Kolzenburg et al. 2012).

Although Volcán de Colima is characterised by persistent edifice subsidence (Murray and Wooller 2002; Pinel et al. 2011), interpreted as due to the compaction and settling of the edifice (Murray and Wooller 2002). There is no clear evidence of volcano spreading at Volcán de Colima (Murray and Wooller 2002), a key contributor to volcano instability (e.g. McGuire 1996; van Wyk de Vries and Francis 1997; Borgia et al. 2000). The lack of definitive evidence for volcano spreading may be explained by the relatively young age of Volcán de Colima (about 4000 years old; Murray and Wooller 2002). Volcanic spreading is one of the final stages of the development of a volcanic structure, preceded by periods of building, compressing, thrusting and intruding (Borgia 1994). Inelastic compaction of the edifice rocks may therefore be one of the principal mechanisms driving the "compressing" stage of the growth of a stratovolcano, representing an early stage in the growth and destruction cycles that have dominated the history of the Colima volcanic complex (Stoopes and Sheridan 1992; Cortés et al. 2010). Volcano growth and destruction cycles at the Colima volcanic complex are exemplified by the fact that Volcán de Colima is constructed within the amphitheatre of an earlier collapse structure (Fig. 1a). We speculate that, later in the life cycle of the volcano, the inelastic compaction of edifice-forming rock may also greatly assist volcano spreading and destabilisation.

The substantial volume and distribution of previous collapses (Stoopes and Sheridan 1992 and references therein) highlight the extreme danger posed by Volcán de Colima.

Concluding remarks and perspectives

The failure mode of edifice-forming lava depends on the physical attributes of the lava, primarily the porosity and the pore size, and the conditions under which it deforms. At shallow depths (<1 km), both low- and high-porosity lavas dilate and fail by shear fracturing. However, as depth increases, while low-porosity (<10 %) lava remains dilatant, the failure of high-porosity lava is compactant and driven, on the microscale, by cataclastic pore collapse. Importantly, the choice of failure mode dictates the evolution of key physical properties, such as permeability. Our study has shown that a throughgoing tensile fracture in a sample of porous andesite increases sample permeability by about factor of two and that inelastic compaction can reduce sample permeability by an order of magnitude. The outgassing of volatiles from the conduit may therefore be efficient in the shallow edifice, where rock can fracture, and impeded deeper in the edifice due to compaction. The failure mode of volcanic host rock, and the attendant implications for sidewall outgassing, is thus likely to influence the dominant eruption style: effusive or explosive. If faulting within the shallow edifice cannot compensate for the progressive compaction and permeability reduction of the rocks deeper in the edifice, the explosive potential of a volcano may be subject to increase over time. In terms of volcano stability, fracturing in the upper edifice—which can result in bulging, intense fracturing and landsliding within the flanks— is likely to reduce the integrity of the edifice and lead to an increased risk of flank or large-scale dome collapse. Deeper in the edifice, compactive deformation could explain volcano subsidence and assist in volcano spreading and destabilisation. We highlight that the implications of this study are by no means restricted to Volcán de Colima; due to the comparable construction and eruption histories, and porosity ranges of the edifice host rocks, these implications are likely relevant to similar active andesitic stratovolcanoes, such as Merapi (Indonesia), Santa María (Guatemala), Tungurahua (Ecuador) and Ruapehu (New Zealand).

References

Adelinet M, Fortin J, Schubnel A, Guéguen Y (2013) Deformation modes in an Icelandic basalt: from brittle failure to localized deformation bands. J Volcanol Geotherm Res 255:12–25

Arámbula-Mendoza R, Lesage P, Valdés-González C, Varley NR, Reyes-Dávila G, Navarro C (2011) Seismic activity that accompanied the effusive and explosive eruptions during the 2004–2005 period at Volcán de Colima, Mexico. J Volcanol Geotherm Res 205:30–46

Ayling MR, Meredith PG, Murrell SAF (1995) Microcracking during triaxial deformation of porous rocks monitored by changes in rock physical properties, I. Elastic-wave propagation measurements on dry rocks. Tectonophysics 245:205–221

Baud P, Schubnel A, Wong T-F (2000) Dilatancy, compaction, and failure mode in Solnhofen limestone. J Geophys Res 105(B8):19289–19303

Baud P, Klein E, Wong T-F (2004) Compaction localization in porous sandstones: spatial evolution of damage and acoustic emission activity. J Struct Geol 26:603–624

Baud P, Vajdova V, Wong T-f (2006) Shear-enhanced compaction and strain localization: inelastic deformation and constitutive modeling of four porous sandstones. J Geophys Res 111: B12401. doi: 12410.11029/12005JB004101

Baud P, Townend E, Meredith PG (2012) Permeability evolution during triaxial compaction of an anisotropic porous sandstone. J Geophys Res. doi:10.1029/2012JB009176

Bernard B, Kueppers U, Ortiz H (2015) Revisiting the statistical analysis of pyroclast density and porosity data. Solid Earth Discuss 7:1077–1095

Biggs J, Mothes P, Ruiz M, Amelung F, Dixon TH, Baker S, Hong S-H (2010) Stratovolcano growth by co-eruptive intrusion: the 2008 eruption of Tungurahua Ecuador. Geophys Res Lett 37:21. doi:10.1029/2010GL044942

Borgia A (1994) Dynamic basis of volcanic spreading. J Geophys Res 99: 17791–17804

Borgia A, Linneman SR (1990) On the mechanisms of lava flow emplacement and volcano growth: Arenal, Costa Rica. Lava Flows Domes, IAVCEI Proc Volcanol 2:208–243

Borgia A, Delaney PT, Denlinger RP (2000) Spreading volcanoes. Annu Rev Earth Planet Sci 28:539–570

Brace WF, Paulding BW, Scholz CH (1966) Dilatancy in the fracture of crystalline rocks. J Geophys Res 71:3939–3953

Brantut N, Heap MJ, Meredith PG, Baud P (2013) Time-dependent cracking and brittle creep in crustal rocks: a review. J Struct Geol 52:17–43

Castro J, Bindeman IN, Tuffen H, Schipper CI (2014) Explosive origin of silicic lava: textural and δD–H_2O evidence for pyroclastic degassing during rhyolite effusion. Earth Planet Sci Lett 405:52–61

Cheung C, Baud P, Wong T-f (2012). Effect of grain size distribution on the development of compaction localization in porous sandstone. Geophys Res Lett 39(21). DOI: 10.1029/2012GL053739

Cilona A, Faulkner DR, Tondi E, Agosta F, Mancini L, Rustichelli A, Baud P, Vinciguerra S (2014) The effects of rock heterogeneity on compaction localization in porous carbonates. J Struct Geol 67:75–93

Collinson ASD, Neuberg J (2012) Gas storage, transport and pressure changes in an evolving permeable volcanic edifice. J Volcanol Geotherm Res 243–244:1–13

Collombet M (2009) Two-dimensional gas loss for silicic magma flows: toward more realistic numerical models. Geophys J Int 177:309–318

Cortés A, Garduño VH, Macías JL, Navarro-Ochoa C, Komorowski JC, Saucedo R, Gavilanes JC (2010) Geologic mapping of the Colima volcanic complex (Mexico) and implications for hazard assessment. Geol Soc Am Spec Pap 464:249–264

Cuss RJ, Rutter E, Holloway RF (2003) The application of critical state soil mechanics to the mechanical behaviour of porous sandstones. Int J Rock Mech Min Sci 40:847–862

David C, Wong T-f, Zhu W, Zhang J (1994) Laboratory measurement of compaction-induced permeability change in porous rocks: implications for the generation and maintenance of pore pressure excess in the crust. Pure Appl Geophys 143:425–456

Donnadieu F, Merle O (1998) Experiments on the identation process during cryptodome intrusions: new insights into Mount St. Helens deformation. Geology 26:79–82

Eichelberger JC, Carrigan CR, Westrich HR, Price PH (1986) Non-explosive silicic volcanism. Nature 323:598–602

Evans B, Frederich JT, Wong T-F (1990) The brittle-ductile transition in rocks: recent experimental and theoretical progress. In Duba AG, Durham WB, Handin J, Wang HF (eds) The brittle-ductile transition in rocks. The Heard volume. pp. 1-20, American Geophysical Union, Geophys Monograph 56, Washington

Farquharson IJ, Heap MJ, Varley N, Baud P, Reuschlé T (2015) Permeability and porosity relationships of edifice-forming andesites: a combined field and laboratory study. J Volcanol Geotherm Res 297:52–68

Farrell NJC, Healy D, Taylor CW (2014) Anisotropy of permeability in faulted porous sandstones. J Struct Geol 63:50–67

Faulkner DR, Rutter EH (2001) Can the maintenance of overpressured fluids in large strike-slip fault zones explain their apparent weakness? Geology 29:503–506

Fortin J, Schubnel A, Gueguen Y (2005) Elastic wave velocities and permeability evolution during compaction of Bleurswiller sandstone. Int J Rock Mech Min Sci 42:873–889

Gaunt HE, Sammonds PR, Meredith PG, Smith R, Pallister JS (2014) Pathways for degassing during the lava dome eruption of Mount St. Helens 2004–2008. Geology. doi:10.1130/G35940.1

Gerst A, Savage MK (2004) Seismic anisotropy beneath Ruapehu volcano: a possible eruption forecasting tool. Science 306:1543–1547

Goto Y, Nakata S, Kurokawa M, Shimano T, Sugimoto T, Sakuma S, Hoshizumi H, Yoshimoto M, Uto K (2008) Character and origin of lithofacies in the conduit of Unzen volcano, Japan. Journal of Volcanology and Geothermal Research 175:45–59

Gudmundsson A (2006) How local stresses control magma-chamber ruptures, dyke injections, and eruptions in composite volcanoes. Earth Sci Rev 79:1–31

Gudmundsson A (2011) Rock fractures in geological processes. Cambridge University Press, Cambridge

Guest JE, Chester DK, Duncan AM (1984) The Valle del Bove, Mount Etna: its origin and relation to the stratigraphy and structure of the volcano. J Volcanol Geotherm Res 21:1–23

Hall ML, Robin C, Beate B, Mothes P, Monzier M (1999) Tungurahua Volcano, Ecuador: structure, eruptive history and hazards. J Volcanol Geotherm Res 91:1–21

Heap MJ, Baud P, Meredith PG, Vinciguerra S, Reuschlé T (2014a) The permeability and elastic moduli of tuff from Campi Flegrei, Italy: implications for ground deformation modelling. Solid Earth 5:25–44

Heap MJ, Lavallée Y, Petrakova L, Baud P, Reuschlé T, Varley N, Dingwell DB (2014b) Microstructural controls on the physical and mechanical properties of edifice-forming andesites at Volcán de Colima, Mexico. J Geophys Res 119:2925–2963

Heap MJ, Xu T, Chen C-f (2014c) The influence of porosity and vesicle size on the brittle strength of volcanic rocks and magmas. Bull Volcanol 76:856. doi:10.1007/s00445-014-0856-0

Heap MJ, Kennedy BM, Pernin N, Jacquemard L, Baud P, Farquharson IJ, Scheu B, Lavallée Y, Gilg HA, Letham-Brake M, Mayer K, Jolly AD, Reuschlé T, Dingwell DB (2015) Mechanical behaviour and failure modes in the Whakaari (White Island volcano) hydrothermal system, New Zealand. J Volcanol Geotherm Res 295:26–42

Heiken G, Wohletz K, Eichelberger JC (1988) Fracture fillings and intrusive pyroclasts, Inyo Domes, California. J Geophys Res 93:4335–4350

Hoek E, Bieniawski ZT (1965) Brittle fracture propagation in rock under compression. Int J Fract 1:137–155

Horwell CJ, Williamson BJ, Llewellin EW, Damby DE, Le Blond JS (2013) The nature and formation of cristobalite at the Soufrière Hills volcano, Montserrat: implications for the petrology and stability of silicic lava domes. Bull Volcanol 75:696. doi:10.1007/s00445-013-0696-3

Hutchinson W, Varley N, Pyle DM, Mather TA et al (2013) Airborne thermal remote sensing of the Volcán de Colima (Mexico) lava dome from 2007 to 2010. In: Pyle DL (ed) Remote sensing of volcanoes & volcanic processes: integrating observation & modelling. Geological Society of London, London

James MR, Varley N (2012) Identification of structural controls in an active lava dome with high resolution DEMs: Volcán de Colima, Mexico. Geophys Res Lett 39:22. doi:10.1029/2012GL054245

Jaupart C (1998) Gas loss from magmas through conduit walls during eruption. Geol Soc Lond, Spec Publ 145:73–90

Kaneko K (2002) Exogenous and endogenous growth of the Unzen lava dome examined by satellite infrared image analysis. J Volcanol Geotherm Res 116:151–160

Kendrick JE, Lavallée Y, Hess K-U, Heap MJ, Gaunt HE, Meredith PG, Dingwell DB (2013) Tracking the permeable porous network during strain-dependent magmatic flow. J Volcanol Geotherm Res 260:117–126

Kennedy LA, Russell JK, Nelles E (2009) Origins of mount St. Helens cataclasites: experimental insights. Am Mineral 94:995–1004

Kolzenburg S, Heap MJ, Lavallée Y, Russell JKR, Meredith PG, Dingwell DB (2012) Strength and permeability recovery of tuffisite-bearing andesite. Solid Earth 3:191–198

Kueppers U, Scheu B, Spieler O, Dingwell DB (2005) Field-based density measurements as tool to identify pre-eruption dome structure: set-up and first results from Unzen volcano, Japan. J Volcanol Geotherm Res 141:65–75

Lagmay AMF, van Wyk de Vries B, Kerle N, Pyle DM (2000) Volcano instability induced by strike-slip faulting. Bull Volcanol 62:331–346

Lamb OD, Varley NR, Mather TA, Pyle DM, Smith PJ, Liu EJ (2014) Multiple timescales of cyclical behaviour observed at two dome-forming eruptions. J Volcanol Geotherm Res 284:106–121

Lavallée Y, Varley N, Alatorre-Ibargüengoitia MA, Hess K-U, Kueppers U, Mueller S, Richard D, Scheu B, Spieler O, Dingwell DB (2012) Magmatic architecture of dome-building eruptions at Volcán de Colima, Mexico. Bull Volcanol 74:249–260

Lavallée Y, Benson PM, Heap MJ, Hess K-U, Flaws A, Schillinger B, Meredith PG, Dingwell DB (2013) Reconstructing magma failure and the degassing network of dome-building eruptions. Geology 41:515–518

Lavallée Y, Heap MJ, Kueppers U, Kendrick JE, Dingwell DB (2015) The fragility of Volcán de Colima—a material constraint. In: Varley N, Komorowski JC (eds) Volcán de Colima: managing the threat. Springer, Berlin

Lesage P, Reyes-Dávila G, Arámbula-Mendoza R (2014) Large tectonic earthquakes induce sharp temporary decreases in seismic velocity in Volcán de Colima, Mexico. J Geophys Res 119:4360–4376

Loaiza S, Fortin J, Schubnel A, Guéguen Y, Vinciguerra S, Moreira M (2012) Mechanical behavior and localized failure modes in a porous basalt from the Azores. Geophys Res Lett 39. doi:10.1029/2012GL053218

Lockner D (1993) The role of acoustic emission in the study of rock fracture. Int J Rock Mech Min Sci Geomech Abstr 30:883–889

Lockner D, Byerlee J, Kuksenko V, Ponomarev A, Sidorin A (1991) Quasi-static fault growth and shear fracture energy in granite. Nature 350:39–42

Luhr JF (2002) Petrology and geochemistry of the 1991 and 1998-1999 lava flows from Volcán de Colima, México: implications for the end of the current eruptive cycle. J Volcanol Geotherm Res 117(1-2):169–194

McGuire WJ (1996) Volcano instability: a review of contemporary themes. Geol Soc Lond 110:1–23

Melnik O, Sparks RSJ (2002) Dynamics of magma ascent and lava extrusion at Soufrière Hills Volcano, Montserrat. In Druitt TH, Kokelaar BP (eds) The eruption of Soufrière Hills volcano, Montserrat, from 1995 to 1999. London, Geological Society of London, Memoirs, 21, 153-171

Menéndez B, Zhu W, Wong T-f (1996) Micromechanics of brittle faulting and cataclastic flow in Berea sandstone. J Struct Geol 18:1–16

Mitchell TM, Faulkner DR (2008) Experimental measurements of permeability evolution during triaxial compression of initially intact crystalline rocks and implications for fluid flow in fault zones. J Geophys Res 113:B11. doi:10.1029/2008JB005588

Mitchell TM, Faulkner DR (2012) Towards quantifying the matrix permeability of fault damage zones in low porosity rocks. Earth Planet Sci Lett 339–340:24–31

Mollema PN, Antonellini MA (1996) Compaction bands: a structural analog for anti-mode I cracks in aeolian sandstone. Tectonophysics 267:209–228

Mueller S, Scheu B, Spieler O, Dingwell DB (2008) Permeability control on magma fragmentation. Geology 36:399–402

Mueller S, Scheu B, Spieler O, Richard D, Dingwell DB (2011) The porosity of pyroclasts as an indicator of volcanic explosivity. J Volcanol Geotherm Res 203:168–174

Mueller SB, Varley NR, Kueppers U, Lesage P, Reyes Davila GÁ, Dingwell DB (2013) Quantification of magma ascent rate through rockfall monitoring at the growing/collapsing lava dome of Volcán de Colima, Mexico. Solid Earth 4:201–213

Murray JB, Wooller LK (2002) Persistent summit subsidence at Volcan de Colima, Mexico, 1982–1999: strong evidence against Mogi deflation. J Volcanol Geotherm Res 117:69–78

Nara Y, Meredith PG, Yoneda T, Kaneko K (2011) Influence of macro-fractures and micro-fractures on permeability and elastic wave velocities in basalt at elevated pressure. Tectonophysics 503:52–59

Nguyen CT, Gonnermann HM, Houghton BF (2014) Explosive to effusive transition during the largest volcanic eruption of the 20th century (Novarupta 1912, Alaska). Geology. doi:10.1130/G35593.1

Ngwenya BT, Kwon O, Elphick SC, Main IG (2003) Permeability evolution during progressive development of deformation bands in porous sandstones. J Geophys Res 108:B7. doi:10.1029/2002JB001854

Okumura S, Sasaki O (2014) Permeability reduction of fractured rhyolite in volcanic conduits and its control on eruption cyclicity. Geology 42:843–846

Paterson MS, Wong T-F (2005) Experimental rock deformation—the brittle field. Springer, New York. ISBN 978-3-540-26339-5

Pinel V, Hooper A, De la Cruz-Reyna S, Reyes-Davila GA, Doin MP, Bascou P (2011) The challenging retrieval of the displacement field from InSAR data for andesitic stratovolcanoes: case study of Popocatepetl and Colima Volcano, Mexico. J Volcanol Geotherm Res 200:49–61

Read MD, Ayling MR, Meredith PG, Murrell SAF (1995) Microcracking during triaxial deformation of porous rocks monitored by changes in rock physical properties, II. Pore volumometry and acoustic emission measurements on water-saturated rocks. Tectonophysics 245: 223–235

Roman DC, Moran SC, Power JA, Cashman KV (2004) Temporal and spatial variation of local stress fields before and after the 1992 eruptions of crater peak vent, Mount Spurr Volcano, Alaska. Bull Seismol Soc Am 94:2366–2379

Rust AC, Cashman KV, Wallace PJ (2004) Magma degassing buffered by vapor flow through brecciated conduit margins. Geology 32:349–352

Rutter E (1986) On the nomenclature of mode of failure transitions in rocks. Tectonophysics 122(3-4):381–387

Sammis CG, Ashby MF (1986). The failure of brittle porous solids under compressive stress states. Acta Metall 34: 511-526. doi: 510.1016/0001-6160(1086)90087-90088

Savov IP, Luhr JF, Navarro-Ochoa C (2008) Petrology and geochemistry of lava and ash erupted from Volcán Colima, Mexico, during 1998–2005. J Volcanol Geotherm Res 174:241–256

Schipper CI, Castro JM, Tuffen H, Wadsworth FB, Chappell D, Pantoja AE, Simpson MP, Le Ru EC (2015) Cristobalite in the 2011–2012 Cordón Caulle eruption (Chile). Bull Volcanol 77:34. doi:10.1007/s00445-015-0925-z

Schock RN, Heard HC, Stephans DR (1973) Stress-strain behavior of a granodiorite and two graywackes on compression to 20 kilobars. J Geophys Res 78:5922–5941

Scholz CH (1968) Microfracturing and the inelastic deformation of rock in compression. J Geophys Res 73:1417–1432

Shipton ZK, Evans JP, Robeson KR, Forster CB, Snelgrove S (2002) Structural heterogeneity and permeability in faulted eolian sandstone: implications for subsurface modeling of faults. AAPG Bull 86:863–883

Smith R, Sammonds P, Tuffen H, Meredith PG (2011) Evolution of the mechanics of the 2004–2008 Mt. St. Helens lava dome with time and temperature. Earth Planet Sci Lett 307:191–200

Stevenson JA, Varley N (2008) Fumarole monitoring with a handheld infrared camera: Volcán de Colima, Mexico, 2006-2007. J Volcanol Geotherm Res 177:911–924

Stoopes GR, Sheridan MF (1992) Giant debris avalanches from the Colima Volcanic Complex, Mexico: implications for long-runout landslides (>100 km) and hazard assessment. Geology 20:299–302

Taran YA, Bernard A, Gavilanes JC, Lunezheva E, Cortés A, Armienta MA (2001) Chemistry and mineralogy of high-temperature gas discharges from Colima volcano, Mexico. Implications for magmatic gas–atmosphere interaction. J Volcanol Geotherm Res 108:245–264

Taran Y, Gavilanes JC, Cortés A (2002) Chemical and isotopic composition of fumarolic gases and the SO2 flux from Volcán de Colima, Mexico, between the 1994 and 1998 eruptions. J Volcanol Geotherm Res 117:105–119

Tibaldi A (2001) Multiple sector collapses at stromboli volcano, Italy: how they work. Bull Volcanol 63:112–125

van Wyk de Vries B, Borgia A (1996) The role of basement in volcano deformation. Geol Soc Lond Spec Publ 110:95–110

van Wyk de Vries B, Francis PW (1997) Catastrophic collapse at stratovolcanoes induced by gradual volcano spreading. Nature 387:387–390

Varley NR, Taran YA (2003) Degassing processes of Popocatépetl and Volcán de Colima, Mexico. In: Oppenheimer C, Pyle DM, Barclay J (eds) Volcanic degassing. Geological Society of London, London, pp 263–280. ISBN 1-86239-136-X

Varley N, Arámbula-Mendoza R, Reyes-Dávila G, Stevenson J, Harwood R (2010) Long-period seismicity during magma movement at Volcán de Colima. Bull Volcanol 72:1093–1107

Violay M, Gibert B, Mainprice D, Burg J-P (2015) Brittle versus ductile deformation as the main control of the deep fluid circulation in oceanic crust. Geophys Res Lett. doi:10.1002/2015GL063437

Voight B (2000) Structural stability of andesite volcanoes and lava domes, philosophical transactions: mathematical, physical and engineering sciences, 358, No. 1770, causes and consequences of eruptions of andesite volcanoes (May 15, 2000), 1663-1703

Voight B, Janda RJ, Glicken H, Douglass PM (1983) Nature and mechanics of the Mount St. Helens rockslide avalanche of 18 May. Geotechnique 33:243–273

Wang B, Chen Y, Wong T-f (2008). A discrete element model for the development of compaction localization in granular rock. J Geophys Res 113: B03202. doi:03210.01029/02006JB004501

Webb EB, Varley N, Pyle DM, Mather TA (2014) Thermal imaging and analysis of short-lived Vulcanian explosions at Volcán de Colima, Mexico. J Volcanol Geotherm Res 278–279:132–145

Wibberley CAJ, Shimamoto T (2003) Internal structure and permeability of major strike-slip fault zones: the median tectonic line in Mie Prefecture, southwest Japan. J Struct Geol 25:59–78

Wong T-f, Baud P (2012) The brittle-ductile transition in rocks: a review. J Struct Geol 44:25–53

Wong T-f, David C, Zhu W (1997) The transition from brittle faulting to cataclastic flow in porous sandstones: mechanical deformation. J Geophys Res 102(B2):3009–3025

Woods AW, Koyaguchi T (1994) Transitions between explosive and effusive eruptions of silicic magmas. Nature 370:641–644

Young NK, Gottsmann J (2015) Shallow crustal mechanics from volumetric strain data: insights from Soufrière Hills Volcano, Montserrat. J Geophys Res 120:1559–1571

Zhu W, Wong T-f (1997a) The transition from brittle faulting to cataclastic flow: permeability evolution. J Geophys Res 102(B2): 3027–3041

Zhu W, Montesi LGJ, Wong T-f (1997b) Shear-enhanced compaction and permeability reduction: triaxial extension tests on porous sandstone. Mech Mater 25:199–214

Zhu W, Baud P, Wong T-F (2010) Micromechanics of cataclastic pore collapse in limestone. J Geophys Res. doi:10.1029/2009JB006610

Zhu W, Baud P, Vinciguerra S, Wong T-F (2011). Micromechanics of brittle faulting and cataclastic flow in Alban Hills tuff. J Geophys Res 116: B06209. doi:06210.01029/02010JB008046

Zoback MD, Byerlee JD (1975) The effect of microcrack dilatancy on the permeability of westerly granite. J Geophys Res 80:752–755

Zobin VM, González-Amezcua M, Reyes-Dávila GA (2002) Seismotectonic deformation of the volcanic edifice prior to the 1998 lava eruption of Volcán de Colima, México. Bull Volcanol 64:349–355

CrossMark

From rock to magma and back again: The evolution of temperature and deformation mechanism in conduit margin zones

Michael J. Heap [a,*], Marie Violay [b], Fabian B. Wadsworth [c], Jérémie Vasseur [c]

[a] *Géophysique Expérimentale, Institut de Physique de Globe de Strasbourg (UMR 7516 CNRS, Université de Strasbourg/EOST), 5 rue René Descartes, 67084 Strasbourg cedex, France*
[b] *Laboratory of Experimental Rock Mechanics, École Polytechnique Fédérale de Lausanne, Station 18, CH-1015, Lausanne, Switzerland*
[c] *Earth and Environmental Sciences, Ludwig-Maximilians-Universität, Theresienstr. 41, 80333 Munich, Germany*

A B S T R A C T

Explosive silicic volcanism is driven by gas overpressure in systems that are inefficient at outgassing. The zone at the margin of a volcanic conduit—thought to play an important role in the outgassing of magma and therefore pore pressure changes and explosivity—is the boundary through which heat is exchanged from the hot magma to the colder country rock. Using a simple heat transfer model, we first show that the isotherm for the glass transition temperature (whereat the glass within the groundmass transitions from a glass to an undercooled liquid) moves into the country rock when the magma within the conduit can stay hot, or into the conduit when the magma is quasi-stagnant and cools (on the centimetric scale over days to months). We then explore the influence of a migrating viscous boundary on compactive deformation micromechanisms in the conduit margin zone using high-pressure (effective pressure of 40 MPa), high-temperature (up to 800 °C) triaxial deformation experiments on porous andesite. Our experiments show that the micromechanism facilitating compaction in andesite is localised cataclastic pore collapse at all temperatures below the glass transition of the amorphous groundmass glass T_g (i.e., rock). In this regime, porosity is only reduced within the bands of crushed pores; the porosity outside the bands remains unchanged. Further, the strength of andesite is a positive function of temperature below the threshold T_g due to thermal expansion driven microcrack closure. The micromechanism driving compaction above T_g (i.e., magma) is the distributed viscous flow of the melt phase. In this regime, porosity loss is distributed and is accommodated by the widespread flattening and closure of pores. We find that viscous flow is much more efficient at reducing porosity than cataclastic pore collapse, and that it requires stresses much lower than those required to form bands of crushed pores. Our study therefore highlights that temperature excursions can result in a change in deformation micromechanism that drastically alters the mechanical and hydraulic properties of the material within the conduit margin zone, with possible implications for pore pressure augmentation and explosive behaviour.

© 2017 Elsevier B.V. All rights reserved.

1. Introduction

Magma vesiculation is the consequence of volatile oversaturation during decompression (Gonnermann and Manga, 2012) or heating (Lavallée et al., 2015). Once exsolved, the ease with which these volatiles can escape, governed by the permeability of the system, is thought to impact volcanic explosivity (Eichelberger et al., 1986; Woods and Koyaguchi, 1994; Melnik et al., 2005; Mueller et al., 2008). The conduit margin zone (comprising the magma at the conduit margin and the adjacent wall rock) is thought to be the annulus through which degassed volatiles dominantly escape, a result of its highly fractured, brecciated, and banded nature (Rust et al., 2004; Tuffen and Dingwell, 2005; Lavallée et al., 2013; Gaunt et al., 2014).

The fractured physical state of the conduit margin zone is a consequence of the shear stresses in the magma-filled conduit (e.g., Tuffen and Dingwell, 2005). In the shallow edifice, a brittle response to an applied stress can be expected from (1) country rock adjacent to the conduit (Heap et al., 2015a), (2) volcanic material at the conduit margin without a substantial melt phase (i.e., high-crystallinity; Smith et al., 2011; Violay et al., 2012), and (3) magma with a substantial melt phase at the conduit margin deforming at a strain rate that exceeds the structural re-

laxation timescale of its melt phase (Ichihara and Rubin, 2010; Lavallée et al., 2013). Brittle deformation (i.e., fracture formation) increases the porosity and permeability of volcanic materials (Nara et al., 2011; Lavallée et al., 2013; Violay et al., 2015; Heap and Kennedy, 2016; Farquharson et al., 2016a), thus locally increasing the efficiency of outgassing and potentially decreasing the likelihood or intensity of an explosive eruption (Mueller et al., 2008; Lavallée et al., 2013; Castro et al., 2014).

Deeper in the edifice (≥1 km), the country rock adjacent to the conduit will accommodate stresses in a dominantly ductile manner (Shimada, 1986; Loaiza et al., 2012; Adelinet et al., 2013; Heap et al., 2015a). Ductile deformation in both the solid and liquid regimes can decrease the porosity, and therefore permeability, of the materials within the conduit margin zone, thus potentially increasing the likelihood or intensity of an explosive eruption (Kennedy et al., 2010; Kendrick et al., 2013; Heap et al., 2015a, 2015b; Schauroth et al., 2016). The micromechanical mechanism responsible for ductile deformation in volcanic rocks (or magmas without a substantial melt phase) is distributed (Shimada, 1986; Zhu et al., 2011) or localised (Loaiza et al., 2012; Adelinet et al., 2013; Heap et al., 2015a) cataclastic pore collapse. Viscous flow of the amorphous melt phase is the mechanism responsible for ductile deformation in magma containing a substantial melt phase residing at a temperature above its glass transition temperature T_g (Quane et al., 2009; Lavallée et al., 2013; Kendrick et al., 2013; Vasseur et al., 2013; Heap et al., 2015b). We note that high strain rates can shift the transition from ductile to brittle deformation to greater depths (Webb and Dingwell, 1990; Cordonnier et al., 2012; Lavallée et al., 2013; Kushnir et al., 2017).

The zone at the margin of a volcanic conduit is the boundary through which heat is exchanged from the hot magma to the colder country rock. Temperature excursions, resulting from the injection of hot magma batches or the cooling of the magma within the conduit, will move the T_g isotherm thus modifying the operative micromechanism of deformation, with attendant implications for the mechanical response and the physical property evolution (e.g., porosity and permeability) of the materials within the margin zone. At a depth ≥1 km, where ductile deformation will dominate, the materials within the margin zone may repeatedly transition between the micromechanisms of cataclastic pore collapse and viscous flow. The transition between these compaction micromechanisms, and the accompanying changes in mechanical and hydraulic behaviour, has never been explicitly studied. Experimental studies of compaction in magmas have largely been limited to uniaxial experiments (Quane et al., 2009; Kendrick et al., 2013; Heap et al., 2014a) or isobaric conditions in which other forces, such as surface tension, dominate (Vasseur et al., 2013; Kennedy et al., 2015), while deformation experiments designed to study compaction in volcanic rocks have all been performed at ambient-temperature (Loaiza et al., 2012; Adelinet et al., 2013; Heap et al., 2015a). High-pressure and high-temperature studies of magma deformation have focussed on magma viscosity determination (e.g., Champallier et al., 2008) or the onset of fracturing (e.g., Kushnir et al., 2017) and, so far, have not provided *in-situ* measurements of porosity during deformation. A recent study however has shown, by means of a pore fluid volumometer, that compactive behaviour is encountered in low-porosity basalt at a confining pressure of 100 MPa and a temperature of 950 °C (Violay et al., 2015).

Our aim here is to investigate compaction processes in the conduit margin zone of a typical andesitic stratovolcano as the materials are heated or cooled. To achieve this goal we performed a series of high-pressure (at a pressure analogous to ~1 km depth) triaxial experiments on porous andesite at temperatures from ambient to 800 °C in which we monitored sample porosity during deformation. A detailed understanding of the micromechanical processes
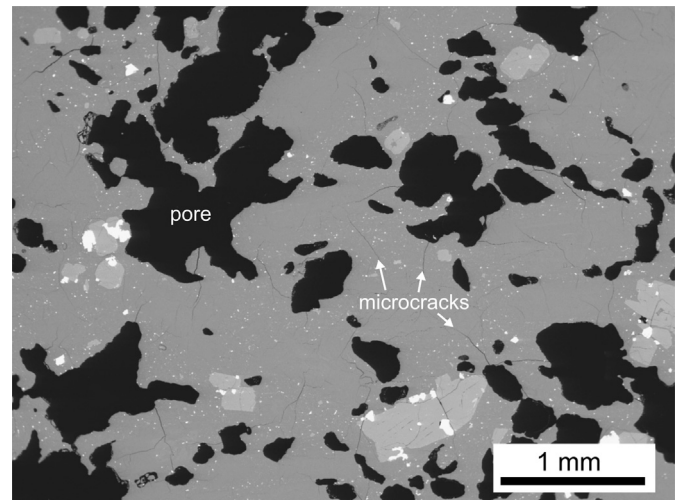
Fig. 1. Backscattered scanning electron microscope (BSEM) image of the as-collected andesite studied herein. Porosity is black. A pore and microcracks are labelled on the image.

responsible for compaction in the conduit margin zone, and how they influence mechanical behaviour and hydraulic properties, is paramount to our comprehension of pore pressure changes and the likelihood of explosive behaviour at active volcanoes worldwide.

2. Experimental material

We use an andesite block collected from the La Lumbre debris-flow track at Volcán de Colima, an active stratovolcano located in the Trans-Mexican Volcanic Belt (Mexico) (Varley and Komorowski, 2017). Although our block was sourced from Volcán de Colima, we consider the implications presented in this study to be applicable to active and frequently collapsing andesitic stratovolcanoes worldwide. Cylindrical core samples used for this study were all drilled from this block in the same orientation.

The andesite collected has a porphyritic texture consisting of a glassy groundmass (with abundant microlites) that hosts pores and a phenocryst cargo (long axis <1.5 mm; Fig. 1). The phenocrysts and groundmass contain many randomly oriented microcracks up to a few mm in length (Fig. 1). The average connected and total porosity is 0.265 and 0.268 (isolated porosity ~0.03), respectively (determined by helium pycnometry; the connected porosity of each sample is given in Table 1). The phenocryst volume fraction is ~0.4 and the groundmass consists of glass (volume fraction ~0.135) containing ~0.2 volume fraction of microlites (of mainly plagioclase with subordinate high-density Fe–Ti oxides), estimated from 2D scanning electron microscope (SEM) images using ImageJ. The bulk composition of the here-studied andesite includes 61.5 wt.% SiO_2, measured using X-ray fluorescence (XRF; complete XRF analysis is presented in the Supplementary Information), and is very similar to that of the products erupted over the last two decades (Heap et al., 2014b).

The temperature at which the glass within the groundmass transitions from a glass to an undercooled liquid—the glass transition temperature (T_g)—was determined using a Netzsch Pegasus 404 simultaneous thermal analysis device at a heating rate of 20 °C min^{-1}. The glass transition is manifest as a non-linear endothermic peak in heat flow relative to the smoothly changing baseline value. During heating from the unknown natural cooling path during which the rock was formed, this peak occurred at ~750.2 ± 3.5 °C (see Supplementary Information for further details).

Table 1
Summary of the experiments performed for this study.

Connected porosity	Confining pressure (MPa)	Pore fluid pressure (MPa)	Pore fluid	Effective pressure (MPa)	Temperature (°C)	Strain rate (s^{-1})	Failure mode	Dominant deformation micromechanism
0.278	25	20	Water	5	Ambient	10^{-5}	Brittle	Microcracking
0.267	30	20	Water	10	Ambient	10^{-5}	Brittle	Microcracking
0.268	40	20	Water	20	Ambient	10^{-5}	Brittle	Microcracking
0.269	50	20	Water	30	Ambient	10^{-5}	Ductile	Cataclastic pore collapse
0.274	60	20	Water	40	Ambient	10^{-5}	Ductile	Cataclastic pore collapse
0.275	70	20	Water	50	Ambient	10^{-5}	Ductile	Cataclastic pore collapse
0.291	50	20	Argon	30	200	10^{-5}	Ductile	Cataclastic pore collapse
0.248	50	20	Argon	30	400	10^{-5}	Ductile	Cataclastic pore collapse
0.294	50	20	Argon	30	600	10^{-5}	Ductile	Cataclastic pore collapse
0.281	50	20	Argon	30	800	10^{-5}	Ductile	Viscous flow

3. Modelling

We will now consider whether, and to what extent, the spatial position of T_g will move with respect to the conduit margin. To do this, we apply a simple conductive solution to the 1D heat equation in cylindrical coordinates. We explore two end-member scenarios. First, where the magma remains at the initial maximum temperature and heat continuously conducts toward the far-field into the country rock. And second, where the magma in the conduit is stagnant and loses heat conductively into the country rock, leading to wholescale cooling of the system. While simplistic, to a first order the former scenario may be analogous to rapidly ascending magma (rapid advection end-member) while the latter may be analogous to very slowly ascending or stagnant conduit magma (no advection end-member). The 1D heat equation in cylindrical coordinates is:

$$\frac{\partial T}{\partial t} = \frac{1}{r}\frac{\partial}{\partial r}\left(rD\frac{\partial T}{\partial r}\right), \tag{1}$$

where r is the radial coordinate distance, t is the time since the onset of heat transfer, R is the conduit cylindrical radius, T is the temperature, and D is the thermal diffusivity. In both end-member cases we have the same initial conditions that are $T = T_m$ for $r \leq R$ at $t = 0$ and $T = T_r$ at $R \leq r \leq L$, where T_m and T_r are the initial temperature of the magma and the country rock, respectively. We take $T_m = 940\,°C$ (estimated magmatic temperature for Volcán de Colima; Luhr and Carmichael, 1980) and $T_r = 50\,°C$. We assume a first order estimate for the dependence of the thermal diffusivity D on temperature T is $D = D_0 \exp(\beta T)$, where D_0 is the diffusivity at $T = 0$ (in units of °C) and β is a constant (after Schauroth et al., 2016). Following Schauroth et al. (2016), we compare the exponential form for D with the experimental data of Bagdassarov and Dingwell (1994) for pore-free volcanic material over the range of $550 \leq T \leq 1100\,°C$. In this range we find that best fit values are $D_0 = 2.89 \times 10^{-7}$ m^2 s^{-1} and $\beta = 1.58 \times 10^{-3}\,°C^{-1}$. In the case where the magma and country rock are porous, we scale the effect of porosity by decomposing D into $D = k/\rho C$, the first-order scaling for porosity is then as follows:

$$D' = \frac{k(1-\phi)}{(\rho C(1-\phi) + \rho_f C_f \phi)(1+\phi)} \tag{2}$$

where D' is the value of D scaled for ϕ, k is the pore-free thermal conductivity, ρ is the pore-free density, C is the pore-free specific heat capacity, ρ_f is the density of the pore fluid, C_f is the specific heat capacity of the pore fluid, and ϕ is the porosity. The bulk value of k is taken to be $D\rho C$ of the pore-free material. When $\phi = 0$, we then have the desirable limit that $D' = D$. Herein we take approximate values $\rho = 2000$ kg m^{-3}, $C = 1000$ J kg^{-1} K^{-1}, $\rho_f = 1.275$ kg m^{-3}, and $C_f = 1007$ J kg^{-1} K^{-1}. For a case where we invoke porosity, we replace D in Equation (1) with D' from Equation (2).

In our simulations of heat transfer, the conduit centre is insulated in both scenarios (Neumann boundary condition of 0) such that $\partial T/\partial r = 0$ for all t at $r/R = 0$. In the case where the magma remains hot throughout, we additionally have that $T = T_m$ for all t at $r/R \leq 1$. The scenario in which the magma is effectively stagnant and can cool, there is no boundary condition at $r/R = 1$ as we assume the material either side of the conduit wall follows the same $D(T)$ or $D'(T)$ law (see above). These assumptions are justified as the data from Bagdassarov and Dingwell (1994) show no discontinuity over this temperature range, even across T_g for any porosity. With these conditions, we solve Equation (1) numerically by using a fully implicit finite difference scheme (backward time, central space) coupled with a relaxed fixed-point method to ensure convergence at each time step, with a dimensionless spatial and temporal resolution of 10^{-3} and 10^{-4}, respectively. The results are shown in Fig. 2 for initial conduit radii of 15 and 50 m and initial country rock porosities of 0 and 0.4.

The model presented herein (Fig. 2) is a simplified numerical rendering of heat-transfer through conduit margin zones. In modelling conduction of heat from stagnant magma, repetitively injected magma, and continuously flowing magma to wall rocks, Petcovic and Dufek (2005) found that, for their conditions of a basaltic magma intruding a tonalitic wall rock, the amount of melting achieved in the wall rocks depended dominantly on the time since injection, the frequency of injection, and the time since the onset of continuous flow, in each case, respectively. Their model is composed of a coupled solution of the flow profile in the intrusion, the crystallisation and chemical mass transfer, and the heat transfer in both the magma and the wall rocks. Despite the complexity, a scaling between the time available for heat transfer t and the thermal diffusion length L holds such that $L \approx \sqrt{Dt}$, such that the half-fall distance of the temperature in published simulations scales with L until distances of $\sim$10 m from the conduit. These authors use a temperature independent diffusivity of $D = 1.1 \times 10^{-6}$ m^2 s^{-1} so that this scaling is easily computed (see Supplementary Information). This simple scaling implies that L can be used to approximately predict heat transfer at the conduit boundary to a first order even for more complex conditions than the explicit solution given here (Fig. 2).

We find the intuitive result that T_g moves into the country rock in the case where the conduit magma does not cool (rapidly ascending magma), and that T_g moves into the conduit magma in the case where the conduit magma is quasi-stagnant and cools (Fig. 2). In the former case, the volume of material capable of viscous deformation will increase, enlarging the effective conduit radius (by 1–8 cm over days to months; Fig. 2a). These estimations are consistent with the observations of 0.1–2 cm-thick welded and densified rinds in the baked country rock at Tarawera volcano, New Zealand (Schauroth et al., 2016). Longer lengthscales (5–10 cm) of country rock viscous mobilisation will occur over timescales approaching a year (Fig. 2a). Conversely, in the latter case, cooling
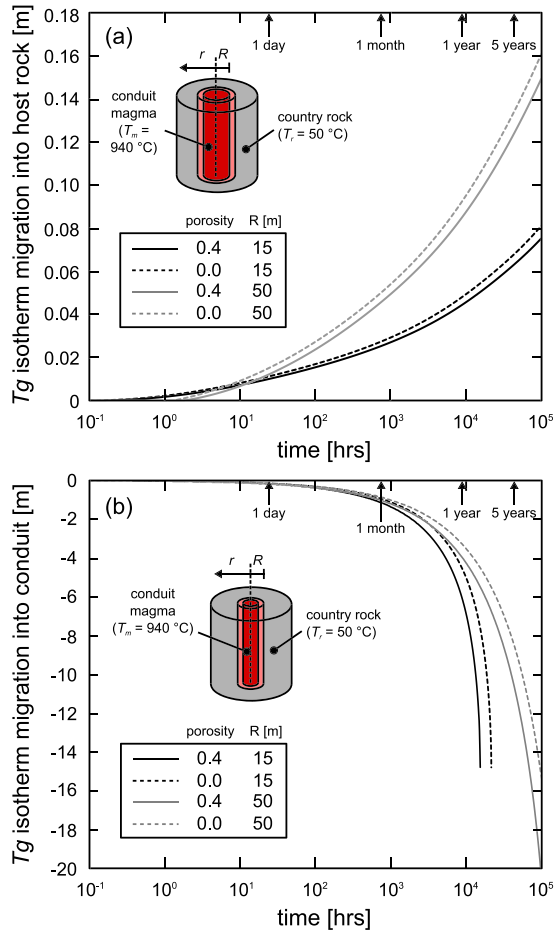
Fig. 2. The solution to the 1D heat equation in cylindrical coordinates for conductive heat transfer from a high-temperature magma-filled conduit ($T_m = 940\,^\circ$C) to the adjacent country rock ($T_r = 50\,^\circ$C). (a) Scenario in which the temperature of the magma is constant ($T = T_m$ for all t at $r/R \leq 1$). (b) Scenario in which the magma is allowed to cool (there is no boundary condition at $r/R = 1$). Curves are given for dense (porosity = 0) and porous (porosity = 0.4) country rock for two conduit radii, 15 and 50 m.

will result in a narrowing of the viscous radius of the magma conduit (by 15–100 cm over days to months; Fig. 2b). In this scenario, the viscous radius can be reduced by 4–5 m within one year (Fig. 2b).

It can be inferred from these models that the conduit margin zone—an important region of the edifice for magmatic outgassing—is subject to fluctuations in temperature that will modify the mechanical response and the physical property evolution (e.g., porosity and permeability) of the materials within the zone. We will now explore the influence of a migrating viscous deformation front on compactive deformation micromechanisms in the conduit margin zone using high-pressure and high-temperature triaxial deformation experiments.

4. Experimental considerations

Since our goal is to perform experiments at high-temperature, it is important to first understand whether exposure to high-temperature alters the physical state of the andesite (e.g., thermal microcracking). To this end, we measured the connected porosity, P-wave velocity, and permeability of two cylindrical samples (20 mm in diameter and precision-ground to a nominal length of 40 mm) at ambient temperature and after exposure to temperatures between 200 and 900 °C. The samples were heated in a furnace at room pressure at a rate of 1 °C min^{-1} and 20 °C min^{-1},
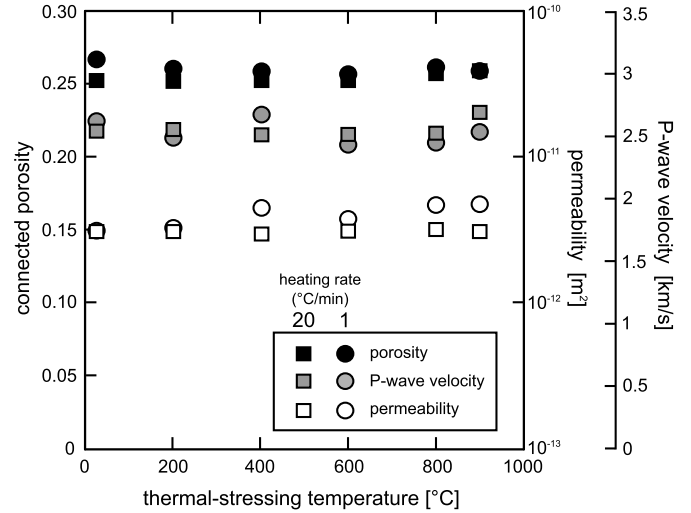

Fig. 3. Rock physical property evolution (connected porosity, permeability, and P-wave velocity) as a function of thermal stressing temperature (at two heating/cooling rates, 1 and 20 °C min^{-1}).

respectively, left at the target temperature for 2 h, before being cooled back to room temperature at 1 °C min^{-1} and 20 °C min^{-1}, respectively. Connected porosity was measured using a helium pycnometer. P-wave velocity was measured along the axis of the sample under an axial stress of $\sim$1 MPa. Permeability was measured along the sample axis in a steady-state gas (nitrogen) permeameter under a confining pressure P_c of 1 MPa (see the Supplementary Information for further details).

Our physical property data show that connected porosity, P-wave velocity, and permeability do not change upon transient (2 h) exposure to high-temperature (Fig. 3). Negligible changes to volcanic rock physical properties following thermal stressing has been previously noted in basalt heated to 900 °C (Vinciguerra et al., 2005) and andesite heated to 450 °C (Heap et al., 2014b). The absence of additional thermal microcracks in these thermally stressed samples was attributed to their high pre-existing microcrack density (Vinciguerra et al., 2005; Heap et al., 2014b), an observation that holds true for the andesite used herein (Fig. 1). Since rock physical properties are unaffected by thermal stressing (Fig. 3), the *in-situ* changes in mechanical behaviour can be wholly attributed to the *in-situ* pressure and temperature conditions, rather than changes to the physical state of the samples during heating to the target experimental temperature.

5. Experiments

5.1. Experimental methods

5.1.1. Ambient-temperature triaxial experiments

The focus of this study is to investigate ductile compactive micromechanisms in the conduit margin zone. To guide the effective pressure P_{eff} to be used in the high-temperature triaxial experiments, we first performed a suite of ambient-temperature triaxial deformation experiments ($\sigma_1 > \sigma_2 = \sigma_3$) to assess the pressure conditions under which the andesite is brittle and under which andesite is ductile (see 5.2.1 for a description of material failure modes). We assume here a simple effective pressure law of $P_{eff} = P_c - \alpha P_p$, where P_p is the pore fluid pressure. Here, the poroelastic constant α is taken to be unity, an assumption that is validated by a recent study in which this is explored for porous andesite (Farquharson et al., 2016b). We treat compressive stresses and strains as positive.

For the ambient-temperature triaxial experiments, cylindrical samples (20 mm in diameter and precision-ground to a nomi-

nal length of 40 mm) were prepared and vacuum saturated in deionised water. The samples were deformed at a range of P_c (confining fluid used was kerosene) at a constant P_p of 20 MPa (pore fluid used was deionised water). Samples were deformed in compression at a constant axial strain rate of 10^{-5} s^{-1}. Sample drainage at this strain rate was assured by their high permeability of $\sim 10^{-12}$ m^2 (fluid flow timescale is much shorter than the deformation timescale; see Heap and Wadsworth, 2016). A load cell and an LVDT recorded axial force and axial displacement, respectively, and a pore pressure intensifier monitored pore volume changes. These measurements were then converted to axial stress, axial strain, and connected porosity change using the sample dimensions. The deformation of the load train was removed from the measured axial displacement.

5.1.2. High-temperature triaxial experiments

For the high-temperature experiments, cylindrical samples 15 mm in diameter and precision-ground to between 33–36 mm in length were prepared and oven-dried at 70 °C for at least 48 h. Argon was used for the confining and pore fluid. Experiments were performed at temperatures between 200 and 800 °C and at a constant P_p of 20 MPa. Samples were heated at ~ 20 °C min^{-1} to the target experimental temperature and, following deformation, cooled at the same rate. Copper jackets were used at temperatures ≤ 400 °C; iron jackets were used for the experiments ≥ 600 °C. Two iron jackets were used for the experiment performed at 800 °C to avoid a leak due to the substantial volumetric decrease of the sample. The contribution of the jacket strength was removed from the measured force using the estimates provided by Frost and Ashby (1982). Surface pores were filled with hardened ceramic paste to prevent jacket puncture. All samples were deformed in compression at an axial strain rate of 10^{-5} s^{-1}. An internal load cell and an LVDT recorded axial force and axial displacement, respectively, and a pore fluid volumometer monitored pore volume change. The difference between the temperature of the sample and that of the volumometer was accounted for by multiplying the ratio of the molar volumes of argon at both temperatures (ratios derived from Fischer and Paterson, 1989). These measurements were then converted to axial stress, axial strain, and connected porosity change using the sample dimensions. The deformation of the load train was removed from the measured axial displacement. A schematic of the high-temperature triaxial deformation apparatus can be found in Violay et al. (2015).

5.2. Experimental results

5.2.1. Ambient-temperature triaxial experiments

The relationship between increasing stress and increasing strain, and the evolution of connected porosity with strain for the ambient-temperature triaxial experiments ($5 < P_{eff} < 50$ MPa) are presented in Fig. 4. The terms brittle and ductile are used here to describe the failure mode on the sample lengthscale. A brittle experiment involves an increase in porosity or decrease in the rate of compaction (dilatational microcracking) as strain increases towards macroscopic failure (grey curves in Fig. 4b) and strain softening (stress drop) following a peak stress (grey curves in Fig. 4a). A brittle failure mode is confirmed by the presence of a shear fracture preserved in the sample after the experiment. We use here the definition of ductility provided by Rutter (1986): the capacity of a material to deform to a substantial strain without the tendency to localise the deformation into faults (although there are instances of compaction localisation in the ductile domain, see Heap et al., 2015a). The concept of ductility, as interpreted by Rutter (1986) and herein, is not dependent on the deformation micromechanism. Ductile experiments are purely compactional (grey curves in Fig. 4b). From these data (Fig. 4) we conclude that the andesite
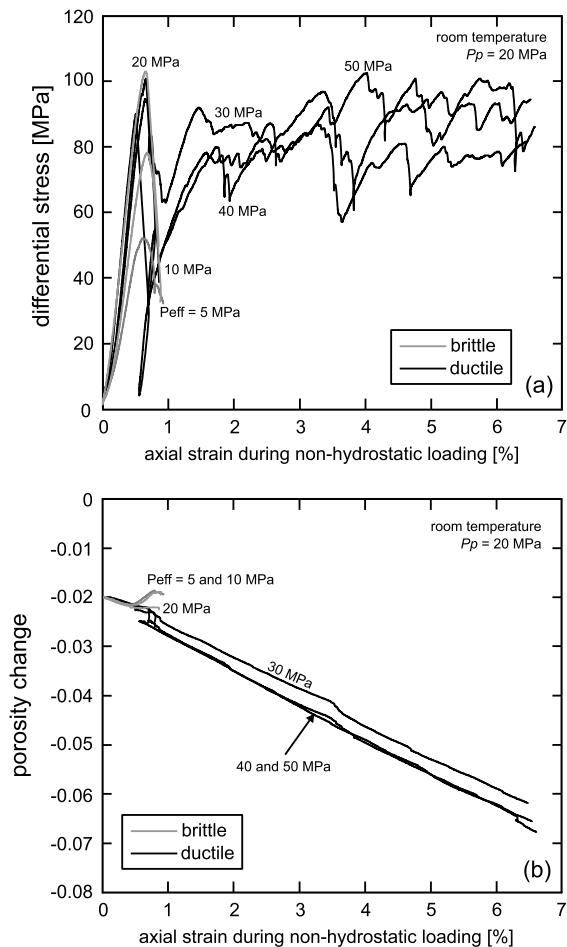
Fig. 4. Ambient-temperature triaxial experiments. (a) Ambient-temperature stress–strain curves for andesite samples deformed at a range of effective pressures (P_{eff}; the experimental pressure is indicated next to each curve). (b) Connected porosity change as a function of axial strain for the experiments shown in panel (a). The connected porosity decrease during the hydrostatic portion of the experiment (i.e., prior to differential stressing) was subtracted from each curve. Brittle curves are shown in grey and ductile curves are shown in black.

is brittle at $5 < P_{eff} < 20$ MPa and ductile at $P_{eff} > 30$ MPa. In the brittle regime, the peak stress increases as P_c is increased from 5 to 20 MPa (black curves in Fig. 4a). The evolution of stress with increasing strain in the ductile regime is characterised by small stress drops (black curves in Fig. 4a); stress drops during compactant behaviour in volcanic rocks have been previously attributed to compaction localisation (Heap et al., 2015a). Since our interest here is compaction, we used $P_{eff} = 40$ MPa ($P_c = 60$ MPa; $P_p = 20$ MPa) for our high-temperature deformation experiments.

5.2.2. High-temperature triaxial experiments

The stress–strain curves and connected porosity reduction curves for the high-temperature (up to 800 °C) triaxial experiments ($P_{eff} = 40$ MPa) are presented in Fig. 5. The stress–strain curves at temperatures between 200 and 600 °C (i.e., below T_g on the timescale of the experiment) are qualitatively similar to those at ambient-temperature (Fig. 4a) in that many small stress drops are observed (Fig. 5a). We also note that the samples deformed at temperatures between 200 and 600 °C are stiffer than the ambient-temperature sample, and that the differential stress before the first stress drop increases as temperature increases, from ~ 90 MPa at ambient-temperature to ~ 200 MPa at 600 °C (Fig. 5a). The mechanical behaviour is markedly different for the sample deformed at 800 °C (Fig. 5). The sample is considerably weaker and shows strain hardening up to the maximum axial

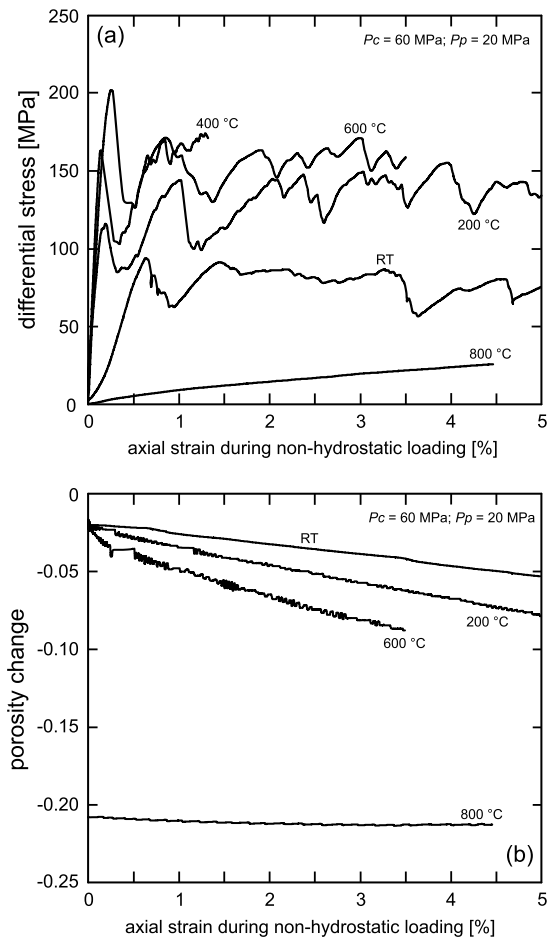**Fig. 5.** High-temperature triaxial experiments. (a) Stress–strain curves for andesite samples deformed at a range of temperatures (ambient-temperature to 800 °C; the experimental temperature is indicated next to each curve) at P_{eff} = 40 MPa. (b) Connected porosity change as a function of axial strain for the experiments shown in panel (a). Connected porosity change was not monitored during the hydrostatic portion of the high-temperature experiments. Hydrostatic connected porosity change for the tests performed below T_g was assumed to be the same as those performed at ambient-temperature (porosity reduction of 0.02). Hydrostatic porosity change for the 800 °C sample was estimated using the initial porosity of the sample, the 2D porosity of the sample following deformation (determined using ImageJ), and the connected porosity change measured *in-situ* during deformation.

strain of 4.5% (Fig. 5a). Porosity decreased from the initial 0.265 to 0.065 during the hydrostatic portion of the experiment (estimated from the 2D porosity determined from a post-deformation SEM photomicrograph minus the connected porosity change measured during the experiment). During deformation at constant strain rate, the connected porosity decreased by a further ∼0.05 at the maximum axial strain of 4.5% (Fig. 5b).

6. Discussion

6.1. Strengthening of andesite below T_g

Our mechanical data show that there is a progressive strengthening as temperature is increased below the threshold T_g (Fig. 5a). For example, the differential stress before the first stress drop at 600 °C is more than twice that at ambient-temperature (Fig. 5a). We interpret this strengthening as a consequence of the closure of pre-existing microcracks (abundant in this material; Fig. 1) due to the thermal expansion of the mineral assemblage. Previous studies have reported an increase in the strength of volcanic rock at high temperature. For example, Meredith and Atkinson (1985) measured an increase in fracture toughness in gabbro from ambient-

temperature to 100 °C and Duclos and Paquet (1991) reported an increase in the compressive strength of basalt, from ∼340 MPa at ambient-temperature to ∼450 MPa at 650 °C. We note that the strengthening of the samples as temperature is increased in the regime below T_g may be reduced at strain rates lower than 10^{-5} s^{-1} due to temperature-sensitive subcritical crack growth processes such as stress corrosion (Brantut et al., 2013).

6.2. Micromechanical mechanisms of compaction

The micromechanism driving the compaction in the samples deformed at ambient-temperature and up to 600 °C (i.e., below T_g) is cataclastic pore collapse (Fig. 6a). The compaction is localised into bands (∼2 mm in width) orientated subperpendicular to the maximum principal stress; these bands of crushed pores are similar to those observed in previously published ambient-temperature experiments (Loaiza et al., 2012; Adelinet et al., 2013; Heap et al., 2015a). The experiments reported here are the first to document localised pore collapse in volcanic rocks at temperatures greater than ambient. The porosity within the band is ∼0.12 (measured on 2D SEM images using ImageJ). Due to the localised nature of the deformation, the porosity is largely unchanged outside of the band (porosity ≈0.26). Contrastingly, the micromechanism facilitating compaction at 800 °C (i.e., above T_g) was distributed viscous flow of the melt phase (Fig. 6b). Substantial porosity loss is the result of the flattening and closing of connected pores (Fig. 6b), as previously documented in uniaxial (Quane et al., 2009; Kendrick et al., 2013) and isobaric (Vasseur et al., 2013; Kennedy et al., 2015) experiments. We observe no significant change to the crystal cargo, and no preferred orientation for the crystals and flattened pores (Fig. 6b). We note that isolated pores may deform under applied shear stresses (e.g., Llewellin et al., 2002), shrink slightly at high pressures (e.g., Proussevitch et al., 1993), or resorb, if the volatile phase is soluble in the melt (e.g., McIntosh et al., 2014), but will not compact in the same way as connected pores. Herein, the porosity change we measure during deformation is that of the interconnected pore space that can readily outgas the pore fluid phase and close shut as a result.

6.3. Volcanological significance

The conduit margin zone is thought to assist magmatic outgassing (Rust et al., 2004; Tuffen and Dingwell, 2005; Lavallée et al., 2013; Gaunt et al., 2014; Farquharson et al., 2016c; Kendrick et al., 2016), a key factor for the dissipation of pore pressure and therefore the cessation of explosive behaviour. This zone will be subject to fluctuations in temperature as heat is transferred from the hot, conduit-dwelling magma to the colder country rock. At a depth ≥1 km, the migration of the T_g isotherm (Fig. 2) in the conduit margin zone will promote a change in compaction deformation micromechanism (Fig. 6) that drastically influences strength and porosity loss during compaction (Fig. 5).

Material below T_g will accommodate small stresses elastically, while larger stress perturbations will result in the formation of bands of crushed pores (Fig. 6a). Such bands—that are of lower porosity than the rock in which they are hosted—have been previously shown to reduce permeability by up to an order of magnitude in porous andesite (initial connected porosity ≈0.19; Heap et al., 2015a). If the differential stress imposed on the conduit margin zone is subperpendicular to the conduit wall, we would expect these features to be orientated parallel to the conduit margin (Fig. 7). Bands of crushed pores that form in the conduit margin zone are thus expected to impede the outgassing of the nearby magma-filled conduit, although it is at present unclear whether such features can form a coherent low-permeability barrier.
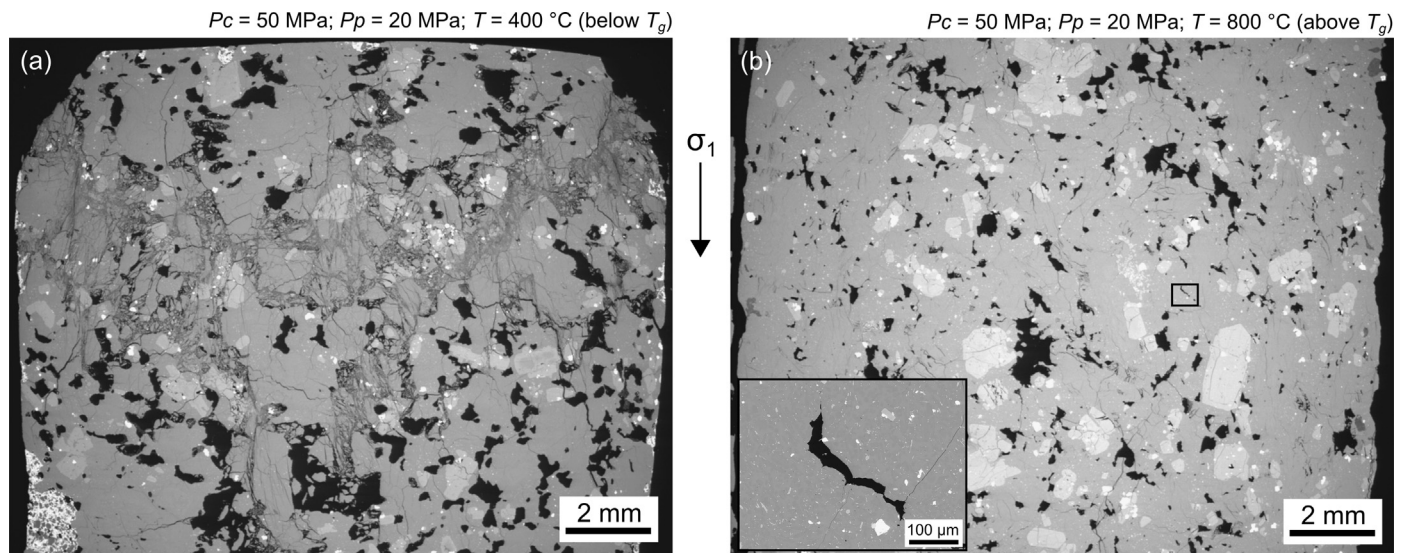
Pc = 50 MPa; Pp = 20 MPa; T = 400 °C (below T_g)   Pc = 50 MPa; Pp = 20 MPa; T = 800 °C (above T_g)

Fig. 6. Ductile deformation microstructures below and above T_g. (a) Backscattered scanning electron microscope (BSEM) image of the sample deformed at 400 °C ($P_{eff} = 40$ MPa) showing the band of crushed pores (running across the diameter of the sample). (b) BSEM image of the sample deformed at 800 °C ($P_{eff} = 40$ MPa) showing distributed viscous compaction. Inset shows a viscously flattened pore.

Material above T_g will accommodate stress through viscous flow (Fig. 6b). The change in micromechanism from cataclastic pore collapse to viscous flow is accompanied by a significant reduction to the strength (Fig. 5a) and a substantial and distributed loss of porosity as pores are flattened and closed (Fig. 6b). Since a porosity loss from ∼0.256 to ∼0.06 is likely to reduce permeability by four orders of magnitude (Farquharson et al., 2015), the migration of the T_g isotherm into the country rock (increasing the effective conduit radius) will significantly lower permeability of the conduit margin zone (Fig. 7a). The reduction in porosity and permeability is expected to inhibit the outgassing of the nearby magma-filled conduit, leading to the preservation of high overpressures and thus increasing the probability of explosive behaviour (Kennedy et al., 2010; Schauroth et al., 2016).

If magma is emplaced in the conduit and then remains stagnant for a period of time before the next episode of up-flow and emplacement (as explored by Petcovic and Dufek, 2005) or if the conduit ascent rate is variable (as suggested for Volcán de Colima by Cassidy et al., 2015), then the spatial position of the T_g isotherm is likely to fluctuate outward and inward with respect to an initial conduit margin. Such a spatially mobile T_g isotherm implies that parts of the conduit margin zone are likely repeatedly cycled above and below T_g. Due to the particle-size dependence of viscous sintering (e.g., Wadsworth et al., 2016), any bands of collapsed pores in a material taken above T_g will efficiently heal thus creating a band of very low porosity and permeability. Material compacted viscously—and therefore low-porosity—taken below T_g will likely respond in a brittle manner to an applied stress, due to the porosity dependence of brittle versus ductile behaviour in volcanic rocks (Heap et al., 2015a). This cyclicity of deformation micromechanisms at the conduit margin has implications for the distribution of outgassing pathways that can be formed or destroyed in that zone (see the varied textures and overprinting textures presented in Tuffen and Dingwell, 2005 and Farquharson et al., 2016c, for example) and for the switch between seismogenic and aseismic periods of flow (Tuffen et al., 2003; Neuberg et al., 2006; Lavallée et al., 2008).

Fluctuations in the permeability of the conduit margin zone should now be considered in models of conduit outgassing (Collinson and Neuberg, 2012) and in the interpretation of outgassing fluctuations monitored at active volcanoes (Edmonds et al., 2003).

7. Conclusions

The conduit margin zone—defined as the country rock and the magma close to the conduit margin—is thought to be the annulus through which magmas outgas (e.g., Rust et al., 2004; Tuffen and Dingwell, 2005; Lavallée et al., 2013; Farquharson et al., 2016c; Kendrick et al., 2016). Therefore, a decrease of porosity and permeability for the material within this zone could impede outgassing and lead to pressure build-up and explosive behaviour. Since the conduit margin zone is the boundary through which heat is exchanged from the hot magma to the colder country rock, it is prone to fluctuations in temperature. A simple model of heat transfer shows that the T_g isotherm can move (on the centimetric scale over days to months) into the country rock when the magma within the conduit can stay hot, or move into the conduit when the magma is quasi-stagnant and cools.

Triaxial deformation experiments designed to explore the micromechanisms of compaction above and below T_g show that while ductile deformation below T_g is localised, manifest as bands of crushed pores oriented perpendicular to the maximum principal stress, ductile deformation above T_g is facilitated by distributed viscous flow. Our experiments show that viscous flow requires stresses much lower than those required to form bands of collapsed pores in volcanic rock, and that it is a much more efficient at reducing the porosity, and therefore permeability, of the materials within the conduit margin zone.

Our study therefore highlights that fluctuations in temperature can result in a change in deformation micromechanism that drastically alters the mechanical and hydraulic properties of the material within the conduit margin zone, with possible implications for pore pressure augmentation and explosive behaviour.
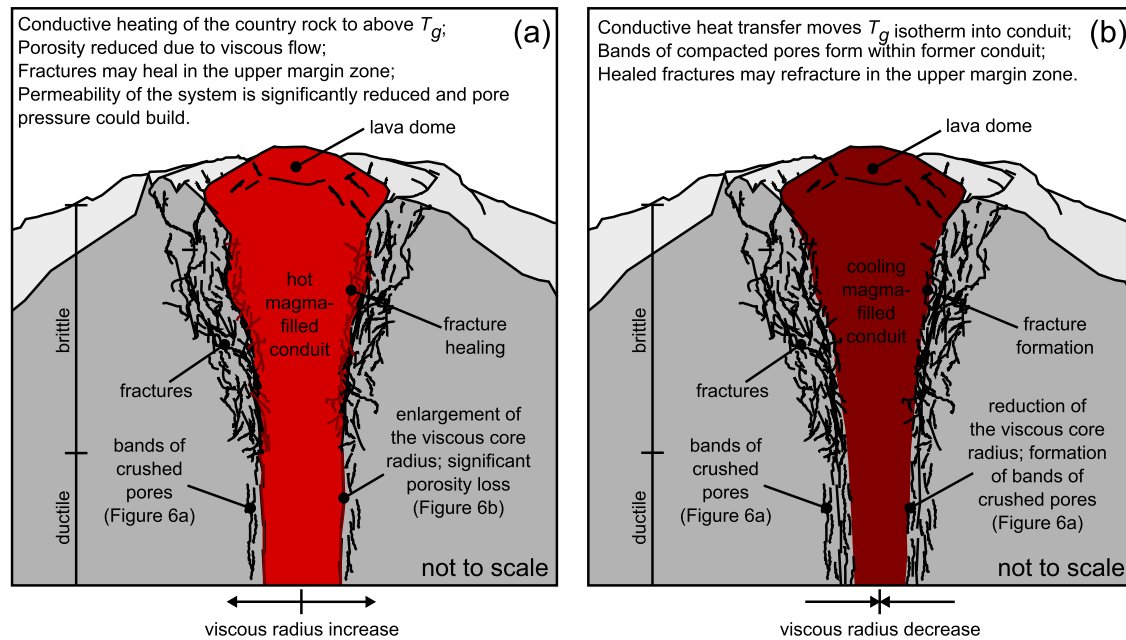
Fig. 7. Cartoons (not to scale) highlighting the salient implications of this study. (a) Country rock within the conduit margin zone is heated above T_g (e.g., rapidly ascending magma), expanding the effective conduit radius. Viscous compaction leads to a large reduction in porosity and permeability of the conduit margin zone, potentially reducing outgassing capability and augmenting pore pressure. (b) Magma cools and the T_g isotherm retreats inside the conduit (e.g., slow-moving or stagnant magma), reducing the effective conduit radius. Stresses within the conduit margin zone may create bands of crushed pores (subparallel to the conduit margin) within the former conduit. Bands of crushed pores are expected to disrupt outgassing, although it is at present unclear whether such features can form a coherent low-permeability barrier.

Appendix A. Supplementary material

Supplementary material related to this article can be found on-line at http://dx.doi.org/10.1016/j.epsl.2017.01.021.

References

Adelinet, M., Fortin, J., Schubnel, A., Guéguen, Y., 2013. Deformation modes in an Icelandic basalt: from brittle failure to localized deformation bands. J. Volcanol. Geotherm. Res. 255, 12–25.

Bagdassarov, N.S., Dingwell, D.B., 1994. Thermal properties of vesicular rhyolite. J. Volcanol. Geotherm. Res. 60, 179–191.

Brantut, N., Heap, M.J., Meredith, P.G., Baud, P., 2013. Time-dependent cracking and brittle creep in crustal rocks: a review. J. Struct. Geol. 52, 17–43.

Cassidy, M., Cole, P.D., Hicks, K.E., Varley, N.R., Peters, N., Lerner, A.H., 2015. Rapid and slow: varying magma ascent rates as a mechanism for Vulcanian explosions. Earth Planet. Sci. Lett. 420, 73–84.

Castro, J., Bindeman, I.N., Tuffen, H., Schipper, C.I., 2014. Explosive origin of silicic lava: textural and δD–H_2O evidence for pyroclastic degassing during rhyolite effusion. Earth Planet. Sci. Lett. 405, 52–61.

Champallier, R., Bystricky, M., Arbaret, L., 2008. Experimental investigation of magma rheology at 300 MPa: from pure hydrous melt to 76 vol.% of crystals. Earth Planet. Sci. Lett. 267, 571–583.

Collinson, A.S.D., Neuberg, J., 2012. Gas storage, transport and pressure changes in an evolving permeable volcanic edifice. J. Volcanol. Geotherm. Res. 243–244, 1–13.

Cordonnier, B., Caricchi, L., Pistone, M., Castro, J., Hess, K.U., Gottschaller, S., Manga, M., Dingwell, D.B., Burlini, L., 2012. The viscous–brittle transition of crystal-bearing silicic melt: direct observation of magma rupture and healing. Geology 40 (7), 611–614.

Duclos, R., Paquet, J., 1991. High-temperature behaviour of basalts—role of temperature and strain rate on compressive strength and K_{IC} toughness of partially glassy basalts at atmospheric pressure. Int. J. Rock Mech. Min. Sci. Geomech. Abstr. 28, 71–76.

Edmonds, M., Herd, R.A., Galle, B., Oppenheimer, C.M., 2003. Automated, high time-resolution measurements of SO_2 flux at Soufrière Hills Volcano, Montserrat. Bull. Volcanol. 65, 578–586.

Eichelberger, J.C., Carrigan, C.R., Westrich, H.R., Price, P.H., 1986. Non-explosive silicic volcanism. Nature 323, 598–602.

Farquharson, J.I., Heap, M.J., Varley, N., Baud, P., Reuschlé, T., 2015. Permeability and porosity relationships of edifice-forming andesites: a combined field and laboratory study. J. Volcanol. Geotherm. Res. 297, 52–68.

Farquharson, J.I., Heap, M.J., Baud, P., 2016a. Strain-induced permeability increase in volcanic rock. Geophys. Res. Lett. 43. http://dx.doi.org/10.1002/2016GL071540.

Farquharson, J.I., Heap, M.J., Baud, P., Reuschlé, T., Varley, N., 2016b. Pore pressure embrittlement in a volcanic edifice. Bull. Volcanol. 78 (6).

Farquharson, J.I., Heap, M.J., Lavallée, Y., Varley, N., Baud, P., 2016c. Evidence for the development of permeability anisotropy in lava domes and volcanic conduits. J. Volcanol. Geotherm. Res. 323, 163–185.

Fischer, G.J., Paterson, M.S., 1989. Dilatancy during rock deformation at high temperatures and pressures. J. Geophys. Res. 94 (B12), 17607–17617.

Frost, H.J., Ashby, M.F., 1982. Deformation-Mechanism Maps. Pergamon, Oxford.

Gaunt, H.E., Sammonds, P.R., Meredith, P.G., Smith, R., Pallister, J.S., 2014. Pathways for degassing during the lava dome eruption of Mount St. Helens 2004–2008. Geology 42 (11), 947–950.

Gonnermann, H.M., Manga, M., 2012. Dynamics of magma ascent in the volcanic conduit. In: Fagents, S.A., Gregg, T.K.P., Lopes, R.M.C. (Eds.), Modeling Volcanic Processes: the Physics and Mathematics of Volcanism. Cambridge University Press, Cambridge.

Heap, M.J., Kolzenburg, S., Russell, J.K., Campbell, M.E., Welles, J., Farquharson, J.I., Ryan, A., 2014a. Conditions and timescales for welding block-and-ash flow deposits. J. Volcanol. Geotherm. Res. 289, 202–209.

Heap, M.J., Lavallée, Y., Petrakova, L., Baud, P., Reuschlé, T., Varley, N., Dingwell, D.B., 2014b. Microstructural controls on the physical and mechanical properties of edifice-forming andesites at Volcán de Colima, Mexico. J. Geophys. Res. 119 (4), 2925–2963.

Heap, M.J., Farquharson, I.J., Baud, P., Lavallée, Y., Reuschlé, T., 2015a. Fracture and compaction of andesite in a volcanic edifice. Bull. Volcanol. 77, 55. http://dx.doi.org/10.1007/s00445-015-0938-7.

Heap, M.J., Farquharson, I.J., Wadsworth, F.B., Kolzenburg, S., Russell, J.K., 2015b. Timescales for permeability reduction and strength recovery in densifying magma. Earth Planet. Sci. Lett. 429, 223–233.

Heap, M.J., Kennedy, B.M., 2016. Exploring the scale-dependent permeability of fractured andesite. Earth Planet. Sci. Lett. 447, 139–150.

Heap, M.J., Wadsworth, F.B., 2016. Closing an open system: pore pressure changes in permeable edifice rock at high strain rates. J. Volcanol. Geotherm. Res. 315, 40–50.

Ichihara, M., Rubin, M.B., 2010. Brittleness of fracture in flowing magma. J. Geophys. Res. 115. http://dx.doi.org/10.1029/2010JB007820.

Kendrick, J.E., Lavallée, Y., Hess, K.-U., Heap, M.J., Gaunt, H.E., Meredith, P.G., Dingwell, D.B., 2013. Tracking the permeable porous network during strain-dependent magmatic flow. J. Volcanol. Geotherm. Res. 260, 117–126.

Kendrick, J.E., Lavallée, Y., Varley, N.R., Wadsworth, F.B., Lamb, O.D., Vasseur, J., 2016. Blowing off stream: tuffisite formation as a regulator for lava dome eruptions. Front. Earth Sci. 4. http://dx.doi.org/10.2289/feart.2016.00041.

Kennedy, B.M., Jellinek, A.M., Russell, J.K., Nichols, A.R.L., Vigouroux, N., 2010. Time- and temperature-dependent conduit wall porosity: a key control on degassing and explosivity at Tarawera volcano, New Zealand. Earth Planet. Sci. Lett. 299, 126–137.

Kennedy, B.M., Wadsworth, F.B., Vasseur, J., Schipper, C.I., Jellinek, A.M., von Aulock, F.W., Hess, K.-U., Russell, J.K., Lavallée, Y., Nichols, A.R.L., Dingwell, D.B., 2015. Surface tension driven processes densify and retain permeability in magma and lava. Earth Planet. Sci. Lett. 433, 116–124.

Kushnir, A.R., Martel, C., Champallier, R., Arbaret, L., 2017. In situ confirmation of permeability development in shearing bubble-bearing melts and implications for volcanic outgassing. Earth Planet. Sci. Lett. 458, 315–326.

Lavallée, Y., Meredith, P.G., Dingwell, D.B., Hess, K.-U., Wassermann, J., Cordonnier, B., Gerik, A., Kruhl, J.H., 2008. Seismogenic lavas and explosive eruption forecasting. Nature 453, 507–510.

Lavallée, Y., Benson, P.M., Heap, M.J., Hess, K.-U., Flaws, A., Schillinger, B., Meredith, P.G., Dingwell, D.B., 2013. Reconstructing magma failure and the degassing network of dome-building eruptions. Geology 41, 515–518.

Lavallée, Y., Dingwell, D.B., Johnson, J.B., Cimarelli, C., Hornby, A.J., Kendrick, J.E., von Aulock, F.W., Kennedy, B.M., Andrews, B.J., Wadsworth, F.B., Rhodes, E., Chinga, G., 2015. Thermal vesiculation during volcanic eruptions. Nature 528, 544–547.

Llewellin, E.W., Mader, H.M., Wilson, S.D.R., 2002. The rheology of a bubbly liquid. Proc. R. Soc. A 458. http://dx.doi.org/10.1098/rspa.2001.0924.

Loaiza, S., Fortin, J., Schubnel, A., Guéguen, Y., Vinciguerra, S., Moreira, M., 2012. Mechanical behavior and localized failure modes in a porous basalt from the Azores. Geophys. Res. Lett. 39. http://dx.doi.org/10.1029/2012GL053218.

Luhr, J.F., Carmichael, I.S., 1980. The Colima volcanic complex, Mexico. Contrib. Mineral. Petrol. 71 (4), 343–372.

McIntosh, I.M., Llewellin, E.W., Humphreys, M.C.S., Nichols, A.R.L., Burgisser, A., Schipper, C.I., Larsen, J., 2014. Distribution of dissolved water in magmatic glass recores growth and resorption of bubbles. Earth Planet. Sci. Lett. 401, 1–11.

Melnik, O., Barmin, A.A., Sparks, R.S.J., 2005. Dynamics of magma flow inside volcanic conduits with bubble overpressure buildup and gas loss through permeable magma. J. Volcanol. Geotherm. Res. 142, 53–68.

Meredith, P.G., Atkinson, B.K., 1985. Fracture toughness and subcritical crack growth during high-temperature tensile deformation of Westerly granite and Black gabbro. Phys. Earth Planet. Inter. 39, 33–51.

Mueller, S., Scheu, B., Spieler, O., Dingwell, D.B., 2008. Permeability control on magma fragmentation. Geology 36, 399–402.

Nara, Y., Meredith, P.G., Yoneda, T., Kaneko, K., 2011. Influence of macro-fractures and micro-fractures on permeability and elastic wave velocities in basalt at elevated pressure. Tectonophysics 503, 52–59.

Neuberg, J.W., Tuffen, H., Collier, L., Green, D., Powell, T., Dingwell, D.B., 2006. The trigger mechanism of low-frequency earthquakes on Montserrat. J. Volcanol. Geotherm. Res. 153, 37–50.

Petcovic, H.L., Dufek, J.D., 2005. Modeling magma flow and cooling in dikes: implications for emplacement of Columbia River flood basalts. J. Geophys. Res. 110. http://dx.doi.org/10.1029/2004JB003432.

Proussevitch, A.A., Sahagian, D.L., Anderson, A.T., 1993. Dynamics of diffusive bubble growth in magmas: isothermal case. J. Geophys. Res. 98, 22283–22307.

Quane, S.L., Russell, J.K., Friedlander, E.A., 2009. Time scales of compaction in volcanic systems. Geology 37, 471–474.

Rust, A.C., Cashman, K.V., Wallace, P.J., 2004. Magma degassing buffered by vapor flow through brecciated conduit margins. Geology 32, 349–352.

Rutter, E., 1986. On the nomenclature of mode of failure transitions in rocks. Tectonophysics 122, 381–387.

Schauroth, J., Wadsworth, F.B., Kennedy, B.M., von Aulock, F.W., Lavallée, Y., Damby, D.E., Vasseur, J., Scheu, B., Dingwell, D.B., 2016. Conduit margin heating and deformation during the AD 1886 basaltic Plinian eruption at Tarawera volcano, New Zealand. Bull. Volcanol. 78 (2). http://dx.doi.org/10.1007/s00445-016-1006-7.

Shimada, M., 1986. Mechanism of deformation in a dry porous basalt at high pressures. Tectonophysics 121, 153–173.

Smith, R., Sammonds, P., Tuffen, H., Meredith, P.G., 2011. Evolution of the mechanics of the 2004–2008 Mt. St. Helens lava dome with time and temperature. Earth Planet. Sci. Lett. 307, 191–200.

Tuffen, H., Dingwell, D.B., Pinkerton, H., 2003. Repeated fracture and healing of silicic magma generate flow banding and earthquakes? Geology 31, 1089–1092.

Tuffen, H., Dingwell, D.B., 2005. Fault textures in volcanic conduits: evidence for seismic trigger mechanisms during silicic eruptions. Bull. Volcanol. 67, 370–387.

Varley, N., Komorowski, J.-C., 2017. Volcán de Colima: Managing the Threat. Springer. ISBN 978-3-642-25911-1.

Vasseur, J., Wadsworth, F.B., Lavallée, Y., Hess, K.-U., Dingwell, D.B., 2013. Volcanic sintering: timescales of viscous densification and strength recovery. Geophys. Res. Lett. 40, 5658–5664.

Vinciguerra, S., Trovato, C., Meredith, P.G., Benson, P.M., 2005. Relating seismic velocities, thermal cracking and permeability in Mt. Etna and Iceland basalts. Int. J. Rock Mech. Min. Sci. 42, 900–910.

Violay, M., Gibert, B., Mainprice, D., Evans, B., Dautria, J.-M., Azias, P., Pezard, P., 2012. An experimental study of the brittle–ductile transition of basalt at oceanic crust pressure and temperature conditions. J. Geophys. Res. 117 (B3). http://dx.doi.org/10.1029/2011JB008884.

Violay, M., Gibert, B., Mainprice, D., Burg, J.-P., 2015. Brittle versus ductile deformation as the main control of the deep fluid circulation in oceanic crust. Geophys. Res. Lett. 42. http://dx.doi.org/10.1002/2015GL063437.

Wadsworth, F.B., Vasseur, J., Llewellin, E.W., Schauroth, J., Dobson, K.J., Scheu, B., Dingwell, D.B., 2016. Sintering of viscous droplets under surface tension. Proc. R. Soc. A 472. http://dx.doi.org/10.1098/rspa.2015.0780.

Webb, S.L., Dingwell, D.B., 1990. The onset of non-Newtonian rheology of silicate melts—a fiber elongation study. Phys. Chem. Mater. 17, 125–132.

Woods, A.W., Koyaguchi, T., 1994. Transitions between explosive and effusive eruptions of silicic magmas. Nature 370, 641–644.

Zhu, W., Baud, P., Vinciguerra, S., Wong, T.-F., 2011. Micromechanics of brittle faulting and cataclastic flow in Alban Hills tuff. J. Geophys. Res. 116, B06209. http://dx.doi.org/10.1029/2010JB008046.

CHAPTER THREE – The permeability of volcanic rocks

This chapter outlines recent work from laboratory at IPG Strasbourg on the permeability of volcanic rocks. One of the first studies from our laboratory to focus on the permeability of volcanic rocks was "The permeability and elastic moduli of tuff from Campi Flegrei, Italy: Implications for ground deformation modelling" (Heap et al., 2014b, *Solid Earth*). This paper showed that high-porosity tuffs (porosity > 0.45) can be characterised by a permeability of ∼10^{-15} m², many orders of magnitude lower than a sandstone of the same porosity. This paper also studied the influence of confining pressure and thermal stressing on the permeability of high-porosity tuffs.
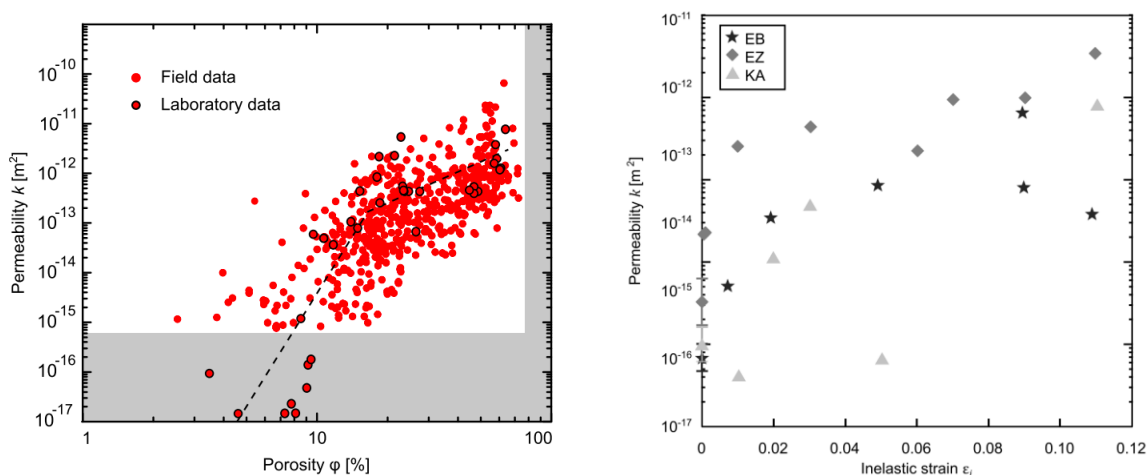
Figure 11. *Left graph: Permeability as a function of porosity for nearly 600 samples from Volcán de Colima. The graph also shows the two-power-law model, as determined by our Bayesian Information Criterion (BIC) analysis (graph from Farquharson et al., 2015). Right graph: Permeability of volcanic samples (EB – basalt; EZ – andesite; KA – andesite) as a function of inelastic strain (from Farquharson et al., 2016b).*

In a paper that combines field and laboratory studies, "Permeability and porosity relationships of edifice-forming andesites: A combined field and laboratory study" (Farquharson et al., 2015, *Journal of Volcanology and Geothermal Research*), Jamie Farquharson (during his Ph.D at IPG Strasbourg, 2013-2016) measured the porosity and permeability of more than 500 rock samples from Volcán de Colima. Using this large dataset, we found that the porosity-permeability trend for these andesites is best described using two power laws, as confirmed by modified Bayesian Information Criterion (BIC) analysis (Figure 11). This paper also highlighted the huge variability in microstructure, porosity, and permeability of the volcanic rocks comprising a typical andesitic stratovolcano.

Jamie Farquharson expanded on this work in 2016 and 2017 in the following papers: "Strain-induced permeability increase in volcanic rock" (Farquharson et al., 2016b, *Geophysical Research Letters*), "Inelastic compaction and permeability evolution in volcanic rock" (Farquharson et al., 2016c, *Solid Earth*), "Evidence for the development of permeability anisotropy in lava domes and volcanic conduits" (Farquharson et al., 2016d, *Journal of Volcanology and Geothermal Research*), and "Time-dependent permeability evolution in compacting volcanic fracture systems and implications for gas overpressure" (Farquharson et al., 2017, *Journal of Volcanology and Geothermal Research*). The first two of these papers demonstrated the influence of deformation (brittle and ductile, respectively) on the permeability of volcanic materials (Figure 11). Farquharson et al. (2016d) focused on the permeability of naturally fractured volcanic rocks from Volcán de Colima and the latter paper (Farquharson et al., 2017) provides a model to determine the time-dependent permeability evolution of volcanic systems.

The final paper of Jamie Farquharson (Farquharson et al., 2017) was inspired by a paper published in 2015 entitled "Timescales for permeability reduction and strength recovery in densifying magma" (Heap et al., 2015c, *Earth and Planetary Science Letters*). In this paper, the permeability of naturally welded block-and-ash flow deposits was used in conjunction with a rheological model for viscous compaction to provide timescales for permeability loss at active volcanoes (Figure 12). We found that the timescales for permeability loss can be short, helping to explain the regular gas-and-ash explosions seen at many active volcanoes.

The scale-dependence of permeability is well known (e.g., Guéguen et al., 1996). However, this topic has not received much attention in volcanology. To help address this problem, I published a paper in 2016 with Ben Kennedy entitled "Exploring the scale-dependent permeability of fractured andesite" (Heap and Kennedy, 2016, *Earth and Planetary Science Letters*). This paper determined the permeability of fractures within andesites from Ruapehu (New Zealand) by measuring the permeability of laboratory samples before and after failure in tension. These permeabilities could then be used to model, using a simple model that considers flow in parallel layers, to provide estimates of the equivalent permeability of a volcanic rock mass (Figure 12).
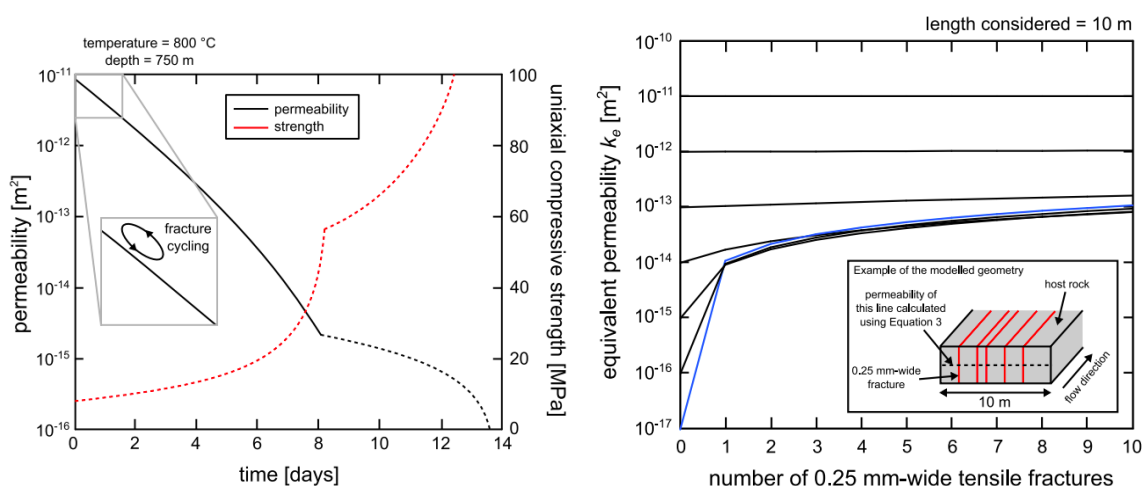
Figure 12. *Left graph: Permeability and uniaxial compressive strength as a function of time (graph from Heap et al., 2015c). Right graph: Equivalent permeability as a function of the number of fractures, for a 10 m length of rock (from Heap and Kennedy, 2016).*

Following these works, I published a multidisciplinary study (again combining field and laboratory analyses) that focussed on the permeability of a volcano with an aggressive hydrothermal system (Whakaari volcano, New Zealand): "A multidisciplinary approach to quantify the permeability of the Whakaari/White Island volcanic hydrothermal system (Taupo Volcanic Zone, New Zealand)" (Heap et al., 2017b, *Journal of Volcanology and Geothermal Research*). More recently, we investigated the difference between the gas and water permeability of volcanic rocks: "Permeability of volcanic rocks to gas and water" (Heap et al., 2018a, *Journal of Volcanology and Geothermal Research*).

Attached to this chapter are three of the most relevant papers on this topic (all the of papers published on this topic can be found in Appendix B).

➢ "**Permeability and porosity relationships of edifice-forming andesites: A combined field and laboratory study**" (Farquharson et al., 2015).
➢ "**Timescales for permeability reduction and strength recovery in densifying magma**" (Heap et al., 2015c).
➢ "**Exploring the scale-dependent permeability of fractured andesite**" (Heap and Kennedy, 2016).

Permeability and porosity relationships of edifice-forming andesites: A combined field and laboratory study

Jamie Farquharson [a,*], Michael J. Heap [a], Nick R. Varley [b], Patrick Baud [a], Thierry Reuschlé [a]

[a] Laboratoire de Déformation des Roches, Équipe de Géophysique Expérimentale, Institut de Physique de Globe de Strasbourg (UMR 7516 CNRS, Université de Strasbourg/EOST), 5 rue René Descartes, 67084 Strasbourg cedex, France
[b] Facultad de Ciencias, University of Colima, Colima 28045, Mexico

ABSTRACT

Permeability of the edifice is one of the key parameters governing eruptive style, magnitude, and frequency of active stratovolcanoes. This study presents a suite of density and permeability field measurements from 572 samples of edifice-forming andesite from Volcán de Colima, Mexico. The breadth of the density distribution of the rocks collected (corresponding to porosity values from 2.5 to 73%), and the increasing bimodality towards the vent, are indicative of the explosive–effusive behaviour that characterises active composite volcanoes. Measured field permeabilities are in the range of 10^{-16} to 10^{-11} m^2, encompassing values significantly greater than those generally assumed for fluid transport in magma, and thus emphasising the importance of host-rock permeability in facilitating outgassing of volatiles and, in turn, governing eruption dynamics. For any given porosity we observe up to four orders of magnitude in permeability. This range of scatter was found to be unaffected for the most part by meso-scale textural differences, oxidation, or alteration. A complementary laboratory and microstructural study reveals that the andesites collected are microstructurally diverse and complex. For example, anomalously high surface areas are measured in samples with significant inter-microlite microporosity. However, these micropores do not serve to significantly increase porosity or pore connectivity, resulting in under-estimation of fluid pathway tortuosities using the Kozeny–Carman relation. Indeed, calculated tortuosity values highlight that the Kozeny–Carman relation poorly predicts connectivity and does not therefore capture the microstructural complexity of the studied volcanic rocks. A changepoint porosity value, where the permeability–porosity power-law exponent changes, is identified at around 14% porosity using a Bayesian Information Criterion analysis. Here we assume a change in the dominant microstructural element controlling fluid flow, i.e. from crack- to pore-dominated flowpath geometries. Microstructural analysis indicates that fluid flow in the low porosity andesites (<14%) of this study is governed by tortuous microcracks, while the more porous samples (>14%) display relatively large, interconnected pores. While the supposition that the power-law exponent changes at a distinct changepoint is a simplification, we find that it well describes permeability data from Volcán de Colima (from this study and those of previous authors). The exceptional heterogeneity of edifice-forming rocks is thought to have significant implications for lateral outgassing, eruption dynamics, as well as influencing regional edifice strength and stability.

© 2015 Elsevier B.V. All rights reserved.

1. Introduction

1.1. Permeability of a volcanic edifice

Permeability, quantifying the capacity of a material to transmit fluids, is fundamental in controlling a variety of processes in geological systems, and can vary over twelve orders of magnitude in natural rocks (Guéguen and Palciauskas, 1994). In volcanic settings, permeability is a

key parameter controlling eruptive style and magnitude by influencing the capacity for a volcano to outgas (Jaupart, 1998; Edmonds et al., 2003; Costa, 2006; Taisne and Jaupart, 2008; Castro et al., 2014). As magma ascends, volatile species exsolve (degas) from the melt phase due to oversaturation; the relative ease by which these volatiles can then outgas depends on the permeability of the rocks forming the edifice (e.g., Jaupart, 1998), and the connectivity and mobility of bubbles in conduit magma (i.e. outgassing through a permeable network in the magma, e.g., Plail et al. (2014); Shields et al. (2014)). Efficiently degassed and outgassed magma tends to erupt effusively (e.g. Lev et al., 2012), constituting a hazard only in the immediate vicinity of a volcano. On the other hand, inefficient outgassing can result in volatile

oversaturation and pressure build-up within the volcano, ultimately fostering catastrophic explosive eruptions, flank collapse, and pyroclastic density currents (e.g. Wallace and Anderson, 2000). In these latter cases, impacts may be widespread, long-lived, and lethal.

Stratovolcanoes comprise an edifice constructed by indiscriminate emplacement of explosive and effusive products, surrounding a central magma conduit or cluster of dykes (e.g., Biggs et al., 2010; Gudmundsson, 2012). Continual accumulation of these products results in a structure with spatially variable physical properties, with pervasive differences in porosity and permeability down to the intra-clast scale. Thus transport networks for magmatic volatiles are dependant not only on large-scale fault systems (which may not necessarily provide a direct pathway for volcanic gas species: see Varley and Taran (2003)), but also on the fluid transport properties of the constituent edifice-forming rocks.

Models of volcanic processes must be built on a foundation of observed or experimentally derived parameters; however, as we often wish to understand fluid flow in regions of the edifice that are difficult or indeed impossible to access, permeability cannot necessarily be determined in situ. It is thus of importance to relate transport properties of porous volcanic rocks to the governing physical properties, such as porosity. Though it is evident that the capacity for fluid transport through a porous rock is somewhat dependent on its connected pore space (porosity φ), it is nontrivial to define a precise relationship due to the microstructural complexity of the medium involved (e.g. Zhu and Wong, 1996; Bernabé et al., 2003). Generally, permeability k is estimated as some function of connected porosity, such that $k = f(\varphi)$, where f may include further parameters such as tortuosity (τ) or pore aperture radius. This relation then forms the basis of permeability modelling reliant on empirical or semi-empirical Kozeny–Carman equations (geometrical models), or network modelling (statistical models) (see Guéguen and Palciauskas (1994) for a review).

It is recognised that no all-encompassing theory exists to describe this relationship in all media, due primarily to the fact that some pore geometries may be more effective than others at transporting fluid (e.g. Bernabé et al., 2003). Nevertheless, models such as the Kozeny–Carman (see Kozeny (1927); Carman (1937)), or percolation theory (Sahimi, 1994) have been employed and modified in order to describe the behaviour of volcanic rocks (e.g. Klug and Cashman, 1996; Klug et al., 2002; Mueller et al., 2005; Costa, 2006). In turn, estimates of permeability can be included in numerical simulations of various volcanic processes, with the ultimate aim of predicting the behaviour of a given volcanic system (e.g. Lacey et al., 1981; Day, 1996; Clarke et al., 2002a, b; Reid, 2004; Collinson and Neuberg, 2012; Lavallée et al., 2013).

Previous experimental studies concerning the permeability and porosity of volcanic rocks (e.g. Eichelberger et al., 1986; Klug and Cashman, 1996; Tait et al., 1998; Saar and Manga, 1999; Blower, 2001; Klug et al., 2002; Melnik and Sparks, 2002; Sruoga et al., 2004; Mueller et al., 2005; Wright et al., 2006; Bernard et al., 2007; De Maisonneuve et al., 2009; Yokoyama and Takeuchi, 2009; Heap et al., 2014a,b; Gaunt et al., 2014; Okumura and Sasaki, 2014) have highlighted a vast range of measured values. Porosity of the various volcanic materials—as determined in these laboratory-based studies—has been shown to range between 3 and 90%, while permeabilities in the range of 10^{-17}–10^{-8} m^2 have been measured. The spatiotemporal variation of the physical properties of volcanic rocks necessitates the sampling of a statistically robust dataset (Kueppers et al., 2005; Bernard et al., 2015). In light of these factors, the research herein comprises a systematic field campaign assessing the permeability of edifice-forming rocks representative of a typical andesitic volcano. Combined with field-based density measurements and a complementary laboratory-based study, we further explore the microstructural processes governing permeability in volcanic rocks. While we focus herein on cooled, variably fractured rock, the incidence of fracturing in magma—for example due to strain localisation close to the conduit margins (e.g. Lavallée et al., 2013; Gaunt et al., 2014)—means that the

following discussions and conclusions may also be extended to outgassing processes at the periphery of the conduit, as well as in the edifice.

1.2. Case study: Volcán de Colima

Volcán de Colima is situated at 19°30′45.82″N, 103°37′2.07″W on the Colima–Jalisco border at the south-western margin of the Trans-Mexican Volcanic Belt (Fig. 1). Along with the extinct Nevado edifice, the volcano comprises the Colima Volcanic Complex, marking the conjunction of the Colima rift zone and the Tamazula fault (Rodríguez-Elizarrarás, 1995; Norini et al., 2010). Overlying a Cretaceous basement consisting of deformed volcanic and sedimentary rocks (Rodríguez-Elizarrarás, 1995), Volcán de Colima forms a typical stratocone, with eruptive products varying little in bulk composition: crystal-rich andesites with SiO$_2$ contents typically between ~58 and 61 wt.% (Luhr, 2002; Mora et al., 2002; Valdez-Moreno et al., 2006; Reubi and Blundy, 2008; Savov et al., 2008). Historic volcanism has been characterised by periods of effusive activity (dome formation and lava flows, determined by magma ascent rates, topography, etc.), punctuated by frequent Vulcanian explosions and commonly culminating in voluminous Plinian eruptions (e.g. Luhr, 2002; Varley et al., 2010; James and Varley, 2012; Lavallée et al., 2012). The most recent period of sustained activity began in January 2013, consisting of dome extrusion, pyroclastic density current generation, and intermittent Vulcanian activity. As of April 2015, frequent explosive events were still ongoing.

Volcán de Colima exhibits many characteristics common to convergent margin volcanoes, such as Santa Maria (Guatemala), Ruapehu (New Zealand), Lascar (Chile), Mount Merapi (Indonesia), Citlaltépetl (Mexico), or Egmont Volcano (New Zealand): the steep conical edifice structure overlying a sedimentary basement (e.g. Carrasco-Núñez, 2000; Smyth et al., 2005; Gaylord and Neall, 2012) fosters frequent collapse events (e.g. Rose et al., 1977; Gardeweg et al., 1998; Gamble et al., 1999; Camus et al., 2000; Carrasco-Núñez, 2000), with cyclic eruptive behaviour interspersed with periods of dome effusion (e.g. Rose et al., 1977; Houghton et al., 1987; Gardeweg et al., 1998; Gamble et al., 1999; Camus et al., 2000; Carrasco-Núñez, 2000; Gaylord and Neall, 2012). Combined with its consistently intermediate composition, we maintain that Volcán de Colima can be viewed as generally representative of andesitic stratovolcanoes worldwide.

2. Methods

2.1. Field methods

We collected 572 hand samples from sites around the volcano, shown in Fig. 1, comprising over half a metric ton of andesitic edifice rock. The sites are debris-flow tracks, locally termed *barrancas*: La Lumbre, Montegrande, and El Zarco; as well as a site at El Playón, the area between the summit cone and the ancient caldera wall (Fig. 1). These sites were chosen due to their accessibility and because they all contain abundant loose surface material of a size suitable for our methods (i.e. approximately fist-sized clasts). The collected samples comprise a range of variably remobilised and reworked explosive and effusive products, representative of the edifice-forming materials. A portable air permeameter (Vindum Engineering TinyPerm II) was used to measure the permeability of each hand sample. By evacuating air from a rock, the TinyPerm II unit calculates a value based on the monitored response function of the transient vacuum at the nozzle-rock interface, which corresponds to the sample permeability. The relation between the given TinyPerm value and Darcian permeability is discussed in Appendix A.

The ability to make autonomous and rapid measurements is extremely useful when working in the field; as such these permeameters have seen increasing use in volcanology and related geoscience disciplines (e.g. Possemiers et al., 2012; Invernizzi et al., 2014; Vignaroli
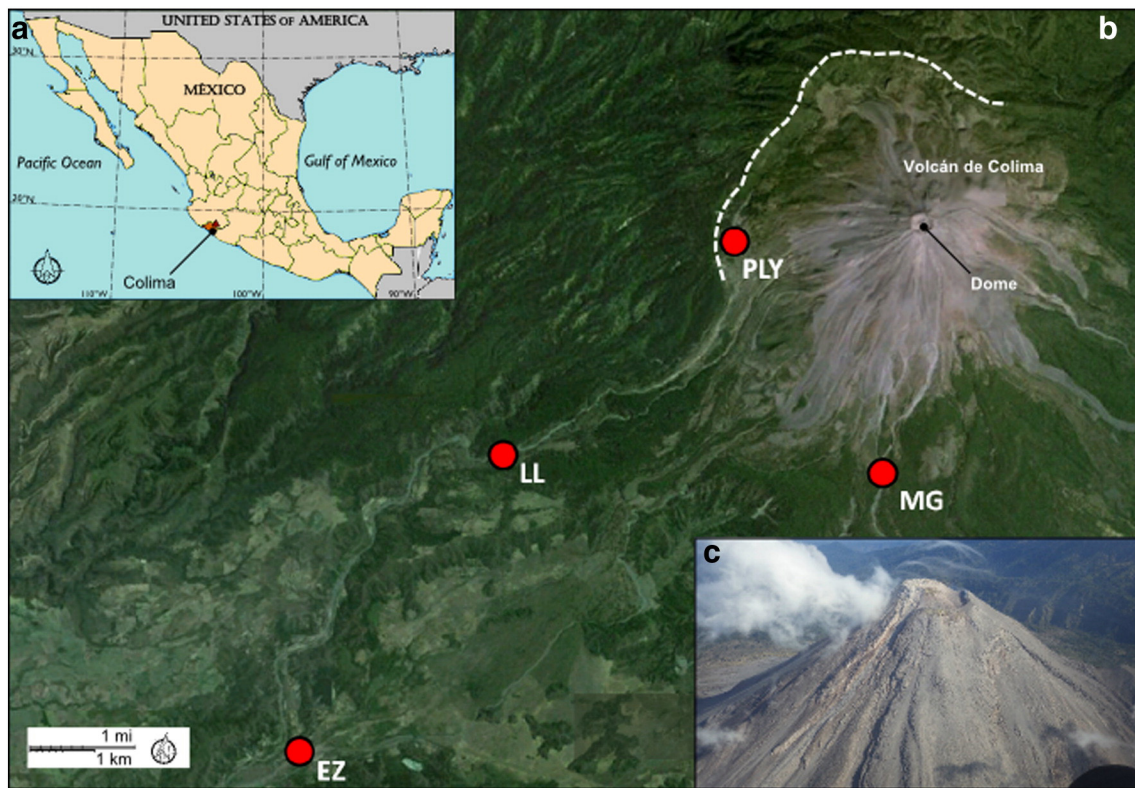
Fig. 1. Volcán de Colima. Inset (a) gives location of Volcán de Colima, (b) shows sample collection sites El Playón (PLY), Montegrande (MG), La Lumbre (LL), and El Zarco (EZ). Active dome and the ancient caldera amphitheatre (dashed line) are also shown. Map is a composite of Google Earth™ imagery (19°30′45.82″N, 103°37′2.07″W). Inset (c) is an aerial photograph of the active summit area, taken on 3rd June, 2014.

et al., 2014). For this reason, Appendix A also includes systematic assessment (comprising 400 measurements) of the capabilities, accuracy, and repeatability of a TinyPerm unit.

Permeability anisotropy in volcanic rocks has been discussed by several authors (e.g. Clavaud et al., 2008; Wright et al., 2009; Gaunt et al., 2014), resulting as a function of anisotropic bubble growth and crack propagation during ascent, eruption, and emplacement of volcanic materials. In laboratory measurements, the pathway for fluid flow can be approximated as we peripherally confine a cylindrical sample and control the rate of flow or the up- and downstream pressures. The field process, on the other hand, involves the evacuation of irregularly shaped, unconfined samples, meaning that measurement is nominally isotropic, even if the actual permeability of the sample is not. As the edifice is constructed of rocks chaotically oriented with respect to any existing anisotropy, we measured field permeability on an average of three faces for each sample (where this was possible: given the heterogeneous shape and size of the hand samples, this procedure was not always feasible). This further ensured a robust methodological procedure.

Bulk rock density was also determined for each sample using an Archimedean weighting method similar to that employed by Kueppers et al. (2005). Our method differs in that it accounts for imbibition in the post-processing stage, rather than during the measurement itself: specifically, Kueppers et al. (2005) vacuum-sealed samples in plastic bags to avoid the imbibition of water. The setup consisted of a balance mounted on a tripod, with a water-filled bag suspended underneath (Fig. 2). A windbreak was used in the field in order to minimise the effects of wind on the balance. The balance, with a precision of 0.1 g and a load limit of 5000 g, was used to measure the weight of the rock in air (point 1 in Fig. 2), and the apparent immersed weight taken in a sample basket (point 2). Assuming the fluid (water) density to be

1000 kg m^{-3} (1 g cm^{-3}), then bulk rock density ρ can be determined from the Archimedes principle, such that:

$$\rho = \frac{W}{W - W_I} \quad (1)$$
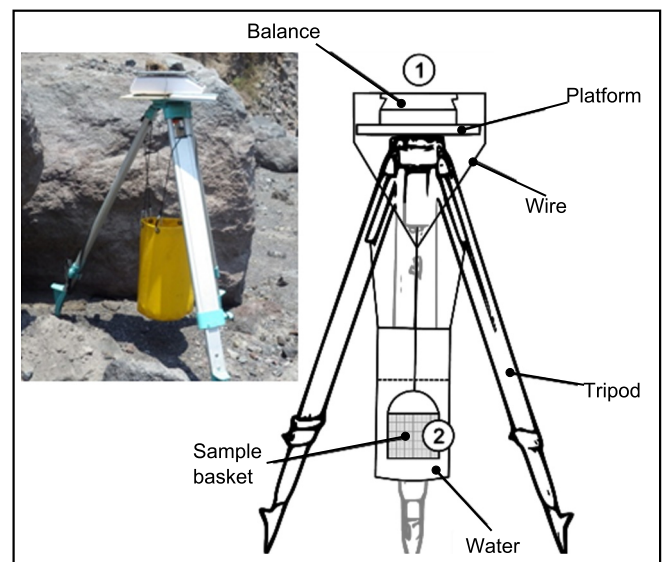
Fig. 2. Schematic of the field setup for measuring sample density (inset shows a photograph), based on the method employed by Kueppers et al. (2005). Weight measurements are performed at points 1 and 2 (see text for discussion). Bag provided by Landjoff Ltd.

where W is weight in air, W_I is the apparent immersed weight, and the denominator is hence equal to the weight of displaced fluid. Measurements of density were subsequently transformed into porosity data; full details are presented in Appendix B. A limit to this method arises in the measurement of some highly pumiceous samples: highly porous pyroclasts with a specific gravity <1 could not be immersed in water due to their buoyancy. While samples could be weighed down with an object of known mass, this method was not employed in this study, mainly due to the fact that so few ($n = 7$) of these highly pumiceous samples were observed in our study areas.

In addition to quantitative measurements, each hand sample was also categorised in terms of visible alteration or structure, or differences in colour; examples of each of these categories are given in Fig. 3. In order to be of practical use in the field, classifications are based on differences readily discernible in hand samples, as such none of the following descriptors are used with a compositional or genetic connotation. "Pumiceous" samples are defined by their high vesicularity, low density, and pale grey colour (Fig. 3c). Samples containing an abundance of large pores and being dark grey to black in colour are referred to as "scoracious", although these textures can extend to lower porosities as well, and occasionally exhibit additional comagmatic features (Fig. 3d). Volcanic material that cannot be texturally described as pumiceous or scoracious is simply referred to hereafter as "lava" (Fig. 3b). "Lava" is generally grey aphanitic to porphorytic juvenile andesite; however rocks in these three categories could also display a variable degree of alteration, including oxidation (examples of which are given in Fig. 3e–h).
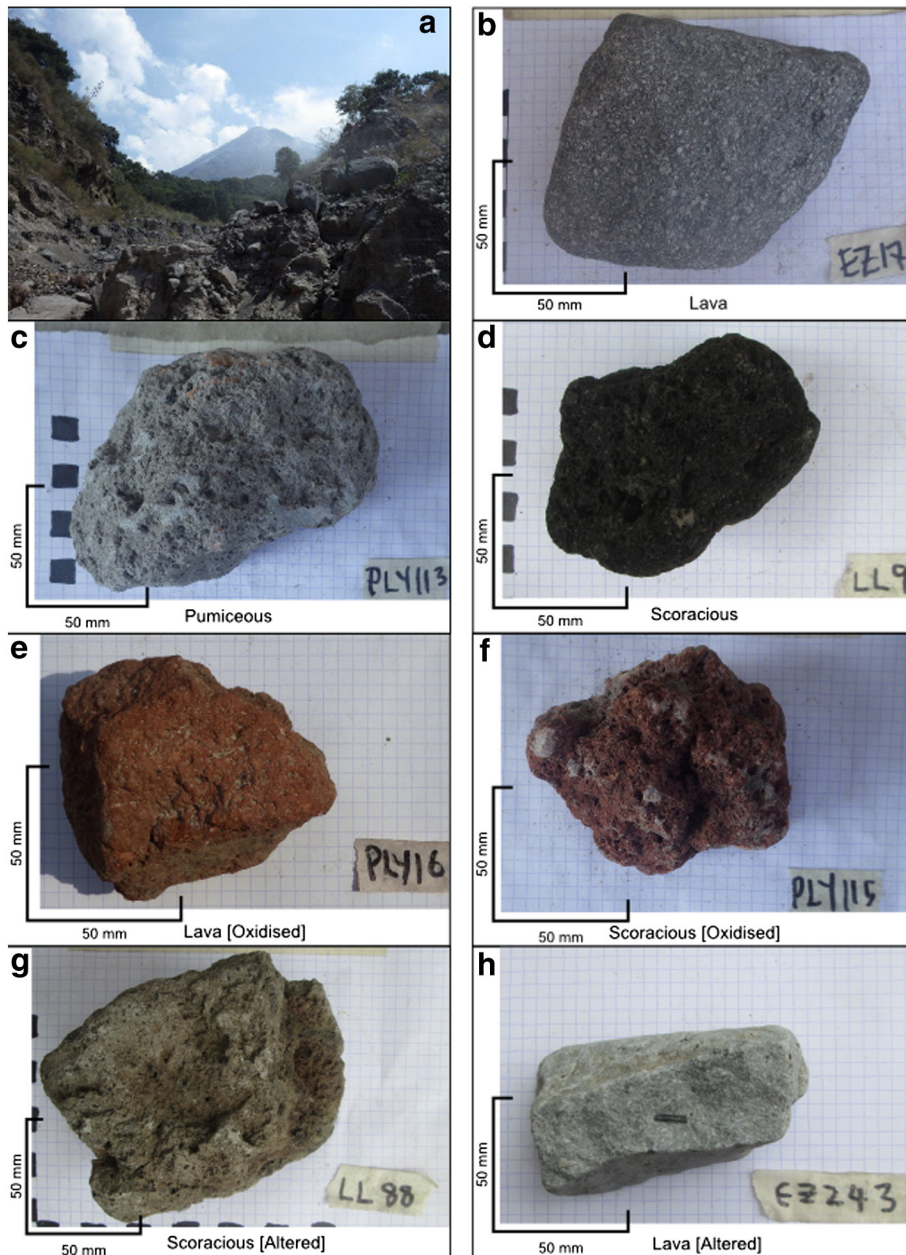
Fig. 3. Rock classification scheme. (a) Barranca Montegrande, a representative debris-flow-track from which samples were collected. Summit of Volcán de Colima can be seen in the background. (b) Pristine porphyritic lava. (c) Pumiceous pyroclast. (d) Scoracious sample, characterised by large, variably elongated pores (vesicles), and typically dark in colour, (e) and (f) show oxidised samples, as evidenced by their brick red colour. Texturally (f) is described as scoracious, respectively. (g) and (h) both show examples of altered clasts: in (g) significant post-emplacement weathering can be observed; in (h) evidence of hydrothermal vapour-phase alteration can be seen. (For interpretation of the references to colour in this figure legend, the reader is referred to the web version of this article.)

Alteration is also manifest in general weathering of the rocks (e.g., due to rainfall, fluvial reworking, and other transport processes), as well as mineral phase replacement resulting from hydrothermal processes (John et al., 2008; Lavallée et al., 2012). The strong correlation between connected porosity and density determined in the following section attests to there being very little variation in bulk composition across the range of samples (see Appendix B).

2.2. Laboratory methods

To complement the field study, a selection of samples was collected to be analysed in the Experimental Geophysics laboratory at Université de Strasbourg. Not only does this afford a more robust exploration of their physical properties and the opportunity to image their microstructure, but also allows us to access permeability data in a range below that measurable by the TinyPerm unit. Based solely on their density, eleven rocks were sub-sampled from the entire dataset to represent the range of porosities observed in the field. Variations in texture or permeability were not considered at this point (the selection process was thus a stratified-random sampling method). Seventeen cylindrical cores, 20 mm in diameter, were obtained from the sub-sample set and precision ground to a nominal length of 40 mm. Connected water porosity was measured for each core using the triple-weight water saturation method (Guéguen and Palciauskas, 1994), and connected gas porosity and skeletal density were measured using helium pycnometry (AccuPyc II 1340). Total porosity (φ_T) was determined as $1 - (\rho_B/\rho_S)$, i.e. the ratio of bulk and skeletal densities for each sample, allowing unconnected porosity (φ_U) to be calculated as $\varphi_T - \varphi$. The double-weight field method was also tested in the laboratory by performing an equivalent

set of measurements (i.e. dry mass and apparent immersed dry weight), shown in Appendix B (Fig. B1). Gas permeability of each oven-dry (vacuum dried at 40 °C) core was measured using a benchtop steady-state permeameter. All measurements were performed under 1 MPa confining pressure in order to preclude fluid (nitrogen) flow around the sides of the sample. Samples were left for at least one hour prior to measurement to ensure microstructural equilibration. Volumetric flow rate measurements were taken (using a gas flow meter) under several pressure gradients to determine the permeability using Darcy's law, and to assess the need for the Klinkenberg or Forchheimer correction, which were applied where appropriate. It should be noted that cores were obtained in only one direction from each of the 11 hand samples; consequently, the subsequent analyses and discussion do not account for potential anisotropy in these rocks. Hydraulic radii of samples were determined with Brunauer, Emmett, and Teller krypton adsorption (BET), in order to use the modified Kozeny–Carman relation (after Heap et al. (2014a)) to assess microstructural controls on the permeability of these rocks. The revised Kozeny–Carman equation can be shown as (Yokoyama and Takeuchi, 2009; Heap et al., 2014a):

$$k_{KC} = \frac{\varphi^3}{b\tau^2 \rho_B^2 S_{BET}^2} \tag{2}$$

where ρ_B is bulk density, S_{BET} is the specific surface area, and b is a geometric constant. Assuming that porosity is either crack-controlled ($b = 12$), or a pore-controlled ($b = 8$) (Bernabé et al., 2010) we can thus solve for tortuosity τ.
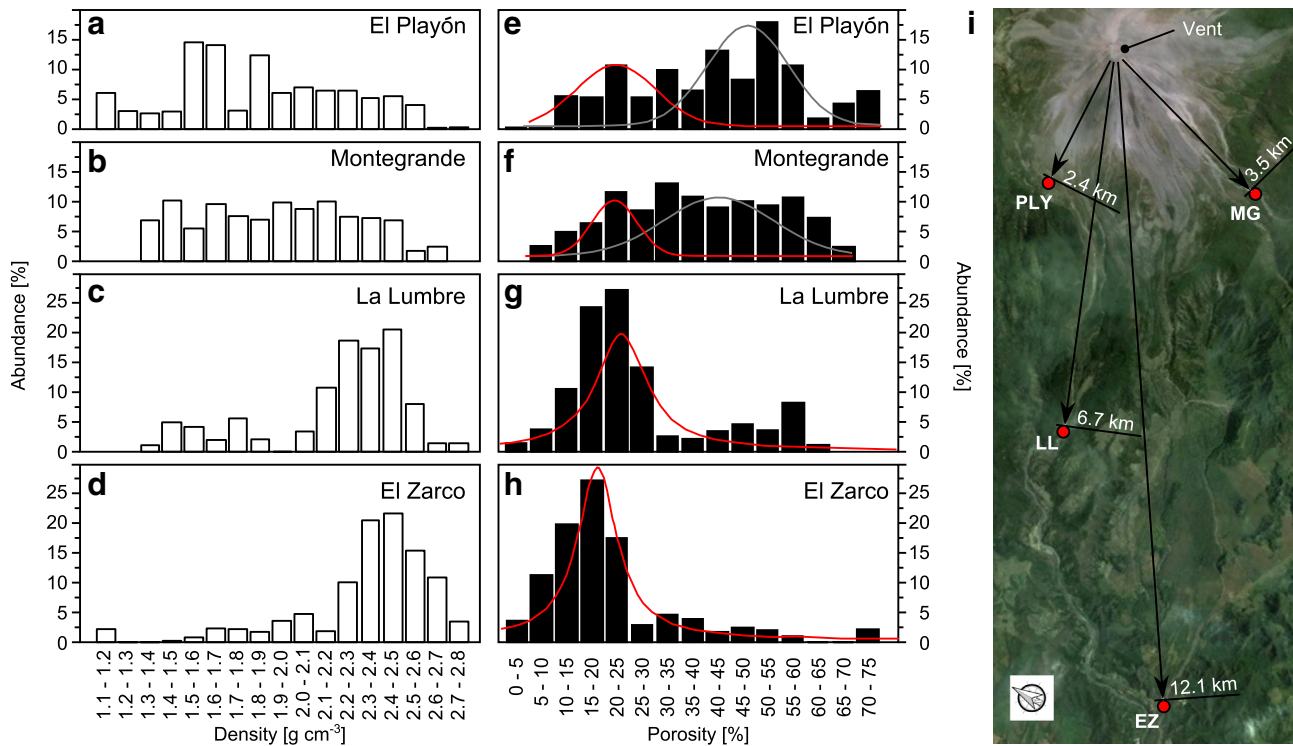
Fig. 4. (a)–(d) show the density distribution of collected samples for each of the collection sites. (e)–(h) shows the porosity distribution across the sample sites. Data are shown in terms of their weighted abundance, after Bernard et al. (2015). The map (i) indicates the distance of each site from the active vent. Note that distance indicated is the minimum transport distance (i.e. straight-line distance). PLY = El Playón; MG = Montegrande; LL = La Lumbre; EZ = El Zarco. Peaks in the low-end of the porosity distributions are described by the red curves. High-porosity peaks are shown by grey curves. For El Playón and Montegrande, the distribution is bimodal; La Lumbre and El Zarco show increasingly skewed distributions. Curves fitted using Origin® data analysis software. Data comprises 118, 94, 97, and 232 samples at each study site, respectively. (For interpretation of the references to colour in this figure legend, the reader is referred to the web version of this article.)

3. Results and discussion

3.1. Density distribution from the vent

Of the 572 collected samples, density could not be determined for samples too buoyant for our field density method. Fig. 4 shows the density (a–d) and porosity (e–h) of the remaining samples collected at each of the sampling sites shown in (i) (also Fig. 1). Relatively uniform or bimodal distributions in density and porosity are seen at the site closest to the active summit region (i.e. El Playón), while the distribution becomes unimodal and notably skewed towards high densities (low porosities) as one moves to sites increasingly more distal: Montegrande, La Lumbre, and El Zarco, respectively. This phenomenon has been noted in previous field studies (e.g. Kueppers et al., 2005), and can be attributed to the increased transport distance and associated degradation of more friable, porous materials. As volcanic deposits are remobilised away from the vent, higher-porosity rocks will be preferentially comminuted into smaller size classes by processes such as abrasion, collision, and fluvial reworking (as shown experimentally by Manga et al. (2011); Kueppers et al. (2012)). As such, the proportion of relatively dense rocks should increase with distance from the vent, as we observe in our data.

The array of porous media collected and measured in the course of this study indicates that edifice material (and hence, the edifice of Volcán de Colima) exhibits extraordinary heterogeneity in terms of its physical properties. A wide range of densities can be observed in the dataset ($n = 542$), from 1142.40 to 2813.79 kg m^{-3}, indicating a correspondingly broad variance in porosities (2.5–72.7%). The porosity within volcanic materials can either be in the form of cracks (due to thermal,

mechanical, or chemical stresses) or pores, the frozen-in relicts of bubble formation, growth, and coalescence. As the volatile content in magma comprises one of the fundamental driving forces of explosive activity, the post-eruptive porosity allows us to glean insight into the eruption dynamics and pre- and syn-eruptive conditions within the conduit (e.g. Cashman et al., 1994; Kueppers et al., 2005; Gonnermann and Manga, 2007; Mueller et al., 2011). A tendency towards relatively high porosity values (e.g. as observed at El Playón: Fig. 4e) is indicative of deposits of predominantly explosive origin, while low-porosity rocks are associated with predominantly extrusive material (Cashman et al., 1994; Mueller et al., 2011); the range of measured porosities thus attests to the array of observed eruption styles at Volcán de Colima (e.g. Bretón-González et al., 2002; Mueller et al., 2011). Variability of host-rock porosity also exerts a significant influence over strength and deformation modes within the edifice, in turn affecting outgassing through the edifice and flank stability (Heap et al., submitted for publication). As such, it is imperative that future models of volcanic processes—such as conduit outgassing or mechanical stressing of the edifice—account for the potential diversity of the physical rock properties which underpin these processes.

The density distribution of the erupted material at Volcán de Colima over time is best approximated by that of samples measured at El Playón, closest to the active summit crater: Fig. 4 shows that this distribution is bimodal. If we assume that the initial volatile content of magma is roughly equivalent through time, we can surmise that—in general—dense rocks result from efficiently outgassed magma, likely to have erupted effusively. On the other hand, the lower density peak represents inefficient outgassing of magma and the retention of explosive potential energy. The low porosity and permeability of dense
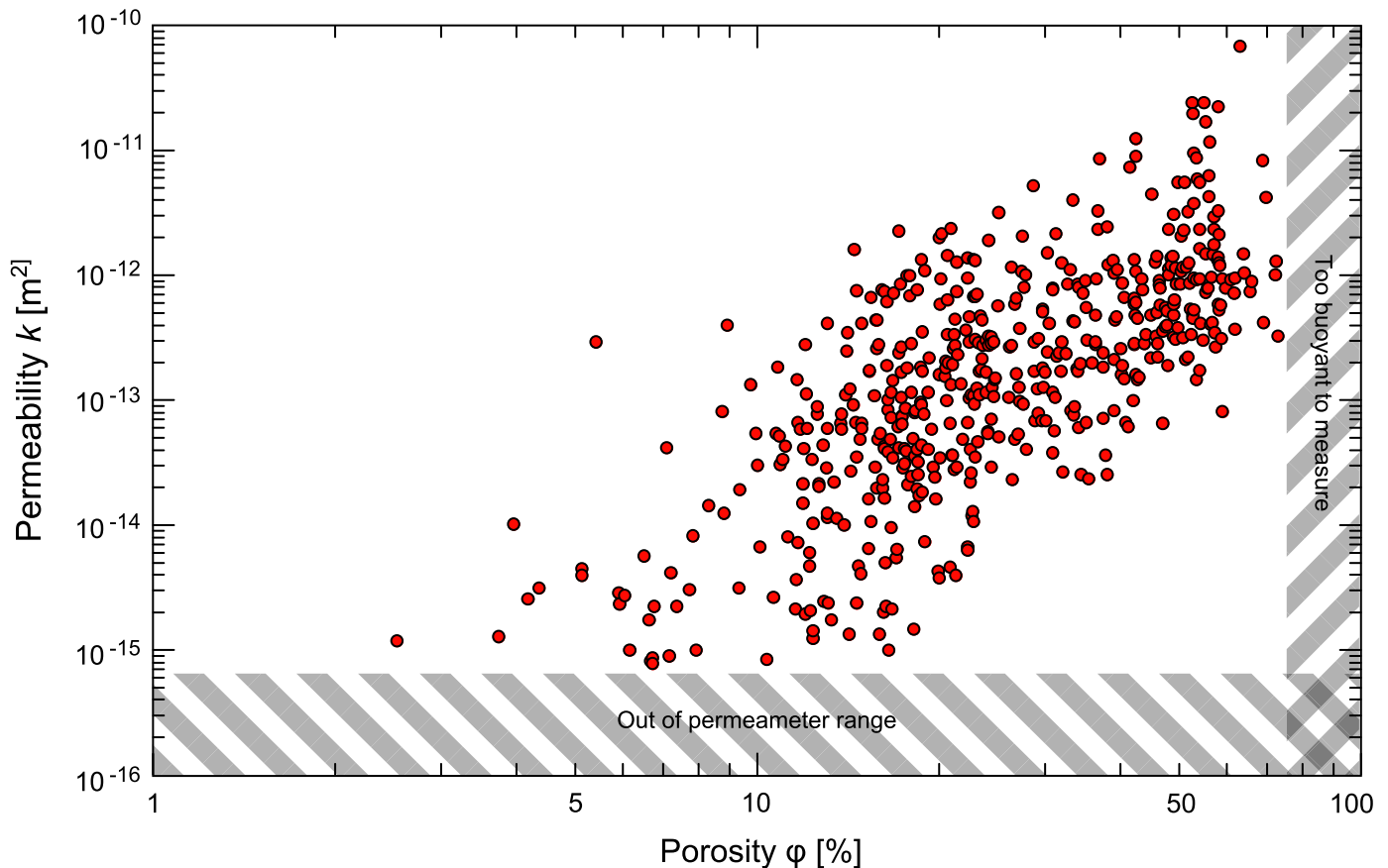
Fig. 5. Permeability–porosity data for 542 samples (i.e. excluding the 30 samples which were either too buoyant to obtain a density measurement, or have a permeability below the limit of field permeameter) across all sample sites and all classifications, as measured in the field. Hatched areas indicate regions where the field methods were ineffective, either because sample permeability was below the limit of the permeameter, or because samples were too buoyant to measure using the double-weight method outlined in the text. Each point is a mean value from multiple measurements, as discussed in the text.

lavas will consequently limit outgassing, resulting in the eruption of less dense material. In turn, this material will increase the permeability of the edifice, fostering extrusion of dense products, and so the cycle continues. Thus, explosive decompression and fragmentation serve to facilitate outgassing in future eruptive cycles (e.g. Gonnermann and Manga, 2003). It is probable that the range of porosities is therefore linked to the frequency and cyclicity of highly explosive eruptions at Volcán de Colima (e.g. Robin et al., 1991; Luhr, 2002), and at least partially dictates the observed transition between explosive and effusive behaviours.

Further, previous works have shown that porosity has a significant influence on the strength and failure mode of volcanic rocks (e.g. Zhu et al., 2011; Heap et al., 2014a). The increased proportion of high-porosity material near the vent and proximal flanks of the volcano will consequently decrease stability in this region, leading to more frequent, local slope failure than observed distal to the vent.

3.2. The relationship between porosity and permeability

The initial dataset of 572 hand samples contained 30 samples which were either too buoyant to measure porosity or of a permeability too low to measure permeability in the field: the lower limit of the field permeameter (6.92×10^{-16} m^2) did not permit measurements of permeability for some of the very low porosity samples. Samples for which a value for either porosity or permeability could not be obtained are not included in any further analysis. Transformed field data are displayed in Fig. 5: our data show that there is a general trend of increasing permeability with increasing porosity. Porosity values range from 2.5 to 72.7%, while permeabilities lie between 7.6×10^{-16} and 6.5×10^{-11} m^2.

For rocks of comparable porosity, a difference in permeability of up to four orders of magnitude can be observed, as has been noted in previous studies of volcanic materials (e.g. Saar and Manga, 1999; Klug et al., 2002; Mueller et al., 2005; De Maisonneuve et al., 2009; Wright et al., 2009; Yokoyama and Takeuchi, 2009). Notably, comparable values of permeability can also be associated with rocks with very different porosities. While part of this distribution may be explained by permeability anisotropy (as discussed previously; see e.g. Clavaud et al. (2008); Wright et al. (2009); Gaunt et al. (2014)), microstructural attributes such pore geometry will contribute significantly to permeability. For instance, a rock with a single through-running crack could have a very low porosity, while providing an effective fluid conduit. On the other hand, a rock structure consisting of many large pores connected by tortuous microcracks could be poor at transmitting fluids, despite having a relatively high porosity. It is important to note that the edifice is haphazardly constructed of variably porous material with differing eruptive and emplacement histories: in reality, a representative suite of edifice-forming rocks is bound to contain both these end-members and a range of more or less effective pore geometries in between (discussed in detail below). Due to this inherent natural variability, it is therefore unsurprising that a large degree of scatter is evident in our field data.

Fig. 6 displays the field permeability data grouped by our rock classification scheme (i.e. lava, scoracious, pumiceous, altered and oxidised). Notably, the degree of scatter observed in Fig. 5 appears to be largely unaffected by meso-scale textural differences, or by syn- or post-eruption alteration. Lava (Figs. 3b, 6a) comprises the

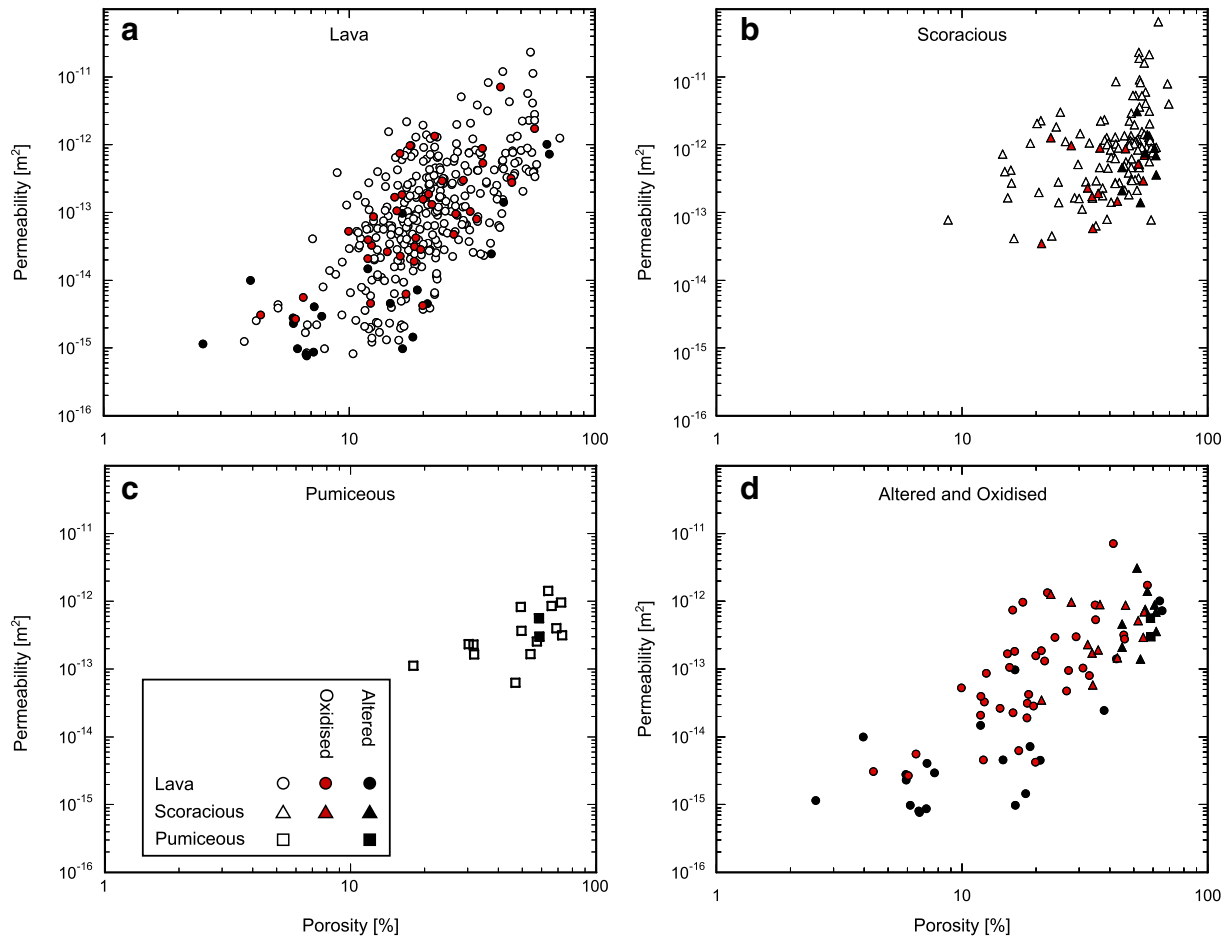**Fig. 6.** Field permeability–porosity data sorted by sample classification; a: lava ($n = 390$); b: scoracious material ($n = 136$); c: pumiceous material ($n = 16$); and d: altered (including oxidised) samples ($n = 95$). By definition, scoracious and pumiceous rocks (b, c) occupy only the higher-porosity domain. Lava, altered, and oxidised samples (a, d), on the other hand encompass the whole range of porosities and permeabilities.

majority of field samples ($n = 378$), and encompasses the range of measured permeabilities and porosities. For any given porosity, permeability may differ by up to four orders of magnitude, a phenomenon which is consistent for the oxidised and altered rocks (denoted by the red and black filled symbols, respectively). Scoracious samples (Figs. 3d, 6b) display a similar range of permeability for a given porosity, with porosities of around 60% yielding permeability values from 7.8×10^{-14} to 6.5×10^{-11} m^2. It is possible that the elongation of vesicles associated with scoracious deposits fosters a significant degree of permeability anisotropy, as discussed by Wright et al. (2009). Pumiceous samples (Fig. 3c) show a narrower extent of permeabilities, from 6.3×10^{-14} to 1.4×10^{-12} m^2 (Fig. 6c), however this may merely be a product of their low sample number ($n = 16$) relative to the other classes. While hydrothermal alteration, weathering, or oxidation will influence the porosity and permeability of an individual sample, we note that, following the subdivision of the data into these categories, the general permeability–porosity trend (as observed in Fig. 5) is unaffected, as shown in the synopsis plot of Fig. 6d.

3.3. Volcán de Colima andesites: microstructural complexity

To provide deeper insight into the observed variability in the field samples, we now provide laboratory measurements of physical rock properties (including permeability), and an assessment of the micro-scale complexities in andesites representative of the observed porosity range of edifice-forming rocks. Measuring permeabilities in the laboratory allows us to include samples that would otherwise fall below the measurable limit imposed by the field method. Given that meso-scale textural differences have been shown to explain little of the variation in the field data (Fig. 6), the sample set comprised lava, scoracious, and pumiceous material in order to maximise the porosity range (from 3.5 to 59.4%, in 17 cylindrical cores; see Table 1).

Fig. 7 displays the laboratory-determined values for permeability and connected gas porosity against other measured or calculated physical properties: specific surface area, tortuosity (Eq. (2)), and overall connectivity. To assess the degree of overall pore connectivity within these andesites, we examine the ratio of connected and unconnected porosity for each of our laboratory samples, deriving a dimensionless parameter Γ as a proxy for pore connectivity, such that $\Gamma = 1 - (\varphi_U/\varphi)$. Physical property data for each sample are given in Table 1.

As observed in our field data (Fig. 5), permeability increases with increasing connected porosity (Fig. 7a). We observe that the increase is nonlinear; rather, the data appears to describe a dogleg or kink (in log–log space). This phenomenon is discussed in detail in the following section. Specific surface areas of these andesites appear to fall into two distinct families (Fig. 7b), with the majority of samples containing a specific surface area of less than 100 m^2 kg^{-1}, and showing an increasing trend with increasing porosity. However, for the two samples containing the lowest porosities, we measure much higher surface areas, in excess of 500 m^2 kg^{-1} (Table 1). For perspective, the surface area within a cylindrical sample (EZ_94: length = 41.11 mm; diameter = 19.91 mm) is greater than the area between the goalposts in a football (soccer) goal. Notably, Scanning Electron Microscope (SEM) analysis has shown that the high surface area data are associated with a pilotaxitic groundmass containing abundant high aspect ratio microlites, attributed to syn- and post-eruptive differentiation. Between these microlites we observe micro-scale pore space (microporosity), which we define as pores less than 30 μm in diameter (see Zhu et al., 2010, and references therein). Microporosity can be observed in the SEM photomicrographs of Fig. 8a–c, and serves to greatly increase the internal surface area while contributing little to overall porosity and fluid transport. Samples with only microporosity (e.g. EZ_69; EZ_94) show very low permeabilities (Fig. 7a; Table 1), thus we can infer that micropores may not contribute significantly to fluid transport in the samples with higher permeabilities (see also Saar and Manga (1999)). The fact that a large proportion of the internal surface does not contribute to fluid flow highlights that the permeability of these samples are poorly approximated by the Kozeny–Carman relation (Eq. (2)). In contrast, the specific surface area within sandstone, a rock with a much simpler microstructure, has been shown to correspond strongly with both porosity and permeability (e.g. Rabbani and Jamshidi, 2014).

Calculated tortuosities of all samples were low ($0 < \tau < 2.2$), with the majority <1 (Fig. 7c; Table 1). In reality a tortuosity less than one is impossible (this representing a perfectly straight flow path); however, values in this range have been predicted previously for volcanic rocks, such as highly-porous andesite (Heap et al., 2014a), and rhyolitic pumice (Degruyter et al., 2010; Wright et al., 2009). In contrast to Heap et al. (2014a) however, we do not observe high tortuosities at values of low connected porosity. It is a peculiarity of our data that the anomalously high surface areas cancel out the effects of low connected porosity when using Eq. (2), yielding low tortuosity values. Even disregarding these two values, we note that internal surface area alone does not appear to exert a dominant control on permeability and is thus a poor predictor of permeability in the volcanic rocks of this study (Fig. 7d).

Overall connectivity Γ lies between zero and one, where zero represents a pore network completely isolated from the outside of the sample, and one corresponds to a sample where all of the porosity is connected. Fig. 7e shows the relation of this parameter to connected porosity (on linear axes), while Fig. 7f illustrates the

Table 1
Physical properties of a suite of Volcán de Colima andesites, including porosity, bulk density, specific surface area, permeability, tortuosity, and connectivity. Tortuosity has been calculated according to Eq. (2), assuming $b = 8$ or 12 (see text for discussion). Letter in brackets refers to sample classification: L = lava; S = scoracious; P = pumiceous.

Sample	Connected porosity φ [%]	Unconnected porosity φ_U [%]	Connectivity Γ	Bulk density ρ_B [kg/m^3]	Specific surface area S [m^2/kg]	Permeability k [m^2]	Tortuosity τ
EZ_120 (L)	18.5	1.7	0.91	2139.32	28	2.72×10^{-13}	0.90
EZ_121 (L)	9.6	0.3	0.97	2454.39	18	6.05×10^{-14}	0.79
EZ_69 (L)	4.6	1.1	0.76	2670.47	522	1.62×10^{-17}	0.50
EZ_94 (L)	3.5	0.6	0.82	2658.23	546	9.47×10^{-17}	0.13
LL_43a (S)	46.8	0.8	0.98	1422.23	96	4.17×10^{-13}	1.29
LL_43b (S)	48.1	0.9	0.98	1386.71	82	4.48×10^{-13}	1.55
LL_74a (L)	10.6	0.7	0.93	2396.42	59	5.29×10^{-14}	0.31
LL_74b (L)	8.5	0.9	0.90	2448.07	47	1.25×10^{-15}	1.76
LL_96 (S)	44.9	1.7	0.96	1450.14	212	4.37×10^{-13}	0.52
MG_02 (L)	23.4	0.8	0.97	2054.79	36	4.37×10^{-13}	0.82
MG_22a (L)	27.4	<0.1	1.00	1943.45	42	4.39×10^{-13}	0.94
MG_22b (L)	24.5	<0.1	1.00	2024.24	36	4.39×10^{-13}	0.89
MG_28 (S)	46.6	1.0	0.98	1436.68	53	4.67×10^{-13}	2.16
PLY_116a (P)	57.5	2.0	0.96	1094.30	56	3.94×10^{-12}	1.27
PLY_116b (P)	57.9	2.1	0.96	1081.20	70	1.75×10^{-12}	1.56
PLY_116c (P)	59.4	2.0	0.97	1042.74	63	1.40×10^{-12}	2.08
PLY_116d (P)	58.6	2.2	0.96	1060.52	61	1.77×10^{-12}	1.84
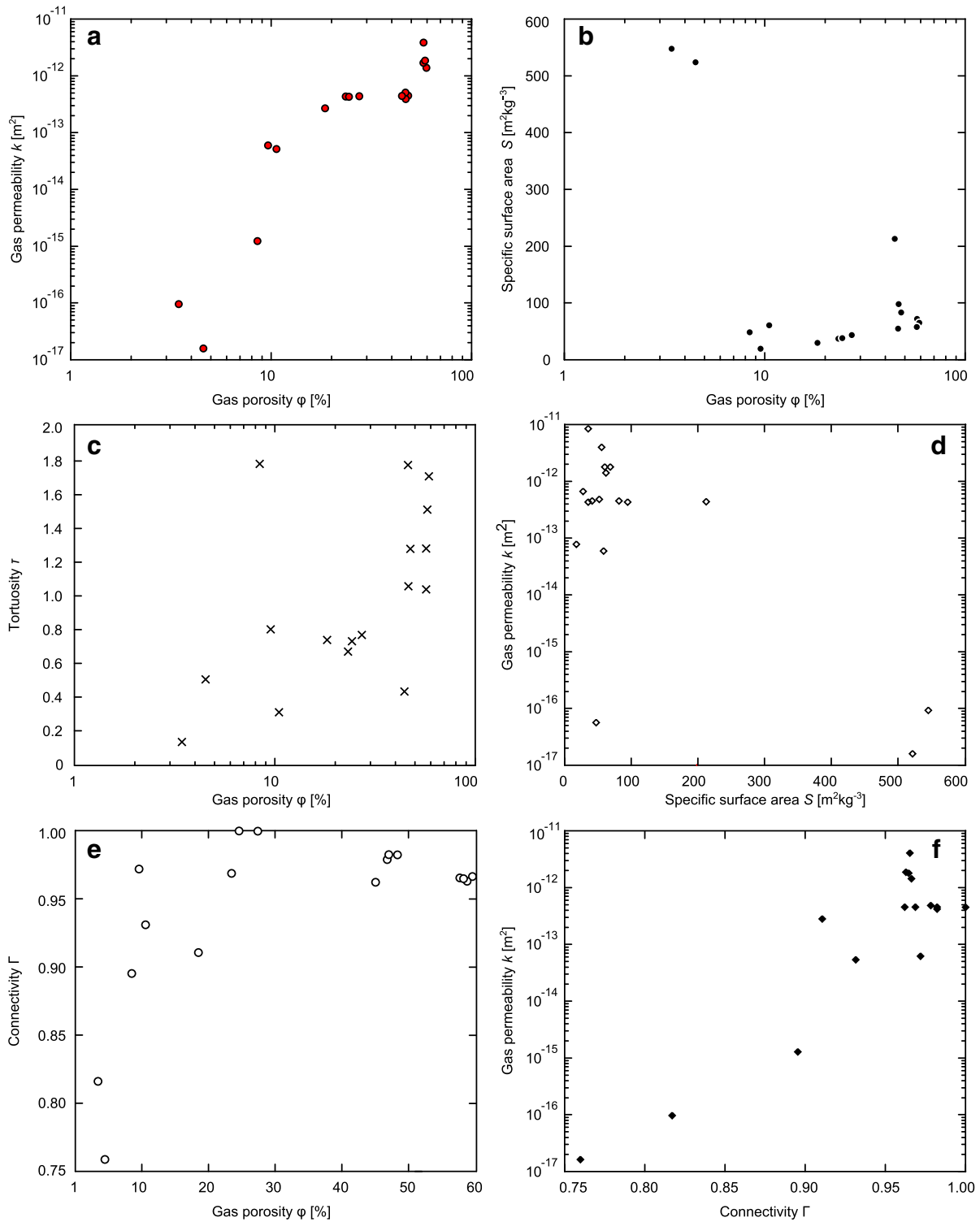
Fig. 7. Physical property data of laboratory samples. (a) shows connected gas porosity against gas permeability on log–log axes. Gas porosity versus specific surface area is given in (b), and tortuosities calculated according to Eq. (2) in panel (c). (d) shows specific surface area against gas permeability. (e) shows pore connectivity, plotted against connected porosity (note that porosity is here shown in a linear axis, in contrast to the logged axes of the other panels. See text for discussion). Finally, (f) displays gas permeability against connectivity in semi-log space.

approximately exponential increase in permeability with pore connectivity. While this parameter affords insight into the degree of connectivity to the outside of the sample, it does not indicate the relative efficiency of each pore interconnection. Ostensibly, measuring properties such as connected porosity or surface area makes use of all available pore space. On the other hand, pathways perpendicular to flow, excessively tortuous, or which involve very

narrow pore apertures may be redundant to flow, and thus not included in measurements of permeability.

3.4. A critical porosity: microstructural changepoint

When describing permeability as proportional to integer powers of geometrical parameters (i.e. φ, τ, S), as in Eq. (2), is it generally given
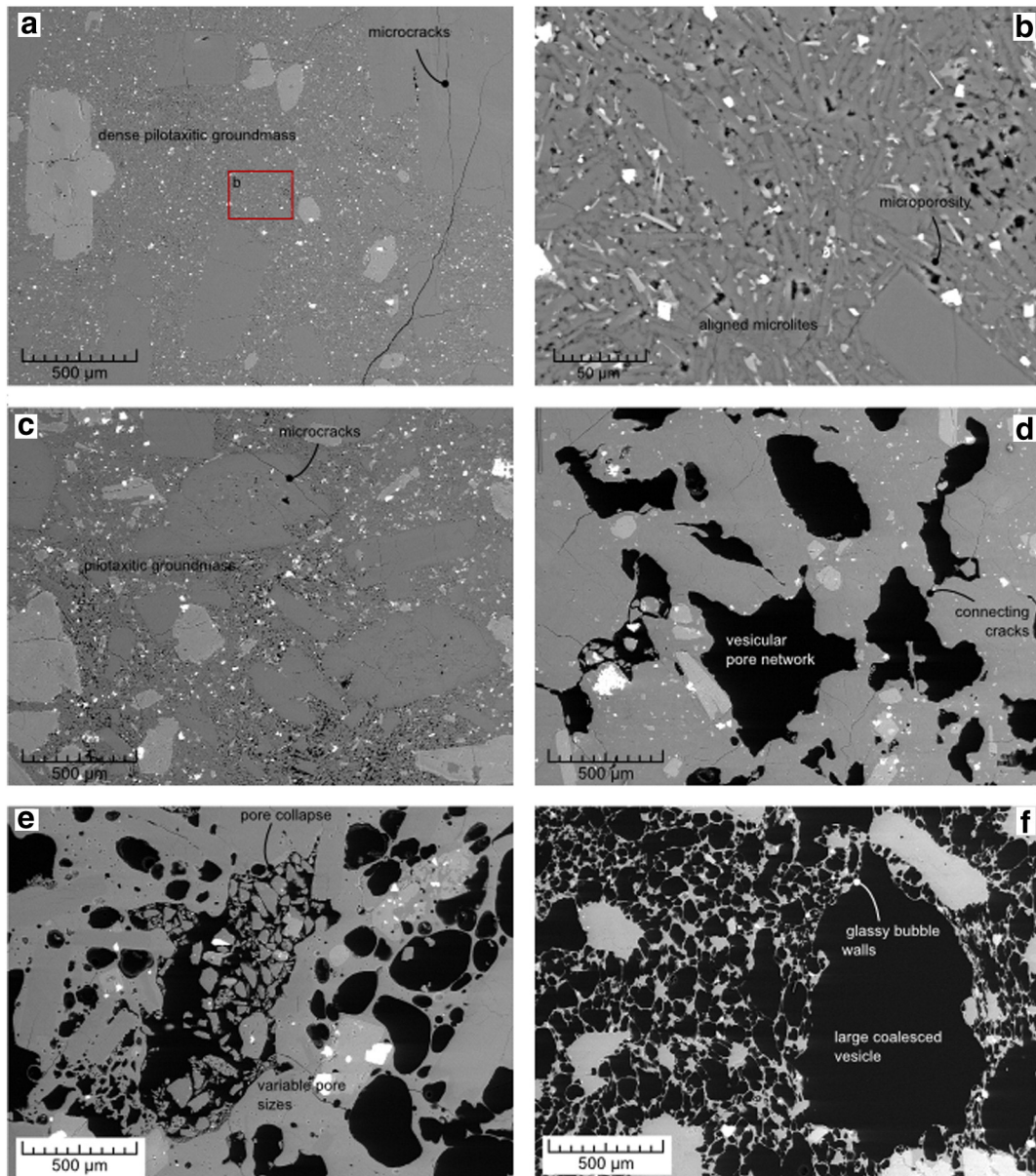
Fig. 8. Microstructures. Scanning electron microscope backscatter photomicrographs of an array of andesites from Volcán de Colima. (a) is from sample EZ94, with a porosity around 3.5%. The sample has a highly dense pilotaxitic groundmass containing thin and tortuous microcracks. Panel (b) shows a close-up view of the abundant microlites in (a), highlighting their flow-alignment and intercrystalline of microporosity. Similar textures can be observed in (c), sample EZ69 (porosity ~5%). The marginally higher porosity may be due to the relatively greater degree of microporosity compared to the samples shown in (a) and (b). The pilotaxitic textures observe in these samples correspond to anomalously high surface area measurements. In (d), a more porous rock (MG22: ~25%) shows large subspherical pores, variably well connected with cracks. Panel (e) shows connected vesicles in a glassy groundmass (sample LL96: ~45%). Finally, (f) shows a pumiceous sample (PLY116: ~58%), with characteristically large pores and thin glassy bubble walls. The sequence of images shows a transition between crack- and pore-dominated geometries (as discussed in Section 3.4).

that these parameters are similarly correlated by power-law relations (Bernabé et al., 2003). We can thus infer that the slope m of a fitted curve is the exponent of the relation $k = f(\varphi^m)$. However, and as seen in Fig. 7a, the assumption that permeability can be simply described by porosity to a single power-law exponent m is false in the case of the andesites of this study. In previous laboratory studies involving physical properties of volcanic rocks (andesites from Volcán de Colima: Heap et al., 2014a; welded block-and-ash flow deposits from Mount Meager, Canada: Heap et al., 2014b), a critical "crossover" porosity, at which the value of m changes significantly, was observed. A crossover porosity has similarly been observed in sandstone (Bourbie and Zinszner, 1985). In each case, the crossover porosity was interpreted as the result of a distinct change in rock microstructure. These studies by Heap et al. (2014a, 2014b) on volcanic materials estimate the thresh-old value of porosity to exist between 12 and 15%, though this value is

assigned on a best-estimate basis. When plotted in log–log space this threshold resembles a piecewise linear model, as has been applied in other geoscientific studies, notably that of Hatton et al. (1994). The piecewise linear model assumes that log transformed data are described by one linear relationship until a defined changepoint (crossover), whereafter data are described by a linear relation with a different slope (correspondingly, the original data may be described by two distinct power-law relations).

The existence of such a changepoint in our field data cannot be definitively argued, the reasons for which are twofold: firstly, data obtained in the field does not extend to lower permeabilities ($< 10^{-16}$ m^2). Secondly, any fitted curve is influenced by the porosity distribution of the sample set, which causes the paired permeability–porosity data to cluster between 10 and 25%. How-ever, our laboratory-derived data (and laboratory data of other

authors) are not hindered by either issue, thus we can determine whether a statistically justifiable crossover value exists. As well as data from this study, the following analysis was performed on compiled data from Mueller (2006), Kolzenburg et al. (2012), Kendrick et al. (2013), Richard et al. (2013), and Heap et al. (2014a).

Although increasing the complexity of a model can yield curves that better fit the data (in the sense that the residual sum of squares S_R^2 is minimised), arbitrarily increasing model complexity without accounting for the increased number of model parameters can yield false relationships or models which cannot be generally applied. With this in mind, we adopt the modified Bayesian Information Criterion approach outlined by Main et al. (1999), which enacts a penalty for each additional parameter introduced into the model. We compare the cases of a one- and two-slope model, respectively.

Herein, $y_i = \gamma(x_i) + \varepsilon_i$, for i = 1, …, n, where y_i is the ith iteration of the variable to be predicted (in this case, $\log_{10}k$), $\gamma(x_i)$ is the predicted value of y_i and a function of x_i, the explanatory variable (in this case $\log_{10}\varphi$), and ε_i is an error term. The residual sum of squares is defined as:

$$S_R^2 = \sum_{i=1}^{n} [y_i - \gamma(x_i)]^2 \tag{3}$$

where n is the sample size. The independent x_i, y_i data pairs are resampled using a bootstrapping procedure, and the position of a potential changepoint x^* is determined by piecewise linear regression. The two cases for determining $\gamma(x_i)$ are as follows:

$$\gamma(x_i) = a_0 + b_0(x_i); p = 3 \tag{4}$$

$$\gamma(x_i) = a_1 + \{b_1 x_i [\forall x_i < x^*]\} + \{x^*(b_1 - b_2) + b_2 x_i [\forall x_i \geq x^*]\}; p = 5 \tag{5}$$

The simple linear case (Eq. (4)) is described by intercept a_0 and slope b_0, while Eq. (5) comprises an intercept a_1, a slope term b_1 for all values below the changepoint x^*, and a slope b_2, corresponding to the slope for all values equal to or greater than x^*. For each model, p is the number of unknown parameters (including the error term).

As in Main et al. (1999), the information criteria for the linear and changepoint models are given by:

$$BIC_R = L(y) - \frac{1}{2} p \ln\left(\frac{n}{2\pi}\right) \tag{6}$$

$$BIC(x^*) = L(y, x^*) - \frac{1}{2} p \ln\left(\frac{n}{2\pi}\right) \tag{7}$$

respectively, where $L(y)$ is the maximised log-likelihood function, given by $-n/2 \ln(S_R^2)$. We find, for the data of this study, that $BIC(x^*) > BIC_R$, for values of x^* to be around 1.14, corresponding to a porosity of around 14% and permeability of around 1.8×10^{-13} m². For our laboratory data, the difference between Eqs. (6) and (7) is greater than 3; typically this analysis is considered robust if $BIC(x^*) - BIC_R \geq 1$.

Despite the fact that the compiled laboratory data were collected using different permeants, under different pressures, and with different experimental setups and methods, a re-examination of these data using the information criterion analysis described above supports the prediction of a changepoint or crossover. Specifically, $BIC(x^*) > BIC_R$ when x^* is close to 1.18 (around 15% porosity). Fig. 9a and b displays the laboratory data of this study and that of other authors, respectively, indicating the model exponents and changepoint locations. The high-porosity exponent for each dataset is remarkably similar (1.7 and 1.5; Fig. 9). While the lower exponents differ somewhat, this difference is greatly exaggerated by the logged x-axis and the fact that low-porosity data are relatively more scarce in the literature. Importantly, this comparison indicates that a changepoint in the permeability–porosity data is not merely an artefact of our selected laboratory samples. The preceding
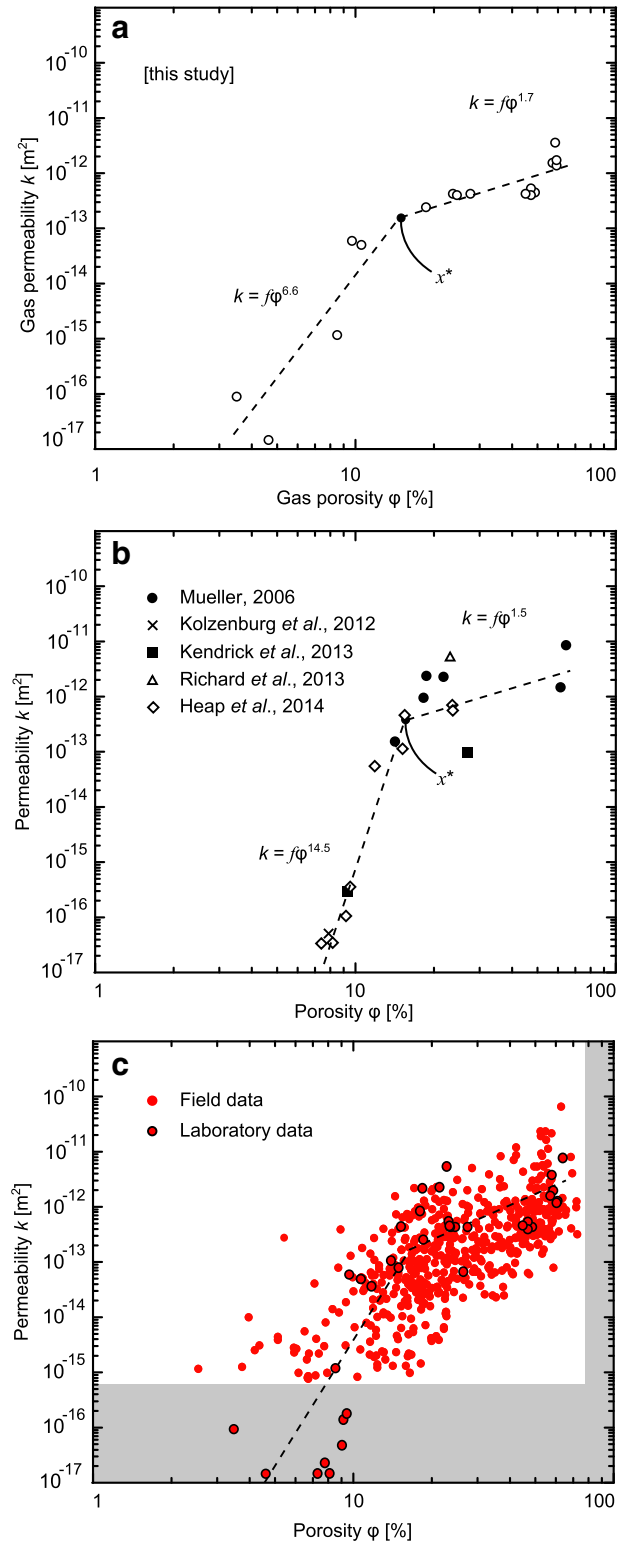
Fig. 9. Microstructural changepoint. Piecewise regression curve fit through the data of this study (a), with the changepoint x^* ~14%. (b) shows compiled Volcán de Colima data from Mueller (2006), Kolzenburg et al. (2012), Kendrick et al. (2013), Richard et al. (2013), and Heap et al. (2014a). Data from Mueller (2006) and Richard et al. (2013) were measured with argon, using the pulse decay method (with an initial pressure differential of 2.5 MPa and 4 MPa, respectively). The Kolzenburg et al. (2012) and Kendrick et al. (2013) data were obtained using water, under a confining pressure of 5 MPa. The data from Heap et al. (2014a) are water permeabilities performed under 2 MPa of confining pressure. The changepoint is maximised at a porosity ~15%. In (c), the field data of this study are overlain with the combined laboratory data of this study and that shown in (b), with a piecewise regression curve derived from the laboratory data ($x^* \approx 16\%$).

analysis is useful as it identifies the porosity (and permeability) where we can expect to observe a significant change in microstructure. The differences discernible between the SEM photomicrographs in Fig. 8a–c (below the changepoint) and Fig. 8d–f (above the changepoint), are congruent with this conclusion: in the former, pathways available for fluid flow consist primarily of microcracks and microporosity. The latter show relatively large subspherical to spherical pores, which could provide relatively less constricted and tortuous pathways for flow. By extension, rocks in the field should largely follow one power-law trend below a porosity around 14–16% (where fluid flow is crack controlled), and another trend above this threshold (where fluid flow is pore controlled). Fig. 9c shows our field data overlain with a relation derived from all of the compiled Volcán de Colima laboratory data ($x^* = 16.2\%$): it can be seen that despite the scatter observed in the field data—and the attendant issues with compiling laboratory data—the permeability–porosity trend is congruent with a changepoint model. In fact, essentially all of the variability between laboratory measurements is encapsulated by the natural variability observed in the field data. While a discrete changepoint x^* is probably an over-simplification of the transition from a low to a high exponent (and vice versa), these data strongly suggest that this model captures a significant component of the microstructural complexity displayed by edifice-forming volcanic rocks. Further, the close agreement between the optimal changepoints determined for our data and compiled data from other authors hints that the changepoint must occur within a relatively small porosity range (i.e. within a few percent of $\varphi = 14\%$).

As discussed by Heap et al. (2014a), the changepoint is likely to represent a critical porosity threshold beneath which fluid transport is dominated by tortuous microcracks. Although the genesis of porosity is initially pre- or syneruptive (i.e. formation porosity), we observe ubiquitous microcracks across the range of collected porosities (i.e. porosity likely formed during emplacement and transport; Fig. 8a, c, d). As a result, the values of permeability measured on edifice-forming rocks are likely to be higher than their pre- or syneruptive permeabilities. In samples with low initial porosity (Fig. 8a–c), fluid flow is restricted largely to these tortuous microcracks. Where the initial porosity is higher (Fig. 8d–f), the cracks serve to link existing porosity. If effective fluid pathways exist, then additional porosity (formed by bubble growth, thermal cracking, or transport processes) has a marginal impact on permeability, explaining why the power-law exponent is lower above the changepoint porosity.

Overall pore connectivity (given by Γ) can be seen to follow two distinct patterns (Fig. 7e) as porosity increases: connectivity increases linearly until the predicted changepoint, after which it plateaus around $\Gamma = 1$. This indicates that any additional porosity below the changepoint serves to connect a correspondingly larger fraction of the pore space. Above around 14% porosity, essentially all porosity is connected to the outside of the sample, and thus constitutes a potential fluid pathway. The permeability is thus little influenced by additional porosity; rather, the effectiveness of pore connections—determined largely by pore apertures—must govern the flow of fluid through the rock.

4. Conclusions

The goal of this combined field and laboratory study was to explore the relationship between porosity and permeability of edifice-forming andesitic rocks at Volcán de Colima, and to identify the likely microstructural controls governing this relationship (given its structural and eruptive characteristics, we assert that Volcán de Colima is typical of many andesitic stratovolcanoes). Our study highlights a wide range of bulk density of samples at Volcán de Colima, suggesting of a wide range of eruptive styles. With increasing distance from the active vent, the measured samples tend towards a skewed density distribution,

as dense, low-porosity rocks typically survive comminution during remobilisation more so than less indurate rocks. The measured densities (between 1142.40 and 2813.79 kg m^{-3}) correspond to porosity values between 2.5 and 73%. Measured field permeabilities are in the range of 10^{-16} to 10^{-11} m^2, encompassing values significantly greater than those generally assumed for fluid transport in magma, and thus emphasising the importance of host-rock permeability in facilitating outgassing of volatiles and, in turn, governing eruption dynamics. For any given porosity we observe a permeability range of up to four orders of magnitude, which can be partially explained by natural variability in microstructural attributes (pore geometries and pore connectivity). This range of stochasticity is little affected by meso-scale textural differences, oxidation, or alteration, although the bubble elongation associated with scoracious deposits fosters the largest degree of scatter. In the laboratory, permeabilities as low as 9.5×10^{-17} m^2 were measured, corresponding to low porosities (≤5%) and high internal surface areas. Microstructural analysis reveals that high surface areas are associated with an inter-microlite microporosity, which does not appear to significantly increase porosity or pore connectivity, resulting in underestimation of fluid pathway tortuosities. We observe that low porosity samples are dominated by tortuous microcracks, whereas highly-porous samples contain large interconnected pores. Consistently low calculated tortuosity values highlight that the Kozeny–Carman relation is a poor predictor of connectivity and cannot adequately capture the microstructural complexity of volcanic rocks. The ratio of total and unconnected porosity Γ comprises a useful proxy for determining the overall connectivity of a sample, although it does not describe the efficiency of fluid flow through pore networks. The relationship of permeability to connected porosity was observed to follow two distinct power-law trends: a threshold in connected porosity was identified at approximately 14% using piecewise regression and Bayesian Information Criterion analyses. At this changepoint, we assume that the permeable network of these volcanic rocks becomes pore-dominated rather than microcrack-dominated. The changepoint is congruent with a change in the relation between Γ and connected porosity. The improved connectivity of fluid pathways above ~14–16% is manifest in a reduced exponent in the power-law relation between permeability and porosity. While the supposition that this exponent changes at a distinct changepoint is a simplification, we find that it describes well our permeability trend, as well as data from previous studies. A firmer understanding of the microstructural attributes and physical properties controlling permeability is important for the long-term goal of understanding volcanic outgassing and the attendant controls on the frequent transition between effusive and explosive behaviour characteristic of many active andesitic volcanoes.

Appendix A

The field permeameter used in this study was the TinyPerm II, developed by New England Research, Inc. and Vindum Engineering, Inc. The

unit comprises a nozzle and chamber attached to a volume syringe with a plunger. An absolute air pressure transducer is housed near the nozzle, and a volume transducer situated within the syringe. To use the permeameter, the nozzle is pressed against a rock surface, then the plunger is depressed, evacuating air from the sample. The sample at ambient pressure is thus subjected to a pressure profile as air is drawn from the rock; this pressure differential returns to ambient after some time interval, dependent on the permeability of the rock. A microcontroller unit records the absolute pressure at the nozzle-rock interface, while monitoring the internal syringe volume and computing the response function of the pressure transient. The underlying semi-empirical theory is described fully in Brown and Smith (2013). Note that this permeameter uses atmospheric air as a permeant, rather than a truly inert fluid as would be used in laboratory measurements.

The resultant value, here called $\dot{k}$, is displayed onscreen, and corresponds to Darcian permeability such that $\dot{k} = (-0.8206 \log_{10}(k) + 12.8737)$. In order to convert $\dot{k}$ into SI units, we rearrange such that

$$k = \frac{10^{\left((\dot{k}-12.8737)/-0.8206\right)}}{9.869233 \times 10^{10}} \tag{A1}$$

in m^2.

To test the accuracy and repeatability of the field permeameter, we performed a suite of permeability measurements on sedimentary samples for comparison with laboratory-derived permeability measurements. Blocks of eight sedimentary rocks were cored and a cylindrical sample obtained, nominally 40 mm long and 20 mm in diameter. Gas permeability was measured on these cores using the benchtop steady-state gas permeameter described in the main body of the text. TinyPerm measurements were performed on each of the blocks, parallel to the coring direction. Each block was measured at five or more points, with ten measurements performed at each point. The measured rocks are Bentheim Main (MA) and Basis (BA) sandstone, Bleurswiller sandstone (BWS), Monti Climiti limestone (MCL), Boise sandstone (BO), Darley Dale sandstone (DD), Leitha limestone (L41), and Saint Maximin limestone (SML); physical properties are given in Table A1. These well-studied materials were chosen for this assessment as they exhibit notable homogeneity in their microstructure and pore size distribution; we

Fig. A2. Comparison of field based whole-clast permeability–porosity measurements and laboratory core measurements.

can thus be confident that a core sample derived from one of these blocks will represent the physical properties of the block as a whole. Notably, the steady-state method yielded results that were consistently within one standard deviation of the mean TinyPerm value. Fig. A1 compares the steady-state permeability measured on cored cylinders with the range of values determined with the TinyPerm unit. When obtaining cores from volcanic rocks that are highly heterogeneous in their pore size distribution, we observe that the measured porosity (and by extension, permeability) can differ from the bulk clast values, as shown in Fig. A2. Notably, despite these differences, the overall permeability–porosity trend, as discussed in the text, remains the same.

Repeatability of results from the TinyPerm unit was found to be high, measurements on the same point (i.e. A, B, C, D, E) always being within one order of magnitude, and generally less than 20% either side of mean. Data are given in Table A2.

Two main issues were identified when using the TinyPerm to measure volcanic rock samples. Firstly, obtaining accurate and precise measurements depends on creating an airtight contact between the permeameter nozzle and the sample surface. If the rock surface is non-ideal, then leakage of air into the permeameter chamber can result in over an order of magnitude error in measurements. To preclude this we use a malleable putty on the end of the nozzle (as suggested by the manufacturer) to seal the nozzle to the sample. With sufficient pressure against the sample, use of the putty seal was effective in preventing the premature decay of the pressure gradient. Secondly, the maximum $\dot{k}$ value observable on the microcontroller display is 13, corresponding

Fig. A1. Box-and-whisker distribution of TinyPerm permeability measurements. Central horizontal line of each box represents the mean measured value. Outliers are shown as circles. Crosses show the results of benchtop steady-state measurements for each sample. The measured rocks were Bentheim Main (MA) and Basis (BA) sandstone, Bleurswiller sandstone (BWS), Monti Climiti limestone (MCL), Boise sandstone (BO), Darley Dale sandstone (DD), Leitha limestone (L41), and Saint Maximin limestone (SML).

Table A1
Laboratory physical property data (porosity and permeability) for cores of selected sedimentary rocks, alongside TinyPerm results from blocks.

Sample	Gas porosity [%]	Gas permeability [m^2]	Mean TinyPerm permeability [m^2]	TinyPerm standard deviation
MA	22.96	3.72×10^{-13}	3.34×10^{-13}	6.65×10^{-14}
BWS	25.78	2.85×10^{-13}	3.47×10^{-13}	1.09×10^{-13}
MCL	28.53	1.70×10^{-13}	1.58×10^{-13}	5.94×10^{-14}
BO	26.00	8.65×10^{-13}	7.26×10^{-13}	2.5×10^{-13}
DD	17.07	2.11×10^{-14}	2.49×10^{-14}	6.78×10^{-15}
L41	24.32	4.47×10^{-13}	5.01×10^{-13}	4.71×10^{-13}
SML	37.82	5.50×10^{-13}	4.26×10^{-13}	1.49×10^{-13}
BA	24.05	4.09×10^{-13}	3.45×10^{-12}	6.02×10^{-13}

Table A2
Full table of (transformed) results from permeability measurements on sedimentary blocks. A, B, C, D, and E represent five randomly selected points on the surface of each block, whereat ten repeat measurements were made.

| Measurement	Sample							
	MCL	DD	SML	L41	MA	BA	BWS	BO
A1	1.05×10^{-13}	4.53×10^{-14}	4.04×10^{-13}	7.72×10^{-14}	2.58×10^{-13}	3.71×10^{-12}	3.14×10^{-13}	6.89×10^{-13}
A2	1.35×10^{-13}	4.16×10^{-14}	3.93×10^{-13}	1.84×10^{-13}	4.28×10^{-13}	3.82×10^{-12}	3.14×10^{-13}	7.71×10^{-13}
A3	1.32×10^{-13}	3.33×10^{-14}	5.2×10^{-13}	2.06×10^{-13}	3.05×10^{-13}	3.92×10^{-12}	2.73×10^{-13}	7.71×10^{-13}
A4	1.18×10^{-13}	2.81×10^{-14}	2.81×10^{-13}	1.47×10^{-13}	3.14×10^{-13}	3.82×10^{-12}	2.73×10^{-13}	8.38×10^{-13}
A5	1.43×10^{-13}	3.06×10^{-14}	4.16×10^{-13}	2.81×10^{-13}	2.73×10^{-13}	4.27×10^{-12}	2.81×10^{-13}	8.87×10^{-13}
A6	1.24×10^{-13}	2.44×10^{-14}	4.04×10^{-13}	2.97×10^{-13}	3.61×10^{-13}	2.58×10^{-12}	2.89×10^{-13}	9.12×10^{-13}
A7	1.32×10^{-13}	3.06×10^{-14}	3.32×10^{-13}	2.81×10^{-13}	3.23×10^{-13}	2.65×10^{-12}	2.65×10^{-13}	5.99×10^{-13}
A8	1.32×10^{-13}	2.89×10^{-14}	4.52×10^{-13}	1.9×10^{-13}	3.82×10^{-13}	2.96×10^{-12}	2.44×10^{-13}	5.5×10^{-13}
A9	1.65×10^{-13}	2.58×10^{-14}	3.93×10^{-13}	2.51×10^{-13}	4.04×10^{-13}	2.88×10^{-12}	2.81×10^{-13}	7.09×10^{-13}
A10	2.51×10^{-13}	4.53×10^{-14}	4.52×10^{-13}	2.18×10^{-13}	3.93×10^{-13}	2.96×10^{-12}	3.14×10^{-13}	6.33×10^{-13}
B1	1.24×10^{-13}	2.06×10^{-14}	3.82×10^{-13}	2.58×10^{-14}	2.89×10^{-13}	4.91×10^{-12}	3.14×10^{-13}	7.49×10^{-13}
B2	3.93×10^{-13}	1.47×10^{-14}	4.52×10^{-13}	4.28×10^{-14}	2.89×10^{-13}	4.04×10^{-12}	2.97×10^{-13}	6.7×10^{-13}
B3	1.43×10^{-13}	1.9×10^{-14}	5.2×10^{-13}	3.15×10^{-14}	3.72×10^{-13}	4.51×10^{-12}	2.89×10^{-13}	8.87×10^{-13}
B4	2.06×10^{-13}	2.44×10^{-14}	3.05×10^{-13}	5.21×10^{-14}	3.14×10^{-13}	4.51×10^{-12}	2.81×10^{-13}	9.38×10^{-13}
B5	1.79×10^{-13}	2.18×10^{-14}	3.32×10^{-13}	5.83×10^{-14}	3.32×10^{-13}	4.78×10^{-12}	2.73×10^{-13}	6.89×10^{-13}
B6	1.6×10^{-13}	2.25×10^{-14}	3.72×10^{-13}	1.95×10^{-13}	2.89×10^{-13}	3.82×10^{-12}	2.37×10^{-13}	7.71×10^{-13}
B7	1.95×10^{-13}	1.95×10^{-14}	3.14×10^{-13}	8.88×10^{-14}	3.05×10^{-13}	3.82×10^{-12}	2.73×10^{-13}	7.09×10^{-13}
B8	1.9×10^{-13}	1.9×10^{-14}	3.23×10^{-13}	5.67×10^{-14}	3.23×10^{-13}	3.92×10^{-12}	2.81×10^{-13}	8.62×10^{-13}
B9	1.79×10^{-13}	1.9×10^{-14}	3.42×10^{-13}	5.21×10^{-14}	3.05×10^{-13}	4.04×10^{-12}	2.65×10^{-13}	9.38×10^{-13}
B10	1.74×10^{-13}	1.85×10^{-14}	3.93×10^{-13}	5.67×10^{-14}	2.97×10^{-13}	4.78×10^{-12}	2.89×10^{-13}	8.38×10^{-13}
C1	1.05×10^{-13}	1.32×10^{-14}	2.31×10^{-13}	1.11×10^{-12}	2.97×10^{-13}	3.71×10^{-12}	3.32×10^{-13}	3.93×10^{-13}
C2	1.74×10^{-13}	1.7×10^{-14}	3.05×10^{-13}	1.28×10^{-12}	3.72×10^{-13}	2.96×10^{-12}	3.23×10^{-13}	3.51×10^{-13}
C3	1.74×10^{-13}	2.12×10^{-14}	3.23×10^{-13}	1.28×10^{-12}	4.4×10^{-13}	2.96×10^{-12}	3.32×10^{-13}	3.82×10^{-13}
C4	1.35×10^{-13}	2.18×10^{-14}	3.05×10^{-13}	1.28×10^{-12}	3.32×10^{-13}	3.51×10^{-12}	2.51×10^{-13}	3.42×10^{-13}
C5	1.08×10^{-13}	2.58×10^{-14}	2.81×10^{-13}	1.02×10^{-12}	2.97×10^{-13}	3.41×10^{-12}	3.61×10^{-13}	3.82×10^{-13}
C6	1.32×10^{-13}	$2.44 \times 10_{-14}$	1.79×10^{-13}	9.38×10^{-13}	2.65×10^{-13}	3.13×10^{-12}	3.72×10^{-13}	4.16×10^{-13}
C7	1.43×10^{-13}	2.18×10^{-14}	2.24×10^{-13}	1.21×10^{-12}	3.42×10^{-13}	3.71×10^{-12}	8.62×10^{-13}	4.04×10^{-13}
C8	2.73×10^{-13}	2.01×10^{-14}	2.31×10^{-13}	1.21×10^{-12}	3.51×10^{-13}	2.65×10^{-12}	3.32×10^{-13}	4.78×10^{-13}
C9	1.32×10^{-13}	2.18×10^{-14}	3.32×10^{-13}	1.14×10^{-12}	4.4×10^{-13}	2.58×10^{-12}	3.61×10^{-13}	4.28×10^{-13}
C10	1.05×10^{-13}	2.01×10^{-14}	5.66×10^{-13}	1.17×10^{-12}	3.61×10^{-13}	3.22×10^{-12}	3.51×10^{-13}	4.28×10^{-13}
D1	1.47×10^{-13}	2.73×10^{-14}	5.99×10^{-13}	1.08×10^{-13}	3.72×10^{-13}	3.32×10^{-12}	5.66×10^{-13}	1.14×10^{-12}
D2	1.02×10^{-13}	2.31×10^{-14}	6.51×10^{-13}	1.18×10^{-13}	4.16×10^{-13}	3.13×10^{-12}	5.35×10^{-13}	1.08×10^{-12}
D3	1.39×10^{-13}	2.89×10^{-14}	5.5×10^{-13}	1.35×10^{-13}	4.28×10^{-13}	3.82×10^{-12}	4.4×10^{-13}	1.31×10^{-12}
D4	1.24×10^{-13}	3.33×10^{-14}	6.16×10^{-13}	5.67×10^{-14}	5.06×10^{-13}	3.13×10^{-12}	4.78×10^{-13}	1.11×10^{-12}
D5	1.35×10^{-13}	2.81×10^{-14}	7.49×10^{-13}	1.51×10^{-13}	4.28×10^{-13}	3.22×10^{-12}	4.92×10^{-13}	1.08×10^{-12}
D6	1.32×10^{-13}	1.7×10^{-14}	7.09×10^{-13}	9.94×10^{-14}	3.72×10^{-13}	2.8×10^{-12}	4.92×10^{-13}	1.14×10^{-12}
D7	1.56×10^{-13}	2.38×10^{-14}	7.09×10^{-13}	1.18×10^{-13}	3.93×10^{-13}	2.65×10^{-12}	5.35×10^{-13}	1.11×10^{-12}
D8	1.14×10^{-13}	3.06×10^{-14}	7.29×10^{-13}	1.74×10^{-13}	3.32×10^{-13}	2.96×10^{-12}	2.97×10^{-13}	1.02×10^{-12}
D9	1.84×10^{-13}	3.15×10^{-14}	7.09×10^{-13}	6.9×10^{-14}	3.51×10^{-13}	3.13×10^{-12}	4.04×10^{-13}	1.14×10^{-12}
D10	1.69×10^{-13}	1.85×10^{-14}	5.82×10^{-13}	1.84×10^{-13}	4.4×10^{-13}	3.41×10^{-12}	4.16×10^{-13}	9.92×10^{-13}
E1	8.88×10^{-14}	2.31×10^{-14}	5.5×10^{-13}	1.02×10^{-12}	1.84×10^{-13}	3.82×10^{-12}	3.14×10^{-13}	5.2×10^{-13}
E2	2.58×10^{-13}	2.44×10^{-14}	2.44×10^{-13}	9.65×10^{-13}	2.44×10^{-13}	2.96×10^{-12}	2.81×10^{-13}	5.35×10^{-13}
E3	9.94×10^{-14}	2.06×10^{-14}	2.97×10^{-13}	8.87×10^{-13}	2.97×10^{-13}	2.88×10^{-12}	2.97×10^{-13}	5.06×10^{-13}
E4	1.43×10^{-13}	2.81×10^{-14}	2.12×10^{-13}	9.38×10^{-13}	2.51×10^{-13}	3.13×10^{-12}	3.42×10^{-13}	5.66×10^{-13}
E5	9.94×10^{-14}	3.06×10^{-14}	3.72×10^{-13}	1.08×10^{-12}	2.31×10^{-13}	3.61×10^{-12}	3.14×10^{-13}	5.06×10^{-13}
E6	1.51×10^{-13}	2.06×10^{-14}	4.52×10^{-13}	8.38×10^{-13}	2.81×10^{-13}	3.22×10^{-12}	3.23×10^{-13}	5.82×10^{-13}
E7	1.56×10^{-13}	2.51×10^{-14}	4.78×10^{-13}	9.38×10^{-13}	2.18×10^{-13}	3.32×10^{-12}	3.72×10^{-13}	6.16×10^{-13}
E8	1.21×10^{-13}	2.31×10^{-14}	4.16×10^{-13}	8.62×10^{-13}	2.73×10^{-13}	3.22×10^{-12}	3.51×10^{-13}	6.51×10^{-13}
E9	1.56×10^{-13}	2.38×10^{-14}	4.4×10^{-13}	9.38×10^{-13}	3.05×10^{-13}	3.13×10^{-12}	2.89×10^{-13}	6.16×10^{-13}
E10	3.51×10^{-13}	2.51×10^{-14}	4.65×10^{-13}	9.38×10^{-13}	3.42×10^{-13}	2.96×10^{-12}	3.05×10^{-13}	6.7×10^{-13}

to a k of 6.92×10^{-16} m^2. Any and all samples with a permeability $\leq 6.92 \times 10^{-16}$ m^2 are thus indistinguishable; accordingly, a $\dot{k}$ value of 12.99 has been implemented as the limit in our study.

Appendix B

Fig. B1 shows the densities yielded by two methods performed on the sample suite at the Experimental Geophysics laboratory, Strasbourg. The double-weight method is equivalent to that carried out in the field; the second method comprises the volumetric mass density determined by the ratio of the geometric volume and dry mass of a cylindrical sample. As evidenced in Fig. B1, the double-weight values are progressively higher than the geometric values at decreasing densities (i.e. higher porosities). This is a function of the capacity for water imbibition through surface pores over the timescale of each measurement (typically about 5 s); incorporating the parameters of the fitted line into further analyses of density data allows this deviation to be accounted for. Porosity is a direct function of the ratio of bulk and particle densities: the relationship between porosity and volumetric mass density can thus be well constrained, as in Fig. B1b, where the inverse of the absolute value of the slope corresponds to the particle density. The strong linear correlation between these values attests to a relative lack of variation in bulk composition and thus particle density between samples. The correlations described by Fig. B1a and B1b have been encompassed in an empirical relation (Fig. B1c), subsequently used to estimate connected porosity from the initial field density data.
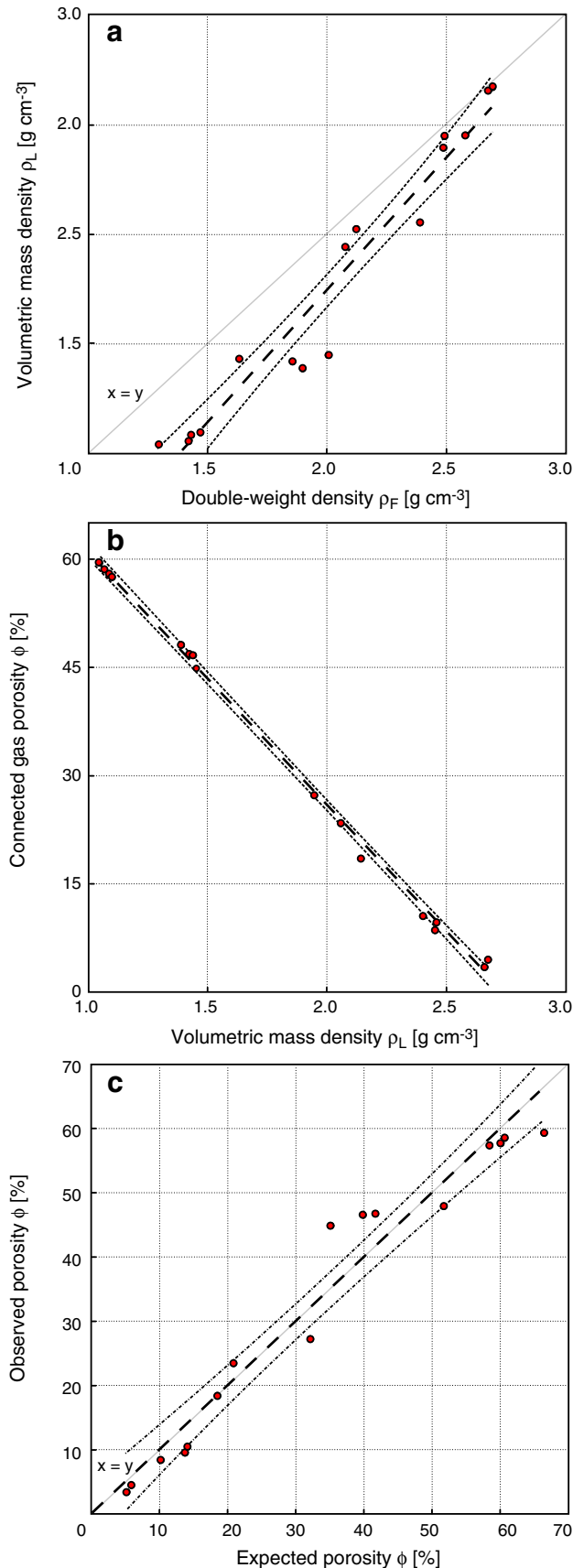
References

Bernabé, Y., Mok, U., Evans, B., 2003. Permeability–porosity relationships in rocks subjected to various evolution processes. Pure Appl. Geophys. 160 (5-6), 937–960.

Bernabé, Y., Li, M., Maineult, A., 2010. Permeability and pore connectivity: a new model based on network simulations. J. Geophys. Res. 155, B10203. http://dx.doi.org/10.1023/2010JB007444.

Bernard, B., Kueppers, U., Ortiz, H., 2015. Revisiting the statistical analysis of pyroclast density and porosity data. Solid Earth Discuss. 7, 1077–1095. http://dx.doi.org/10.5194/sed-7-1077-2015 (2015).

Bernard, M.L, Zamora, M., Géraud, Y., Boudon, G., 2007. Transport properties of pyroclastic rocks from Montagne Pelée volcano (Martinique, Lesser Antilles). Journal of Geophysical Research: Solid Earth (1978–2012) 112 (B5). http://dx.doi.org/10.1029/2006JB004385.

Biggs, J., Mothes, P., Ruiz, M., Amelung, F., Dixon, T.H., Baker, S., Hong, S.H., 2010. Stratovolcano growth by co-eruptive intrusion: the 2008 eruption of Tungurahua Ecuador. Geophys. Res. Lett. 37 (21). http://dx.doi.org/10.1029/2010GL044942.

Blower, J., 2001. Factors controlling permeability–porosity relationships in magma. Bull. Volcanol. 63 (7), 497–504. http://dx.doi.org/10.1007/s004450100172.

Bourbie, T., Zinszner, B., 1985. Hydraulic and acoustic properties as a function of porosity in Fontainebleau sandstone. J. Geophys. Res. Solid Earth (1978–2012) 90 (B13), 11524–11532. http://dx.doi.org/10.1029/JB090iB13p11524.

Bretón-González, M., Ramírez, J.J., Navarro, C., 2002. Summary of the historical eruptive activity of Volcán De Colima, Mexico 1519–2000. J. Volcanol. Geotherm. Res. 117 (1-2), 21–46. http://dx.doi.org/10.1016/S0377-0273(02)00233-0.

Brown, S., Smith, M., 2013. A transient-flow syringe air permeameter. Geophysics 78 (5), D307–D313. http://dx.doi.org/10.1190/geo2012-0534.1.

Camus, G., Gourgaud, A., Mossand-Berthommier, P.C., Vincent, P.M., 2000. Merapi (Central Java, Indonesia): an outline of the structural and magmatological evolution, with a special emphasis to the major pyroclastic events. J. Volcanol. Geotherm. Res. 100 (1), 139–163. http://dx.doi.org/10.1016/S0377-0273(00)00135-9.

Carman, P.C., 1937. Fluid flow through granular beds. Trans. Inst. Chem. Eng. 15, 150–166.

Carrasco-Núñez, G., 2000. Structure and proximal stratigraphy of Citlaltepetl volcano (Pica de Orizaba), Mexico. Cenozoic Tectonics Volcan. Mex. 334, 247. http://dx.doi.org/10.1130/0-8137-2334-5.247.

Cashman, K.V., Mangan, M.T., Newman, S., 1994. Surface degassing and modifications to vesicle size distributions in active basalt flows. J. Volcanol. Geotherm. Res. 61 (1), 45–68. http://dx.doi.org/10.1016/0377-0273(94)00015-8.

Castro, J.M., Bindeman, I.N., Tuffen, H., Schipper, C.I., 2014. Explosive origin of silicic lava: textural and δD–H2O evidence for pyroclastic degassing during rhyolite effusion. Earth Planet. Sci. Lett. 405, 52–61. http://dx.doi.org/10.1016/j.epsl.2014.08.012.

Clarke, A.B., Neri, A., Voight, B., Macedonio, G., Druitt, T.H., 2002a. Computational modelling of the transient dynamics of the August 1997 Vulcanian explosions at Soufriere Hills Volcano, Montserrat: influence of initial conduit conditions on near-vent pyroclastic dispersal. Geol. Soc. Lond. Mem. 21, 319–348.

Clarke, A.B., Voight, B., Neri, A., Macedonio, G., 2002b. Transient dynamics of vulcanian explosions and column collapse. Nature 415 (6874), 897–901. http://dx.doi.org/10.1038/415897a.

Clavaud, J.B., Maineult, A., Zamora, M., Rasolofosaon, P., Schlitter, C., 2008. Permeability anisotropy and its relations with porous medium structure. J. Geophys. Res. Solid Earth (1978–2012) 113 (B1). http://dx.doi.org/10.1029/2007JB005004.

Collinson, A.S.D., Neuberg, J.W., 2012. Gas storage, transport and pressure changes in an evolving permeable volcanic edifice. J. Volcanol. Geotherm. Res. 243, 1–13. http://dx.doi.org/10.1016/j.jvolgeores.2012.06.027.

Costa, A., 2006. Permeability–porosity relationship: a reexamination of the Kozeny–Carman equation based on a fractal pore-space geometry assumption. Geophys. Res. Lett. 33 (2). http://dx.doi.org/10.1029/2005GL025134.

Day, S.J., 1996. Hydrothermal pore fluid and the stability of porous, permeable volcanoes. Q. J. Geol. Soc. Lond. 111, 77–93. http://dx.doi.org/10.1144/GSL.SP.1996.110.01.06.

De Maisonneuve, C.B., Bachmann, O., Burgisser, A., 2009. Characterization of juvenile pyroclasts from the Kos Plateau Tuff (Aegean Arc): insights into the eruptive dynamics of a large rhyolitic eruption. Bulletin of volcanology 71 (6), 643–658. http://dx.doi.org/10.1007/s00445-008-0250-x.

Degruyter, W., Bachmann, O., Burgisser, A., 2010. Controls on magma permeability in the volcanic conduit during the climactic phase of the Kos Plateau Tuff eruption (Aegean Arc). Bulletin of Volcanology 72 (1), 63–74. http://dx.doi.org/10.1007/s00445-009-0302-x.

Edmonds, M., Oppenheimer, C., Pyle, D.M., Herd, R.A., Thompson, G., 2003. SO2 emissions from Soufrière Hills Volcano and their relationship to conduit permeability,

Fig. B1. (a) gives a comparison between density values yielded by the double-weight (field) method ρ_F and the volumetric mass (laboratory) method ρ_L. The deviation from $x = y$ can be described empirically such that $\rho_L = m_A\rho_F + c_A$, [$R^2 = 0.95$]. Thin dashed lines represent the upper and lower 95% confidence intervals (CI) around the fit line (thick dashed line). In (b), connected gas porosity φ as measured by helium pycnometry is shown against volumetric mass density for andesite cores. The relationship is of the form $\varphi = m_B\,\rho_L + c_B$, [$R^2 = 1.00$]. Thin dashed lines represent the upper and lower 95% confidence intervals (CI) around the fit line (thick dashed line). (c) shows the results of semi-empirical transformation of double-weight core density measurements (Expected) against measured gas porosity (Observed) described by the dashed line [$R^2 = 0.99$]. Transformation is of the form $\varphi = \alpha[m_B(m_A\rho_L + c_A) + c_B]$, where m_A, c_A, m_B and, c_B are fit components from (a) and (b). The coefficient α is an empirical constant close to 1. Grey line describes Observed = Expected porosity. (For interpretation of the references to colour in this figure legend, the reader is referred to the web version of this article.)

hydrothermal interaction and outgassing regime. J. Volcanol. Geotherm. Res. 124, 23–43. http://dx.doi.org/10.1016/S0377-0273(03)00041-6.

Eichelberger, J.C., Carrigan, C.R., Westrich, H.R., Price, R.H., 1986. Non-explosive silicic volcanism. Nature 323 (6089), 598–602. http://dx.doi.org/10.1038/323598a0.

Gamble, J.A., Wood, C.P., Price, R.C., Smith, I.E.M., Stewart, R.B., Waight, T., 1999. A fifty year perspective of magmatic evolution on Ruapehu Volcano, New Zealand: verification of open system behaviour in an arc volcano. Earth Planet. Sci. Lett. 170 (3), 301–314. http://dx.doi.org/10.1016/S0012-821X(99)00106-5.

Gardeweg, M.C., Sparks, R.S.J., Matthews, S.J., 1998. Evolution of Lascar volcano, northern Chile. J. Geol. Soc. 155 (1), 89–104. http://dx.doi.org/10.1144/gsjgs.155.1.0089.

Gaunt, H.E., Sammonds, P.R., Meredith, P.G., Smith, R., Pallister, J.S., 2014. Pathways for degassing during the lava dome eruption of Mount St. Helens 2004–2008. Geology 42 (11), 947–950. http://dx.doi.org/10.1130/G35940.1.

Gaylord, D.R., Neall, V.E., 2012. Subedifice collapse of an andesitic stratovolcano: the Maitahi Formation, Taranaki Peninsula, New Zealand. Geol. Soc. Am. Bull. 124 (1-2), 181–199. http://dx.doi.org/10.1130/B30141.1.

Gonnermann, H.M., Manga, M., 2003. Explosive volcanism may not be an inevitable consequence of magma fragmentation. Nature 426 (6965), 432–435. http://dx.doi.org/10.1038/nature02138.

Gonnermann, H.M., Manga, M., 2007. The fluid mechanics inside a volcano. Annu. Rev. Fluid Mech. 39, 321–356. http://dx.doi.org/10.1146/annurev.fluid.39.050905.110207.

Gudmundsson, A., 2012. Magma chambers: formation, local stresses, excess pressures, and compartments. J. Volcanol. Geotherm. Res. 237, 19–41. http://dx.doi.org/10.1016/j.jvolgeores.2012.05.015.

Guéguen, Y., Palciauskas, V., 1994. Introduction to the Physics of Rocks. Princeton University Press, UK.

Hatton, C.G., Main, I.G., Meredith, P.G., 1994. Non-universal scaling of fracture length and opening displacement. Nature 367 (6459), 160–162. http://dx.doi.org/10.1038/367160a0.

Heap, M.J., Lavallée, Y., Petrakova, L., Baud, P., Reuschlé, T., Varley, N.R., Dingwell, D.B., 2014a. Microstructural controls on the physical and mechanical properties of edifice-forming andesites at Volcán de Colima, Mexico. J. Geophys. Res. Solid Earth 119. http://dx.doi.org/10.1002/2013JB010521.

Heap, M.J., Kolzenburg, S., Russell, J.K., Campbell, M.E., Welles, J., Farquharson, J.I., Ryan, A., 2014b. Conditions and timescales for welding block-and-ash flow deposits. J. Volcanol. Geotherm. Res. 289, 202–209. http://dx.doi.org/10.1016/j.jvolgeores.2014.11.010.

Heap, M.J., Farquharson, Y., Baud, P., Lavallée, Y., Reuschlé, T., 2015. Fracture and compaction of andesite in a volcanic edifice. Bull. Volcanol. (submitted for publication).

Houghton, B.F., Latter, J.H., Hackett, W.R., 1987. Volcanic hazard assessment for Ruapehu composite volcano, Taupo volcanic zone, New Zealand. Bull. Volcanol. 49 (6), 737–751. http://dx.doi.org/10.1007/BF01079825.

Invernizzi, C., Pierantoni, P.P., Chiodi, A., Maffucci, R., Corrado, S., Baez, W., Viramonte, J., 2014. Preliminary assessment of the geothermal potential of Rosario de la Frontera area (Salta, NW Argentina): insight from hydro-geological, hydro-geochemical and structural investigations. J. S. Am. Earth Sci. 54, 20–36. http://dx.doi.org/10.1016/j.jsames.2014.04.003.

James, M.R., Varley, N., 2012. Identification of structural controls in an active lava dome with high resolution DEMs: Volcán de Colima, Mexico. Geophys. Res. Lett. 39, L22303. http://dx.doi.org/10.1029/2012GL054245.

Jaupart, C., 1998. Gas loss from magmas through conduit walls during eruption. J. Geol. Soc. 145, 73–90. http://dx.doi.org/10.1144/GSL.SP.1996.145.01.05.

John, D.A., Sisson, T.W., Breit, G.N., Rye, R.O., Vallance, J.W., 2008. Characteristics, extent and origin of hydrothermal alteration at Mount Rainier Volcano, Cascades Arc, USA: implications for debris-flow hazards and mineral deposits. J. Volcanol. Geotherm. Res. 175 (3), 289–314. http://dx.doi.org/10.1016/j.jvolgeores.2008.04.004.

Kendrick, J.E., Lavallée, Y., Hess, K.U., Heap, M.J., Gaunt, H.E., Meredith, P.G., Dingwell, D.B., 2013. Tracking the permeable porous network during strain-dependent magmatic flow. J. Volcanol. Geotherm. Res. 260, 117–126. http://dx.doi.org/10.1016/j.jvolgeores.2013.05.012.

Klug, C., Cashman, K.V., 1996. Permeability development in vesiculating magmas: implications for fragmentation. Bull. Volcanol. 58 (2-3), 87–100. http://dx.doi.org/10.1007/s004450050012.

Klug, C., Cashman, K., Bacon, C., 2002. Structure and physical characteristics of pumice from the climactic eruption of Mount Mazama (Crater Lake). Or. Bull. Volcanol. 64 (7), 486–501. http://dx.doi.org/10.1007/s00445-002-0230-5.

Kolzenburg, S., Heap, M.J., Lavallée, Y., Russell, J.K., Meredith, P.G., Dingwell, D.B., 2012. Strength and permeability recovery of tuffisite-bearing andesite. Solid Earth 3 (2), 191–198. http://dx.doi.org/10.5194/se-3-191-2012.

Kozeny, J., 1927. Über kapillare Leitung des Wassers im Boden:(Aufstieg, Versickerung und Anwendung auf die Bewässerung). Hölder-Pichler-Tempsky.

Kueppers, U., Scheu, B., Spieler, O., Dingwell, D.B., 2005. Field-based density measurements as tool to identify preeruption dome structure: set-up and first results from Unzen volcano, Japan. J. Volcanol. Geotherm. Res. 141 (1), 65–75. http://dx.doi.org/10.1016/j.jvolgeores.2004.09.005.

Kueppers, U., Putz, C., Spieler, O., Dingwell, D.B., 2012. Abrasion in pyroclastic density currents: insights from tumbling experiments. Phys. Chem. Earth A B C 45, 33–39. http://dx.doi.org/10.1016/j.pce.2011.09.002.

Lacey, A., Ockendon, J.R., Turcotte, D.L., 1981. On the geometrical form of volcanoes. Earth Planet. Sci. Lett. 54 (1), 139–143. http://dx.doi.org/10.1016/0012-821X(81)90074-1.

Lavallée, Y., Varley, N.R., Alatorre-Ibargüengoitia, M.A., Hess, K.U., Kueppers, U., Mueller, S., Richard, D., Scheu, B., Spieler, O., Dingwell, D.B., 2012. Magmatic architecture of dome building eruptions at Volcán de Colima, Mexico. Bull. Volcanol. 74, 249–260. http://dx.doi.org/10.1007/s00445-011-0518-4.

Lavallée, Y., Benson, P.M., Heap, M.J., Hess, K.U., Flaws, A., Schillinger, B., Dingwell, D.B., 2013. Reconstructing magma failure and the degassing network of dome-building eruptions. Geology 41 (4), 515–518. http://dx.doi.org/10.1130/G33948.1.

Lev, E., Spiegelman, M., Wysocki, R.J., Karson, J.A., 2012. Investigating lava flow rheology using video analysis and numerical flow models. J. Volcanol. Geotherm. Res. 247–248, 62–73. http://dx.doi.org/10.1016/j.jvolgeores.2012.08.002.

Luhr, J.F., 2002. Petrology and geochemistry of the 1991 and 1998–1999 lava flows from Volcán de Colima, México: implications for the end of the current eruptive cycle. J. Volcanol. Geotherm. Res. 117, 169–194. http://dx.doi.org/10.1016/S0377-0273(02)00243-3.

Main, I.G., Leonard, T., Papasouliotis, O., Hatton, C.G., Meredith, P.G., 1999. One slope or two? Detecting statistically significant breaks of slope in geophysical data, with application to fracture scaling relationships. Geophys. Res. Lett. 26 (18), 2801–2804. http://dx.doi.org/10.1029/1999GL005372.

Manga, M., Patel, A., Dufek, J., 2011. Rounding of pumice clasts during transport: field measurements and laboratory studies. Bull. Volcanol. 73 (3), 321–333. http://dx.doi.org/10.1007/s00445-010-0411-6.

Melnik, O., Sparks, R.S.J., 2002. Dynamics of magma ascent and lava extrusion at Soufrière Hills Volcano, Montserrat. J. Geol. Soc. Lond. Mem. 21 (1), 153–171. http://dx.doi.org/10.1144/GSL.MEM.2002.021.01.07.

Mora, J.C., Macías, J.L., Saucedo, R., Orlando, A., Manetti, P., Vaselli, O., 2002. Petrology of the 1998–2000 products of Volcán de Colima, México. J. Volcanol. Geotherm. Res. 117 (1), 195–212. http://dx.doi.org/10.1016/S0377-0273(02)00244-5.

Mueller, S.P., 2006. Permeability and porosity as constraints on the explosive eruption of magma: laboratory experiments and field investigations. (PhD Thesis). University of Munich, Munich, Germany.

Mueller, S., Melnik, O., Spieler, O., Scheu, B., Dingwell, D.B., 2005. Permeability and degassing of dome lavas undergoing rapid decompression: an experimental determination. Bull. Volcanol. 67 (6), 526–538. http://dx.doi.org/10.1007/s00445-004-0392-4.

Mueller, S., Scheu, B., Kueppers, U., Spieler, O., Richard, D., Dingwell, D.B., 2011. The porosity of pyroclasts as an indicator of volcanic explosivity. J. Volcanol. Geotherm. Res. 203 (3), 168–174. http://dx.doi.org/10.1016/j.jvolgeores.2011.04.006.

Norini, G., Capra, L., Groppelli, G., Agliardi, F., Pola, A., Cortes, A., 2010. Structural architecture of the Colima Volcanic Complex. J. Geophys. Res. Solid Earth (1978–2012) 115 (B12). http://dx.doi.org/10.1029/2010JB007649.

Okumura, S., Sasaki, O., 2014. Permeability reduction of fractured rhyolite in volcanic conduits and its control on eruption cyclicity. Geology 42 (10), 843–846. http://dx.doi.org/10.1130/G35855.1.

Plail, M., Edmonds, M., Humphreys, M., Barclay, J., Herd, R.A., 2014. Geochemical evidence for relict degassing pathways preserved in andesite. Earth Planet. Sci. Lett. 386, 21–33. http://dx.doi.org/10.1016/j.epsl.2013.10.044.

Possemiers, M., Huysmans, M., Peeters, L., Batelaan, O., Dassargues, A., 2012. Relationship between sedimentary features and permeability at different scales in the Brussels Sands. Geol. Belg. 15 (3).

Rabbani, A., Jamshidi, S., 2014. Specific surface and porosity relationship for sandstones for prediction of permeability. Int. J. Rock Mech. Min. Sci. 71, 25–32. http://dx.doi.org/10.1016/j.ijrmms.2014.06.013.

Reid, M.E., 2004. Massive collapse of volcano edifices triggered by hydrothermal pressurization. Geology 32 (5), 373–376. http://dx.doi.org/10.1130/G20300.1.

Reubi, O., Blundy, J., 2008. Assimilation of plutonic roots, formation of high-K 'exotic' melt inclusions and genesis of andesitic magmas at Volcán de Colima, Mexico. J. Petrol. 49 (12), 2221–2243. http://dx.doi.org/10.1093/petrology/egn066.

Richard, D., Scheu, B., Mueller, S.P., Spieler, O., Dingwell, D.B., 2013. Outgassing: influence on speed of magma fragmentation. J. Geophys. Res. Solid Earth 118, 862–877. http://dx.doi.org/10.1002/jgrb.50080.

Robin, C., Camus, G., Gourgaud, A., 1991. Eruptive and magmatic cycles at Fuego de Colima volcano (Mexico). J. Volcanol. Geotherm. Res. 45 (3), 209–225. http://dx.doi.org/10.1016/0377-0273(91)90060-D.

Rodríguez-Elizarrarás, S.R., 1995. Estratigrafía y estructura del Volcán de Colima, México. Rev. Mex. Cienc. Geol. 12, 22–46.

Rose, W.I., Grant, N.K., Hahn, G.A., Lange, I.M., Powell, J.L., Easter, J., Degraff, J.M., 1977. The evolution of Santa Maria volcano, Guatemala. J. Geol. 63–87.

Saar, M.O., Manga, M., 1999. Permeability-porosity relationship in vesicular basalts. Geophys. Res. Lett. 26 (1), 111–114. http://dx.doi.org/10.1029/1998GL900256.

Sahimi, M., 1994. Applications of Percolation Theory. Taylor Francis, London, UK.

Savov, I.P., Luhr, J.F., Navarro-Ochoa, C., 2008. Petrology and geochemistry of lava and ash erupted from Volcán Colima, Mexico, during 1998–2005. J. Volcanol. Geotherm. Res. 174, 241–256. http://dx.doi.org/10.1016/j.jvolgeores.2008.02.007.

Shields, J.K., Mader, H.M., Pistone, M., Caricchi, L., Floess, D., Putlitz, B., 2014. Strain-induced outgassing of three-phase magmas during simple shear. J. Geophys. Res. Solid Earth 119 (9), 6936–6957. http://dx.doi.org/10.1002/2014JB011111.

Smyth, H., Hall, R., Hamilton, J., Kinny, P., 2005. East Java: Cenozoic basins, volcanoes and ancient basement. Indonesian Petroleum Association, Proceedings 30th Annual Convention, pp. 251–266.

Sruoga, P., Rubinstein, N., Hinterwimmer, G., 2004. Porosity and permeability in volcanic rocks: a case study on the Serie Tobífera, South Patagonia, Argentina. J. Volcanol. Geotherm. Res. 132 (1), 31–43. http://dx.doi.org/10.1016/S0377-0273(03)00419-0.

Taisne, B., Jaupart, C., 2008. Magma degassing and intermittent lava dome growth. Geophys. Res. Lett. 35 (20). http://dx.doi.org/10.1029/2008GL035432.

Tait, S., Thomas, R., Gardner, J., Jaupart, C., 1998. Constraints on cooling rates and permeabilities of pumice in an explosive eruption jet from colour and magnetic mineralogy. J. Volcanol. Geotherm. Res. 86 (1), 79–91. http://dx.doi.org/10.1016/S0377-0273(98)00075-4.

Valdez-Moreno, G., Schaaf, P., Macías, J.L., Kusakabe, M., 2006. New Sr–Nd–Pb–O isotope data for Colima volcano and evidence for the nature of the local basement. Geol. Soc. Am. Spec. Pap. 402, 45–63.

Varley, N.R., Taran, Y., 2003. Degassing processes of Popocatépetl and Volcán de Colima, Mexico. Geol. Soc. Lond., Spec. Publ. 213 (1), 263–280. http://dx.doi.org/10.1144/GSL.SP.2003.213.01.16.

Varley, N., Arámbula-Mendoza, R., Sanderson, R., Stevenson, J., 2010. Generation of Vulcanian activity and long-period seismicity at Volcán de Colima, Mexico. J. Volcanol. Geotherm. Res. 198 (1 - 2), 45–56. http://dx.doi.org/10.1016/j.jvolgeores.2010.08.009.

Vignaroli, G., Aldega, L., Balsamo, F., Billi, A., De Benedetti, A.A., De Filippis, L., Rossetti, F., 2014. A way to hydrothermal paroxysm, Colli Albani volcano, Italy. Geol. Soc. Am. Bull. B31139-1 http://dx.doi.org/10.1130/B31139.1.

Wallace, P., Anderson Jr., A.T., 2000. Volatiles in Magmas. In: Sigurdsson, H., Houghton, B., McNutt, S.R., Rymer, H., Stix, J. (Eds.), Encyclopedia of Volcanoes. Academic Press.

Wright, H., Cashman, K.V., Gottesfeld, E.H., Roberts, J.J., 2009. Pore structure of volcanic clasts: measurements of permeability and electrical conductivity. Earth Planet. Sci. Lett. 280 (1), 93–104. http://dx.doi.org/10.1016/j.epsl.2009.01.023.

Wright, H., Roberts, J.J., Cashman, K.V., 2006. Permeability of anisotropic tube pumice: model calculations and measurements. Geophysical research letters 33 (17). http://dx.doi.org/10.1029/2006GL027224.

Yokoyama, T., Takeuchi, S., 2009. Porosimetry of vesicular volcanic products by a water-expulsion method and the relationship of pore characteristics to permeability. J. Geophys. Res. Solid Earth (1978–2012) 114 (B2). http://dx.doi.org/10.1029/2008JB005758.

Zhu, W., Wong, T.F., 1996. Permeability reduction in a dilating rock: network modeling of damage and tortuosity. Geophys. Res. Lett. 23 (22), 3099–3102. http://dx.doi.org/10.1029/96GL03078.

Zhu, W., Baud, P., Wong, T.F., 2010. Micromechanics of cataclastic pore collapse in limestone. Journal of Geophysical Research: Solid Earth (1978–2012) 115 (B4). http://dx.doi.org/10.1029/2009JB006610.

Zhu, W., Baud, P., Vinciguerra, S., Wong, T.F., 2011. Micromechanics of brittle faulting and cataclastic flow in Alban Hills tuff. J. Geophys. Res. Solid Earth (1978–2012) 116 (B6). http://dx.doi.org/10.1029/2010JB008046.

Timescales for permeability reduction and strength recovery in densifying magma

M.J. Heap [a,*], J.I. Farquharson [a], F.B. Wadsworth [b], S. Kolzenburg [c], J.K. Russell [d]

[a] *Géophysique Expérimentale, Institut de Physique de Globe de Strasbourg (UMR 7516 CNRS, Université de Strasbourg/EOST), 5 rue René Descartes, 67084 Strasbourg cedex, France*
[b] *Department for Earth and Environmental Sciences, Ludwig-Maximilians-Universität, Munich, Theresienstr. 41/III, 80333 Munich, Germany*
[c] *Dipartimento di Scienze della Terra, Università degli Studi di Torino, 35 Via Valperga Caluso, 10125, Torino, Italy*
[d] *Volcanology and Petrology Laboratory, Department of Earth and Ocean Sciences, University of British Columbia, Vancouver, V6T 1Z4, Canada*

A B S T R A C T

Transitions between effusive and explosive behaviour are routine for many active volcanoes. The permeability of the system, thought to help regulate eruption style, is likely therefore in a state of constant change. Viscous densification of conduit magma during effusive periods, resulting in physical and textural property modifications, may reduce permeability to that preparatory for an explosive eruption. We present here a study designed to estimate timescales of permeability reduction and strength recovery during viscous magma densification by coupling measurements of permeability and strength (using samples from a suite of variably welded, yet compositionally identical, volcanic deposits) with a rheological model for viscous compaction and a micromechanical model, respectively. Bayesian Information Criterion analysis confirms that our porosity–permeability data are best described by two power laws that intersect at a porosity of 0.155 (the "changepoint" porosity). Above and below this changepoint, the permeability–porosity relationship has a power law exponent of 8.8 and 1.0, respectively. Quantitative pore size analysis and micromechanical modelling highlight that the high exponent above the changepoint is due to the closure of wide ($\sim$200–300 µm) inter-granular flow channels during viscous densification and that, below the changepoint, the fluid pathway is restricted to narrow ($\sim$50 µm) channels. The large number of such narrow channels allows porosity loss without considerable permeability reduction, explaining the switch to a lower exponent. Using these data, our modelling predicts a permeability reduction of four orders of magnitude (for volcanically relevant temperatures and depths) and a strength increase of a factor of six on the order of days to weeks. This discrepancy suggests that, while the viscous densification of conduit magma will inhibit outgassing efficiency over time, the regions of the conduit prone to fracturing, such as the margins, will likely persistently re-fracture and keep the conduit margin permeable. The modelling therefore supports the notion that repeated fracture-healing cycles are responsible for the successive low-magnitude earthquakes associated with silicic dome extrusion. Taken together, our results indicate that the transition from effusive to explosive behaviour may rest on the competition between permeability reduction within the conduit and outgassing through fractures at the conduit margin. If the conditions for explosive behaviour are satisfied, the magma densification clock will be reset and the process will start again. The timescales of permeability reduction and strength recovery presented in this study may aid our understanding of the permeability evolution of conduit margin fractures, magma fracture-healing cycles, surface outgassing cycles, and the timescales required for pore pressure augmentation and the initiation of explosive eruptions.

© 2015 Elsevier B.V. All rights reserved.

1. Introduction

Welding of volcanic materials occurs through the viscous sintering, compaction, and agglutination of melt particles above their glass transition temperature (e.g., Grunder and Russell, 2005). Welding can occur in the absence of an external load through surface relaxation (Vasseur et al., 2013), but can be assisted by the additional stress provided by the mass of any overlying material (e.g., Quane et al., 2009) or by shear strain (e.g., Tuffen et al., 2003; Kolzenburg and Russell, 2014). The prevalence of welding examples in volcanic environments highlights the importance for thor-

* Corresponding author.
  E-mail address: heap@unistra.fr (M.J. Heap).

ough investigation of the influence of viscous densification on magma physical properties. For example, evidence for welding has been observed in pyroclastic deposits (e.g., Wright and Cashman, 2013) including block-and-ash flow deposits (e.g., Michol et al., 2008; Andrews et al., 2014; Heap et al., 2014a), lava spatter (e.g., Mellors and Sparks, 1991), autobreccias in blocky-lavas and dome lavas (e.g., Sparks et al., 1993), autobreccias at the base of rheo-morphic ignimbrites (e.g., Branney et al., 1992), conduit-filling pyroclastic deposits (e.g., Kano et al., 1997; Kolzenburg and Russell, 2014), and rhyolitic dykes and conduits (e.g., Tuffen et al., 2003; Tuffen and Dingwell, 2005; Okumura and Sasaki, 2014). Welding results in densification, modifying the physical and textural properties of the material. Indeed, welding has been shown to increase the density and strength and decrease the porosity and permeability of volcanic materials and analogues (e.g., Quane et al., 2009; Vasseur et al., 2013; Wright and Cashman, 2013; Okumura and Sasaki, 2014; Heap et al., 2014a). Ultimately, the evolution of physical properties can govern the timescales and extent of welding, the potential for rheomorphic flow, and volcanic explosivity. For example, the ease with which magma can outgas, controlled by the permeability of the system, can influence eruption style, magnitude, and frequency (e.g., Eichelberger et al., 1986; Woods and Koyaguchi, 1994). While the majority of laboratory studies considering the relationships between porosity and permeability for volcanic rocks have focussed on the consequence of ascent-driven vesiculation and bubble growth (porosity increase) for magma permeability (e.g., Eichelberger et al., 1986; Klug and Cashman, 1996; Saar and Manga, 1999; Blower, 2001; Rust and Cashman, 2004; Heap et al., 2014b; Farquharson et al., 2015, amongst others), there are comparatively few laboratory investigations that consider the impact of porosity destruction through magma densification (e.g., Wright and Cashman, 2013; Kendrick et al., 2013; Okumura and Sasaki, 2014; Heap et al., 2014a). Between individual explosive events, porous magma residing in a conduit spends a significant portion of time deforming under the mass of the overlying magmatic column at temperatures above the glass transition of the melt phase. During these intervals, a reduction in the magma permeability through viscous densification could lead to the build-up of pore pressure required for the development of an explosive eruption (e.g., Melnik et al., 2005; Diller et al., 2006). Here we report on a coupled experimental and modelling study that aims to better understand the timescales required to reduce permeability and increase strength during viscous magma densification.

2. Materials and methods

2.1. Materials and sample preparation

This study utilises a suite of natural blocks (about $30 \times 30 \times 30$ cm) collected from the variably-welded block-and-ash flow (BAF) deposits that formed following the 2360 B.P. eruption of Mount Meager volcano (part of the Garibaldi Volcanic Belt, the northernmost segment of the Cascade Volcanic Arc of North America; see Michol et al., 2008; Andrews et al., 2014). The BAF deposits—initially >160 m thick—filled and dammed the Lillooet River valley. The densely-welded portions of the deposit are currently exposed in a 100 m rock wall that formed following the collapse of the pyroclastic dam and erosion from the concomitant flood. The clast sizes in the deposits are typically 5–15 cm in diameter, with rare large clasts up to 1 m. The matrix comprises vitric and crystal fragments (and occasional lithics) that are generally less than 1–2 mm in diameter (see Michol et al., 2008 and Andrews et al., 2014 for a full description of the deposit). The welding intensity of these compositionally similar BAF deposits (Stewart, 2002) ranges from incipient (>0.2 porosity) to

Table 1
Whole rock geochemistry (determined by X-ray fluorescence) and glass geochemistry (determined using an electron microprobe) for the materials of this study (data from Stewart, 2002).

Oxide	Whole rock (wt.%)	Glass (wt.%)
SiO_2	67.51	76.41
TiO_2	0.47	0.30
Al_2O_3	15.78	13.11
Fe_2O_3	3.40	1.20
MgO	1.48	0.26
CaO	3.44	1.18
Na_2O	4.60	4.41
K_2O	2.51	3.52
P_2O_5	0.16	–
LOI	0.70	–
Total	100.06	99.38

dense (<0.1 porosity) (Michol et al., 2008; Heap et al., 2014a) and therefore provides the perfect opportunity to study the influence of viscous densification on material physical properties. Typical welding microtextures (e.g., clast elongation/flattening) found within the deposit are described in detail in Michol et al. (2008) and Heap et al. (2014a) (but also provided here as Figs. 3b and 3c). Using field texture maps, Michol et al. (2008) measured the average volumetric and pure shear strain recorded in these BAF deposits to be 42% (highest 92%) and 31% (highest 82%), respectively. We also sampled a fresh (non-oxidised), glassy block from the incipiently welded facies; we anticipate that this material best represents the source material for the BAF deposit. We analysed optical microscope photomicrographs of a sample of this lava using image processing software ImageJ to estimate the average crystal content of our welded materials. We estimated crystal content to be 0.25 (phenocrysts and minor microlites), the remainder of the sample comprising porosity (0.04–0.05) and a glassy groundmass (Fig. 3a). The dominant crystal size within the source material is between 100 and 400 μm, although we note the presence of occasional phenocrysts as large as a couple of mm and minor microlites (<100 μm) (Fig. 3a).

We prepared cylindrical samples, 20 mm in diameter and precision-ground to nominal lengths of 40 mm, from the blocks collected (the welded blocks and the lava block). Due to the size of our experimental samples, cores from the welded blocks were prepared so as to avoid any large (5–15 cm) clasts. Our welded BAF samples therefore contain vitric and crystal fragments (and occasional lithics) that are generally less than 1–2 mm in diameter (as shown in Figs. 3b and 3c; Michol et al., 2008). We further note that, in general, vitric fragments are larger than the crystal fragments (a consequence of the dominant crystal size, 100–400 μm, in the source material). The cores were then vacuum-dried at 40 °C for at least two days prior to measurement and experimentation.

The bulk composition of our materials is dacitic ($SiO_2 =$ 68 wt.%) with a rhyolitic glass groundmass ($SiO_2 = 76$ wt.%); the wt.% of major oxides for both the bulk material and the glass are provided in Table 1 (data from Stewart, 2002).

2.2. Methods

Porosity and permeability were measured for each of the prepared cylindrical cores at the Université de Strasbourg (France). Connected porosity was measured using a helium pycnometer (for brevity, connected porosity will be simply referred to as "porosity" in the remainder of this manuscript). Steady-state gas (nitrogen) permeability was measured under a confining pressure of 1 MPa. Flow rate measurements were taken (using a gas flowmeter) under several pressure gradients (typically from 0.05 to 0.2 MPa) to determine the permeability using Darcy's law, and to assess the need for

the Klinkenberg or Forchheimer correction. Klinkenberg corrections were applied where appropriate, but our flow rates were never high enough to warrant a Forchheimer correction in these materials. Physical property data of five additional samples (25.4 mm in diameter and nominally 50 mm in length) were measured at the University of British Columbia (Canada). Porosity was again determined using helium pycnometry, while permeability (helium) was measured using the pulse decay technique under confining pressures between 2.5 and 15 MPa, corresponding to depths up to 1000 m (estimated using $\sigma = \rho g h$, where ρ is taken as the skeletal density of the lava sample—measured to be 2500 kg m^{-3} using helium pycnometry—multiplied by 0.6, and g as 10 m s^{-2}). To aid our understanding of the progression of microstructural modification during viscous densification, we performed complementary P-wave velocity measurements. P-wave velocity was measured along the axis of the samples under a constant axial stress of 0.3 MPa. Finally, uniaxial compressive strength was measured using a uniaxial compression apparatus under a constant strain rate of 10^{-5} s^{-1}. A displacement transducer (LVDT) monitored the axial shortening of the sample by recording the movement of the axial piston relative to the static baseplate. Measurements of axial shortening were corrected for the elastic deformation of the loading train. A load cell monitored the axial force. Displacement and load were converted to strain and stress using the sample dimensions. The broken samples were then powdered, the density of which (the skeletal density) was used to calculate total porosity. Isolated porosity was simply taken as total porosity minus connected porosity. All physical property measurements were performed under ambient laboratory pressure (with the exception of the permeability measurements), temperature, and humidity.

3. Results

Measured values of permeability, P-wave velocity, and uniaxial compressive strength are plotted as a function of porosity in Fig. 1. A summary of the physical property characterisation is provided in Tables 2, 3, and 4. The data show that, as porosity decreases, permeability decreases (Fig. 1a), and P-wave velocity (Fig. 1b) and strength (Fig. 1c) increase. The highest permeabilities, $\sim 10^{-13}$ m^2, were measured for the most porous welded BAF samples (porosity = 0.25); at the lowest porosity—the lava samples with a porosity of 0.04—values of permeability are about two orders of magnitude lower ($\sim 10^{-15}$ m^2). The decrease in permeability with decreasing porosity is nonlinear. In detail, the permeability decrease with decreasing porosity is large between a porosity of 0.25 to 0.15–0.16, and markedly smaller between porosities of 0.16 and 0.04 (Fig. 1a). By contrast, the increase in P-wave velocity (Fig. 1b) and strength (Fig. 1c) with decreasing porosity are very nearly linear, although a break in slope in the strength data may exist at 0.15–0.16 porosity. P-wave velocity increases from ~ 2.0 km s^{-1} at 0.25 porosity to ~ 3.0 km s^{-1} at a porosity of 0.04. The strength at 0.25 porosity is ~ 15 MPa, which increases to ~ 85 MPa at a porosity of 0.07.

The influence of confining pressure (up to 15 MPa, corresponding to a maximum depth of 1000 m) on the permeability of two welded BAF samples (with initial porosities of 0.172 and 0.195, respectively) and a sample of lava (porosity = 0.047) is presented in Fig. 2. We find that the permeability of the welded BAF samples does not change up to 15 MPa. However, the permeability of the lava sample was reduced from 1×10^{-16} m^2 at 2.5 MPa to 1×10^{-17} m^2 at 15 MPa, a decrease of an order of magnitude.

We find that, although the volume of isolated porosity (which ranges between 0.005 and 0.025; i.e., similar to that measured by Michol et al., 2008) does not systematically vary with connected porosity (Fig. 2b), there is an increase therefore in the proportion of isolated porosity as total porosity decreases.
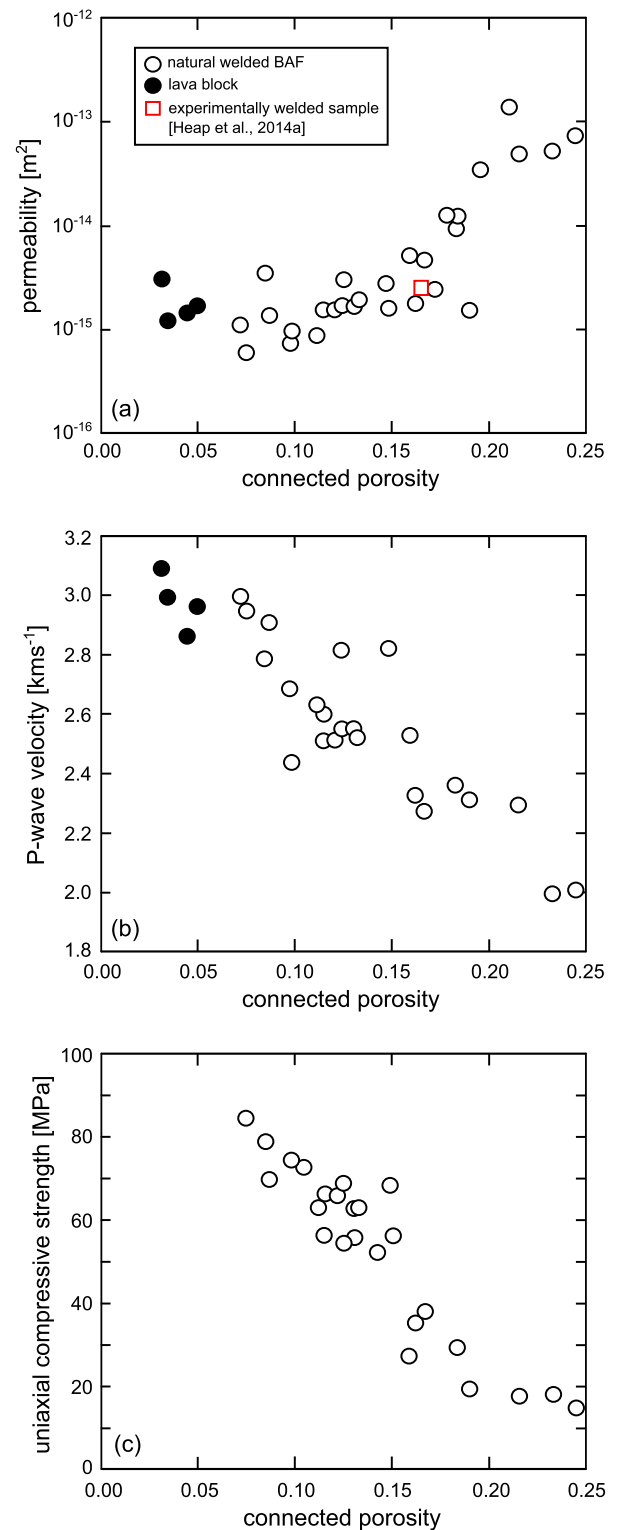

Fig. 1. The impact of viscous densification on physical properties. (a) Permeability as a function of connected porosity. Some of the data (see Tables 2, 3, and 4) are taken from Heap et al. (2014a). (b) P-wave velocity as a function of connected porosity. (c) Uniaxial compressive strength as a function of connected porosity.

4. Discussion

4.1. The evolution of permeability during densification

Previous studies have shown that the permeability of volcanic rock increases nonlinearly as porosity increases (Klug and Cashman, 1996; Saar and Manga, 1999; Rust and Cashman, 2004;

Table 2
Rock physical property summary for the 5 lava samples.

Connected porosity	Total porosity	Isolated porosity	Confining pressure of permeability measurement (MPa)	Permeability (m^2)	P-wave velocity $(km\,s^{-1})$
0.031	0.046	0.015	1	3.08×10^{-15}[a]	3.09
0.034	0.045	0.011	1	1.22×10^{-15}[a]	2.99
0.040	0.054	0.014	2.5	1.09×10^{-16}	–
			5.0	4.74×10^{-17}	
			7.5	2.99×10^{-17}	
			10.0	2.28×10^{-17}	
			14.9	1.17×10^{-17}	
0.044	0.061	0.017	1	1.48×10^{-15}[a]	2.86
0.050	0.063	0.013	1	1.72×10^{-15}[a]	2.96

[a] Datum taken from Heap et al. (2014a).

Table 3
Rock physical property summary for the 20 welded block-and-ash flow samples containing porosities below the changepoint porosity.

Connected porosity	Total porosity	Isolated porosity	Confining pressure of permeability measurement (MPa)	Permeability (m^2)	P-wave velocity $(km\,s^{-1})$	Uniaxial compressive strength (MPa)	Pore size estimated using the model of Sammis and Ashby (1986) (µm)
0.072	0.087	0.015	1	1.11×10^{-15}[a]	2.99	–	–
0.075	0.088	0.013	1	6.14×10^{-16}[a]	2.95	84.6	30
0.085	0.097	0.012	1	3.54×10^{-15}[a]	2.79	79.1	31
0.087	0.099	0.012	1	1.38×10^{-15}[a]	2.91	69.7	39
0.098	0.123	0.025	1	9.81×10^{-16}[a]	2.44	–	–
0.098	0.109	0.011	1	7.67×10^{-16}	2.69	74.3	31
0.104	0.112	0.008	–	–	–	72.4	31
0.111	0.121	0.010	1	8.87×10^{-16}	2.63	63.1	39
0.115	0.125	0.010	1	1.55×10^{-15}	2.60	56.7	47
0.115	0.123	0.008	1	1.57×10^{-15}	2.51	66.0	35
0.121	0.129	0.008	1	1.61×10^{-15}	2.51	65.5	34
0.124	0.133	0.009	1	1.73×10^{-15}	2.81	68.9	30
0.125	0.130	0.005	1	3.11×10^{-15}	2.55	54.4	48
0.130	0.137	0.007	–	–	–	55.6	44
0.130	0.136	0.006	1	1.74×10^{-15}	2.55	62.9	34
0.132	0.138	0.006	1	1.90×10^{-15}	2.52	62.8	34
0.142	0.148	0.004	–	–	–	52.0	47
0.147	0.163	0.016	2.5	2.79×10^{-15}	–	–	–
0.148	0.155	0.007	1	1.58×10^{-15}	2.82	68.3	26
0.150	0.161	0.011	–	–	–	55.6	39

[a] Datum taken from Heap et al. (2014a).

Table 4
Rock physical property summary for the 14 welded block-and-ash flow samples containing porosities above the changepoint porosity.

Connected porosity	Total porosity	Isolated porosity	Confining pressure of permeability measurement (MPa)	Permeability (m^2)	P-wave velocity $(km\,s^{-1})$	Uniaxial compressive strength (MPa)	Pore size estimated using the model of Sammis and Ashby (1986) (µm)
0.165[b]	0.183	0.018	1	2.64×10^{-15}[a]	2.72	–	–
0.159	0.167	0.008	1	5.29×10^{-15}[a]	2.53	27.0	158
0.162	0.181	0.019	1	1.78×10^{-15}[b]	2.32	35.0	93
0.167	0.182	0.015	1	4.65×10^{-15}[a]	2.27	37.6	78
0.172	0.185	0.013	2.6	2.49×10^{-15}	–	–	–
			5.1	2.49×10^{-15}			
			7.5	2.49×10^{-15}			
			10.0	2.51×10^{-15}			
			14.9	2.51×10^{-15}			
0.179	0.197	0.018	2.5	1.26×10^{-14}	–	–	–
0.183	0.187	0.005	1	9.34×10^{-15}[a]	2.36	29.5	118
0.183	0.201	0.018	2.5	1.22×10^{-14}	–	–	–
0.190	0.215	0.025	1	1.53×10^{-15}[a]	2.31	19.6	259
0.195	0.209	0.014	2.5	3.44×10^{-14}	–	–	–
			5.1	3.57×10^{-14}			
			7.5	3.62×10^{-14}			
			10.0	3.36×10^{-14}			
			15.0	3.58×10^{-14}			
0.210	0.211	0.013	2.5	1.41×10^{-13}	–	–	–
0.215	0.234	0.019	1	4.99×10^{-14}[a]	2.29	15.1	280
0.233	0.246	0.013	1	5.29×10^{-14}[a]	2.00	18.2	254
0.244	0.259	0.015	1	7.27×10^{-14}[a]	2.01	15.1	354

[a] Datum taken from Heap et al. (2014a).
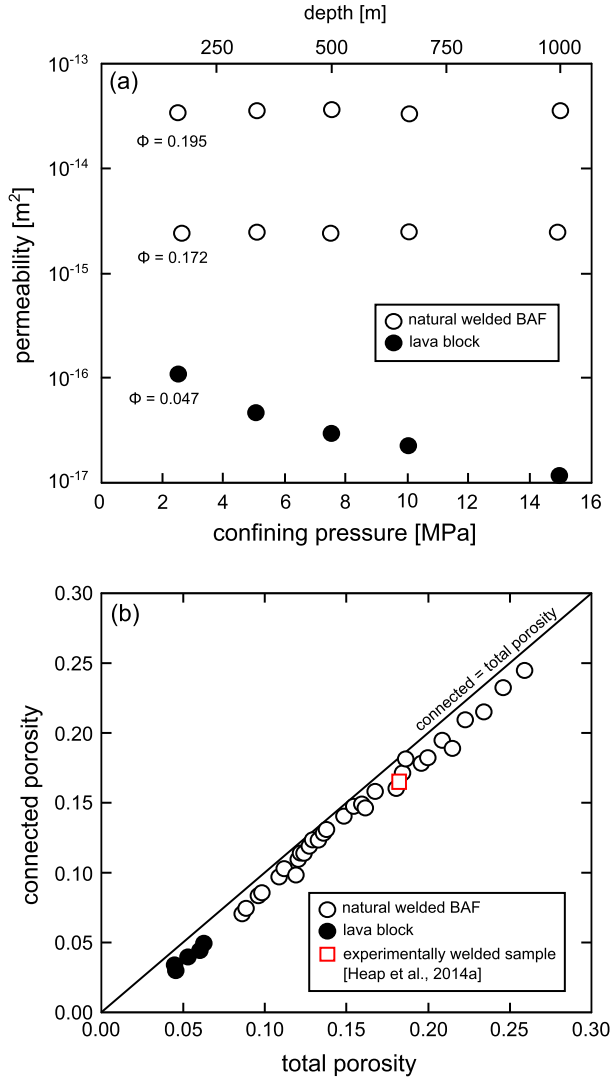[b] Experimentally welded block-and-ash deposit from Heap et al. (2014a).

Fig. 2. (a) Permeability as a function of confining pressure (or depth) for two welded block-and-ash flow samples (connected porosity = 0.172 and 0.195) and a lava sample (connected porosity = 0.047). (b) Connected porosity as a function of total porosity. The black line represents the line of connected = total porosity.

Heap et al., 2014b; Farquharson et al., 2015). While many of these studies describe this relationship with a single power law, a recent study (Farquharson et al., 2015) suggested that the porosity–permeability relationship for volcanic rocks can be described by an empirical changepoint model, whereby the data are described by a certain power law permeability–porosity model until a threshold value of porosity (the porosity changepoint), after which the data are best described by a model with a much lower power law exponent (i.e., the porosity–permeability trend is concave down in log–log space). Our study however concerns the evolution of permeability as porosity decreases during viscous densification, rather than the trend during porosity increasing processes such as vesiculation and bubble growth. Thus, we find a very different relationship where the high and low porosity data are described by a high and low power law exponent, respectively (i.e., the porosity–permeability trend is concave up in log–log space; Figs. 1a and 3f).

Recent studies have demonstrated microstructural modifications, influencing pore connectivity, as a governing factor for permeability reduction during viscous densification (Wright and Cashman, 2013; Kendrick et al., 2013; Okumura and Sasaki, 2014; Heap et al., 2014a). The largest pores and channels are closed, re-

stricting fluid flow to tortuous pathways of flattened "crack-like" pores in melt-dominated materials (Wright and Cashman, 2013) or pores sandwiched between crystals in crystal-bearing materials (Heap et al., 2014a). All studies show that densification reduces permeability (Wright and Cashman, 2013; Kendrick et al., 2013; Okumura and Sasaki, 2014; Heap et al., 2014a). Heap et al. (2014a) speculated that there is an abrupt change in the permeability–porosity power law exponent during viscous densification, due to a sudden change in the pore shape and pore volume connectivity. Here we employ a more rigorous method—a modified Bayesian Information Criterion (BIC) method, as described by Main et al. (1999)—to statistically assess whether the permeability decrease can be best described by one or two discrete power law relationships. This approach determines whether increasing the complexity of a model is statistically justifiable when accounting for the additional unknown parameters. The BIC analysis compares two models: linear and piecewise regressions of log-transformed permeability–porosity data, such that:

$$\gamma(x_i) = a_0 + b_0(x_i), \tag{1}$$

and

$$\gamma(x_i) = a_1 + \left\{ b_1 x_i \left[\forall x_i < x^* \right] \right\} \\ + \left\{ x^*(b_1 - b_2) + b_2 x_i \left[\forall x_i \geq x^* \right] \right\}, \tag{2}$$

where $\gamma(x_i)$ is the predicted value of y_i (log-transformed permeability) as a function of x_i (log-transformed porosity), for each iteration i. The linear case includes the intercept a_0 and a single slope b_0, whereas the piecewise model consists of an intercept a_1, a slope b_1 for all values of x_i below the changepoint x^*, and a slope b_2 pertaining to all values of x_i equal to or greater than x^*. The more complex two-slope model can be statistically justified when BIC(x^*)—the maximised information criterion for Equation (2)—is greater that for Equation (1) (BIC$_R$). We find this to be the case at a changepoint value of $x^* = 1.19$ (equating to a porosity of approximately 0.155), both in terms of the root-mean-square-error and the information criterion analysis (i.e., BIC(x^*) > BIC$_R$). Details on the determination and implementation of these criteria are discussed in Main et al. (1999) and Farquharson et al. (2015). Correspondingly, our data is therefore best described by two power law exponents: 8.8 at porosity values above the changepoint porosity and 1.0 below the changepoint (Fig. 3f).

The appearance of a changepoint as porosity decreases below 0.155 can be explained by the evolution of the microstructure during progressive viscous densification (Fig. 3). Above the changepoint, fluids can utilise pores that are as wide as 200–300 μm (Figs. 3c and 3g). Below the changepoint, however, the microstructure is characterised by the absence of large pores (Fig. 3b); the largest pores are typically about 50 μm (Fig. 3d). This observation is supported by pore size analysis of SEM photomicrographs using image processing software ImageJ. Pore diameters were estimated using the average Feret diameter d_F where $d = 3/2(d_F)$ and d is the estimated pore diameter. These data show that there are many pores with a diameter of 150 μm and higher within the sample above the changepoint (Fig. 3h); below the changepoint, there are considerably fewer pores with a diameter above 150 μm (Fig. 3e). The changepoint therefore presumably represents the porosity at which the wide flow channels are efficiently closed, restricting fluid flow to narrower flow paths. The wide flow channels are closed over a small porosity interval and reduce permeability by two orders of magnitude, yielding the relatively high power law exponent above the changepoint. By contrast, a much lower power law exponent describes the permeability–porosity trend below the changepoint: the large number of narrow channels (Figs. 3b and 3e) must be sufficient to allow continued porosity
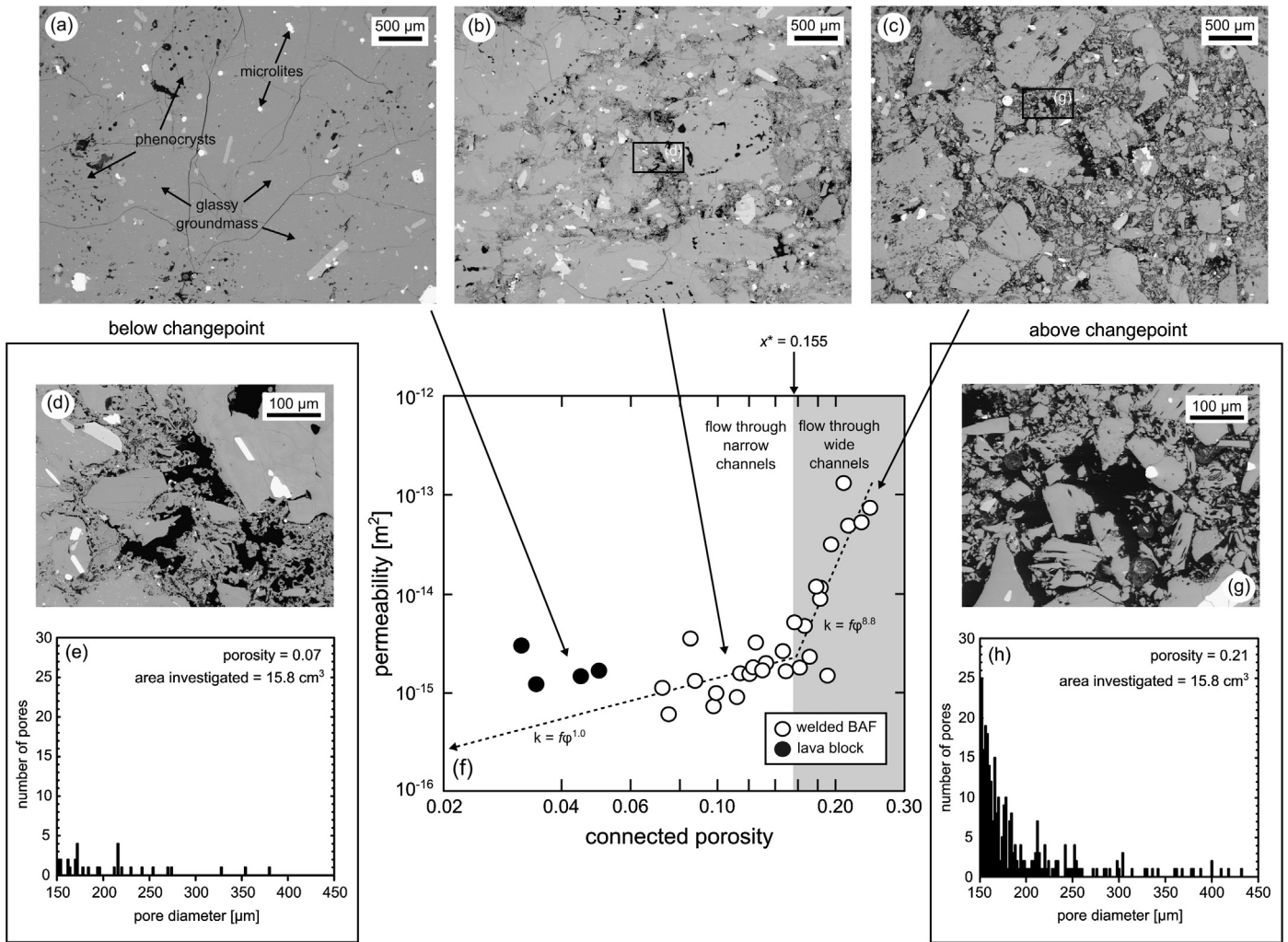
Fig. 3. The evolution of permeability during viscous densification. (a) Back-scattered electron (BSE) photomicrograph of the lava block (the source material). The rock is characterised by phenocrysts (typically 100–400 μm in diameter, but occasionally reaching a couple of mm) within a glassy groundmass containing sparse microlites. (b) BSE photomicrograph of welded block-and-ash flow below the microstructural changepoint. Note that the porosity (in black) is much reduced from the incipiently welded sample in panel (c). We highlight here that the porosity reduction is the result of the sintering and amalgamation of vitric fragments. The largest clast size, where discernible, is on the order of 1–2 mm. (c) BSE photomicrograph of welded block-and-ash flow above the microstructural changepoint. The porosity (in black) is clearly higher than the densely welded sample in panel (b). Many of the vitric shards (up to 1–2 mm in diameter) retain their angular, post-fragmentation shape. (d) BSE photomicrograph showing a zoomed in image of panel (b) to better show the size of the pores below the changepoint. Pores are typically less than 50 μm. (e) Number of pores with a diameter greater than 150 μm within an area of 15.8 cm^2 in the welded block-and-ash flow sample below the microstructural changepoint shown in panel (b). (f) The porosity–permeability data of Fig. 1a with the best-fit slopes provided by the modified Bayesian Information Criterion (BIC) method (see text for details). We provide the relevant power law exponent next to the slopes. The microstructural changepoint (x^*) is also indicated (porosity = 0.155). Above the changepoint fluid flow is assisted by the presence of wide channels (grey zone) and below the changepoint fluid flow is restricted to narrow channels (white zone). (g) BSE photomicrograph showing a zoomed in image of panel (c) to better show the size of the pores above the changepoint. Pores can be as large as 200–300 μm. (h) Number of pores with a diameter greater than 150 μm within an area of 15.8 cm^2 in the welded block-and-ash flow sample above the microstructural changepoint shown in panel (c).

loss without considerable permeability reduction. The permeability of the coherent (i.e., not fragmented and viscously welded) lava samples, not considered in our changepoint analysis, plot above this trend because the connection of the pore network is assisted by a pervasive population of tortuous microcracks (as shown in the SEM photomicrograph of Fig. 3a). This assertion is confirmed by our permeability measurements at elevated pressure (Fig. 2a). When the permeability relies on a network of microcracks, permeability is greatly reduced at low confining pressures due to the ease of microcrack closure at low pressure, a consequence of their high aspect ratio (e.g., Nara et al., 2011). By contrast, the permeability of two welded BAF deposits (porosity 0.172 and 0.195) did not change as the confining pressure increased to 15 MPa (Fig. 2a), indicating that their permeability does not rely on microcracks.

Although the switch from the higher to the lower power law exponent is probably a more gradual transition (e.g., a "change-zone" over a porosity range of 0.14 to 0.17), rather than the discrete changepoint assumed in the model, our data nevertheless show that there exists a microstructurally-controlled break in slope in the permeability–porosity relationship during magma densification. We note that the absolute porosity at which the microstructural changepoint occurs may well be dependent on the initial attributes and textural evolution (e.g., crystal content, grain and crystal size distribution, degree of strain, amongst others) of the granular material during densification. Here therefore we only consider materials with polydisperse grain size distributions; further work is likely required to parameterise the changepoint, or the existence of a changepoint, for different volcanic materials.

The timescales for the viscous densification of volcanic materials have been discussed by several authors (e.g., Quane et al., 2009; Kolzenburg and Russell, 2014; Heap et al., 2014a; Okumura and Sasaki, 2014). The study of Heap et al. (2014a) used the rheological model of Russell and Quane (2005),

$$\Delta t = \frac{\eta_0(1-\phi^i)}{\alpha\sigma}\left[\exp\left(\frac{-\alpha\phi}{1-\phi}\right) - \exp\left(\frac{-\alpha\phi^i}{1-\phi^i}\right)\right], \qquad (3)$$

to estimate densification timescales using data from high temperature viscous welding experiments conducted on disaggregated glassy material from the Mount Meager welded BAF deposit (i.e., the same materials used in the present study). Here η_0 is the effective viscosity of the melt plus crystal cargo at zero porosity (extrapolated from the experimental data of Heap et al., 2014a), α is a dimensionless empirical coefficient (equal to 2, as determined from the experiments of Heap et al., 2014a), σ is the lithostatic (or "magmastatic") stress acting on the deposit, ϕ is the time-dependent porosity, and ϕ^i is the initial porosity of the deposit (taken here to be 0.4, a typical porosity for polydisperse granular materials close to their maximum packing, see Heap et al., 2014a). The applicability of this model for our permeability data is highlighted by the coincidence between the permeability of the natural samples and that of the viscously welded experimental sample used for the determination of η_0 and α (the unfilled square in Figs. 1a and 2b; see Heap et al., 2014a). First, we modelled the porosity loss with time for melt viscosities at three temperatures (800, 900, and 1000 °C; using the temperature dependence of the melt viscosity from Heap et al., 2014a) and a stress of 3.75 MPa (corresponding to a depth of 250 m; estimated as before using $\sigma = \rho gh$) (Fig. 4a). To demonstrate the influence of depth on viscous porosity loss, we provide an additional curve for 800 °C and 750 m. Our permeability data measured at 1 MPa are likely to also represent those at the depths implicated here: we note that the permeability of the welded BAF samples does not decrease up to confining pressures of 15 MPa (corresponding to depths of 1000 m) (Fig. 2a). We find that the rate of porosity decrease is very much dependent on the stress/depth and viscosity/temperature (see also Quane et al., 2009; Kolzenburg and Russell, 2014; Heap et al., 2014a). For example, the time to halve the porosity (i.e., to reach a porosity of 0.2) is 19 and 5 days for temperatures of 800 and 900 °C, respectively (for a depth of 250 m). As depth is increased from 250 to 750 m (at a constant temperature of 800 °C), the time required to reach a porosity of 0.2 is reduced from 19 to 6.5 days. Using these modelled porosity curves, we can plot the time required to densify to the changepoint (i.e., a porosity of 0.155—the porosity at which flow is no longer aided by wide flow channels—corresponding to a permeability of 2.1×10^{-15} m^2) (Fig. 4b). We do this by inserting a constant porosity of 0.155 into Equation (3) and computing the values of Δt for all values of η_0 (which in turn correspond to values of temperature). At a temperature of 900 °C it takes 6 and 2 days to reach the changepoint at depths of 250 and 750 m, respectively (Fig. 4b). In other words, at a starting porosity of 0.4, permeability can be reduced by about four orders of magnitude in timescales from days to weeks. Using the power laws defined by our changepoint model (Fig. 3f), and the modelled evolution of porosity with time (Fig. 4a), we can predict the evolution of permeability with time for different temperatures and depths (Fig. 4c). The rate of permeability decrease is very much dependent on the stress/depth, viscosity/temperature, and time. It takes 24 days at a temperature of 800 °C and a depth of 250 m to reduce the permeability from 1×10^{-11} to 2×10^{-15} m^2 (i.e., the changepoint), but a further 16 days to reduce the permeability by an additional order of magnitude (i.e., to 2×10^{-16} m^2). At 750 m, these times are reduced to 8 and 5 days, respectively (Fig. 4c). These permeability reduction timescales are much larger than those estimated by Okumura and Sasaki (2014) for crystal-free melts (100 to 1000 s), highlighting the significant impact of crystals on permeability reduction timescales, a consequence of their large influence on the effective viscosity (e.g., Andrews et al., 2014; Heap et al., 2014a).
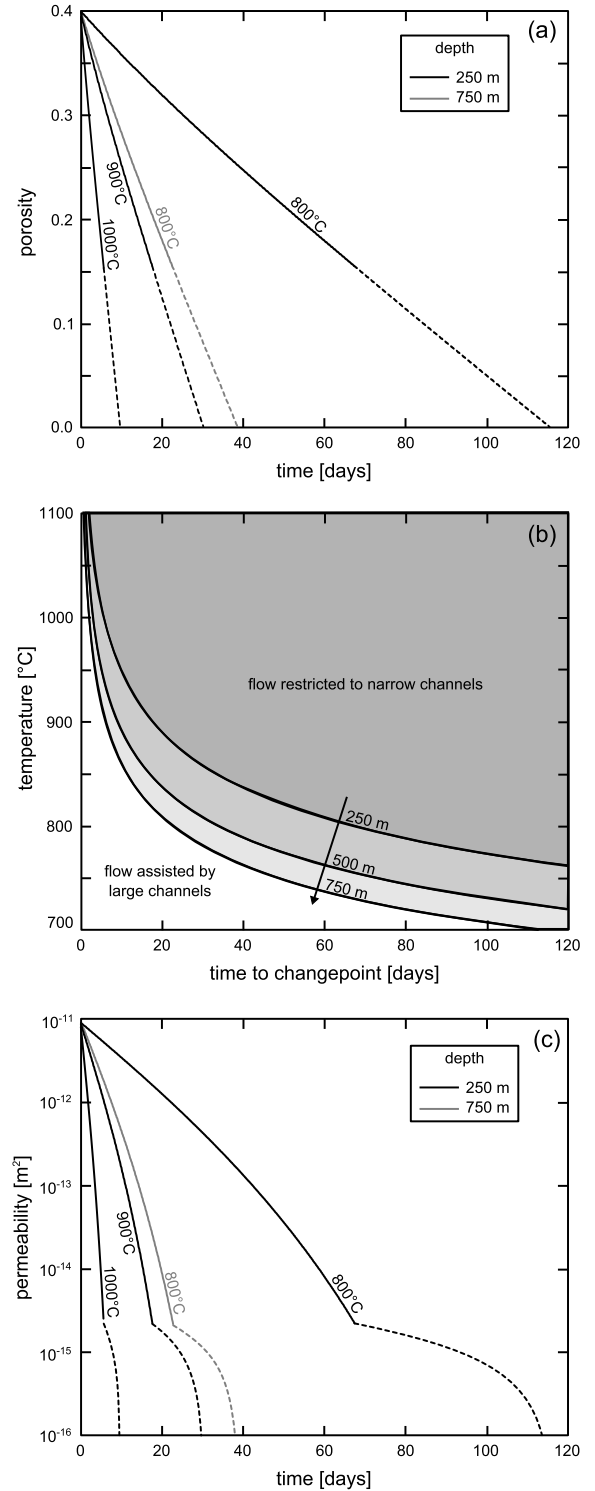

Fig. 4. (a) Compaction timescales. Modelled porosity-time curves using the rheological model of Russell and Quane (2005) (Equation (3)) for melt viscosities at three temperatures (800, 900, and 1000 °C) and lithostatic stresses of 3.75 and 11.25 MPa (depths corresponding to 250 and 750 m, respectively; see text for details). (b) Curves showing the time required to reach the microstructural changepoint (porosity = 0.155) as a function of temperature for different depths (250–750 m). (c) Permeability reduction timescales. Modelled permeability-time curves (using the modelled output of Fig. 4a and the discrete power law permeability–porosity relationships defined by the changepoint model) for melt viscosities at three temperatures (800, 900, and 1000 °C) and lithostatic stresses of 3.75 and 11.25 MPa (depths corresponding to 250 and 750 m, respectively; see text for details). The curves are dashed below the changepoint porosity in panels (a) and (b) because the model may not accurately capture the porosity evolution due to the change in pore geometry.

4.2. The evolution of P-wave velocity and uniaxial compressive strength during densification

The data of this study show that P-wave velocity and strength increase as porosity decreases (Figs. 1b and 1c), behaviour consistent with previous experimental studies on rocks (e.g., Chang et al., 2006) and viscously welded materials (Vasseur et al., 2013). The linear increase of P-wave velocity with decreasing porosity is not influenced by the microstructural changepoint; it is likely that the closure of the largest pores does not influence the first arrival (elastic wave velocities are much more sensitive to void space with a high aspect ratio, like cracks; O'Connell and Budiansky, 1974). However, the strength data (Fig. 1c) show a break in slope at approximately the same position as the microstructural changepoint (porosity = 0.155). The strength of rocks is not only a function of porosity, but very much depends on the pore size (Vasseur et al., 2013; Heap et al., 2014c). An explanation for the mechanical behaviour of these materials therefore requires a model that considers both porosity and pore size, such as the pore-emanating crack model of Sammis and Ashby (1986). Sammis and Ashby's (1986) micromechanical model has successfully described the mechanical behaviour of volcanic materials (e.g., Zhu et al., 2011; Vasseur et al., 2013). The model describes a two-dimensional elastic medium populated by circular holes of uniform radius r. Cracks emanate from the circular holes (parallel to the direction of the applied stress) when the stress at the tip of a small crack on the circular surface reaches a critical value (the fracture toughness, K_{IC}). The newly-formed cracks propagate to a distance l in the direction of the maximum principal stress. The cracks interact when they reach a certain length, thus increasing the local tensile stress intensity. Eventually, the coalescence of these cracks induces the macroscopic failure of the elastic medium. In the case of uniaxial compression, Zhu et al. (2010) derived an analytical approximation of Sammis and Ashby's (1986) pore-emanating crack model to estimate the uniaxial compressive strength (σ_p) as a function of the porosity (ϕ):

$$\sigma_p = \frac{1.325}{\phi^{0.414}} \frac{K_{IC}}{\sqrt{\pi r}}. \tag{4}$$

If the pore-emanating cracks grow through the particles, the value of K_{IC} would closely resemble the values of the mineral constituents: $K_{IC} = 0.3$–0.4 MPa m$^{0.5}$ for feldspar (Atkinson and Meredith, 1987) and $K_{IC} = 0.7$ MPa m$^{0.5}$ for glass (borosilicate glass; Wiederhorn, 1969). However, cracks are likely to grow along particle boundaries that will serve to significantly lower K_{IC} (Atkinson and Meredith, 1987). For example, the K_{IC} of a tuff from the Alban Hills (Italy) was estimated to be 0.1–0.2 MPa m$^{0.5}$ as a result of cracks growing along weak clast interfaces (Zhu et al., 2011). If we assume an intermediate $K_{IC} = 0.15$ MPa m$^{0.5}$, curves of uniaxial compressive strength against porosity can be modelled for different pore diameters, as in Fig. 5a. We find that the strength of the samples below the changepoint can be described by a single characteristic pore size (= 40 μm). However, there is no unique curve for the data above the changepoint, the model suggests that the pore size is decreasing (from 300 to 40 μm; Fig. 5a) as porosity is reduced to the changepoint. This is best observed when the pore size is calculated for each experiment using Equation (4) ($K_{IC} = 0.15$ MPa m$^{0.5}$), as shown in Fig. 5b. The model predicts that the pore size is reduced from ∼350 μm at a porosity of 0.25 to a pore size of ∼50 μm at the changepoint porosity (= 0.155). The pore size does not change as porosity is decreased below 0.155 (Fig. 5b). These predicted pore diameters are in close agreement with our microstructural observations and quantitative pore size analysis (Fig. 3) and therefore add rigour to our above interpretation of the changepoint (i.e., wide channels are progressively closed above the changepoint, while the numerous narrow channels below the changepoint allow porosity loss without considerable permeability reduction).

As discussed, strength versus porosity below the changepoint is well described by Equation (4) using a constant pore size of 40 μm. However, we can also compute the strength above the changepoint using Equation (4) by calculating pore size using the slope of pore size change with decreasing porosity to the changepoint (which is approximately linear; Fig. 5b). These modelled curves are presented in Fig. 5c. The models of strength increase with decreasing porosity above and below the changepoint can then be used in conjunction with the rheological compaction model (Equation (3)) to provide timescales of strength increase during magma densification (Fig. 5d). The rate of strength increase is very much dependent on the stress/depth, viscosity/temperature, and time. It takes 24.5 days at a temperature of 800 °C and a depth of 250 m to increase the strength from ∼8 to ∼56 MPa, but only a further 13 days to almost double the strength to ∼100 MPa. At 750 m, these times are reduced to 8 and 4.5 days, respectively (Fig. 5d).

Although we report uniaxial compressive strengths here (this is a standard way to assess strength and allows us to use models optimised for uniaxial compressive strengths, such as the Sammis and Ashby, 1986 model), we highlight that the fracture of magma is more likely to occur in either shear (e.g., Cordonnier et al., 2012) or in tension (e.g., Heiken et al., 1988). Further, we highlight that the model assumes that the pores are circular and may not therefore capture the behaviour of compacted deposits containing pores with a high aspect ratio (which may be the case for highly-sheared and/or melt-dominated materials; e.g., Wright and Cashman, 2013).

5. Densification, permeability reduction, and strength recovery in volcanic environments

The permeability and strength data and modelling presented herein are relevant to the viscous densification of porous, polydisperse granular materials of crystal-bearing melts in the absence of significant differential/shear stresses.

Lava dome extrusion at the surface is often accompanied by repetitive, low-magnitude and low-frequency earthquakes at depth (e.g., Neuberg et al., 2006), considered to be the result of magma fracture (e.g., Tuffen et al., 2003; Thomas and Neuberg, 2012) or slip events on fractures containing shards of juvenile material (Tuffen and Dingwell, 2005). Preserved and extruded examples of these fractures expose them to be filled with fragmented ash shards, and they are thought to play a key—albeit transient—role in the outgassing of magmatic volatiles through the edifice or into the permeable country rock (e.g., Stasiuk et al., 1996; Rust et al., 2004; Kolzenburg et al., 2012; Castro et al., 2014). Such transient channels in highly viscous magma help to bleed the overpressure that is generated by gas exsolution in silicic volcanic conduits (e.g., Gonnermann and Manga, 2007) and complicate eruptive scenarios such that both explosive and effusive behaviour can be coincident at the same vent (e.g., Woods and Koyaguchi, 1994; Schipper et al., 2013). Once formed, the permeability of these fragment-filled fractures, and their strength recovery, may be approximated using the simple model presented in this study (provided that the material remains hot; we note that some the fractures may propagate to significant distances into the country rock (Heiken et al., 1988), allowing the fragmental fracture fill to cool below its glass transition temperature). The modelled changes in strength and permeability with time are plotted together in Fig. 6, for an isothermal melt viscosity at 800 °C and a lithostatic stress of 11.25 MPa (i.e., a depth of 750 m). Fig. 6 shows that the strength increase after 6 days is only a factor of two; the permeability change over the same timeframe is more than two orders of magnitude. As magma near the conduit margin ascends through regions that sat-
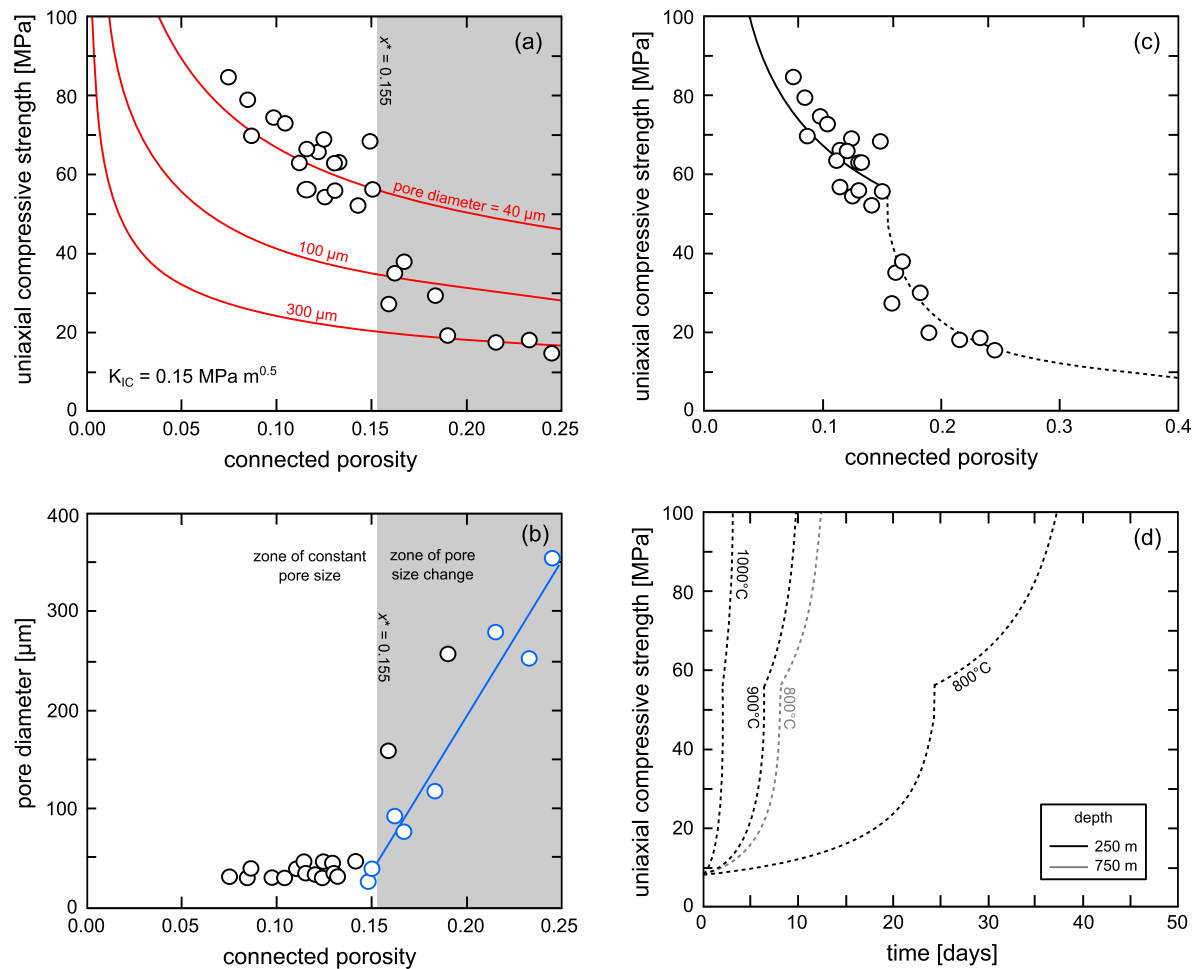
Fig. 5. (a) Micromechanical modelling. Uniaxial compressive strength as a function of connected porosity (the data of Fig. 1c) plotted with the modelled curves, for different pore diameters, from Sammis and Ashby's pore-emanating crack model (Equation (4); using $K_{IC} = 0.15$ MPa m$^{0.5}$). The microstructural changepoint (x^*) is also indicated (porosity = 0.155). (b) Pore size as a function of porosity. Pore diameters were calculated using Sammis and Ashby's pore-emanating crack model (Equation (4); using $K_{IC} = 0.15$ MPa m$^{0.5}$). The blue data highlight those used to determine the pore size change with decreasing porosity to the changepoint; the blue curve represents a linear fit through those data. The microstructural changepoint (x^*) is also indicated (porosity = 15.5%). (c) Uniaxial compressive strength as a function of connected porosity. The panel shows the experimental data of Fig. 1a together with curves modelled using the Sammis and Ashby (1986) pore-emanating crack model. A pore diameter of 40 µm is used below the changepoint, and a pore diameter that changes as a function of porosity (see panel (b)) is used above the changepoint (Equation (4); using $K_{IC} = 0.15$ MPa m$^{0.5}$). The curves are dashed above the changepoint porosity because the pore sizes used to calculate the curve were determined using Sammis and Ashby's (1986) model (see panel (b) and text for details). (d) Strength increase timescales. Modelled strength-time curves (using the modelled output of Fig. 4a and the strength-porosity models shown in panel (c)) for melt viscosities at three temperatures (800, 900, and 1000 °C) and lithostatic stresses of 3.75 and 11.25 MPa (depths corresponding to 250 and 750 m, respectively; see text for details). The curves are dashed below the changepoint porosity because the viscous compaction model may not accurately capture the porosity evolution due to the change in pore geometry, and above the changepoint porosity because the pore sizes used to calculate the curve were determined using Sammis and Ashby's (1986) model (see panel (b) and text for details). (For interpretation of the references to color in this figure legend, the reader is referred to the web version of this article.)

isfy the criteria for fracturing (e.g., Gonnermann and Manga, 2003; Thomas and Neuberg, 2012), the relatively long timescales required for permeability reduction (Fig. 6) may keep the edges of the conduit sufficiently permeable to facilitate outgassing into the country rock (e.g., Shields et al., 2014), or via a permeable halo surrounding the conduit (e.g., Rust et al., 2004). The repeat times between successive low-magnitude and low-frequency earthquakes during silicic lava dome extrusion (from minutes to hours, see Tuffen et al., 2003 and references therein) suggest that magma re-fracturing takes place long before permeability can decrease, keeping the conduit margin permeable (see inset on Fig. 6). The ease of magma re-fracturing is supported here by our estimates of the timescales of strength recovery, which are much greater than our permeability reduction timescales. We further note that magma re-fracturing may be assisted by small (0.5 MPa) pore overpressures (Heap et al., 2015); increased pore fluid pressures are thought to transiently occur in magma fractures (Castro et al., 2014). To conclude, any repetition of fracturing events likely occurs prior to significant in-

creases in strength and must therefore occur more frequently than the viscous densification timescale (as argued in Tuffen and Dingwell, 2005).

We note here that, melt viscosity may decrease, and the viscous densification timescales lowered, if exsolved volatiles passing through the fractured magma can be reabsorbed into the melt phase (Sparks et al., 1999). However, we highlight that the ratio of the timescales of strength recovery and permeability reduction (i.e., that the timescale for strength recovery is longer than that for permeability reduction) will be independent of effective viscosity and imposed stress. We further note that stresses additional to that of the lithostatic (e.g., the high shear stresses anticipated close to the conduit margin; Gonnermann and Manga, 2003), not considered in our simple model, may accelerate densification and reduce the timescales required for permeability decrease and strength increase. However, while in-conduit densification is expected to be accelerated by significant shear stresses driving shear strain, significant pore fluid pressure can retard densification. This is especially
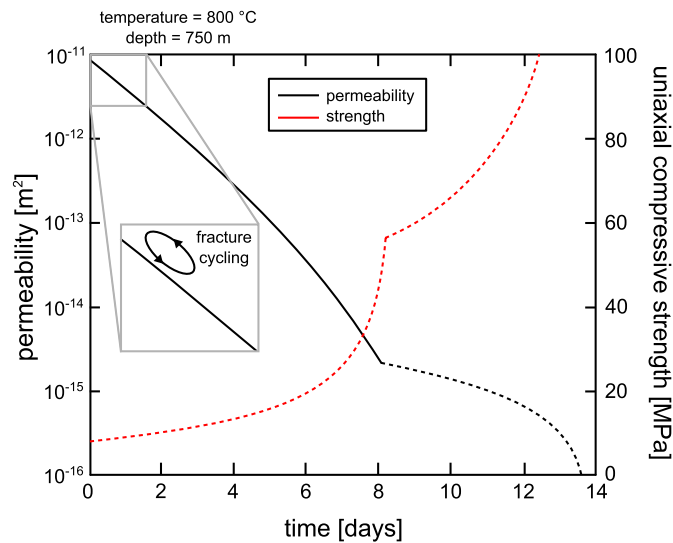
Fig. 6. Permeability reduction and strength increase timescales for the melt viscosity at 800 °C and a lithostatic stress of 11.25 MPa (or a depth of 750 m; see text for details). The permeability-time curve was modelled using the output of Fig. 4a and the discrete power law permeability–porosity relationships defined by the changepoint model (Fig. 3f). The strength-time curve was modelled using the output of Fig. 4a and the strength-porosity models shown in Fig. 5c. The curves are dashed below the changepoint porosity because the model may not accurately capture the porosity evolution due to the change in pore geometry. The strength increase curve is also dashed above the changepoint porosity because the pore sizes used to calculate the curve were determined using Sammis and Ashby's (1986) model. Inset shows a zoom of the start of the permeability reduction curve showing the permeability evolution of conduit margin fractures based on re-fracture timescales provided by low-magnitude and low-frequency earthquakes during silicic lava dome extrusion (from minutes to hours, see Tuffen et al., 2003 and references therein).

true in the volumetric pressure case where densification will halt when the hydrostatic pressure matches the pore fluid pressure. As mentioned above, increased pore fluid pressures are thought to occur, albeit transiently, in particle-filled fractures within magma (e.g., Castro et al., 2014). It is clear that much experimental and theoretical work is required on the viscous densification of granular magma in various stress regimes to facilitate this discussion.

The conduit zone of Unzen volcano (Japan) chiefly comprises volcanic breccia, as revealed by the cores recovered from the 2003–2004 Unzen Scientific Drilling Project (Goto et al., 2008). This conduit-filling breccia is thought to have formed during the growth of the edifice through the disintegration of previous infill material and wall rocks by explosive eruptions and gravitational failures, a model considered applicable to other polygenetic volcanoes developed through explosive followed by effusive behaviour (Goto et al., 2008). Other examples of polydisperse granular conduit fill include: pyroclastic shallow conduit infill at Mount Meager (Canada) (Kolzenburg and Russell, 2014) and Shiotani (Japan) (Kano et al., 1997) following an explosive eruption, the rheomorphic flow of densified pyroclastic material back into the vent at Las Cañadas caldera, Tenerife (Canary Islands) (Soriano et al., 2009), and intra-caldera brecciation at Scafell caldera (Lake District, England) as a result of subaerial caldera collapse (Branney and Kokelaar, 1994). The permeability reduction and strength recovery of these conduit-filling deposits may be approximated using the modelling of the present study (Figs. 4c, 5d and 6). For example, the reduction in permeability may restrict the efficiency with which gases can escape up through the conduit (within days to weeks; e.g., Edmonds et al., 2003; Nicholson et al., 2013). If pore pressure builds as a result of the permeability reduction, the conditions preparatory to a subsequent explosive eruption may be satisfied (e.g., Melnik et al., 2005; Diller et al., 2006). However, the relatively slow initial increase

in strength during viscous densification (Fig. 6) coupled with the fact that pore overpressures drastically reduce strength (Heap et al., 2015) may facilitate magma fracturing within the conduit—as seen in the conduit-filling breccia of Unzen volcano (Goto et al., 2008)—thus providing pathways for the lateral outgassing of magmatic volatiles.

The results of this study may therefore provide support for models of conduit outgassing (e.g., Collinson and Neuberg, 2012).

6. Concluding remarks

Transitions between effusive and explosive behaviour are commonplace at many active volcanoes. If the outgassing efficiency, controlled by the permeability of the system, exerts a crucial control on eruption style, then a constantly changing permeability may be responsible for the observed fluctuations in eruption style. Our study highlights that the progressive densification of magma by viscous sintering during dome-building extrusion, driven by the load provided by the magmatic column, will decrease the porosity and permeability and increase the strength of conduit magma and ash-filled fractures that form at the conduit margin. The viscous magma densification will therefore inhibit outgassing efficiency over time. However, the slow strength recovery of densifying ash-filled fractures, shown herein, suggests that conduit margin fractures may continually re-fracture and remain permeable, allowing the conduit to outgas into the edifice rock and up through the damage zone enveloping the conduit. Therefore, the permeability and outgassing efficiency of the system will depend on the competition between permeability reduction within the conduit and outgassing through conduit margin fractures. If fluid escape can be ultimately disrupted, pore pressure will increase and, if pore pressure increases sufficiently, the conditions required to switch from effusive to explosive (e.g., Vulcanian eruptions) behaviour may be realised. An explosive episode will then reset the magma densification clock, and the process will start again. The timescales of permeability reduction and strength recovery in densifying magma presented in this study may aid our understanding of, amongst others, surface outgassing cycles, magma fracture-healing cycles, and the timescales required for pore pressure augmentation and the initiation of explosive eruptions.

paper was improved following the constructive comments of Hugh Tuffen, one anonymous reviewer, and the editor, Tamsin Mather.

References

Andrews, G.D.M., Russell, J.K., Stewart, M.I., 2014. The history and dynamics of a welded pyroclastic dam and its failure. Bull. Volcanol. 76, 811.

Atkinson, B.K., Meredith, P.G., 1987. Experimental fracture mechanics data for rocks and minerals. In: Atkinson, B.K. (Ed.), Fracture Mechanics of Rock. Academic Press, London, pp. 477–525.

Blower, J., 2001. Factors controlling permeability–porosity relationships in magma. Bull. Volcanol. 63, 497–504.

Branney, M.J., Kokelaar, B.P., McConnell, B.J., 1992. The Bad Step Tuff: a lava-like rheomorphic ignimbrite in a calc-alkaline piecemeal caldera, English Lake District. Bull. Volcanol. 54, 187–199.

Branney, M.J., Kokelaar, B.P., 1994. Volcanotectonic faulting, soft-state deformation, and rheomorphism of tuffs during development of a piecemeal caldera, English Lake District. Bull. Geol. Soc. Am. 106, 507–530.

Castro, J., Bindeman, I.N., Tuffen, H., Schipper, C.I., 2014. Explosive origin of silicic lava: textural and δD–H_2O evidence for pyroclastic degassing during rhyolite effusion. Earth Planet. Sci. Lett. 405, 52–61.

Chang, C., Zoback, M.D., Khaksar, A., 2006. Empirical relations between rock strength and physical properties in sedimentary rocks. J. Pet. Sci. Eng. 51, 223–237.

Collinson, A.S.D., Neuberg, J., 2012. Gas storage, transport and pressure changes in an evolving permeable volcanic edifice. J. Volcanol. Geotherm. Res. 243–244, 1–13.

Cordonnier, B., Caricchi, L., Pistone, M., Castro, J., Hess, K.-U., Gottschaller, S., Manga, M., Dingwell, D.B., Burlini, L., 2012. The viscous-brittle transition of crystal-bearing silicic melt: direct observation of magma rupture and healing. Geology 40, 611–614.

Diller, K., Clarke, A.B., Voight, B., Neri, M., 2006. Mechanisms of conduit plug formation: implications for vulcanian explosions. 33, 20. http://dx.doi.org/10.1029/2006GL027391.

Edmonds, M., Oppenheimer, C., Pyle, D.M., Herd, R.A., Thompson, G., 2003. SO_2 emissions from Soufrière Hills Volcano and their relationship to conduit permeability, hydrothermal interaction and degassing regime. J. Volcanol. Geotherm. Res. 124, 23–43.

Eichelberger, J.C., Carrigan, C.R., Westrich, H.R., Price, P.H., 1986. Non-explosive silicic volcanism. Nature 323, 598–602.

Farquharson, J.I., Heap, M.J., Varley, N., Baud, P., Reuschlé, T., 2015. Permeability and porosity relationships of edifice-forming andesites: a combined field and laboratory study. J. Volcanol. Geotherm. Res. 297, 52–68.

Gonnermann, H.M., Manga, M., 2003. Explosive volcanism may not be an inevitable consequence of magma fragmentation. Nature 426, 432–435.

Gonnermann, H.M., Manga, M., 2007. The fluid mechanics inside a volcano. Annu. Rev. Fluid Mech. 39, 321–356.

Goto, Y., Nakata, S., Kurokawa, M., Shimano, T., Sugimoto, T., Sakuma, S., Hoshizumi, H., Yoshimoto, M., Uto, K., 2008. Character and origin of lithofacies in the conduit of Unzen volcano, Japan. J. Volcanol. Geotherm. Res. 175, 45–59.

Grunder, A., Russell, J.K.R., 2005. Welding processes in volcanology: insights from field, experimental, and modeling studies. J. Volcanol. Geotherm. Res. 142, 1–9.

Heap, M.J., Kolzenburg, S., Russell, J.K., Campbell, M.E., Welles, J., Farquharson, I.J., Ryan, A., 2014a. Conditions and timescales for welding block-and-ash flow deposits. J. Volcanol. Geotherm. Res. 289, 202–209.

Heap, M.J., Lavallée, Y., Petrakova, L., Baud, P., Reuschlé, T., Varley, N., Dingwell, D.B., 2014b. Microstructural controls on the physical and mechanical properties of edifice-forming andesites at Volcán de Colima, Mexico. J. Geophys. Res. 119, 2925–2963.

Heap, M.J., Xu, T., Chen, C.-f., 2014c. The influence of porosity and vesicle size on the brittle strength of volcanic rocks and magmas. Bull. Volcanol. 76, 856. http://dx.doi.org/10.1007/s00445-014-0856-0.

Heap, M.J., Xu, T., Kushnir, A.R.L., Kennedy, B., Chen, C.-f., 2015. Fracture of magma containing overpressurised pores. J. Volcanol. Geotherm. Res. 301, 180–190.

Heiken, G., Wohletz, K., Eichelberger, J.C., 1988. Fracture fillings and intrusive pyroclasts, Inyo Domes, California. J. Geophys. Res. 93, 4335–4350.

Kano, K., Matsuura, H., Yamauchi, S., 1997. Miocene rhyolitic welded tuff infilling a funnel-shaped eruption conduit Shiotani, southeast of Matsue, SW Japan. Bull. Volcanol. 59, 125–135.

Kendrick, J.E., Lavallée, Y., Hess, K.-U., Heap, M.J., Gaunt, H.E., Meredith, P.G., Dingwell, D.B., 2013. Tracking the permeable porous network during strain-dependent magmatic flow. J. Volcanol. Geotherm. Res. 260, 117–126.

Klug, C., Cashman, K.V., 1996. Permeability development in vesiculating magmas: implications for fragmentation. Bull. Volcanol. 58, 87–100.

Kolzenburg, S., Heap, M.J., Lavallée, Y., Russell, J.K., Meredith, P.G., Dingwell, D.B., 2012. Strength and permeability recovery of tuffisite-bearing andesite. Solid Earth 3, 191–198.

Kolzenburg, S., Russell, J.K., 2014. Welding of pyroclastic conduit infill: a mechanism for cyclical explosive eruptions. J. Geophys. Res. 119, 5305–5323.

Main, I.G., Leonard, T., Papasouliotis, O., Hatton, C.G., Meredith, P.G., 1999. One slope or two? Detecting statistically significant breaks of slope in geophysical data, with application to fracture scaling relationships. Geophys. Res. Lett. 26, 2801–2804.

Mellors, R.A., Sparks, R.S.J., 1991. Spatter-rich pyroclastic flow deposits on Santorini, Greece. Bull. Volcanol. 53, 327–342.

Melnik, O., Barmin, A.A., Sparks, R.S.J., 2005. Dynamics of magma flow inside volcanic conduits with bubble overpressure buildup and gas loss through permeable magma. J. Volcanol. Geotherm. Res. 143, 53–68.

Michol, K.A., Russell, J.K.R., Andrews, G.D.M., 2008. Welded block and ash flow deposits from Mount Meager, British Columbia, Canada. J. Volcanol. Geotherm. Res. 169, 121–144.

Nara, Y., Meredith, P.G., Yoneda, T., Kaneko, K., 2011. Influence of macro-fractures and micro-fractures on permeability and elastic wave velocities in basalt at elevated pressure. Tectonophysics 503, 52–59.

Neuberg, J.W., Tuffen, H., Collier, L., Green, D., Powell, T., Dingwell, D.B., 2006. The trigger mechanism of low-frequency earthquakes on Montserrat. J. Volcanol. Geotherm. Res. 153, 37–50.

Nicholson, E.J., Mather, T.A., Pyle, D.M., Odbert, H.M., Christopher, T., 2013. Cyclical patterns in volcanic degassing revealed by SO_2 flux timeseries analysis: an application to Soufrière Hills Volcano, Montserrat. Earth Planet. Sci. Lett. 375, 209–221.

O'Connell, R.J., Budiansky, B., 1974. Seismic velocities in dry and saturated cracked solids. J. Geophys. Res. 79, 5412–5426.

Okumura, S., Sasaki, O., 2014. Permeability reduction of fractured rhyolite in volcanic conduits and its control on eruption cyclicity. Geology 42, 843–846.

Quane, S.L., Russell, J.K., Friedlander, E.A., 2009. Time scales of compaction in volcanic systems. Geology 37, 471–474.

Russell, J.K., Quane, S.L., 2005. Rheology of welding: inversion of field constraints. J. Volcanol. Geotherm. Res. 142, 173–191.

Rust, A., Cashman, K.V., 2004. Permeability of vesicular silicic magma: inertial and hysteresis effects. Earth Planet. Sci. Lett. 228, 93–107.

Rust, A.C., Cashman, K.V., Wallace, P.J., 2004. Magma degassing buffered by vapor flow through brecciated conduit margins. Geology 32, 349–352.

Saar, M.O., Manga, M., 1999. Permeability–porosity relationship in vesicular basalts. Geophys. Res. Lett. 26, 111–114.

Sammis, C.G., Ashby, M.F., 1986. The failure of brittle porous solids under compressive stress states. Acta Metall. 34, 511–526. http://dx.doi.org/10.1016/0001-6160(86)90087-8.

Schipper, C.I., Castro, J.M., Tuffen, H., James, M.R., How, P., 2013. Shallow vent architecture during hybrid explosive–effusive activity at Cordón Caulle (Chile, 2011–12): evidence from direct observations and pyroclast textures. J. Volcanol. Geotherm. Res. 262, 25–37.

Shields, J.K., Mader, H.M., Pistone, M., Caricchi, L., Floess, D., Putlitz, B., 2014. Strain induced outgassing of three-phase magmas during simple shear. J. Geophys. Res. 119, 6936–6957.

Soriano, C., Giordano, D., Galindo, I., Hürlimann, M., Ardia, P., 2009. Giant gas bubbles in a rheomorphic vent fill at the Las Cañadas caldera, Tenerife (Canary Islands). Bull. Volcanol. 71, 919–932.

Sparks, R.S.J., Stasiuk, M.V., Gardeweg, M., Swanson, D.A., 1993. Welded breccias in andesite lavas. J. Geol. Soc. 150, 897–902.

Sparks, R.S.J., Tait, S.R., Yanev, Y., 1999. Dense welding caused by volatile resorption. J. Geol. Soc. 156, 217–225.

Stasiuk, M.V., Barclay, J., Carroll, M.R., Jaupart, C., Ratté, J.C., Sparks, R.S.J., Tait, S.R., 1996. Degassing during magma ascent in the Mule Creek vent (USA). Bull. Volcanol. 58, 117–130.

Stewart, M.L., 2002. Dacite block and ash avalanche hazards in mountainous terrains: 2360 yr. BP eruption of Mount Meager, British Columbia. Master of Science thesis. University of British, Columbia.

Thomas, M.E., Neuberg, J., 2012. What makes a volcano tick—a first explanation of deep multiple seismic sources in ascending magma. Geology 40, 351–354.

Tuffen, H., Dingwell, D.B., Pinkerton, H., 2003. Repeated fracture and healing of silicic magma generate flow banding and earthquakes? Geology 31, 1089–1092.

Tuffen, H., Dingwell, D.B., 2005. Fault textures in volcanic conduits: evidence for seismic trigger mechanisms during silicic eruptions. Bull. Volcanol. 67, 370–387.

Vasseur, J., Wadsworth, F.B., Lavallée, Y., Hess, K.-U., Dingwell, D.B., 2013. Volcanic sintering: timescales of viscous densification and strength recovery. Geophys. Res. Lett. 40, 5658–5664.

Wiederhorn, S.M., 1969. Fracture surface energy of glass. J. Am. Ceram. Soc. 52 (2), 99–105.

Woods, A.W., Koyaguchi, T., 1994. Transitions between explosive and effusive eruptions of silicic magmas. Nature 370, 641–644.

Wright, H.M., Cashman, K.V., 2013. Compaction and gas loss in welded pyroclastic deposits as revealed by porosity, permeability, and electrical conductivity measurements of the Shevlin Park Tuff. Geol. Soc. Am. Bull. http://dx.doi.org/10.1130/B30668.1. http://gsabulletin.gsapubs.org/content/early/2013/12/13/B30668.1.

Zhu, W., Baud, P., Wong, T.-F., 2010. Micromechanics of cataclastic pore collapse in limestone. J. Geophys. Res. 115 (B4). http://dx.doi.org/10.1029/2009JB006610.

Zhu, W., Baud, P., Vinciguerra, S., Wong, T.-F., 2011. Micromechanics of brittle faulting and cataclastic flow in Alban Hills tuff. J. Geophys. Res. 116, B06209. http://dx.doi.org/10.1029/2010JB008046.

CrossMark

Exploring the scale-dependent permeability of fractured andesite

Michael J. Heap [a,*], Ben M. Kennedy [b]

[a] *Géophysique Expérimentale, Institut de Physique de Globe de Strasbourg (UMR 7516 CNRS, Université de Strasbourg/EOST), 5 rue René Descartes, 67084 Strasbourg cedex, France*
[b] *Department of Geological Sciences, University of Canterbury, Private Bag 4800, Christchurch, New Zealand*

A B S T R A C T

Extension fractures in volcanic systems exist on all scales, from microscopic fractures to large fissures. They play a fundamental role in the movement of fluids and distribution of pore pressure, and therefore exert considerable influence over volcanic eruption recurrence. We present here laboratory permeability measurements for porous (porosity = 0.03–0.6) andesites before (i.e., intact) and after failure in tension (i.e., the samples host a throughgoing tensile fracture). The permeability of the intact andesites increases with increasing porosity, from 2×10^{-17} to 5×10^{-11} m^2. Following fracture formation, the permeability of the samples (the equivalent permeability) falls within a narrow range, $2–6 \times 10^{-11}$ m^2, regardless of their initial porosity. However, laboratory measurements on fractured samples likely overestimate the equivalent permeability due to the inherent scale-dependence of permeability. To explore this scale-dependence, we first determined the permeability of the tensile fractures using a two-dimensional model that considers flow in parallel layers. Our calculations highlight that tensile fractures in low-porosity samples are more permeable (as high as 3.5×10^{-9} m^2) than those in high-porosity samples (as low as 4.1×10^{-10} m^2), a difference that can be explained by an increase in fracture tortuosity with porosity. We then use our fracture permeability data to model the equivalent permeability of fractured rock (with different host rock permeabilities, from 10^{-17} to 10^{-11} m^2) with increasing lengthscale. We highlight that our modelling approach can be used to estimate the equivalent permeability of numerous scenarios at andesitic stratovolcanoes in which the fracture density and width and host rock porosity or permeability are known. The model shows that the equivalent permeability of fractured andesite depends heavily on the initial host rock permeability and the scale of interest. At a given lengthscale, the equivalent permeability of high-permeability rock (10^{-12} to 10^{-11} m^2) is essentially unaffected by the presence of numerous tensile fractures. By contrast, a single tensile fracture increases the equivalent permeability of low-permeability rock ($<10^{-15}$ m^2) by many orders of magnitude. We also find that fractured, low-permeability rock (e.g., 10^{-17} m^2) can have an equivalent permeability higher than that of similarly fractured rock with higher host rock permeability (e.g., 10^{-15} m^2) due to the low-tortuosity of fractures in low-porosity andesite. Our modelling therefore outlines the importance of fractures in low-porosity, low-permeability volcanic systems. While our laboratory measurements show that, regardless of the initial porosity, the equivalent permeability of fractured rock on the laboratory scale is $2–6 \times 10^{-11}$ m^2, the equivalent permeability of low-permeability rock is significantly reduced as the scale of interest is increased. Therefore, due to the scale-dependence of permeability, laboratory measurements on pristine, low-permeability rocks significantly underestimate the equivalent permeability of fractured volcanic rock. Further, measurements on fractured rock samples can significantly overestimate the equivalent permeability. As a result, care must be taken when selecting samples in the field and when using laboratory data in volcano outgassing models. The data and modelling presented herein provide insight into the scale-dependence of the permeability of fractured volcanic rock, a prerequisite for understanding outgassing at active volcanoes.

© 2016 Elsevier B.V. All rights reserved.

1. Introduction

Extension fractures (tensile fractures and hydrofractures) are ubiquitous in volcanic systems, a consequence of the mechani-

* Corresponding author.
  E-mail address: heap@unistra.fr (M.J. Heap).

cal (e.g., Heiken et al., 1988) and thermal stresses (e.g., Aydin and DeGraff, 1988) inherent to these environments and the low tensile strength of rock (strength in tension is typically an order of magnitude lower than compressive strength; Jaeger et al., 2007). Extension fractures commonly seen within volcano environments include: microscopic cooling fractures (e.g., Heap et al., 2014), macroscopic polygonal cooling fractures in lavas and lava domes (e.g., Aydin and DeGraff, 1988; Spörli and Rowland, 2006), hydrofractures and tuffisites (e.g., Knapp and Knight, 1977; Heiken et al., 1988; Stasiuk et al., 1996; Sparks, 1997; Tuffen and Dingwell, 2005; Kolzenburg et al., 2012; Castro et al., 2014), crease structures (e.g., Anderson and Fink, 1992), lava dome fractures that form due to a combination of subsurface overpressures and regional stresses (such as that formed following the 2013 explosion at Mt. Merapi, Indonesia; Walter et al., 2015), and large crevasses/fissures (e.g., Gudmundsson, 2011; Fitzgerald et al., 2014). In many cases, magma fragmentation in conduits is dominated by extension fractures with a wide range of orientations (Kennedy et al., 2005). Extension fractures form due to the high overpressures generated by exsolving magmatic fluids, the thermal expansion of pore fluids, and/or the magmatic stresses (hydrofractures; e.g., Knapp and Knight, 1977; Heiken et al., 1988; Benson et al., 2012) or simply as a result of the tensile stresses exceeding the local tensile strength (tensile fractures; e.g., see the experiments presented in Lavallée et al., 2012). Both mechanisms require that, if the temperature exceeds the glass transition of the melt phase Tg, strain rates are high enough to exceed the structural relaxation timescale of the melt (Dingwell and Webb, 1990).

The extension fractures outlined above occur on a wide range of scale, from the microscale (Fig. 1a shows a back-scattered scanning electron photomicrograph of a cooling microcrack within one of the andesite samples of this study) to the hand sample or laboratory-scale (Fig. 1b shows a photograph of a block collected from Volcán de Colima (Mexico) containing a tensile fracture; inset shows a cylindrical laboratory sample (20 mm in diameter and 40 mm in length) prepared from the block) to the meso- or outcrop-scale (Fig. 1c shows columnar cooling fractures at Mt. Ruapehu, New Zealand) to, finally, the macroscale (Fig. 1d shows the fissure exposed following the 2012 eruption from the Te Maari vent at Mt Tongariro, New Zealand). Once formed, extension fractures principally perform two functions at active volcanoes: (1) they reduce the structural stability of the volcano and lava dome (e.g., Voight, 2000) and, (2) they act as pathways for fluids. The ease with which exsolved magmatic gases can escape the conduit—governed by the permeability of the rock and magma—is thought to impact volcanic explosivity (as discussed by many authors, e.g., Eichelberger et al., 1986; Sparks, 1997; Mueller et al., 2005; Melnik et al., 2005; Edmonds and Herd, 2007; Lavallée et al., 2013; Castro et al., 2014). Extension fractures in particular are considered to be a key component in facilitating the outgassing of the conduit magma (e.g., Castro et al., 2014). Indeed, overpressure-driven fractures can propagate to considerable distances and are thought to form efficient fluid pathways (Heiken et al., 1988; Gudmundsson et al., 2002).

Laboratory studies designed to measure the impact of tensile fracture formation on permeability are few, especially for volcanic rocks. Well-constrained laboratory measurements have shown that sample-scale tensile fractures increase permeability of very low-porosity basalt (porosity <0.05) and porous andesite (porosity = 0.17–0.18) by many orders of magnitude (Nara et al., 2011) and by a factor of almost two (Heap et al., 2015a), respectively. The few number of studies, and the discrepancy between measurements performed on rock with different porosity (Nara et al., 2011; Heap et al., 2015a), highlight the need for systematic laboratory studies to better understand the influence of tensile fractures on the permeability of variably-porous volcanic rock. How-
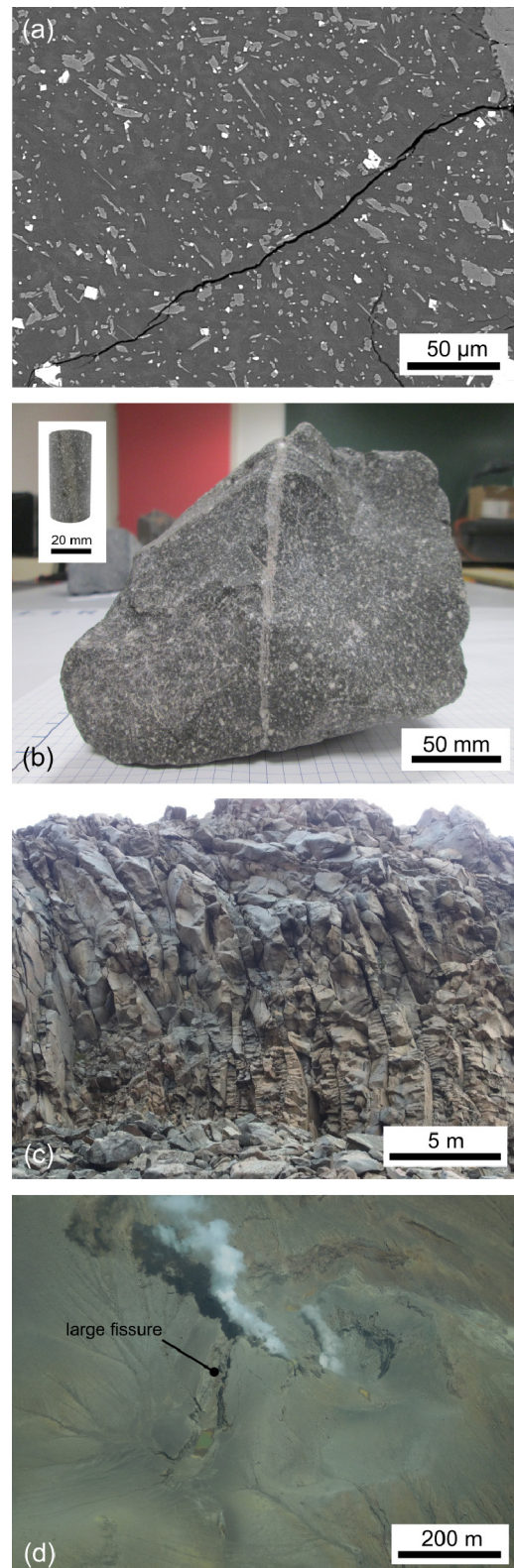

Fig. 1. A voyage through scales. (a) A microscopic cooling fracture in one of the andesites of this study (sample R10). The fracture, seen here to cut through a glassy groundmass containing microlites, is only a few microns wide. (b) A hand- or laboratory-scale block (roughly 20 × 20 × 20 cm) of andesite from Volcán de Colima (Mexico) containing a fracture. The fracture is a couple of mm wide. Inset shows a cylindrical laboratory sample cored from the block shown (20 mm in diameter and 40 mm in length). (c) Macroscopic polygonal columnar cooling fractures in an outcrop at Mt. Ruapehu (New Zealand). Photo credit: Ben Kennedy. (d) Aerial photograph of the large fissure formed following the 2012 eruption from the Te Maari vent at Tongariro (New Zealand). Photo credit: Tetsuo Kobayashi.
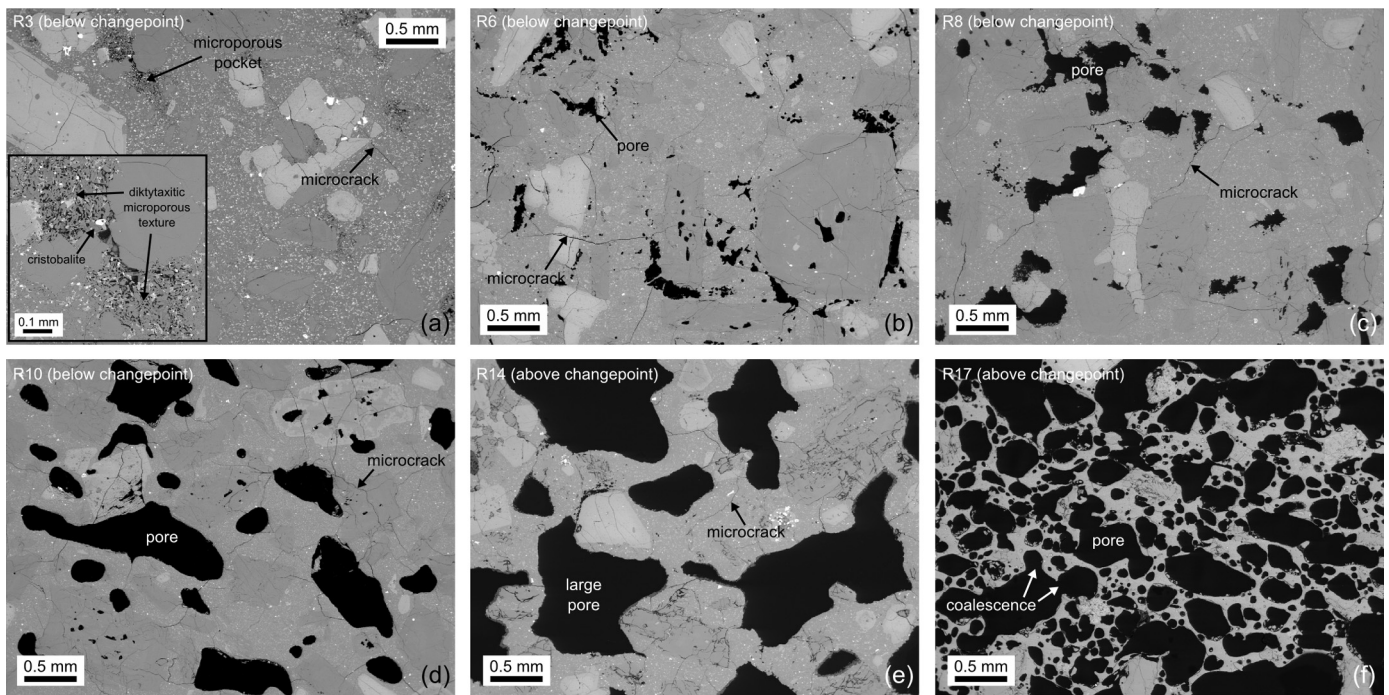
Fig. 2. Intact microstructure. Back-scattered electron microscope images of some of the andesites of this study, arranged from low to high porosity. (a) Image of sample R3 ("altered lava"). A microporous pocket and a microcrack are labelled on the image. The inset shows a zoomed-in image of one of the microporous pockets; diktytaxitic microtextures and "fish-scale" cristobalite are labelled on the inset. (b–e) Images of samples R6, R8, R10, and R14 ("lavas"). A pore and a microcrack are labelled on each of the images. (f) Image of sample R17 ("scoracious"). A pore and pore coalescence are labelled on the image.

ever, while well-constrained laboratory measurements offer considerable insight, it is well known that permeability exhibits a scale effect (Brace, 1984; Clauser, 1992; Neuman, 1994). Laboratory measurements on pristine samples do not account for meso- and macroscale fractures (Figs. 1c and 1d) and therefore underestimate the equivalent permeability of rock (e.g., Clauser, 1992). Similarly, laboratory measurements on samples containing heterogeneities (such as fractures and layering; Fig. 1b) will likely under- or overestimate the equivalent permeability of rock depending on whether the feature(s) serves as a barrier to flow or a conduit for flow, respectively. The extrapolation of laboratory data to larger scales is an outstanding challenge in volcanology. Currently, such extrapolations for fractured volcanic rock are hampered by the paucity of well-constrained laboratory data.

Our aim here is to explore upscaling in fractured andesites using a new laboratory dataset. We first present new laboratory measurements of permeability for a suite of variably-porous (porosity = 0.03–0.6) andesites before and after the formation of a macroscopic tensile (extension) fracture. We use these data to extract the permeability of the fractures, which are then used to explore the role of lengthscale on the equivalent permeability of rock using a two-dimensional model that considers flow in parallel layers. A grasp of the scale-dependence of the permeability of fractured volcanic rock is a prerequisite for understanding and modelling outgassing at active volcanoes (e.g., Collombet, 2009; Collinson and Neuberg, 2012).

2. Materials and methods

A suite of variably porous andesites was selected for this study. The andesite blocks (roughly $10 \times 10 \times 10$ cm in size) were collected on the northern flank of Mt. Ruapehu—an active stratovolcano at the southern end of the Taupo Volcanic Zone (TVZ) in New Zealand's North Island—and are all part of the Whakapapa Formation, the youngest of the units that comprise the present-day edifice (Hackett and Houghton, 1989). Although the materials

are sourced from the edifice of Mt. Ruapehu, the data presented in this study are likely applicable to other active andesitic stratovolcanoes, such as Volcán de Colima, Soufrière Hills (Montserrat), Merapi, Santa María (Guatemala), and Tungurahua (Ecuador). Fifteen blocks were collected in total: four "altered lavas", ten "lavas", and one "scoracious" sample (using the classification scheme of Farquharson et al., 2015). We note that none of the blocks contained fractures visible to the naked eye. The microstructure of samples selected to best represent the measured range in porosity is presented in Fig. 2. We find that the porosity in the low-porosity (0.03–0.04) altered sample is not distributed throughout the sample, but exists as pockets of microporosity commonly sandwiched between crystals (Fig. 2a). This microporous texture—termed diktytaxitic (Kushnir et al., 2016 and references therein)—is associated with cristobalite (a high-temperature, low-pressure silica polymorph; Deer et al., 1992), identifiable by its characteristic fish-scale texture (Deer et al., 1992) (see inset in Fig. 2a). Photomicrographs of the lava samples show that the increase in porosity is coupled with an increase in the pore diameter; the lava samples are also pervasively microcracked (Figs. 2b–e). The microstructure of the scoracious sample is characterised by a bimodal distribution of sub-equant pores, with peaks at diameters of about 100 µm and 500 µm (Fig. 2f). The scoracious sample also shows evidence of bubble coalescence (Fig. 2f).

Two cylindrical samples, 20 mm in diameter and precision-ground flat and parallel to a nominal length of 20 mm (length to width ratios lower than one are not recommended for laboratory permeability measurements), were prepared from each of the fifteen blocks collected (apart from sample R15, for which there is only one sample). 29 samples were prepared in total: 8 altered lava samples, 19 lava samples, and 2 scoracious samples (using the classification scheme of Farquharson et al., 2015) (see Tables 1 and 2). The connected porosity of each sample was measured using a helium pycnometer. Their initial, pre-fracture gas (nitrogen) permeability was measured using a benchtop steady-state permeameter (Figs. 3a and 3b). All measurements were conducted under
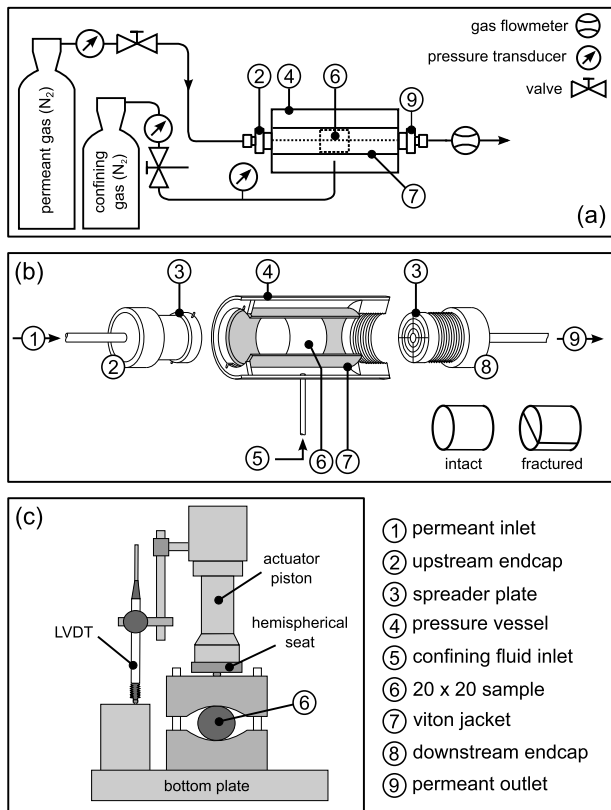
Fig. 3. Schematics of the experimental apparatus. (a–b) Schematic diagrams (not to scale) of the benchtop permeameter. Inset in panel (b) shows a schematic of an intact sample and a fractured sample showing the geometry of the fracture plane. (c) Schematic diagram (not to scale) of the uniaxial load frame used to deform the samples.
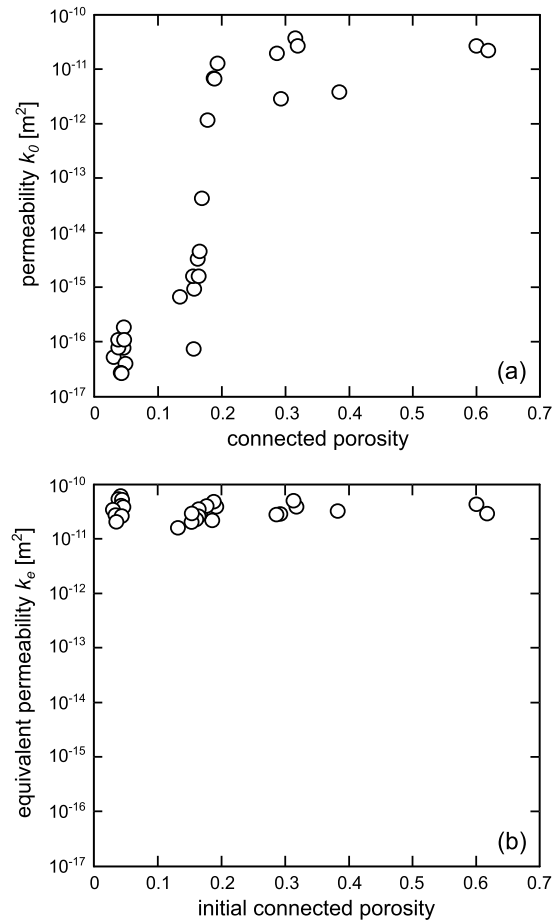

Fig. 4. Laboratory measurements. (a) Intact permeability (k_0) as a function of connected porosity. (b) Equivalent permeability (k_e) of the fractured samples as a function of initial connected porosity. Experimental error is captured by the symbol size.

a confining pressure of 1 MPa. Flow rate measurements were taken (using either a low- or high-flow gas flowmeter, depending on the permeability of the sample) under several pressure gradients (typically from 0.05 to 0.2 MPa, equating to flow rates between 0.2 and 400 ml/min) to determine the permeability using Darcy's law and to assess the need for the Klinkenberg or Forchheimer corrections, which were applied on a case-by-case basis. The samples were then double-wrapped in tape and loaded diametrically in compression (at a constant displacement rate of 0.004 mm/s) until tensile failure using a servo-controlled uniaxial load frame (Fig. 3c). The samples were unloaded following the formation of the first macrofracture (a throughgoing tensile fracture in each case) and their post-fracture permeability was measured using the same procedure described above. The plane of the throughgoing fracture was oriented parallel to the direction of fluid flow (see inset in Fig. 3b). While the fracture experiments yielded a load at failure, indirect tensile strengths are not reported here because the diameter of our samples does not meet the recommended minimum requirement (54 mm) of the International Society of Rock Mechanics (Ulusay and Hudson, 2007). All experiments and measurements were conducted on dry samples (dried in a vacuum oven at 40 °C for a minimum of 48 h) at room temperature.

3. Results

Measured values of intact (pre-fracture) permeability are plotted as a function of connected porosity in Fig. 4a. Intact permeability k_0 increases as connected porosity increases (Fig. 4a). In detail, permeability was measured to be between 1–2×10^{-16} and 2×10^{-17} m^2 at the lowest porosities of 0.03–0.04 and to be about 5×10^{-11} m^2 at the highest porosity of 0.6 (Fig. 4a;

Tables 1 and 2). A single power law cannot describe the porosity–permeability trend on the log-linear graph of Fig. 4a: permeability increases significantly as porosity is increased from 0.03 to about 0.18–0.19, while the increase in permeability between a porosity of about 0.18–0.19 and 0.6 is modest. The permeability of the samples following the formation of a macroscopic tensile fracture—termed here the equivalent permeability k_e (Renard and de Marsily, 1997)—is plotted as a function of initial connected porosity in Fig. 4b. The equivalent permeabilities of all the fractured samples fall within a narrow range, 2–6×10^{-11} m^2, regardless of the initial porosity (Fig. 4b; Tables 1 and 2).

4. Discussion

4.1. Porosity–permeability relationships

The nonlinearity in the porosity–permeability trend of volcanic rock has been considered by some authors to be well captured by a single power law model (e.g., Mueller et al., 2005). Recently however, Bayesian Information Criterion (BIC) analysis has revealed that the porosity–permeability trend for some volcanic materials is better described by two or more discrete power law models that intersect at so-called "porosity changepoints" x^* (Farquharson et al., 2015; Heap et al., 2015b; Kushnir et al., 2016). These changepoints are thought to exist due to microstructural differences between high- and low-porosity volcanic materials. For example, low-porosity rocks (below about 0.15) often contain a poorly-connected or tortuous network of pores, and fluids are often obliged to travel through narrow microcracks that

Table 1
Summary of the laboratory data collected for this study below the microstructural changepoint. AL—"altered lava"; L—"lava". Fracture permeabilities were calculated using Equation (2). The intact area A_{intact} used in Equation (2) was taken as the sample area A (calculated using the sample width W) minus the fracture area $A_{fracture}$ (calculated using the fracture length and a fracture width of 0.25 mm).

Sample	Sample width W (mm)	Connected porosity	Confining pressure (MPa)	Pre-fracture permeability k_0 (m^2)	Post-fracture permeability k_e (m^2)	Fracture length (mm)	Fracture permeability k_f (m^2)
R1 T1 (AL)	20.00	0.043	1	2.63×10^{-17}	6.10×10^{-11}	20.87	1.75×10^{-9}
R1 T2 (AL)	19.99	0.041	1	2.74×10^{-17}	5.08×10^{-11}	20.55	3.10×10^{-9}
R2 T1 (AL)	19.99	0.038	1	1.09×10^{-16}	2.34×10^{-11}	21.12	1.39×10^{-9}
R2 T2 (AL)	20.00	0.031	1	5.23×10^{-17}	3.31×10^{-11}	20.52	2.03×10^{-9}
R3 T1 (AL)	20.00	0.047	1	3.87×10^{-17}	2.46×10^{-11}	21.06	1.47×10^{-9}
R3 T2 (AL)	19.99	0.048	1	3.96×10^{-17}	3.56×10^{-11}	20.97	2.13×10^{-9}
R4 T1 (AL)	20.01	0.046	1	1.87×10^{-16}	4.51×10^{-11}	20.59	2.76×10^{-9}
R4 T2 (AL)	20.01	0.045	1	7.65×10^{-17}	5.75×10^{-11}	20.73	3.49×10^{-9}
R6 T1 (L)	20.00	0.038	1	7.92×10^{-17}	1.97×10^{-11}	21.67	1.14×10^{-9}
R6 T2 (L)	20.00	0.047	1	1.11×10^{-16}	3.83×10^{-11}	20.72	2.32×10^{-9}

Table 2
Summary of the laboratory data collected for this study above the microstructural changepoint. L—"lava"; S—"scoracious". Fracture permeabilities were calculated using Equation (2). The intact area A_{intact} used in Equation (2) was taken as the sample area A (calculated using the sample width W) minus the fracture area $A_{fracture}$ (calculated using the fracture length and a fracture width of 0.25 mm).

Sample	Sample width W (mm)	Connected porosity	Confining pressure (MPa)	Pre-fracture permeability k_0 (m^2)	Post-fracture permeability k_e (m^2)	Fracture length (mm)	Fracture permeability k_f (m^2)
R7 T1 (L)	20.01	0.193	1	1.32×10^{-11}	3.70×10^{-11}	20.96	1.44×10^{-9}
R7 T2 (L)	20.00	0.188	1	6.71×10^{-12}	4.82×10^{-11}	21.47	2.44×10^{-9}
R8 T1 (L)	20.02	0.155	1	1.62×10^{-15}	1.94×10^{-11}	21.77	1.12×10^{-9}
R8 T2 (L)	20.02	0.162	1	3.34×10^{-15}	2.20×10^{-11}	21.32	1.30×10^{-9}
R9 T1 (L)	20.01	0.157	1	9.21×10^{-16}	2.95×10^{-11}	22.68	1.64×10^{-9}
R9 T2 (L)	20.01	0.156	1	7.35×10^{-17}	2.97×10^{-11}	21.11	1.77×10^{-9}
R10 T1 (L)	20.01	0.134	1	6.71×10^{-16}	1.62×10^{-11}	21.37	9.53×10^{-10}
R10 T2 (L)	20.02	0.163	1	1.62×10^{-15}	2.56×10^{-11}	21.46	1.50×10^{-9}
R11 T1 (L)	19.99	0.169	1	4.33×10^{-14}	2.79×10^{-11}	21.81	1.60×10^{-9}
R11 T2 (L)	20.00	0.165	1	4.60×10^{-15}	3.37×10^{-11}	21.47	1.97×10^{-9}
R12 T1 (L)	20.02	0.187	1	6.85×10^{-12}	2.21×10^{-11}	22.09	8.76×10^{-10}
R12 T2 (L)	20.03	0.178	1	1.19×10^{-12}	3.99×10^{-11}	21.88	2.23×10^{-9}
R13 T1 (L)	19.98	0.293	1	2.89×10^{-11}	2.81×10^{-11}	22.05	1.44×10^{-9}
R13 T2 (L)	20.00	0.287	1	1.98×10^{-11}	2.80×10^{-11}	22.27	4.82×10^{-10}
R14 T1 (L)	20.01	0.384	1	3.89×10^{-12}	3.20×10^{-11}	22.96	1.54×10^{-9}
R14 T2 (L)	19.99	0.316	1	3.97×10^{-11}	4.92×10^{-11}	23.59	5.45×10^{-10}
R15 T1 (L)	19.99	0.319	1	2.72×10^{-11}	3.86×10^{-11}	21.72	6.86×10^{-10}
R17 T1 (S)	20.00	0.600	1	2.74×10^{-11}	4.40×10^{-11}	23.33	9.21×10^{-10}
R17 T2 (S)	19.97	0.618	1	2.25×10^{-11}	2.95×10^{-11}	22.58	4.11×10^{-10}

connect the pore network (Heap et al., 2014; Farquharson et al., 2015; Kushnir et al., 2016). Moderate- to high-porosity rocks (above about 0.15), by contrast, often contain a well-connected network of large pores and channels (Rust and Cashman, 2004; Wright et al., 2006; Farquharson et al., 2015; Kennedy et al., 2015; Kushnir et al., 2016). The break-in-slope in the data presented in Fig. 4a also suggests a changepoint porosity, which was calculated using BIC analysis to be at a porosity of 0.19 (Fig. 5a). Data from the altered lavas, and low-porosity lava sample R6, were excluded from our BIC analysis. Kushnir et al. (2016) also found that andesites containing porosities below 0.05 do not align with a model containing two power laws. In our data, while these low-porosity samples could indicate the presence of another porosity changepoint at a porosity between 0.11–0.15 (with the data described by a power law with a low exponent), we highlight that most of these samples contain complex microstructures due to low-pressure, high-temperature alteration (Fig. 2a; Kushnir et al., 2016) and that we have insufficient data to draw firm conclusions. The existence of a changepoint in the rocks presented here is interpreted as a change in void space connectivity at a porosity of 0.19, the same conclusion drawn by previous authors (Farquharson et al., 2015; Heap et al., 2015b; Kushnir et al., 2016). This interpretation is supported by microstructural observations: rocks below the changepoint contain few pores and a pervasive microcrack network (thought to be a consequence of their cooling history, as previously

inferred for similar edifice-forming andesites; Heap et al. (2014)) (Figs. 2b–d), while rocks above the changepoint contain a dense network of large pores (Figs. 2e–f).

4.2. Modelling the equivalent permeability of rock containing tensile fractures

A fundamental model for flow through a fracture is the parallel plate model, which assumes that the fracture walls are smooth, parallel plates separated by a fracture of width h. The derivation of this model yields an exact solution for fracture permeability k_f (Zimmerman and Bodvarsson, 1996):

$$k_f = \frac{h^2}{12} \tag{1}$$

Constraining the width of our experimental fractures is challenging however. While the width of the fractures varies little between different samples of varying porosity (Figs. 5b and 5c), a fracture within a particular sample can vary from $\sim$0.1 to $\sim$0.6 mm (Fig. 5c). Further, our permeability measurements were conducted at a confining pressure of 1 MPa, and therefore the crack width associated with the permeability measurement may be lower than that depicted in Figs. 5b and 5c. Additionally, fracture width may vary along its plane. Since we cannot well constrain our fracture
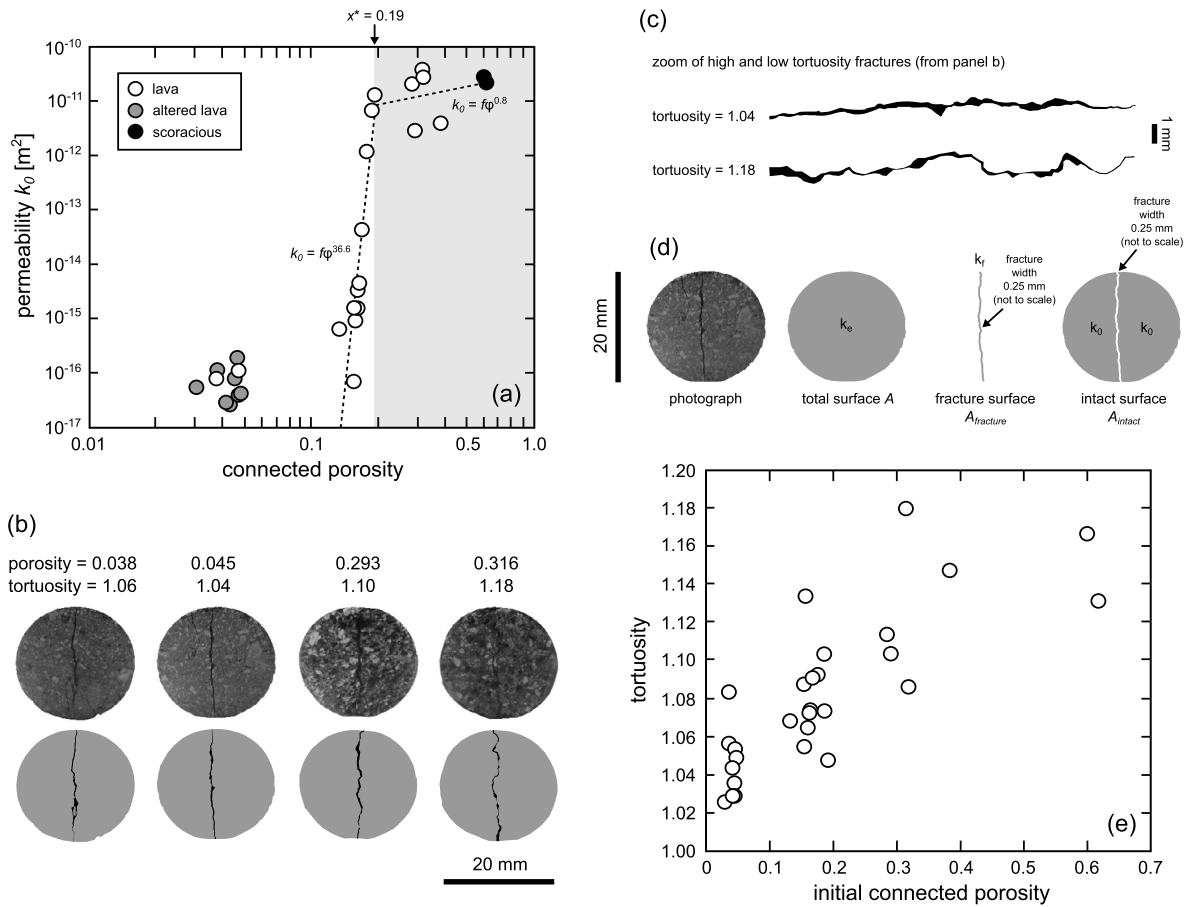
Fig. 5. (a) Microstructural changepoint. Log–log plot of intact permeability (k_0) as a function of connected porosity (i.e., the data of Fig. 4a). Best-fit slopes provided by the Bayesian Information Criterion (BIC) method are also shown (see text for details). The power law exponent for each of the slopes is provided next to the relevant curve. The colour of each data point corresponds to the classification of the sample (using the classification scheme of Farquharson et al., 2015). White—lava. Grey—altered lava. Black—scoracious. The porosity changepoint x^* is labelled on the figure, those points above and below the changepoint lie in the grey and white zones, respectively. (b) Examples of the tensile fractures formed in the experimental samples (top—photograph of the end face of the sample; bottom—schematic diagram of the sample with the main fracture indicated), ordered from low to high porosity. (c) Magnified images of two of the fractures shown in panel (b), the least and most tortuous fracture. (d) Model setup for the determination of fracture permeability using Equation (2) (see text for details). Surface in question is indicated in grey. k_0 = intact permeability, k_f = fracture permeability, and k_e = equivalent permeability. (e) Fracture tortuosity as a function of initial connected porosity.

widths at our experimental pressure, we will assume a conservative and constant fracture width of 0.25 ± 0.1 mm for all of the fractures. Assuming a constant h of 0.25 ± 0.1 mm, Equation (1) yields a fracture permeability of $2.08 \times 10^{-8} \pm 8.33 \times 10^{-12}$ m². Inspection of our experimental samples reveals however that the assumption of smooth, parallel fracture walls is invalid (Fig. 5c). Generally speaking, rough-walled fractures are less permeable than fractures with smooth walls (e.g., Brown, 1987; Thompson and Brown, 1991; Zimmerman et al., 1992). Better estimations of the permeability of fractures with more realistic geometries are possible using the contact surface area of the fracture surfaces (Zimmerman and Bodvarsson, 1996). However, and due to the difficulty in measuring the contact surface (especially under a confining pressure), we adopt here a different approach that interrogates our new experimental dataset.

If we consider the permeability of a sample containing a fracture as an equivalent permeability (k_e), we can extract the fracture permeability (k_f) using the following two-dimensional model that considers flow in parallel layers (a fracture between two layers of host rock):

$$k_f = \frac{Ak_e - A_{intact} \cdot k_0}{A_{fracture}} \qquad (2)$$

Where k_0 is the intact permeability and A is the area of the sample end face. A can be subdivided into the area of fracture ($A_{fracture}$)

and the area of intact rock (A_{intact}). The model setup is shown in Fig. 5d. k_0 and k_e were measured for each rock, and we determine A using the measured sample diameter (Tables 1 and 2). Calculating $A_{fracture}$ requires the length and width of each fracture. While we assume a fixed value of fracture width (0.25 ± 0.1 mm) for this calculation (see reasoning above), we note that the fracture length, which varies between the samples (Figs. 5b and 5c), will not be modified upon the application of a 1 MPa confining pressure. The fracture length, which was measured on the end face of each sample (Figs. 5b and 5c; Tables 1 and 2), also defines a fracture tortuosity. If we plot fracture tortuosity as a function of the initial connected porosity we find that the tortuosity of a tensile fracture increases as the initial connected porosity is increased (Fig. 5e). The path of tensile fractures in the higher porosity samples is influenced by the distribution of large diameter pores; in our samples, pore size tends to increase with porosity (see Figs. 2b–d). In the low-porosity samples, the stress field is not perturbed by the presence of large pores and the fracture is much straighter as a result (Figs. 5b and 5c). We highlight that our model assumes that the fracture area and tortuosity at the end face of the sample is representative of the internal geometry of the fracture in a particular sample. The intact area A_{intact} used in Equation (2) was simply taken as the sample area A minus the fracture area $A_{fracture}$ (all of the values required for the calculation of k_f are provided in Tables 1 and 2). Fracture permeability
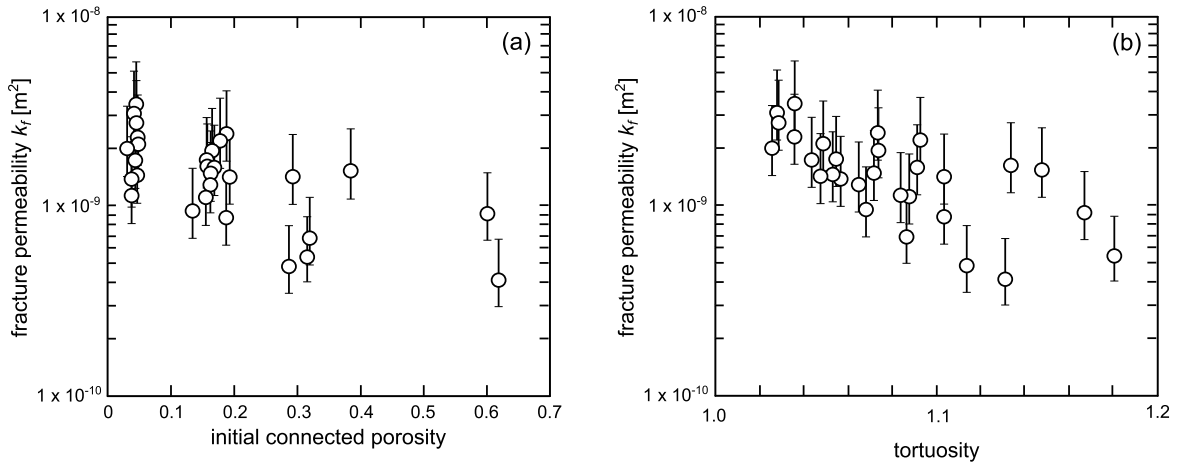
Fig. 6. Tensile fracture permeability (k_f), calculated using Equation (2), as a function of (a) initial connected porosity and (b) fracture tortuosity. Error bars represent the anticipated variability of the fracture width at a confining pressure of 1 MPa (0.25 ± 0.1 mm) (see text for details).

k_f (determined using Equation (2)) is plotted as a function of initial connected porosity and fracture tortuosity in Figs. 6a and 6b, respectively (the error bars account for the anticipated variability of the fracture width, 0.25 ± 0.1 mm). Our data show that fracture permeability decreases as the initial connected porosity (Fig. 6a) or tortuosity increases (Fig. 6b). Our calculated fracture permeabilities are all lower (some by a couple of orders of magnitude) than that predicted using Equation (1) for smooth, parallel fracture walls.

Using our fracture permeability data (Tables 1 and 2), we can model the equivalent permeability of a given length of rock (with chosen host rock permeability) containing a 0.25 mm-wide tensile fracture using the following one-dimensional relation:

$$k_e = \frac{(w_{intact} \cdot k_0) + (w_{fracture} \cdot k_f)}{W} \tag{3}$$

Where W is the total rock width considered, which is subdivided into the width of the fracture $w_{fracture}$ and the width of the intact rock w_{intact}. The model setup is provided as an inset in Fig. 7a. Since fracture permeability decreases with increasing initial connected porosity (Fig. 6a), values of k_f for a given host rock permeability were determined using the empirical power law relationship between the initial permeability and fracture permeability. Our model not only allows us to consider a single fracture: we can increase the number of fractures in a given length of rock by increasing $w_{fracture}$ accordingly. We can now explore the influence of lengthscale on the equivalent permeability of fractured andesitic rock.

There are a few important upscaling considerations however. (1) Although increasing $w_{fracture}$ also allows us to increase the width of the fracture(s), we highlight that this extrapolation may not be appropriate. First, it is unclear whether heterogeneities on the mm-scale (pores and/or crystals) will influence the tortuosity of wider fractures; the tortuosity of larger fractures is likely a product of meso- or macro-scale heterogeneities. Second, an increase in fracture width will likely lead to changes in flow inertia. As a result, the upscaling of laboratory data to wide fissures (e.g., Fig. 1d) will likely require further consideration. Therefore, we restrict our modelling to rock containing one or more 0.25 mm-wide tensile fractures. (2) Fractures observed in the field are often wider than 0.25 mm (e.g., Gudmundsson, 2011). While this may restrict our upscaling discussion to short lengthscales for shallow rock (fluid flow at long lengthscales are likely controlled by fractures wider than those modelled herein), we highlight that wide fractures may not exist at depth unless they are propped open by, for example, high pore fluid pressures (e.g., Rust et al., 2004). Therefore, while the relevance of discussing lengthscales up to 100 m

may be brought into question for subsurface fluid flow (or for zones where wide fractures are propped open), upscaling to long lengthscales (~100 m) may be relevant for the equivalent permeability of fractured rock at depths where the lithostatic pressure inhibits the presence of wide fractures.

If we consider a 10 m length of rock (Fig. 7a), we find that the increase in equivalent permeability with number of tensile fractures (i.e., fracture density) depends heavily on the permeability of the host rock. We also highlight that these modelled equivalent permeabilities differ considerably from the laboratory measurements of equivalent permeability, which were all in the range 2–6×10^{-11} m^2 (Fig. 4b). The modelled curves in Fig. 7a show that the equivalent permeability of a 10 m length of rock is essentially unaffected by fractures when the host rock permeability is between 10^{-13} and 10^{-11} m^2; by contrast, the addition of a single tensile fracture in low-permeability rock (between 10^{-15} and 10^{-17} m^2) increases the equivalent permeability by many orders of magnitude.

Counterintuitively, the equivalent permeability of fractured andesite does not decrease as the host rock permeability is decreased below 10^{-13} m^2. This is a consequence of the porosity dependence of the fracture permeability: fracture permeability increases as initial porosity/permeability is decreased due to the reduction in fracture tortuosity (Fig. 6). As a result, the equivalent permeability when the host rock has a permeability of 10^{-17} m^2 (highlighted in blue) is higher than that for the modelled curve at 10^{-16} m^2, which is higher than that for the 10^{-15} m^2 curve, and so on (Fig. 7a). The equivalent permeability of the 10^{-17} m^2 curve (highlighted in blue) is also higher than the 10^{-14} m^2 curve at five fractures and above (Fig. 7a).

Another way to consider the influence of lengthscale on the equivalent permeability is by increasing the considered lengthscale for a rock containing a fixed fracture number, as in Fig. 7b for a single 0.25 mm-wide fracture. We emphasise that this figure is for illustrative purposes only; in nature rock is increasingly likely to contain more than one fracture as the lengthscale is increased. Further, we highlight that our model assumes that lengthscale is shorter than the macrofracture spacing (and therefore may not be relevant for shallow rock at long lengthscales). The equivalent permeability of rock containing a single 0.25 mm-wide fracture is high (~10^{-11} m^2) when the length considered is within the range of laboratory samples (the grey zone in Fig. 7b), regardless of the initial host rock permeability (as was the case for our laboratory measurements of equivalent permeability, see Fig. 4b). As the scale of interest increases from that considered in the laboratory (generally up to 100 mm), the equivalent permeability decreases by
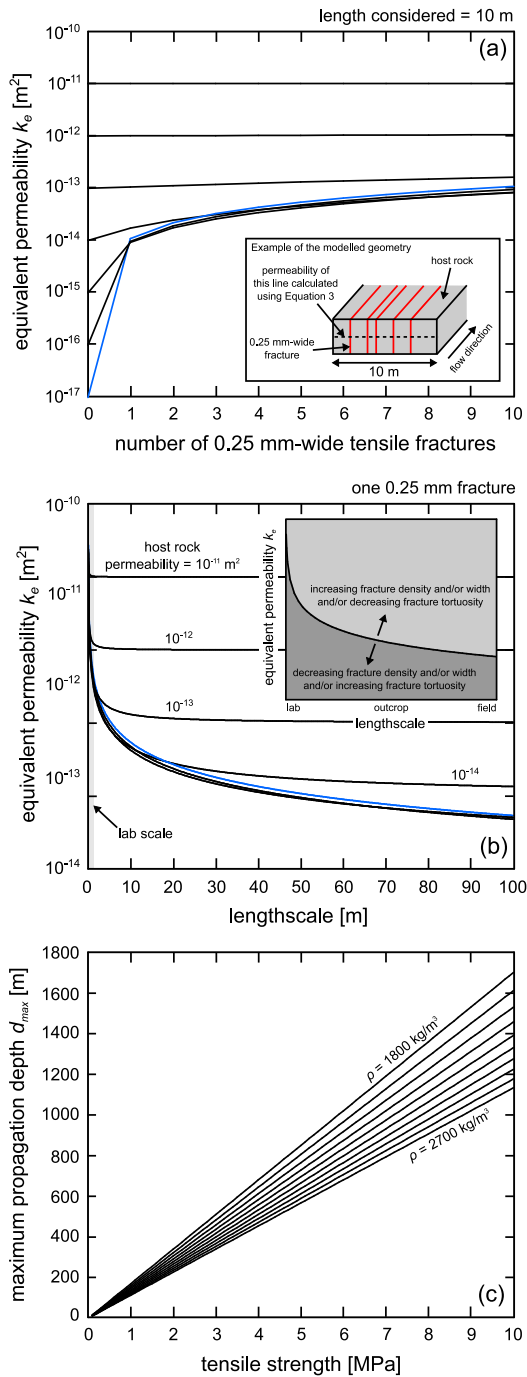
Fig. 7. (a) Equivalent permeability (k_e) of a 10 m length of rock with host rock permeabilities from 10^{-17} to 10^{-11} m^2 as a function of the number of tensile fractures (modelled using Equation (3)). Each fracture is 0.25 mm wide. Fracture permeability for each host rock was determined through the power law relationship between host rock permeability and fracture permeability. The modelled curve for a host rock permeability of 10^{-17} m^2 is highlighted in blue. The inset in panel (a) shows an example of the modelled geometry. (b) Equivalent permeability (k_e) of rock containing one 0.25 mm-wide fracture with increasing lengthscale (up to 100 m). Modelled curves (using Equation (3)) are for rock with host rock permeabilities from 10^{-17} to 10^{-11} m^2. Fracture permeability for each host rock was determined through the power law relationship between host rock permeability and fracture permeability. The laboratory scale (0 to 0.1 m) is labelled on the graph. Modelled curve for a host rock permeability of 10^{-17} m^2 is highlighted in blue. Inset shows a schematic diagram indicating the shift of the curves with increasing/decreasing fracture density, width, and tortuosity. (c) The maximum depth of a downward-propagating tensile fracture as a function of the tensile strength of the host rock, modelled for different host rock densities (from 1800 to 2700 km/m^3) using Equation (4) (from Gudmundsson, 2011). (For interpretation of the references to colour in this figure, the reader is referred to the web version of this article.)

one or more orders of magnitude when the permeability of the host rock is 10^{-12} m^2 or lower (Fig. 7b). The equivalent permeability of andesite containing one fracture, as modelled here for a lengthscale up to 100 m, is not simply a function of the host rock permeability. As discussed above, this is a result of the porosity dependence of tortuosity and therefore fracture permeability (for emphasis we again highlight the 10^{-17} m^2 curve in blue). Despite the somewhat illustrative scenario, we highlight that the equivalent permeability of a 100 m of rock is greatly influenced by one 0.25 mm-wide fracture (Fig. 7b).

We emphasise that the curves of Fig. 7b will shift towards higher equivalent permeabilities in the likely scenario where the number or width of fractures increases (and/or the fracture tortuosity decreases) with increasing lengthscale. By contrast, equivalent permeabilities will be lowered if the fracture density and/or width are decreased (and/or the fracture tortuosity is increased). This is summarised in the schematic diagram presented as an inset in Fig. 7b. As discussed above, it is increasingly likely that more fractures will be encountered at longer lengthscales. Similarly, wide fractures may also be encountered as lengthscale is increased, particularly for shallow rock or rock containing elevated pore pressures (e.g., Rust et al., 2004). Therefore, in a shallow volcanic system, the curves will be significantly shifted to higher equivalent permeabilities at long lengthscales (although we are unable to use our experimental data to explore the influence of wider fractures, the permeability of wider fractures will be higher, see Equation (1)). As the considered depth is increased, or pore pressure decreased, the increasing lithostatic pressure will decrease fracture width, and the curve will be shifted to lower equivalent permeabilities, even at long lengthscales. A final consideration is fracture tortuosity or roughness. The ability of a fracture to close at depth depends on the roughness of the fracture surface: straight or smooth fractures close more readily than rough fractures (Gavrilenko and Guéguen, 1989). Rough fractures, which could be expected for high-porosity materials, may therefore hold the potential to remain open at depth.

The approach here demonstrates how laboratory-measured permeabilities can be used to better approximate equivalent (i.e., "up-scaled") permeabilities. To emphasise, if we imagine a rock outcrop (host rock permeability $= 1.0 \times 10^{-17}$ m^2) that contains 15 fractures (0.25 mm-wide) over a length of 10 m, the equivalent permeability of the rock outcrop, using a k_f of 2.18×10^{-9} m^2 (determined using the power law relationship between the initial permeability and fracture permeability), is estimated using the model presented herein to be 8.2×10^{-13} m^2. Collecting samples for laboratory measurements would therefore yield an underestimate of the permeability is the sample is pristine (the permeability of this sample would be 1.0×10^{-17} m^2) or an overestimation if the sample (length $= 0.02$ m) contains one throughgoing fracture (the equivalent permeability of this sample would be 2.7×10^{-11} m^2).

4.3. Implications for volcanic systems

The data presented herein show that a tensile fracture will have a permeability of between 10^{-10} and 10^{-9} m^2, depending on the initial porosity of the rock (Fig. 6a; Tables 1 and 2): fractures in low-porosity rock are more permeable (as high as 3.5×10^{-9} m^2) than those formed in high-porosity rock (as low as 4.1×10^{-10} m^2) due to their low tortuosity. Modelling these data shows that, at longer lengthscales, fractures greatly influence the equivalent permeability of rock with a low-permeability, but do not significant affect the equivalent permeability of rock with a high-permeability (Figs. 7a and 7b). In detail, fractured, low-permeability rock can have an equivalent permeability higher than that of similarly fractured rock with higher host rock permeability (Figs. 7a and 7b) due to the porosity dependence of tortuosity and therefore fracture

permeability (Fig. 6). As a result, fractures in low-porosity, low-permeability materials—such as those at Chaitén volcano (Chile) (Castro et al., 2014)—will increase the equivalent permeability by many orders of magnitude. By contrast, tensile fractures in the porous materials at Volcán de Colima (Lavallée et al., 2016) may only increase the equivalent permeability by a factor of two or three. These data and modelling highlight an extremely important role for tensile fractures in diffusing explosive behaviour at systems dominated by low-porosity, low-permeability materials.

We note that the outgassing lifespan of these fractures depends on, amongst others, their depth and the temperature at which they reside. First, tensile fractures can partially close as a result of the overburden pressure. Nara et al. (2011) show that the permeability of a low-porosity (porosity <0.05) sample containing a macroscopic tensile fracture can be reduced by about an order of magnitude as the effective pressure is increased from 5 MPa (equivalent to a lithostatic depth of a couple of hundred m) to 50 MPa (depth ∼2 km). Importantly, these data show that the fracture is not completely closed even at 90 MPa (depth of ∼3.5–4 km). As discussed above, straight or smooth fractures close more readily than rough fractures (e.g., Gavrilenko and Guéguen, 1989). Our study has shown that tensile fractures can be more tortuous in high-porosity andesites (Fig. 6a). Therefore, we surmise that the decrease in permeability (from 5 to 50 MPa) for fractured porous materials would be less than the order of magnitude decrease in permeability seen for the low-porosity sample of Nara et al. (2011). Future experimental studies should focus on the role of confining pressure on the permeability of variably-porous rocks containing tensile fractures. Second, if the fracture resides at a temperature above T_g it can heal through the viscous sintering of the fracture surfaces or of any fragmental material within the fracture (Quane et al., 2009; Vasseur et al., 2013; Wadsworth et al., 2014; Heap et al., 2015b). However, Heap et al. (2015b) recently suggested that the slow strength recovery of sintering material could keep the conduit margins permeable through repeated fracturing. Fracture sealing/healing below T_g could occur as a result of hydrothermal mineral precipitation (Figs. 8a and 8b show sulphur deposits at active fumaroles at the edge of the lava dome at Volcán de Colima and hydrothermal precipitation within fractures at Whakaari volcano (New Zealand), respectively; see also Edmonds et al., 2003) or hot isostatic pressing (Kolzenburg et al., 2012). Therefore, either a fracture remains open and creates a pathway for fluids (which may depend on the continuous flow of fluids; Rust et al., 2004) or, and perhaps more likely, the fracture is transient and allows a "pulse" of volatiles to leave the system before succumbing to time-dependent healing or sealing by one or more of the mechanisms described above.

We also highlight here some of the constraints for extension fracture propagation. First, the length (vertically and laterally) of a propagating extension fracture can also be compromised by the presence of pre-existing discontinuities such as joints, faults, dykes, and layering (e.g., Warpinksi and Teufel, 1987; Renshaw and Pollard, 1995; Gudmundsson and Brenner, 2002). Second, downward-propagating tensile fractures will convert to a normal fault once the following relation has been satisfied (Gudmundsson, 2011):

$$d_{max} = \frac{3\sigma_t}{\rho g} \qquad (4)$$

Therefore, if one assumes a typical bulk density ($\rho = 2400$ kg/m^3) and tensile strength ($\sigma_t = 3$ MPa) for porous andesite (Lavallée et al., 2016), then the maximum penetration depth for a downward-propagating tensile crack d_{max} would be 375 m (where g is the acceleration due to gravity). Once a tensile fracture converts to a shear fault, its influence on permeability will be likely governed by the porosity of the host rock (shear fractures in high-porosity rock can reduce permeability (e.g., Zhu and Wong, 1997), while

shear fractures can increase the permeability of low-porosity rock (e.g., Mitchell and Faulkner, 2008). Large sub-vertical tensile fractures that propagate down from the surface are a common feature of andesitic lava domes (Fig. 8e shows a fracture adjacent to the dome at Santa María); other examples of large lava dome fractures exist at Merapi (Walter et al., 2015) and Soufrière Hills (Watts et al., 2002). However, we note that weak dome material could result in much lower penetration depths (as modelled in Fig. 7c); while there is a general paucity in tensile strength data for volcanic rocks, Heap et al. (2012) have shown that high porosity (porosity = 0.5) volcanic rocks can have an indirect tensile strength as low as 0.45 MPa. We further note that laboratory tensile strength measurements likely overestimate "rock mass" tensile strength (e.g., Schultz, 1996). Shallow penetration depths could provide a limit to the outgassing potential of these fractures and their ability to act as conduits from pressurised magma to the surface.

The permeable pathways formed by tensile fractures do not only allow exsolving volatiles to escape, but also permit the ingress of fluids. These fluids may be sourced from the magma, the hydrothermal system, or from the Earth's surface (glaciers or lakes). This can have two, not necessarily mutually exclusive, effects. First, if the fluids are cooler than the host material, the hot host rock cools and contracts adjacent to the fracture resulting in the formation of additional tensile fractures perpendicular to the cooling surface (i.e., the fracture) (e.g., Forbes et al., 2012). Many spectacular examples of this process exists at Mt. Ruapehu, where smaller secondary columns formed on the side of large primary cooling columns due to the rapid ingress of water (Fig. 8d; Spörli and Rowland, 2006; Conway et al., 2015). Second, the circulation of hot hydrothermal fluids can encourage the hydrothermal alteration of the host rock and/or further tensile fracturing through the build-up of fluid overpressures. Since hydrothermally-altered rocks are generally weaker than pristine rock (Pola et al., 2014; Wyering et al., 2014; Heap et al., 2015c), alteration can also lead to further fracturing. Examples of intense hydrothermal alteration and mineral precipitation can be seen in the fractured andesites at Pinnacle Ridge on Mt. Ruapehu (Figs. 8f and 8g; Hackett and Houghton, 1989) and in fractured lavas at Whakaari volcano (Fig. 8b; Heap et al., 2015c).

5. Concluding remarks

The permeability of a volcanic system is expected to impact explosivity: low-permeability rocks and magma can allow the pore pressure to build to that preparatory for an explosive eruption (e.g., Sparks, 1997; Melnik et al., 2005), while high-permeability rocks and magma will permit outgassing, compaction, and encourage quiescence (Kennedy et al., 2015). Extension fractures at volcanoes are expected to play an important role in outgassing (e.g., Stasiuk et al., 1996; Castro et al., 2014), although laboratory permeability data on volcanic rocks are scarce (e.g., Nara et al., 2011; Heap et al., 2015a). Our experimental and modelling approach offers some novel insights. First, we find here that, irrespective of the initial porosity, a single fracture in a laboratory sample (in which the fracture plane is parallel to the flow direction) will result in a permeability of between 2–6 × 10^{-11} m^2. Second, that the permeability of a fracture is influenced by the initial porosity and pore size of the rock: the more heterogeneous the rock, the more tortuous the resultant tensile fracture, and the lower the fracture permeability. Third, when these data are used to model the equivalent permeability of fractured rock, we find that equivalent permeability depends heavily on the scale of interest and the initial permeability of the host rock. Our modelling highlights that the equivalent permeability of a low-permeability rock is greatly increased upon the formation of a single fracture, while the equivalent permeability of high-permeability rock is largely unaffected
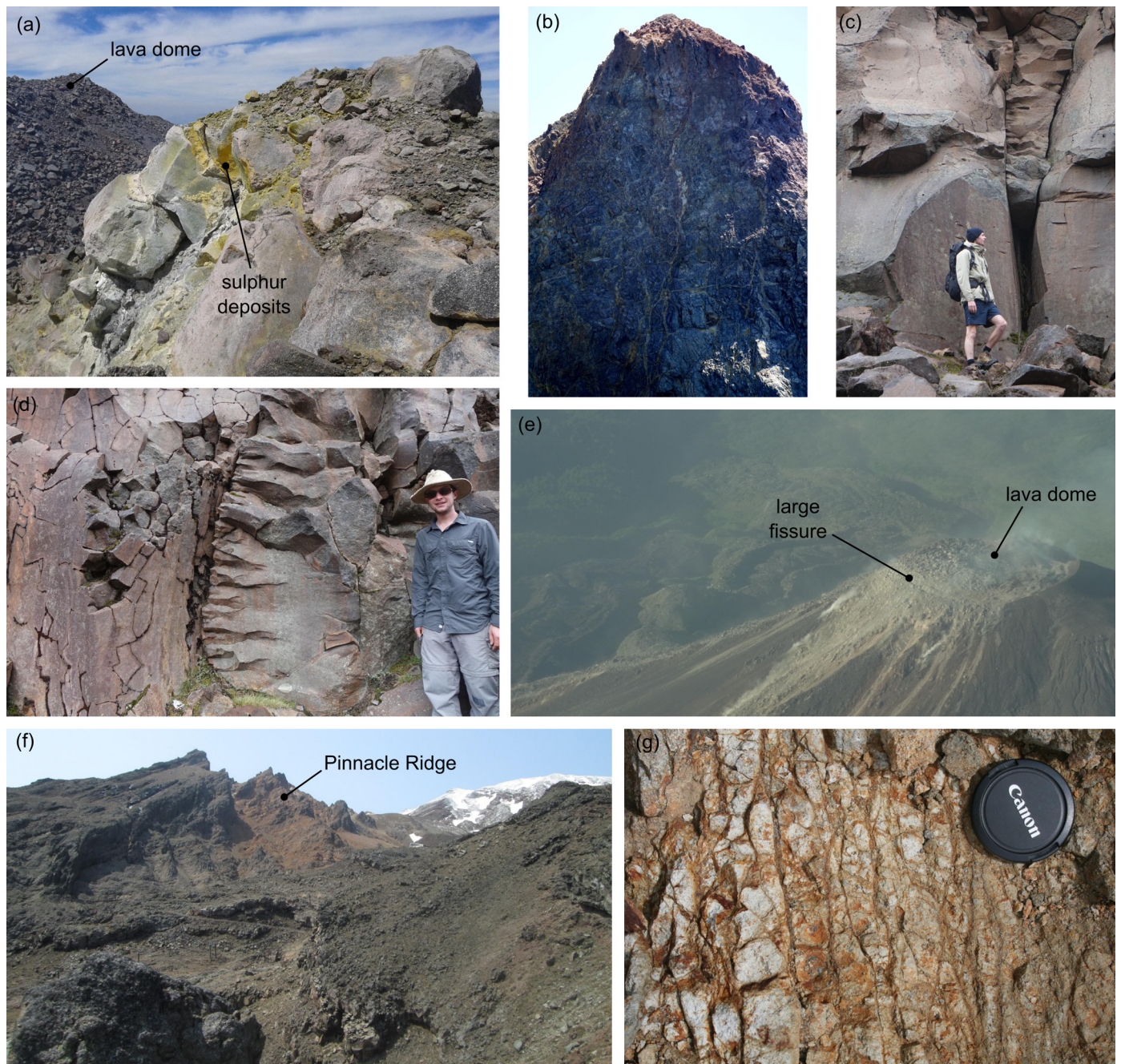
Fig. 8. Field photographs. (a) Photograph of sulphur deposits near a fumarole next to the dome at Volcán de Colima (Mexico) on March 2012 (photo credit: Jamie Farquharson). Photograph of the highly fractured and altered host rock at Whakaari volcano (New Zealand) (photo credit: Ben Kennedy). (c) Photograph of large fractures in the andesite of the Whakapapa Formation (Ruapehu, New Zealand) (photo credit: Ben Kennedy). Chris Conway for scale. (d) Photograph of column-on-column cooling fractures in the andesite of the Whakapapa Formation (Ruapehu) (photo credit: Ben Kennedy). Stan Mordensky for scale. (e) Photograph of the lava dome at Santa María (Guatemala) in 2012 (photo credit: Ben Kennedy). (f) View of Pinnacle Ridge on Mt. Ruapehu (New Zealand) (photo credit: Michael Heap). (g) Photograph of the highly fractured and altered host rock at Pinnacle Ridge (photo credit: Ben Kennedy).

by the presence of many fractures. We also find that fractured, low-permeability rock (e.g., 10^{-17} m^2) can have an equivalent permeability higher than that of similarly fractured rock with higher host rock permeability (e.g., 10^{-15} m^2) due to the porosity dependence of fracture tortuosity and therefore permeability. The modelling therefore highlights an important role for extension fractures in outgassing low-porosity and low-permeability volcanic systems. While our laboratory measurements show that, regardless of the initial porosity, the equivalent permeability of fractured rock on the laboratory scale is 2–6×10^{-11} m^2, the equivalent permeability of low-permeability rock containing a single frac-

ture is significantly reduced as the scale of interest is increased. We find that this role of lengthscale on equivalent permeability diminishes for high-permeability rocks. In summary, due to the scale-dependence of permeability, laboratory measurements on pristine rocks significantly underestimate the equivalent permeability of a fractured volcanic system, and measurements on fractured rocks can significantly overestimate the equivalent permeability. As a result, care must be taken when selecting representative samples from the field for laboratory experiments and input parameters for volcano outgassing models (e.g., Collombet, 2009; Collinson and Neuberg, 2012). We highlight that our modelling

approach can be used to estimate the equivalent permeability of numerous scenarios at andesitic stratovolcanoes in which the fracture density and width and host rock porosity or permeability are known.

Acknowledgements

References

Anderson, S.W., Fink, J.H., 1992. Crease structures: indicators of emplacement rates and surface stress regimes of lava flows. Bull. Geol. Soc. Am. 104, 615–625.

Aydin, A., DeGraff, J.M., 1988. Evolution of polygonal fracture patterns in lava flows. Science 239, 471–476.

Benson, P.M., Heap, M.J., Lavallée, Y., Flaws, A., Hess, K.-U., Selvadurai, A.P.S., Dingwell, D.B., Schillinger, B., 2012. Laboratory simulations of tensile fracture development in a volcanic conduit via cyclic magma pressurisation. Earth Planet. Sci. Lett. 349–350, 231–239.

Brace, W.F., 1984. Permeability of crystalline rocks: new in situ measurements. J. Geophys. Res. 89, 4327–4330.

Brown, S.R., 1987. Fluid flow through rock joints: the effect of surface roughness. J. Geophys. Res. 92, 1337–1347.

Castro, J., Bindeman, I.N., Tuffen, H., Schipper, C.I., 2014. Explosive origin of silicic lava: textural and δD–H_2O evidence for pyroclastic degassing during rhyolite effusion. Earth Planet. Sci. Lett. 405, 52–61.

Clauser, C., 1992. Permeability of crystalline rocks. Earth Space Sci. News 73, 233–238.

Collinson, A.S.D., Neuberg, J., 2012. Gas storage, transport and pressure changes in an evolving permeable volcanic edifice. J. Volcanol. Geotherm. Res. 243–244, 1–13.

Collombet, M., 2009. Two-dimensional gas loss for silicic magma flows: toward more realistic numerical models. Geophys. J. Int. 177, 309–318.

Conway, C.E., Townsend, D.B., Leonard, G.S., Wilson, C.J.N., Calvert, A.T., Gamble, J.A., 2015. Lava–ice interaction on a large composite volcano: a case study from Ruapehu, New Zealand. Bull. Volcanol. 77 (21).

Deer, W.A., Howie, R.A., Zussman, J., 1992. An Introduction to the Rock-Forming Minerals. Longman Scientific and Technical, Harlow.

Dingwell, D.B., Webb, S.L., 1990. Relaxation in silicate melts. Eur. J. Mineral. 2, 427–449.

Edmonds, M., Oppenheimer, C., Pyle, D.M., Herd, R.A., Thompson, G., 2003. SO_2 emissions from Soufrière Hills Volcano and their relationship to conduit permeability, hydrothermal interaction and degassing regime. J. Volcanol. Geotherm. Res. 124, 23–43.

Edmonds, M., Herd, R.A., 2007. A volcanic degassing event at the explosive–effusive transition. Geophys. Res. Lett. 37 (21). http://dx.doi.org/10.1029/2007GL031379.

Eichelberger, J.C., Carrigan, C.R., Westrich, H.R., Price, P.H., 1986. Non-explosive silicic volcanism. Nature 323, 598–602.

Farquharson, I.J., Heap, M.J., Varley, N., Baud, P., Reuschlé, T., 2015. Permeability and porosity relationships of edifice-forming andesites: a combined field and laboratory study. J. Volcanol. Geotherm. Res. 297, 52–68.

Fitzgerald, R.H., Tsunematsu, K., Kennedy, B.M., Breard, E.C.P., Lube, G., Wilson, T.M., Jolly, A.D., Pawson, J., Rosenberg, M.D., Cronin, S.J., 2014. The application of a calibrated 3D ballistic trajectory model to ballistic hazard assessments at Upper Te Maari, Tongariro. J. Volcanol. Geotherm. Res. 286, 248–262.

Forbes, A.E.S., Blake, S., McGarvie, D.W., Tuffen, H., 2012. Pseudopillow fracture systems in lavas: insights into cooling mechanisms and environments from lava flow fractures. J. Volcanol. Geotherm. Res. 245–246, 68–80.

Gavrilenko, P., Guéguen, Y., 1989. Pressure dependence of permeability: a model for cracked rocks. Geophys. J. Int. 98, 159–172.

Gudmundsson, A., 2011. Rock Fractures in Geological Processes. Cambridge University Press, Cambridge.

Gudmundsson, A., Brenner, S.L., 2002. How hydrofractures become arrested. Terra Nova 13, 456–462.

Gudmundsson, A., Fjeldskaar, I., Brenner, S.L., 2002. Propagation pathways and fluid transport of hydrofractures in jointed and layered rocks in geothermal fields. J. Volcanol. Geotherm. Res. 116, 257–278.

Hackett, W.R., Houghton, B.F., 1989. A facies model for a quaternary andesitic composite volcano, Ruapehu, New Zealand. Bull. Volcanol. 51, 51–68.

Heap, M.J., Lavallée, Y., Laumann, A., Hess, K.-U., Meredith, P.G., Dingwell, D.B., 2012. How tough is tuff in the event of fire? Geology 40, 311–314.

Heap, M.J., Lavallée, Y., Petrakova, L., Baud, P., Reuschlé, T., Varley, N., Dingwell, D.B., 2014. Microstructural controls on the physical and mechanical properties of edifice-forming andesites at Volcán de Colima, Mexico. J. Geophys. Res. 119, 2925–2963.

Heap, M.J., Farquharson, I.J., Baud, P., Lavallée, Y., Reuschlé, T., 2015a. Fracture and compaction of andesite in a volcanic edifice. Bull. Volcanol. 77, 55. http://dx.doi.org/10.1007/s00445-015-0938-7.

Heap, M.J., Farquharson, I.J., Wadsworth, F.B., Kolzenburg, S., Russell, J.K., 2015b. Timescales for permeability reduction and strength recovery in densifying magma. Earth Planet. Sci. Lett. 429, 223–233.

Heap, M.J., Kennedy, B.M., Pernin, N., Jacquemard, L., Baud, P., Farquharson, I.J., Scheu, B., Lavallée, Y., Gilg, H.A., Letham-Brake, M., Mayer, K., Jolly, A.D., Reuschlé, T., Dingwell, D.B., 2015c. Mechanical behaviour and failure modes in the Whakaari (White Island volcano) hydrothermal system, New Zealand. J. Volcanol. Geotherm. Res. 295, 26–42.

Heiken, G., Wohletz, K., Eichelberger, J.C., 1988. Fracture fillings and intrusive pyroclasts, Inyo Domes, California. J. Geophys. Res. 93, 4335–4350.

Jaeger, J., Cook, N.G.W., Zimmerman, R., 2007. Fundamentals in Rock Mechanics, 4th edition. Blackwell Publishing, London.

Kennedy, B.M., Spieler, O., Scheu, B., Kueppers, U., Taddeucci, J., Dingwell, D.B., 2005. Conduit implosion during vulcanian eruptions. Geology 33 (7), 581–584.

Kennedy, B.M., Wadsworth, F.B., Vasseur, J., Schipper, C.I., Jellinek, A.M., von Aulock, F.W., Hess, K.-U., Russell, J.K., Lavallée, Y., Nichols, A.R.L., Dingwell, D.B., 2015. Surface tension driven processes densify and retain permeability in magma and lava. Earth Planet. Sci. Lett. 433, 116–124.

Knapp, R.B., Knight, J.E., 1977. Differential thermal expansion of pore fluids: fracture propagation and microearthquake production in hot pluton environments. J. Geophys. Res. 82, 2515–2522.

Kolzenburg, S., Heap, M.J., Lavallée, Y., Russell, J.K.R., Meredith, P.G., Dingwell, D.B., 2012. Strength and permeability recovery of tuffisite-bearing andesite. Solid Earth 3, 191–198.

Kushnir, A.R.L., Martel, C., Bourdier, J.-L., Heap, M.J., Reuschlé, T., Erdmann, S., Komorowski, J.C., Cholik, N., 2016. Probing permeability and microtexture: unravelling the role of a low-permeability dome on the explosivity of Merapi (Indonesia). http://dx.doi.org/10.1016/j.jvolgeores.2016.02.012.

Lavallée, Y., Varley, N., Alatorre-Ibargüengoitia, M.A., Hess, K.-U., Kueppers, U., Mueller, S., Richard, D., Scheu, B., Spieler, O., Dingwell, D.B., 2012. Magmatic architecture of dome-building eruptions at Volcán de Colima, Mexico. Bull. Volcanol. 74, 249–260.

Lavallée, Y., Benson, P.M., Heap, M.J., Hess, K.-U., Flaws, A., Schillinger, B., Meredith, P.G., Dingwell, D.B., 2013. Reconstructing magma failure and the degassing network of dome-building eruptions. Geology 41, 515–518.

Lavallée, Y., Heap, M.J., Kueppers, U., Kendrick, J.E., Dingwell, D.B., 2016. The fragility of Volcán de Colima—a material constraint. In: Varley, N., Komorowski, J.C. (Eds.), Volcán de Colima: Managing the Threat. Springer-Verlag, Berlin, Heidelberg.

Melnik, O., Barmin, A.A., Sparks, R.S.J., 2005. Dynamics of magma flow inside volcanic conduits with bubble overpressure buildup and gas loss through permeable magma. J. Volcanol. Geotherm. Res. 143, 53–68.

Mitchell, T.M., Faulkner, D.R., 2008. Experimental measurements of permeability evolution during triaxial compression of initially intact crystalline rocks and implications for fluid flow in fault zones. J. Geophys. Res. 113 (B11). http://dx.doi.org/10.1029/2008JB005588.

Mueller, S., Melnik, O., Spieler, O., Scheu, B., Dingwell, D.B., 2005. Permeability and degassing of dome lavas undergoing rapid decompression: an experimental study. Bull. Volcanol. 67, 526–538.

Nara, Y., Meredith, P.G., Yoneda, T., Kaneko, K., 2011. Influence of macro-fractures and micro-fractures on permeability and elastic wave velocities in basalt at elevated pressure. Tectonophysics 503, 52–59.

Neuman, S.P., 1994. Generalized scaling of permeabilities: validation and effect of support scale. Geophys. Res. Lett. 21, 349–352.

Pola, A., Crosta, G.B., Fusi, N., Castellanza, R., 2014. General characterization of the mechanical behaviour of different volcanic rocks with respect to alteration. Eng. Geol. 169, 1–13.

Quane, S.L., Russell, J.K., Friedlander, E.A., 2009. Time scales of compaction in volcanic systems. Geology 37, 471–474.

Renard, P., de Marsily, G., 1997. Calculating equivalent permeability: a review. Adv. Water Resour. 20, 253–278.

Renshaw, C.E., Pollard, D.D., 1995. An experimentally verified criterion for propagation across unbounded frictional interfaces in brittle, linear elastic materials. Int. J. Rock Mech. Min. Sci. Geomech. Abstr. 32, 237–249.

Rust, A., Cashman, K.V., 2004. Permeability of vesicular silicic magma: inertial and hysteresis effects. Earth Planet. Sci. Lett. 228, 93–107.

Rust, A.C., Cashman, K.V., Wallace, P.J., 2004. Magma degassing buffered by vapor flow through brecciated conduit margins. Geology 32, 349–352.

Schultz, R.A., 1996. Relative scale and the strength and deformability of rock masses. J. Struct. Geol. 18, 1139–1149.

Sparks, R.S.J., 1997. Causes and consequences of pressurisation in lava dome eruptions. Earth Planet. Sci. Lett. 150, 177–189.

Spörli, K.B., Rowland, J.V., 2006. 'Column on column' structures as indicators of lava/ice interaction, Ruapehu andesite volcano, New Zealand. J. Volcanol. Geotherm. Res. 157, 297–310.

Stasiuk, M.V., Barclay, J., Carroll, M.R., Jaupart, C., Ratté, J.C., Sparks, R.S.J., Tait, S.R., 1996. Degassing during magma ascent in the Mule Creek vent (USA). Bull. Volcanol. 58, 117–130.

Thompson, M.E., Brown, S.R., 1991. The effect of anisotropic surface roughness on flow and transport in fractures. J. Geophys. Res. 96, 21923–21932.

Tuffen, H., Dingwell, D.B., 2005. Fault textures in volcanic conduits: evidence for seismic trigger mechanisms during silicic eruptions. Bull. Volcanol. 67, 370–387.

Ulusay, R., Hudson, J.A., 2007. The Complete ISRM Suggested Methods for Rock Characterization, Testing and Monitoring: 1974–2006. International Society for Rock Mechanics, ISBN 978-975-93675-4-1. 628 pp.

Vasseur, J., Wadsworth, F.B., Lavallée, Y., Hess, K.-U., Dingwell, D.B., 2013. Volcanic sintering: timescales of viscous densification and strength recovery. Geophys. Res. Lett. 40, 5658–5664.

Voight, B., 2000. Structural stability of andesite volcanoes and lava domes. Philos. Trans. R. Soc., Math. Phys. Eng. Sci. 358 (1770), 1663–1703. Causes and consequences of eruptions of andesite volcanoes (May 15, 2000), 1663–1703.

Wadsworth, F.B., Vasseur, J., von Aulock, F.W., Hess, K.-U., Scheu, B., Lavallée, Y., Dingwell, D.B., 2014. Nonisothermal viscous sintering of volcanic ash. J. Geophys. Res. 119, 8792–8804.

Walter, T.R., Subandriyo, J., Kirbani, S., Bathke, H., Suryanto, W., Aisyah, N., Darmawan, H., Jousset, P., Luehr, B.-G., Dahm, T., 2015. Volcano-tectonic control of Merapi's lava dome splitting: the November 2013 fracture observed from high resolution TerraSAR-X data. Tectonophysics 639, 23–33.

Warpinksi, N.R., Teufel, L.W., 1987. Influence of geologic discontinuities on hydraulic fracture propagation. J. Pet. Technol. 39. http://dx.doi.org/10.2118/13224-PA.

Watts, R.B., Herd, R.A., Sparks, R.S.J., Young, S.R., 2002. Growth patterns and emplacement of the andesitic lava dome at Soufrière Hills Volcano, Montserrat. Mem. Geol. Soc. Lond. 21, 115–152. http://dx.doi.org/10.1144/GSL.MEM.2002.021.01.06.

Wright, H.M.N., Roberts, J.J., Cashman, K.V., 2006. Permeability of anisotropic tube pumice: model calculations and measurements. Geophys. Res. Lett. 33. http://dx.doi.org/10.1029/2006GL027224.

Wyering, L.D., Villeneuve, M.C., Wallis, I.C., Siratovich, P., Kennedy, B., Gravely, D.M., Cant, J.L., 2014. Mechanical and physical properties of hydrothermally altered rocks, Taupo Volcanic Zone, New Zealand. J. Volcanol. Geotherm. Res. 288, 76–93.

Zhu, W., Wong, T.-f., 1997. The transition from brittle faulting to cataclastic flow: permeability evolution. J. Geophys. Res. 102 (B2), 3027–3041.

Zimmerman, R.W., Chen, D.-W., Cook, N.W.G., 1992. The effect of contact area on the permeability of fractures. J. Hydrol. 139, 79–96.

Zimmerman, R.W., Bodvarsson, G.S., 1996. Hydraulic conductivity of rock fractures. Transp. Porous Media 23, 1–30.

CHAPTER FOUR – The use of volcanic rocks in construction

This chapter outlines recent work from laboratory at IPG Strasbourg on the use of volcanic rocks in construction. In particular, our laboratory has focussed on the use of tuffs in construction. The first study from our laboratory to focus on the use of tuffs in construction was "How tough is tuff in the event of fire?" (Heap et al., 2012, *Geology*). This paper found that only tuffs that contained zeolites were weakened following exposure to the high temperatures of fire. Unfortunately, at least for Naples (Italy), the most widespread dimension stone—the Neapolitan Yellow Tuff—contains zeolites and is therefore weakened following fire (Figure 13). This study concluded that zeolite-rich tuffs would be weak in the event of fire.
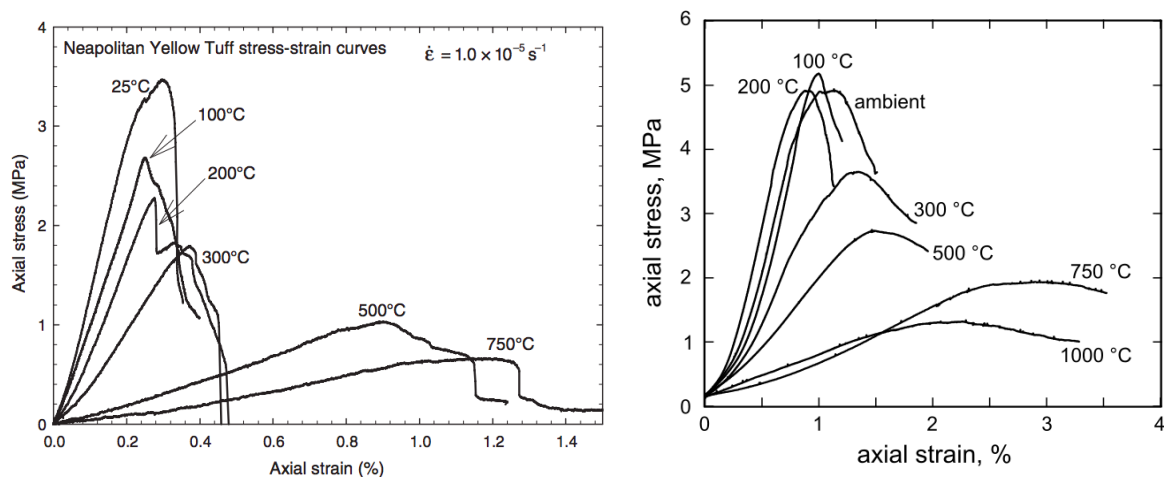
Figure 13. *The weakening of tuff following exposure to the high temperatures of fire. Left graph: Axial stress as a function of axial strain (stress-strain curves) for Neapolitan Yellow Tuff (graph from Heap et al., 2012). Right graph: Axial stress as a function of axial strain (stress-strain curves) for Mt. Epomeo Green Tuff (from Heap et al., 2018b, in revision).*

This work was followed-up by a recent paper entitled "Fire resistance of the Mt. Epomeo Green Tuff, a widely-used building stone on Ischia Island (Italy)" (Heap et al., 2018b, *in revision*). In this study, the fire resistance of another tuff, the use of which is widespread in construction on Ischia Island (Italy), was tested. However, using measured values of thermal diffusivity, we provided thermal modelling that shows that, although the tuffs are weakened following exposure to high temperature (Figure 13), their low thermal diffusivity requires that the fire

must burn for many hours. This paper (Heap et al., 2018b, *in revision*) concludes that, for this reason, tuffs may actually be tough in the event of fire.

In another recent paper, "The influence of water on the strength of Neapolitan Yellow Tuff, the most widely-used building stone in Naples (Italy)" (Heap et al., 2018c, *Bulletin of Volcanology*), we investigated the water-weakening of the most popular natural building stone in Naples – the Neapolitan Yellow Tuff. This paper shows that the Neapolitan Yellow Tuff is systematically weaker when wet (Figure 14), which can help explain weathering damage in building stones (due to rainfall, rising damp, and proximity to the sea or water table) and the observed link between rainfall and landslides, rock falls, and sinkhole formation in Naples.
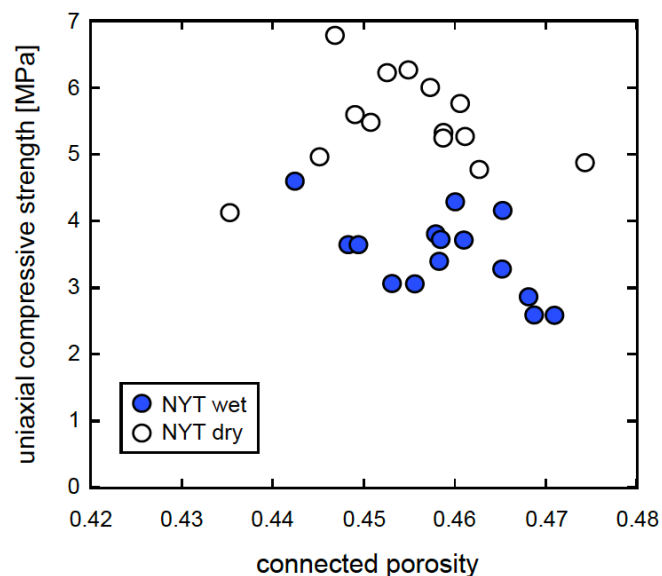
Figure 14. Water-weakening in the Neapolitan Yellow Tuff. Uniaxial compressive strength as a function of porosity for dry and wet Neapolitan Yellow Tuff (from Heap et al., 2018c).

Attached to this chapter are three of the most relevant papers on this topic (all the of papers published on this topic can be found in Appendix B).

 ➢ "**How tough is tuff in the event of fire?** " (Heap et al., 2012).
 ➢ "**Fire resistance of the Mt. Epomeo Green Tuff, a widely-used building stone on Ischia Island (Italy)**" (Heap et al., 2018b).
 ➢ "**The influence of water on the strength of Neapolitan Yellow Tuff, the most widely-used building stone in Naples (Italy)**" (Heap et al., 2018c).

Geology

How tough is tuff in the event of fire?

M.J. Heap, Y. Lavallée, A. Laumann, K.-U. Hess, P.G. Meredith and D.B. Dingwell

---

Email alerting services	click www.gsapubs.org/cgi/alerts to receive free e-mail alerts when new articles cite this article
Subscribe	click www.gsapubs.org/subscriptions/ to subscribe to Geology
Permission request	click http://www.geosociety.org/pubs/copyrt.htm#gsa to contact GSA

Notes

THE GEOLOGICAL SOCIETY OF AMERICA

How tough is tuff in the event of fire?

M.J. Heap[1], Y. Lavallée[2], A. Laumann[2], K.-U. Hess[2], P.G. Meredith[3], and D.B. Dingwell[2]

[1]Laboratoire de Géophysique Expérimentale, Institut de Physique de Globe de Strasbourg (UMR 7516 Centre National de la Recherche Scientifique, Université de Strasbourg/Ecole et Observatoire des Sciences de la Terre), 5 rue René Descartes, 67084 Strasbourg cedex, France
[2]Earth and Environment, LMU (Ludwig Maximilian University) University of Munich, Theresienstrasse 41/III, 80333 Munich, Germany
[3]Rock & Ice Physics Laboratory, Department of Earth Sciences, University College London, Gower Street, London WC1E 6BT, UK

ABSTRACT

Tuff has been extensively used as a building material in volcanically and tectonically active areas over many centuries, despite its inherent low strength. A common and unfortunate secondary hazard accompanying both major volcanic eruptions and tectonic earthquakes is the initiation of catastrophic fires. Here we report new experimental results on the influence of high temperatures on the strength of three tuffs that are commonly used for building in the Neapolitan region of Italy. Our results show that a reduction in strength was only observed for one tuff; the other two were unaffected by high temperatures. The cause of this strength discrepancy was found to be a product of the initial mineralogical composition, or more specifically, the presence of thermally unstable zeolites within the initial rock matrix. The implications of these data are that, in the event of fire, only the stability of buildings or structures built from tuff containing thermally unstable zeolites will be reduced. Unfortunately, this includes the most widespread dimension stone in Neapolitan architecture. We recommend that this knowledge should be considered during fire hazard mitigation in the Neapolitan area and that other tuffs used in construction worldwide should be tested in a similar way to assess their fire resistance.

INTRODUCTION

Tuff is a very weak geomaterial (Schultz and Li, 1995; Hall et al., 2006; Tuccimei et al., 2010; Zhu et al., 2011). It has nevertheless been extensively used as a building material in volcanically and tectonically active areas (e.g., in Naples and Rome, Italy) due to the combination of local availability and its easy workability. Given its widespread use, we examined the high-temperature stability of tuff in the event of fire; catastrophic fire (especially in urban areas) is also a common secondary hazard accompanying major volcanic eruptions and tectonic earthquakes. Here we report new experimental results on the influence of high temperatures on the strength of three tuffs from the Campanian region of Italy.

MATERIALS AND METHODS

We performed uniaxial compressive and indirect tensile strength tests on thermally stressed samples of Neapolitan Yellow Tuff (NYT), gray Campanian Ignimbrite (welded gray ignimbrite, WGI), and Piperno Tuff (PT). The tuffs were formed during large explosive eruptions from the Campi Flegrei caldera (Orsi et al., 1996; de Gennaro and Langella, 1996; de Gennaro et al., 2000), located a few kilometers west of the city of Naples, and have all been used in construction throughout the Neapolitan area (see Morra et al., 2010, and references therein). Our sample materials were collected from open quarries (that supply material for construction) within the Campanian area.

Prior to experimentation, the "as-received" materials (i.e., samples that have undergone no heating) were characterized using optical microscopy (carried out using a Leica DM2500 microscope; see GSA Data Repository[1])

and X-ray diffraction (XRD) (carried out using a Stoe Kristalloflex diffractometer; see the Data Repository). NYT, a trachytic pyroclastic deposit characterized by both pyrogenic and authigenic phases (de Gennaro et al., 2000), was found to contain phenocrysts of sanidine, plagioclase, clinopyroxene, biotite, and minor amounts of titaniferous magnetite and apatite within a matrix of lapilli and glass shard ash (Fig. 1A). The glass shards frequently contain microscopic vesicles, as well as nanoscopic crystals. Xenoliths of fine-grained gabbro (altered and near pristine) were also found. XRD pattern analysis confirmed the presence of the above-mentioned crystals and also indicated the presence of segelerite and three zeolites, phillipsite, chabazite, and analcime (Fig. 2A). The presence of these zeolites in NYT has been reported in previous studies, and their mean content can exceed 50 wt% (de Gennaro et al., 1990, 2000). The WGI, feldspathized by authigenic mineralization processes, is made up of reversely graded black scoriae embedded in an ashy matrix with subordinate lithics and crystals (Cappelletti et al., 2003). The WGI was found to contain hypidiomorphic phenocrysts of alkali feldspars with minor amounts of clinopyroxene, as well as microlites of alkali feldspar, titaniferous magnetite, and apatite, giving the matrix a trachytic appearance (Fig. 1E). The matrix comprises well-sorted glass shards with occasional accretionary ash clots and porous lapilli fragments (Fig. 1F). PT is characterized by a eutaxitic texture with black flattened scoriae set in a light gray matrix (Calcaterra et al., 2000), and was found to contain hypidiomorphic phenocrysts of alkali feldspars with minor amounts of clinopyroxene. The microlites are not well developed and tend to be fragments of alkali feldspar. Titaniferous magnetite and apatite are present as accessory minerals. The matrix comprises well-sorted glass shards surrounding porous lapilli fragments (Fig. 1H). NYT, WGI, and PT contain average porosities of 44%, 49%, and 48%, respectively (measured using an AccuPyc II 1340 helium pycnometer).

Experimental samples comprised cylindrical cores 25 mm in diameter by 75 mm long (resulting in a length:diameter ratio of 3:1) for uniaxial compressive strength tests, and discs 40 mm in diameter by 20 mm thick for indirect tensile strength tests (within the thickness-diameter ratio suggested by the International Society for Rock Mechanics [ISRM, 1978]). Prior to strength testing, samples were either (1) held at ambient temperature, or (2) thermally stressed to predetermined temperatures of 100, 200, 300, 500, or 750 °C. Thermal stressing was achieved by heating the sample to the target temperature at a rate of 1 °C/min without load, holding the temperature constant for 60 min, and then cooling at the same rate. Strength tests were then performed on all samples using special testing jigs mounted in a servo-controlled uniaxial load frame. In our uniaxial compression tests, core samples were loaded at a constant strain rate of 1.0×10^{-5} s^{-1} until failure. Indirect tensile tests were conducted using the Brazil-disc technique (ISRM, 1978), in which discs are loaded diametrically in compression to produce a maximum tensile stress at their center. Indirect tensile strengths were then calculated using standard rock mechanics relationships (ISRM, 1978).

RESULTS AND DISCUSSION

Results demonstrate that, whereas the strength of NYT decreased with thermal stressing, the strengths of WGI and PT remained unaffected
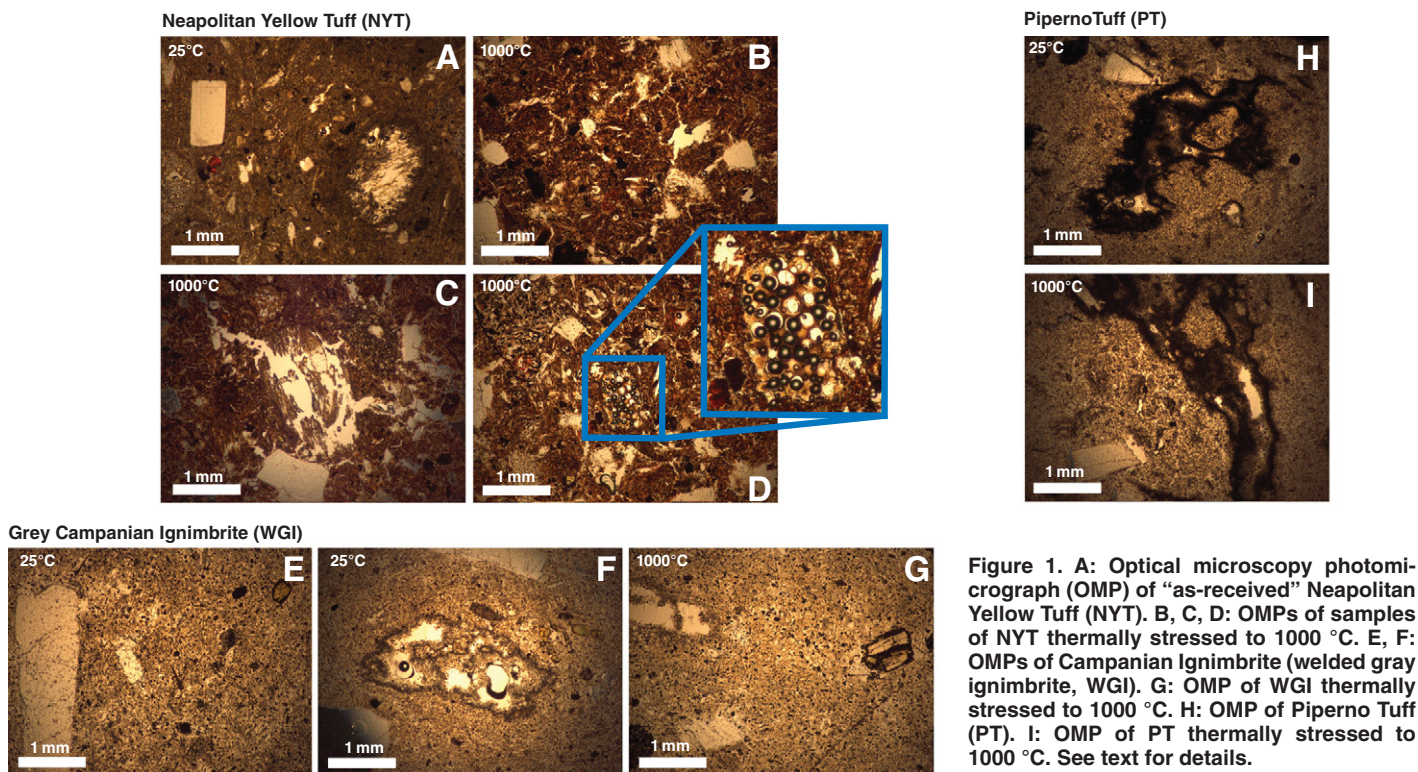
Neapolitan Yellow Tuff (NYT)

PipernoTuff (PT)

Grey Campanian Ignimbrite (WGI)

Figure 1. A: Optical microscopy photomicrograph (OMP) of "as-received" Neapolitan Yellow Tuff (NYT). B, C, D: OMPs of samples of NYT thermally stressed to 1000 °C. E, F: OMPs of Campanian Ignimbrite (welded gray ignimbrite, WGI). G: OMP of WGI thermally stressed to 1000 °C. H: OMP of Piperno Tuff (PT). I: OMP of PT thermally stressed to 1000 °C. See text for details.

(Figs. 3A and 3B). The compressive strength and indirect tensile strength of NYT were reduced by 80% (from 3.4 to 0.7 MPa) and 90% (from 1 to 0.1 MPa), respectively. The gradual degradation of strength with thermal stressing in NYT is also illustrated in the stress-strain curves of Figure 3C.

To investigate the cause of this discrepancy in strength reduction, we first performed thermogravimetric analysis (carried out using a Netzsch STA 449 C thermobalance apparatus; see the Data Repository) on all three samples (Fig. 3D). Thermogravimetric analysis permits us to evaluate the amount of hydrated minerals contained within the three tuffs. Figure 3D shows that, at 1000 °C, NYT had lost 18% of its initial mass, whereas WGI and PT had only lost ~2%. It follows that the more mass lost during heating, the more hydrated minerals contained within the material (see also de Gennaro and Colella, 1989). The nature of these hydrated minerals was further investigated using a combination of XRD and optical microscopy on samples thermally stressed to 1000 °C, to be compared with our observations of the as-received materials. Thermally stressing the NYT to 1000 °C resulted in the disintegration of the matrix, revealed by the presence of distributed and nonpreferentially oriented 1–100-μm-wide microcracks (Fig. 1B). The cores of lapilli were sometimes strongly affected and act as a point of nucleation for the propagation of microcracks (Fig. 1C). Some areas show the presence of foamed glass as much as 1 mm wide (Fig. 1D). The crystals of biotite appear relatively more oxidized (see the diminished XRD peak of Fig. 2A), whereas those of feldspar, pyroxenes, and apatite remain unaffected. Phillipsite, chabazite, analcime, and segelerite, which were originally present in the matrix, are no longer visible on the XRD patterns (Fig. 2A). Zeolites are micro-porous minerals with an open framework structure capable of storing both exchangeable cations and water molecules. As a consequence, they are prone to changes in temperature (and/or water vapor pressure). Detailed studies on the thermal decomposition of the zeolites in NYT have highlighted that analcime irreversibly loses water and chabazite and phillipsite undergo a partial reversible dehydration at 240 °C; phillipsite breaks down during dehydration and chabazite undergoes reversible hydration at 350 °C; and at 900 °C,

the structure of the zeolites will be so damaged that no further water molecules can be stored (de Gennaro and Colella, 1989). Our thermogravimetric analysis (Fig. 3D) corroborates these observations: NYT had lost 16.5% of its mass by 350 °C (total mass lost at 1000 °C was 18%). Thermally stressing both WGI and PT to 1000 °C did not produce any changes to the matrix, glass, or the crystals (Figs. 1G and 1I) and XRD pattern analysis did not reveal any mineralogical changes (Figs. 2B and 2C).

We therefore conclude that the thermal liability of the zeolites in NYT, particularly phillipsite and chabazite (see also de Gennaro et al., 1983, 1984), can explain the strength discrepancy between the three tuffs. Phillipsite and chabazite represent the "cement" that promoted the lithification of the originally incoherent pozzolanic material (de Gennaro et al., 2000) and consequently, upon its loss, the structural integrity of NYT deteriorates significantly (see Figs. 1B and 1C). The WGI and PT, both of which do not contain zeolites, are therefore unaffected by thermal stressing.

The implications of these data are that, in the event of fire, the stability of buildings or structures built from WGI and PT will not be jeopardized. Unfortunately, the most widespread dimension stone in Neapolitan architecture, NYT, will deteriorate considerably. One of the most infamous fires in a building constructed from NYT is that of the Church of Santa Chiara, Naples (built between A.D. 1310 and 1340), in 1943. The fire, initiated after an air raid attack during the Second World War accidently hit the church, roared for 10 days and almost destroyed the church entirely. Restoration work on the church, back to its original Gothic style, was completed in 1953.

Current worldwide zeolitized tuff consumption as a dimension stone is at ~3 × 10⁶ t/yr (Colella et al., 2001). This widespread utilization demands extra consideration during fire hazard mitigation. We recommend that the results of our study should be considered during fire hazard mitigation in the Neapolitan area (including any original material incorporated into restorations after fires), and that other tuffs used in construction worldwide should be tested in a similar way to assess their fire resistance.
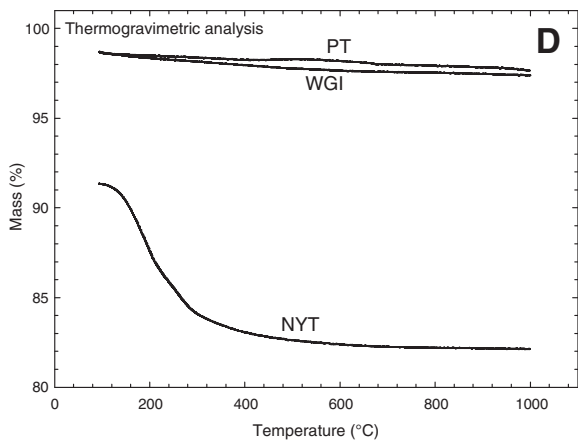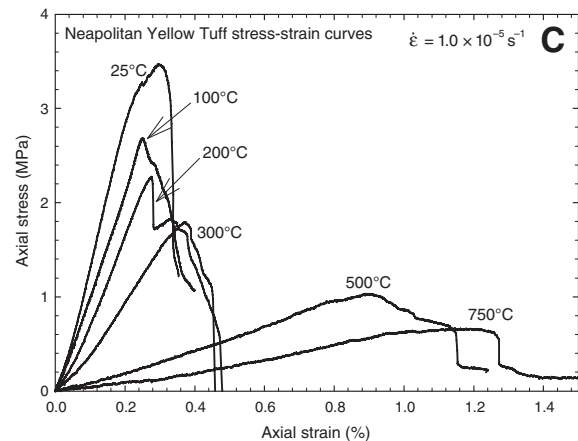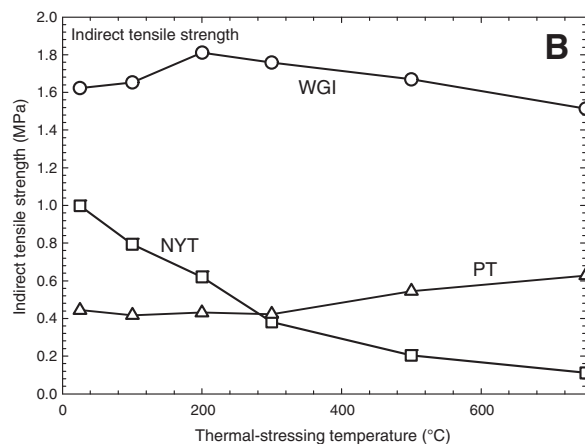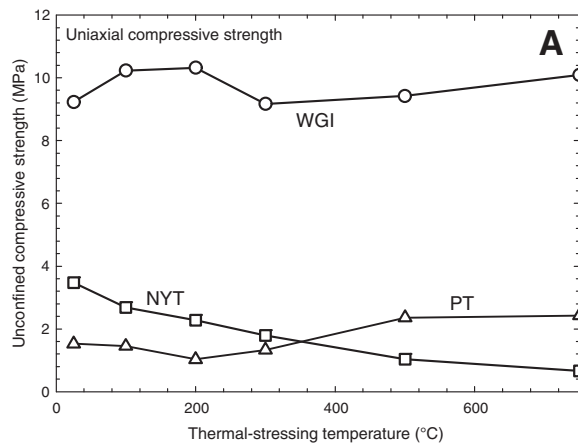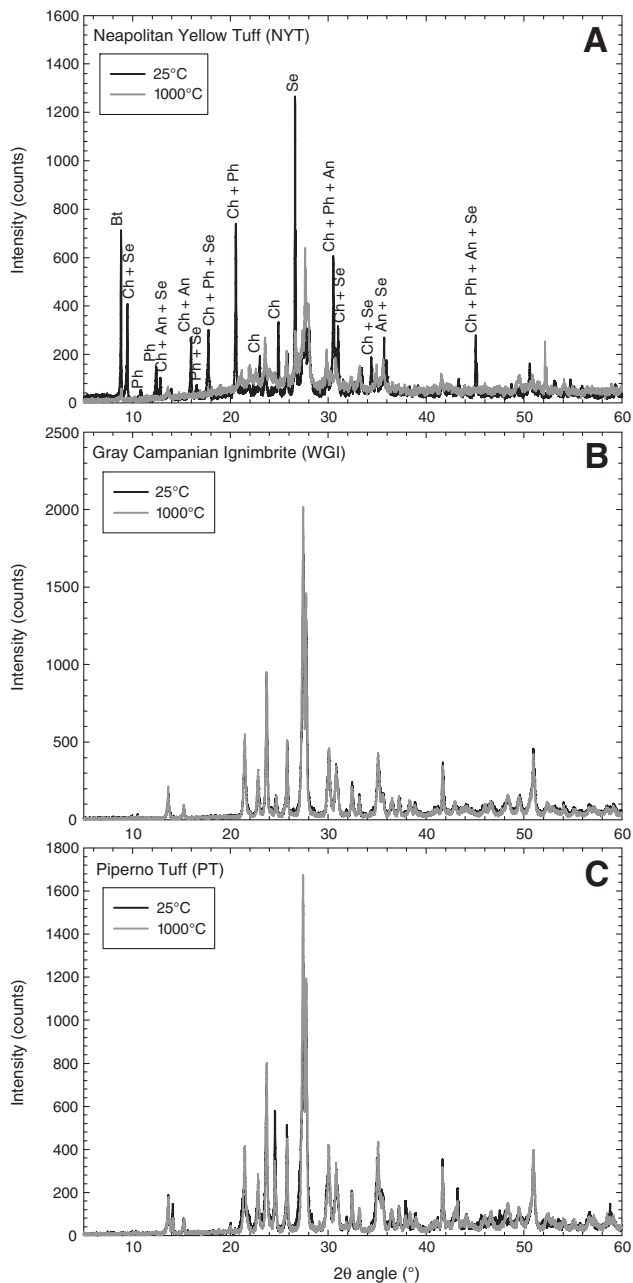
Figure 2. X-ray diffraction (XRD) patterns. A: Neapolitan Yellow Tuff. Only hydrated minerals and biotite (Bt) are labeled in A. Ph—phillipsite; Ch—chabazite; An—analcime; Se—segelerite. B: Gray Campanian Ignimbrite (welded gray ignimbrite, WGI). C: Piperno Tuff. Panels show both "as-received" XRD patterns (black lines) and XRD patterns for samples thermally stressed to 1000 °C (gray lines).

Figure 3. A: Influence of thermal stressing on uniaxial compressive strength (one sample per temperature). NYT—Neapolitan Yellow Tuff; WGI— welded grayCampanian Ignimbrite; PT—Piperno Tuff. B: Influence of thermal stressing on indirect tensile strength (average of two samples per temperature). C: Stress-strain curves for constant strain rate uniaxial compressive tests on samples of thermally stressed NYT. Temperature next to each curve indicates thermal stressing temperature for that sample. D: Mass loss with temperature for each sample, by means of thermogravimetric analysis.

REFERENCES CITED

Calcaterra, D., Cappelletti, P., Langella, A., Morra, V., Colella, A., and de Gennaro, R., 2000, The building stones of the ancient centre of Naples (Italy): Piperno from Campi Flegrei. A contribution to the knowledge of a long-time-used stone: Journal of Cultural Heritage, v. 1, p. 415–427, doi:10.1016/S1296-2074(00)01097-9.

Cappelletti, P., Cerri, G., Colella, A., de Gennaro, M., Langella, A., Perrotta, A., and Scarpati, C., 2003, Post-eruptive processes in the Campanian Ignimbrite: Mineralogy and Petrology, v. 79, p. 79–97, doi:10.1007/s00710-003-0003-7.

Colella, C., de Gennaro, M., and Aiello, R., 2001, Use of zeolitic tuff in the building industry: Reviews in Mineralogy and Geochemistry, v. 45, p. 551–587, doi:10.2138/rmg.2001.45.16.

de Gennaro, M., and Colella, C., 1989, Use of thermal analysis for the evaluation of zeolite content in mixtures of hydrated phase: Thermochimica Acta, v. 154, p. 345–353, doi:10.1016/0040-6031(89)85472-3.

de Gennaro, M., and Langella, A., 1996, Italian zeolitized rocks of technological interest: Mineralium Deposita, v. 31, p. 451–472, doi:10.1007/BF00196127.

de Gennaro, M., Colella, C., Franco, E., and Aiello, R., 1983, Italian zeolites 1. Mineralogical and technical features of Neapolitan yellow tuff: Industrial Minerals, v. 186, p. 47–53.

de Gennaro, M., Colella, C., Aiello, R., and Franco, E., 1984, Italian zeolites 2. Mineralogical and technical features of Campanian tuff: Industrial Minerals, v. 204, p. 97–109.

de Gennaro, M., Petrosino, P., Conte, M.T., Munno, R., and Colella, C., 1990, Zeolite chemistry and distribution in a Neapolitan Yellow Tuff deposit: European Journal of Mineralogy, v. 2, p. 779–786.

de Gennaro, M., Cappelletti, P., Langella, A., Perrotta, A., and Scarpati, C., 2000, Genesis of zeolites in the Neapolitan Yellow Tuff: Geological, volcanological and mineralogical evidences: Contributions to Mineralogy and Petrology, v. 139, p. 17–35, doi:10.1007/s004100050571.

Hall, S.A., de Sanctis, F., and Viggiani, G., 2006, Monitoring fracture propagation in a soft rock (Neapolitan Tuff) using acoustic emissions and digital images: Pure and Applied Geophysics, v. 163, p. 2171–2204, doi:10.1007/s00024-006-0117-z.

ISRM (International Society for Rock Mechanics), 1978, SM for Determining Tensile Strength of Rock Materials–1978 [EUR 4], Part 2; SM for Determining Indirect Tensile Strength by the Brazil Test, in Ulusay, R., and Hudson, J.A., eds., The complete ISRM suggested methods for rock characterization, testing and monitoring: Lisbon, Portugal, International Society for Rock Mechanics, 628 p.

Morra, V., Calcaterra, D., Cappelletti, P., Colella, A., Fedele, L., de' Gennaro, R., Langella, A., Mercurio, M., and de' Gennaro, M., 2010, Urban geology: Relationships between geological setting and architectural heritage of the Neapolitan area, in Beltrando, M., et al., eds., The geology of Italy: Tectonics and life along plate margins: Journal of the Virtual Explorer (electronic edition), v. 36, paper 27, doi:10.3809/jvirtex.2010.00261.

Orsi, G., de Vita, S., and di Vito, M., 1996, The restless, resurgent Campi Flegrei nested caldera (Italy): Constraints on its evolution and configuration: Journal of Volcanology and Geothermal Research, v. 74, p. 179–214, doi:10.1016/S0377-0273(96)00063-7.

Schultz, R.A., and Li, Q., 1995, Uniaxial strength testing of non welded Calico Hills tuff, Yucca Mountain, Nevada: Engineering Geology, v. 40, p. 287–299, doi:10.1016/0013-7952(95)00041-0.

Tuccimei, P., Mollo, S., Vinciguerra, S., Castelluccio, M., and Soligo, M., 2010, Radon and thoron emission from lithophysae-rich tuff under increasing deformation: An experimental study: Geophysical Research Letters, v. 37, L05305, doi:10.1029/2009GL042134.

Zhu, W., Baud, P., Vinciguerra, S., and Wong, T.-f., 2011, Micromechanics of brittle faulting and cataclastic flow in Alban Hills tuff: Journal of Geophysical Research, v. 116, B06209, doi:10.1029/2010JB008046.

Fire resistance of the Mt. Epomeo Green Tuff, a widely-used building stone on Ischia Island (Italy)

Michael J. Heap[*α], Alexandra R. L. Kushnir[α], Luke Griffiths[α], Fabian B. Wadsworth[†β], Gian Marco Marmoni[γ], Matteo Fiorucci[γ], Salvatore Martino[γ], Patrick Baud[α], H. Albert Gilg[δ], Thierry Reuschlé[α]

[α] *Géophysique Expérimentale, Institut de Physique de Globe de Strasbourg (UMR 7516 CNRS, Université de Strasbourg/EOST), 5 rue René Descartes, 67084 Strasbourg cedex, France.*
[β] *Earth & Environmental Sciences, Ludwig Maximilians Universität, Theresienstr. 41/III, 80333 Munich, Germany.*
[γ] *Earth Science Department, Sapienza University of Rome, Piazzale Aldo Moro 5, 00185 Rome, Italy.*
[δ] *Lehrstuhl für Ingenieurgeologie, Technische Universität München, Munich, Germany.*

Abstract

The use of Mt. Epomeo Green Tuff (MEGT) as a building stone is widespread on Ischia Island (Italy). We assess here the fire resistance of MEGT by thermally stressing samples to temperatures up to 1000 °C. Porosity and uniaxial compressive strength increase and decrease from 44% and 4.5 MPa at ambient temperature to 48% and 1.5 MPa following exposure to 1000 °C, respectively. Complementary thermogravimetric and X-ray powder diffraction analyses, experiments that monitor acoustic emissions during heating/cooling, and microstructural observations highlight that these changes are the result of thermal microcracks, formed due to the breakdown of zeolites and clays (MEGT contains 35 wt.% analcime, 15 wt.% smectite, and 3 wt.% illite) at high temperature. Although the stability of structures built from MEGT will be jeopardised at high temperature, a very low thermal diffusivity requires that fires must burn for many hours to compromise the strength of a typical dimension stone: tuffs are tough in the event of fire.

Résumé

Le tuf vert de Mt. Epomeo (MEGT) est très utilisé comme matériau de construction dans l'ile d'Ischia (Italie). Nous avons analysé la résistance au feu du MEGT en soumettant cette roche à des traitements thermiques à des températures allant jusqu'à 1000°C. Si la porosité du MEGT augmente de 44% à température ambiante, à 48% à 1000 °C, sa résistance en compression uniaxiale décroit de 4,5 à 1,5 MPa sur le même intervalle de température. Des analyses thermogravimétriques et par diffractométrie de rayons X, l'enregistrement des émissions acoustiques durant le chauffage et le refroidissement, ainsi que des observations de la microstructure montrent que les changements observés sur le MEGT après traitement thermique sont liés au développement de microfissures. Ces microfissures se forment à cause de la rupture des zéolites et des argiles à haute température. Le MEGT contient 35% d'analcime, 15% de smectite et 3% d'illite. Bien que la stabilité de structures construites avec le MEGT puisse être compromise à haute température, la très faible diffusivité thermique de cette roche nécessite un incendie très long (plusieurs heures) pour vraiment réduire la résistance des blocs de roche typiquement utilisés dans les édifices de l'ile d'Ischia. Le tuf peut de ce fait être considéré comme une roche résistante en cas d'incendie.

1 Introduction

Tuffs—deposits from explosive eruptions—have been used worldwide as a building stone for millennia [Heiken 2006]. The use of tuff as a building stone is particularly prevalent in Italy. Notable examples include the cities of Naples [e.g. Calcaterra et al. 2000; de'Gennaro et al. 2000; Evangelista et al. 2000; Colella et al. 2001; Calcaterra et al. 2005; Heap et al. 2012; Benedetto et al. 2015; Heap et al. 2018] and Rome [e.g. De Casa et al. 1994; Jackson et al. 2005]. The use of green-coloured tuff from Mt. Epomeo as a building stone is widespread on Ischia Island (a volcanic island in the Tyrrhenian Sea at the northern end of the Gulf of Naples, Italy). The Mt. Epomeo Green Tuff

---

[*]Corresponding author: heap@unistra.fr
[†]now at: Department of Earth Sciences, Durham University, Science Labs, Durham DH1 3LE, UK

(MEGT), a massive green-coloured alkali-trachytic pyroclastic flow deposit, was formed following an explosive caldera-forming eruption about 55 ka [Orsi et al. 1991; Tibaldi and Vezzoli 1998; Brown et al. 2007]. The MEGT represents the largest known eruption on Ischia Island and has an estimated volume of 40 km³ [Tomlinson et al. 2014]. MEGT is commonly used to construct walls and houses (Figure 1), including the striking San Ciro church (Figure 1A). Statues are found hewn from blocks of the green tuff (Figure 1B) and many houses and restaurants are built on top of, or inside, large blocks that litter the slopes of Mt. Epomeo and Mt. Nuovo as a result of historic rock avalanches [Seta et al. 2012; Della Seta et al. 2015] (Figure 1C–D).

Due to the widespread use of tuff as a building stone worldwide, many studies are devoted to understanding, for example, their resistance to fire [e.g. Duvarcı et al. 2007; Gomez-Heras et al. 2006; Heap et al. 2012], resistance to salt weathering [e.g. Török et al. 2004; Zedef et al. 2007; Vacchiano et al. 2008; Oguchi and Yuasa 2010; Yavuz 2012; Russa et al. 2017], resistance to freeze-thaw weathering [e.g. Chen et al. 2004; Török et al. 2004; Oguchi and Yuasa 2010; Nijland et al. 2010; Ruedrich et al. 2011; Yavuz 2012], and their strength in the presence of water and following wetting-drying cycles [e.g. Jackson et al. 2005; Siedel 2010; Oguchi and Yuasa 2010; Zhu et al. 2011; Benedetto et al. 2015; Heap et al. 2018].

The vulnerability of tuffs often used in construction in the Neapolitan area of Italy to the high temperatures of fire was the focus of a recent study by Heap et al. [2012]. These authors found that the strength of only one of the three tuffs was reduced following exposure to high temperature (up to 1000 °C). The weakening of this tuff—the Neapolitan Yellow Tuff—was found to be the result of microcracking and the disintegration of the matrix due to the dehydration and breakdown of zeolites (phillipsite, chabazite, and analcime) at high temperature; the other two tuffs did not contain any zeolites and were therefore unaffected by exposure to high temperature [Heap et al. 2012]. Since the MEGT contains zeolites (Pola et al. [2012] and Marmoni et al. [2017a]), we may expect similar reductions in strength. However, Marmoni et al. [2017a] found that the strength of MEGT did not change systematically following exposure to temperatures up to 300 °C. The influence of higher temperatures, such as those experienced during fires, on the physical properties of MEGT is currently unknown.

Fires are a secondary hazard in tectonically and volcanically active areas, and a Mediterranean climate consisting of hot and dry summers can exacerbate natural and accidental fires. For example, a fire of vast proportions (covering an area of ~1 km²) engulfed the wooded southwestern slope of Mt. Epomeo (MEGT forms a significant component of Mt. Epomeo: Marmoni et al. [2017a]), between the towns of Forio and Serrara Fontana, in August 2017 (Figure 2). We present

a study designed to better understand the influence of the high temperatures (up to 1000 °C) of fire (or from inundation by lava flows) on the physical properties (porosity and strength) of MEGT. Uniaxial compressive strength tests on thermally stressed samples of MEGT are supported by X-ray powder diffraction analyses (XRPD) on "as collected" (i.e. material that has undergone no heating or deformation) and thermally stressed MEGT, thermal property data (thermal diffusivity, thermal conductivity, and specific heat capacity), thermogravimetric data, acoustic emission (AE)—a proxy for microcracking—monitoring during heating and cooling, and microstructural observations of thermally stressed samples. Finally, we modelled heat conduction in an MEGT dimension stone to assess time-dependent physical property modifications during fire.

2 Experimental materials and methods

The microstructure and mineral content of our block of MEGT was first investigated using scanning electron microscopy (SEM) and X-ray powder diffraction (XRPD), respectively. The block—collected from the northern slope of Mt. Epomeo—is the same block used in recent mechanical studies focussed on gravitational slope deformation [Marmoni et al. 2017a; Marmoni et al. 2017b]. Thin sections were prepared from the as collected material and imaged using a Tescan Vega 2 XMU scanning electron microscope (SEM). The mineral content was quantified using XRPD using a powdered sample of the as collected MEGT. 10 wt.% ZnO (internal standard) was added to the MEGT powder and the powdered mixture was ground for 8 min with 10 ml of isopropyl alcohol in a McCrone Micronising Mill using agate cylinder elements. The XRPD analyses were performed on powder mounts using a PW 1800 X-ray diffractometer (CuKα, graphite monochromator, 10 mm automatic divergence slit, step-scan 0.02°2θ increments per second, counting time one second per increment, 30 mA, 40 kV). The phases in the whole rock powders were quantified using the Rietveld program BGMN [Bergmann et al. 1998]. To identify the clay minerals, we also separated < 2 µm fractions by gravitational settling and prepared oriented mounts that were X-rayed in an air-dried and an ethylene-glycolated state.

The studied block of MEGT is a heterogeneous green-coloured ignimbrite deposit that contains lithic fragments (< 10 mm in diameter), porous lapilli (i.e. pumice) fragments (< 20 mm in diameter), and phenocrysts hosted within an altered matrix (Figure 3; Table 1). The phenocrysts are mainly Na-rich sanidine (17 wt.%), Na-poor K-feldspar (25 wt.%), plagioclase (50 wt.%), and biotite (2 wt.%) (Figure 3; Table 1). The altered matrix comprises analcime (35 wt.%), smectite (12 wt.%), and Fe-rich illite (3 wt.%) (Table 1). Our block of MEGT is therefore similar in mineral con-

Figure 1: The use of Mt. Epomeo Green Tuff (MEGT) in construction on Ischia Island (Italy). [A] The San Ciro church. [B] Statue carved from a block of MEGT. [C] Restaurant built using MEGT on top of a block of MEGT. [D] House built inside a block of MEGT. [E] Wall constructed using blocks of MEGT. Photo credit for all pictures: M.J. Heap.
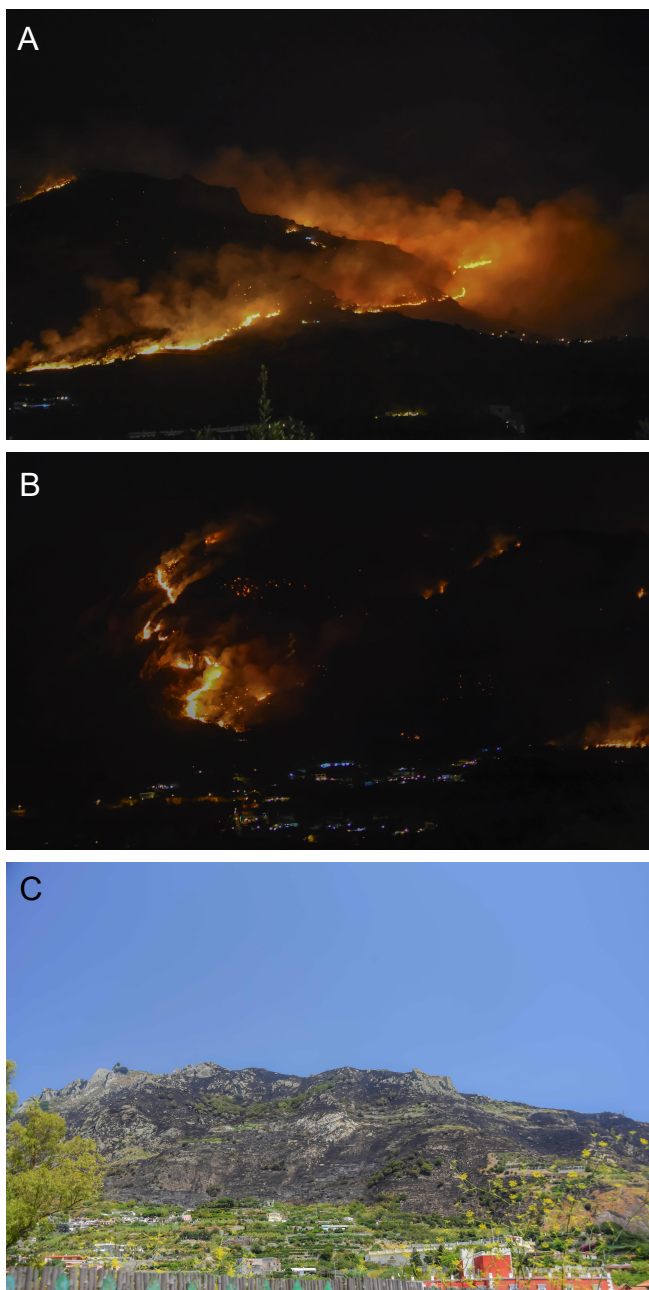
Figure 2: [A] and [B] Photographs of the August 2017 fire that engulfed the wooded southwestern slopes of Mt. Epomeo. [C] Photograph of the charred volcanic slope following the fire. Photographs taken by, and used with permission from, Michele Abbagnara.

Table 1 – Quantitative bulk mineralogical composition, determined using X-ray powder diffraction (XRPD), for the "as collected" (i.e. material that has undergone no heating or deformation) Mt. Epomeo Green Tuff (MEGT) used in this study.

Mineral	Mineral content (wt.%)
Na-rich sanidine	17 ± 2
Plagioclase	5 ± 1
Biotite	2 ± 1
Analcime	35 ± 2
Na-poor K-feldspar	25 ± 2
Cristobalite	< 1
Calcite	1 ± 2
Smectite	12 ± 3
Fe-rich illite	3 ± 2

(Figure 3). Our XPRD analysis found no residual glass (Table 1). Microstructurally, the MEGT is very heterogeneous and contains pores of various sizes (from a few tens of microns up to a few millimetres in diameter) (Figure 3) and large (often several millimetres long) altered porous fragments (Figure 3).

Cylindrical samples were cored in the same orientation from a single block of MEGT to a diameter of 25 mm and cut and precision-ground to a nominal length of 60 mm. Samples were cored so as to avoid centimetric-scale juvenile lapilli and lithic fragments. To avoid the washout of porous lapilli and the fine fraction, the sample block was first soaked in water and then cored dry (i.e. samples were cored without running water). A total of 25 cylindrical samples were prepared, gently washed to remove any water-soluble grinding fluid, and then dried in a vacuum at 40 °C for at least 48 h. Their connected porosities were determined using a helium pycnometer (Micromeritics AccuPyc II 1340). The average connected porosity of these 25 samples was measured to be 44.7% (standard deviation of 1.6%). To avoid problems with sample variability, we selected a subset of 14 cores with similar connected porosities (average of 44.8% and a standard deviation of 0.7%). Pairs of samples were heated to target temperatures of 100, 200, 300, 500, 750, and 1000 °C in an oven at ambient pressure. Samples were heated at a constant heating rate of $1\,°C\,min^{-1}$, left at the target temperature for 2 h, before being cooled back to ambient temperature at $1\,°C\,min^{-1}$. The colour of the samples changed from pale green to yellow-orange following exposure to 500 °C and, finally, to blood-orange following exposure to 1000 °C (Figure 4). The connected porosities of the thermally stressed samples were then remeasured using the helium pycnometer. A pair of samples was left unheated to serve as a comparison. Finally, the 14 samples were deformed uniaxially at ambient temperature at a strain rate of $1.0 \times$

tent to the clasts (pebble- to boulder-sized) of MEGT found in polymictic breccia that covers large portions of the area from just downslope of the summit of Mt. Epomeo to the southern coast several km away [Altaner et al. 2013]. This mineral content indicates a high alteration temperature (> 70 °C) in a mostly closed chemical system [Altaner et al. 2013]. Our XRPD analysis also found subordinate calcite (1 wt.%) and cristobalite (< 1 wt.%) (Table 1) and our microstructural analysis highlighted the presence of iron and titanium oxides
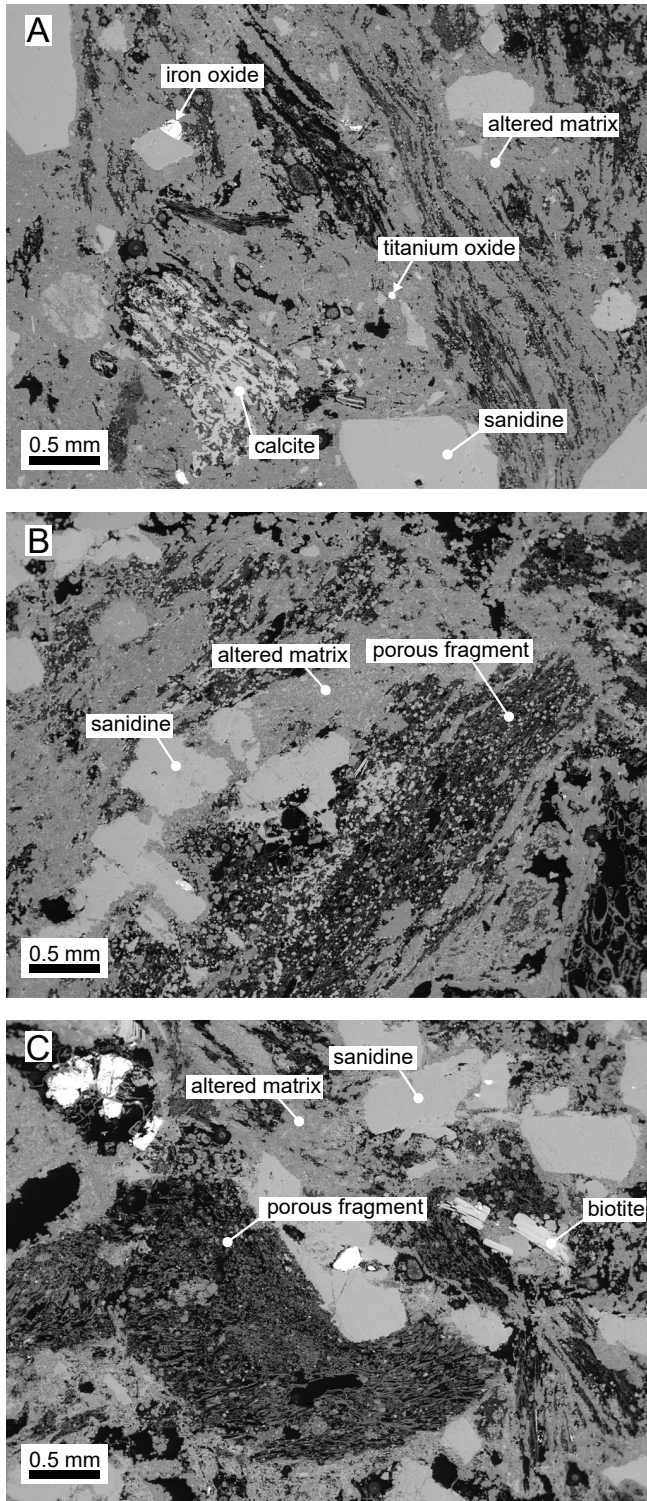
Figure 3: Backscattered scanning electron microscope images of "as collected" (i.e. material that has undergone no heating or deformation) Mt. Epomeo Green Tuff (MEGT).

10^{-5} s^{-1} until macroscopic failure. A lubricating wax was applied to the ends of the samples to reduce frictional constraint at the interface between the sample and the pistons [Labuz and Bridell 1993]. The output of AE during deformation was monitored using a

wideband (bandwidth of 100-1000 kHz; from Physical Acoustics) AE sensor—embedded within the bottom endcap—connected to a USB AE node (a single channel AE digital signal processor with a built-in 26 dB pre-amplifier; from Physical Acoustics). AEs are high frequency elastic wave packets generated by the rapid release of strain energy and are frequently used as a proxy for microcracking in laboratory experiments [e.g. Lockner 1993]. In our experiments, an AE "hit" was counted if the amplitude of the received signal exceeded the detection threshold (set at 30 dB). The AE energy (in arbitrary units) of an AE hit was calculated as the area under the received waveform.

We also performed thermo-gravimetric analysis (TGA) on a powdered sample (~40 mg) of MEGT using a Netzsch Pegasus 404 thermal analysis device. The powdered sample was heated in an atmosphere flushed with argon at a flow rate of 20 ml min^{-1} inside a platinum crucible (with lid). The powders were first heated to 100 °C. This temperature was kept constant for 20 minutes to ensure that any free water (i.e. not structurally bound) was removed. The powder was then heated at 1 °C min^{-1} to 1000 °C. This type of analysis tracks the mass loss of a sample as a result of, for example, the dehydroxylation of zeolites during heating (see, for example, de'Gennaro and Colella [1989] and Heap et al. [2012]).

The output AE during heating and cooling was recorded on an additional cylindrical sample (20 mm in diameter and nominally 40 mm in length) using a system specifically designed to record AE at high temperature. The setup consists of a servo-controlled uniaxial press and a tube furnace [Griffiths et al. 2018]. The sample was held between the pistons of the uniaxial press, under a constant servo-controlled load of 100 N. The tube furnace was placed around the sample and pistons and programmed to heat the sample at a rate of 1 °C min^{-1} to a target temperature of 700 °C, dwell for 2 h at the target temperature, before cooling the sample back to ambient temperature at a rate of 1 °C min^{-1}. AE activity was detected using a micro80 AE sensor (bandwidth of 200-900 kHz and a resonant frequency of 325 kHz; from Physical Acoustics) embedded in the centre of the upper piston, which acts as a continuous wave guide. The AE sensor was connected to a USB AE node, and the detection threshold was set at 40 dB. This system is optimised for recording AE during heating: (1) the upper piston acts as a continuous wave guide, circumventing attenuation due to surface interfaces; (2) the sensor is embedded within the centre of the piston rather than on the side, improving amplitude and frequency content of the signal; (3) the piston is cooled (to protect the sensor) using a custom-built air-cooling system that does not generate detectable electrical or mechanical noise; (4) the servo-controlled displacement of the lower piston during heating and cooling compensates for their thermal expansion and contraction, providing a constant load on the sample to avoid any oscil-
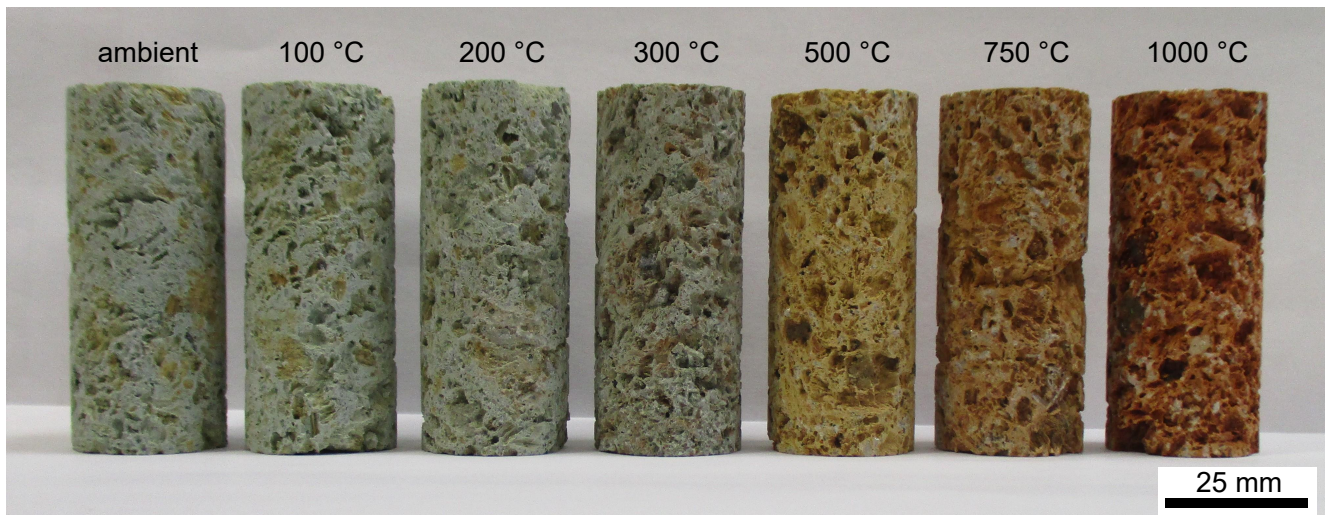
Figure 4: Photograph of a suite of thermally stressed samples of Mt. Epomeo Green Tuff (MEGT). Temperature quoted above each sample is the thermal stressing temperature. "Ambient" (i.e. ambient temperature) indicates a sample that underwent no thermal stressing.

lation in coupling and, ultimately, in the AE detection threshold [Griffiths et al. 2018].

The thermal diffusivity, thermal conductivity, and specific heat capacity of the MEGT were measured using a Hot Disk TPS 500 Thermal Constants Analyser using the Hot Disk method [Gustafsson 1991; Gustavsson et al. 1994]. A Kapton sensor 6.403 mm in radius was sandwiched between two 40 mm-diameter cylindrical samples (20 mm long) and measurements were conducted at a system output power of 150 mW for 40 s. The measurements were conducted at ambient temperature (21 °C). Specific heat capacity was calculated by the system after measurement. A series of four consecutive measurements was performed on different sample surfaces to account for sample heterogeneity. Individual measurements were performed at least 5 min apart, to ensure that the sample temperature returned to 21 °C before the subsequent measurement. No corrections were made to the measured value of thermal conductivity [see Nabelek et al. 2010, for example].

Microstructural analyses were performed on thin sections prepared from samples of MEGT thermally stressed to 500 and 750 °C using the aforementioned SEM.

3   RESULTS

3.1   Connected porosity and uniaxial compressive strength

The stress-strain curves of selected experiments at each thermal stressing temperature are shown in Figure 5, and are typical of those for brittle rock in compression [e.g. Hoek and Bieniawski 1965; Brace et al. 1966; Scholz 1968]. Figure 5 shows that the strength of MEGT

is clearly reduced as thermal stressing temperature increases, best shown on a plot of uniaxial compressive strength (UCS) as a function of thermal stressing temperature (Figure 6A). We also find that connected porosity increases with thermal stressing temperature (Figure 6B). In detail, connected porosity and UCS increase and decrease from 44% and 4.5 MPa at ambient temperature to 48% and 1.5 MPa following exposure to 1000 °C, respectively (Figure 6; Table 2). The stress-strain curves and cumulative AE energy curves are plotted for a sample left at ambient temperature and for samples thermally stressed to temperatures of 500 and 1000 °C in Figure 7. While the output of AE accelerates up to failure in the ambient and 500 °C sample (Figure 7A and 7B), typical for brittle rock in compression [e.g. Scholz 1968], AE activity for the sample thermally stressed to 1000 °C does not accelerate up to failure. These data also show that the cumulative AE energy during deformation and failure is much greater for the 1000 °C sample than for the ambient and 500 °C samples (Figure 7).

3.2   Thermogravimetric analysis

Relative mass as a function of temperature is shown in Figure 8. The data show that MEGT loses ~3.2% of its mass up to a temperature of ~300 °C, and a further ~1.1% from ~300 to ~630 °C (Figure 8). There is little change in mass from ~630 °C up to the maximum temperature of 1000 °C (Figure 8).

3.3   Acoustic emission activity during heating and cooling

The output of AE during heating to and cooling from 700 °C are shown in Figure 9. Significant AE activity

Table 2 – Summary of the experimental data collected for this study.

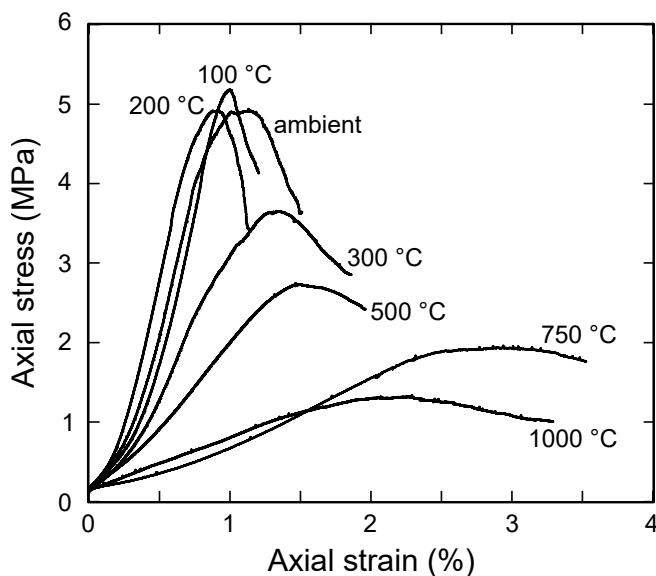| Sample number	Thermal stressing temperature (°C)	Connected porosity (%)	Uniaxial compressive strength (MPa)
MEGT 1	-	43.5	4.94
MEGT 3	-	44.4	4.05
MEGT 6	100	44.9	3.98
MEGT 8	100	44.1	5.18
MEGT 7	200	46.1	2.60
MEGT 9	200	44.6	4.91
MEGT 10	300	47.3	2.57
MEGT 12	300	47.1	3.65
MEGT 13	500	47.2	2.74
MEGT 14	500	46.1	4.19
MEGT 15	750	49.3	2.69
MEGT 16	750	48.6	1.94
MEGT 17	1000	47.9	1.72
MEGT 18	1000	48.1	1.32

MEGT = Mt. Epomeo Green Tuff.

Figure 5: Uniaxial stress-strain curves for samples of Mt. Epomeo Green Tuff (MEGT). Temperature next to each curve corresponds to the thermal stressing temperature. "Ambient" (i.e. ambient temperature) indicates a sample that underwent no thermal stressing.

starts at ~200 °C during the heating cycle and continues up to the maximum temperature of 700 °C (Figure 9B). There are two large spikes in AE activity during heating, at a temperature of ~370–380 °C and a temperature of ~540–580 °C (Figure 9A). Far fewer AE were recorded during the cooling phase than during the heating phase (Figure 9B).

3.4 Thermal property data

Values of thermal conductivity, thermal diffusivity, and volume-specific heat capacity for MEGT are $0.499 \, \mathrm{W \, mK^{-1}}$, $0.451 \, \mathrm{mm^2 \, s^{-1}}$, and $1.132 \, \mathrm{MJ \, m^{-3} \, K^{-1}}$, respectively (Table 3).

3.5 Microstructural observations

Backscattered SEM images of samples of MEGT exposed to temperatures of 500 and 700 °C (i.e. before and after the large spike in AE activity at temperatures of ~540–675 °C; Figure 9) are shown in Figure 10. Microcracks are observed within the altered matrix of these thermally stressed samples (Figure 10B). Many more microcracks are seen in the 750 °C sample (Figure 10C and 10D) than in the sample heated to 500 °C (Figure 10A and 10B). The formed microcracks appear very tortuous and often deflect around the small crystals that form the altered matrix (Figure 10B). The large microcrack seen in the sample heated to 750 °C appears to have originated from inside one of the porous fragments Figure 10C and 10D).

3.6 Mineral content of MEGT following exposure to high temperature

To better understand the changes to the mineral content of the MEGT following exposure to high temperature, we performed XRPD analysis on a sample of powdered MEGT that had been thermally stressed to 1000 °C. The XRPD procedure was performed as de-

Table 3 – Thermal properties of Mt.Epomeo Green Tuff, Neapolitan Yellow Tuff, Grey Campanian Ignimbrite, and high-strength concrete.

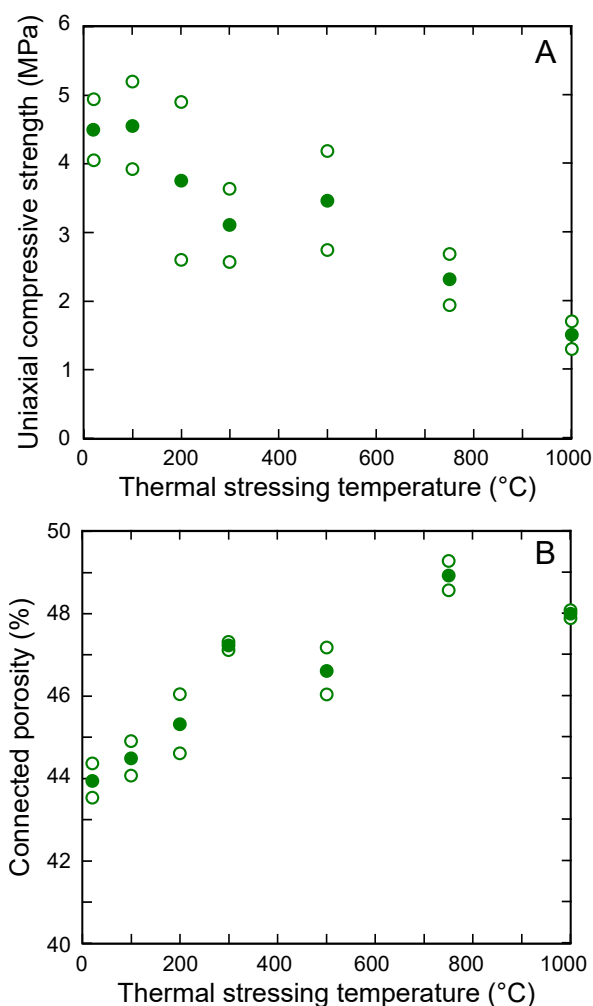| Sample	Thermal conductivity $(W\,mK^{-1})$	Thermal diffusivity $(mm^2\,s^{-1})$	Volume-specific heat capacity $(MJ\,m^{-3}\,K^{-1})$
Mt.Epomeo Green Tuff	0.4990	0.4513	1.1324
Neapolitan Yellow Tuff	0.4004	0.2902	1.3801
Grey Campanian Ignimbrite	0.4148	0.4360	0.9246
High-strength concrete	3.0997	1.4537	2.1729

Figure 6: [A] Uniaxial compressive strength (UCS) as a function of thermal stressing temperature for Mt. Epomeo Green Tuff (MEGT) (open symbols). The filled symbols are the averages of two measurements (Table 2). [B] Connected porosity as a function of thermal stressing temperature for MEGT (open symbols). The filled symbols are the averages of two measurements (Table 2).

scribed above. The XRPD profiles for an as collected sample and a sample exposed to 1000 °C are shown in Figure 11. The curves show that, following exposure to 1000 °C, the sample has lost analcime, smectite, and Fe-rich illite (Figure 11). The curves also indicate a slight decrease in biotite and the growth of an amorphous phase and other hitherto unidentified phases (Figure 11).

4   Discussion

4.1   The weakening of MEGT following exposure to high temperature

Our data show that the strength of MEGT is reduced from ~4.5 MPa at ambient temperature down to ~1.5 MPa following exposure to 1000 °C (Figure 6A; Table 2), a reduction in strength of ~70%. A similar reduction in strength was seen for Neapolitan Yellow Tuff following exposure to high temperature: strength was reduced from ~3.4 MPa at ambient temperature to ~0.7 MPa following exposure to 750 °C, a reduction of ~80% (Figure 12; Heap et al. [2012]). The weakening of the Neapolitan Yellow Tuff following exposure to high temperature was found to be the result of microcracking due to the dehydration and breakdown of zeolites (phillipsite, chabazite, and analcime) [Heap et al. 2012].

Our thermogravimetric analysis can be interpreted here to record the dehydration and dehydroxylation of the zeolites and clays within the matrix (Figure 8). Indeed, our XRPD analyses (Figure 11) show that MEGT loses analcime, smectite, and illite following exposure to high temperature. Our thermogravimetric analysis can provide the temperature ranges at which these reactions take place, to guide our mechanical and microstructural interpretations. Smectite typically dehydrates at temperatures ~100–150 °C and undergoes mass loss due to dehydroxylation at temperatures ~400–600 °C [Girgis et al. 1987]. However, the smectite within our block of MEGT is probably characterised by a cis-vacant dioctahedral structure due to the abundance of Al and therefore likely dehydroxylates at slightly higher temperatures, between 650 and
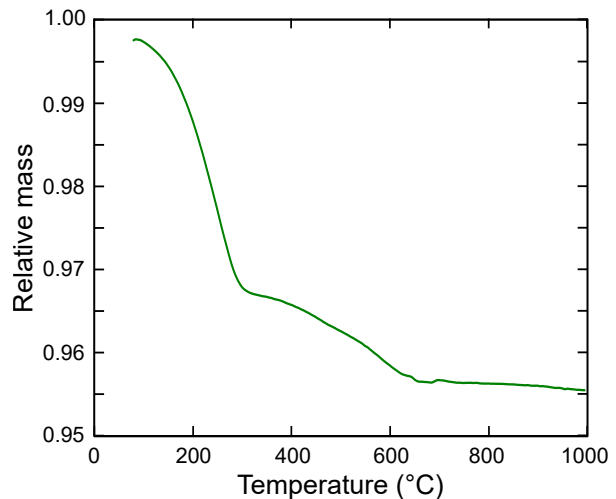
Figure 8: Relative mass as a function of temperature for Mt. Epomeo Green Tuff (MEGT).

tion of Fe-illite occurs at a temperature of ~100 °C and large mass losses due to dehydroxylation occur at temperatures from ~350 °C [Murad 1996]. Mass losses due to the dehydroxylation of Fe-illite peak at ~565 °C and Mössbauer spectroscopy highlighted the disappearance of Fe_2^+ at temperatures of ~250 °C [Murad 1996]. Analcime irreversibly loses water and phillipsite undergoes a partial reversible dehydration at ~240 °C [de'Gennaro and Colella 1989]. The structure of analcime reaches a maximum distortion at ~375 °C, associated with the complete loss of water and a reduction in volume [Cruciani and Gualtieri 1999]. Our thermogravimetric analysis shows that the majority of the mass loss occurs up to a temperature of ~300 °C (Figure 8), a likely result of the high proportion of analcime (35 wt.%) compared to smectite and Fe-rich illite (12 and 3 wt.%, respectively). The mass loss between ~400 and ~650 °C is likely associated with the dehydroxylation Fe-rich illite [Murad 1996] and perhaps the start of the dehydroxylation of the Al-rich smectite [Wolters and Emmerich 2007]. The thermogravimetric data for MEGT (Figure 8) are similar to data for other zeolite-bearing tuffs [e.g. de'Gennaro and Colella 1989; Heap et al. 2012].

Our AE data show that MEGT undergoes thermal microcracking during heating and cooling (Figure 9). The output of AE has been previously used to monitor thermal microcracking in rock during heating [e.g. Glover et al. 1995] and during heating and cooling [e.g. Heap et al. 2014a; Browning et al. 2016; Griffiths et al. 2018]. Thermal microcracks are thought to be the consequence of stresses that arise due to the mismatch in thermal expansion and contraction of the mineral constituents. We observed two large spikes in AE activity at temperatures of ~370–380 °C and ~540–580 °C (Figure 9). The temperature of the first AE spike corresponds to the temperature of the maximum volume reduction in analcime (~375 °C; Cruciani and Gualtieri [1999]). We suggest that the breakdown of analcime—which likely
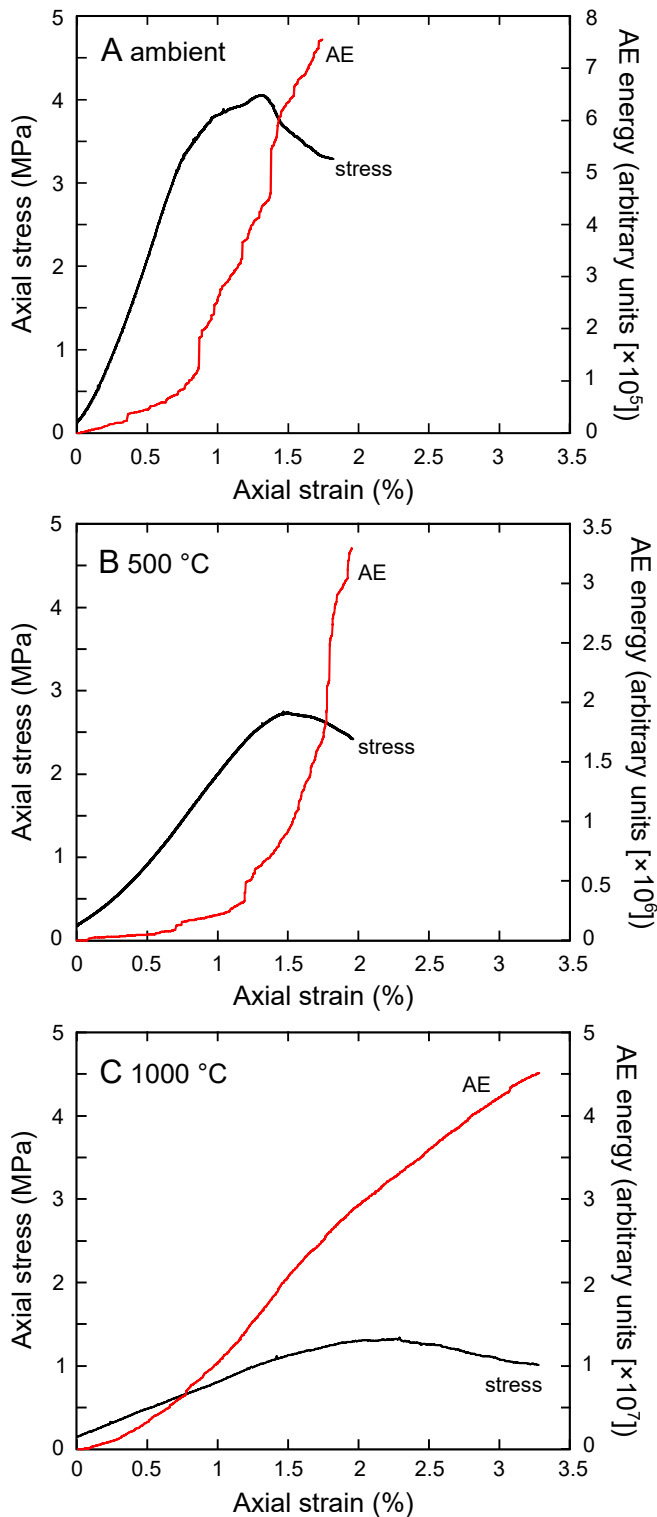

Figure 7: Uniaxial stress-strain curves for samples of Mt. Epomeo Green Tuff (MEGT) together with the cumulative output of AE energy. [A] MEGT sample left at ambient temperature (i.e. a sample that underwent no thermal stressing). [B] MEGT sample thermally stressed to 500 °C. [C] MEGT sample thermally stressed to 1000 °C.

700 °C [Wolters and Emmerich 2007]. The dehydra-
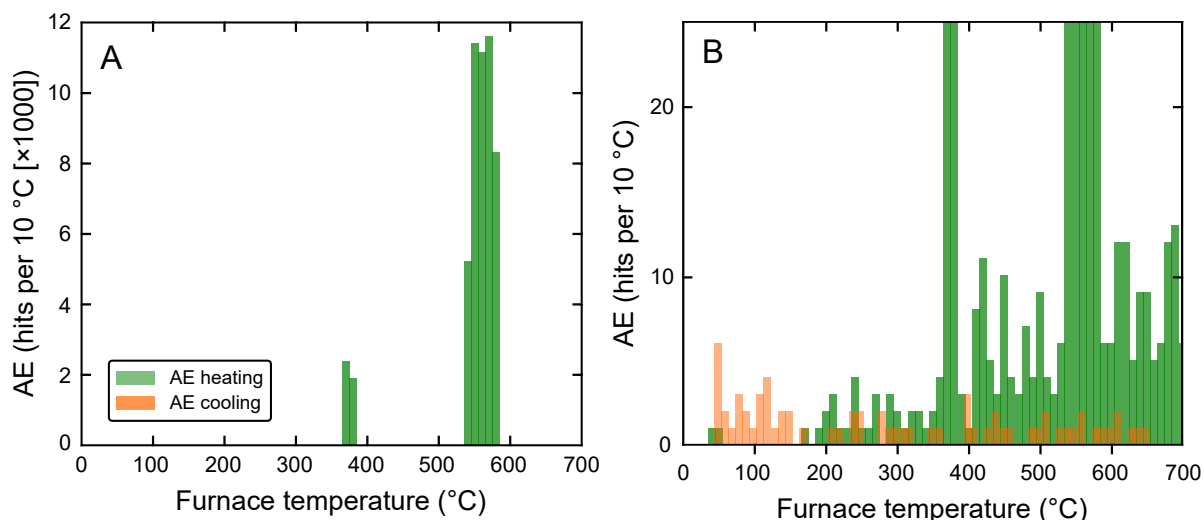
Figure 9: [A] The number of acoustic emission (AE) hits per 10 °C recorded during a thermal stressing experiment on Mt. Epomeo Green Tuff (MEGT) to a maximum temperature of 700 °C. [B] A graph showing a zoom of the data shown in panel [A] to highlight the AE hits recorded during cooling.
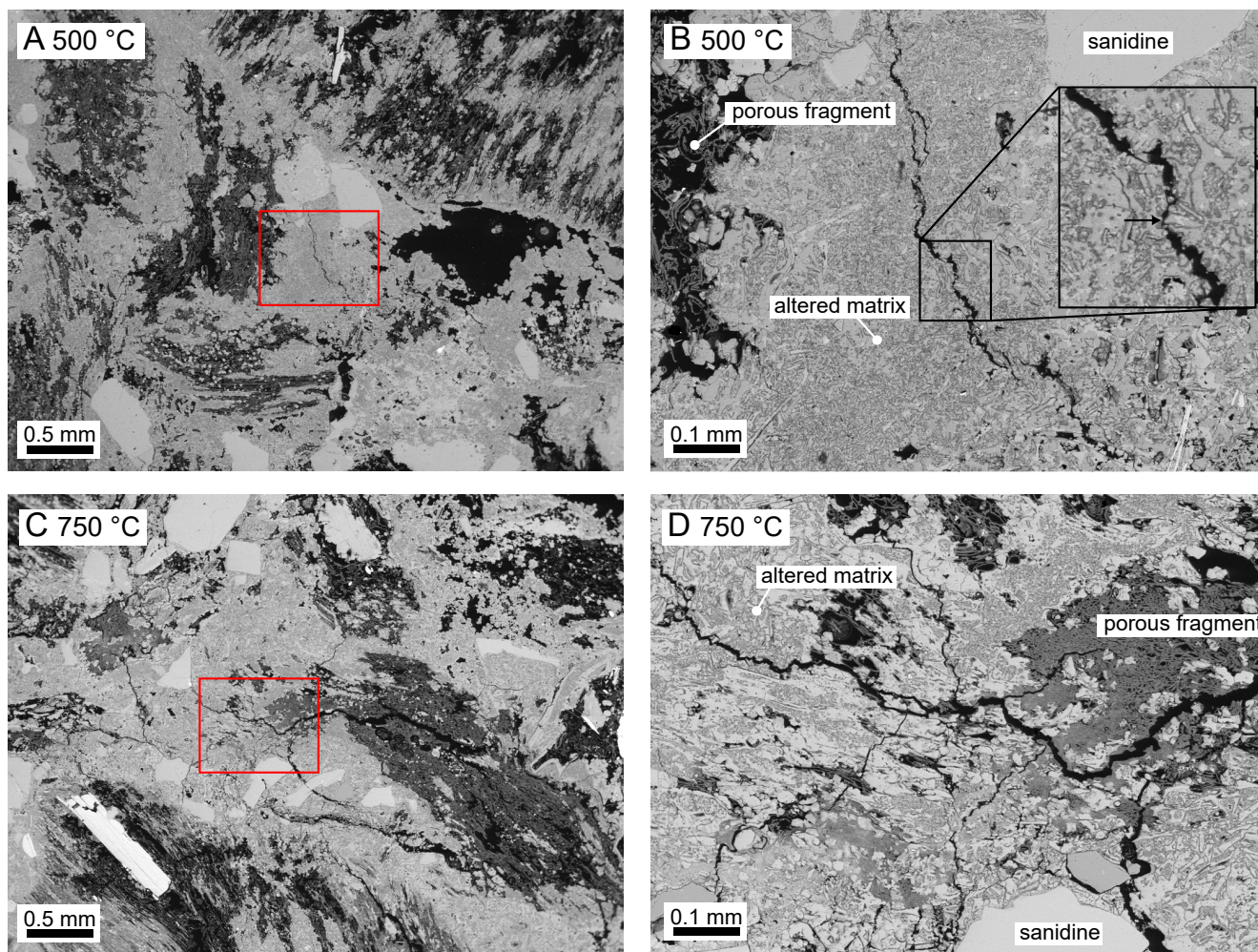
Figure 10: Backscattered scanning electron microscope images of Mt. Epomeo Green Tuff (MEGT) that have been thermally stressed to 500 °C (panel [A]) and 750 °C (panel [D]). Panels [B] and [D] show zoomed-in images from panels [A] and [B], respectively (indicated by the red rectangles). Inset in panel [B] shows a close-up of the fracture; the arrow indicates a crystal fragment that has deflected the path of the tortuous fracture.
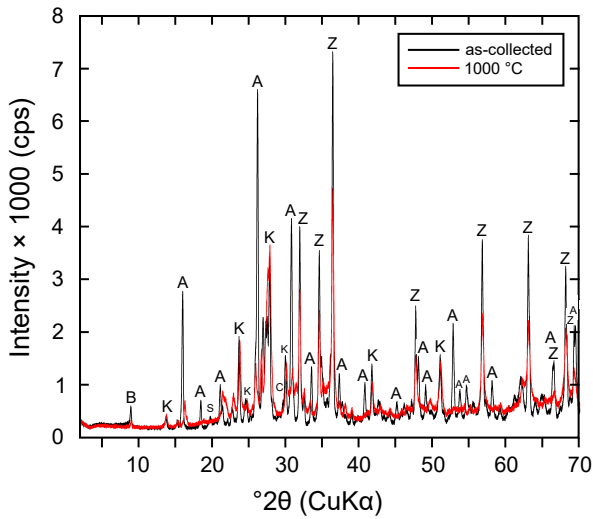
Figure 11: X-ray powder diffraction (XRPD) profile for a sample of "as collected" (i.e. material that has undergone no heating or deformation) Mt. Epomeo Green Tuff (MEGT) and a sample of MEGT exposed to 1000 °C. Z – ZnO; B – biotite; A – analcime; S – smectite; C – calcite; K – K-feldspar.
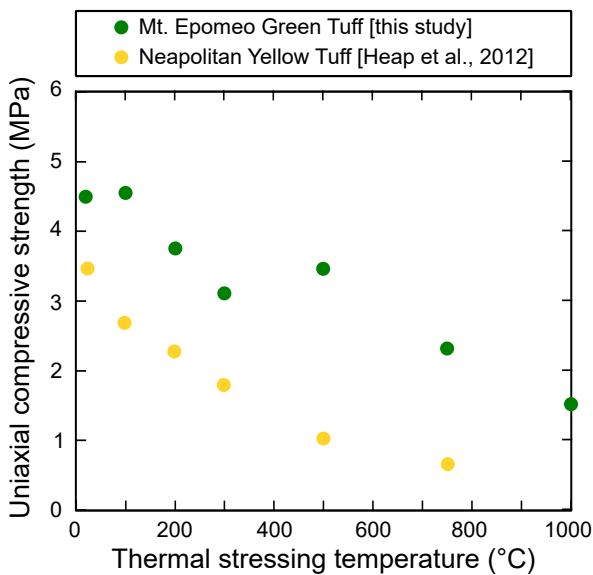
Figure 12: Uniaxial compressive strength (UCS) as a function of thermal stressing temperature for Mt. Epomeo Green Tuff (MEGT) (data from this study; symbols represent the average of two experiments, see Table 2) and Neapolitan Yellow Tuff (data from Heap et al. [2012]).

contributed to the lithification of ignimbrite deposits [e.g. de'Gennaro et al. 2000]—resulted in microcracking, as exhibited by our AE data (Figure 9) and observed in our microstructural analysis (Figure 10B). We attribute the second spike in AE activity (∼540–580 °C; Figure 9) primarily to the dehydroxylation of Fe-rich illite, for which the maximum mass loss occurs at a temperature of ∼565 °C [Murad 1996]. We note that this temperature is slightly below that required for the dehydroxylation of Al-rich smectite (between 650 and 700 °C) [Wolters and Emmerich 2007], although we cannot definitively rule out that some of the smectite within the MEGT dehydroxylated within this lower temperature range. The large number of AE hits detected within this temperature range (∼540–580 °C; Figure 9) are reflected in the microstructure: we observe many, tortuous microcracks in the sample thermally stressed to 750 °C (Figure 10C and 10D).

We therefore conclude that the observed weakening in MEGT following exposure to high temperature (Figures 5 and 6) is primarily due to the dehydration and breakdown of analcime up to a temperature of ∼400 °C and the dehydroxylation of Fe-rich illite and smectite at temperatures between ∼350 and ∼700 °C – both of which contribute to thermal microcracking (Figures 8, 9 and 10).

4.2 Heat conduction modelling: how tough is tuff in the event of fire?

To assess fire resistance of buildings constructed using MEGT, we consider the diffusion of heat through a half-space of MEGT. The diffusion of heat through a Cartesian half-space can be determined by solving:

$$\frac{dT(z)}{dt} = \frac{1}{\alpha}\frac{\partial^2 T}{\partial z^2} \qquad (1)$$

where T is temperature, z is the distance from the heat source, t is time, and α is the thermal diffusivity of the material. Our determination of α was not dependent on temperature, and so we can make a simplification to Equation 1 that results in the error function solution that is analytical:

$$\frac{T(z) - T_w}{T_i - T_w} = 1 - \mathrm{erf}\left(\frac{z}{2\sqrt{\alpha t}}\right) \qquad (2)$$

where the limits of T_w and T_i represent the temperature of the wall heat source and the initial temperature of block, respectively. In this formulation, $2\sqrt{\alpha t}$ is the lengthscale of diffusion used to normalize z on the right hand side of Equation 2. Our conceptual model considers a width of MEGT consistent with a typical dimension stone (300 mm; see, for example, the stones used in the San Ciro church shown in Figure 1A) and assumes a fire temperature of $T_w = 1000$ °C. We solve Equation 2 for temperature at $0 < z < 300$ mm and at times: 1,

5, 10, and 20 hours. The results of our thermal modelling are presented in Figure 13A. Figure 13A shows a rectangle for each time step, designed to represent the dimension stone (300 mm). The fire (at a constant temperature of 1000 °C) is exposed to the left hand side of the dimension stone and the isotherms (indicated by a colour-coded scale: black – cold; white – hot) migrate into the stone from left to right. When $t = 0$ h (i.e. the first rectangle), for example, the dimension stone is entirely black, indicating that the temperature is 20 °C. Figure 13A shows that the 750 °C isotherm (the temperature at which the microstructure is greatly affected (Figure 10C and 10D) and the strength is notably lower (Figures 5 and 6)) reaches 18 mm into the block after 1 h, 39.5 mm after 5 h, 57.5 mm after 10 h, and 81 mm after 20 h (Figure 13A).

If we compare these model predictions with those for siliceous-aggregate, high-strength concrete (HSC) (the same material used in Heap et al. [2013]; $\alpha = 1.4537$ mm^2 s^{-1}; Table 2) (Figure 13B), we find, due to its higher thermal diffusivity, that the 750 °C isotherm (also an important isotherm for the physical degradation of HSC due to the decarbonation of calcium carbonate between 650 and 740 °C; Heap et al. [2013]) requires much shorter timescales to traverse the block (Figure 13B). In the case of the HSC, the 750 °C isotherm reaches 29 mm into the block after 1 h, 73 mm after 5 h, 103 mm after 10 h, and 145.5 mm after 20 h (Figure 13B). Thermal property measurements on two other types of tuff commonly used in construction in Italy—the Neapolitan Yellow Tuff and the grey Campanian Ignimbrite (the same materials used in Heap et al. [2012] and Heap et al. [2014b])—show that similarly porous tuffs also have very low thermal diffusivities (Table 3). These tuffs will therefore show similar heating profiles to the MEGT shown in Figure 13A. Therefore, although the connected porosity and uniaxial compressive strength of MEGT increase and decrease, respectively, with increasing thermal stressing temperature (Figures 5 and 6), our modelling shows that the low thermal diffusivity of MEGT (and other similarly porous tuffs) requires that fires must burn for many hours to jeopardise the stability of a typical dimension stone (Figure 13).

5   CONCLUDING REMARKS

Due to its widespread use as a building material on Ischia Island (Italy; Figure 1), we examined the fire resistance of Mt. Epomeo Green Tuff (MEGT). Although the connected porosity and uniaxial compressive strength of MEGT increase and decrease, respectively, with increasing thermal stressing temperature (Figure 6)—due to the formation microcracks (Figure 11) as a result of the dehydration and breakdown of analcime and clays (illite and smectite)—the low thermal diffusivity of MEGT requires that fires must burn for many
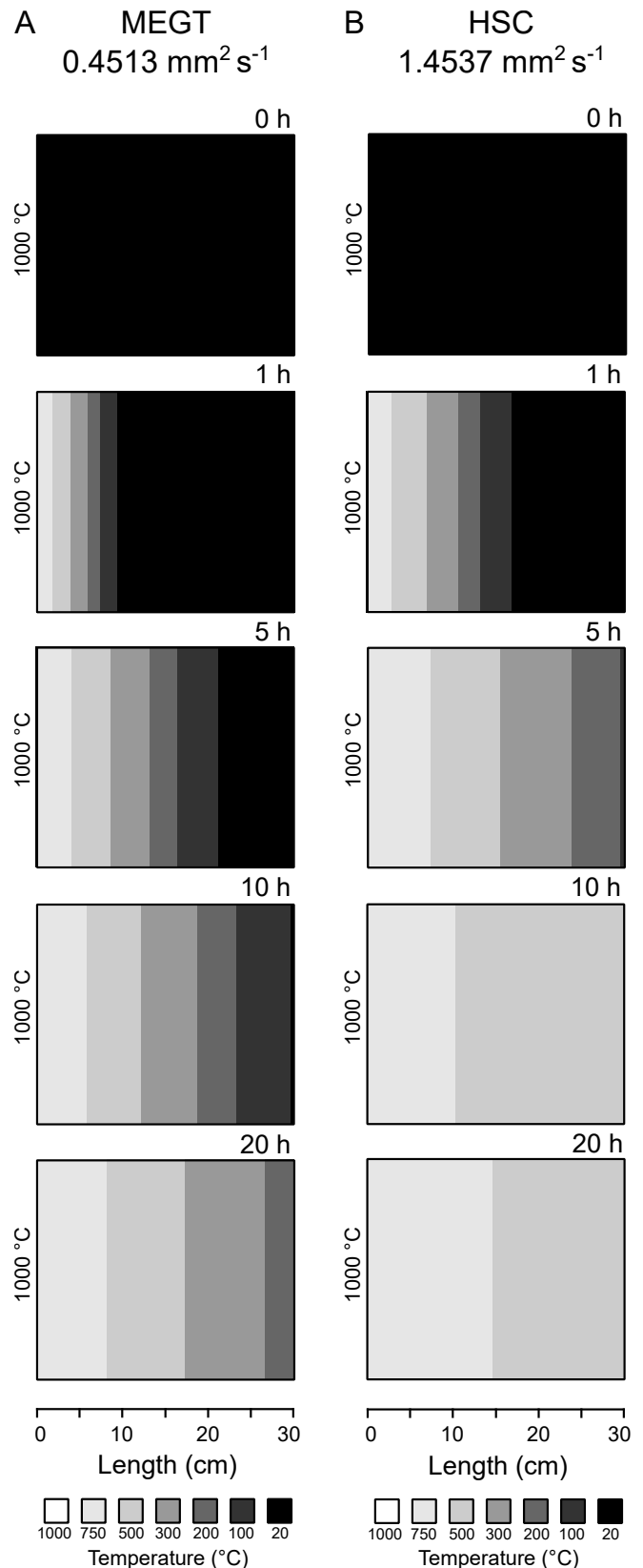

Figure 13: Thermal modelling showing the isotherms within a 300 mm block (represented by the rectangles) of [A] Mt. Epomeo Green Tuff (MEGT) and [B] high-strength concrete (HSC) for a constant fire temperature of 1000 °C (from the left) after 0, 1, 5, 10, and 20 hours.

hours to jeopardise the stability of a typical dimension stone (Figure 13). We further note that concrete walls are generally thinner than walls constructed using natural dimension stones and, as such, the 750 °C isotherm would likely travel through a concrete wall on a timescale shorter than that depicted in Figure 13. We conclude therefore that, in spite of the reported weakening, tuffs are tough in the event of fire. We recommend, in areas with a volcanically active past, that natural volcanic materials are used in modern construction due to their fire resistance, sustainability, and aesthetic qualities, rather than relying on concretes that are associated with an additional CO_2 fingerprint [e.g. Worrell et al. 2001], a low resistance to fire (compared to the tuffs discussed herein), and a short service life. In the case of Ischia Island we also highlight that, although the temperature of the fumaroles on the volcanic slopes currently rarely exceeds 100 °C, and that the temperatures of the present-day shallow hydrothermal system are estimated to be ~300 °C [Chiodini et al. 2004], an increase in temperature during renewed volcanic unrest could weaken the MEGT forming the volcanic slopes, increasing the risk of catastrophic slope failure [e.g. Marmoni et al. 2017a].

Acknowledgements

Author contributions

M.J. Heap prepared the samples, performed the measurements of porosity and strength, took the photograph of the buildings, performed the microstructural analysis, and wrote the manuscript. A.R.L. Kushnir performed the thermal property measurements, and assisted with the thermal modelling and microstructural analysis. L. Griffiths performed the acoustic emission experiment and analysed the data. F.B. Wadsworth performed the thermogravimetric analysis and the thermal modelling. H.A. Gilg performed the XRPD analysis and analysed the data. G.M. Marmoni, M. Fiorucci, and S. Martino led the field campaign and collected the block of tuff. P. Baud translated the abstract. T. Reuschlé provided instrumental experimental support. All authors had a hand in the interpretation of the data and the writing of the manuscript.

Data availability

The stress-strain data, thermogravimetric data, and the AE data during heating and cooling are hosted on figshare: https://figshare.com/s/22dc2d3077893b36e1ca.

Copyright notice

References

Altaner, S., C. Demosthenous, A. Pozzuoli, and G. Rolandi (2013). "Alteration history of Mount Epomeo Green Tuff and a related polymictic breccia, Ischia Island, Italy: evidence for debris avalanche". *Bulletin of Volcanology* 75.5. DOI: 10.1007/s00445-013-0718-1.

Benedetto, C. D., P. Cappelletti, M. Favaro, S. Graziano, A. Langella, D. Calcaterra, and A. Colella (2015). "Porosity as key factor in the durability of two historical building stones: Neapolitan Yellow Tuff and Vicenza Stone". *Engineering Geology* 193, pp. 310–319. DOI: 10.1016/j.enggeo.2015.05.006.

Bergmann, J., P. Friedel, and R. Kleeberg (1998). "BGMN—a new fundamental parameters based Rietveld program for laboratory X-ray sources, its use in quantitative analysis and structure investigations". *CPD Newsletter* 20.5.

Brace, W. F., B. W. Paulding, and C. Scholz (1966). "Dilatancy in the fracture of crystalline rocks". *Journal of Geophysical Research* 71.16, pp. 3939–3953. DOI: 10.1029/jz071i016p03939.

Brown, R. J., G. Orsi, and S. de Vita (2007). "New insights into Late Pleistocene explosive volcanic activity and caldera formation on Ischia (southern Italy)". *Bulletin of Volcanology* 70.5, pp. 583–603. DOI: 10.1007/s00445-007-0155-0.

Browning, J., P. Meredith, and A. Gudmundsson (2016). "Cooling-dominated cracking in thermally stressed volcanic rocks". *Geophysical Research Letters* 43.16, pp. 8417–8425. DOI: 10.1002/2016gl070532.

Calcaterra, D., P. Cappelletti, A. Langella, V. Morra, A. Colella, and R. de'Gennaro (2000). "The building stones of the ancient centre of Naples (Italy): Piperno from Campi Flegrei. A contribution to the knowledge of a long-time-used stone". *Journal of Cultural Heritage* 1.4, pp. 415–427. DOI: 10.1016/s1296-2074(00)01097-9.

Calcaterra, D., A. Langella, R. de'Gennaro, M. de'Gennaro, and P. Cappelletti (2005). "Piperno from Campi Flegrei: a relevant stone in the historical and monumental heritage of Naples (Italy)". *Environmental Geology* 47.3, pp. 341–352. DOI: 10.1007/s00254-004-1156-3.

Chen, T., M. Yeung, and N. Mori (2004). "Effect of water saturation on deterioration of welded tuff due to freeze-thaw action". *Cold Regions Science and Technology* 38.2-3, pp. 127–136. DOI: 10.1016/j.coldregions.2003.10.001.

Chiodini, G., R. Avino, T. Brombach, S. Caliro, C. Cardellini, S. D. Vita, F. Frondini, D. Granirei, E. Marotta, and G. Ventura (2004). "Fumarolic and diffuse soil degassing west of Mount Epomeo, Ischia, Italy". *Journal of Volcanology and Geothermal Research* 133.1-4, pp. 291–309. DOI: 10.1016/s0377-0273(03)00403-7.

Colella, C., M. de'Gennaro, and R. Aiello (2001). "Use of Zeolitic Tuff in the Building Industry". *Reviews in Mineralogy and Geochemistry* 45.1, pp. 551–587. DOI: 10.2138/rmg.2001.45.16.

Cruciani, G. and A. Gualtieri (1999). "Dehydration dynamics of analcime by in situ synchrotron powder diffraction". *American Mineralogist* 84.1-2, pp. 112–119. DOI: 10.2138/am-1999-1-212.

De Casa, G., G. Giglio, G. Lombardi, and M. Mariottini (1994). "Characterization and state of decay of the volcanic tuff of the Tabularium in the Roman Forum, Italy". *Lavas and volcanic tuffs: proceedings of the international meeting, Easter Island, Chile, 25–31 October, 1990*. International Centre for the Study of the Preservation and the Restoration of Cultural Property, pp. 107–127.

de'Gennaro, M., D. Calcaterra, P. Cappelletti, A. Langella, and V. Morra (2000). "Building stone and related weathering in the architecture of the ancient city of Naples". *Journal of Cultural Heritage* 1.4, pp. 399–414. DOI: 10.1016/s1296-2074(00)01096-7.

de'Gennaro, M. and C. Colella (1989). "Use of thermal analysis for the evaluation of zeolite content in mixtures of hydrated phases". *Thermochimica Acta* 154.2, pp. 345–353. DOI: 10.1016/0040-6031(89)85472-3.

Della Seta, M., C. Esposito, G. M. Marmoni, S. Martino, A. Paciello, C. Perinelli, and G. Sottili (2015). "Geological constraints for a conceptual evolutionary model of the slope deformations affecting Mt. Nuovo at Ischia (Italy)". *Italian Journal of Engineering Geology and Environment* 15.2, pp. 15–28.

Duvarcı, Ö. Ç., Y. Akdeniz, F. Özmıhçı, S. Ülkü, D. Balköse, and M. Çiftçioğlu (2007). "Thermal behaviour of a zeolitic tuff". *Ceramics International* 33.5, pp. 795–801. DOI: 10.1016/j.ceramint.2006.01.003.

Evangelista, A., S. Aversa, T. Pescatore, and F. Pinto (2000). "Soft rocks in southern Italy and role of volcanic tuffs in the urbanization of Naples". *Proceedings of the II International Symposium on 'The Geotechnics of Hard Soils and Soft Rocks', Napoli*. Vol. 3, pp. 1243–1267.

Girgis, B., K. El-Barawy, and N. Felix (1987). "Dehydration kinetics of some smectites: a thermogravimetric study". *Thermochimica Acta* 111, pp. 9–19. DOI: 10.1016/0040-6031(87)88029-2.

Glover, P. W. J., P. Baud, M. Darot, P. G. Meredith, S. A. Boon, M. LeRavalec, S. Zoussi, and T. Reuschlé (1995). "α/β phase transition in quartz monitored using acoustic emissions". *Geophysical Journal International* 120.3, pp. 775–782. DOI: 10.1111/j.1365-246x.1995.tb01852.x.

Gomez-Heras, M., M. Hajpál, M. Álvarez de Buergo, A. Török, R. Fort, and M. Varas (2006). "Evolution of porosity in Hungarian building stones after simulated burning". *Heritage Weathering and Conservation HWC-2006. Taylor & Francis, Rotterdam*, pp. 513–519.

Griffiths, L., O. Lengliné, M. J. Heap, P. Baud, and J. Schmittbuhl (2018). "Thermal Cracking in Westerly Granite Monitored Using Direct Wave Velocity, Coda Wave Interferometry, and Acoustic Emissions". *Journal of Geophysical Research: Solid Earth* 123.3, pp. 2246–2261. DOI: 10.1002/2017jb015191.

Gustafsson, S. E. (1991). "Transient plane source techniques for thermal conductivity and thermal diffusivity measurements of solid materials". *Review of Scientific Instruments* 62.3, pp. 797–804. DOI: 10.1063/1.1142087.

Gustavsson, M., E. Karawacki, and S. E. Gustafsson (1994). "Thermal conductivity, thermal diffusivity, and specific heat of thin samples from transient measurements with hot disk sensors". *Review of Scientific Instruments* 65.12, pp. 3856–3859. DOI: 10.1063/1.1145178.

Heap, M. J., P. Baud, P. G. Meredith, S. Vinciguerra, and T. Reuschlé (2014b). "The permeability and elastic moduli of tuff from Campi Flegrei, Italy: implications for ground deformation modelling". *Solid Earth* 5.1, pp. 25–44. DOI: 10.5194/se-5-25-2014.

Heap, M. J., J. I. Farquharson, A. R. L. Kushnir, Y. Lavallée, P. Baud, H. A. Gilg, and T. Reuschlé (2018). "The influence of water on the strength of Neapolitan Yellow Tuff, the most widely-used building stone in Naples (Italy)". *Bulletin of Volcanology*. DOI: 10.1007/s00445-018-1225-1.

Heap, M. J., Y. Lavallee, A. Laumann, K.-. U. Hess, P. G. Meredith, and D. B. Dingwell (2012). "How tough is tuff in the event of fire?" *Geology* 40.4, pp. 311–314. DOI: 10.1130/g32940.1.

Heap, M. J., Y. Lavallée, L. Petrakova, P. Baud, T. Reuschlé, N. R. Varley, and D. B. Dingwell (2014a). "Microstructural controls on the physical and mechanical properties of edifice-forming andesites at Volcán de Colima, Mexico". *Journal of Geophysical Research: Solid Earth* 119.4, pp. 2925–2963. DOI: 10.1002/2013jb010521.

Heap, M., Y. Lavallée, A. Laumann, K.-U. Hess, P. Meredith, D. Dingwell, S. Huismann, and F. Weise (2013). "The influence of thermal-stressing (up to 1000°C) on the physical, mechanical, and chemical properties of siliceous-aggregate, high-strength concrete". *Construction and Building Materials* 42, pp. 248–265. doi: 10.1016/j.conbuildmat.2013.01.020.

Heiken, G. (2006). *Tuffs: their properties, uses, hydrology, and resources*. Vol. 408. Geological Society of America.

Hoek, E. and Z. Bieniawski (1965). "Brittle fracture propagation in rock under compression". *International Journal of Fracture Mechanics* 1.3. doi: 10.1007/bf00186851.

Jackson, M. D., F. Marra, R. L. Hay, C. Cawood, and E. M. Winkler (2005). "The judicious selection and preservation of tuff and travertine building stone in ancient Rome". *Archaeometry* 47.3, pp. 485–510. doi: 10.1111/j.1475-4754.2005.00215.x.

Labuz, J. and J. Bridell (1993). "Reducing frictional constraint in compression testing through lubrication". *International Journal of Rock Mechanics and Mining Sciences & Geomechanics Abstracts* 30.4, pp. 451–455. doi: 10.1016/0148-9062(93)91726-y.

Lockner, D. (1993). "The role of acoustic emission in the study of rock fracture". *International Journal of Rock Mechanics and Mining Sciences & Geomechanics Abstracts* 30.7, pp. 883–899. doi: 10.1016/0148-9062(93)90041-b.

Marmoni, G., S. Martino, M. Heap, and T. Reuschlé (2017a). "Gravitational slope-deformation of a resurgent caldera: New insights from the mechanical behaviour of Mt. Nuovo tuffs (Ischia Island, Italy)". *Journal of Volcanology and Geothermal Research* 345, pp. 1–20. doi: 10.1016/j.jvolgeores.2017.07.019.

– (2017b). "Multiphysics Laboratory Tests for Modelling Gravity-driven Instabilities at Slope Scale". *Procedia Engineering* 191, pp. 142–149. doi: 10.1016/j.proeng.2017.05.165.

Murad, E. (1996). "The Thermal Behaviour of an Fe-Rich Illite". *Clay Minerals* 31.1, pp. 45–52. doi: 10.1180/claymin.1996.031.1.04.

Nabelek, P. I., A. G. Whittington, and A. M. Hofmeister (2010). "Strain heating as a mechanism for partial melting and ultrahigh temperature metamorphism in convergent orogens: Implications of temperature-dependent thermal diffusivity and rheology". *Journal of Geophysical Research* 115.B12. doi: 10.1029/2010jb007727.

Nijland, T. G., R. P. J. V. Hees, and L. Bolondi (2010). "Evaluation of three Italian tuffs (Neapolitan Yellow Tuff, Tufo Romano and Tufo Etrusco) as compatible replacement stone for Römer tuff in Dutch built cultural heritage". *Geological Society, London, Special Publications* 333.1, pp. 119–127. doi: 10.1144/sp333.12.

Oguchi, C. T. and H. Yuasa (2010). "Simultaneous wetting/drying, freeze/thaw and salt crystallization experiments of three types of Oya tuff". *Geological Society, London, Special Publications* 333.1, pp. 59–72. doi: 10.1144/sp333.6.

Orsi, G., G. Gallo, and A. Zanchi (1991). "Simple-shearing block resurgence in caldera depressions. A model from Pantelleria and Ischia". *Journal of Volcanology and Geothermal Research* 47.1-2, pp. 1–11. doi: 10.1016/0377-0273(91)90097-j.

Pola, A., G. Crosta, N. Fusi, V. Barberini, and G. Norini (2012). "Influence of alteration on physical properties of volcanic rocks". *Tectonophysics* 566-567, pp. 67–86. doi: 10.1016/j.tecto.2012.07.017.

Ruedrich, J., D. Kirchner, and S. Siegesmund (2011). "Physical weathering of building stones induced by freeze–thaw action: a laboratory long-term study". *Environmental Earth Sciences* 63.7-8, pp. 1573–1586. doi: 10.1007/s12665-010-0826-6.

Russa, M. F. L., S. A. Ruffolo, M. Á. de Buergo, M. Ricca, C. M. Belfiore, A. Pezzino, and G. M. Crisci (2017). "The behaviour of consolidated Neapolitan yellow Tuff against salt weathering". *Bulletin of Engineering Geology and the Environment* 76.1, pp. 115–124. doi: 10.1007/s10064-016-0874-6.

Scholz, C. H. (1968). "Microfracturing and the inelastic deformation of rock in compression". *Journal of Geophysical Research* 73.4, pp. 1417–1432. doi: 10.1029/jb073i004p01417.

Seta, M. D., E. Marotta, G. Orsi, S. de Vita, F. Sansivero, and P. Fredi (2012). "Slope instability induced by volcano-tectonics as an additional source of hazard in active volcanic areas: the case of Ischia island (Italy)". *Bulletin of Volcanology* 74.1, pp. 79–106. doi: 10.1007/s00445-011-0501-0.

Siedel, H. (2010). "Historic Building Stones and Flooding: Changes of Physical Properties due to Water Saturation". *Journal of Performance of Constructed Facilities* 24.5, pp. 452–461. doi: 10.1061/(asce)cf.1943-5509.0000066.

Tibaldi, A. and L. Vezzoli (1998). "The space problem of caldera resurgence: an example from Ischia Island, Italy". *Geologische Rundschau* 87.1, pp. 53–66. doi: 10.1007/s005310050189.

Tomlinson, E. L., P. G. Albert, S. Wulf, R. J. Brown, V. C. Smith, J. Keller, G. Orsi, A. J. Bourne, and M. A. Menzies (2014). "Age and geochemistry of tephra layers from Ischia, Italy: constraints from proximal-distal correlations with Lago Grande di Monticchio". *Journal of Volcanology and Geothermal Research* 287, pp. 22–39. doi: 10.1016/j.jvolgeores.2014.09.006.

Török, A., M. Gálos, and K. Kocsanyi-Kopecsko (2004). "Experimental weathering of rhyolite tuff building stones and the effect of an organic polymer conserving agent". *Stone Decay: Its Causes and Controls*. London/ New York: Routledge. Chap. 7, pp. 109–127.

Vacchiano, C. D., L. Incarnato, P. Scarfato, and D. Acierno (2008). "Conservation of tuff-stone with polymeric resins". *Construction and Building Materials* 22.5, pp. 855–865. DOI: 10.1016/j.conbuildmat.2006.12.012.

Wolters, F. and K. Emmerich (2007). "Thermal reactions of smectites—Relation of dehydroxylation temperature to octahedral structure". *Thermochimica Acta* 462.1-2, pp. 80–88. DOI: 10.1016/j.tca.2007.06.002.

Worrell, E., L. Price, N. Martin, C. Hendriks, and L. O. Meida (2001). "Carbon Dioxide Emissions from the Global Cement Industry". *Annual Review of Energy and the Environment* 26.1, pp. 303–329. DOI: 10.1146/annurev.energy.26.1.303.

Yavuz, A. B. (2012). "Durability assessment of the Alaçatı tuff (Izmir) in western Turkey". *Environmental Earth Sciences* 67.7, pp. 1909–1925. DOI: 10.1007/s12665-012-1632-0.

Zedef, V., K. Kocak, A. Doyen, H. Ozsen, and B. Kekec (2007). "Effect of salt crystallization on stones of historical buildings and monuments, Konya, Central Turkey". *Building and Environment* 42.3, pp. 1453–1457. DOI: 10.1016/j.buildenv.2005.12.010.

Zhu, W., P. Baud, S. Vinciguerra, and T.-f. Wong (2011). "Micromechanics of brittle faulting and cataclastic flow in Alban Hills tuff". *Journal of Geophysical Research* 116.B6. DOI: 10.1029/2010jb008046.

RESEARCH ARTICLE

CrossMark

The influence of water on the strength of Neapolitan Yellow Tuff, the most widely used building stone in Naples (Italy)

Michael J. Heap[1] · Jamie I. Farquharson[1] · Alexandra R. L. Kushnir[1] · Yan Lavallée[2] · Patrick Baud[1] · H. Albert Gilg[3] · Thierry Reuschlé[1]

Abstract

Neapolitan Yellow Tuff (NYT) has been used in construction in Naples (Italy) since the Greeks founded the city—then called Neapolis—in the sixth century BCE. We investigate here whether this popular building stone is weaker when saturated with water, an issue important for assessments of weathering damage and monument preservation. To this end, we performed 28 uniaxial compressive strength measurements on dry and water-saturated samples cored from a block of the lithified Upper Member of the NYT. Our experiments show that the strength of the zeolite-rich NYT is systematically reduced when saturated with water (the ratio of wet to dry strength is 0.63). Complementary experiments show that two other common Neapolitan building stones—Piperno Tuff and the grey Campanian Ignimbrite (both facies of the Campanian Ignimbrite deposit devoid of zeolites)—do not weaken when wet. From these data, and previously published data for tuffs around the globe, we conclude that the water-weakening in NYT is a consequence of the presence of abundant zeolites (the block tested herein contains 46 wt.% of zeolites). These data may help explain weathering damage in NYT building stones (due to rainfall, rising damp, and proximity to the sea or water table) and the observed link between rainfall and landslides, rock falls, and sinkhole formation in Naples, and the weathering of other buildings built from zeolite-rich tuffs worldwide.

Keywords Zeolites · Uniaxial compressive strength · Porosity · Mercury porosimetry

Introduction

For millennia, tuffs have been used worldwide as a building stone (Heiken 2006). Cities built on and constructed using tuff span six of the seven continents (all except Antarctica). Tuff has been used as a building material in Naples (Italy; Fig. 1) since the city's birth as Neapolis in the sixth century BCE (e.g., Calcaterra et al. 2000; de'Gennaro et al. 2000a;

Evangelista et al. 2000a; Colella et al. 2001, Calcaterra et al. 2005; Morra et al. 2010; Aversa et al. 2013; Colella et al. 2017). The most commonly used tuff in Naples is the Neapolitan Yellow Tuff (NYT), the product of a large phreatoplinian eruption from the adjacent Campi Flegrei volcanic district (e.g., Orsi et al. 1992; Scarpati et al. 1993; Wohletz et al. 1995; Orsi et al. 1996; Civetta et al. 1997) about 15,000 years ago (Deino et al. 2004). However, laboratory experiments on tuff show that they are sometimes weaker when saturated with water (e.g., Schultz and Li 1995; Yassaghi et al. 2005; Jackson et al. 2005; Montanaro et al. 2016). The metric "water-weakening", the ratio of the wet to dry strength of a material, is often used to describe this affect (Zhu et al. 2011), where low values (close to zero) indicate a strong water-weakening effect and values at or close to unity indicate that there is little or no water-weakening. A water-weakening assessment of the NYT is particularly important due to the prevalence of water related weathering typologies seen on buildings in Naples (e.g., de'Gennaro et al. 1993 2000a; Di Benedetto et al. 2015).

✉ Michael J. Heap
   heap@unistra.fr

1   Géophysique Expérimentale, Institut de Physique de Globe de Strasbourg (UMR 7516 CNRS, Université de Strasbourg/EOST), 5 rue René Descartes, 67084 Strasbourg cedex, France

2   Earth, Ocean and Ecological Sciences, University of Liverpool, L693GP, Liverpool, UK

3   Lehrstuhl für Ingenieurgeologie, Technische Universität München, Munich, Germany

🍁 Springer

Fig. 1 Maps showing the location of Naples (inset is a map of Italy). The inferred Campi Flegrei caldera is indicated by the dashed circle, and the main towns with blue dots. The Neapolitan Yellow Tuff (NYT) used in this study was collected from an open quarry at Monte San Severino, on the border of the inferred Campi Flegrei caldera
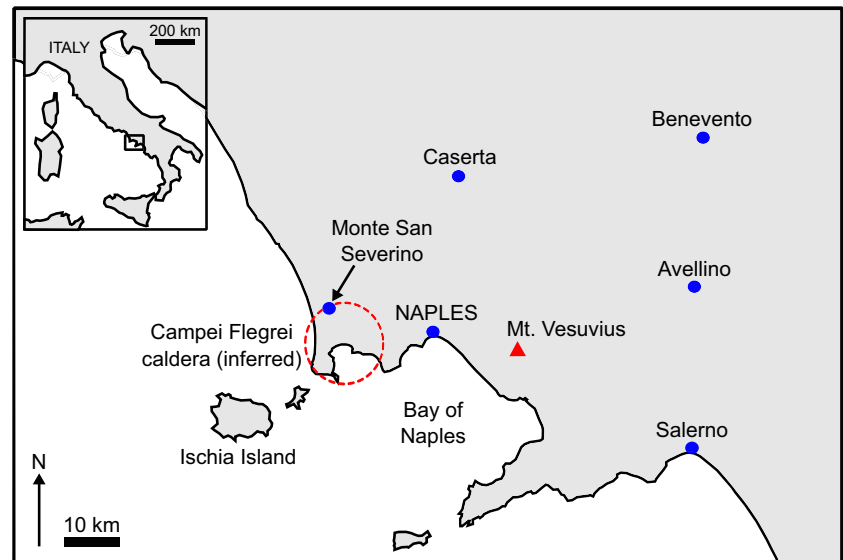

Fig. 2 Photographs of buildings constructed using Neapolitan Yellow Tuff (NYT) in Naples. (**a**) Castel dell'Ovo, (**b**) Castel Nuovo, (**c**) the church of Santa Chiara, (**d**) the church of San Domenico Maggiore, (**e**) the Academy of Fine Arts, and (**f**) a plastered wall constructed using NYT within the ancient city centre of Naples

The stratigraphy of the NYT is divided into two members: a Lower Member (comprising fall deposits and pyroclastic flow deposits) and an Upper Member (comprising pyroclastic flow deposits) (Scarpati et al. 1993; Cole and Scarpati 1993). The Upper Member is composed of the deposits of a non-turbulent pyroclastic density flow and five low- and high-concentration turbulent pyroclastic density flows (Cole and Scarpati 1993). The Upper Member is variably lithified and is preserved as either unlithified grey "pozzolana" material or a lithified yellow rock (e.g., Scarpati et al. 1993; Cole and Scarpati 1993; de'Gennaro et al. 2000b). The lithified Upper Member has been divided into four texturally distinct units, classified by the size and quantity of lithic and porous juvenile fragments (Colella et al. 2017). The lithified Upper Member of the NYT has not only been used in the construction of monuments such as Castel dell'Ovo, Castel Nuovo, the churches of Santa Chiara and San Domenico Maggiore, and the Academy of Fine Arts, but also in many of the walls and houses within the ancient city centre of Naples (Fig. 2).

The lithified Upper Member of the NYT is a particularly well-studied material, for a number of reasons. First, due to its prevalent use in construction in the Neapolitan area (de'Gennaro et al. 1993; Aversa and Evangelista 1998; de'Gennaro et al. 2000a; Evangelista et al. 2000a; Augenti and Parisi 2010; Nijland et al. 2010; Calderoni et al. 2010; Heap et al. 2012; Di Benedetto et al. 2015; La Russa et al. 2017; Colella et al. 2017). Second, due to the alarming frequency of landslide and rock fall hazards (Calcaterra et al. 2002; Di Martire et al. 2002; Calcaterra et al. 2007; Nocilla et al. 2009) and underground cavity collapse and anthropogenic sinkhole formation (Evangelista et al. 2000b; Hall et al. 2006; Guarino and Nisio 2012; Guarino et al. 2018) associated with the NYT. Third, the NYT contains abundant zeolites, aluminosilicate minerals of commercial, industrial, and environmental importance (de'Gennaro et al., 1990, 2000a; Coppola et al. 2002; Colella 2005). Finally, since NYT is one of the principal lithologies forming the increasingly restless Campi Flegrei caldera (Orsi et al. 1996; Di Vito et al. 1999; Chiodini et al. 2001; Heap et al. 2014; Chiodini et al. 2015; Mayer et al. 2016; Montanaro et al. 2016; Kilburn et al. 2017; Chiodini et al. 2017; Cardellini et al. 2017), a detailed understanding of the physical and mechanical properties of the NYT form an important component of volcanic risk assessment and mitigation.

These studies, amongst others, have shown that the lithified Upper Member of the NYT is a heterogeneous trachytic pyroclastic deposit that is characterised by both pyrogenic and authigenic phases (de'Gennaro et al., 1990). It contains variably quantities of porous juvenile lapilli (i.e., pumice) fragments (between ~8 and ~40%) and lithic fragments (between ~7 and ~16%) (Colella et al. 2017). The NYT typically contains a large proportion of plagioclase phenocrysts (between ~14 and ~36 wt.%; Colella et al. 2017), amorphous phases
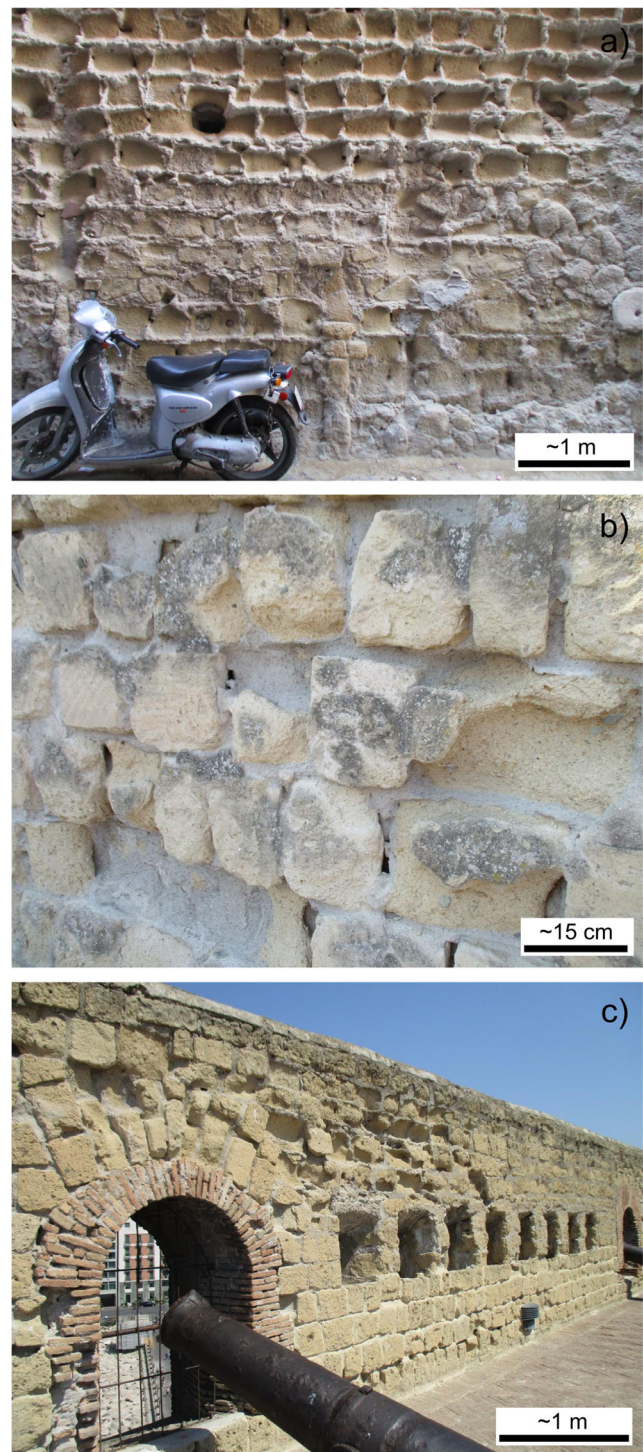
Fig. 3 (a) Weathering on a wall constructed using Neapolitan Yellow Tuff (NYT) within the ancient city centre of Naples. (b) and (c) Weathering on NYT walls within the Castel dell'Ovo

(~10 wt.%; Di Benedetto et al. 2015; Colella et al. 2017), and zeolites, namely K-rich phillipsite, chabazite, and analcime (Gatta et al. 2010; Heap et al. 2012; Di Benedetto et al. 2015; Colella et al. 2017). The mean content of zeolites within the NYT can exceed 50 wt.% (de'Gennaro et al., 1990, 2000a;

Fig. 4 A photograph (**a**) and an optical photomicrograph (**b**) of the Neapolitan Yellow Tuff (NYT) used in this study (modified from Heap et al., 2012). A K-feldspar and clinopyroxene phenocryst and a porous juvenile lapilli fragment are labelled on the photomicrograph
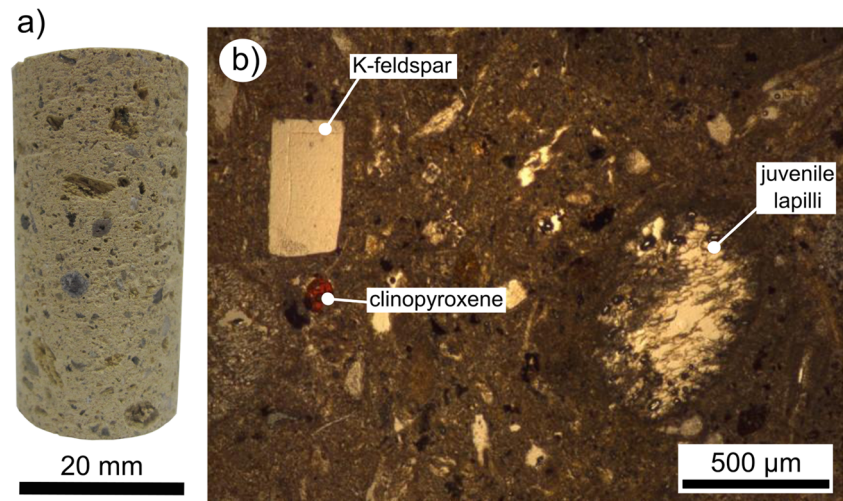
Di Benedetto et al. 2015; Colella et al. 2017). Also found within the NYT are subordinate smectite (between 0 and 6 wt.%; Di Benedetto et al. 2015; Colella et al. 2017) and phenocrysts of sanidine, clinopyroxene, biotite, and minor quantities of Ti-magnetite and apatite (Heap et al. 2012; Di Benedetto et al. 2015).

Due to the heterogeneity of the lithified Upper Member of the NYT (e.g., Scarpati et al. 1993; Cole and Scarpati 1993; Colella et al. 2017), its physical properties are equally heterogeneous. For example, its porosity and permeability can range from 0.35 and 0.65 (Colella et al. 2017) and 10^{-17} and 10^{-13} m^2 (Peluso and Arienzo 2007; Heap et al. 2014; Montanaro et al. 2016), respectively. Reported values of uniaxial compressive strength (UCS) of NYT typically vary between ~1 and ~10 MPa, although it can be as strong as ~40 MPa (Evangelista and Aversa 1994; Hall et al. 2006; Augenti and Parisi 2009; Heap et al. 2012; Montanaro et al. 2016; Colella et al. 2017). Further, and due to its high porosity, triaxial deformation experiments have shown that NYT is compactant (i.e. ductile) even at very low effective pressures (< 5 MPa) and under ambient laboratory temperatures (Aversa and Evangelista 1998; Heap et al. 2014).

The physical and mechanical properties of tuffs are well known to be influenced by exposure to the elements, as recognised by Vitruvius as far back as pre-Christian Rome (Italy), where he wrote: "*There are also many other kinds, such as red and black tuff in Campania, [and] in Umbria, Piceno and in Venetia white, which, indeed, can be cut like wood by means of a serrated or toothed saw. So long as these soft stones are sheltered under plaster they will hold up and do their work but if they are laid bare or exposed in the open air, ice and frost accumulate within them and they crumble apart and dissolve. Also along the sea coast salt eats at them and they dissolve apart; neither do they endure sea tides and spray.*" (from De Architectura 2.7.1–2 as quoted in Jackson et al. 2006). Indeed, and more recently, NYT has been shown

to degrade during salt crystallisation tests (La Russa et al. 2017) and the UCS and indirect tensile strength of zeolite-rich NYT was found to decrease following exposure to the high-temperatures of fire (Heap et al. 2012). However, since the early work of Evangelista (1980), an unpublished report containing experiments that show that the peak strength of NYT is reduced when water-saturated, the water-weakening behaviour of the lithified Upper Member of the NYT has received little attention in the literature. To the authors' knowledge, only Montanaro et al. (2016) provide a handful of UCS experiments (three dry and three water-saturated) that show that NYT is weaker when saturated with water (dry UCS = 6.1–7.3 MPa; wet UCS = 1.2–2.3 MPa). The lack of a comprehensive study is surprising on two counts. First, deformation experiments on tuffs have highlighted that they are weaker when saturated with water (e.g., Schultz and Li 1995; Yassaghi et al. 2005; Jackson et al. 2005; Montanaro et al. 2016). Second, a survey of weathering typologies in buildings in Naples constructed with NYT found that the most prevalent weathering type was the result of moisture (due to rising damp) and rainfall (de'Gennaro et al. 2000a). This type of weathering results in alveolisation (detachment of lithic and

Table 1 Quantitative bulk mineralogical composition, determined using X-ray powder diffraction (XRPD), for the Neapolitan Yellow Tuff used in this study

Mineral	Mineral content [wt.%]
Amorphous phase	36 ± 5
K-feldspar	10 ± 1
Biotite	2 ± 1
Clinopyroxene	3 ± 1
Chabazite	30 ± 2
Phillipsite	16 ± 2
Smectite	3 ± 1

porous juvenile fragments), scaling, exfoliation, and disaggregation, as shown in Fig. 3 (see also de'Gennaro et al. 1993 2000a; Di Benedetto et al. 2015). We thus report, herein, on the results of an experimental study that quantifies the water-weakening behaviour of a facies of the NYT often used in construction in the Neapolitan area.

Experimental material and methods

We performed uniaxial compressive strength (UCS) measurements on cylindrical samples of NYT cored in the same orientation from a single block. The block of NYT (from the lithified yellow Upper Member) was sourced from an open quarry at Monte San Severino, at the boundary of the inferred Campi Flegrei caldera (the same block used in Heap et al.

2012 2014; see Fig. 1 for sample location). Importantly, this quarry has supplied dimension stones (natural stone or rock that has been selected and finished to a specific size or shape) for building projects within the Neapolitan area. Due to the presence of centimetric juvenile lapillis, the NYT tested herein is similar to the facies "MC" described by Colella et al. (2017).

A total of 28 samples were cored to a diameter of either 25 or 20 mm and cut and precision-ground to a nominal length of 60 or 40 mm, respectively (a photograph of a 20 mm-diameter sample is provided as Fig. 4a). Samples were cored so as to avoid centimetric juvenile lapillis and lithic fragments. To avoid the washout of juvenile lapilli and the fine fraction, the sample block was first soaked in water and then cored dry (i.e., samples were cored without running water). The prepared cylindrical samples were then washed with water to remove any water-soluble

Table 2 Summary of the 28 experiments performed on Neapolitan Yellow Tuff (NYT) for this study. Wet—vacuum-saturated in deionised water (see text for details). Dry—dried in a vacuum oven at 40 °C for at least 48 h. The uniaxial compressive strength for a sample of 50 mm diameter was calculated using the empirical relation given as Eq. (1) (see text for details). The average connected porosities for the samples deformed in the dry and wet condition are 0.456 and 0.459, respectively

Sample	Sample diameter [mm]	Connected porosity	Uniaxial compressive strength [MPa]	Experimental condition	Uniaxial compressive strength (diameter = 50 mm) (Eq. 1) [MPa]
NYT-1	19.83	0.46	3.71	Wet	3.14
NYT-2	19.82	0.46	5.76	Dry	4.88
NYT-3	19.87	0.44	4.60	Wet	3.90
NYT-4	19.77	0.47	4.87	Dry	4.12
NYT-5	19.83	0.47	3.28	Wet	2.78
NYT-6	19.86	0.45	4.96	Dry	4.20
NYT-8	19.84	0.46	5.32	Dry	4.51
NYT-9	19.84	0.45	3.64	Wet	3.08
NYT-10	19.86	0.45	6.26	Dry	5.30
NYT*-1	19.86	0.46	4.29	Wet	3.63
NYT25-1	24.97	0.47	2.87	Wet	2.53
NYT25-2	24.93	0.47	2.59	Wet	2.29
NYT25-3	25.58	0.46	3.73	Wet	3.31
NYT25-4	24.97	0.47	4.16	Wet	3.67
NYT25-5	24.98	0.46	3.40	Wet	3.00
NYT25-6	25.58	0.46	3.81	Wet	3.38
NYT25-7	24.95	0.45	3.07	Wet	2.71
NYT25-8	24.92	0.45	3.65	Wet	3.22
NYT25-9	25.42	0.46	3.06	Wet	2.71
NYT25-10	25.00	0.47	2.58	Wet	2.28
NYT25-11	24.93	0.45	6.23	Dry	5.50
NYT25-12	25.48	0.46	5.22	Dry	4.62
NYT25-13	25.58	0.46	5.26	Dry	4.66
NYT25-14	24.79	0.45	5.59	Dry	4.93
NYT25-15	24.89	0.45	5.48	Dry	4.83
NYT25-16	24.90	0.45	6.78	Dry	5.98
NYT25-17	24.98	0.46	6.00	Dry	5.30
NYT25-19	25.56	0.46	4.77	Dry	4.23
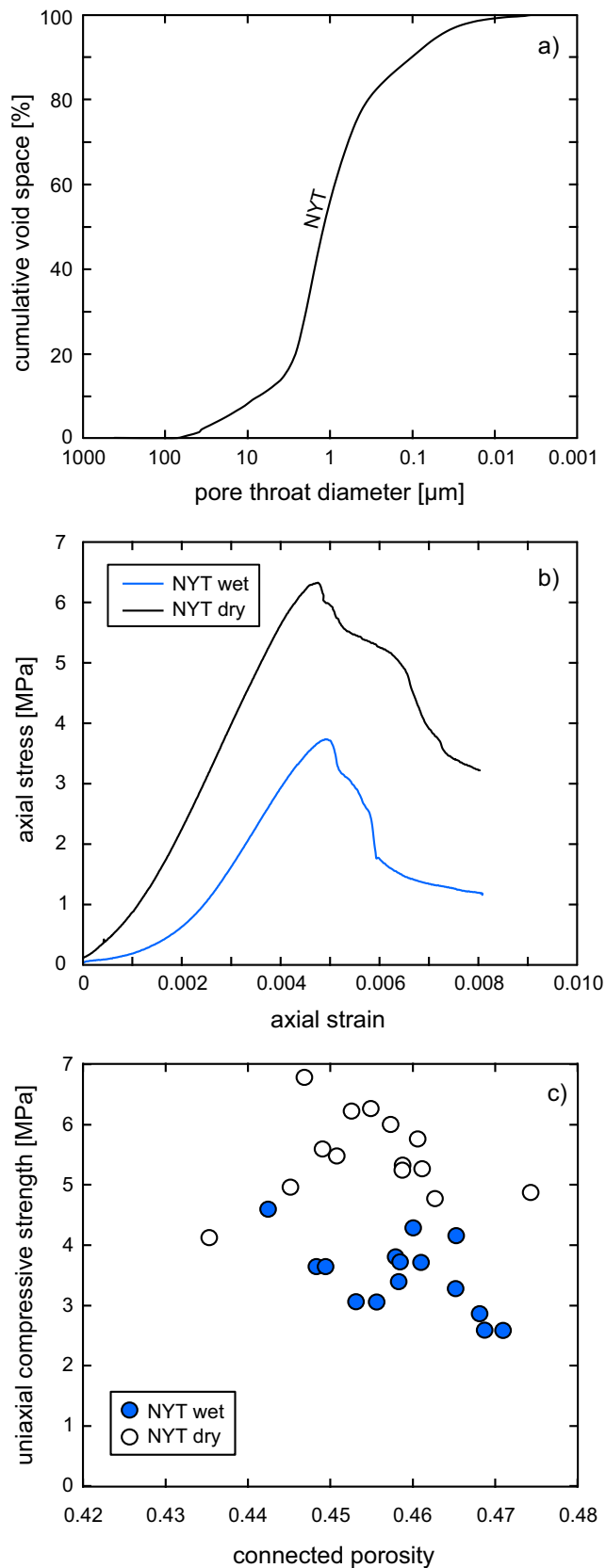
grinding fluid and vacuum-dried in an oven for at least 48 h at 40 °C. The connected porosity of each sample was then determined using the skeletal (connected) volume of the sample given by a helium pycnometer (Micromeritics AccuPyc II 1340) and the bulk volume of the sample calculated using the sample dimensions. Finally, the samples were deformed uniaxially at a strain rate of 1.0×10^{-5} s^{-1} until macroscopic failure. Thirteen of the samples were deformed "dry" (dried in a vacuum-oven for at least 48 h prior to deformation) and 15 were deformed "wet" (vacuum-saturated in deionised water and deformed in a water bath). The water saturation procedure for the samples deformed in the "wet" condition consisted of two steps:

(1) the vacuum-dried samples were placed inside a belljar which was then vacuumed for at least 12 h and, finally,
(2) degassed (using a Venturi siphon with municipal water as the motive fluid) deionised water was introduced into the belljar whilst under vacuum.

A mercury injection test was performed on a small vacuum-dried offcut (~3.5 g) of NYT using the Micromeritics Autopore IV 9500 at the University of Aberdeen (Scotland). The evacuation pressure and evacuation time were 50 μm Hg and 5 min, respectively, and the mercury filling pressure and equilibration time were 3.59 MPa and 10 s, respectively. The pressure range was 0.69 to 413.69 MPa. Mercury injection data permit the estimation of connected porosity and pore throat size distribution. The mercury injection data were corrected for the "low pressure correction" recommended by the American Section of the International Association for Testing Materials (ASTM D4404-10 2010).

The mineral content of the studied NYT was quantified using X-ray powder diffraction (XRPD). A powder, prepared from the deformed NYT cores and containing 10 wt.% ZnO as internal standard, was ground for 8 min with 10 ml of isopropyl alcohol in a McCrone Micronising Mill using agate cylinder elements. The XRPD analyses were performed on powder mounts using a PW 1800 X-ray diffractometer (CuKα, graphite monochromator, 10 mm automatic divergence slit, step-scan 0.02° with 2θ increments per second, counting time one second per increment, 30 mA, 40 kV). The phases in the whole rock powders were quantified using the Rietveld

Table 3 Summary of the published (including data from this study) wet and dry uniaxial compressive strength of tuffs from around the globe. UCS_{dry}—dry uniaxial compressive strength; UCS_{wet}—wet uniaxial compressive strength

Tuff	Outcrop	Connected porosity	±	UCS_{dry} [MPa]	±	UCS_{wet} [MPa]	±	$\frac{UCS_{wet}}{UCS_{dry}}$	Source	Notes
Anatolian tuff	White	0.39	0.008	10.00	0.88	3.76	0.53	0.376	Topal and Sözmen (2003)	No zeolites. Smectite and Illite present
	Pink	0.33	0.021	16.95	0.54	10.89	1.82	0.642	Ayday and Göktan (1990)	No zeolites. Smectite, Illite, and Kaolinite present
	White	0.28		8.15		3.55		0.436		No zeolites. Smectite and Illite present
	Pink	0.24		18.23		10.46		0.574		No zeolites. Smectite, Illite, and Kaolinite present
Cappadoccian tuff	Vertical	0.38	0.005	6.53	0.67	2.16	0.34	0.331	Topal and Doyuran (1997)	Volcanic glass shards are partly altered to smectite
	Horizontal	0.38	0.005	4.87	0.43	0.93	0.29	0.191		
	Vertical	0.29		6.50		3.00		0.462	Erdoğan (1986)	
	Vertical	0.29		6.50		3.00		0.462	Erguvanlı et al. (1989)	
	Kavak	0.27		3.60		1.10		0.306	Tuncay (2009)	Clinoptilolite
		0.21		5.00		1.56		0.312		
		0.24		5.00		1.33		0.266		
	Zelve	0.26		4.20		0.83		0.198		Substantially clinptilolite-rich, but also
	Cemilköy	0.35		1.20		0.44		0.367		containing minor erionite, chabazite and phillipsite[1]
		0.28		2.20		0.52		0.236		No zeolites
	Kızılkaya	0.27		6.30		3.88		0.616		
		0.37		3.40		3.27		0.962		
	Ortahisar	0.34		6.60		1.30		0.197	Erguler and Ulusay (2009)	81% clay (montmorillonite)
	Ürgüp	0.26		12.90		1.60		0.124		27% clay minerals
		0.26		9.70		1.30		0.134		40% clay minerals
Yucca Mountain tuff	Calico Hills	0.30	0.015	29.09	3.19	5.34	0.77	0.184	Schultz and Li (1995)	Low temperature zeolitic alteration products in Calico Hills rocks include clinoptilolite zeolite, mordenite and smectite[2]
		0.38		36.85	4.15	30.40	7.45	0.825	Price (1983); Price and Jones (1982)	
	Paintbrush tuff	0.40	0.011	4.70	1.20	11.30		2.404	Martin et al. (1994)	Heulandite-clinoptilolite and smectite[3]
Karaj tuff	Crystalline	0.10	0.005	121.00	21.00	92.00	14.00	0.760	Yassaghi et al. (2005)	No zeolites
	Vitric	0.13	0.022	92.50	12.50	52.00	3.00	0.562		20% clay minerals
	Lithic	0.09	0.023	98.50	11.50	64.50	6.50	0.655		45% clay minerals
Mt. Nuovo	Upper unit	0.46	0.021	4.85	0.45	2.68	0.88	0.552	Marmoni et al. (2017a)	Glass partially replaced by zeolites (incl. Analcime and phillipsite)
	Lower unit	0.21	0.005	33.77	4.03	26.00		0.770		
Urumieh-Dokhtar tuff		0.03		124.30		78.20		0.629	Heidari et al. (2014)	Data not available
Challis tuff	Perpendicular to bedding	0.24		75.01		29.27		0.390	Behre Jr. (1929)	Contains montmorillonite clay andmordenite (zeolite)[4]
	Parallel to bedding	0.24		78.92		28.52		0.361		
Alaçatı tuff		0.26	0.009	14.90	1.95	6.90	1.03	0.463	Yavuz (2012)	Contains smectite and mordenite
Ayazini tuff		0.37	0.022	22.21	1.47	12.44	0.49	0.560	Celik et al. (2014)	Illite and smectite present
Seydiler tuff		0.36	0.027	19.07	1.69	9.07	0.25	0.476	Çelik and Ergul (2015)	
Sárospatak rhyolite tuff		0.20		19.47		8.95		0.460	Török et al. (2004)	Montmorillonite and other clay minerals
Oya tuff		0.34		11.20	0.92	5.00	0.51	0.446	Okubo and Chu (1994)	Contains clinoptilolite and mordenite
Tage tuff		0.25		16.10	0.92	9.10	0.59	0.565		
Monti Sabatini tuff	Tufo Giallo della Prima Porta	0.23		20.40	0.35	9.80	0.11	0.480	Jackson et al. (2005)	Analcime, phillipsite, and chabazite
	Tufo Giallo della Via Tibernia	0.20		22.90	0.94	7.60	0.05	0.332		
Monti Albani tuff	Tufo Lionato	0.15		28.50	0.68	15.90	0.40	0.558		
	Lapis Albanus	0.11		31.30	0.25	16.30	0.39	0.521		
	Tufo di Tusculo	0.15		36.70	1.80	17.30	0.48	0.471		
	Lapis Gabinus	0.14		39.50	4.15	15.50	0.53	0.392		
	Peperino della Via Flaminia	0.13		43.40	6.21	28.80	3.48	0.664		
	Pisolitico di Trigoria	0.35	0.002					0.500	Zhu et al. (2011)	Phillipsite and chabazite
	Palatino	0.32	0.004					0.683		
Eger-Demjéntuff		0.19		39.75		25.96		0.653		Contains 10–20% smectite[7]

Table 3 (continued)

Tuff	Outcrop	Connected porosity	±	UCS_{dry} [MPa]	±	UCS_{wet} [MPa]	±	$\frac{UCS_{wet}}{UCS_{dry}}$	Source	Notes
		0.40		8.49		3.35		0.395	Vásárhelyi, (pers. Comm.)	
		0.39		4.95		1.59		0.321		
		0.51		3.03		0.74		0.244		
		0.37		7.61		2.60		0.342		
		0.36		6.11		1.37		0.224		
		0.36		5.60		1.91		0.341		
		0.38		7.66		2.24		0.292		
		0.40		4.67		1.74		0.373		
		0.58		2.59		1.15		0.444		
		0.34		8.40		2.76		0.329		
		0.38		4.40		0.87		0.198		
		0.39		5.54		2.02		0.365		
		0.41		3.53		0.55		0.156		
		0.34		5.32		2.21		0.415		
		0.35		7.81		2.94		0.376		
		0.37		3.13		0.63		0.201		
		0.38		5.36		1.20		0.224		
Tuff from Hungary	Rhyolite tuff	0.45		2.59		1.18		0.444	Vásárhelyi (2002)	Data not available
		0.30		4.95		1.59		0.321		
		0.32		4.69		1.74		0.371		
		0.29		5.54		2.02		0.365		
		0.27		5.60		1.91		0.341		
		0.30		8.49		3.35		0.395		
		0.30		7.66		2.24		0.292		
		0.30		10.03		7.83		0.781		
		0.28		7.81		2.94		0.376		
		0.29		5.36		1.20		0.224		
		0.29		21.81		21.27		0.975		
		0.15		39.75		26.90		0.677		
	Andesite tuff	0.20		26.00		20.20		0.78		
		0.15		33.50		27.74		0.83		
		0.17		30.33		22.32		0.74		
		0.16		16.30		8.62		0.53		
		0.07		32.60		21.50		0.66		
		0.11		19.80		10.10		0.51		
		0.08		15.60		11.30		0.72		
		0.14		28.60		19.80		0.69		
	Basalt tuff	0.27		8.50		8.30		0.98		
		0.20		3.34		2.48		0.74		
		0.30		3.05		1.76		0.58		
		0.22		4.36		3.40		0.78		
		0.31		8.30		14.04		1.69		
		0.24		8.34		12.88		1.54		
		0.00		3.83		3.10		0.81		
		0.09		14.12		13.07		0.93		
		0.09		40.29		18.43		0.46		
		0.03		63.36		53.2		0.84		
Neapolitan Yellow Tuff		0.49	0.011	6.65	0.65	1.88	0.68	0.28	Montanaro et al. (2016)	Zeolites
La Pietra Tuff 1		0.49	0.004	4.56	0.94	2.27	0.97	0.50		

Table 3 (continued)

Tuff	Outcrop	Connected porosity	±	UCS_{dry} [MPa]	±	UCS_{wet} [MPa]	±	$\frac{UCS_{wet}}{UCS_{dry}}$	Source	Notes
La Pietra Tuff 2		0.47	0.013	9.74	0.84	3.68	1.32	0.38		
Gauro Tuff		0.46	0.009	11.78	1.17	4.82	0.49	0.41		
Neapolitan Yellow Tuff (this study)	Monte San Severino	0.46	0.017	5.44	0.83	3.81	0.79	0.701	This study	Phillipsite, chabazite, and smectite
Grey Campanian Ignimbrite (WGI; this study)	Open quarry to the north-west of the town of Caserta (Italy)	0.50	0.005	10.59	1.31	9.94	1.04	0.939		No zeolites or clays present
Piperno tuff (PT; this study)	Open quarry in the Neapolitan area (Italy)	0.51	0.004	3.17		3.29		1.038	This study	No zeolites or clays present

1. Cejka et al. (2007); Temel and Gündoğdu (1996)

2. Broxton et al. (1993)

3. Levy and O''Neil (1989)

4. Ross and Shannon (1924)

5. Estimated from P* wet/dry ratio

6. Estimated from P* wet/dry ratio

7. Wedekind et al. (2013)

program BGMN (Bergmann et al. 1998). To identify the clay minerals, we also separated <2 μm fractions by gravitational settling and prepared oriented mounts that were X-rayed in an air-dried and ethylene-glycolated state. Since some of the constituents of the NYT are delicate (juvenile lapilli), and/or may be affected by vacuum-drying (zeolites and clays), we chose to prepare our powdered sample for XRPD analysis using the deformed core samples so that the mineral content determined is representative of the deformed samples, rather than the block prior to sample preparation. Although our samples were prepared with the utmost care, we cannot definitively rule out that their mineral content was slightly modified by the sample preparation procedure.

Results

Mineral content and microstructure

The microstructure of the NYT used in this study contains phenocrysts (of K-feldspar, clinopyroxene, and biotite) and juvenile lapilli within a fine-grained matrix (Fig. 4b). Table 1 gives the XRPD analysis, which shows that the main minerals within the NYT are amorphous phases (36 wt.%, Table 1) and two zeolites: chabazite (30 wt.%, Table 1) and phillipsite (16 wt.%, Table 1). The block of NYT also contains 10 wt.% K-feldspar, 3 wt.% clinopyroxene, 3 wt.% smectite, and 2 wt.% biotite (Table 1). The total proportion of zeolites (chabazite and phillipsite) is therefore 46 wt.%. We note that the amorphous phase (36 wt.%, Table 1) measured is likely to contain little residual glass (Colella et al. 2017) and could include an aluminosilicate gel-like component (de'Gennaro and Colella 1989; Colella et al. 2017).

Experimental data

The NYT studied has an average dry bulk density of 1240 kg.m^{-3} and an average connected porosity of 0.458 (standard deviation: 0.0079) (Table 2). A connected porosity of 0.446 was determined from the mercury injection data. The pore throat size distribution for NYT is shown in Fig. 5a. These data show that pore throats of diameter ≥ 10 μm constitute ~10% of the pores by volume (Fig. 5a). The majority of pores (~65%) have a diameter between 0.3 and 3 μm (Fig. 5a). The average pore throat diameter was determined to be 0.21 μm.

Representative uniaxial stress-strain curves for dry and wet NYT samples are shown in Fig. 5b, and the UCS is plotted as a function of connected porosity in Fig. 5c (data given in Table 2). The average wet and dry strength was found to be 3.50 and 5.58 MPa, respectively. The ratio of wet to dry strength—a metric commonly used to assess water-weakening in rocks (Zhu et al. 2011)—is 0.63.

Table 4 Summary of the published wet and dry tensile strengths of tuffs from around the globe. τ_{dry}—dry tensile strength; τ_{wet}—wet tensile strength

Tuff	Core orientation	Connected porosity	±	τ_{dry} [MPa]	±	τ_{wet} [MPa]	±	$\frac{\tau_{wet}}{\tau_{dry}}$	Source	Notes
Eger-Demjén		0.35	0.010	3.30	0.57	2.78	0.36	0.844	Stück et al.	Data not available
Eger-Tihamér		0.36	0.002	0.81	0.14	0.31	0.08	0.386	(2008)	
Weibern tuff		0.43	0.004	1.64	0.22	1.23	0.14	0.754		Fine grained matrix of zeolite minerals
Rochlitz tuff		0.28	0.005	2.42	0.28	1.47	0.26	0.608		Presence of kaolinite
Habichtswald tuff		0.22	0.013	2.68	0.91	2.37	0.6	0.887		Smectite-zeolite matrix
Loseros tuff	X	0.07		6.29		5.82		0.925	Wedekind et al.	Kaolinite, illite, and smectite
	Z	0.07		8.25		6.69		0.811	(2013)	
Cantera Rosa tuff	X	0.41		3.94		2.61		0.662		Smectite and kaolinite
	Z	0.41		4.02		3.00		0.746		
Chiluca tuff	X	0.08		5.13		4.56		0.889		Small amounts of illite and smectite
	Z	0.08		5.61		4.79		0.854		
Gris de los Remedios tuff	X	0.31		2.27		1.39		0.612		Smectites and traces of muscovite/illite
	Z	0.31		2.24		1.58		0.773		
Cantera Formación tuff	X	0.13		10.65		8.23		0.773		Kaolinite and halloysite
	Z	0.13		9.89		8.71		0.881		
Cantera Blanca tuff	X	0.15		6.90		3.99		0.578		Mordenite, clinoptilolite, and montmorillonite
	Z	0.15		5.89		3.11		0.528		
Bufa tuff	X	0.18		6.04		3.65		0.604		Illite and smectite
	Z	0.18		6.95		4.57		0.658		
Tenayocátetl tuff	X	0.05		5.43		3.94		0.726		Smectite
	Z	0.05		5.71		4.12		0.722		
Cantera Amarilla tuff	X	0.42		0.99		0.49		0.495		Smectite, kaolinite, and halloysite
	Z	0.42		1.05		0.56		0.533		
Hilbersdorf tuff	X	0.30		3.70		1.14		0.308		Illite
	Z	0.30		4.62		3.10		0.671		

Discussion

We have performed UCS tests on cylindrical cores of dry and water-saturated NYT either 20 or 25 mm in diameter. Although these diameters are standard in volcanological studies, the strength of engineering materials is typically determined on samples that are 50 mm in diameter. Due to the influence of sample geometry on the UCS (Hawkes and Mellor 1970; Hoek and Brown 1980), we provide here UCS values for 50 mm-diameter core samples using the following empirical relation (Hoek and Brown 1980):

$$UCS = UCS_{50}\left(\frac{50}{d}\right)^{0.18},   (1)$$

where UCS is the uniaxial compressive strength measured for a cylindrical sample of diameter d (in mm) and UCS_{50} is the uniaxial compressive strength of a 50-mm-diameter core sample. The UCS_{50} values for our experiments are given in Tables 2 and 5. However, although this allows us to better compare our UCS values with those from the engineering

literature, we highlight that the goal of this contribution was to understand whether NYT is weaker when water-saturated. In this case, the metric of interest—the ratio of wet to dry UCS—is independent of sample diameter.

Our data show that the UCS of water-saturated NYT is weaker than dry NYT (Fig. 5c). These data are in accordance with tuffs sourced from Italy and elsewhere. For example, studies have shown that the tuffs from the Cappadocia (Erdoğan 1986; Erguvanlı et al. 1989; Topal and Doyuran 1997; Tuncay 2009; Erguler and Ulusay 2009) and Afyonkarahisar (Çelik et al. 2014; Çelik and Ergul 2015) regions of Turkey, tuffs from different locations in Hungary (Vásárhelyi 2002), and tuffs from Rome (Jackson et al. 2005) and the Neapolitan area (Montanaro et al. 2016; Marmoni et al. 2017a) are weaker when wet. To test the hypothesis that the presence of zeolites and/or clays is responsible for the observed water-weakening in tuffs, we have collated the available published data on the wet versus dry compressive (Table 3) and tensile (Table 4) strength of tuffs from around the world (Fig. 6). All the data are presented in Fig. 6a, and Fig. 6b shows only UCS data for which the composition is known. The data in Fig. 6b have been divided into three
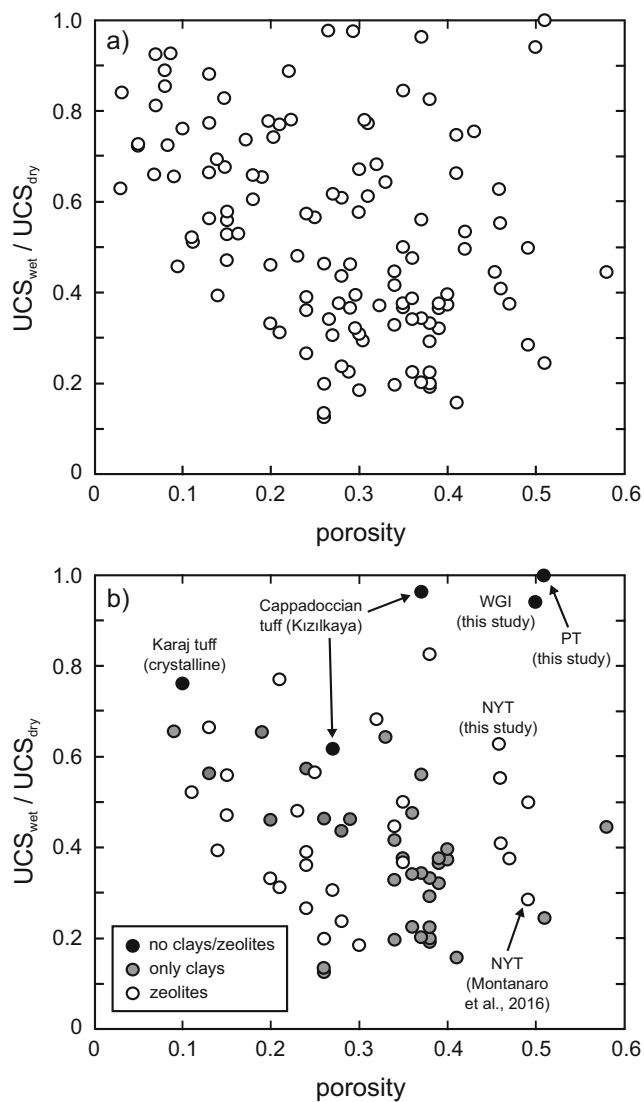
Fig. 6 (a) Water-weakening (ratio of wet to dry strength) as a function of porosity for tuffs all over the world. (b) Ratio of wet to dry uniaxial compressive strength as a function of porosity (data for which the composition is known). Data are in three groups (1) tuffs that contain zeolites (white circles), (2) tuffs that contain clays but no zeolites (grey circles), and (3) tuffs that contain neither zeolites nor clays (black circles). Data from: this study, Behre Jr. (1929), Price (1983), Price and Jones (1982), Erdoğan (1986), Erguvanlı et al. (1989), Ayday and Göktan (1990), Martin et al. (1994), Okubo and Chu (1994), Schultz and Li (1995), Topal and Doyuran (1997), Vásárhelyi (2002), Topal and Sözmen (2003), Török et al. (2004), Yassaghi et al. (2005), Jackson et al. (2005), Tuncay (2009), Stück et al. (2008), Erguler and Ulusay (2009), Zhu et al. (2011), Heidari et al. (2014), Wedekind et al. (2013), Çelik et al. (2014), Çelik and Ergul (2015), Montanaro et al. (2016), Marmoni et al. (2017a), Marmoni et al. (2017b), and Vásárhelyi (pers. comm.)

groups: (1) tuffs that contain zeolites, (2) tuffs that contain clays but no zeolites, and (3) tuffs that contain neither zeolites nor clays.

To complement these data, we performed ancillary experiments on two tuffs that contain no zeolites or clays—the grey Campanian Ignimbrite (welded grey ignimbrite, WGI) and the Piperno Tuff (PT). Both rocks are facies of the Campanian Ignimbrite deposit (e.g., Barberi et al. 1978; Rosi et al. 1996; Fedele et al. 2016) and have been used in construction within the Neapolitan area (e.g., Calcaterra et al. 2000; de'Gennaro et al. 2000a; Calcaterra et al. 2005; Morra et al. 2010). The use of PT is particularly widespread in the ancient city centre of Naples, the church of Gesù Nuovo providing a spectacular example (Fig. 7). Piperno Tuff was also used to construct the corner towers of Castel Nuovo (Fig. 2b). Cylindrical samples (20 mm in diameter and nominally 40 mm in length) were prepared from both the WGI block described in Heap et al. (2012 2014) and the PT block described in Heap et al. (2012), as described in the methods section above. The WGI samples tested contain hypidiomorphic phenocrysts of alkali feldspar with minor clinopyroxene within a matrix composed of microlites of alkali feldspar, Ti-magnetite, and apatite, as well as well-sorted glass shards with occasional accretionary ash clots and porous lapilli fragments (Heap et al. 2012). Piperno Tuff is characterised by a eutaxitic texture with black flattened scoriae and phenocrysts of alkali feldspar and clinopyroxene set within a light grey matrix of well-sorted glass shards and microlites of alkali feldspar and Ti-magnetite (Heap et al. 2012). Importantly, no zeolites or clays are present within these blocks (see XRD data presented in Heap et al. 2012). The connected porosities of the WGI and PT samples were first determined; the samples were then deformed in either the dry or wet condition (as described in the methods section above). The results of these experiments are summarised in Table 5. The ratio of wet to dry strength in WGI and PT is 0.939 and 1.038, respectively (Fig. 6b; Table 3). In other words, based on these data, WGI and PT are not weaker in the presence of water.

Figure 6b suggests that the presence of zeolites and clays promote water-weakening in tuffs, although firm conclusions cannot be drawn due to the paucity of data for zeolite-free tuff. The four samples of zeolite-free tuff (Karaj (crystalline), Cappadoccian (Kızılkaya), the WGI, and the PT) show consistently high ratios of UCS_{wet}/UCS_{dry}—between ~0.6 and ~1.0 (Fig. 6b; Table 3). By contrast, zeolite- and clay-bearing tuffs have average UCS_{wet}/UCS_{dry} ratios of 0.54 and 0.37, respectively (Fig. 6b; Table 3). We therefore conclude that the water-weakening in NYT is the result of the presence of abundant zeolites (46 wt.% in total; Table 1), although the influence of subordinate clay (3 wt.%; Table 1), thought to promote water-weakening in sandstones (Dyke and Dobereiner 1991; Schmitt et al. 1994; Demarco et al. 2007; Shakoor and Barefield 2009), cannot be discounted. We attribute the observed weakening in the presence of water to the hydric expansion of zeolites and clays (e.g., Nijland et al. 2010; Wedekind et al. 2013; López-Doncel et al. 2013). However, based on the available data, we cannot definitively rule out the influence of porosity type (pores versus

Fig. 7 (**a**) Photograph of the church of Gesù Nuovo in Naples. (**b**) Photograph of front of the church of Gesù Nuovo showing the pyramid-shaped bossage constructed using Piperno Tuff

microcracks), pore shape, average pore size, and pore size distribution, amongst others, on the water-weakening behaviour of tuffs. Indeed, Wedekind et al. (2013) found a correlation between microporosity, average pore radius, and moisture expansion for a variety of tuffs from Mexico, Germany, and Hungary.

We also highlight that, in our study, we compare the strength of dry and fully saturated samples. In reality, it is unlikely that building stones will be fully saturated with water. However, experimental studies have shown that even low levels of water saturation can result in measurable water-weakening in tuffs (Kleb and Vásárhelyi 2003; Çelik and Ergül 2015). For example, Çelik and Ergül (2015) found that immersion in water for 1 h was sufficient to reduce the strength of tuff by ~32%. Water-weakening at low levels of water saturation has also been observed in clay-rich sandstones (Dyke and Dobereiner 1991; Schmitt et al. 1994; Demarco et al. 2007; Shakoor and Barefield 2009). Therefore, we consider our conclusions, drawn from experiments on dry and fully saturated samples, are relevant for monuments and buildings constructed using NYT. We further note that we have only tested one facies of the heterogeneous

lithified Upper Member of the NYT (Colella et al. 2017). However, yellow-coloured tuffs associated with more recent (post-NYT) eruptions at Campi Flegrei (Gauro and La Pietra Tuffs) also show water-weakening (Montanaro et al. 2016; Table 3). Importantly, these tuffs are texturally different to the facies studied herein. Indeed, one of the La Pietra Tuffs contained very few lapilli-sized lithic and porous juvenile fragments (similar to the "NP" end-member facies of the NYT reported in Colella et al. 2017). Based on these data, we expect the NYT facies that are texturally different to that studied herein will also be weaker when wet (as long as they contain zeolites), although more experiments should now be performed to test this hypothesis.

Conclusions

We have shown that a block of the lithified Upper Member of the NYT, often used in construction within the Neapolitan region of Italy, is weaker when water-saturated (Fig. 5c). Compiled data on the wet and dry strength of tuffs from across the globe suggest that the cause of the water-weakening is the

Table 5 Summary of the experiments performed on Piperno Tuff (labelled "PIP") and the grey Campanian Ignimbrite (labelled "CI") for this study. Wet—vacuum-saturated in deionised water (see text for details). Dry—dried in a vacuum oven at 40 °C for at least 48 h. The uniaxial compressive strength for a sample of 50 mm diameter was calculated using the empirical relation given as Eq. (1) (see text for details)

Sample	Sample diameter [mm]	Connected porosity	Uniaxial compressive strength [MPa]	Experimental condition	Uniaxial compressive strength (diameter = 50 mm) (Eq. 1) [MPa]
PIP-1	20.26	0.51	3.17	Dry	2.69
PIP-2	20.29	0.50	3.29	Wet	2.80
CI-4	19.85	0.50	10.97	Wet	9.29
CI-9	19.79	0.50	9.54	Wet	8.07
CI-10	19.82	0.50	9.59	Wet	8.12
CI-11	19.83	0.50	9.65	Wet	8.17
CI-13	19.81	0.50	10.88	Dry	9.21
CI-19	19.81	0.50	10.17	Dry	8.61
CI-20	19.83	0.50	11.05	Dry	9.36
CI-21	19.83	0.50	8.95	Dry	7.58
CI-22	19.84	0.50	11.90	Dry	10.08
CI*-2	19.83	0.50	10.94	Wet	9.26

due to the presence of zeolites (Fig. 6b). Water-weakening in the zeolite-rich NYT may help explain the widespread weathering observed in Naples due to moisture (as a result of rising damp) and rainfall (Fig. 3; de'Gennaro et al. 1993 2000a; Di Benedetto et al. 2015) and the apparent link between rainfall and landslide and rock fall hazards (Calcaterra et al. 2002; Di Martire et al. 2012; Calcaterra et al. 2007; Nocilla et al. 2009) and sinkhole formation (Guarino and Nisio 2012). We additionally conclude that the buildings constructed using zeolite-free tuffs, such as the church of Gesù Nuovo (Fig. 7), will be less prone to weathering associated with moisture and rainfall. This latter hypothesis is supported by the observation that, while the WGI is only subject to physical weathering, the zeolitised facies of the Campanian Ignimbrite is more affected by chemical action (de'Gennaro et al. 1995). We anticipate that the implications of this study will be important not only for building and monument preservation in Naples, but also in other cities worldwide constructed using tuff.

References

ASTM D4404-10, (2010) Standard test method for determination of pore volume and pore volume distribution of soil and rock by mercury intrusion porosimetry, ASTM International, West Conshohocken, PA, www.astm.org

Augenti N, Parisi F (2009) Mechanical characterization of tuff masonry. Proc. Protection Hist Build, PROHITECH 9:1579–1584

Augenti N, Parisi F (2010) Constitutive models for tuff masonry under uniaxial compression. J Mater Civ Eng 22(11):1102–1111

Aversa S, Evangelista A (1998) The mechanical behaviour of a pyroclastic rock: yield strength and "destructuration" effects. Rock Mech Rock Eng 31(1):25–42

Aversa S, Evangelista A, Scotto Di Santolo A (2013) Influence of the subsoil on the urban development of Napoli In Proc. Of the 2nd Int Symp On Geotechnical Engineering for the Preservation of Monuments and Historic Sites, 15–43

Ayday C, Göktan RM (1990) A preliminary engineering geology study directed to the conservation of Midas monument. In Proc. International Earth Sciences Colloquium on the Aegean Region (IESCA), DE University, Izmir (pp. 102–108)

Barberi F, Innocenti F, Lirer L, Munno R, Pescatore T, Santacroce R (1978) The Campanian ignimbrite: a major prehistoric eruption in the Neapolitan area (Italy). Bull Volcanol 41(1):10–31

Behre Jr, CD (1929) Volcanic tuffs and sandstones used as building stones in the upper Salmon River valley, Idaho. Contributions to Economic Geology, Part 1

Bergmann J, Friedel P, Kleeberg R (1998) BGMN—a new fundamental parameters based Rietveld program for laboratory X-ray sources, its use in quantitative analysis and structure investigations. CPD Newsletter, 20:5–8

Broxton DE, Chipera SJ, Byers FM Jr, Rautman CA (1993) Geologic evaluation of six nonwelded tuff sites in the vicinity of Yucca Mountain, Nevada for a surface-based test facility for the Yucca Mountain project (No. LA–12542-MS). Los Alamos National Lab, NM (United States)

Calcaterra D, Cappelletti P, Langella A, Morra V, Colella A, de Gennaro R (2000) The building stones of the ancient Centre of Naples (Italy): Piperno from Campi Flegrei. A contribution to the knowledge of a long-time-used stone. J Cult Herit 1(4):415–427

Calcaterra D, De Riso R, Nave A, Sgambati D (2002) The role of historical information in landslide hazard assessment of urban areas: the case of Naples (Italy). In Proc. 1st European Conference on Landslides, Prague (pp. 129–135)

Calcaterra D, Langella A, De Gennaro R, de'Gennaro M, Cappelletti P (2005) Piperno from Campi Flegrei: a relevant stone in the historical and monumental heritage of Naples (Italy). Environ Geol 47(3):341–352

Calcaterra D, Coppin D, De Vita S, Di Vito MA, Orsi G, Palma B, Parise M (2007) Slope processes in weathered volcaniclastic deposits within the city of Naples: the Camaldoli Hill case. Geomorphology 87(3):132–157

Calderoni B, Cecere G, Cordasco EA, Guerriero L, Lenza P, Manfredi G (2010) Metrological definition and evaluation of some mechanical properties of post-medieval Neapolitan yellow tuff masonry. J Cult Herit 11(2):163–171

Cardellini C, Chiodini G, Frondini F, Avino R, Bagnato E, Caliro S, Lelli M, Rosiello A (2017) Monitoring diffuse volcanic degassing during volcanic unrests: the case of Campi Flegrei (Italy). Sci Rep 7:6757

Cejka J, Van Bekkum H, Corma A, Schueth F, (2007) Introduction to zeolite molecular sieves, vol. 168. Elsevier, Amsterdam

Çelik MY, Akbulut H, Ergül A (2014) Water absorption process effect on strength of Ayazini tuff, such as the uniaxial compressive strength (UCS), flexural strength and freeze and thaw effect. Environ Earth Sci 71(9):4247–4259

Çelik MY, Ergül A (2015) The influence of the water saturation on the strength of volcanic tuffs used as building stones. Environ Earth Sci 74(4):3223–3239

Chiodini G, Frondini F, Cardellini C, Granieri D, Marini L, Ventura G (2001) CO2 degassing and energy release at Solfatara volcano, Campi Flegrei, Italy. J Geophys Res: Solid Earth 106(B8):16213–16221

Chiodini G, Vandemeulebrouck J, Caliro S, D'Auria L, De Martino P, Mangiacapra A, Petrillo Z (2015) Evidence of thermal-driven processes triggering the 2005–2014 unrest at Campi Flegrei caldera. Earth Planet Sci Lett 414:58–67

Chiodini G, Selva J, Del Pezzo E, Marsan D, De Siena L, D'Auria L, Bianco F, Caliro S, De Martino P, Ricciolino P, Petrillo Z (2017) Clues on the origin of post-2000 earthquakes at Campi Flegrei caldera (Italy). Sci Rep 7:4472

Civetta L, Orsi G, Pappalardo L, Fisher RV, Heiken G, Ort M (1997) Geochemical zoning, mingling, eruptive dynamics and depositional processes—the Campanian ignimbrite, Campi Flegrei caldera, Italy. J Volcanol Geotherm Res 75(3):183–219

Cole PD, Scarpati C (1993) A facies interpretation of the eruption and emplacement mechanisms of the upper part of the Neapolitan

Yellow Tuff, Campi Flegrei, southern Italy. Bull Volcanol 55(5): 311–326

Colella C, de'Gennaro M, Aiello R (2001) Use of zeolitic tuff in the building industry. Rev Mineral Geochem 45(1):551–587

Colella C (2005) Natural zeolites. Stud Surf Sci Catal 157:13–40

Colella A, Di Benedetto C, Calcaterra D, Cappelletti P, D'Amore M, Di Martire D, Graziano SF, Papa L, de Gennaro M, Langella A (2017) The Neapolitan yellow tuff: an outstanding example of heterogeneity. Constr Build Mater 136:361–373

Coppola E, Battaglia G, Bucci M, Ceglie D, Colella A, Langella A et al (2002) Neapolitan yellow tuff for the recovery of soils polluted by potential toxic elements in illegal dumps of Campania region. Stud Surf Sci Catal 142:1759–1766

Deino AL, Orsi G, de Vita S, Piochi M (2004) The age of the Neapolitan yellow tuff caldera-forming eruption (Campi Flegrei caldera–Italy) assessed by 40 Ar/39 Ar dating method. J Volcanol Geotherm Res 133(1):157–170

de'Gennaro M, Colella C (1989) Use of thermal analysis for the evaluation of zeolite content in mixtures of hydrated phases. Thermochim Acta 154(2):345–353

de'Gennaro M, Fuscaldo MD, Colella C (1993) Weathering mechanisms of monumental tuff-stone masonries in downtown Naples. Sci Technol Cult Herit 2:53–62

de'Gennaro M, Colella C, Langella A, Cappelletti P (1995) Decay of Campanian ignimbrite stoneworks in some monuments of the Caserta area. Sci Technol Cult Herit, 4, 75–86

de'Gennaro M, Calcaterra D, Cappelletti P, Langella A, Morra V (2000a) Building stone and related weathering in the architecture of the ancient city of Naples. J Cult Herit 1(4):399–414

de'Gennaro M, Cappelletti P, Langella A, Perrotta A, Scarpati C (2000b) Genesis of zeolites in the Neapolitan yellow tuff: geological, volcanological and mineralogical evidence. Contrib Mineral Petrol 139(1):17–35

Demarco MM, Jahns E, Rüdrich J, Oyhantcabal P, Siegesmund S (2007) The impact of partial water saturation on rock strength: an experimental study on sandstone [Der Einfluss einer partiellen Wassersättigung auf die mechanischen Gesteinseigenschaften: eine Fallstudie an Sandsteinen]. Z Dtsch Ges Geowiss 158(4):869–882

Di Benedetto C, Cappelletti P, Favaro M, Graziano SF, Langella A, Calcaterra D, Colella A (2015) Porosity as key factor in the durability of two historical building stones: Neapolitan yellow tuff and Vicenza stone. Eng Geol 193:310–319

Di Martire D, De Rosa M, Pesce V, Santangelo MA, Calcaterra D (2012) Landslide hazard and land management in high-density urban areas of Campania region, Italy. Nat Hazards Earth Syst Sci 12(4):905–926

Di Vito MA, Isaia R, Orsi G, Southon J, De Vita S, d'Antonio M, Pappalardo L, Piochi M (1999) Volcanism and deformation since 12,000 years at the Campi Flegrei caldera (Italy). J Volcanol Geotherm Res 91(2):221–246

Dyke CG, Dobereiner L (1991) Evaluating the strength and deformability of sandstones. In Quarterly Journal of Engineering Geology and Hydrogeology (Vol. 24, No. 1, pp. 123-134). Geological Society of London

Erdoğan M (1986) Nevşehir-Ürgup yöresi tüflerinin malzeme jeolojisi açısından araştırılması. Unpublished doctoral dissertation, Istanbul Technical University (ITU), Faculty of Mining, Istanbul

Erguler ZA, Ulusay R (2009) Water-induced variations in mechanical properties of clay-bearing rocks. Int J Rock Mech Min Sci 46(2):355–370

Erguvanlı K, Yorulmaz M, Çılı F, Ahunbay Z, Erdoğan M (1989) Göreme yapısal koruma ve sağlamlaştırma projesi, E1 Nazar kilisesi, Istanbul Technical University (ITU). Faculty of Mining, Istanbul p 46

Evangelista A (1980) Influenza del contenuto d'acqua sul comportamento del tufo giallo napoletano. Atti del XIV Convegno Nazionale di Geotecnica, Firenze

Evangelista A, Aversa S (1994) Experimental evidence of non-linear and creep behaviour of pyroclastic rocks. In Visco-plastic behaviour of geomaterials (pp. 55–101). Springer, Vienna

Evangelista A, Aversa S, Pescatore TS, Pinto F (2000a) Soft rocks in southern Italy and role of volcanic tuffs in the urbanization of Naples. In Proceedings of the II International Symposium on 'The Geotechnics of Hard Soils and Soft Rocks', Napoli (Vol. 3, pp. 1243–1267)

Evangelista A, Flora A, Lirer S, Feola A, Maiorano RMS (2000b) Numerical analysis of roof failure mechanisms of cavities in a soft rock. In ISRM International Symposium. International Society for Rock Mechanics

Fedele L, Scarpati C, Sparice D, Perrotta A, Laiena F (2016) A chemostratigraphic study of the Campanian ignimbrite eruption (Campi Flegrei, Italy): insights on magma chamber withdrawal and deposit accumulation as revealed by compositionally zoned stratigraphic and facies framework. J Volcanol Geotherm Res 324:105–117

Gatta GD, Cappelletti P, Langella A (2010) Crystal-chemistry of phillipsites from the Neapolitan yellow tuff. Eur J Mineral 22(6):779–786

Guarino PM, Nisio S (2012) Anthropogenic sinkholes in the territory of the city of Naples (southern Italy). Phys Chem Earth, Parts A/B/C 49:92–102

Guarino PM, Santo A, Forte G, De Falco M, Niceforo DMA (2018) Analysis of a database for anthropogenic sinkhole triggering and zonation in the Naples hinterland (southern Italy). Nat Hazards, 91(1), 173–192

Hall SA, De Sanctis F, Viggiani G (2006) Monitoring fracture propagation in a soft rock (Neapolitan tuff) using acoustic emissions and digital images. Pure Appl Geophys, 163(10), 2171–2204

Hawkes I, Mellor M (1970) Uniaxial testing in rock mechanics laboratories. Eng Geol 4(3):179–285

Heap MJ, Lavallée Y, Laumann A, Hess KU, Meredith PG, Dingwell DB (2012) How tough is tuff in the event of fire? Geology 40(4):311–314

Heap MJ, Baud P, Meredith PG, Vinciguerra S, Reuschlé T (2014) The permeability and elastic moduli of tuff from Campi Flegrei, Italy: implications for ground deformation modelling. Solid Earth 5(1):25–44

Heidari M, Khanlari GR, Torabi-Kaveh M, Kargarian S, Saneie S (2014) Effect of porosity on rock brittleness. Rock Mech Rock Eng 47(2):785–790

Heiken, G. (Ed.). (2006). Tuffs: their properties, uses, hydrology, and resources (Vol. 408). Geological Society of America

Hoek E, Brown ET (1980) Underground excavations in rock, Institution of Mining and Metallurgy, London

Jackson MD, Marra F, Hay RL, Cawood C, Winkler EM (2005) The judicious selection and preservation of tuff and travertine building stone in ancient Rome. Archaeometry 47(3):485–510

Jackson MD, Kosso C, Marra F, Hay R (2006) Geological basis of Vitruvius' empirical observations of material characteristics of rock utilized in Roman masonry. In Proceedings of the Second International Congress of Construction History Queen's College, University of Cambridge (Vol. 2, 1685–1702)

Kleb B, Vásárhelyi B (2003) Test results and empirical formulas of rock mechanical parameters of rhyolitic tuff samples from Eger's cellars. Acta Geol Hung 46(3):301–312

Kilburn CR, De Natale G, Carlino S (2017) Progressive approach to eruption at Campi Flegrei caldera in southern Italy. Nature Communications, 8

La Russa MF, Ruffolo SA, de Buergo MÁ, Ricca M, Belfiore CM, Pezzino A, Crisci GM (2017) The behaviour of consolidated

Neapolitan yellow tuff against salt weathering. Bull Eng Geol Environ 76(1):115–124

Levy SS, O'Neil JR (1989) Moderate-temperature zeolitic alteration in a cooling pyroclastic deposit. Chem Geol 76(3–4):321–326.

López-Doncel R, Wedekind W, Dohrmann R, Siegesmund S (2013) Moisture expansion associated to secondary porosity: an example of the Loseros tuff of Guanajuato, Mexico. Environ Earth Sci 69(4): 1189–1201

Marmoni GM, Martino S, Heap MJ, Reuschlé T (2017a) Gravitational slope-deformation of a resurgent caldera: new insights from the mechanical behaviour of Mt. In: Nuovo tuffs (Ischia Island, Italy), vol 345. Research, Journal of Volcanology and Geothermal, pp 1–20. https://doi.org/10.1016/j.jvolgeores.2017.07.019

Marmoni GM, Martino S, Heap MJ, Reuschlé T (2017b) Multiphysics laboratory tests for modelling gravity-driven instabilities at slope scale. Proc Eng 191:142–149

Martin RJ, Boyd PJ, Noel JS, Price RH (1994) Bulk and mechanical properties of the paintbrush tuff recovered from borehole USW NRG-6: data report (no. SAND—93-4020). Sandia National Labs., Albuquerque, NM (United States)

Mayer K, Scheu B, Montanaro C, Yilmaz TI, Isaia R, Aßbichler D, Dingwell DB (2016) Hydrothermal alteration of surficial rocks at Solfatara (Campi Flegrei): petrophysical properties and implications for phreatic eruption processes. J Volcanol Geotherm Res 320:128–143

Montanaro C, Scheu B, Mayer K, Orsi G, Moretti R, Isaia R, Dingwell DB (2016) Experimental investigations on the explosivity of steam-driven eruptions: a case study of Solfatara volcano (Campi Flegrei). J Geophys Res: Solid Earth 121(11):7996–8014

Morra V, Calcaterra D, Cappelletti P, Colella A, Fedele L, de' Gennaro R, Langella A, Mercurio M, de' Gennaro M (2010) Urban geology: relationships between geological setting and architectural heritage of the Neapolitan area. In: (Eds.) Marco Beltrando, Angelo Peccerillo, Massimo Mattei, Sandro Conticelli, and Carlo Doglioni, journal of the virtual explorer, volume 36, paper 26, doi: https://doi.org/10.3809/jvirtex.2010.00261

Nijland TG, Van Hees RP, Bolondi L (2010) Evaluation of three Italian tuffs (Neapolitan yellow tuff, Tufo Romano and Tufo Etrusco) as compatible replacement stone for Römer tuff in Dutch built cultural heritage. Geol Soc Lond, Spec Publ 333(1):119–127

Nocilla N, Evangelista A, Di Santolo AS (2009) Fragmentation during rock falls: two Italian case studies of hard and soft rocks. Rock Mech Rock Eng 42(5):815–833

Okubo S, Chu SY (1994) Uniaxial compression creep of Tage and Oya tuff in air-dried and water-saturated conditions. J Soc Mat Sci, Japan 43(490):819–825

Orsi G, D'Antonio M, de Vita S, Gallo G (1992) The Neapolitan yellow tuff, a large-magnitude trachytic phreatoplinian eruption: eruptive dynamics, magma withdrawal and caldera collapse. J Volcanol Geotherm Res 53(1):275–287

Orsi G, De Vita S, Di Vito M (1996) The restless, resurgent Campi Flegrei nested caldera (Italy): constraints on its evolution and configuration. J Volcanol Geotherm Res 74(3–4):179–214

Peluso F, Arienzo I (2007) Experimental determination of permeability of Neapolitan yellow tuff. J Volcanol Geotherm Res 160(1):125–136

Price RH (1983) Analysis of the rock mechanics properties of volcanic tuff units from Yucca Mountain, Nevada Test Site. Sandia National Laboratories

Price RH, Jones AK (1982) Uniaxial and triaxial compression test series on Calico Hills tuff (no. SAND—82-1314). Sandia National Labs., Albuquerque, NM (United States)

Rosi M, Vezzoli L, Aleotti P, De Censi M (1996) Interaction between caldera collapse and eruptive dynamics during the Campanian ignimbrite eruption, Phlegraean fields, Italy. Bull Volcanol 57(7):541–554

Ross CS, Shannon EV (1924) Mordenite and associated minerals from near Challis, Custer County, Idaho. Proc US Nat Museum 64(19):1–9

Scarpati C, Cole P, Perrotta A (1993) The Neapolitan yellow tuff—a large volume multiphase eruption from Campi Flegrei, southern Italy. Bull Volcanol 55(5):343–356

Schmitt L, Forsans T, Santarelli FJ (1994) Shale testing and capillary phenomena. In International Journal of Rock Mechanics and Mining Sciences & Geomechanics Abstracts (Vol. 31, No. 5, pp. 411–427). Pergamon

Schultz RA, Li Q (1995) Uniaxial strength testing of non-welded Calico Hills tuff, Yucca Mountain, Nevada. Eng Geol 40(3–4):287–299

Shakoor A, Barefield EH (2009) Relationship between unconfined compressive strength and degree of saturation for selected sandstones. Environ Eng Geosci 15(1):29–40

Stück H, Forgó LZ, Rüdrich J, Siegesmund S, Török A (2008) The behaviour of consolidated volcanic tuffs: weathering mechanisms under simulated laboratory conditions. Environ Geol 56(3–4):699–713

Temel A, Gündoğdu MN (1996) Zeolite occurrences and the erionite-mesothelioma relationship in Cappadocia, central Anatolia, Turkey. Mineralium Deposita, 31(6):539–547

Topal T, Doyuran V (1997) Engineering geological properties and durability assessment of the Cappadocian tuff. Eng Geol 47(1–2):175–187

Topal T, Sözmen B (2003) Deterioration mechanisms of tuffs in Midas monument. Eng Geol 68(3):201–223

Török A, Gálos M, Kocsanyi-Kopecsko K (2004) Experimental weathering of rhyolite tuff building stones and the effect of an organic polymer conserving agent. Stone Decay: Its Causes and Controls, 109–127

Tuncay E (2009) Rock rupture phenomenon and pillar failure in tuffs in the Cappadocia region (Turkey). Int J Rock Mech Min Sci 46(8): 1253–1266

Vásárhelyi B (2002) Influence of the water saturation on the strength of volcanic tuffs. In ISRM international symposium-EUROCK 2002. International Society for Rock Mechanics

Wedekind W, López-Doncel R, Dohrmann R, Kocher M, Siegesmund S (2013) Weathering of volcanic tuff rocks caused by moisture expansion. Environ Earth Sci 69(4):1203–1224

Wohletz K, Orsi G, De Vita S (1995) Eruptive mechanisms of the Neapolitan yellow tuff interpreted from stratigraphie, chemical, and granulometric data. J Volcanol Geotherm Res 67(4):263–290

Yassaghi A, Salari-Rad H, Kanani-Moghadam H (2005) Geomechanical evaluations of Karaj tuffs for rock tunnelling in Tehran–Shomal freeway, Iran. Eng Geol 77(1):83–98

Yavuz AB (2012) Durability assessment of the Alaçatı tuff (Izmir) in western Turkey. Environ Earth Sci 67(7):1909–1925

Zhu W, Baud P, Vinciguerra S, Wong T-f (2011) Micromechanics of brittle faulting and cataclastic flow in Alban Hills tuff. Journal of Geophysical Research: Solid Earth, 116(B6)

CHAPTER FIVE – Some perspectives for future work

5.1 The mechanical behaviour of porous rocks

The data presented in Heap et al. (2015a) show that the failure envelope for the highest porosity andesite (porosity = 0.24) is larger than that for the andesite containing a porosity of 0.18. In other words, over the entire stress space, the andesite with a porosity of 0.24 is stronger than the andesite with a porosity of 0.18. However, based on data for sedimentary rocks, the sample with the highest porosity should be the weakest (Wong and Baud, 2012). It was noted by Heap et al. (2015a) that the highest porosity sample contained smaller pores than the sample containing a porosity of 0.18. We speculated in this paper that the average pore size, the maximum pore size, and the pore size distribution could therefore greatly influence the mechanical behaviour of these andesites. However, there were not enough data to draw firm conclusions. A full understanding of the influence of pore size on the mechanical behaviour would require samples that preserve the same porosity (and other attributes) but contain pores of different sizes – not a simple task with natural volcanic materials (for which pore size often increases as porosity increases, for example).

Further, although Heap et al. (2015a) determined the pore size and pore size distribution for each of the studied andesites, pore shape was not quantified. However, a recent study has shown that pore shape can play a first-order role in the strength of volcanic rocks (Bubeck et al., 2017). Bubeck et al. (2017) showed that the strength of porous basalts with elliptical pores is 80-102 MPa when the pores are orientated with their long axis parallel to the applied stress and 16-30 MPa when the pores are orientated with their long axis perpendicular to the applied stress. Based on these results they encourage future studies to accurately determine the shape of the pore population and their preferred orientation. Therefore, to better understand the mechanical behaviour of volcanic rocks, studies should characterise not only the porosity (a scalar), but also the shape, size, and preferred orientation of the pores (using, for example, X-ray computed tomography; XCT).

Heap et al. (2015b) found that high-porosity tuffs deformed in the ductile regime without forming compaction bands, as also observed for tuff from the Alban Hills (Italy; Zhu et al., 2011). Other studies have found that porous andesites (e.g., Heap et al., 2015a), basalts (Loaiza et al.,

2012; Adelinet et al., 2013), and dacites (e.g., Heap et al., 2016) formed compaction bands. However, it is currently unclear why some volcanic rocks form compaction bands and others do not. Based on data on sandstones, which suggest that compaction bands form in rocks with a narrow grain size distribution (Cheung et al., 2012), it is perhaps intuitive that compaction bands in porous volcanic rocks would form in samples with a narrow pore size distribution. However, the andesites that developed compaction bands, documented by Heap et al. (2015a), were characterised by a very wide pore size distribution. More experiments are therefore required to understand compaction localisation in volcanic rocks.

It is clear based on the above discussion that more experimental campaigns are required to better understand how volcanic rocks deform. However, due to the extreme variability of volcanic rocks, further insight into their mechanical behaviour is best achieved using synthetic samples (using methods such as 3D printing, or preparing samples by hot pressing glass beads or volcanic powders). Only using synthetic samples can we accurately control microstructural variables such as porosity, pore size shape, and grain size and shape, amongst other factors. Controlling these parameters is considered here to be an important prerequisite for a deeper understanding of the mechanical behaviour and failure mode of volcanic rocks.

5.2 The permeability of volcanic rocks

The porosity-permeability data for more than 500 rock samples presented in Farquharson et al. (2015) show that, even for the same rock type (andesite) sourced from the same volcano, permeability at a constant porosity can vary by orders of magnitude (Figure 11). This is a result of the extremely variable microstructure of volcanic rocks. Similar to the conclusion for the previous section (section 5.1), it could be concluded here that a deeper understanding requires the use of synthetic samples. Only when we can control the microstructural attributes (such as porosity, pore size shape, and grain size and shape, amongst other factors) can we use microstructural models (such as those presented in Guéguen and Dienes, 1989) to better understand the physical parameters important for fluid flow in volcanic rocks. This deeper understanding also requires a more complete comprehension of the microstructure of volcanic materials that can, for example, be exposed by routine X-ray computed tomography on volcanic rocks sourced from volcanoes worldwide.

5.3 The use of volcanic rocks in construction

The data presented in Heap et al. (2012, 2018b) highlight that zeolites and clays are responsible for the observed weakening following exposure to fire. However, there is still a paucity of data for tuffs that do not contain such minerals and, as such, there is room for further study in this area. Similarly, water-weakening data for tuffs devoid of zeolites and clays would help reinforce the conclusions drawn by Heap et al. (2018c) – most of the data (for tuffs worldwide) have been, so far, collected on zeolite- or clay-bearing tuffs (Heap et al., 2018).

Appendix A – Reference list

Aben, F. M., Doan, M. L., Mitchell, T. M., Toussaint, R., Reuschlé, T., Fondriest, M., ... & Renard, F. (2016). Dynamic fracturing by successive coseismic loadings leads to pulverization in active fault zones. Journal of Geophysical Research: Solid Earth, 121(4), 2338-2360.

Aben, F. M., Doan, M. L., Gratier, J. P., & Renard, F. (2017). Coseismic Damage Generation and Pulverization in Fault Zones. Fault Zone Dynamic Processes: Evolution of Fault Properties during Seismic Rupture, 47-80.

Adelinet, M., Fortin, J., Schubnel, A., & Guéguen, Y. (2013). Deformation modes in an Icelandic basalt: from brittle failure to localized deformation bands. Journal of Volcanology and Geothermal Research, 255, 15-25.

Apuani, T., Corazzato, C., Cancelli, A., & Tibaldi, A. (2005). Physical and mechanical properties of rock masses at Stromboli: a dataset for volcano instability evaluation. Bulletin of Engineering Geology and the Environment, 64(4), 419.

Ashby, M. F., & Sammis, C. G. (1990). The damage mechanics of brittle solids in compression. Pure and Applied Geophysics, 133(3), 489-521.

Barbier, E. (2002). Geothermal energy technology and current status: an overview. Renewable and Sustainable Energy Reviews, 6(1-2), 3-65.

Baud, P., Vajdova, V., & Wong, T.-f. (2006). Shear-enhanced compaction and strain localization: Inelastic deformation and constitutive modeling of four porous sandstones. Journal of Geophysical Research: Solid Earth, 111(B12).

Baud, P., Zhu, W., & Wong, T.-f. (2000). Failure mode and weakening effect of water on sandstone. Journal of Geophysical Research: Solid Earth, 105(B7), 16371-16389.

Baud, P., Vinciguerra, S., David, C., Cavallo, A., Walker, E., & Reuschlé, T. (2009). Compaction and failure in high porosity carbonates: Mechanical data and microstructural observations. In Rock Physics and Natural Hazards (pp. 869-898). Birkhäuser Basel.

Baud, P., Meredith, P., & Townend, E. (2012). Permeability evolution during triaxial compaction of an anisotropic porous sandstone. Journal of Geophysical Research: Solid Earth, 117(B5).

Baud, P., Exner, U., Lommatzsch, M., Reuschlé, T., & Wong, T.-f. (2017a). Mechanical behavior, failure mode, and transport properties in a porous carbonate. Journal of Geophysical Research: Solid Earth, 122(9), 7363-7387.

Baud, P., Schubnel, A., Heap, M., & Rolland, A. (2017b). Inelastic Compaction in High-Porosity Limestone Monitored Using Acoustic Emissions. Journal of Geophysical Research: Solid Earth.

Benson, P., Schubnel, A., Vinciguerra, S., Trovato, C., Meredith, P., & Young, R. P. (2006). Modeling the permeability evolution of microcracked rocks from elastic wave velocity inversion at elevated isostatic pressure. Journal of Geophysical Research: Solid Earth, 111(B4).

Bernabé, Y., Li, M., & Maineult, A. (2010). Permeability and pore connectivity: a new model based on network simulations. Journal of Geophysical Research: Solid Earth, 115(B10).

Bourbié, T., & Zinszner, B. (1985). Hydraulic and acoustic properties as a function of porosity in Fontainebleau sandstone. Journal of Geophysical Research: Solid Earth, 90(B13), 11524-11532.

Bubeck, A., Walker, R. J., Healy, D., Dobbs, M., & Holwell, D. A. (2017). Pore geometry as a control on rock strength. Earth and Planetary Science Letters, 457, 38-48.

Brace, W., Walsh, J. B., & Frangos, W. T. (1968). Permeability of granite under high pressure. Journal of Geophysical Research, 73(6), 2225-2236.

Caine, J. S., Evans, J. P., & Forster, C. B. (1996). Fault zone architecture and permeability structure. Geology, 24(11), 1025-1028.

Carrier, A., Got, J. L., Peltier, A., Ferrazzini, V., Staudacher, T., Kowalski, P., & Boissier, P. (2015). A damage model for volcanic edifices: Implications for edifice strength, magma pressure, and eruptive processes. Journal of Geophysical Research: Solid Earth, 120(1), 567-583.

Chen, T. C., Yeung, M. R., & Mori, N. (2004). Effect of water saturation on deterioration of welded tuff due to freeze-thaw action. Cold Regions Science and Technology, 38(2), 127-136.

Cheung, C. S., Baud, P., & Wong, T.-f. (2012). Effect of grain size distribution on the development of compaction localization in porous sandstone. Geophysical Research Letters, 39(21).

Cilona, A., Faulkner, D. R., Tondi, E., Agosta, F., Mancini, L., Rustichelli, A., ... & Vinciguerra, S. (2014). The effects of rock heterogeneity on compaction localization in porous carbonates. Journal of Structural Geology, 67, 75-93.

Darot, M., & Reuschlé, T. (2000). Acoustic wave velocity and permeability evolution during pressure cycles on a thermally cracked granite. International Journal of Rock Mechanics and Mining Sciences, 37(7), 1019-1026.

David, C., Wong, T.-f., Zhu, W., & Zhang, J. (1994). Laboratory measurement of compaction-induced permeability change in porous rocks: Implications for the generation and maintenance of pore pressure excess in the crust. Pure and Applied Geophysics, 143(1-3), 425-456.

David, C., Menéndez, B., & Bernabé, Y. (1998). The mechanical behaviour of synthetic sandstone with varying brittle cement content. International Journal of Rock Mechanics and Mining Sciences, 35(6), 759-770.

David, C., Menéndez, B., & Darot, M. (1999). Influence of stress-induced and thermal cracking on physical properties and microstructure of La Peyratte granite. International Journal of Rock Mechanics and Mining Sciences, 36(4), 433-448.

David, C., Menéndez, B., Zhu, W., & Wong, T.-f. (2001). Mechanical compaction, microstructures and permeability evolution in sandstones. Physics and Chemistry of the Earth, Part A: Solid Earth and Geodesy, 26(1-2), 45-51.

Delcamp, A., van Wyk de Vries, B., & James, M. R. (2008). The influence of edifice slope and substrata on volcano spreading. Journal of Volcanology and Geothermal Research, 177(4), 925-943.

Di Benedetto, C., Cappelletti, P., Favaro, M., Graziano, S. F., Langella, A., Calcaterra, D., & Colella, A. (2015). Porosity as key factor in the durability of two historical building stones: Neapolitan Yellow Tuff and Vicenza Stone. Engineering Geology, 193, 310-319.

Doan, M. L., Brodsky, E. E., Kano, Y., & Ma, K. F. (2006). In situ measurement of the hydraulic diffusivity of the active Chelungpu Fault, Taiwan. Geophysical Research Letters, 33(16).

Doyen, P. M. (1988). Permeability, conductivity, and pore geometry of sandstone. Journal of Geophysical Research: Solid Earth, 93(B7), 7729-7740.

Duvarcı, Ö. Ç., Akdeniz, Y., Özmıhçı, F., Ülkü, S., Balköse, D., & Çiftçioğlu, M. (2007). Thermal behaviour of a zeolitic tuff. Ceramics International, 33(5), 795-801.

Eichelberger, J. C., Carrigan, C. R., Westrich, H. R., & Price, R. H. (1986). Non-explosive silicic volcanism. Nature, 323(6089), 598.

Farquharson, J., Heap, M. J., Varley, N. R., Baud, P., & Reuschlé, T. (2015). Permeability and porosity relationships of edifice-forming andesites: a combined field and laboratory study. Journal of Volcanology and Geothermal Research, 297, 52-68.

Farquharson, J., Heap, M. J., Baud, P., Reuschlé, T., & Varley, N. R. (2016a). Pore pressure embrittlement in a volcanic edifice. Bulletin of Volcanology, 78(1), 6.

Farquharson, J. I., Heap, M. J., & Baud, P. (2016b). Strain-induced permeability increase in volcanic rock. Geophysical Research Letters, 43(22).

Farquharson, J. I., Baud, P., & Heap, M. J. (2016c). Inelastic compaction and permeability evolution in volcanic rock. Solid Earth, 8(2), 561.

Farquharson, J. I., Heap, M. J., Lavallée, Y., Varley, N. R., & Baud, P. (2016d). Evidence for the development of permeability anisotropy in lava domes and volcanic conduits. Journal of Volcanology and Geothermal Research, 323, 163-185.

Farquharson, J. I., Wadsworth, F. B., Heap, M. J., & Baud, P. (2017). Time-dependent permeability evolution in compacting volcanic fracture systems and implications for gas overpressure. Journal of Volcanology and Geothermal Research, 339, 81-97.

Gavrilenko, P., & Guéguen, Y. (1989). Pressure dependence of permeability: a model for cracked rocks. Geophysical Journal International, 98(1), 159-172.

Gomez-Heras, M., Hajpál, M., Álvarez de Buergo, M., Török, A., Fort, R., & Varas, M. J. (2006). Evolution of porosity in Hungarian building stones after simulated burning. Heritage Weathering and Conservation HWC-2006. Taylor & Francis, Rotterdam, 513-519.

Got, J. L., Peltier, A., Staudacher, T., Kowalski, P., & Boissier, P. (2013). Edifice strength and magma transfer modulation at Piton de la Fournaise volcano. Journal of Geophysical Research: Solid Earth, 118(9), 5040-5057.

Got, J. L., Carrier, A., Marsan, D., Jouanne, F., Vogfjörd, K., & Villemin, T. (2017). An analysis of the nonlinear magma-edifice coupling at Grimsvötn volcano (Iceland). Journal of Geophysical Research: Solid Earth, 122(2), 826-843.

Guéguen, Y., & Dienes, J. (1989). Transport properties of rocks from statistics and percolation. Mathematical Geology, 21(1), 1-13.

Guéguen, Y., Gavrilenko, P., & Le Ravalec, M. (1996). Scales of rock permeability. Surveys in Geophysics, 17(3), 245-263.

Guéguen, Y., Chelidze, T., & Le Ravalec, M. (1997). Microstructures, percolation thresholds, and rock physical properties. Tectonophysics, 279(1-4), 23-35.

Guéguen, Y., & Schubnel, A. (2003). Elastic wave velocities and permeability of cracked rocks. Tectonophysics, 370(1-4), 163-176.

Heap, M. J., Lavallée, Y., Laumann, A., Hess, K. U., Meredith, P. G., & Dingwell, D. B. (2012). How tough is tuff in the event of fire?. Geology, 40(4), 311-314.

Heap, M. J., Lavallée, Y., Petrakova, L., Baud, P., Reuschlé, T., Varley, N. R., & Dingwell, D. B. (2014a). Microstructural controls on the physical and mechanical properties of edifice-forming andesites at Volcán de Colima, Mexico. Journal of Geophysical Research: Solid Earth, 119(4), 2925-2963.

Heap, M. J., Baud, P., Meredith, P. G., Vinciguerra, S., & Reuschlé, T. (2014b). The permeability and elastic moduli of tuff from Campi Flegrei, Italy: implications for ground deformation modelling. Solid Earth, 5(1), 25.

Heap, M. J., Farquharson, J. I., Baud, P., Lavallée, Y., & Reuschlé, T. (2015a). Fracture and compaction of andesite in a volcanic edifice. Bulletin of volcanology, 77(6), 55.

Heap, M. J., Kennedy, B. M., Pernin, N., Jacquemard, L., Baud, P., Farquharson, J. I., ... & Mayer, K. (2015b). Mechanical behaviour and failure modes in the Whakaari (White Island volcano) hydrothermal system, New Zealand. Journal of Volcanology and Geothermal Research, 295, 26-42.

Heap, M. J., Farquharson, J. I., Wadsworth, F. B., Kolzenburg, S., & Russell, J. K. (2015c). Timescales for permeability reduction and strength recovery in densifying magma. Earth and Planetary Science Letters, 429, 223-233.

Heap, M. J., Russell, J. K., & Kennedy, L. A. (2016). Mechanical behaviour of dacite from Mount St. Helens (USA): A link between porosity and lava dome extrusion mechanism (dome or spine)?. Journal of Volcanology and Geothermal Research, 328, 159-177.

Heap, M. J., & Wadsworth, F. B. (2016). Closing an open system: pore pressure changes in permeable edifice rock at high strain rates. Journal of Volcanology and Geothermal Research, 315, 40-50.

Heap, M. J., & Kennedy, B. M. (2016). Exploring the scale-dependent permeability of fractured andesite. Earth and Planetary Science Letters, 447, 139-150.

Heap, M. J., Violay, M., Wadsworth, F. B., & Vasseur, J. (2017a). From rock to magma and back again: The evolution of temperature and deformation mechanism in conduit margin zones. Earth and Planetary Science Letters, 463, 92-100.

Heap, M. J., Kennedy, B. M., Farquharson, J. I., Ashworth, J., Mayer, K., Letham-Brake, M., ... & Siratovich, P. (2017b). A multidisciplinary approach to quantify the permeability of the Whakaari/White Island volcanic hydrothermal system (Taupo Volcanic Zone, New Zealand). Journal of Volcanology and Geothermal Research, 332, 88-108.

Heap, M. J., Reuschlé, T., Farquharson, J. I., & Baud, P. (2018a). Permeability of volcanic rocks to gas and water. Journal of Volcanology and Geothermal Research, 354, 29-38.

Heap, M.J., Kushnir, A.R.L., Griffiths, L., Wadsworth, F.B., Marmoni, G.M., Fiorucci, M., Martino, S., Baud, P., Gilg, H.A., & Reuschlé, T. (2018b). Fire resistance of the Mt. Epomeo Green Tuff, a widely-used building stone on Ischia Island (Italy). Volcanica. In revision.

Heap, M.J., Farquharson, J.I., Kushnir, A.R.L., Lavallée, Y., Baud, P., Gilg, H.A., and Reuschlé, T. (2018c). The influence of water on the strength of Neapolitan Yellow Tuff, the most widely-used building stone in Naples (Italy). Bulletin of Volcanology. Accepted.

Heiken, G. (Ed.). (2006). Tuffs: their properties, uses, hydrology, and resources (Vol. 408). Geological Society of America.

Holloway, S. (2005). Underground sequestration of carbon dioxide—a viable greenhouse gas mitigation option. Energy, 30(11-12), 2318-2333.

Jackson, M. D., Marra, F., Hay, R. L., Cawood, C., & Winkler, E. M. (2005). The judicious selection and preservation of tuff and travertine building stone in ancient Rome. Archaeometry, 47(3), 485-510.

Jackson, M. D., Kosso, C., Marra, F., & Hay, R. (2006). Geological basis of Vitruvius' empirical observations of material characteristics of rock utilized in Roman masonry. In Proceedings of the Second International Congress of Construction History Queen's College, University of Cambridge (Vol. 2, 1685-1702).

Keating, B. H., & McGuire, W. J. (2000). Island edifice failures and associated tsunami hazards. Pure and Applied Geophysics, 157(6-8), 899-955.

Klug, C., & Cashman, K. V. (1996). Permeability development in vesiculating magmas: implications for fragmentation. Bulletin of Volcanology, 58(2-3), 87-100.

Farrell, N. J. C., Healy, D., & Taylor, C. W. (2014). Anisotropy of permeability in faulted porous sandstones. Journal of Structural Geology, 63, 50-67.

Faulkner, D. R., Jackson, C. A. L., Lunn, R. J., Schlische, R. W., Shipton, Z. K., Wibberley, C. A. J., & Withjack, M. O. (2010). A review of recent developments concerning the structure, mechanics and fluid flow properties of fault zones. Journal of Structural Geology, 32(11), 1557-1575.

Fortin, J., Schubnel, A., & Guéguen, Y. (2005). Elastic wave velocities and permeability evolution during compaction of Bleurswiller sandstone. International Journal of Rock Mechanics and Mining Sciences, 42(7-8), 873-889.

Fortin, J., Stanchits, S., Dresen, G., & Guéguen, Y. (2006). Acoustic emission and velocities associated with the formation of compaction bands in sandstone. Journal of Geophysical Research: Solid Earth, 111(B10).

Fortin, J., Stanchits, S., Vinciguerra, S., & Guéguen, Y. (2011). Influence of thermal and mechanical cracks on permeability and elastic wave velocities in a basalt from Mt. Etna volcano subjected to elevated pressure. Tectonophysics, 503(1-2), 60-74.

La Russa, M. F., Ruffolo, S. A., de Buergo, M. Á., Ricca, M., Belfiore, C. M., Pezzino, A., & Crisci, G. M. (2017). The behaviour of consolidated Neapolitan yellow Tuff against salt weathering. Bulletin of Engineering Geology and the Environment, 76(1), 115-124.

Lagmay, A. M. F., van Wyk de Vries, B., Kerle, N., & Pyle, D. M. (2000). Volcano instability induced by strike-slip faulting. Bulletin of Volcanology, 62(4-5), 331-346.

Lavallée, Y., Benson, P. M., Heap, M. J., Hess, K. U., Flaws, A., Schillinger, B., ... & Dingwell, D. B. (2013). Reconstructing magma failure and the degassing network of dome-building eruptions. Geology, 41(4), 515-518.

Le Ravalec, M., & Guéguen, Y. (1994). Permeability models for heated saturated igneous rocks. Journal of Geophysical Research: Solid Earth, 99(B12), 24251-24261.

Loaiza, S., Fortin, J., Schubnel, A., Guéguen, Y., Vinciguerra, S., & Moreira, M. (2012). Mechanical behavior and localized failure modes in a porous basalt from the Azores. Geophysical Research Letters, 39(19).

Lockner, D., Byerlee, J. D., Kuksenko, V., Ponomarev, A., & Sidorin, A. (1991). Quasi-static fault growth and shear fracture energy in granite. Nature, 350(6313), 39.

McGuire, W. J. (1996). Volcano instability: a review of contemporary themes. Geological Society, London, Special Publications, 110(1), 1-23.

Melnik, O., Barmin, A. A., & Sparks, R. S. J. (2005). Dynamics of magma flow inside volcanic conduits with bubble overpressure buildup and gas loss through permeable magma. Journal of Volcanology and Geothermal Research, 143(1-3), 53-68.

Menéndez, B., Zhu, W., & Wong, T. F. (1996). Micromechanics of brittle faulting and cataclastic flow in Berea sandstone. Journal of Structural Geology, 18(1), 1-16.

Menéndez, B., David, C., & Darot, M. (1999). A study of the crack network in thermally and mechanically cracked granite samples using confocal scanning laser microscopy. Physics and Chemistry of the Earth, Part A: Solid Earth and Geodesy, 24(7), 627-632.

Meredith, P. G., Main, I. G., Clint, O. C., & Li, L. (2012). On the threshold of flow in a tight natural rock. Geophysical Research Letters, 39(4).

Mitchell, T. M., & Faulkner, D. R. (2008). Experimental measurements of permeability evolution during triaxial compression of initially intact crystalline rocks and implications for fluid flow in fault zones. Journal of Geophysical Research: Solid Earth, 113(B11).

Mueller, S., Melnik, O., Spieler, O., Scheu, B., & Dingwell, D. B. (2005). Permeability and degassing of dome lavas undergoing rapid decompression: an experimental determination. Bulletin of Volcanology, 67(6), 526-538.

Nara, Y., Meredith, P. G., Yoneda, T., & Kaneko, K. (2011). Influence of macro-fractures and micro-fractures on permeability and elastic wave velocities in basalt at elevated pressure. Tectonophysics, 503(1-2), 52-59.

Nelson, P. H. (1994). Permeability-porosity relationships in sedimentary rocks. The Log Analyst, 35(03).

Nijland, T. G., Van Hees, R. P., & Bolondi, L. (2010). Evaluation of three Italian tuffs (Neapolitan Yellow Tuff, Tufo Romano and Tufo Etrusco) as compatible replacement stone for Römer tuff in Dutch built cultural heritage. Geological Society, London, Special Publications, 333(1), 119-127.

Oguchi, C. T., & Yuasa, H. (2010). Simultaneous wetting/drying, freeze/thaw and salt crystallization experiments of three types of Oya tuff. Geological Society, London, Special Publications, 333(1), 59-72.

Okubo, C. H. (2004). Rock mass strength and slope stability of the Hilina slump, Kīlauea volcano, Hawai'i. Journal of Volcanology and Geothermal Research, 138(1-2), 43-76.

Paterson, M. S., & Wong, T. F. (2005). Experimental rock deformation-the brittle field. Springer Science & Business Media.

Read, M. D., Ayling, M. R., Meredith, P. G., & Murrell, S. A. (1995). Microcracking during triaxial deformation of porous rocks monitored by changes in rock physical properties, II. Pore volumometry and acoustic emission measurements on water-saturated rocks. Tectonophysics, 245(3-4), 223-235.

Ruedrich, J., Kirchner, D., & Siegesmund, S. (2011). Physical weathering of building stones induced by freeze–thaw action: a laboratory long-term study. Environmental Earth Sciences, 63(7-8), 1573-1586. https://doi.org/10.1007/s12665-010-0826-6.

Rust, A. C., & Cashman, K. V. (2004). Permeability of vesicular silicic magma: inertial and hysteresis effects. Earth and Planetary Science Letters, 228(1-2), 93-107.

Saar, M. O., & Manga, M. (1999). Permeability-porosity relationship in vesicular basalts. Geophysical Research Letters, 26(1), 111-114.

Siedel, H. (2010). Historic building stones and flooding: changes of physical properties due to water saturation. Journal of Performance of Constructed Facilities, 24(5), 452-461.

Shimada, M. (1986). Mechanism of deformation in a dry porous basalt at high pressures. Tectonophysics, 121(2-4), 153-173.

Sparks, R. S. J. (1997). Causes and consequences of pressurisation in lava dome eruptions. Earth and Planetary Science Letters, 150(3-4), 177-189.

Stanchits, S., Fortin, J., Guéguen, Y., & Dresen, G. (2009). Initiation and propagation of compaction bands in dry and wet Bentheim sandstone. Pure and Applied Geophysics, 166(5-7), 843-868.

Tembe, S., Baud, P., & Wong, T.-f. (2008). Stress conditions for the propagation of discrete compaction bands in porous sandstone. Journal of Geophysical Research: Solid Earth, 113(B9).

Török, A., Gálos, M., & Kocsanyi-Kopecsko, K. (2004). Experimental weathering of rhyolite tuff building stones and the effect of an organic polymer conserving agent. Stone Decay: Its Causes and Controls, 109-127.

Vacchiano, C. D., Incarnato, L., Scarfato, P., & Acierno, D. (2008). Conservation of tuff-stone with polymeric resins. Construction and Building Materials, 22(5), 855-865.

Vajdova, V., Baud, P., & Wong, T.-f. (2004). Compaction, dilatancy, and failure in porous carbonate rocks. Journal of Geophysical Research: Solid Earth, 109(B5).

Vajdova, V., Zhu, W., Chen, T. M. N., & Wong, T.-f. (2010). Micromechanics of brittle faulting and cataclastic flow in Tavel limestone. Journal of Structural Geology, 32(8), 1158-1169.

Vajdova, V., Baud, P., Wu, L., & Wong, T.-f. (2012). Micromechanics of inelastic compaction in two allochemical limestones. Journal of Structural Geology, 43, 100-117.

van Wyk de Vries, B. V. W., & Borgia, A. (1996). The role of basement in volcano deformation. Geological Society, London, Special Publications, 110(1), 95-110.

van Wyk de Vries, B. V. W., & Francis, P. W. (1997). Catastrophic collapse at stratovolcanoes induced by gradual volcano spreading. Nature, 387(6631), 387.

Voight, B. (2000). Structural stability of andesite volcanoes and lava domes." Philosophical Transactions of the Royal Society of London A: Mathematical, Physical and Engineering Sciences, 358(1770), 1663-1703.

Watters, R. J., Zimbelman, D. R., Bowman, S. D., & Crowley, J. K. (2000). Rock mass strength assessment and significance to edifice stability, Mount Rainier and Mount Hood, Cascade Range volcanoes. Pure and Applied Geophysics, 157(6-8), 957-976.

Wong, T.-f., David, C., & Zhu, W. (1997). The transition from brittle faulting to cataclastic flow in porous sandstones: Mechanical deformation. Journal of Geophysical Research: Solid Earth, 102(B2), 3009-3025.

Wong, T.-f., & Baud, P. (2012). The brittle-ductile transition in porous rock: A review. Journal of Structural Geology, 44, 25-53.

Worrell, E., Price, L., Martin, N., Hendricks, C., & Meida, L. O. (2001). Carbon dioxide emissions from the global cement industry. Annual Review of Energy and the Environment, 26, 303-329.

Wright, H. M., Cashman, K. V., Gottesfeld, E. H., & Roberts, J. J. (2009). Pore structure of volcanic clasts: measurements of permeability and electrical conductivity. Earth and Planetary Science Letters, 280(1-4), 93-104.

Yavuz, A. B. (2012). Durability assessment of the Alaçatı tuff (Izmir) in western Turkey. Environmental Earth Sciences, 67(7), 1909-1925.

Zedef, V., Kocak, K., Doyen, A., Ozsen, H., & Kekec, B. (2007). Effect of salt crystallization on stones of historical buildings and monuments, Konya, Central Turkey. Building and Environment, 42(3), 1453-1457.

Zhang, J., Wong, T.-f., & Davis, D. M. (1990). Micromechanics of pressure-induced grain crushing in porous rocks. Journal of Geophysical Research: Solid Earth, 95(B1), 341-352.

Zhu, W., & Wong, T.-f. (1997). The transition from brittle faulting to cataclastic flow: Permeability evolution. Journal of Geophysical Research: Solid Earth, 102(B2), 3027-3041.

Zhu, W., Montesi, L. G., & Wong, T.-f. (1997). Shear-enhanced compaction and permeability reduction: Triaxial extension tests on porous sandstone. Mechanics of Materials, 25(3), 199-214.

Zhu, W., Baud, P., & Wong, T.-f. (2010). Micromechanics of cataclastic pore collapse in limestone. Journal of Geophysical Research: Solid Earth, 115(B4).

Zhu, W., Baud, P., Vinciguerra, S., & Wong, T.-f. (2011). Micromechanics of brittle faulting and cataclastic flow in Alban Hills tuff. Journal of Geophysical Research: Solid Earth, 116(B6).

Zoback, M. D., & Byerlee, J. D. (1975). The effect of microcrack dilatancy on the permeability of Westerly granite. Journal of Geophysical Research, 80(5), 752-755.

Appendix B – Full publication list

RANK A papers in peer-reviewed international journals.
* denotes student first author

[80] **Heap, M.J.**, Farquharson, J.I., Kushnir, A.R.L., Lavallée, Y., Baud, P., Gilg, H.A., and Reuschlé, T. (2018). The influence of water on the strength of Neapolitan Yellow Tuff, the most widely-used building stone in Naples (Italy). Bulletin of Volcanology. Accepted.

[79] Soueid Ahmed A., A. Revil, S. Byrdina, A. Coperey, L. Gailler, N. Grobbe, F. Viveiros, C. Silva, D. Jougnot, A. Ghorbani, C. Hogg, D. Kiyan, V. Rath, **M.J. Heap**, H. Grandis, H. Humaida (2018). 3D electrical conductivity tomography of volcanoes. Journal of Volcanology and Geothermal Research, doi: 10.1016/j.jvolgeores.2018.03.017.

[78] Kushnir, A.R.L., **Heap, M.J.**, and Baud, P. (2018) Assessing the role of fractures on the permeability of the Permo-Triassic sandstones at the Soultz-sous-Forêts (France) geothermal site. Geothermics, 74, 181-189.

[77] Lesage, Ph., **Heap, M.J.**, and Kushnir, A.R.L. (2018). A generic model for the shallow velocity structure of volcanoes. Journal of Volcanology and Geothermal Research, doi: 10.1016/j.jvolgeores.2018.03.003.

*[76] Griffiths, L., Lengliné, O., **Heap, M.J.**, Baud, P., and Schmittbuhl, J. (2018). Thermal microcracking in Westerly Granite using direct wave velocity, coda wave interferometry and acoustic emissions. Journal of Geophysical Research, doi: 10.1002/2017JB015191.

[75] **Heap, M.J.**, Reuschlé, T., Farquharson, J.I., and Baud, P. (2018). Permeability of volcanic rocks to gas and water. Journal of Volcanology and Geothermal Research, 354, 29-38.

*[74] Ryan, A., Freidlander, B., Russell, J.K., **Heap, M.J.**, and Kennedy, L. (2018) Hot pressing in conduit faults during lava dome extrusion: Insights from Mount St. Helens 2004-2008, Earth and Planetary Science Letters, 482, 171-180.

[73] Baud, P., Schubnel, A., **Heap, M.J.**, Rolland, A. (2018) Inelastic Compaction in High-Porosity Limestone Monitored Using Acoustic Emissions, Journal of Geophysical Research, doi: 10.1002/2017JB014627.

[72] **Heap, M.J.**, Kushnir, A.R.L, Gilg, H.A., Wadsworth, F.B., Reuschlé, T., and Baud, P. (2017) Microstructural and petrophysical properties of the Permo-Triassic sandstones (Buntsandstein) from the Soultz-sous-Forêts geothermal site (France), Geothermal Energy, 5:26.

[71] Rizzo, R., Healy, D., Farrell, N., and **Heap, M.J.** (2017) Riding the right wavelet: Quantifying scale transitions in fractured rocks, Geophysical Research Letters, 44, 11808-11815.

*[70] Griffiths, L., **Heap, M.J.**, Baud, P., and Schmittbuhl, J. (2017) Quantification of microcrack characteristics and implications for stiffness and strength of granite, International Journal of Rock Mechanics and Mining Sciences, 100, 138-150.

[69] Marmoni, G., Martino, S., **Heap, M.J.**, Reuschlé, T. (2017) Gravitational slope-deformation of a resurgent caldera: new insights from the mechanical behaviour of Mt. Nuovo tuffs (Ischia Island, Italy), Journal of Volcanology and Geothermal Research, 345, 1-20.

[68] Violay, M., **Heap, M.J.**, Acosta, M.A., and Madonna, C., 2017. Porosity evolution at the brittle-ductile transition in the continental crust: Implications for deep hydro-geothermal circulation. Nature Scientific Reports, 7, Article Number 7705, doi: 10.1038/s41598-017-08108-5.

[67] Vasseur, J., Wadsworth, F.B., **Heap, M.J.**, Main, I.G., Lavallée, Y., and Dingwell, D.B., 2017. Does an inter-flaw length control the accuracy of rupture forecasting in geological materials? Earth and Planetary Science Letters, 475, 181-189.

[66] Tang, S.B., Huang, R.Q., Tang, C.A., Liang, Z.Z., and **Heap, M.J.**, 2017. The failure processes analysis of rock slope using numerical modelling techniques, Engineering Failure Analysis, 79, 999-1016. DOI: doi.org/10.1016/j.engfailanal.2017.06.029.

[65] Marmoni, G., Martino, S., **Heap, M.J.**, and Reuschlé, T., 2017. Multiphysics Laboratory Tests for Modelling Gravity-Driven Instabilities at Slope Scale, Procedia Engineering, 191, 142-149. DOI: 10.1016/j.proeng.2017.05.165.

[64] Mikhail, S. and **Heap, M.J.**, 2017. Hot climate inhibits volcanism on Venus: Constraints from rock deformation experiments and argon isotope geochemistry, Physics of the Earth and Planetary Interiors, 268, 18-34. DOI: doi.org/10.1016/j.pepi.2017.05.007.

*[63] Farquharson, J.I., Wadsworth, F.B., **Heap, M.J.**, and P. Baud, 2017. Time-dependent permeability evolution in compacting volcanic fracture systems and implications for gas overpressure, Journal of Volcanology and Geothermal Research, 339, 81-97. DOI: doi.org/10.1016/j.jvolgeores.2017.04.025.

[62] Xu, T., G.L. Zhou, **M.J. Heap**, W.C. Zhu, C.F. Chen, and P. Baud, 2017. The influence of temperature on time-dependent deformation and failure in granite: A mesoscale modeling approach, Rock Mechanics and Rock Engineering, 10.1007/s00603-017-1228-9.

*[61] Farquharson, J. I., P. Baud, and **M. J. Heap** (2017), Inelastic compaction and permeability evolution in volcanic rock, Solid Earth, 8, 561–581.

*[60] Griffiths, L., **Heap, M.J.**, Xu, T., Chen, C.-f., Baud, P., 2017. The influence of pore geometry and orientation on the strength and stiffness of porous rock, Journal of Structural Geology, 96, 149-160. DOI: 10.1016/j.jsg.2017.02.006.

[59] **Heap, M.J.**, Violay, M., Wadsworth, F.B., and Vasseur, J., 2017. From rock to magma and back again: The evolution of temperature and deformation mechanism in conduit margin zones, Earth and Planetary Science Letters, 463, 92-100. DOI: 10.1016/j.epsl.2017.01.021.

[58] Wadsworth, F.B., **Heap, M.J.**, Damby, D.E., Hess, K.-U., Najorka, J., Vasseur, J., Fahrner, D., and Dingwell, D.B., 2017. Local geology controlled the feasibility of vitrifying Iron Age buildings, Nature Scientific Reports, 7, Article number: 40028, DOI: 10.1038/srep40028.

[57] **Heap, M. J.**, P. Byrne, and S. Mikhail (2017), Low surface gravitational acceleration of Mars results in a thick and weak lithosphere: Implications for topography, volcanism, and hydrology, Icarus, 281, 103-114, DOI: 10.1016/j.icarus.2016.09.003.

[56] **Heap, M.J.**, B.M. Kennedy, J.I. Farquharson, J. Ashworth, K. Mayer, M. Letham-Brake, T. Reuschlé, H.A. Gilg, B. Scheu, Y. Lavallée, P. Siratovich, J. Cole, A.D. Jolly, P. Baud, D.B. Dingwell, (2016), A multidisciplinary approach to quantify the permeability of the Whakaari/White Island volcanic hydrothermal system (Taupo Volcanic Zone, New Zealand), Journal of Volcanology and Geothermal Research, 332, 88-108. DOI: 10.1016/j.jvolgeores.2016.12.004.

[55] Dondin, F., **Heap, M.J.**, Robertson, R.E.A., Dorville, J.-F., and Carey, S. (2016), Flank Instability Assessment at Kick-'em-Jenny Submarine Volcano (Grenada, Lesser Antilles): A Multidisciplinary Approach Using Experiments and Modeling, Bulletin of Volcanology, 79:5.

*[54] Farquharson, J. I., **M. J. Heap**, and P. Baud (2016), Strain-induced permeability increase in volcanic rock, Geophysical Research Letters, 43, DOI:10.1002/2016GL071540.

[53] **Heap, M.J.**, J.K Russell, and L.A. Kennedy (2016), Mechanical behaviour of dacite from Mount St. Helens (USA): A link between porosity and lava dome extrusion mechanism (dome or spine)?, Journal of Volcanology and Geothermal Research, 328, 159-177, DOI: 10.1016/j.jvolgeores.2016.10.015.

*[52] Griffiths, L., **M.J. Heap**, F. Wang, D. Daval, H.A. Gilg, P. Baud, J. Schmittbuhl, and A. Genter (2016). Geothermal implications for fracture-filling hydrothermal precipitation. Geothermics, 64, 235-245, DOI: 10.1016/j.geothermics.2016.06.006.

[51] Siratovich, P.A., **M.J. Heap**, M.C. Villeneuve, J. Cole, B.M. Kennedy, J. Davidson, T. Reuschlé (2016). Mechanical behaviour of the Rotokawa Andesites (New Zealand): Insight into permeability evolution and stress-induced behaviour in an actively utilised geothermal. Geothermics, 64, 163-179. DOI: 10.1016/j.geothermics.2016.05.005.

*[50] Farquharson, J. I., **M. J. Heap**, Y. Lavallée, N. Varley, and P. Baud, 2016. Evidence for the development of permeability anisotropy in lava domes and volcanic conduits. Journal of Volcanology and Geothermal Research, 323, 163–185.

[49] **Heap, M. J.**, and Kennedy B. M. (2016). Exploring the scale-dependent permeability of fractured andesite. Earth and Planetary Science Letters, 447, 139-150. DOI: 10.1016/j.epsl.2016.05.004.

[48] Baud, P., Rolland, A., **Heap, M.J.**, Xu, T., Nicolé, M., Ferrand, T., Reuschlé, T., Toussaint, R., and Conil, N. (2016). Impact of stylolites of the mechanical strength of limestone. Tectonophysics, 690, Part A, 4-20.

[47] **Heap, M. J.**, Wadsworth, F. B., Xu, T., Chen, C.-f., and Tang, C.-a. 2016. The strength of heterogeneous volcanic rocks: A 2D approximation. Journal of Volcanology and Geothermal Research, 319, 1-11.

[46] **Heap, M. J.**, and Wadsworth, F. B., 2016. Closing an open system: Pore pressure changes in permeable edifice rock at high strain rates. Journal of Volcanology and Geothermal Research, 315, 40-50, DOI: 10.1016/j.jvolgeores.2016.02.011.

[45] Kushnir, A. R. L., Martel, C., Bourdier, J.-L., **Heap, M. J.**, Reuschlé, T., Erdmann, S., Komorowski, J.-C., Cholik, N., 2016. Probing permeability and microstructure: Unravelling the role of a low-permeability dome on the explosivity of Merapi (Indonesia). Journal of Volcanology and Geothermal Research, 316, 56-71, DOI: 10.1016/j.jvolgeores.2016.02.012.

[44] Wadsworth, F. B., **M. J. Heap**, and D. B. Dingwell, 2016. Friendly fire: Engineering a fort wall in the Iron Age. Journal of Archaeological Science, 67, 7-13, DOI: 10.1016/j.jas.2016.01.011.

*[43] Farquharson, J. I., **M. J. Heap**, P. Baud, T. Reuschlé, and N. Varley, 2016. Pore pressure embrittlement in a volcanic edifice. Bulletin of Volcanology. 78(6).

[42] **Heap, M. J.**, J. I. Farquharson, F. B. Wadsworth, S. Kolzenburg, and J. K. Russell, 2015. Timescales for permeability reduction and strength recovery in densifying magma. Earth and Planetary Science Letters, 429, 223-233.

[41] Mayer, K., Scheu, B., H. A. Gilg, **M. J. Heap**, B. M. Kennedy, Y. Lavallée, M. Letham-Brake, and D. B. Dingwell, 2015. Experimental constraints on phreatic eruption processes at Whakaari (White Island volcano). Journal of Volcanology and Geothermal Research, 302, 150-162.

[40] Wiesmaier, S., **Heap, M. J.**, Branca, S., Gilg, H. A., Kueppers, U., Hess, K.-U., Lavallée, Y., and Dingwell, D. B., 2015. Variability in composition and physical properties of the sedimentary basement of Mt Etna, Italy. Journal of Volcanology and Geothermal Research, 302, 102-116.

[39] **Heap M. J.**, Brantut, N., Baud, P., and Meredith P. G., 2015. Time-dependent compaction band formation in sandstone. Journal of Geophysical Research. DOI: 10.1002/2015JB012022.

[38] **Heap, M. J.**, T. Xu, A. R. L. Kushnir, B. Kennedy, and C.-f. Chen, 2015. Fracture of magma containing overpressurised pores. Journal of Volcanology and Geothermal Research, 301, 180-190.

[37] **Heap, M. J.**, J. I. Farquharson, P. Baud, Y. Lavallée, and T. Reuschlé, 2015. Fracture and compaction of andesite in a volcanic edifice. Bulletin of Volcanology. 77: 55. DOI: 10.1007/s00445-015-0938-7.

*[36] Farquharson, J. I., **M. J. Heap**, N. Varley, P. Baud, and T. Reuschlé, 2015. Permeability and porosity relationships of edifice-forming andesites: A combined field and laboratory study. Journal of Volcanology and Geothermal Research. 297, 52-68.

[35] **Heap, M. J.**, B. Kennedy, N. Perrin, L. Jacquemard, P. Baud, J. I. Farquharson, B. Scheu, Y. Lavallée, H. A. Gilg, M. Letham-Brake, K. Mayer, A. D. Jolly, T. Reuschlé, and D. B. Dingwell, 2015. Mechanical behaviour and failure modes in the Whakaari (White Island volcano) hydrothermal system, New Zealand. Journal of Volcanology and Geothermal Research. DOI: 10.1016/j.jvolgeores.2015.02.012.

[34] **Heap, M. J.**, S. Kolzenburg, J. K. Russell, M. E. Campbell, J. Welles, J. I. Farquharson, A. Ryan, 2014. Conditions and timescales for welding block-and-ash flow deposits. Journal of Volcanology and Geothermal Research. 289, 202-209.

[33] **Heap, M. J.**, T. Xu, and C.-f. Chen, 2014. The influence of porosity and vesicle size on the brittle strength of volcanic rocks and magmas. Bulletin of Volcanology. 76:856, doi; 10.1007/s00445-014-0856-0.

[32] Brantut, N., **M. J. Heap**, P. Baud, and P. G. Meredith, 2014. Mechanisms of time-dependent deformation in porous limestone. Journal of Geophysical Research, DOI: 10.1002/2014JB011186.

[31] Siratovich, P., **Heap, M. J.**, Villeneuve, M. C., Cole, J. W., and Reuschlé, T., 2014. Physical property relationships of the Rotokawa Andesite, a significant geothermal reservoir rock in the Taupo Volcanic Zone, New Zealand. Geothermal Energy, 2:10.

[30] **Heap, M. J.**, Lavallée, Y., Petrakova, L., Baud, P., Reuschlé, T., Varley, N., and Dingwell, D. B., 2014. Microstructural controls on the physical and mechanical properties of edifice-forming andesites at Volcán de Colima, Mexico. Journal of Geophysical Research, DOI: 10.1002/2013JB010521.

[29] Brantut, N., **M. J. Heap**, P. Baud, and P. G. Meredith, 2014. Rate and strain-dependent brittle deformation of rocks. Journal of Geophysical Research, 117 (B8), DOI: 10.1002/2013JB010448.

[28] **Heap, M. J.**, Baud, P., Meredith, P. G., Vinciguerra, S., Reuschlé, T., 2014. The permeability and elastic moduli of tuff from Campi Flegrei, Italy: Implications for ground deformation modelling. Solid Earth, 5, 25-44.

[27] **Heap, M. J.**, Baud, P., Reuschlé, T., and Meredith, P. G., 2014. Stylolites in limestones: Barriers to fluid flow? Geology, 42, 51-54, doi:10.1130/G34900.1.

[26] Mollo, S., **Heap, M. J.**, Dingwell, D. B., Hess, K.-U., Iezzi, G., Masotta, M., Scarlato, P., Vinciguerra, S., 2013. Decarbonation and thermal microcracking under magmatic P-T-fCO2 conditions: the role of skarn substrata in promoting volcanic instability. Geophysical Journal International. DOI: 10.1093/gji/ggt265.

[25] Kendrick, J. E., Lavallée, Y., Hess, K.-U., **Heap, M. J.**, Gaunt, H. E., Meredith, P. G., Dingwell, D. B., 2013. Tracking the permeable porous network during strain-dependent magmatic flow. Journal of Volcanology and Geothermal Research, 260, 117-126.

[24] Brantut, N., M**. J. Heap**, P. G. Meredith, and P. Baud, 2013. Time-dependent cracking and brittle creep in crustal rocks: A review. Journal of Structural Geology, 52, 17-43.

[23] **Heap, M. J.**, Lavallée, Y., Laumann, A., Hess, K.-U., Meredith, P. G., Dingwell, D. B., Huismann, S., Weise, F., 2013. The influence of thermal-stressing (up to 1000 °C) on the physical, mechanical, and chemical properties of siliceous-aggregate, high-strength concrete. Construction and Building Materials, 42, 248-265. doi: 10.1016/j.conbuildmat.2013.01.020.

[22] Lavallée, Y., Benson, P. M., **Heap, M. J.**, Hess, K.-U., Flaws, A., Schillinger, B., Meredith, P. G., Dingwell, D. B., 2013. Reconstructing magma failure and the degassing network of dome-building eruptions. Geology, doi:10.1130/G33948.1.

[21] **Heap, M. J.**, S. Mollo, S. Vinciguerra, Y. Lavallée, K.-U. Hess, D. B. Dingwell, P. Baud, G. Iezzi, 2013. Thermal weakening of the carbonate basement under Mt. Etna volcano (Italy): implications for volcano instability. J. Vol. Geo. Res. 250, 42-60.

[20] Kolzenburg, S., **M.J. Heap**, Y. Lavallée, J.K. Russell, P.G. Meredith, and D.B. Dingwell, 2012. Strength and permeability recovery of tuffisite-bearing andesite. Solid Earth, 3, 191–198.

[19] Benson, P. M., **Heap, M. J.**, Lavallée, Y., Flaws, A., Hess, K.-U., Selvadurai, A. P. S., Dingwell, D. B., 2012. Laboratory simulations of tensile fracture development in a volcanic conduit via cyclic magma pressurisation. Earth Plant. Sci. Lett., 349, 231-239.

[18] Brantut, N., P. Baud, **M.J. Heap**, and P.G. Meredith, 2012. Micromechanics of Brittle Creep in Rocks. J. Geophys. Res - Solid Earth, 117 (8), art. no. B08412, doi:10.1029/2012JB009299.

[17] Mollo, S., **Heap, M. J.**, Iezzi, G., Hess, K.-U., Scarlato, P., Dingwell, D. B., 2012. Volcanic edifice weakening via decarbonation: a self-limiting process? Geophysical Research Letters 39 (15), art. no. L15307, doi: 10.1029/2012GL052613.

[16] Xu, T., C.-a. Tang, J. Zhao, L. Li, and **M. J. Heap**, 2012. Modelling the time-dependent rheological behaviour of heterogeneous brittle rocks, Geophysical Journal International, 198, 1781-1796, doi: 10.1111/j.1365-246X.2012.05460.

[15] Lavallée, Y., T. M. Mitchell, **M. J. Heap**, J. Vasseur, K-U. Hess, T. Hirose, and D. B. Dingwell, 2012. Experimental generation of volcanic pseudotachylites: constraining rheology. Journal of Structural Geology, 38, 222-233.

[14] **Heap, M. J.**, Lavallée, Y., Laumann, A., Hess, K-U., Meredith, P. G., and Dingwell, D. B., 2012. How tough is tuff in the event of fire? Geology, doi: 10.1130/G32940.1.

[13] Lavallée, Y., P. M. Benson, **M. J. Heap**, A. Flaws, K.-U. Hess, D. B. Dingwell, 2011. Volcanic conduit failure as a trigger to magma fragmentation. Bulletin of Volcanology, doi: 10.1007/s00445-011-0544-2.

[12] Mollo, S., Vinciguerra, S., Iezzi, G., Iarocci, A., Scarlato, P., **Heap, M. J.**, Dingwell, D. B., 2011. Volcanic edifice weakening via devolatilization reactions, Geophysical Journal International, doi: 10.1111/j.1365-246X.2011.05097.

[11] Bell, A. F., Naylor, M., **Heap, M. J.**, Main, I. G., 2011. Forecasting volcanic eruptions and other material failure phenomena: an evaluation of the failure forecast method. Geophysical Research Letters, doi:10.1029/2011GL048155.

[10] Mollo, S., Tuccimei, P., **Heap, M.J.**, Vinciguerra, S., Soligo, M., Castelluccio, M., Scarlato, P., Dingwell, D. B., 2011. Increase in radon emission due to rock failure: an experimental study. Geophysical Research Letters, 48, L14304, doi:10.1029/2011GL047962.

[9] **Heap, M. J.**, Baud, P., Meredith, P. G., Vinciguerra, S., Bell, A. F. and Main, I. G., 2011. Brittle creep in basalt: implications for time-dependent volcano deformation. Earth and Planetary Science Letters, 307, 71-82.

[8] Bell, A. F., Greenough, J., **Heap, M. J.** and Main, I. G., 2011. Challenges for forecasting based on accelerating rates of earthquakes at volcanoes and laboratory analogues. Geophysical Journal International, 185, 718-723.

[7] **Heap, M. J.**, D. R. Faulkner, P. G. Meredith and S. Vinciguerra, 2010. Elastic moduli evolution and accompanying stress changes with increasing crack damage: implications for stress changes around fault zones and volcanoes during deformation. Geophysical Journal International, 183, 225-236.

[6] Grindrod, P. M., **Heap, M. J.**, Meredith, P. G., Trippetta, F., Sammonds, P. M., Wood, I. G. and Fortes, D., 2010. Experimental Investigation of the Mechanical Properties of Magnesium Sulfate Hydrates under Martian Conditions. J. Geophys. Res., doi:10.1029/2009JE003552.

[5] **Heap, M. J.**, Baud, P., Meredith, P. G., 2009. The influence of temperature on brittle creep in sandstones. Geophys. Res. Lett., doi:10.1029/2009GL039373.

[4] **Heap, M. J.**, Baud, P., Meredith, P. G., Bell, A. F. and Main, I. G., 2009. Time-dependent brittle deformation in Darley Dale sandstone. J. Geophys. Res, 114, B07203, doi: 10.1029/2008JB006212.

[3] **Heap, M. J.**, S. Vinciguerra, P. G. Meredith, 2009. The evolution of elastic moduli with increasing damage during cyclic stressing of a basalt from Mt. Etna volcano. Tectonophysics, 471, 153-160.

[2] **Heap, M. J.** and D. R. Faulkner, 2008. Quantifying the static elastic evolution of crystalline rock approaching failure. International Journal of Rock Mechanics and Mining Sciences, 45/4, 564-573.

[1] Faulkner, D. R., Mitchell, T. M., Healy, D. and **Heap, M. J.**, 2006. Slip on 'weak' faults by the rotation of regional stress in the fracture damage zone. Nature, 444, 922-925.

Appendix C – Short (2-page) curriculum vitae

Michael John Heap

Nationality English
Languages English, French (basic), German (basic)
Age 35 years old
Position Lecturer at University of Strasbourg
Email heap@unistra.fr

Summary
- ➢ **Awarded "Initiative d'Excellence : les Espoirs de l'Université de Strasbourg" ("Initiative of excellence: the hope of the University of Strasbourg") in 2017**
- ➢ **87 papers (metric from SCOPUS)**
- ➢ ***h*-index 25; published with 138 different authors; over 1700 citations (metrics from SCOPUS)**
- ➢ **7 years of teaching experience as a full-time lecturer**
- ➢ **Awarded ~400 000 Euros in research grants (as PI)**
- ➢ **Supervised/supervising 4 Ph.D students and 2 post-docs**
- ➢ **35 years old**

Employment and Education

2010-onwards Maître de conférences (5èmè echelon) at the École et Observatoire des Sciences de la Terre at the University of Strasbourg (France); part of the Géophysique Expérimentale (Experimental Geophysics) team
2009-2010 Post-doc (funded by BV MatWerk and the DFG) at Ludwig Maximilians Universität München (Germany); project: "Modelling of temporal and thermal weakening of volcanic material involved in the construction of historical buildings"
2005-2009 Ph.D at University College London (UK) supervised by Philip Meredith and Patrick Baud; title: Creep: time-dependent brittle deformation in rocks
2001-2005 First class MESci in geology at University of Liverpool (UK)

Teaching experience

- ➢ **7 years of experience as a full-time lecturer (192+ hours per year)**
- ➢ Taught several courses (lectures, laboratory classes, and field classes) at University of Strasbourg (rock physics, mechanics of fluids and flow, geophysical laboratory classes, geophysical field classes, petrophysics, brittle microstructure, rock physics applied to reservoirs and hazards) (level: undergraduate and masters)
- ➢ Taught summer school (16 hours) at Northeastern University (Shenyang, China) in 2016 on "rock physics and natural hazards" (level: under- and postgraduate students)
- ➢ Won an Erskine teaching fellowship to teach at University of Canterbury (New Zealand) between May and August 2017; taught hydrology and a field class to the Taupo Volcanic Zone (with student exchange initiative Frontiers Abroad) (level: undergraduate and masters)

Research supervision

- ➢ Supervised/supervising four Ph.D students:

[4] Amy Ryan (2017-) (based at UBC, Vancouver, Canada): "Permeability evolution in lava domes: a trigger for explosive activity" (co-supervised with Kelly Russell)

[3] Chong-feng Chen (2015-) (based at Northeastern University, Shenyang, spent one year at Strasbourg): "Creep and fatigue in sandstone" (co-supervised with Tao Xu)

[2] Luke Griffiths (2015-2018) (IPG Strasbourg, École Doctorale/LABEX): "Thermal microcracking in rocks" (co supervised with Patrick Baud)

[1] Jamie Farquharson (2013-2016), IPG Strasbourg, Initiative d'Excellence: Contrats Doctoraux): "Permeability evolution through the brittle-ductile transition in volcanic rocks" (co-supervised with Patrick Baud); won an award for his thesis from the University of Strasbourg

➢ Supervising two post-docs:

[2] Alexandra Kushnir (2017-2019), funded by geothermal ANR grant CANTARE "Characterization of the transition zone in the deep basin context for the exploitation of geothermal reservoirs in Alsace" (co-supervised with Patrick Baud)

[1] Jamie Farquharson (2016-2018), funded by European geothermal grant DESTRESS "Demonstration of soft stimulation treatments of geothermal reservoirs" (co-supervised with Patrick Baud)

➢ Supervised many masters projects, diplômes ingénieurs (engineering diplomas), and projets de recherche (undergraduate research projects)

Scientific responsibilities

➢ Topical Editor of European Geosciences Union open-access journal *Solid Earth* since 2012
➢ Editor of diamond open access journal *Volcanica*.
➢ Reviewed manuscripts for a variety of journals, including *Science* and *Geology*
➢ Invited speaker at the European Geosciences Union and American Geophysical Union
➢ Organised and chaired five sessions at the European Geosciences Union

Awards

➢ **Initiative d'Excellence Prix Scientifiques 2017**: "Les Espoirs de l'Université de Strasbourg" ("the hope of the University of Strasbourg") to "reward scientists who have shown originality and dynamism in the implementation of their research and whose future developments look promising"

➢ Awarded the "prime d'excellence scientifique (PES)" at the Université de Strasbourg in 2012 and 2017, an initiative designed to reward teaching staff with a high research output

Funded proposals (PI only)

➢ **Won ~400 000 Euros in research grants (as PI)**
➢ Won "Initiative d'Excellence" grant from the University of Strasbourg worth 200,000 Euros
➢ Won 7 international grants (totalling 36,500 Euros and 11,990 GBP) to collaborate with researchers in Germany, Italy, the U.K., China, and New Zealand
➢ Won several grants from geothermal initiative LABEX "G-Eau-Thermie Profonde", one worth 100,000 Euros

Research output

➢ *__h-index of 25 (metric from SCOPUS)__*
➢ 87 papers (one in *Nature*) (metric from SCOPUS)
➢ Published with 138 different authors (metric from SCOPUS)
➢ Over 1700 citations (metric from SCOPUS)